# Univerzita Karlova v Praze

**Přírodovědecká fakulta**

Studijní program: fyzikální chemie

**RNDr. Martin Ferus**

## Studium nestabilních částic a prekurzorů biomolekul pomocí spektroskopických
technik

## The Study of Transient Species and Precursors of Biomolecules using Spectroscopic Techniques

Disertační práce

Vedoucí závěrečné práce/Školitel:
Prof. RNDr. Svatopluk Civiš, CSc.

Praha, 2012

# Poděkování

Rád bych poděkoval vedoucímu práce panu Prof. RNDr. Svatopluku Civišovi, CSc. za jeho přátelskou vstřícnost, vedení a pomoc při práci i studiu.

Za spolupráci na experimentech, při přípravě publikací a odbornou diskuzi děkuji nejen svému školiteli, ale také svým kolegům a přátelům Mgr. Petru Kubelíkovi, Doc. Ing. Zdeňku Zelingerovi, CSc., RNDr. Pavlu Kubátovi, CSc., Doc. Vladislavu Chernovovi, Ph.D., Prof. Robertu Georgesovi, Mgr. Regině Michalčíkové, Petře Megové, Mgr. Violettě Shestivské, Ph.D., RNDr. Martinu Civišovi, Ph.D., Ing. Evě Grigorové, Ph.D., Ing. Václavu Nevrlému, Ph.D., Ing. Janu Skřínskému, Ph.D., Ing. Petru Bitalovi, Ph.D., Mgr. Petru Jelínkovi a Ing. Michalu Střižíkovi, Ph.D. in memoriam. Za odbornou diskusi a spolupráci patří velký dík panu Prof. RNDr. Patriku Španělovi, Dr. rer. nat., Ing. Liboru Juhovi, CSc., Prof. RNDr. Ladislavu Kavanovi, DSc., RNDr. Markétě Zukalové, Ph.D., Judit Šponerové, Ph.D., Prof. Kentaro Kawaguchimu, Ing. Iloně Spirovové a RNDr. Jiřímu Skálovi. Děkuji také všem ostatním spoluautorům předkládaných odborných prací.

Za oporu a pomoc při mých studiích děkuji své rodině a své manželce.

V Praze 1. 4. 2012

**Tuto práci s velkými díky za podporu v životě a studiu věnuji svým rodičům Marcele a Zdeňkovi a prarodičům Rudolfovi a Haně.**

## Předmětová slova

spektrometrie, astrochemie, chemické modely

## Klíčová slova

Spektrometrie s Fourierovou transformací (FTS), emisní spektrometrie, LIDB, doutnavý výboj, časově rozlišená spektrometrie, radikály, ionty, biomolekuly

## Prohlášení

Prohlašuji, že jsem závěrečnou práci zpracoval/a samostatně a že jsem uvedl/a všechny použité informační zdroje a literaturu. Tato práce ani její podstatná část nebyla předložena k získání jiného nebo stejného akademického titulu.

V Praze 1. 4. 2012

RNDr. Martin Ferus, v. r.

# Abstrakt

Předložená dizertační práce je složena ze studií zaměřených na spektroskopický popis, kinetiku a dynamiku molekul, radikálů a iontů v plazmě výboje a laserové jiskry. Výzkum těchto fragmentů je rozšířen o vznik biomolekul z těchto jednoduchých specií včetně vlivu látek s katalytickým účinkem.

*Dynamika radikálů, iontů a nestabilních molekul* byla studována pomocí časově rozlišené spektrometrie s Fourierovou transformací. Byla měřena časově rozlišená emisní spektra výbojů v $CH_4$, $HCONH_2$, $BrCN$, $CH_3CN$, $CF_3Br$, $(CF_3)_2CHBr$ a dalších plynech. Následně byl výboj simulován pomocí modelu zahrnujícího molekulární dynamiku, kolizní, chemické a radiační procesy. Modely byly porovnány s experimentálními výsledky a byla vysvětlena získaná emisní časově rozlišená spektra. Fitem na komplexní mechanismus byla experimentálně zjištěna hodnota rychlostní konstanty konverze HCN na HNC kolizí s excitovaným atomem vodíku.

V rámci *studia prekurzorů biomolekul* bylo pomocí vysoce rozlišené infračervené absorpční spektrometrie s Fourierovou transformací analyzováno složení plynných látek vznikajících po expozici  par formamidu a plynné směsi oxidu uhelnatého s dusíkem a izotopově značenou vodou laserové jiskře generované vysoce výkonným pražským laserovým systémem Asterix (PALS). Pomocí chemického modelu byla studována dynamika rozkladu těchto látek. Dosud nepublikované výsledky naznačují, že v laserové jiskře ve formamidu vznikají nukleové báze a aminokyseliny. Vzhledem k použití vody značené kyslíkem $^{18}O$ a katalyticky působícího $Ti^{16}O_2$ a $Ti^{18}O_2$ byla následně pomocí infračervené absorpční spektrometrie s Fourierovou transformací studována izotopová výměna mezi pevným vzorkem $Ti^{18}O_2$ a oxidem uhličitým, kyselinou mravenčí a katalitické působení tohoto materiálu. Izotopová výměna mezi $C^{16}O_2$ a $Ti^{18}O_2$ je spontánním procesem, avšak aktivní místa na povrchu $Ti^{18}O_2$ mohou být blokována vodou či HCOOH. Bylo zjištěno, že při ozařování vzorků dochází k fotochemickému vzniku methanu a acetylenu, rozkladu kyseliny mravenčí a opětovné výměně kyslíkových atomů mezi pevnou fází a oxidem uhličitým.

# Abstract

The presented thesis is focused on a spectroscopic study of unstable radicals, ions and molecules in a positive column glow discharge and laser plasma. The research of these fragments is supplemented by a study of biomolecules formation from these species and influence of catalysts.

*Molecular dynamics of radicals, ions and unstable molecules* has been studied using a time resolved Fourier transform infrared spectroscopy. Time resolved spectra of $CH_4$, $HCONH_2$, $BrCN$, $CH_3CN$, $CF_3Br$, $(CF3)_2CHBr$ positive column glow discharges have been measured and simulated using a kinetic model including molecular dynamics, collisions and chemical and radiation transfer processes. The model has been compared with our experimental results and time resolved spectra were described in details. Fit to a complex reaction mechanism has been used to estimate a rate constant of a HCN conversion to HNC by a collision with H radical.

The study of *precursors of biomolecules* was focused on chemical consequences of a laser induced dielectric breakdown in formamide vapor and gaseous carbon monooxide with $^{18}O$ labeled water. Dissociation products have been detected using the Fourier transform absorption spectroscopy. The experimental results have been explained by a help of a chemical laser spark dynamics model. Additionally, our the most recent unpublished results suggest formation of nucleic bases in samples of high power laser irradiated formamide ices. Since the isotopic labeled water and catalytic $Ti^{16}O_2$ and $Ti^{18}O_2$ were used, an isotopic exchange between $CO_2$ and $Ti^{18}O_2$ has been studied using the high resolution Fourier transform spectrometry. This metal oxide is an important catalyst and the isotopic exchange effect suggests that oxygen can be released from the crystal surface, however, these active centers can be blocked by water or HCOOH. Additionally, after an irradiation, formation of methane and acetylene from carbon monoxide and decomposition of HCOOH photocatalyzed by $TiO_2$ has been observed.

# Obsah

# 1. Úvod

Spektrometrie je v současné době jedinou analytickou technikou, pomocí které je možno dálkově studovat nejen chemické složení vybraných objektů, ale zároveň získat některé informace o jejich fyzikálních vlastnostech. Tato výhoda se uplatňuje zejména v astronomii, kde spektroskopické techniky hrají nenahraditelnou roli všude tam, kde nelze provádět průzkum přímo. Laboratorní experimenty za kontrolovaných podmínek a následně v pozemských podmínkách poskytují důležité informace pro interpretaci na dálku pořízených spekter.

Spektrometrie atomů a molekul se stala významnou součástí astronomie v druhé polovině 19. století[1]. V té době byly linie ve spektrech komet, mlhovin a hvězd srovnávány se spektry plamenů a přiřazovány převážně k jednotlivým prvkům[2] (v kometách např. Mg, C, Mn, Pb, Fe, Na, N, H) a až s výjimkou ·CN a $(CN)_2$, oxidu uhelnatého (CO) nebo jednoduchých uhlovodíků $(C_xH_y)$ nebyla podstata emitujících neatomárních částic přesně známa. Spektrum pořízené tehdejší technikou[3,4] je zobrazeno na Obr. 1. Na přelomu 19. a 20. stol. byla publikována série prací (např.[5]) srovnávajících spektra komet nebo hvězd se spektry plynů v elektrických výbojích, což spolu s rozvojem kvantové mechaniky vedlo po roce 1913 a zejména pak ve 20. a 30. letech k postupnému přesnému přiřazení a popisu spekter[6,7] celé řady stabilních i nestabilních specií (·CN, ·$C_2$, ·$C_3$, ·CH; později ·OH, :NH, ·CH, ·$CH_2$, $CO^+$ a $N_2^+$).

Ve vesmíru byla identifikována celá řada molekul, iontů a radikálů jejichž seznam se stále rozrůstá[8]. Současný výzkum je zaměřen např. na doplňování spektroskopických databází[9] z hlediska spektrálního rozsahu, obsahu a molekulárních parametrů. Jsou měřena spektra molekul za extrémních podmínek, např. při velmi nízkých nebo vysokých teplotách[10]. Experimentální data jsou použita např. k vytváření velmi sofistikovaných simulací spekter atmosfér planet solárního systému, exoplanet[11,12] či difúzních
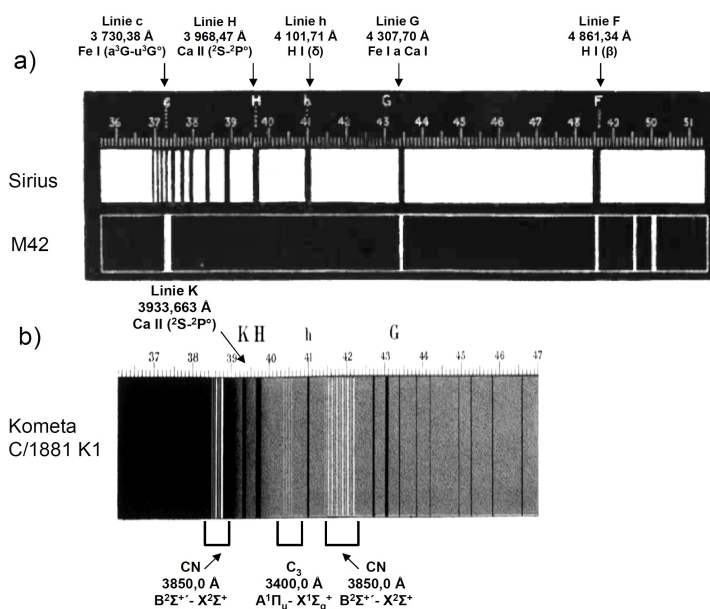


Obr. 1: Spektrum a) Siria a mlhoviny M42 v Orionu, b) tzv. Velké komety z roku 1881 pořízené astronomem Hugginsem. Originální použitá škála vlnové délky odpovídá $10^2$ Å. Přiřazení bylo provedeno podle pozic Fraunhoferových čar v databázi NIST[9]. Obr.: autor za použití původního zdroje[5,6].

interstelárních pásů[13]. Vědecký zájem se rovněž soustředí na problematiku vývoje atmosfér[14,15], původ organických sloučenin[16] a prekurzorů biomolekul[17], původ homochirality[18] a vznik makromolekul majících vlastnosti živé hmoty (schopných replikace, např. RNA[19]).

Cílem této práce bylo právě laboratorní studium chemie nestabilních molekul, iontů a radikálů a vznik biomolekul z těchto sloučenin.

## 2. Dynamika radikálů, iontů a nestabilních molekul

### 2.1 Nukleogeneze a vznik jednoduchých sloučenin ve vesmíru

Na základě dat satelitu WMAP (Wilkinson Microwave Anisotropy Probe) je stáří vesmíru odhadnuto na $13,75 \pm 0,13$ miliard let[20]. Současná zbytková teplota záření[21] po prvotní horké expanzi ($> 10^{32}$ K) byla stanovena na základě měření satelitu COBE (Cosmic Background Explorer) na $2,725 \pm 0,002$ K. Jak je znázorněno na Obr. 2, panel A, při tzv. velkém třesku[22] vznikly nejprve subatomární částice (A1. a A2.), které se v prvních[25] cca 100 s spojily pouze do jader lehkých prvků $^4$He, $^3$He, $^2$H (dále značeno D), $^7$Li a $^{10}$Be (A3.). Vzhledem k odpudivým silám mezi jádry a stabilitě těchto lehkých prvků nedošlo k formování těžších jader.



*Obr. 2: Kosmochemie od prvků po makroskopické objekty. A) Nukleosyntéza po velkém třesku. B) Nukleosyntéza v nitru hvězd. C) Vznik sloučenin v molekulovém oblaku. Sloučeniny se postupně koncentrují do zrn, kde probíhají další reakce. Povrch zrn navíc umožňuje vznik jednoduchých molekul absorpcí energie kolizních partnerů. Zrna následně agregují během procesu akrece oblaku do makroskopických objektů, planetesimálů a komet.*

Chemie vesmíru se omezovala pouze na neutrální atomární vodík[23] H· ($\approx 75\ \%$), helium $^4$He ($\approx 25\ \%$), neutrální atomární deuterium ·D (0.01 %) a na stopy molekulárních plynů ($< 10^{-4}\ \%$ LIH, HD, H$_2$) a iontů [24,25] (např. HeH$^+$, LiH$^+$, H$_3^+$, HD$^+$). V raných stádiích vesmíru mohly být molekuly a molekulární ionty formovány zejména radiačními procesy[26] a reakcemi mezi ionty. Vznik molekulárního vodíku je předpokládán již několik desítek až stovek tisíc let po velkém třesku[26], kdy byla teplota záření $10^4$ K a teplota plynu $10^3$ K, po stovkách milionů let se záření ochladilo na 10 K přičemž nejnižší předpokládaná teplota plynných látek byla již pouze $10^{-3}$ K. V té době[27] se také začaly kolapsem plynu tvořit první hvězdy. Syntéza dalších prvků až po železo probíhala a probíhá právě ve hvězdách, přičemž nejtěžší prvky jsou tvořeny během exploze supernovy. Schématicky jsou tyto procesy pro hvězdu hlavní posloupnosti naznačeny na Obr. 2., panel B (volně podle[28]). Rozprášením prvků z hvězd do vesmíru a následným shlukování vzniklé materie jsou pak tvořena nová mezihvězdná oblaka, která jsou již obohacena o těžší prvky a z nichž vznikají nové hvězdy, planety a další tělesa.

## 2.2 Chemie molekulových oblaků

V současné době je předpokládáno, že chemii ve vesmíru obecně dominují sloučeniny uhlíku, které tvoří asi tři čtvrtiny ve výčtu sloučenin identifikovaných v mezihvězdném prostoru[a] i kolem hvězd[29]. Většina elementů pochází z pozůstatků hvězd, např. ke složení typického molekulového oblaku významně přispívá materiál pocházející z rudých obrů[b], kteří jsou posledním stádiem života Slunci podobných hvězd předchozích generací. V závislosti na typu prostředí se molekuly vyskytují ve vesmírných objektech v různých formách (molekuly, ionty, radikály), takže i chemie těchto systémů je velice rozmanitá.

Mezihvězdný prostor je vyplněn z 90 % atomárním či ionizovaným vodíkem, 10 % He a stopovými koncentracemi iontů či atomů ostatních prvků. Hmota se v prostoru shlukuje za tvorby oblaků, jejichž chemické složení[33] se liší podle jejich hustoty, teploty a stupně vývoje. Jedná se o heterogenní systémy, jak ukazuje Obr. 3 na následující straně, kde je vyobrazen molekulární oblak TMC v souhvězdí Býka[30] spolu s emisními maximy některých typických látek a také výčet některých dalších molekul v hlavní části TMC−1[31] ve srovnání s mezihvězdným oblakem OMC−1 v souhvězdí Orionu[32] a kometou Hale−Bopp[33] (C/1995 O1) v Tab. 1 uvedené samostatně na str. 5. Materiál v hustých mezihvězdných oblacích tvoří základní stavební kameny pro formování hvězd a protoplanetárních disků, ve kterých následným shlukováním vznikají planety, komety, asteroidy, hvězdy a jiné makroskopické objekty.

Chemismus molekulárního oblaku je naznačen na Obr. 2, panel C. V současné době je

a) V anglosaské literatuře se vžila zkratka ISM, interstellar medium.
b) Evoluční větev AGB (Asymptotic Giant Branch) hvězd o hmotnosti 0,6 − 10 x Slunce.
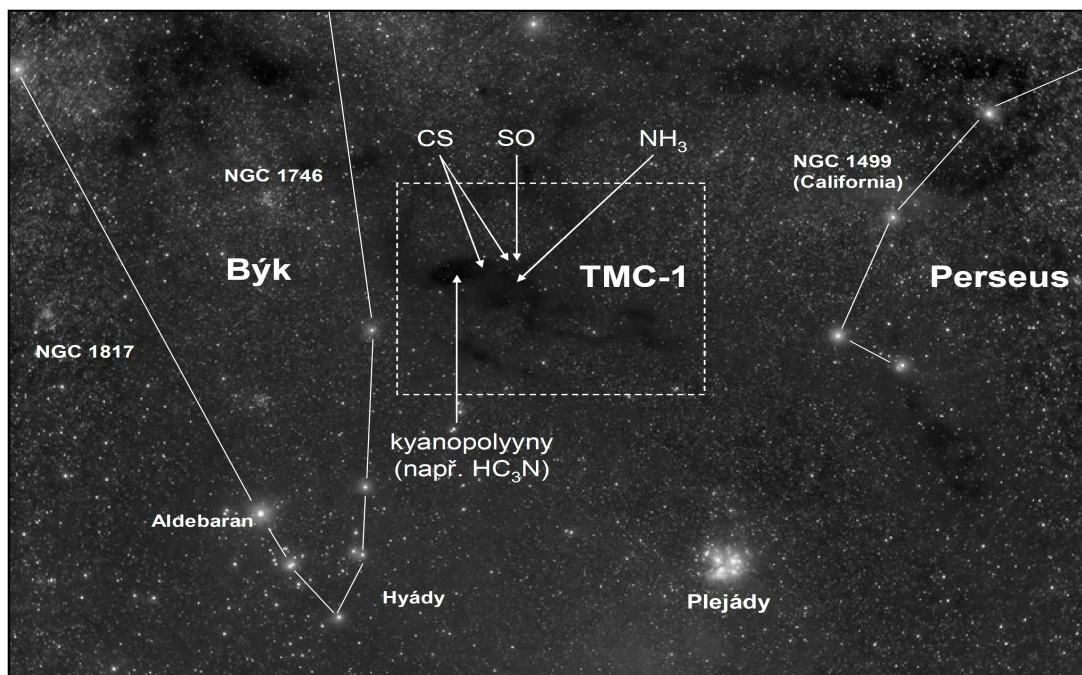
Obr. 3: Obrázek molekulárního oblaku TMC v souhvězdí Býka. Naznačeny jsou polohy emisních maxim některých sloučenin. Emise CO je rozprostřena rovnoměrně po celém oblaku, distribuce ostatních specií (na obr. CS·, SO·, NH3 a kyanopolyynový peak) již není zcela homogenní. Teplota oblaku je odhadnuta na ≈10 K. Obr: autor, s použitím své původní fotografie pro tuto ilustraci laskavě svolil Jerry Lodriguss (http://www.astropix.com/).

předpokládáno, že je řízen nejen reakcemi mezi ionty, ale velký význam mají také exotermické reakce mezi neutrálními speciemi[34] (radikály, stabilní látky). Reakce neprobíhají pouze v plynné fázi. Zrnka prachu tvoří matrici, která absorpcí kinetické energie reakčních partnerů usnadňuje vznik molekul a agreguje chemické sloučeniny i atomy přítomné v mateřském oblaku. Zároveň však desorpcí zpětně uvolňuje řadu sloučenin do plynné fáze.

Aby mohla proběhnout chemická reakce, musí dojít i za nízkých teplot (≈10 K) k setkání reakčních partnerů. Na zrnech prachu vykazují dostatečnou mobilitu[35] pouze atomy H, D, C, O a N. V tomto ohledu nelze nezmínit fakt, že ve výčtu elementů s dostatečnou mobilitou figurují kromě D zároveň všechny čtyři základní prvky tvořící biomolekuly! Zmíněné prvky na povrchu prachu vytváří nejprve jednoduché sloučeniny ve formě ledu např. $H_2O$, CO, $O_2$, $N_2$, $NH_3$ či $CH_4$, přičemž látky vzniklé na povrchu následně migrují kvantovým tunelováním[35] dovnitř zrn a vznikají další molekuly, např. oxid uhličitý ($CO_2$), formaldehyd ($H_2CO$), acetaldehyd ($CH_3CHO$), v oblacích výrazně zastoupený methanol ($CH_3OH$), keteny ($R_1,R_2C=C=O$), propynal ($HC_2CHO$), kyselina isokyanatá (HNCO), formamid ($HCONH_2$). Materiál se na zrnu ukládá ve vrstvách, jak je vidět na Obr. 4.

Ve studených (< 20 K) a hustých oblacích je povrch zrn tvořen
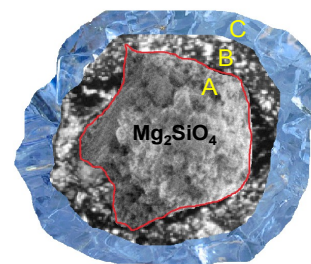


Obr. 4: Stavba prachového zrna v mezihvězdném oblaku: A) Jádro je tvořeno křemičitanem (typicky forsteritem) a pokryto vrstvou B) organického materiálu různého složení (cyklické i alifatické řetězce uhlíku, karbonyly, kyanidy, dusíkové heterocykly aj.). C) Obal je tvořen ledem z $H_2O$, CO, $N_2$, $CO_2$, $NH_3$ či $CH_4$ (záleží na teplotě prostředí, kde se prach nalézá). Obr.: autor.

*Tab 1: Abundance některých molekul v molekulových oblacích TMC−1, OMC−1 a kometě Hale−Bopp vzhledem k zastoupení CO. Přepočteno podle[31,32,33].*

| Molekula | OMC−1 | TMC−1 | Hale−Bopp |
|---|---|---|---|
| CO | 1 | 1 | 1 |
| $NH_3$ | $1,00 \cdot 10^{-2}$ | $2,50 \cdot 10^{-4}$ | $1,20 \cdot 10^{-1}$ |
| $CH_3OH$ | $2,33 \cdot 10^{-3}$ | $3,75 \cdot 10^{-5}$ | $1,33 \cdot 10^{-1}$ |
| $H_2O$ | $1,00 \cdot 10^{-1}$ | $8,75 \cdot 10^{-4}$ | 6,67 |
| NO | $1,00 \cdot 10^{-3}$ | $3,75 \cdot 10^{-4}$ | |
| $CO_2$ | $1,00 \cdot 10^{-2}$ | | $2,00 \cdot 10^{-1}$ |
| $H_2CO$ | $3,33 \cdot 10^{-4}$ | $6,25 \cdot 10^{-4}$ | $6,67 \cdot 10^{-2}$ |
| $CH_3COCH_3$ | $2,00 \cdot 10^{-4}$ | | |
| $HCOOCH_3$ | $1,73 \cdot 10^{-4}$ | | $4,00 \cdot 10^{-3}$ |
| $C_2H$ | $1,07 \cdot 10^{-4}$ | $2,50 \cdot 10^{-4}$ | |
| HCN | $1,00 \cdot 10^{-4}$ | $2,50 \cdot 10^{-4}$ | $1,67 \cdot 10^{-2}$ |
| $CH_3C_2H$ | $6,67 \cdot 10^{-5}$ | | |
| $SO_2$ | $6,67 \cdot 10^{-5}$ | $1,25 \cdot 10^{-5}$ | $3,33 \cdot 10^{-2}$ |
| OCS | $6,67 \cdot 10^{-5}$ | $2,50 \cdot 10^{-5}$ | $6,67 \cdot 10^{-3}$ |
| CN | $6,67 \cdot 10^{-5}$ | $6,25 \cdot 10^{-5}$ | |
| CS | $5,00 \cdot 10^{-5}$ | $5,00 \cdot 10^{-5}$ | |
| $HCO^+$ | $4,67 \cdot 10^{-5}$ | $1,00 \cdot 10^{-4}$ | |
| HNCO | $4,33 \cdot 10^{-5}$ | | $6,67 \cdot 10^{-3}$ |
| $H_2CS$ | $3,20 \cdot 10^{-5}$ | $8,75 \cdot 10^{-6}$ | $1,33 \cdot 10^{-3}$ |
| $CH_3NH_2$ | $2,00 \cdot 10^{-5}$ | | |
| SO | $1,87 \cdot 10^{-5}$ | $2,50 \cdot 10^{-5}$ | $5,33 \cdot 10^{-2}$ |
| HNC | $1,07 \cdot 10^{-5}$ | $2,50 \cdot 10^{-4}$ | $2,67 \cdot 10^{-3}$ |
| HCOOH | $1,00 \cdot 10^{-5}$ | $2,50 \cdot 10^{-6}$ | $4,00 \cdot 10^{-3}$ |
| $CH_3CN$ | $6,40 \cdot 10^{-6}$ | $7,50 \cdot 10^{-6}$ | $1,33 \cdot 10^{-3}$ |
| $CH_3CHO$ | $3,33 \cdot 10^{-6}$ | $7,50 \cdot 10^{-6}$ | |
| $HC_3N$ | $2,67 \cdot 10^{-6}$ | $2,50 \cdot 10^{-4}$ | $1,33 \cdot 10^{-3}$ |
| $NH_2CHO$ | $2,00 \cdot 10^{-6}$ | | $6,67 \cdot 10^{-4}$ |
| $NH_2CN$ | $2,00 \cdot 10^{-6}$ | | |
| $C_3H_2$ | $1,73 \cdot 10^{-6}$ | $1,25 \cdot 10^{-4}$ | |
| $HCS^+$ | $1,07 \cdot 10^{-6}$ | $5,00 \cdot 10^{-6}$ | |
| HCO | $6,67 \cdot 10^{-7}$ | | |
| $HC_5N$ | $4,67 \cdot 10^{-7}$ | $5,00 \cdot 10^{-5}$ | |
| $C_3N$ | $3,33 \cdot 10^{-7}$ | $7,50 \cdot 10^{-6}$ | |
| $C_4H$ | $1,67 \cdot 10^{-7}$ | $1,13 \cdot 10^{-3}$ | |

nepolárními ledy složenými z vysoce těkavých molekul (CO, O$_2$, N$_2$),[36] oproti tomu v teplejších oblacích (< 90 K), ve kterých vlivem vnějšího impulzu dochází k akreci vedoucí ke zrodu hvězdy, je ledový obal tvořen polární méně těkavou fází převážně z vodního ledu[37]. Zmíněné teplotně odlišné typy oblaků reprezentují např. TMC v souhvězdí Býka, kde je podle měření teplota[30] asi 10 K a oblast formování hvězd v oblaku OMC v Orionu, kde byla zjištěna teplota mezi[38] 300 − 500 K. V chladném oblaku, je materie vystavena pouze pronikavému kosmickému záření, avšak zrnka prachu u rodících se hvězd jsou výrazně exponována také tvrdému UV záření nebo i vyšší teplotě, tedy dalším iniciátorům následných chemických reakcí uvnitř zrn, při kterých vzniká široká paleta nových látek (např. CH$_3$CH$_2$CN, CH$_2$CHCN, CH$_3$CN, CH$_3$NH$_2$).

Složení různých objektů ve vesmíru shrnuje Tab. 2., nicméně představu o složení původního materiálu, ze kterého se formovala sluneční soustava, nám mohou dát komety[33]. Typická kometa je složena z 26 % silikátů, kolem 30 % vodního ledu, až 23 % tvoří zmíněný druhotně formovaný organický materiál a pouze 9 % prvotní malé organické molekuly (CO, CO$_2$, CH$_3$OH, HCN, H$_2$CO, CH$_4$, C$_2$H$_2$ a další).

*Tab 2: Uhlík a ostatní materiál ve vybraných prostředích ve vesmíru.*

| Systém | Specie | Pevná fáze |
|---|---|---|
| Obálky hvězd, rudí obři AGB | CO, C$_2$H$_2$, C$_x$H$_y$, PAH, CH$_y$C$_x$−CN vysoké koncentrace HNC, HCN, ·CN, CS | amorfní uhlík, SiC |
| Mezihvězdný prostor a difuzní mezihvězdná oblaka | C$^+$, diatomické molekuly, radikály a ionty (·CH, ·CN, CH$^+$), PAH, řetězce C, fulereny (C$_{60}$) | grafit, ledy, uhlovodíky |
| Studená a hustá mezihvězdná oblaka (10 K) | C$^+$, diatomické molekuly (N$_2$, CO) a radikály (·CN, ·CH), ionty, uhlovodíky, CH$_y$C$_x$−CN, | ledy CO, N$_2$, CO$_2$, CH$_3$OH, uhlíkatá zrnka a silikáty |
| Horká cirkumstelární oblaka (500 K) | >NH$_3$, >H$_2$O, C$_2$H$_2$, komplexní organické látky | ledy H$_2$O, uhlíkatá zrnka, silikáty |
| Meteority | kerogen, PAH | karbidy, grafit, nanodiamanty |
| Komety | H$_2$O, CO, CO$_2$, CH$_3$OH, CH$_4$, HCN | Silikáty podobné diskům kolem rudých obrů AGB, ledy |

### 2.3. Vysoce rozlišená spektrometrie s Fourierovou transformací a její laboratorní. aplikace

(přiložena publikace **Vysoce rozlišená spektrometrie s Fourierovou transformací a její laboratorní aplikace.** Ferus M., Civiš S. *Československý časopis pro fyziku* **57**, 127 (2008))

Spektrometrie umožňuje v laboratoři studovat spektra a molekulární dynamiku řady nestabilních látek včetně těch, které se vyskytují v mezihvězdném prostoru, molekulových mračnech, obálkách hvězd či kometách. V naší laboratoři je k tomuto účelu upraven komerčně dostupný spektrometr Bruker IFS 120 HR, který je přídavnými elektronickými prvky propojen s osobním počítačem, pomocí něhož je softwarem Quartus II (Altera Corp., USA) programován procesor programovatelných hradlových polí (FPGA). Tento procesor synchronizuje snímání dat z detektoru a spínání pulsu výboje nebo laseru.

Postup měření tímto přístrojem se však zásadně odlišuje od klasického přístupu, kdy jsou postupně snímána spektra v časově posunutých sekvencích. V případě spektrometrů využívajících detektor typu CCD (Charge−Couple Device) se tak děje otevřením závěrky vstupní štěrbiny, u spektrometrů s Fourierovou transformací pak velice rychlým pohybem zrcadla tak, aby byl ve velice krátkém časovém úseku získán interferogram (tzv. *fast scan*). Akvizice dat naším systémem probíhá tak, že v pozicích pohyblivého zrcadla definovaných interferečními maximy HeNe laseru je procesorem FPGA sepnut výbojový nebo laserový puls a zároveň je snímána časová sekvence vzájemně časově posunutých signálů z detektoru. Během pohybu zrcadla interferometru se tento postup opakuje v každém interferenčním maximu a následně jsou ze získané matice dat, která obsahuje signály z detektoru ve všech zvolených časech a dráhových rozdílech, rekonstruovány interferogramy odpovídající jednotlivým časovým úsekům. Tato metoda logikou sběru dat odpovídá systému step−scan s tím rozdílem, že zrcadlo není nutné zastavovat.

Technický vývoj shrnuli Kawaguchi a kol.[39,40] v jedné z prvních prací popisujících aplikaci tohoto systému (zde pro měření Ar, ArH a $ArH^+$). Další specie studované touto metodou mají velký význam pro mezihvězdnou chemii, např. iont[41] $H_3^+$, radikál[42] ·CN a excitované atomy (články v příloze). Metoda časově rozlišené spektrometrie byla též využita pro studium dynamiky vzniku a zániku jednoduchých uhlíkatých radikálů ·CH, ·$C_2$, ·CN, vysoce excitovaných molekul $H_2$ a nestabilního izomeru kyanovodíku HNC.

### 2.3.2. Časově rozlišená emisní spektrometrie s Fourierovou transformací He/CH₄ v pozitivním sloupci výboje

(přiložena publikace **Time−Resolved Fourier Transform Emission Spectroscopy of He/CH₄ in a Positive Column Discharge.** Civiš S., Kubelík P., Ferus M. *Journal of Physical Chemistry A* **116** (12), 3137−3147 (2012)).

Chemické děje v plazmatu představují velice komplikovaný systém vzájemných reakcí atomů, radikálů, iontů a molekul. K detailní interpretaci časově rozlišených spekter je nezbytné sestavit chemický model[43], který popíše i proces akvizice dat, tzn. zohlední pulsní režim iniciace chemických reakcí (spínání výboje), kontinuální přísun prekurzoru spojený s kontinuálním odčerpáváním produktů a parametry výboje (elektronové teploty, elektronové hustoty).

Naše studie byly zaměřeny na procesy, při kterých jsou fragmentovány jednoduché molekuly, jako je např. methan, který je významnou složkou atmosféry Saturnova měsíce Titanu a plynných obrů[44], mezihvězdných oblaků[45] a redukčních atmosfér[46] potencionálně vhodných pro syntézu biomolekul. Jako modelové prostředí byl použit doutnavý výboj, ve kterém je methan disociován srážkou s elektronem nebo atomem helia za vzniku jednoduchých radikálů ·CH₃, ·CH₂, ·CH až atomárního uhlíku ·C. Radikál ·CH₃ se nám podařilo detegovat v absorpčních spektrech výboje za použití Whiteovy cely o optické dráze 60 m, avšak v časově rozlišených emisních spektrech byly identifikovány pouze pásy ·CH, ·C a také radikálu ·C₂. Hlavním výsledkem této studie je exaktnější popis podmínek, za jakých je daný molekulární fragment pomocí časově rozlišené spektrometrie měřitelný: Přestože model predikuje vysoké koncentrace radikálu CH₃, nelze tento radikál vzhledem k intenzitě jeho spektra jednoduchým způsobem detegovat vzhledem k jeho emisní intenzitě.

Fragmentaci jakékoliv specie v pulsním výboji vyžaduje komplexní model celé řady simultánních kolizních, radiačních i chemických dějů. Následně lze získat celistvý obraz o jednotlivých krocích procesů v plazmatu s mikrosekundovým časovým rozlišením.

### 2.3.3. Poměr HNC/HCN ve výboji v Acetonitrilu, Formamidu a BrCN

(přiložena publikace **HNC/HCN ratio in Acetonitrile, Formamide and BrCN discharge**. Ferus M., Kubelík P., Kawaguchi K., Dryahina K., Spaněl P., Civiš S. *Journal of Physical Chemistry A* **115** (10), 1885 (2011).

Izomery HCN/HNC a radikál ·CN jsou speciemi hrajícími významnou úlohu v chemii komet, uhlíkatých obálkách hvězd, mezihvězdných oblacích, planetárních atmosférách[47,48,49] a jsou také významnými prekurzory biomolekul (viz kapitola 3). Dobře pochopeno a vysvětleno je formování HNC termálními procesy zahříváním kyanovodíku na teploty[50] nad 1400 K (HNC/HCN < 0,01),

avšak vzájemná izomerace HNC/HCN v molekulových oblacích, kometách či v plazmatu za laboratorních podmínek je stále předmětem diskuze. Při studiu vzniku HNC jsme se zaměřili na molekuly generující HNC/HCN: formamid (HCONH$_2$), který je významným prekurzorem biomolekul, acetonitril (CH$_3$CN), který reprezentuje organickou sloučeninu obsahující skupinu −CN a bromkyan (BrCN) reprezentující anorganický prekurzor. Emisní intenzity pásů HNC a HCN byly korigovány pomocí známých emisních koeficientů a následně byl určen poměr mezi izomery HNC/HCN ≈ 2,2 − 3%. Pomocí komplexního matematického modelu chemismu výboje bylo zjištěno, že za daných podmínek má pro vznik HNC největší význam reakce kyanovodíku s vodíkem

$$HCN + \cdot H \rightarrow HNC + \cdot H \quad (2.2.3.a)$$

a ostatní děje mají zanedbatelný příspěvek. Původně bylo předpokládáno, že HNC vzniká převážně rozpadem iontu HCNH$^+$:

$$HCNH^+ + e^- \rightarrow HNC\ (50\ \%) + HCN\ (50\ \%) \quad\quad (2.2.3.b)$$

Závěry studie nacházejí uplatnění např. pro modelování chemismu komet, ve kterém by měla hrát reakce (2.2.3.a) významnou úlohu[51].


## 2.3.4. Časově rozlišená FT spektroskopie CF$_3$Br a CF$_3$CFHCF$_3$ v pulsním výboji

(přiložena publikace **Time−resolved Fourier transform emission spectroscopy of CF$_3$Br and CF$_3$CFHCF$_3$ in a pulsed electrical discharge**. Ferus M., Civiš S., Kubelík P., Nevrlý V., Bitala P., Grigorová E., Střižík M., Kubát P., Zelinger Z. *Plasma Chemistry and Plasma Processes* **3** (31), 417 (2011).

Z halogenovaných specií byl v mezihvězdném prostoru nalezen ion[52] CF$^+$, sloučeniny chloru[53], HCl, NaCl, AlCl, KCl a fluoru[54,53] HF a AlF. Molekulární dynamika rozkladu CF$_3$Br a (CF$_3$)$_2$CHBr se však stala předmětem studie vzhledem k aplikaci těchto halogenovaných uhlovodíků k likvidaci požárů. Znalost procesů fragmentace těchto látek, které mohou probíhat za vysokých teplot, má význam zejména z hlediska vzniku celé řady agresivních a toxických produktů.

V emisních spektrech obou výbojů byl detegován silný pás reaktivního radikálu ·CF a také několik slabých linií radikálu ·CF$_2$. Radikál ·CF$_3$ nebyl detegován. V naší studii je poprvé prezentováno vysoce rozlišené spektrum radikálu ·CF změřené metodou FT−IR s časovým rozlišením. Dosud byla pro detekci v infračervené oblasti používána pouze diodová spektrometrie (nejnověji např.[55]). Časově rozlišená spektra vzniku a zániku jednoduchých fragmentů byla opět srovnána s výsledky matematického modelu popisujícího disociaci halogenovaných látek za vzniku řady reaktivních

fragmentů, jako jsou radikály $\cdot CF_3, \cdot CF_2$ a $\cdot CF$. Na základě analýzy emisních spekter lze říci, že v plazmě výboje jsou výrazně zastoupeny radikály $\cdot CF_2$ a $\cdot CF$. Tato skutečnost se shoduje jednak s výsledky prezentovaného modelu a také se závěry studie Kim a kol.[56]

# 3. Vznik a zánik biomolekul v raných zemských podmínkách

## 3.1. Biomolekuly a jejich prekurzory na Zemi

Za prekurzory biomolekul lze označit celou řadu sloučenin, které lze rozdělit do skupin uvedených v Tab. 3, a). Nejvíce diskutovanými jsou zejména kyanidy a jejich polymery, sloučeniny s aminoskupinou a sloučeniny s karbonylovou skupinou[62,57]. Mezi často zmiňované prekurzory biomolekul patří kyanovodík, který ve vodném roztoku reaguje za vzniku nukleových bází[94] a také kyanidové polymery, které hydrolyzují za vzniku nukleových bází a aminokyselin[58]. Přehled některých dalších prekurzorů biomolekul spolu s jejich zastoupením[59] poskytuje Tab. 3, b). Samotný původ biomolekul a jejich prekurzorů, které poskytly základní stavební kameny živé hmoty na naší planetě, je vysvětlován dvěma způsoby[60,61]:

**a)** *Hypotézou exogenní syntézy:* Prekurzory biomolekul nebo i samotné biomolekuly vznikají ve vesmíru v oblastech horkých jader protosolárních mlhovin kolem rodících se hvězd[62] a byly dopraveny na Zemi impakty ledových těles (komety) či planetesimálů a poskytly tak materiál ke vzniku života.

*Tab 3: a) Přehled skupin látek majících potencionální význam pro syntézu biomolekul[62] a b) příklady konkrétních sloučenin prekurzorů a příslušných biomolekul spolu s abundancemi[59] těchto látek v kometách.*

**a)**

| Typ molekuly | Příklad, vzorec | Skupina biomolekul |
|---|---|---|
| molekuly se skupinou CN | $HCN$, $H_2NCN$, $CH_3CN$, $C_2N_2$, $HC_3N$, $C_2H_3CN$ | Aminokyseliny, nukleové báze |
| molekuly se skupinou NH | $CH_2NH$, $HCONH_2$, $(NH_2)_2CO$ | Aminokyseliny, nukleové báze |
| molekuly se skupinou CO | $H_2CO$, $HOCH_2CHO$, $CH_3CHO$, $(CH_2OH)_2$ | Cukry |

**b)**

| Název a vzorec molekuly | Abundance (přepočet na HCN) | Poznámka |
|---|---|---|
| $HCN$, kyanovodík | 100,00% | Ve směsi s $NH_3$ polymerace za vzniku nukleových bází[94] |
| $(-C=N-)_n$, HCN polymery | < 10 % | Hydrolýza vede ke vzniku aminokyselin, purinu, kyseliny orotové[37] |
| $HCONH_2$, formamid | < 40 % | Zahříváním a ozařováním vznik nukleových bází a aminokyselin[119,120] |
| $H_2CO$, formaldehyd | max 20 x více | Formózová reakce (polymerace) vede ke vzniku cukrů[57]. |

**b)** *Hypotézou endogenní syntézy:* Biomolekuly byly syntetizovány na Zemi z jednoduchých látek ($N_2$, $NH_3$, $H_2O$, $H_2$, $CH_4$, $CO_2$ atd.) např. intenzivními blesky, UV zářením ze Slunce, působením radioaktivity, vulkanickou činností či rázovými vlnami rozličného původu[63,64].

Tyto dva alternativní scénáře lze srovnat s některými současnými poznatky. Se složením prvotní materie a vznikem biomolekul bylo v dřívějších pracích spojováno zejména složení atmosféry naší planety v době jejího vzniku[93,94]. Stáří našeho solárního systému je v současné době stanoveno na 4,5682 mld. let[65] přičemž formování Země bylo podle Zhanga[66] dokončeno přibližně před 4,45 mld. let. Stáří atmosféry je odhadováno v rozmezí 4,43 až 4,15 mld. let a ve stejné době kolem ≈4,5 mld. let je předpokládán i vznik hydrosféry[67]. Časovou souslednost diskutovaných dějů shrnuje Obr. 5. Izotopové složení neradiogenních vzácných plynů (Ne, Ar, Kr, Xe) přítomných v atmosféře naznačuje,[68,69] že plynný obal Země o teplotě[70] až 1000 K v raných stádiích částečně či zcela unikl

pryč[68] a atmosféra vznikla druhotně z těkavých látek přítomných nejen v horninách, ale zejména z materie na Zemi dopadajících planetesimálů či komet[71], tedy z molekul původně se formujících v pevné fázi akrečního disku (viz. Obr. 2, panel C). Nejnovější práce Traila a
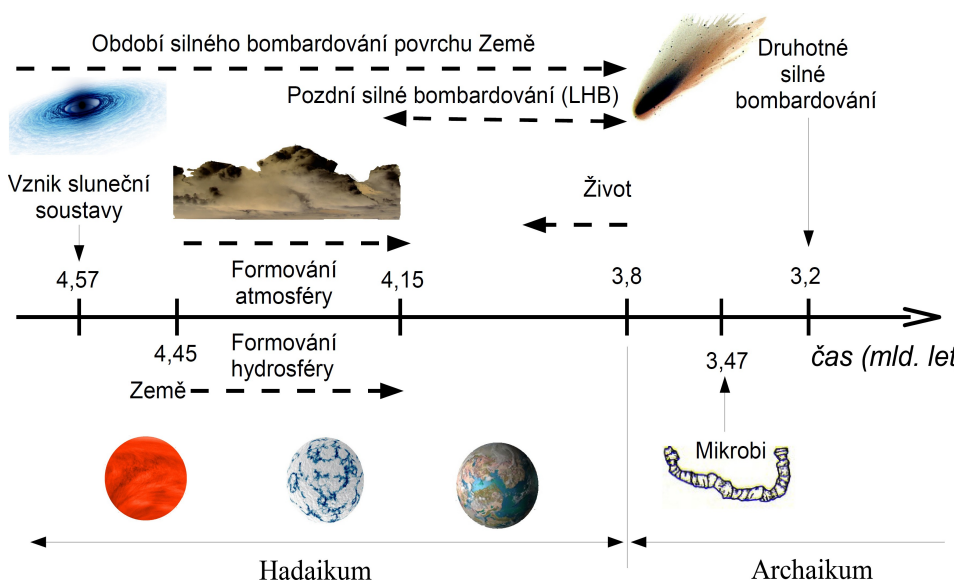


Obr. 5: Časová souslednost dějů raného vývoje Země. Obr.: autor.

kol.[72] naznačuje, že primární atmosféra před ≈4,35 mld. let pravděpodobně nebyla redukční, takže postupná syntéza biomolekul z jednoduchých v atmosféře přítomných redukčních plynů (směs $NH_3$, $CH_4$, $H_2$) podle Millerových a Ureyových experimentů[93] by nepřipadala v úvahu, nebo by byla velmi obtížná[73]. Naopak primární atmosféra patrně nejprve obsahovala významné množství vodíku a vodní páry, která následně kondenzovala za vzniku oceánů a dominantními konstituenty se staly $CO_2$, CO (≈10 atm) a $N_2$ (1 atm)[74]. Pinto a kol.[75] ukázal, že fotochemická syntéza formaldehydu, který je prekurzorem pro syntézu sacharidů je v takové atmosféře možná, avšak vznik kyanovodíku, který je prekurzorem pro vznik nukleových bází a aminokyselin, je podle Chameidese a Walkera[76] obtížná. První překážkou je fakt, že vznik HCN vyžaduje, vzhledem ke své energetické náročnosti, událost

o vysoké hustotě energie (blesk, dopad mimozemského tělesa), druhou pak samotné složení atmosféry, neboť zmíněná událost o vysoké hustotě energie v prostředí bohatém na $CO_2$ nezaručuje dostatečnou produkci HCN.

Jelikož atmosféra se z tohoto pohledu patrně nebyla zdrojem molekul pro vznik života, mohly být organické látky přítomny nebo syntetizovány přímo v oceánu, ve kterém pravděpodobně život vznikl[77]. Cestou tvorby biomolekul a jejich prekurzorů či přímo života samého mohou být chemické reakce poblíž (nikoliv uvnitř[78]) hydrotermálních průduchů (sopouchů)[a]. V práci LaRoweho a Regniera[78] bylo dokázáno, že z jednoduchých směsí jako $N_2$, CO, $CO_2$, $H_2$ může v takovém prostředí vznikat nejen HCN, ale i složité organické molekuly a byly také studovány podmínky, za jakých se tak děje. Bylo zjištěno, že syntéza vyžaduje vyšší koncentrace sopečných plynů, než jaké jsou známy z hydrotermálních průduchů. Je diskutováno, že pokud se složení oceánů či sopečných plynů v dřívějších dobách lišilo od dnešního ve smyslu vysoké koncentrace $N_2$, CO, $CO_2$, $H_2$ (či dokonce přímo HCN) byla by taková syntéza možná a v místě vzniku výpočtem určené nejpříznivější teploty 150 °C a nejpříznivějšího tlaku 500 bar by koncentrace biomolekul dokonce odpovídaly koncentracím v buňce[78,79]. V současné době je známo pouze to, že raný oceán byl kyselejší, než ten dnešní, anoxický a s vyššími koncentracemi solí[84], ale procentuální obsah organických látek není přesně znám. Složení oceánů (i atmosféry[80]) mohlo být významně ovlivněno materiálem mimozemského původu[81] či dokonce mohla oceánská voda z tohoto materiálu přímo pocházet[82,83] a výchozí podmínky mohly být z hlediska koncentrací jednoduchých i složitějších organických látek příznivé, byť tyto příznivé podmínky mohly mít z geologického hlediska krátkodobý či lokální charakter. O sekundárním příspěvku impaktů ke vzniku atmosféry a hydrosféry jsou stále vedeny rozsáhlé diskuze. Jedním z hlavních argumentů je, že teplota v místě formování Země v době jejího vzniku nedovolovala inkorporaci těkavých sloučenin prvků, jako jsou N, C, O, H do hornin tak, aby se tyto komponenty později uvolnily vulkanickou činností a následně vytvořily atmosféru a hydrosféru[84]. Jako pravděpodobní exogenní[84] původci vody a dalších sloučenin N, C, O a H (biomolekuly) jsou označovány uhlíkaté chodrity (obsahují až 22 % vody[85]) a komety přičemž četnost impaktů naznačuje poměr příspěvků[82,83,84] chondritů 90 % a komet 10 %. Chondritické meteority obsahují stovky ppm různých druhů organických látek (aminokyseliny, uhlovodíky, kyslíkaté deriváty atd.[86]) přičemž celkové zastoupení uhlíkatých látek je kolem[87] 8 %, komety obsahují kolem 22 % uhlíkatých látek (prach komety Halley[88]).

Význam impaktů podporují údaje o stáří kráterů na Měsíci. Povrch Země i Měsíce byl vystaven četným impaktům až do doby před 3,8 mld. let[89] a frekvence impaktů dokonce přechodně zesílila v době mezi 4,2 − 3,8 mld. let a v také v době kolem 3,24−3,227 mld. let[90]. Podle dat Chyba a kol.[91]

---

a  V anglosaské literatuře je používán termín „hydrothermal vent".

mohlo být v té době na Zemi doneseno až $10^{11}$ kg/rok organického materiálu[81]. Pokud je tento optimistický odhad správný, pak každý rok bylo úhrnem k dispozici něco pod 1 % organických látek, než kolik je v současné době fixováno fytoplanktonem v oceánu[92] (4,5 x $10^{13}$ kg/rok). Vzhledem k objemu a stupni vývoje současné biosféry by toto číslo nemuselo být považováno za nízké.

Vzhledem k tomu, že impakty mimozemských těles ovlivnily složení atmosféry a hydrosféry, je třeba porozumět transformačním procesům, kterým byl tento materiál vystaven a zodpovědět otázku, zda původní materie

**1)** obsahovala pouze jednoduché těkavé látky typu $N_2$, $NH_3$, $CH_4$, HCN, CO, $CO_2$ atd., které podle původních hypotéz Ureye a Millera[93] či Oró[94] poskytly materiál k syntéze biomolekul, nebo

**2)** složitější sloučeniny přítomné v protoplanetárním disku (viz. Tab. 3) přímo vedly k syntéze biomolekul i na Zemi[62] nebo

**3)** samotné biomolekuly přítomné ve vesmírné materii se staly materiálem pro vznik živé hmoty.

### 3.2. Simulace dopadu mimozemského tělesa

Existence primitivních životních forem na Zemi je předpokládána na základě izotopického složení inkluzí v geologických nálezech již v době před 3,85 mld. let[95]. Zatím nejstarší potvrzené mikrofosilie baktérií pochází z hornin nalezených v Austrálii a datovaných do doby před 3,465 mld. let[96] (viz časová osa na Obr. 5, str. 12). Složení primární materie je možno odhadnout na základě studia transformačních procesů, kterým podléhaly chemické látky v době vzniku života. Jak již bylo konstatováno v předchozí kapitole, tyto chemické látky pravděpodobně pocházely z těles dopadajících do atmosféry a na povrch Země. Prvotním transformačním procesem se bezpochyby stal samotný dopad tělesa. Následovaly další chemické změny vzniklé materie v pozemských podmínkách.

První simulace impaktu předpokládaly, že samotné těleso může být vystaveno teplotám až 40 000 K přičemž by mělo dojít k okamžité pyrolýze materiálu[97]. Pozdější modely ukázaly, že teploty nemusí být takto drastické, pakliže se uvažují různé geometrie dopadu[98] a také tlaková i teplotní závislost rychlostních konstant pyrolýzy spolu s krátkodobou expozicí[99]. Bylo také dokázáno, že část ledového tělesa (kometa) může roztát a dopadnout, rozprášit se ve formě kapaliny[99] nebo se rozptýlit explozí[100].

Chemické děje spojené s impakty jsou stále předmětem výzkumu (přednáška A.−Ch. Levasseur−Regourd[101], Montpellier 2011). Simulace jsou prováděny např. pomocí projektilů vystřelených vysokou rychlostí proti zvolenému terči[102], matematického modelování, laboratorní simulací plazmatu pomocí laserového záření,[103] pyrolýzou[104] či rázovou vlnou[105].

Prvotní výsledky kolizních experimentů Tingle et al.[106], který použil přímo vzorek Murchinsonského meteoritu, ukázaly, že za vysokých tlaků až 36 GPa je degradováno cca 70 % organických látek (při dopadu tělesa však může tlak v závislosti na geometrii narůst až na 100 GPa[99]). Peterson et al.[107] přidal

k materiálu meteoritu vzorek aminokyselin a studoval účinky nárazu za použití původní uhlíkové matrice tak, aby se přiblížil skutečným podmínkám. Při tlaku 30 GPa byly zjištěny menší ztráty mezi 40 − 50 %. Systematickými experimenty bylo potvrzeno, že při zachování stejných podmínek jsou ztráty přímo úměrné tlaku[108], nicméně okolní hmota významně ovlivňuje účinky nárazu. Nejlepší vlastnosti mají v tomto ohledu ledy a kapaliny, ve kterých ztráty organických látek dosahují asi[109] 25 %. Jak již bylo zmíněno v úvodu, právě ledová tělesa jsou typická vysokým obsahem organických látek (≈23 %) pocházejících z mezihvězdného oblaku[33].

Nejnovější práce zabývající se modelováním chemismu plazmy ukázala, že v závislosti na rychlosti dopadu jsou hlavními produkty destrukce organických látek v kometárním ledu $H_2$ a CO přičemž zastoupení organických komponent klesá typicky o jeden až dva řády v závislosti na rychlosti dopadu[110] a největší stabilitu projevuje kyanovodík.

Plazma vznikající při impaktu mimozemského tělesa je v naší laboratoři simulováno pomocí vysoce výkonného laseru PALS[111,112] (Prague Asterix Laser System). Při dielektrickém průrazu v plynu (LIDB)
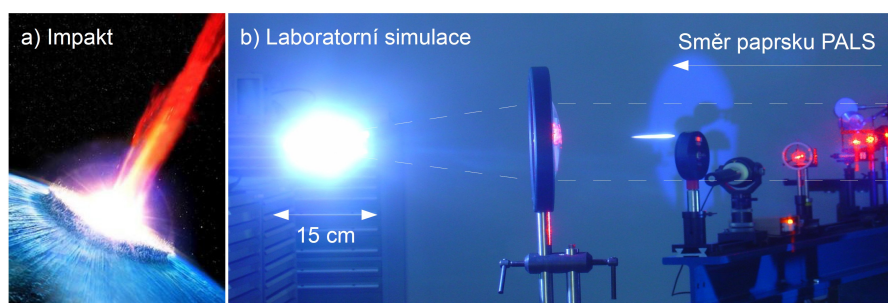


Obr. 6: Plazma vznikající při impaktu mimozemského tělesa a) v představě malíře, b) laboratorní simulace pomocí laseru PALS. Obr.: internet; autorem fotografie b) je RNDr. Jiří Skála z Ústavu fyziky plazmatu AV ČR, schéma autor.

generovaným pomocí laserového pulsu na vlnové délce 1315 nm, energii[113] ≈150 J a době trvání ≈400 ps dochází ke všem projevům spojeným s událostí o vysoké hustotě energie: ke skokovému nárůstu teploty na několik tisíc K[114], vzniku rázové vlny a generování sekundárního tvrdého záření (UV−VUV, XUV, RTG)[115]. Plazma LIDB je zobrazena na Obr. 6. V našich experimentálních modelech plyn reprezentuje atmosféru, ve které vzniká relativně husté impaktní plazma, které působí na kapalný nebo pevný vzorek (led, hornina).

### 3.2.1. Výzkum chemie laserového plazmatu ve směsích CO−N₂−H₂O pomocí izotopově značené vody ¹⁸O

(předkládaná publikace **Investigation of laser−plasma chemistry in CO−N₂−H₂O mixture using ¹⁸O labeled water**. Ferus M., Matulková I., Juha L., Civiš S. *Chemical Physics Letters* **472** (1−3), 14 (2009).

Působení impaktního plazmatu bylo studováno v předkládané práci zabývající se rozkladem oxidu uhelnatého při simulaci impaktu mimozemského tělesa do planetární atmosféry. Transformace CO na $CO_2$ je z hlediska složení rané atmosféry zajímavá zejména proto, že v kometách může být koncentrace CO oproti $CO_2$ až několikanásobně vyšší[116] a CO je též složkou sopečných plynů

(na Jupiterově měsíci[117] Io CO/CO$_2$ ≈ 1:1).

Kyslík se stal významnou složkou atmosféry před ≈2,4 mld. let, tj. asi 300 mil. let po vzniku fotosyntetizujících mikrobů, takže vznik CO$_2$ z CO byl v plazmatu generované v praatmosféře možný buďto disproporcionační reakcí

$$CO + CO \rightarrow CO_2 + C\cdot \qquad (3.1.1.a)$$

nebo oxidací ·OH radikálem pocházejícím z rozkladu vodní páry

$$H_2O \rightarrow \cdot OH + \cdot H \qquad (3.1.1.b)$$

$$CO + \cdot OH \rightarrow CO_2 + \cdot H \qquad (3.1.1.c)$$
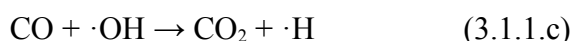
Za účelem sledování molekulární dynamiky těchto dějů byla použita směs C$^{16}$O:N$_2$ 1:1 za atmosférického tlaku a 2 ml izotopově značené vody H$_2{}^{18}$O (tenze par 23,7 Torr). Tato směs byla ozařována deseti pulsy laseru PALS o energii 100 J a délce 400 ps. Po každém pulsu bylo izotopové složení vznikajícího CO$_2$ měřeno pomocí vysoce rozlišené infračervené spektrometrie s Fourierovou transformací, která je velmi vhodným nástrojem k detekci izotopového složení plynných směsí, protože absorpční čáry téže látky odlišného izotopového složení jsou vzhledem k odlišným hmotnostem izotopů vzájemně posunuty.

Mezi C$^{16}$O a H$_2{}^{18}$O nedochází ke spontánní izotopové výměně a vzhledem k nadbytku směsi N$_2$+C$^{16}$O nad CO$_2$ (300 ppm na konci ozařování) lze zanedbat také případnou izotopovou výměnu mezi C$^{16}$O$_2$ a H$_2{}^{18}$O. Jednotlivé složky směsi byly kvantifikovány na základě intenzit vybraných absorpčních linií. Na základě nárůstu koncentrace C$^{16}$O$_2$ (produkt disproporcionace, rovnice (3.1.1.a)) a nárůstu koncentrace C$^{16,18}$O$_2$ (produkt oxidace, rovnice (3.1.1.c)) lze konstatovat, že ačkoliv za daných podmínek hrají roli oba procesy, je disproporcionační reakce v plazmatu 1,56 x rychlejší, než oxidace. Kromě této studie zaměřené čistě na molekulární dynamiku jednoduchých plynů starší experimenty se směsí CO$_2$/CO−N$_2$−H$_2$O prokázaly také abiotickou syntézu nejjednodušší aminokyseliny glycinu[118]. Tento experimentální závěr byl později potvrzen chemickou simulací Goldman a kol.[119].

### 3.2.2. Rozklad formamidu v laserové jiskře studovaný pomocí FT−IR Spektrometrie
(předkládaná publikace **Laser Spark Formamide Decomposition Studied by FT−IR Spectroscopy**. Ferus M., Kubelík P., Civiš S. Journal of Physical Chemistry A 115, 12132 (2011).

Formamid je zajímavým prekurzorem biomolekul, protože jejich vznik iniciují podmínky, které by se daly očekávat na Zemi v raných stádiích jejího vývoje, tj. zvýšená teplota a hlavně silné UV záření[120]. Podle teorií Saladina, Constanza a kol.[121,122,123] je formamid důležitý pro vznik biomolekul, protože je produktem hydrolýzy zředěného roztoku kyanovodíku, který se pravděpodobně vyskytoval v praoceánu[124] a protože jde o stabilní kapalinu s nízkou tenzí páry[125].

Naše první studie byla zaměřena na stabilitu formamidu při události a vysoké hustotě energie. Směs kapalného a plynného formamidu v inertní Ar atmosféře byla ozařována laserovým systémem PALS, produkty rozkladu byly následně vymrazeny a složení plynné fáze bylo analyzováno spektrometrem s vysokým rozlišením. Mezi produkty rozkladu byly identifikovány HCN, $CH_3OH$, CO, $N_2O$, $NH_2OH$, $NH_3$ a $CO_2$. Srovnání těchto spekter se spektry produktů zahřívání a výboje ukazuje Obr. 7. Molekulární dynamika plazmatu byla následně simulována kinetickým modelem jako skoková termolýza formamidu (4500 K po dobu 1.86 μs). Složení směsi predikované modelem odpovídalo experimentálním výsledkům. Tato skutečnost poukazuje na to, že chemismus laserového plazmatu lze aproximovat pomocí modelu vysokoteplotní termolýzy. Protože se však jedná o chemický model laserové jiskry ve kterém byla studována poměrně složitá organická molekula, je nutné provést ještě řadu dalších experimentů. V rámci zatím nepublikovaných studií byly účinky laserové jiskry srovnávány s doutnavým výbojem a reakcemi za vysoké teploty (viz Obr. 7 ). Tyto
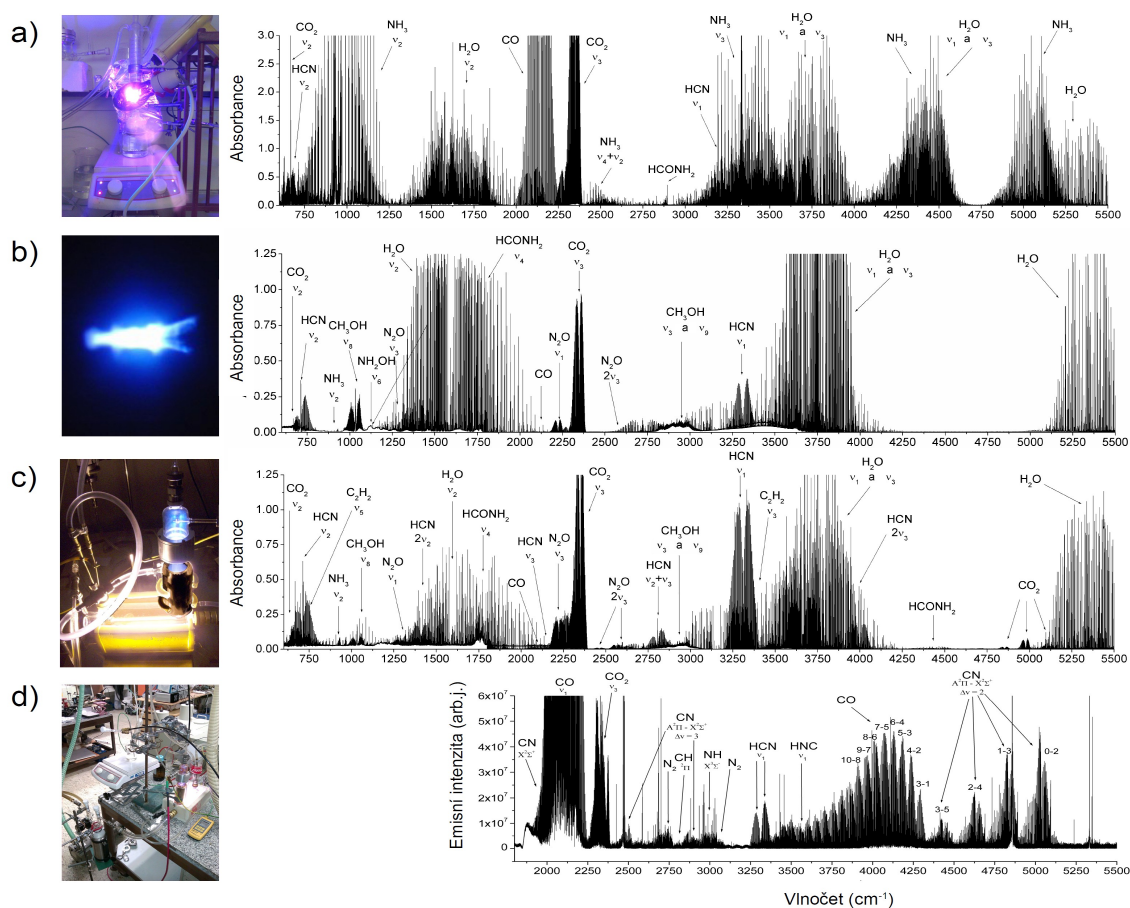


*Obr. 7: Vysoce rozlišená spektra plynných produktů disociace formamidu a) při zahřívání na 180 °C a ozařování UV zářením (lampa 340 nm), b) po expozici deseti laserovým pulsům systému PALS, c) po rozkladu par v doutnavém výboji a d) emisní spektrum stabilních a nestabilních molekul v doutnavém výboji v čase 10 μs po jeho iniciaci. Produkty byly při měřeních b) a d) koncentrovány v tekutém dusíku. Obr. a foto: autor; autorem fotografie b) je RNDr. Jiří Skála z Ústavu fyziky plazmatu AV ČR.*

experimenty potvrdily, že formamid je skutečně termálně rozkládán za vzniku HCN, CH$_3$OH, NH$_3$, HNCO, CO, CO$_2$ a N$_2$O avšak konečná skladba produktů je výrazně ovlivněna jejich stabilitou za podmínek panujících v plazmatu (NH$_3$ a HNCO jsou nestabilní a se dále rozkládají) a také teplotně závislým poměrem mezi disociačními kanály samotné molekuly formamidu. V dosud nepublikované studii se nám podařilo potvrdit, že poměry mezi teoreticky předpovězenými rychlostními konstantami disociace této molekuly v práci Nguyen[126] a kol. odpovídají našim experimentálním výsledkům stejně jako aktivační energie studovaných disociačních kanálů.

Zaměřili jsme se také na vznik nukleových bází při ozařování ledů tvořených pevným formamidem. Ačkoliv panuje obecný předpoklad, že teplota se v průběhu prvních cca 1,5 mld. let vývoje Země držela mezi[127] 80 °C až 70±15 °C (před ≈3,3 mld let), je možné, že docházelo také ke krátkodobým zaledněním[128]. Z tohoto pohledu je možné, že se byť lokálně akumulovaly organické látky z dopadů komet a následně po rozpuštění a ohřátí poskytly dostatečně koncentrovaný roztok. V ozařovaných ledech se podařilo pomocí metody GC−MS detegovat nukleové báze jejichž koncentrace přímo závisely na použitém katalyzátoru (jíl, NiFe meteorit, kamenný meteorit, TiO$_2$)[129].

### 3.3. Studium fotochemických vlastností TiO$_2$

Z hlediska vzniku organických látek či dokonce biomolekul může hrát významnou úlohu katalytický účinek některých látek (jíly, kovové minerály, oxidy kovů). Fotokatalytická aktivita oxidů kovů byla již u některých z nich studována (např.[130,131,132] Fe$_2$O$_3$, CeO$_2$, ZnO, TiO$_2$, SrTiO$_3$, In$_2$O$_3$, ZrO$_2$, InTaO$_4$) a zejména v případě TiO$_2$ je výzkum zaměřen na průmyslové aplikace jako je čištění vody[133], výroba samočistících a antibakteriální povrchů[134] nebo čističek vzduchu[135]. Důležitou vlastností TiO$_2$ z našeho pohledu není pouze fotoindukovaná destrukce molekul, ale hlavně schopnost katalyzovat vznik organických látek z jednoduchých atomárních plynů. Mřížka TiO$_2$ má zajímavé vlastnosti umožňující vazbu mnoha molekul, které pak podléhají fotochemickým změnám přičemž kyslíkové atomy v mřížce vykazují mobilitu umožňující spontánní izotopovou výměnu mezi plynným C$^{16}$O$_2$ a pevným Ti$^{18}$O$_2$.

### 3.3.1. Izotopově značený oxid titaničitý: Ti$^{18}$O$_2$

(předkládaná publikace **Oxygen−isotope labeled titania: Ti$^{18}$O$_2$**. Kavan L., Zukalová M., Ferus M., Kürti J., Koltai J., Civiš S. *Physical Chemistry Chemical Physics* **13**, 11583 (2011).

Výzkum vlastností Ti$^{18}$O$_2$ se v prvé řadě soustředil na izotopovou výměnu mezi tímto materiálem a molekulami C$^{16}$O$_2$, C$^{16}$O a HC$^{16}$O$^{16}$OH. Ti$^{18}$O$_2$ byl syntetizován hydrolýzou TiCl$_4$ vodou H$_2$$^{18}$O a následně pomocí Ramanovy spektrometrie bylo zjištěno, že kalcinací za různých teplot lze získat tři typy krystalických forem TiO$_2$: Anatas při teplotách 200 °C (vzorek A200) a 450 °C (vzorek A450), rutil při 1000 °C (vzorek R1000). Interakce těchto krystalových forem s plynnou fází byla následně

studována pomocí vysoce rozlišené spektrometrie s Fourierovou transformací.

### 3.3.2. Izotopová výměna mezi $CO_2$ a pevným $Ti^{18}O_2$

(předkládaná publikace **Oxygen−isotope exchange between $CO_2$ and solid $Ti^{18}O_2$**. Civiš S., Ferus M., Kubát P., Zukalová M., Kavan L. *Journal of Physical Chemistry C* **115**, 11156 (2011).

Mobilita kyslíkového atomu v krystalové mřížce $TiO_2$ byla prokázána zcela spontánní izotopovou výměnou s $CO_2$. Po kalcinaci byl vzorek A450 přesypán od kyvety, která byla následně napuštěna 2 Torr $CO_2$ přirozeného izotopového složení (0,39 % $C^{16,18}O_2$ a 0,0004 % $C^{18,18}O_2$)[136]. Ukázalo se, že směs se velice rychle obohacuje o plynný $C^{18,18}O_2$ (až $10^4$ x) již během několika desítek minut a rovnováha se ustálí během hodin (2,9 % $C^{16,18}O_2$ a 37,7 % $C^{18,18}O_2$). Mechanismus výměny lze popsat vstupem jednoho z kyslíků $^{16}O$ molekuly $C^{16,16}O_2$ do vakance v krystalové mřížce $Ti^{18}O_2$. Tento atom ve vakanci zůstává a místo něj je na molekulu navázán sousední atom $^{18}O$ patřící do struktury $Ti^{18}O_2$. Vzniká tak molekula $C^{16,18}O_2$ odchází a podstupuje stejný proces za vzniku finálního produktu $C^{18,18}O_2$. Oproti tomu výměna mezi $C^{16}O$ a $Ti^{18}O_2$ neprobíhá vzhledem k tomu, že kyslík do vakance nevstupuje a CO se váže přímo na atom Ti. Při ozařování nevyžíhaného vzorku (A200) v přítomnosti $CO_2$ byl kromě izotopové výměny zjištěn také vznik methanu a acetylenu.

Studium fotokatalytického vzniku methanu na povrchu oxidů kovů ($TiO_2$ a dalších) je pro nás zajímavé z hlediska dodnes uspokojivě nevysvětleného původu methanu na Saturnově měsíci Titanu[137] a zejména na Marsu[138]. Methan v případě Titanu mohl být během formování měsíce částečně generován fotochemicky a v případě Marsu se tak může dít do dnes působením fotoaktivních minerálů[139,140] na $H_2O$ a $CO_2$. V případě Marsu tento argument podporuje zejména sezónní fluktuace obsahu methanu v atmosféře, jehož koncentrace rostou během Marsovského léta[141].

### 3.3.3. Fotochemie a FTIR spektrometrie interakce kyseliny mravenčí s nanočásticemi anatasu $Ti^{18}O_2$

(předkládaná publikace **Photochemistry and gas phase FTIR spectroscopy of formic acid interaction with anatase $Ti^{18}O_2$ nanoparticles.** Civiš, S.; Ferus, M.; Zukalová, M.; Kubát, P.; Kavan, L. *Journal of Physical Chemistry C*, v tisku (DOI: 10.1021/jp303011a), (2012).

Mechanismus izotopové výměny a fotokatalytické vlastnosti $TiO_2$ byly následně studovány za použití kyseliny mravenčí. Vzorek kalcinovaného anatasu $Ti^{18}O_2$ (A450) byl opět umístěn do evakuované kyvety, která byla následně naplněna parami kyseliny mravenčí $HC^{16}O^{16}OH$. Měření izotopového složení plynné fáze pomocí vysoce rozlišené spektrometrie prokázalo, že nedochází k výměně kyslíku $^{18}O$ mezi kyselinou mravenčí a oxidem titaničitým a navíc dochází k zablokování

aktivních míst povrchu, takže nedochází ani k výměně mezi $C^{16}O_2$ a $Ti^{18}O_2$. Pokud je však povrch $Ti^{18}O_2$ ozařován UV zářením (UV lampa a XeCl laser), dochází k rozkladu $HC^{16}O^{16}OH$ za vzniku $C^{16}O$ a $C^{16}O_2$. Uvolněná aktivní místa pak následně umožní vznik $C^{16,18}O_2$ a $C^{18}O_2$, které jsou rozkládány za vzniku stopových množství $C^{18}O$.

## 4. Závěr

Předkládaná dizertační práce je tvořena souborem studií zaměřených na výzkum procesů, při kterých jsou generovány částice mající omezenou dobu života. Studium těchto specií se týká dynamiky jednoduchých molekulárních fragmentů (radikálů, iontů) a nestabilních molekul v mračnech v mezihvězdném prostoru, ve hvězdách a jejich atmosférách či kometách a reakcí těchto jednoduchých látek za vzniku organických molekul, biomolekul a jejich prekurzorů, diskutován je také vliv látek s katalytickým účinkem ($TiO_2$).

Byla studována dynamika nestabilních látek v doutnavém výboji v methanu a vybraných prekurzorech HNC/HCN a radikálů CN, které jsou významnými speciemi v kosmickém chemismu a jsou považovány za prekurzory biomolekul. V laserové jiskře pak byl studován rozklad formamidu, který je předpokládaným prekurzorem nukleových bází a aminokyselin. V souvislosti s použitím izotopově značených sloučenin a $TiO_2$ jako katalyzátoru byly studovány fotochemické vlastnosti tohoto materiálu a izotopová výměna s plynnou fází.

# 5. Použitá Literatura

1  Heidarzadeh, T.: *A history of physical theories of comets, from Aristotle to Whipple.* Springer 2008.
2  Lockyer, J. N.: *Appendix to the Bakerian Lecture. On the Classification of Heavenly Bodies*, 157, (1889). Přístupné z URL: <http://ia700600.us.archive.org/26/items/philtrans07401003/07401003.pdf>, staženo 28.2.2012.
3  Chambers, G. G.: *A Handbook of Descriptive and Practical Astronomy.* IV. ed., Clarendon Press., Oxford 1890.
4  Schmidt, T. W.: C*omputational Spectroscopy: Methods, Experiments and Applications.* Wiley, Weinheim 2010.
5  Fowler, A.: Terrestrial Repuroduction of the Spectra of the Tails of Recent Comets. *Monthly Notices of the Royal Astronomical Society* **70**, 176 (1909).
6  Fowler, A.: The Origin of Spectra. *J. Roy. Astron. Soc. Canad.* **18**, 373 (1924).
7  Mulliken, R. S.: Electronic States and Band Spectrum Structure in Diatomic Molecules. *Phys. Rev.* **28**, 481 (1926).
8  Databáze dostupná on−line z URL: <http://www.astrochymist.org/astrochymist_mole.html>, staženo 28.2.2012.
9  Databáze NIST dostupná on−line z URL: <http://www.nist.gov/pml/data/asd.cfm>, staženo 23.3.2012.
10  Moudens, A.; Georges, R.; Benidar, A.; Amyay, B.; Herman, M.; Fayt, A.; Plez, B. *J. Quant. Rad. Transf.* **112**, 540 − 549 (2011).
11  Vinatier, S., Bézard, B., Coustenis, A. a kol. *Icarus* **188**, 120 − 138 (2007).
12  Seager, S.; Deming, D.; Blandford, R.; Faber, S. M.; Van Dishoeck, E.; Kormendy, *J. Ann. Rev. Astron. Astrophys.* **45**, 631 − 672 (2010).
13  Pendeleton, Y. J.; Allamandola, L. J. *Astrophys. J. Suppl.* **138**, 75 − 98 (2002).
14  Grinn, R. G. *Planet. Space. Sci.* **30**, 741 − 753 (1982).
15  Pepin, R. O. *Earth and Planet. Sci. Lett.* **252**, 1−14 (2006).
16  Kwok, S. *Astrophys. Space Sci.* **319**, 5 − 21 (2009).
17  Balucani, N. *Int. J. Mol. Sci.* **10**, 2304 − 2335 (2009).
18  Podlech, *J. Cell. Mol. Life. Sci.* **58**, 44 − 60 (2001).
19  Orgel, L. E. *Critical Rev. in Biochemistry and Molec. Biol.* **39**, 99 − 123 (2004).
20  Jarosik, N. a kol. *Astrophys. J. Suppl.* **192**, 1 − 15 (2011).
21  Gush, H. P., Halpern, M., Wishnow, E. H.: *Phys. Rev. Lett.* **65**, 537 − 540 (1990).
22  Newton, D. E. Chemistry of Space, Facts on File, Inc.; New York 2007.
23  Glover, S. C. O. *Proc. IAU Symp. "The Molecular Universe"* **280**, 1 − 12.
24  Stancil, P.: *Stellar Evolution, Stellar Explosions and Galactic Chemial Evolution*, 145 − 148 (1998).
25  Puy, D.; Signore, M. *New Astron. Rev.* **51**, 411 − 416 (2007).
26  Dalgarno, A.; Van der Loo, M. P. J. *Astrophys. J.* **646**, L91 − L94 (2006).
27  Bromm, V.; Larson, R. B. *Annu. Rev. Astron. Astrophys.* **42**, 79 − 118 (2004).
28  Kleczek, J. *Velká encyklopedie vesmíru.* Academia, Praha 2002, str. 319.
29  Henning, T.; Salama, F. *Science* **282**, 2204 − 2210 (1998).
30  Pratap, P.; Dickens, J. E.; Snell, R. L.; Miralles, M. P.; Bergin, E. A.; Irvine, W. M.; Schloerb, F. P. *Astrophys. J.* **486**, 862 − 885 (1997).
31  Smith, I. W. M.; Herbst, E.; Chang, Q. *Mon. Not. Roy. Astron. Soc.* **350**, 323 − 330 (2004).
32  Blake, G. A.; Sutton, E. C.; Masson, C. R.; Phillips, T. G. *Astrophys. J.* **315**, 621 − 645 (1987).
33  Ehrenfreund, P.; Charnley, S. B. *Annu. Rev. Astron. Astrophys.* **38**, 427 − 483 (2000).
34  Sims, I. R.; Karthäuser, J.; Smith, I. W. M. *Chem. Phys. Lett.* **211**, 461 − 468 (1993).
35  Tielens, A.; Hagen W. *Astron. Astrophys.* **114**, 245 − 260 (1982).
36  Ehrenfreund, P.; Boogert, A.; Gerakines, P. *Faraday Discussions* **109**, 463–74 (1998).
37  Tielens, A.; Whittet D. C. B. *Molecules in Astrophysics: Probes and Processes*, ed. EF van Dishoeck, pp. 45–60. Dordrecht: Kluwer 1997.
38  Herrmann, F.; Madden, S. C.; Nikola, T.; Poglitsch, A.; Timmermann, R.; Geis, N.; Townes, C. H.; Stacey, G. J. *Astrophys. J.* **481**, 343 − 354 (1997).
39  Kawaguchi, K.; Baskakov, O.; Hosaki, Y.; Hama, Y.; Kugimiya, C. *Chem. Phys. Lett.* **3−4**, 293−298 (2003).
40  Kawaguchi, K.; Hama, Y.; Nishida, S. *J. Mol. Spec.* **232**, 1−13 (2005).
41  Civiš, S.; Kubát, P.; Nishida, S.; Kawaguchi, K. *Chem. Phys. Lett.* **418**, 448−453 (2006).
42  Civiš, S.; Uhlíková−Šedivcová, T.; Kubelík, P.; Kawaguchi, K. J. Mol. Spec. 250, 20−26 (2008).
43  Kubelík, P. dizertační práce, PřF UK, Praha 2012.
44  Perry, J. J.; Kim, Y. H.; Fox, J. L.; Porter, H. S. *J. Geophys. Res.* **104**, 16541−16565 (1999).
45  Wu, Y. J.; Wu, C.Y.R.; Chou, S. L.; Lin, M.Y.; Lu, H.C.; Lo, J.I.; Cheng, B.M. *Astrophys. J.* **746**, art. no. 175 (2012).
46  Zahnle, K.; Schaefer, L.; Fegley, B. Cold. Spring. Harb. Perspect. Biol. 2:a004895 (2010).
47  Fray, N.; Bénilan, Y.; Cottin, H.; Gazeau, M.-C.; Crovisier, J. *Planet. Space Sci.* **53**, 1243-1262 (2005).
48  Nyman, L., A.; Olofsson, H.; Johansson, L. E. B.; Carstrom, U.; Wolstencroft, R. *Astron. Astrophys.* **1**, 377 (1993).
49  Lellouch, E.; Romani, P. N.; Rosenqvist, J. *Icarus* **108**, 112 (1994).
50  Barber, R.J.; Harris, G.J.; Tennyson, J. *J. Chem. Phys.* **24**, 11239 (2002).
51  Rodgers, S. D.; Charnley, S. B. *Astrophys. J.* **501**, L227 (1998).
52  D. A. Neufeld, P. Schilke, K. M. Menten, M. G. Wolfire, J. H. Black, F. Schuller, H. S. P. Müller, S. Thorwirth, R. Güsten, and S. Philipp. *A&A* **454**, L37−L40 (2006).
53  J. Cernicharo and M. Guélin, *A&A* 183:L10−L12 (1987).
54  D. A. Neufeld, J. Zmuidzinas, P. Schilke, and T. G. Phillips, *Astrophys. J.* **488**, L141−L144 (1997).
55  Nagai, M.; Hori, M.; *Jpn. J. Appl. Phys.* **3A**,1176−1180 (2007).

56  Kim, J. H.; Chung, K. H.; Yoo, Y. S. *J. Korean. Pyhs. Soc.* **47**, 249 (2005).

57  Shapiro, R. *Orig. Life Evol. Biosph.* **18**, 71−85 (1987).

58  Ferris, J. P.; Joshi, P. C.; Edelson, E. H.; Lawless, J. G. *J. Mol. Evol.* **11**, 293–311 (1978).

59  Crovisier, J. *Asteroids, Comets, Meteors. Proc. IAU Symp.* **229**, 133−152 (2006).

60  Chyba, Ch.; Sagan, C. *Nature* **355**, 125 − 132 (1992).

61  Berstein, M. *Philos. Trans. Roy. Soc.* B **361**, 1689−1702 (2006).

62  Balucani, N. *Int. J. Mol. Sci.* **10**, 2304 − 2335 (2009).

63  Miller, S. L. *Chem. Scripta* **26B**, 5 − 11 (1986).

64  Cleaves, H. J.; Chalmers, J. H.; Laszano, A.; Miller, S. L. *Orig. Life. Evol. Biosph.* **38**, 105−115, (2008).

65  Bouvier, A.; Wadhwa, M. *Nature Geoscience* **3**, 637 − 641 (2010).

66  Zhang, Y. *Earth−Sci. Rev.* **59**, 235 − 263 (2002).

67  Harrison, T. M. *Ann. Rev. Earth Planet. Sci.* **37**, 479 − 505 (2009).

68  Pepin, R. *Earth and Planetary Sci. Lett.* **252**, 1 − 14 (2006).

69  Marty, B. Earth Planet. Sci. Lett. 94, 45−56 (1989).

70  Bell, K. R.; Cassen, P. M.; Wasson, J. T.; Woolum, D. S. The FU orionis phenomenon and solar nebula material. Protostars and Planets IV (ed. V. Mannings;  A. P.Boss; S. S. Russell), str. 897. Tucson, AZ: University of Arizona Press.

71  Farley, K. A.; Neroda, E. *Annu. Rev. Earth Planet. Sci.* **26**, 189–218 (1998).

72  Trail, D.; Watson, E. B.; Tailby, N. D. *Nature* **480**, 79−82 (2011).

73  Stribling, R.; Miller, S. L. *Orig. Life Evol. Biosph.* **17**, 261–273 (1987).

74  Kasting, J. F. *Science* **259**, 920 − 926 (1993).

75  Pinto, J. P.; Gladstone, G. R.; Yung, Y. L. *Science* **210**, 183 − 184 (1980).

76  Chameides, W. L.; Walker, J. C. G. *Orig. Life Evol. Biosph.* **11**, 291−302 (1981).

77  McClendon, J. H. *Earth Sci. Rev.* **47**, 71 − 93 (1999).

78  LaRowe, D. E.; Regnier, P. *Orig. Life Evol. Biosph.* **38**, 383−397 (2008).

79  Voet, D.; Voet, J.G.; Pratt, C.W. Fundamentals of biochemistry. Wiley, New York (1999).

80  Dauphas, N.  *Icarus* **165**, 326–339 (2003).

81  Ehrenfreund, P.; Irvine, W.; Becker, L.; Blank, J.; Brucato, J. R.; Colangeli, L.; Derenne, S.; Despois, D.; Dutrey, A.; Fraaije, H.; Lazcano, A.; Owen, T.; Robert, F. *Rep. Prog. Phys.* **65**, 1427−1487 (2002).

82  Dauphas, N.; Robert, F.; Marty, B.  *Icarus* **148**, 508–512 (2000).

83  Morbidelli, A.; Chambers, J.; Lunine, J.I.; Petit, J.M.; Robert, F. *Meteorit. Planet. Sci.* **35**, 1309–1320 (2000).

84  Pinti, D. L. *Lectures in Atrobiology* **I**, 83–112 (2005). Springer−Verlag Berlin Heidelberg.

85  Kerridge, J. F. *Geochim. Cosmochim. Acta* **49**, 1707−1714 (1985).

86  Pizzarello, S.; Shock, E. *Cold Spring Harb. Perspect. Biol.* **2**, 1–19 (2010).

87  Cody, G. D.; Alexander, C. M. O. *Geochim. Cosmochim. Acta* **69**, 1085−1097 (2005).

88  Fomenkova, M. N.; Chang, S.; Mukhin, L. M. *Geochim. Cosmochim. Acta* **20**, 4503−4512 (1994).

89  Anders, E.; Owen, T. *Nature* **330**, 632−635 (1989).

90  Glikson, A. Y. *J. Geodynamics* **32**, 205 − 229 (2001).

91  Chyba, C. F.; Sagan, C. *Comets and the Origin and Evolution of Life*, 147−173, Springer, Berlin 1997.

92  Falkowski, P. G.; Barber, R. T.; Smetacek, V. Science 281, 200−206 (1998).

93  Miller, S. L. *Science* **117**, 528–529 (1953).

94  Oró, J. *Nature* **191**, 1193−1194 (1961).

95  Mojzsis, S. J.; Arrhenius, G.; McKeegan, K. D.; Harrison, T. M.; Nutman, A. P.; Friends, C. R. L. *Nature* **384**, 55 − 59 (1996).

96  Schopf, J. W. *Science* **260**, 640−646 (1993).

97  Chyba, C. F.; Thomas, P. J.; Brookshaw L.; Sagan, C. *Science* **249**, 366−373 (1990).

98  Pierazzo, E.; Chyba, C. F. *Meteoritics and Planetary Space* **34**, 909−918 (1998).

99  Blank, J.; Miller, G; Ahrens, M. J.; Winans, R. E. Proc. 21st Symp. on Shock Waves, 1467 − 1472, Panther Press (1998).

100 Chyba, C. F. *Nature* **363**, 701−703 (1993).

101 Levasser−Regourd, A.−Ch.; Lasue, J.; Brouet, Y. ISSOL and Bioastronomy Joint International Conference, pp 28, O7a−3, Montpellier 2011.

102 Srama, R.; Woiwode, W.; Postberg, F.; Armes, S. P.; Fujii, S.; Dupin, D.; Ormond−Prout, J.; Sternovsky, Z.; Kempf, S.; Moragas−Kiostermeyer, G.; Mocker, A.; Grun, E. *Rapid. Communications in Mass Spectrometry* **23**, 3895−3906 (2009).

103 Managadze, G. *Int. J. Astrobiology* **9**, 157−174 (2010).

104 Pierazzo, E.; Chyba, C. F. *Meteoritics Planet. Sci.* **34**, 909−918 (1999).

105 Elert, M. L.; Zybin, S. V.; White, C. T. *J. Chem. Phys.* **118**, 9795−9802 (2003).

106 Tingle, T. N.; Tyburczy, J. A.; Ahrens, T. J.; Becker, C. H. *Orig. Life Evol. Biosph.* **21**, 385−397 (1992).

107 Peterson, E; Horz, F.; Chang, S. *Geochim. Cosmochim. Acta* **61**, 3937–50 (1997).

108 Cooper, G. W.; Horz. F.; Oleary, A.; Chang, S. *Lunar Planet Sci. Conf.* **31**, 3232–3233 (2000).

109 Blank, J.; Miller, G.; Ahrens, M. J.; Winans, R. E. *Orig. Life Evol.  Biosph.* **31**, 15–51 (2001).

110 Ishimaru, R.; Senshu, H.; Sugita, S.; Matsui, T. *Icarus* **210**, 411–423 (2010).

111 Babánková, D.; Civiš, S.; Juha, L. *Progress Quant. Electronics* **30**, 75−88 (2006).

112 Jungwirth K. a kol.: *Phys. Plasma* **8**, 2495 (2001).

113 Civiš, S.; Juha, L.; Babánková, D.; Cvačka, J.; Frank,O.; Jehlička, J.; Králiková, B.; Krása, J.; Kubát, P.; Muck, A.; Pfeifer, M.; Skála, J.; Ullschmied, J. *Chem. Phys. Lett.* **386**, 169 (2004).

114 Babankova, D.; Civis, S.; Juha, L.; Bittner, M.; Cihelka, J.; Pfeifer, M.; Skala, J.; Bartnik, A.; Fiedorowicz, H.; Mikolajczik, J.; Ryc, L.; Sedivcova, T. *J. Phys. Chem. A* **110**, 12113 (2006).

115 Bittner, M.; Babánková, D.; Juha, L.; Civiš, S.; Cihelka, J.; Bartnik, A.; Fiedorovicz, H.; Mikolajczyk, J.; Ryc, L. *WDS´06 Proc. Contrib. Papers* **II**, 86−90 (2006).

116 Cottin, H.; Gazeau, M. C.; Raulin, F. *Planet. Space Sci.* **47**, 1141−1162 (1999).

117 Schaeffer, L.; Fegley, B. *Astrophys. J.* **618**, 1079−1085 (2005).

118 Civis, S; Juha, L.; Babankova, D; Cvacka, J.; Frank, O.; Jehlicka, J.; Kralikova, B.; Krasa, J.; Kubat, P.; Muck, A.; Pfeifer, M.; Skala, J.; Ullschmied, J. *Chem. Phys. Lett.* **386**, 169 (2004).

119 Goldman, N.; Reed, E. J.; Fried, L. E.; Kuo, I. F. W.; Maiti, A. *Nature Chem.* **2**, 949–954 (2010).

120 Barks, H. L.; Buckley, R.; Grieves, G. A.; Di Mauro, E.; Hud, N.; Orlando, T. M. *Chembiochem* **2010**,11, 1240.

121 Saladino, R.; Crestini, C.; Ciciriello, F.; Di Mauro, E.; Costanzo, G. *J. Biol. Chem.* **281**, 5790 (2006).

122 Saladino, R.; Crestini, C.; Costanzo, G.; DiMauro, E. Top. *Curr. Chem.* **259**, 29, (2005).

123 Saladino, R.; Ciambecchini, U.; Crestini, C.; Costanzo, G.; Negri, R.; Di Mauro, E. *ChemBioChem* **4**, 514 (2003).

124 Bada, J. L. *Earth and Planetary Science Letters* **2004**, 226, 1.

125 Miyakawa, S.; Cleaves, H. J.; Miller, S. L. *Origin of Life Evolut. Biosphere* **2002**, 32, 195.

126 Nguyen, V. S.; Abbott, H. L.; Dawley, M. M.; Orlando, T. M.; Leszczynski, J.; Nguyen, M. T. *J. Phys. Chem. A* 115, 841 (2011).

127 Kasting, J. F.; Howard, M. T. *Phil. Trans. Roy. Soc.* B **361**, 1733−1742 (2006).

128 Caldeira, K.; Kasting, J. F. Susceptibility of the early Earth to irreversible glaciation caused by carbon dioxide clouds. *Nature* **359**, 226−228 (1992).

129 Michalčíková R. Diplomová práce. PřF UK, Praha 2012.

130 Bennett, S. W.; Keller, A. A. *Appl. Catal.* B **102**, 600−607 (2011).

131 Reyes−Gil, K. R.; Sun, Y. P.; Reyes−Garcia, E.; Raftery, D. *J. Phys. Chem. C* **113**, 12558−12570 (2009).

132 Emeline, A. V.; Kuzmin, G. N.; Basov, L. L.; Serpone, N. *J. Photochem. Photobiol.* A **174**, 214−221 (2005).

133 Frank, S.N.; Bard, A.J. *J. Am. Chem. Soc.* **99**, 303 (1977).

134 Batzill, M. *Energy Eviron. Sci.* **4**, 3275−3286 (2011).

135 Fujishima, A.; Zhang, X. *C. R. Chimie* **9**, 750−760 (2006).

136 The HITRAN database program, <http://cfa−www.harvard.edu/HITRAN>.

137 Tobie, G.; Choukroun, M.; Grasset, O.; Le Mouélic, S.; Lunine, J. I.; Sotin, C.; Bourgeois, O.; Gautier, D.; Hirtzig, M.; Lebonnois, S.; Le Corre, L. *Phil. Trans. Roy. Soc.* A **1889**, 617−631 (2009).

138 ten Kate, I. L. *Astrobiology* **10**, 589−603 (2010).

139 Quinn, R. C.; Zent, A. P. *Orig. Life Evol. Biosph.* **29**, 59−72 (1999).

140 Pang, K.; Ajello, J. M. *Icarus* **30**, 63−74 (1977).

141 Mumma, M.J., Villanueva, G.L., Novak, R.E., Hewagama, T., Bonev, B.P., DiSanti, M.A., Mandell, A.M., Smith, M.D. Strong release of methane on Mars in northern summer 2003. *Science* **323**, 1041–1045 (2009).

# Předkládané publikace

# Vysoce rozlišená spektrometrie s FOURIEROVOU TRANSFORMACÍ A JEJÍ LABORATORNÍ APLIKACE

**Martin Ferus**[1,2]**, Svatopluk Civiš**[1]

[1] Ústav fyzikální chemie Jaroslava Heyrovského AV ČR, v. v. i., Dolejškova 2155/3, 182 23 Praha 8
[2] Fyzikální ústav AV ČR, v. v. i., Na Slovance 2, 182 21 Praha 8

*Vyložíme zde fyzikální základy spektrometrie s Fourierovou transformací. Ukážeme jednoduchý postup nastiňující odvození základního vztahu Fourierovy transformace, podáme popis uspořádání spektrometru a vysvětlíme princip časově rozlišených spektrálních měření. Článek rovněž stručně seznamuje čtenáře se zajímavými výsledky, dosaženými na našem pracovišti pomocí vysoce rozlišujícího spektrometru s Fourierovou transformací Bruker IFS 120 HR, v současnosti jediném přístroji tohoto druhu u nás. Následující řádky jsou určeny zejména těm, kteří se chtějí podrobněji seznámit s touto metodou a s možnostmi jejího využití.*

## ÚVOD

Spektrometrie s Fourierovou transformací (FT spektrometrie) je padesát šest let starou metodou, která si našla řadu aplikací v laboratořích i ve výzkumu atmosféry a kosmu. V současné době jsou komerčně dostupné přístroje od velikosti stolního počítače až po aparatury dlouhé několik metrů poskytující rozlišení tisícin reciprokého centimetru, tedy v oblastech přirozených šířek absorpčních čar. Jediný vysoce rozlišující spektrometr v ČR se nachází na Ústavu fyzikální chemie Jaroslava Heyrovského. Tento přístroj byl aplikován v oblastech výzkumu životního prostředí, teoretického studia spekter a časově rozlišených měření emisních spekter nestabilních částic. Pořízením vysoce rozlišujícího spektrometru s Fourierovou transformací i další prací spektroskopických laboratoří na zmíněném ústavu je navázáno na spektroskopickou tradici tohoto pracoviště. Skupinou J. Plívy, M. Horáka, R. Sovičky a P. Engsta byl již dříve vyvíjen vysoce rozlišující spektrometr, který byl však založen na použití mřížky jako disperzního prvku.

## KRÁTCE Z HISTORIE

Francouzský matematik Jean Baptista Josef Fourier mohl být spisovatelem, ale ve třinácti letech si vybral jinou oblast svých zájmů: matematiku. V roce 1794 byl přijat na École Normale v Paříži a byl vyučován velikány své doby, jako byli Lagrange a Laplace. Fourier se zúčastnil Napoleonovy výpravy do Egypta a po návratu získal významné místo prefekta. V prvních létech 19. století začíná pracovat na svých nejvýznamnějších matematických pracích. Ačkoliv byla tehdy tato dnes ceněná díla považována za kontroverzní, bylo Fourierovi uděleno několik cen. Jeho závěry byly o desetiletí poté využity pozdějším nositelem Nobelovy ceny Albertem Michelsonem. Kromě toho, že Michelson je autorem experimentu vyvracejícího teorii světového éteru, zabýval se tento vědec rovněž Zeemanovým jevem. Pro tuto činnost sestrojil tzv. harmonický analyzátor pracující s 80 datovými body. Přístrojem byl schopen vzniklé dublety analyzovat právě pomocí algoritmů vycházejících z Fourierových prací. V roce 1952 Peter Fellgett navrhl první spektrometr s Fourierovou transformací. Přístroj byl pak sestrojen a odzkoušen skupinou Johna D. Stronga. S rozvojem počítačů byly ukončeny polemiky o tom, jestli je výhodnější klasická spektrometrie nebo spektrometrie Fourierova. Metoda byla využita při astronomických měřeních spekter planet (Pierre Connes a Janine Connesová), v kosmickém výzkumu pomocí sond (např. VIKING či NIMBUS), pozemských atmosféric-
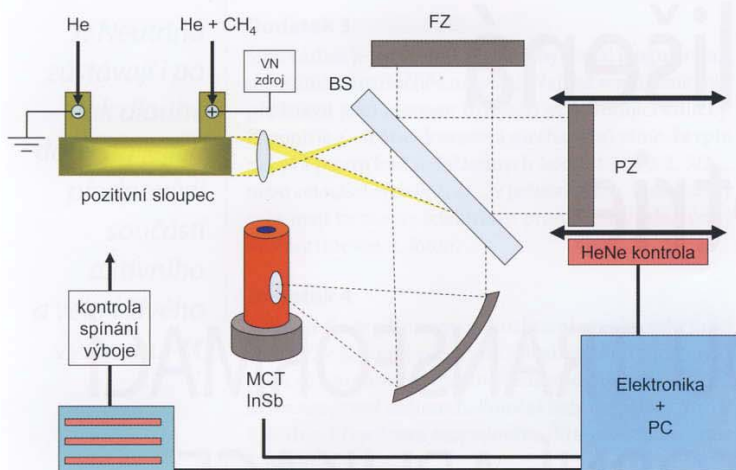
**Obr. 1** Základní částí spektrometru s Fourierovou transformací je interferometr. Na obrázku je ukázán řez spektrometrem s interferometrem Michelsonova typu. Ze zdroje záření (zde v emisním uspořádání se jedná o výbojovou celu) dopadají paprsky na dělič paprsků BS a odrážejí se od pohyblivého (PZ), resp. fixního (FZ) zrcadla. Procházející a odražené paprsky spolu interferují. V absorpčním uspořádání je mezi detektor a interferometr umístěna cela s měřeným vzorkem. Přidané elektronické komponenty slouží k akvizici dat při časově rozlišeném měření.

kých měřeních (Hajime Sakai a Randall E. Murphy) a mnoha laboratorních experimentech. Spektrometrie s Fourierovou transformací znamenala ještě jednu experimentální revoluci: pomocí této metody je možné jednoduše sledovat rychlé časové změny systému. Již v 60. a hlavně v 70. letech byly diskutovány a vyvinuty metody pro sledování časových změn v řádu milisekund i mikrosekund. V dalších letech již následovala měření s rozlišením v řádech nanosekund.

## TEORETICKÉ ZÁKLADY METODY

Algoritmus Fourierovy transformace vychází z rovnic pro interferenci paprsků. Základní částí spektrometru je interferometr, který generuje dva paprsky vzájemně posunuté o jistý dráhový rozdíl. Obr. 1 znázorňuje spektrometr s interferometrem Michelsonova typu v emisním uspořádání. Paprsek ze zdroje dopadá na dělič BS umístěný ve středu optické soustavy. Dělič je z částečně transparentního materiálu a propustí pouze polovinu z procházejícího záření. Toto záření putuje k pohyblivému zrcadlu PZ. Paprsky odražené děličem dopadají na zrcadlo fixní FZ. Obě frakce jsou na děliči opět sloučeny a vycházejí z optické soustavy interferometru ven, kde dopadají na detektor. Pohyblivé zrcadlo uděluje jedné z frakcí paprsků dráhový rozdíl $\delta$ (OPD – *Optical Path Difference*). Pro monochromatické záření platí, že výsledná intenzita $I_{AB}$ interferujících paprsků označených A a B bude dána jako čtverec součtu vlnových funkcí $\psi_A$ a $\psi_B$, tedy

$$I_{AB} = \left( \psi_A + \psi_B \right)^2 . \qquad (1)$$

Výsledná rovnice pro interferenci pak bude mít tvar

$$I_{AB} = I_A + I_B + 2\sqrt{I_A I_B} \cos (k\delta) , \qquad (2)$$

kde $k$ je vlnový vektor světla. V případě polychromatického záření dojdeme k rovnici

$$I(\delta) = \int_0^\infty I_k(k)dk + \int_0^\infty I_k \cos (k\delta)dk , \qquad (3)$$

kde $I_k$ je intenzita $k$-té monochromatické složky záření. Rovnici (3) lze přepsat jako

$$I(\delta) = \int_0^\infty I_k(k)dk + \int_0^\infty I_k(k) \frac{\exp(ik\delta) + \exp(-ik\delta)}{2} dk , \qquad (4)$$

kde $i$ je imaginární jednotka, a upravit do tvaru

$$I(\delta) = \frac{1}{2} I_0 + \frac{1}{2} \int_{-\infty}^\infty I_k(k) \exp(ik\delta) dk . \qquad (5)$$

Jestliže uvažujeme výsledný interferogram jako funkci, pro niž platí

$$S(\delta) = 2I(\delta) - I_0 , \qquad (6)$$

je $S(\delta)$ intenzita záření registrovaného detektorem, kde dosazením výrazu (6) do (5) dostaneme

$$S(\delta) = \int_{-\infty}^\infty I_k(k) \exp(ik\delta)dk . \qquad (7)$$

Protože vlnový vektor je dán rovnicí

$$k = \frac{2\pi}{\lambda} = 2\pi v , \qquad (8)$$

kde $\lambda$ je vlnová délka a $v$ je vlnočet, výsledná rovnice vyjadřující intenzitu záření $S(\delta)$ registrovaného detektorem bude mít tvar

$$S(\delta) = \int_{-\infty}^\infty I(v) \exp(2\pi i v\delta)dv . \qquad (9)$$

Fourierova transformace však má naopak vést ke spektru zdroje. Přepočetní vztah získáme inverzí této rovnice:

$$I(v) = \int_{-\infty}^\infty S(\delta) \exp(-2\pi i v\delta)d\delta . \qquad (10)$$

Tento výraz lze zjednodušit na tvar často zmiňovaný v literatuře použitím vzorce

$$\exp(-2\pi i v\delta) = \cos(2\pi v\delta) - i\sin 2\pi i v\delta; \qquad (11)$$

dostaneme

$$I(v) = \int_{-\infty}^{+\infty} S(\delta) \cos(2\pi v\delta)d\delta . \qquad (12)$$

Právě tato rovnice je klíčem k přepočtu interferogramu $S(\delta)$ registrovaného detektorem na spektrum zdroje $I(v)$.

Přístroj však snímá interferogram jen od dráhového rozdílu nula do maximálního dráhového rozdílu omezeného délkou dráhy pohyblivého zrcadla. Navíc interferogram není registrován spojitě, ale digitalizován v bodech. Každý interferogram se tak skládá z N vzorkovacích bodů. Rovnici Fourierovy transformace přepíšeme na výsledný tvar:

$$I(v_j) = \sum_{i=1}^m S(\delta_i) \cos(2\pi v_j \delta_i)\Delta\delta_i , \qquad (13)$$

kde $I(v_j)$ je intenzita záření zdroje na $j$-té pořadnici vlnočtu $v_j$ a $S(\delta_i)$ je intenzita signálu snímaného detektorem na $i$-té pořadnici dráhového rozdílu $\delta_i$. Přesná kontrola rychlosti a polohy pohyblivého zrcadla je zajištěna HeNe laserem pracujícím na vlnové délce 632,8 nm. Laserový paprsek prochází interferometrem po stejné dráze jako polychromatické záření a dopadá na fotodiodu. Dioda registruje interferogram podobný funkci kosinus s maximy při posunu o celistvé násobky vlnové délky $n \cdot \lambda$ (n = 1, 2, 3, ...) a minimy při posunu o $n \cdot \lambda/2$ (n = 1, 2, 3, ...). Z rovnice 13 vidíme, že bě-

hem jednoho pojezdu pohyblivého zrcadla (tzv. skenu) získáme informaci o celém zvoleném spektrálním rozsahu. Tato výhoda – možnost sledovat celé spektrum v časových relacích omezených pouze jedním skenem – je nazvána multiplexní výhodou nebo také výhodou Fellgettovou.

Ve spektrometru s interferometrem Michelsonova typu jsou interferující paprsky vedeny přes kyvetu se vzorkem a dopadají na detektor. Takto sestavený spektrometr neobsahuje žádný disperzní prvek (mřížku nebo hranol) a průchodnost systému $E$ (v anglosaské literatuře označována *étendue*) je fyzicky dána hlavně velikostí zrcadel a výkonem detektoru $R_{DET}$:

$$E = R_{DET} \cdot \Omega, \qquad (14)$$

kde $\Omega$ je prostorový úhel, pod nímž zrcadla soustřeďují svazek na detektor. Tento úhel je rovněž závislý na rozlišení, které může interferometr poskytnout. Podle svého objevitele je tato výhoda pojmenována Jacquinotova.

Vysoké rozlišení patří k další z výhod spektrometrie s Fourierovou transformací. Rozlišení dané parametrem $\Delta \nu$ (rozdíl vlnočtů dvou linií – interval, kterým je lze oddělit) je totiž dáno jako reciproká hodnota dráhového rozdílu paprsků $\delta_{max}$, resp. dvojnásobku dráhy pohyblivého zrcadla

$$\Delta \nu = 1 / \delta_{max}. \qquad (15)$$

U konvenčních přístrojů je rozlišení omezeno hustotou vrypů na mřížce. Tento parametr je však omezen výrobními možnostmi a dosáhnout lze rozlišení v řádech $10^{-2}$ cm$^{-1}$. To, že rozlišení je úměrné dráhovému rozdílu, vyplývá z vlastností interferogramu. Interferogram linií ve tvaru píku se skládá z pravidelně se opakujících oscilací, které jsou s rostoucím dráhovým rozdílem postupně tlumeny. Platí, že

$$\Delta \delta = 1 / N \Delta \nu, \qquad (16)$$

kde $N$ je počet bodů snímaných přístrojem. Abychom separovali velmi blízké linie, musíme tyto oscilace změřit – získat interferogram s dostatečným dráhovým rozdílem. Interferogram polychromatického spektra tedy obsahuje informace vedoucí k vysokým rozlišením právě v oblastech s nejmenší intenzitou a největším dráhovým rozdílem.

S rozlišením přímo souvisí numerická úprava spektra zvaná apodizace. Linie ve spektru má po provedení Fourierovy transformace jiný tvar než ve skutečnosti.

## K DALŠÍ ČETBĚ O SPEKTROSKOPII VYSOKÉHO ROZLIŠENÍ:

a) Monografie poskytující přehled o rané historii oboru a tradičních experimentálních postupech:
   S. Tolansky: *High Resolution Spectroscopy*, Methuen, London 1947.

b) Patrně nejrozšířenější učebnice-kompendium:
   J. M. Hollas: *High Resolution Spectroscopy*, 2. vyd., J. Wiley & Sons, Chichester-NY-Weinheim-Brisbane-Singapore-Toronto 1998.

c) Pro seznámení s příslušnými metodami laserové spektroskopie je asi nejvhodnější:
   W. Demtröder: *Laser Spectroscopy, Vol. 1 (Basic Principles) + Vol. 2 (Experimental Techniques)*, 4. vydání, Springer-Verlag, Berlin, vyjde v červenci 2008.

**Obr. 2** Řez spektrometrem Bruker IFS 120 v absorpčním uspořádání s charakteristikami jednotlivých komponent

Její intenzita je rozptýlena do podružných maxim. Abychom získali linii tvarem se blížící skutečnosti, je nutné interferogram vynásobit apodizační funkcí vhodného tvaru:

$$S(\nu_j) = \sum_{i=1}^{m} I(\delta_i) A(\delta_i) \cos(2\pi\nu_j \delta_i) \Delta \delta_i. \qquad (17)$$

Touto numerickou úpravou potlačíme podružná maxima (termín apodizace pochází z řeckého 'ά ποδος – bez chodidel). Linie v transformovaném spektru se však použitím apodizace rozšiřují a splývají, čímž klesá možnost separace dvou blízkých linií, roste parametr $\Delta \nu$ a klesá rozlišení.

## BRUKER IFS 120 HR

V České republice je používán zatím jediný vysoce rozlišující spektrometr s Fourierovou transformací v laboratoři FT a laserové spektrometrie na Ústavu fyzikální chemie Jaroslava Heyrovského v Praze. Jedná se o komerčně dostupný přístroj německé firmy Bruker typ IFS 120 HR, který byl obdržen darem od univerzity v německém Wuppertalu v roce 2004. V prodeji je již i pokročilejší verze Bruker IFS 125 HR. Systém pro měření časově rozlišených spekter byl původně sestaven na univerzitě v japonské Okayamě. Po řadě vylepšení je nyní stejný systém napojený na zmíněný spektrometr umístěn v naší laboratoři. V současnosti je tento přístroj za použití interferenčních filtrů schopen měřit absorpční i emisní spektra s rozlišením až 0,003 5 cm$^{-1}$ v intervalu vlnočtů od 400–25 000 cm$^{-1}$. Řez přístrojem a charakteristiky některých prvků znázorňuje obr. 2. Jako zdroje jsou používány wolframová žárovka a globarový zářič, děliče paprsků pro různé spektrální oblasti jsou zhotoveny z bromidu draselného, fluoridu vápenatého a křemene. K detekci signálu jsou použity polovodičové dusíkem chlazené detektory InSb, HgCdTe (tzv. MCT) a Si polovodičový detektor pracující při laboratorní teplotě. Ke kontrole polohy pohyblivého zrcadla je použit HeNe laser.

## SPEKTROMETRIE S ČASOVÝM ROZLIŠENÍM

Časově rozlišená spektrometrie s Fourierovou transformací je výhodná zejména z hlediska zisku spektra v širokém intervalu vlnočtů (multiplexní výhoda) a dobré optické průchodnosti systému (Jacquinoto-
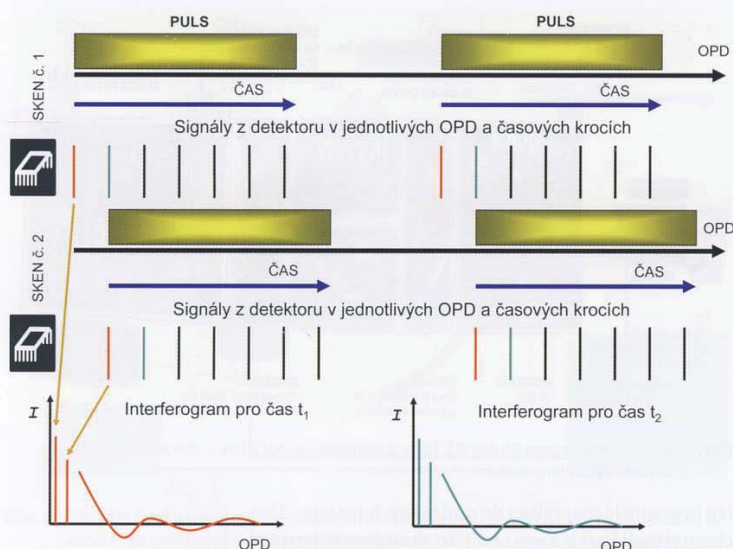
**Obr. 3** Schéma akvizice dat kontinuálním skenováním podle Mantze. Systém využívá pro zisk kompletního interferogramu více skenů. Výboj je přitom zpožděn tak, aby signál z detektoru pro jednotlivé dráhové rozdíly vždy příslušel stejnému časovému úseku.
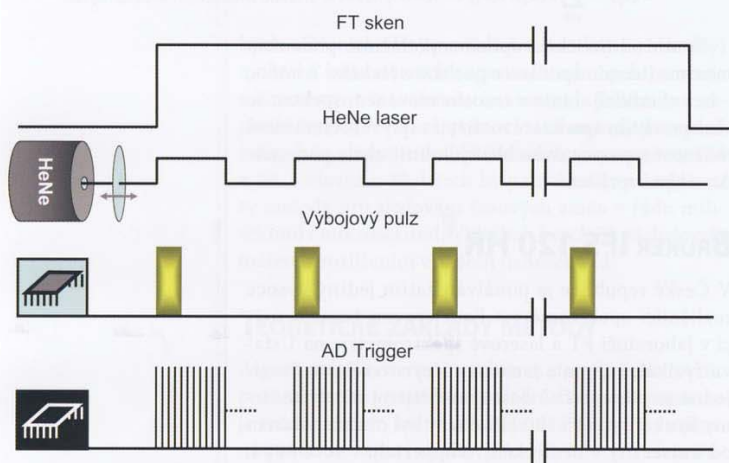


**Obr. 4** Akvizice dat FT. V každém optickém dráhovém rozdílu je iniciován výboj a jsou snímány časově posunuté signály z detektoru (AD trigger). Ze získaných dat je rekonstruován set časově posunutých interferogramů.

va výhoda), která vede k vysokým poměrům signálu k šumu (tzv. SNR, *signal-to-noise ratio*). Rychlost akvizice dat je omezena dobou trvání procesu, rychlostí odezvy detektoru a výkonem elektronických prvků. V zásadě můžeme rozlišit dva přístupy uplatňující se
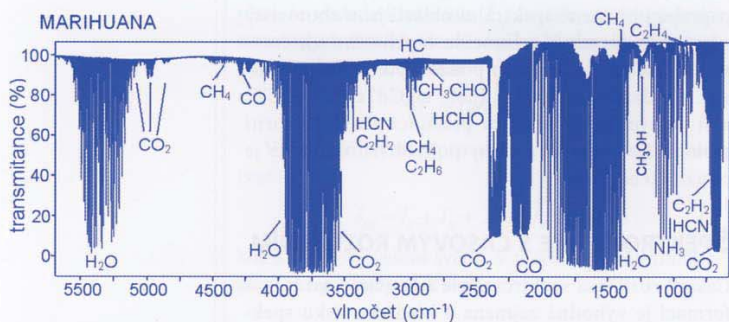


**Obr. 5** Absorpční spektrum kouře z marihuany s označenými absorpčními pásy jednotlivých látek

při zisku časově rozlišených spekter: techniky kontinuálního skenování a nekontinuálního skenování (*step scan*) [1].

Kontinuální skenování lze nejsnáze uplatnit tehdy, je-li délka sledovaného děje delší než čas potřebný k provedení jednoho skenu, tzn. k získání interferogramu až do maximálního dráhového rozdílu. Jednotlivými časově posunutými skeny získáme po sobě jdoucí interferogramy, jež lze přepočítat na konvenční spektrum. Při použití rychlého skenování a pojezdu zrcadla na krátkou vzdálenost lze dosáhnout rozlišení v desetinách vteřiny. Speciálním přístupem vhodným pro zisk časově rozlišených spekter dějů trvajících v řádech milisekund je technika rychlého kontinuálního skenování (setkáme se s termíny *rapid scan* nebo *fast scan*). Tento postup stejně jako další níže zmíněné metody vyžaduje, aby reakci bylo možno iniciovat v pulzním režimu, například za použití laseru, elektrického výboje, bombardování elektrony, UV výbojky apod. Přístroj provádí rychlý kontinuální sken a během pulzu snímá z detektoru signál příslušný k poloze zrcadla a času od počátku pulzní reakce. Při dalším skenu je opět prováděn stejný proces, ale tak, aby byl signál v daných dráhových rozdílech posunut o zvolený časový interval (obr. 3). Po akumulaci dostatečného množství dat z dalších a dalších skenů je rekonstruován interferogram. Při skenovací rychlosti 50 kHz je vzdálenost jednotlivých časových bodů 200 μs. Měření fotolýzy acetonu tímto systémem publikoval A. W. Mantz [2, 3] roku 1976. Metoda se však příliš neujala. Roli v tomto případě sehrála složitost systému, který lze nahradit výhodnějším uspořádáním. Výsledky měření byly navíc dílem artefaktů, na vině bylo hromadění produktů v měřicí cele.

Daleko výhodnější metoda nekontinuálního skenování v krocích (*step scan*) byla aplikována při studiu reakce dusíku s kyslíkem R. E. Murphym a H. Sakaiem [4, 5] v polovině sedmdesátých let. Interferogram je i v tomto případě rekonstruován z dat získaných během měření, avšak v rámci jednoho skenu. Z principu skenování v krocích vychází i akvizice dat realizovaná upraveným spektrometrem Bruker IFS 120 v naší laboratoři. Rozdílné však je, že zrcadlo není třeba zastavovat v definovaných dráhových rozdílech. Systém si přiblížíme následovně:

Poloha pohyblivého zrcadla Michelsonova interferometru je spektrometrem zjišťována pomocí snímání interferenčních maxim záření HeNe laseru. Vstupující signál v podobě kosinové funkce je digitálně zpracován na obdélníkové pulzy a je interním standardem interferometru. Frekvence těchto obdélníkových pulzů závisí na rychlosti pohybu pohyblivého zrcadla. V režimu klasického měření je frekvence obvykle 40 kHz, v případě časově rozlišených měření 10 kHz a menší. Externím procesorem je sledován počátek digitálního pulzu HeNe laseru, jeho pořadí a nulová poloha zrcadla. Během jednoho pulzu je snímán signál z detektoru (30 nebo až 64 signálů), tzv. AD trigger (viz obr. 4). Tyto signály jsou časově posunuty. Získáme tak matici $I(t_k, \delta_i)$ intenzity $I$ v časech $t_k$ ($k = 1, 2, 3, \dots 30$ nebo 64) pro daný optický dráhový rozdíl $\delta_i$ ($i$ je index značící nulový až maximální zvolený optický dráhový rozdíl). Do procesu snímání dat (AD trigger) lze vložit výbojový pulz s proměnnou délkou. Výsledkem je 30 až 64 interferogramů vzájemně časově

posunutých (1, 2 nebo 3 μs). V případě použití výbojového pulzu lze v časově posunutých interferogramech (spektrech) pozorovat procesy před pulzem, během pulzu a po jeho skončení. Velkou výhodou je, že pro každý daný časový interval je získáno vysoce rozlišené FT spektrum obsahující informace o všech liniích specií přítomných ve spektru. Výsledkem je, že každá linie ve spektru má svůj časově rozlišený profil.

## ENVIRONMENTÁLNÍ PROBLEMATIKA

První z mnoha aplikací bylo využití spektrometru Bruker IFS 120 ke stanovení majoritních složek spalin z různých materiálů. Měřená spektra byla získána při tlacích jednotek až desítek kPa. Za daných podmínek spektrometr poskytuje výhodu zejména vysoké citlivosti a širokého spektrálního rozsahu. Dosažení vysokého rozlišení vzhledem k tlakovému rozšíření linií nehraje prvořadou úlohu. Obr. 5, 6 a 7 zobrazují dvě z měřených spekter – spektrum kouře z marihuany, spalování dřeva a spaliny dieselového motoru. Ve spektrech jsou zastoupeny typické produkty spalovacích procesů: jednoduché organické sloučeniny jako methan, ethan, ethylen, acetylen, formaldehyd, acetaldehyd a některé specifické produkty – kyanovodík, metanol, aceton a amoniak v kouři z marihuany. Není bez zajímavosti, že kouř z marihuany se kromě přítomnosti amoniaku kvalitativně neliší od cigaretového kouře.

V jiné studii jsme se zaměřili na produkty spalování plastu: PET (polyethylentereftalátu – obr. 8) a polyuretanů. Ve spalinách byla nalezena řada zmíněných organických látek. Za zmínku stojí přítomnost kyanovodíku ve spalinách z polyuretanu.

Další oblastí aplikace FT spektrometru bylo kvantitativní stanovení zastoupení metanu v bioplynu produkovaném skládkou a čistírnou odpadních vod. Vysoce rozlišená spektra poskytla dostatek silných linií, pro něž jsme stanovili kalibrační závislost absorbance na tlaku plynu. Bylo zjištěno, že bioplyn z čistírny odpadních vod na Císařském ostrově obsahuje v porovnání se skládkovými plyny nejvíce methanu – 71,1 %. Vzorky ze skládky komunálního odpadu v Dolních Chabrech a Ďáblicích obsahovaly 54,7, resp. 58,4 % methanu. Ostatními složkami jsou oxid uhličitý a voda.

Na těchto příkladech lze ukázat, že tato metoda je vzhledem k velkému spektrálnímu rozsahu a citlivosti dobře použitelná pro měření hlavních složek plynných směsí.

## MĚŘENÍ VYSOCE ROZLIŠENÝCH SPEKTER

Měření s vysokým rozlišením jsou důležitá zejména pro teoretické studium absorpčních spekter. Při běžných laboratorních experimentech však nemá smysl vždy trvat na časově náročných měřeních s maximálním roz-

### DALŠÍ ČESKÁ LITERATURA
### O FOURIEROVSKÉ IČ SPEKTROSKOPII:

B. Strauch: „Infračervená spektroskopie s Fourierovou transformací", v: *Nové směry v analytické chemii*, svazek IV, SNTL, Praha 1988, s. 52-88.

D. Papoušek: *O kvantech energie, molekulách a vesmíru*, Academia, Praha 1985, s. 58-61.
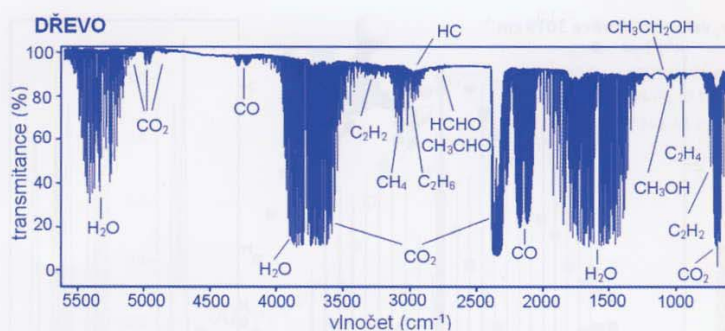
**Obr. 6** Absorpční spektrum spalin hoření dřeva s označenými absorpčními pásy jednotlivých látek
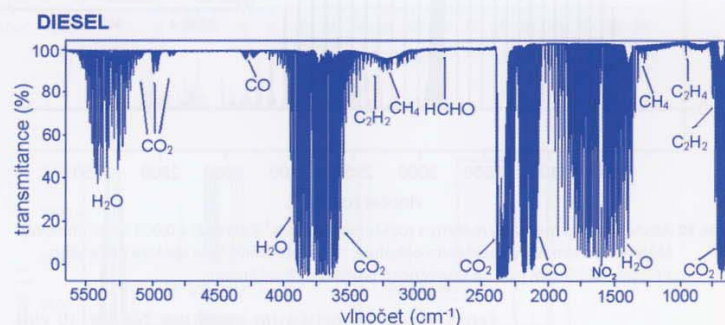


**Obr. 7** Absorpční spektrum spalin dieselového motoru s označenými absorpčními pásy jednotlivých látek
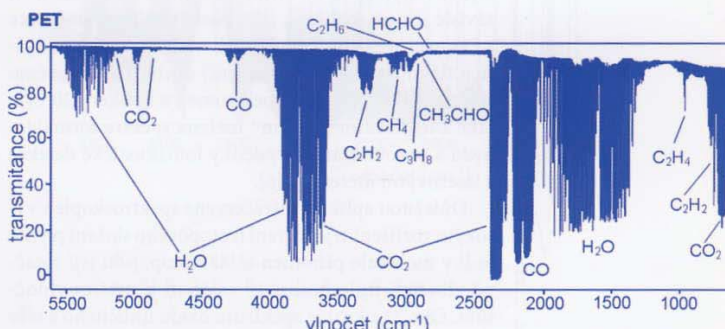


**Obr. 8** Absorpční spektrum spalin PET s označenými absorpčními pásy jednotlivých látek

lišením. Linie rotačně-vibračních přechodů složitějších látek jsou rozšířeny natolik, že fyzicky splynou v jeden pás, a tudíž je nelze ani při nejvyšších rozlišeních vzájemně separovat. Tento případ ukazuje spektrum acetonu měřené s maximálním rozlišením 0,003 5 cm$^{-1}$ na obrázku 9. Je vidět, že i přes vysoké rozlišení je možné pozorovat jen obálku rotačně-vibračního pásu skupiny -CH$_3$. U jednodušších látek, jako je methan, však mě-
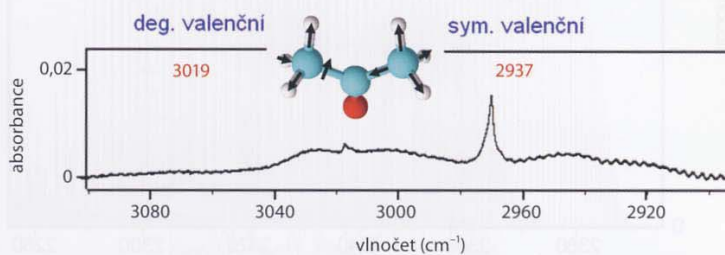


**Obr. 9** Absorpční spektrum acetonu. I při maximálním rozlišení zde splývají jednotlivé linie v jediný pás.

**v₃ valenční vibrace 3019 cm⁻¹**
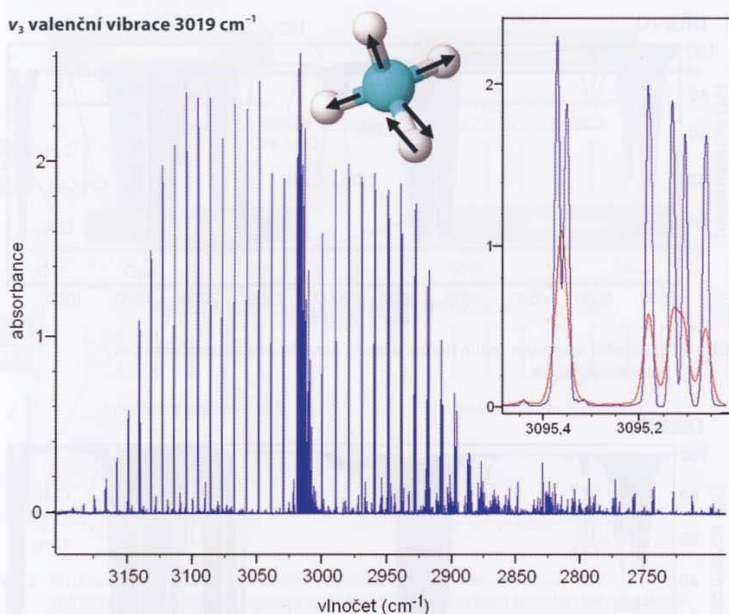


**Obr. 10** Absorpční pás methanu měřený s rozlišením 0,02 cm⁻¹ (červená) a 0,003 5 cm⁻¹ (modrá). Měření s maximálním rozlišením odhalují, že na jednotlivé linie spektra měřeného s nižším rozlišením jsou ve skutečnosti tvořeny dalšími liniemi.

ření s vysokým rozlišením smysl má. Na obr. 10 vidíme, že některé linie ve spektru měřeném s rozlišením 0,02 cm⁻¹ jsou při měření s maximálním rozlišením separovány do dalších linií. Rozšíření linií však není závislé jen na rozlišení, jaké poskytuje instrumentace a Dopplerově jevu. Zejména při měření vzorků za vyšších tlaků (atmosférická měření) dochází k tlakovému rozšíření linií. Pomocí spektrometru Bruker 120 byla také s rozlišením 0,02 cm⁻¹ měřena spektra formaldehydu a porovnávána s výsledky fotoakustické detekce a laserovými měřeními [6].

Důležitou aplikací infračervené spektroskopie s vysokým rozlišením je měření izotopového složení plynů. Je-li v molekule přítomen těžší izotop, jsou její rotačně vibrační linie posunuty směrem k nižším vlnočtům. Obr. 11 ukazuje spektrum oxidu uhličitého a též sloučeniny mající v molekule dva kyslíky ¹⁸O. Pomocí
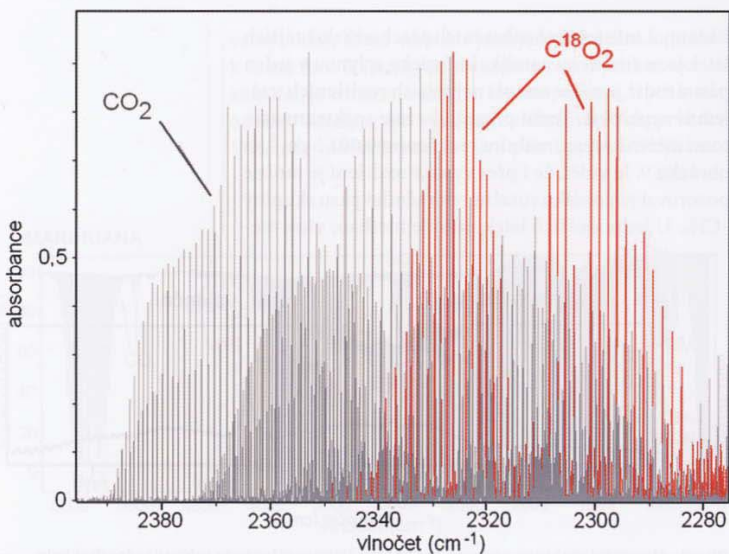
spektrometru byla sledována izotopová výměna mezi vodou $H_2^{18}O$ a oxidem uhličitým $C^{16}O_2$. Experiment byl slepým pokusem k měření vzorků získaných odstřelováním směsi CO:N₂:$H_2^{18}O$ (1:1:2 ml při atmosférickém tlaku) pomocí pražského laserového systému Asterix IV (PALS). Jednodenní měření odhalila nárůst oxidu uhličitého s jedním i dvěma ¹⁸O během několika výstřelů, normální izotopová výměna v téže směsi přitom trvá několik týdnů. Závěry z tohoto experimentu se nyní připravují k publikaci.

## ČASOVĚ ROZLIŠENÁ SPEKTROSKOPIE

Časově rozlišená spektroskopie byla uplatněna při studiu nestabilních meziproduktů reakcí. Pro tyto reaktivní částice se v anglosaské literatuře vžil termín *transient species* – přechodné (krátce žijící, transientní) molekulární částice. Spektroskopická literatura (Herzberg [7]) často hovoří v tomto smyslu o radikálech, ačkoliv podle kvantové teorie může být nazývána radikálem pouze částice s nepárovým elektronem. Vysoce rozlišená spektroskopie nestabilních částic je důležitá zejména pro takové obory, jakými jsou astrochemie a astrofyzika [8], environmentální vědy či průmyslová chemie [9].

S instrumentací v současnosti umístěnou v naší laboratoři byla na univerzitě v japonské Okayamě ve spolupráci s prof. K. Kawaguchim měřena časově rozlišená spektra nestabilních částic. Se starší verzí přístroje byla získána spektra molekulárního iontu $H_3^+$, který hraje velmi důležitou roli iniciátora mnohých reakcí v kosmu [10] (vystupuje jako donor protonu). Bylo potvrzeno, že ve směsi helium – vodík je ion produkován právě vysoce vybuzenými atomy He, přičemž samotný ion vzniká srážkou $H_2^+$ s molekulou vodíku. Byl rovněž pozorován vznik nestabilní částice He₂.

V nedávných experimentech jsme se zabývali doutnavým výbojem ve směsi methanu a helia (obr. 12) s cílem časově rozlišenou spektrometrií pozorovat vznik



**Obr. 11** Ukázka spektra směsi $C^{16}O_2$ s $C^{18}O_2$
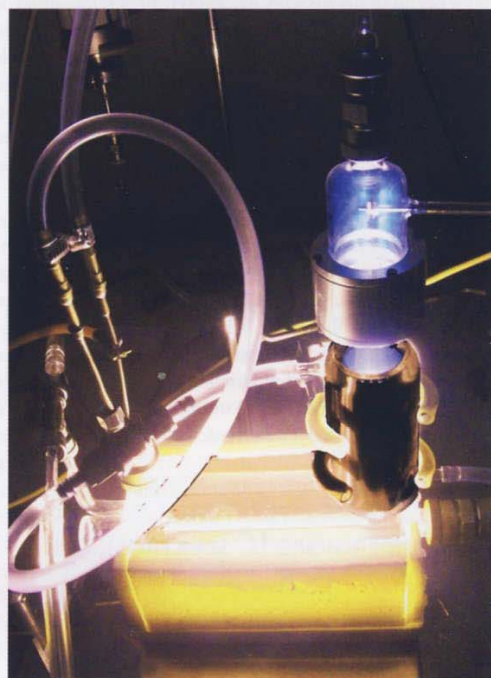


**Obr. 12** Výboj ve směsi helia a methanu v emisní cele
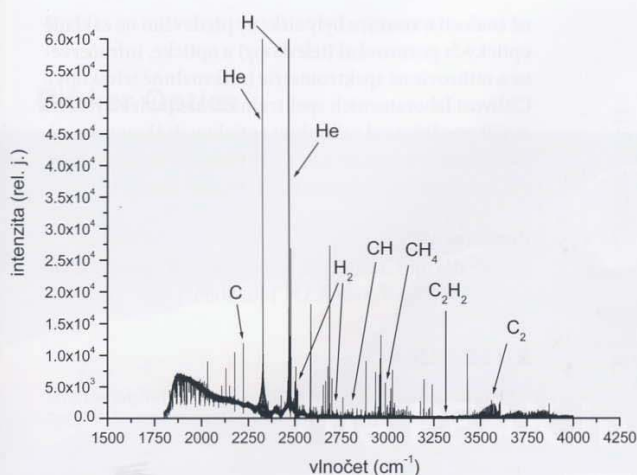
**Obr. 13** *(nahoře)* Spektrum výboje ve směsi methanu a helia

**Obr. 14** *(vpravo nahoře)* Postupný vznik radikálů CH a $C_2$ iniciovaný metastabilním heliem

**Obr. 15** *(vpravo)* Linie rotačně vibračního emisního spektra radikálu CH v základním stavu $^2\Pi_r$. Spektrum výboje ve směsi 0,4 kPa He s 0,007 kPa methanu při 40 μs dlouhém pulsu (rozlišení 0,05 cm$^{-1}$)
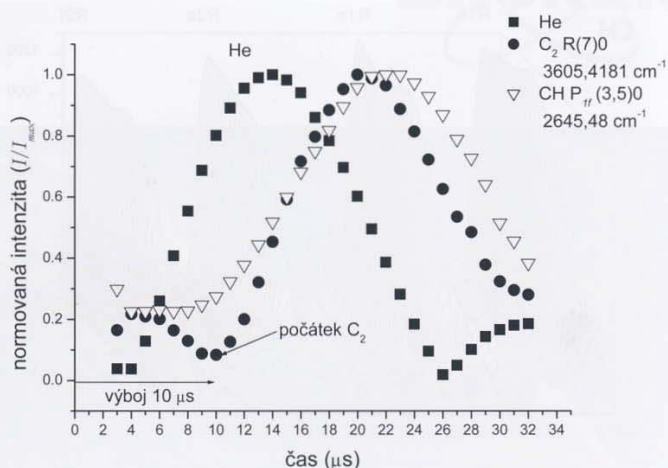
a zánik nestabilních meziproduktů a zjistit doby života energetických hladin těchto částic za daných podmínek. Volba směsi methanu a helia s vodíkem nebyla náhodná, neboť He je schopno dosáhnout vysoce excitovaných stavů s první ionizační energií [11] až 24,588 eV, čímž získává značný potenciál pro destrukci ostatních specií ve směsi, methan je jednoduchý uhlovodík, navíc spolu s He a H významně zastoupený v kosmu. Získali jsme časově rozlišená spektra, která popisují dynamiku vzniku a zániku radikálů $C_2$, CH a některých jednoduchých specií jako atomárního vodíku, molekulárního vodíku (Rydbergovy stavy) a atomárního uhlíku. Identifikováno bylo rovněž emisní spektrum acetylenu, který je produktem reakce. Obr. 13 ukazuje emisní spektrum s identifikovanými liniemi nebo pásy jednotlivých částic a obr. 14 pak postupný vznik $C_2$ a CH během výboje a po něm. Na obr. 15 je ukázáno emisní spektrum radikálu CH a na obr. 16 jeho vyhasínání po výboji.

Důležité je potvrzení faktu, že z jednoduché molekuly, jakou je methan, v těchto podmínkách (resp. obecně v podmínkách plazmy) vznikají komplikovanější specie – radikál $C_2$ či acetylen. Stejné procesy byly pozorovány i v laserových jiskrách [12]. V atmosféře planety Uran a Saturnova měsíce Titanu (stejně jako u ostatních plynných obrů) byl vedle methanu rovněž detekován acetylen spolu s dalšími jednoduššími uhlovodíky [13]. Je předpokládáno, že i atmosféry mnohých z nedávno objevených extrasolárních planet obsahují methan. Infračervená detekce uhlovodíků je prováděna zejména z palub sond (Voyager, Spitzerův dalekohled IRS), neboť požadovaný obor záření není propouštěn zemskou atmosférou. Rozmanitý chemismus vesmíru se ovšem netýká jen methanu, helia a produktů jejich reakcí v plazmě, tak jak byly studovány v naší laboratoři. Dosud bylo ve vesmíru detekováno mnoho organických sloučenin a předpokládá se, že právě chemie uhlíku hraje ve vesmíru velmi důležitou úlohu [14].
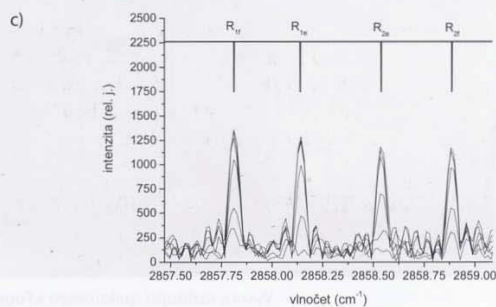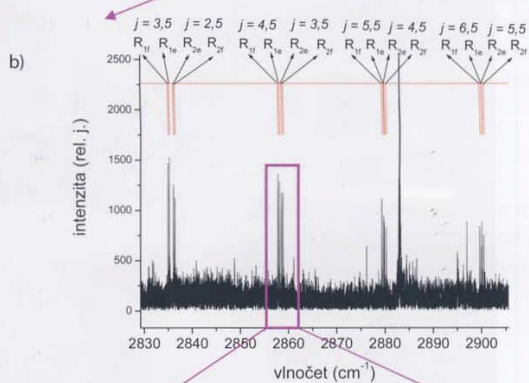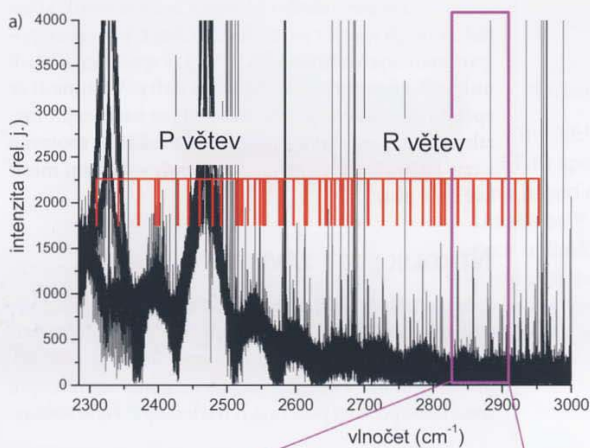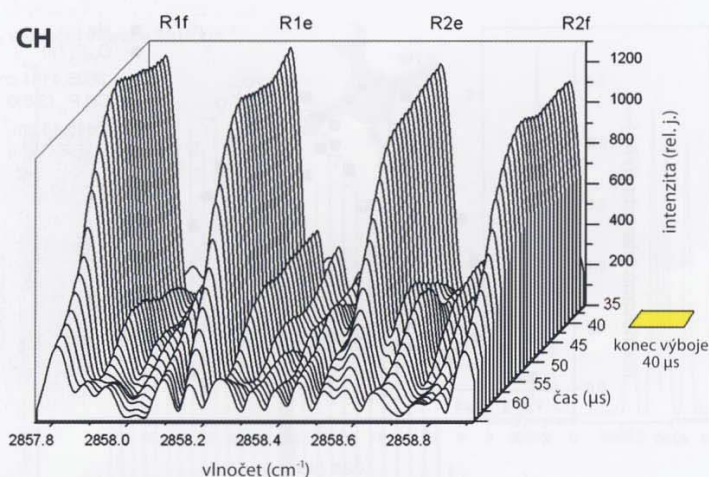
**Obr. 16** Časově rozlišené FT spektrum radikálu CH

Z environmentálního hlediska souvisí vznik komplikovaných specií z jednodušších, např. s emisemi polyaromatických uhlovodíků (PAH) ze spalování lehčích uhlovodíků v podobě benzinu či nafty. Vrátíme-li se zpět do kosmu, má se za to, že i PAH se nacházejí v mezihvězdném prostoru [15] a jejich výskyt je spojován s tzv. DIBs (*Diffuse Interstellar Bands* – difuzní mezihvězdné pásy).

## NĚKOLIK SLOV ZÁVĚREM

Spektrometrie s Fourierovou transformací je hojně využívanou technikou. Emisní a absorpční spektrometrie kromě zmíněných laboratorních aplikací hraje nezastupitelnou úlohu v dálkové detekci z palub kosmických sond nebo pomocí pozemských teleskopů. Naše současné znalosti o vesmíru byly získány především na základě optických pozorování (teleskopy) a optické, infračervené a mikrovlnné spektrometrie (mikrovlnné teleskopy). Citlivost laboratorních spektrálních metod lze výrazně zvýšit použitím cel s dlouhou optickou dráhou nebo vícenásobným odrazem (tzv. *cavity ring down spectroscopy*), kde jsou jako zdroje záření použity lasery.

## LITERATURA

[1] P. R. Griffiths, J. A. de Haseth: *Fourier Transform Infrared Spectrometry*, 2. vyd., Wiley-Interscience, NY 2007, s. 407.

[2] A. W. Mantz: Appl. Spectrosc. **30**, 459 (1976).

[3] A. W. Mantz: Appl. Opt. **17**, 1347 (1978).

[4] R. E. Murphy, H. Sakai: J. Opt. Soc. Am. **65**, 600 (1976).

[5] H. Sakai, R. E. Murphy: Appl. Opt. **17**, 1342 (1978).

[6] M. Ferus, J. Cihelka, S. Civiš: Chem. listy **102**, 417 (2008).

[7] G. Herzberg: *The Spectra and Structures of Simple Free Radicals. An Introduction to Molecular Spectroscopy.* Cornell University Press, Ithaca-London 1971, s. 1.

[8] S. Civiš, T. Šedivcová: Čs. čas. fyz. **A52**, 152 (2002).

[9] E. Hirota: Int. Rev. Phys. Chem. **8**, 171 (1989).

[10] S. Civiš, P. Kubát, S. Nishida, K. Kawaguchi: Phys. Chem. Lett. **418**, 448 (2006).

[11] V. A. Rabinovič, Z. Ja. Chavin: *Stručná chemická příručka.* SNTL Praha, 1985, s. 30.

[12] D. Babánková, S. Civiš, L. Juha: Chem. listy **99**, 109 (2005).

[13] M. Burgdorf, G. Orton, J. van Cleve, W. Meadows, J. Houck: Icarus **184**, 634 (2006).

[14] M. Winnewisser: Chemie in unserer Zeit 18, 1 (1984).

[15] D. M. Hudgins, Ch. W. Bauslicher, L. J. Allamandola: Spectrochim. Acta **A57**, 907 (2001).



Vysoce rozlišující spektrometr s Fourierovou transformací Bruker IFS 120 HR

# Time-Resolved Fourier Transform Emission Spectroscopy of He/CH₄ in a Positive Column Discharge

Svatopluk Civiš,[†] Petr Kubelík,[†,‡] and Martin Ferus*[,†,‡]

[†]J. Heyrovský Institute of Physical Chemistry, Academy of Sciences of the Czech Republic, Dolejškova 3, 18223 Prague 8, Czech Republic

[‡]Institute of Physics, Academy of Sciences of the Czech Republic, Na Slovance 2, 182 21 Prague 8, Czech Republic

**ABSTRACT:** Time-resolved Fourier transform infrared emission spectroscopy was applied to the study of a pulsed discharge in a He/CH₄ mixture. The dynamics of the formation and decay of acetylene $\nu_3$ (3289 cm⁻¹), methane $\nu_3$ (3019 cm⁻¹) and $\nu_1$ (2917 cm⁻¹), the CH radical electronic ground state $X^2\Pi_r$ (2309−2953 cm⁻¹), C₂ Bernath electronic transition $B^1\Delta_g$−$A^1\Pi_u$ (3337−3606 cm⁻¹), molecular hydrogen emission transitions 5g−4f and 2p−2s, atomic hydrogen, and atomic helium were monitored in the 1800−4000 cm⁻¹ region. The time profile of the rotational and vibrational temperature of the CH radical was obtained for a 30 μs time interval during and after the discharge pulse. A kinetic model was used for the study of the chemical dynamics of the formation and decay of the individual fragments. The results from the model were compared to the experimental emission spectra.
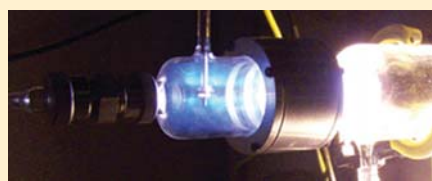
## 1. INTRODUCTION

The motivation for studying the behavior of methane in plasma, which can be created using various methods, arises from various fields of study. Among the most exciting motivations are the following: the plasma-chemical processing of natural resources (e.g., natural gas), the preparation of carbonaceous thin films and coatings, and the laboratory simulation of the chemical consequences of a high-velocity impact by an extraterrestrial body (such as a comet or meteorite) and/or lightning in the Earth's early atmosphere or in the atmosphere of Titan (Saturn's largest moon).

It is assumed that the early, strongly reduced stages of the Earth's atmosphere contained a large amount of methane. We conducted a detailed study on the dynamics of methane decay using an electric pulse discharge and emission spectroscopy in the infrared spectral range. At the same time, laser-induced dielectric breakdown (LIDB) studies were performed using a high-energy laser, PALS (Prague Asterix Laser System), and optical spectroscopy.[1]

The electrical discharge in methane has been the subject of many previous studies.[2−4] These studies showed that a pulsed discharge into CH₄ can lead to the conversion of methane into larger hydrocarbon molecules under the appropriate conditions.[5]

From the infrared spectroscopic observations, the discharge process caused a large concentration of simple radicals (CH ($X^2\Pi$, $A^2\Delta$, $B^2\Sigma^-$), C₂ ($B^1\Delta_g$−$A^1\Pi_u$), C ($^3P$, $^1D$, $^1S$), and H ($n > 1$)) to form. These radicals play a very important role in plasma chemical reactions and have often been the subject of kinetic studies.[6,7] Despite the large amount of kinetic data on the isolated reactions of simple radicals with various species, a satisfactory, unequivocal model that can predict the overall processes that occur in the

plasma of the methane discharge does not exist, particularly for time-resolved measurements.

Among the various methods of plasma generation, the discharge plasma approach is of particular importance because the physical−chemical conditions can be far from equilibrium during such a process. These conditions are due to the complicated interplay of many macroscopic and microscopic processes that occur in the plasma. Therefore, a complete understanding of the potential properties of such a system requires detailed knowledge of the behavior of the various intermediates that form under certain conditions and at certain time intervals.

Traditionally, mass spectrometry methods have been used by several authors to characterize pure methane discharge plasmas,[8] and great effort has been devoted to modeling the system.[9] However, emission spectroscopy in combination with actinometry[10] represents an attractive method for nonintrusive, in situ plasma diagnostics, which have been used relatively less often than mass spectrometry for the characterization of C/H deposition plasmas.[11,12]

The aim of this work was to observe the reaction dynamics of unstable species with the use of time-resolved spectroscopy (TRS-FT). The results of the measurements of the emission spectra acquired over time and the abundance of reactive fragments were used to follow the reaction scheme of a glow discharge, which summarized the formation and decay of the excited individual species during the TRS-FT measurements. This method was first employed for the study of pulsed discharge in less complicated systems (the formation of ArH

and ArH[+] and related atomic species[13] and then for the study of He$_2$ and H$_3$[+]).[14,15]

The use of TRS-FT enabled processes inside of the methane discharge plasma to be studied and permitted the dynamics of the formation and decay of excited atoms, radicals, and ions to be described. The individual processes were investigated using atomic or molecular lines over a wide spectral range of high-resolution FT technology, which extended into the time dimension. The limitation of this method is the sensitivity of the infrared FT emission technique and the considerable number of scans (25 min per measurement) required to acquire the data.

**Methane Plasma Chemistry.** Electrical discharge in methane is a relatively complicated process. The system is dynamic and is determined by a series of reactions, which have been studied both theoretically and experimentally (e.g., numeric simulation and mass spectrometry with the use of isotopic markers). Although numerous reactions are mentioned in the literature, the cleavage of hydrogen from methane[10,16] is proposed to be the main reaction pathway in methane plasma

$$CH_4 + e^- \rightarrow CH_3 + H + e^-$$
$$\sigma(25\ eV) = 1.50 \times 10^{-20}\ m^2 \tag{1}$$

$$CH_4 + e^- \rightarrow CH_2 + 2H + e^-$$
$$\sigma(20\ eV) = 0.75 \times 10^{-20}\ m^2 \tag{2}$$
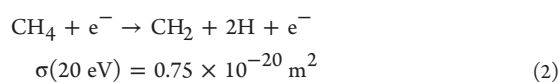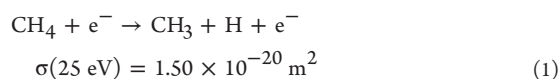
These processes occur due to the collisions of the methane molecules with a fast (high-energy) electron or excited He atom. It should be noted that the dissociation cross sections ($\sigma$) of these reactions are approximately the same for energies under 20 eV.

The reaction pathway in the methane plasma can be altered by adding various gases, varying the pressure, or changing the energy input. If methane is mixed with buffer gases (i.e., hydrogen, oxygen, argon, and helium[3,17]), then the conversion of methane into desired products is more efficient.

According to Kirikov,[18] by adding hydrogen into the methane discharge, the formation of carbon deposits is reduced, and the production of acetylene is increased. If a higher amount of atomic hydrogen is present, then the CH$_2$ radical rapidly transforms into a CH radical, which leads to the direct synthesis of acetylene. At very high applied energies, methane transforms directly into atomic carbon and hydrogen.

The presence of helium, argon, or nitrogen[19] in the discharge leads to a higher degree of methane conversion into the final products (e.g., acetylene), while the abundance of hydrogen increases and the abundance of hydrocarbons decreases. The addition of these gases also leads to a lower consumption of energy during the process of conversion. The authors[19] attributed this observation to the existence of the metastable states of helium and argon.

In the case of hydrocarbon mixtures with helium or other gases with a high ionization potential, a significant role in the discharge is played by Penning ionization, Penning dissociation, and Penning excitation.[17,20] The description of Penning ionization is based on the collisions of metastable[21,22] states of helium (2[3]S with an energy of 19.2 eV and 2[1]S with an energy of 20.61 eV) with the molecule (M), which leads to ionization. The process is schematically described by the equation

$$He^* + M \rightarrow He + M^+ + e^- \tag{3}$$
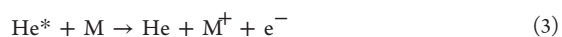
The energy of excited He* is significantly higher compared to the ionization potential of the M species. Highly energetic Penning electrons are produced. Intermediates[23] are assumed to be preferentially formed during Penning ionization. In the case of acetylene, a highly excited molecule in a triplet state is formed; however, the methane molecule is presumed to be directly ionized.

The Penning dissociation can be described by the following scheme

$$He^* + AB \rightarrow He + A + B \tag{4}$$

where A and B are the products of the reaction. The Penning excitation can be assumed to follow a similar scheme

$$He^* + M \rightarrow He + M^* \tag{5}$$

In the case of nitrogen, a similar mechanism is assumed (i.e., a collision of the excited species with a methane molecule) according to the following schemes

$$CH_4 + N_2^* \rightarrow CH_3 + H + N_2 \tag{6}$$

$$CH_4 + N_2^* \rightarrow C + 2H_2 + N_2 \tag{7}$$
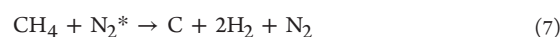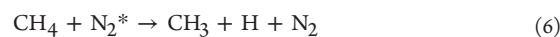
The studies of K.V. Kozlov[19] indicate that an increase in the addition of helium into the methane leads to a higher transfer of charge between the electrodes, and the methane has a lower ignition voltage. The rate of elementary reactions (i.e., the collision reactions of methane with fast electrons) is directly proportional to the curve of the electron energy distribution.

The degree of methane conversion and the composition of products are also influenced by the energy input. The production of acetylene during an RF discharge is more efficient at higher energy inputs; ethane[24] is formed at lower energy inputs. These facts are in agreement with thermodynamic calculations because the formation of an ethane molecule requires 0.7 eV while the formation of the acetylene molecule requires 4 eV. The same results were determined by electrical discharge studies, where the abundance of ethane decreased as the pressure increased.[5,25] The fact that a higher degree of conversion of methane into acetylene in RF discharge is more efficient at higher energies is explained by Kirikov.[18]

Tachibana et al.[26] determined that the total rate constant of methane dissociation increases as the discharge power increases, and the growth rate increases as the pressure of methane increases (in the range of several Torr).

Generally, the molecular dynamics of methane decay in plasma are influenced by the energy input (the particle energy levels of several eV to tens and/or hundreds of eV), pressure (from tenths of Torr to atmospheric pressure), the added impurities of other gases (e.g., nitrogen, helium, argon, and hydrogen), the use of heterogeneous catalysts (e.g., $\gamma$-Al$_2$O$_3$), and the type of discharge (e.g., spark, corona, glow, and arc).

## 2. EXPERIMENTAL SECTION

**A. Continuous Scanning Time-Resolved FT Spectroscopy.** TRS-FT is a wide-spectrum technique used for studying the dynamics of chemical reactions or the dynamic properties of molecules, radicals, and ions in the liquid, gas, and solid states. The main advantage of TR-FTS is that spectra can be obtained over a wide interval of wavenumbers. The speed of data acquisition is limited by the duration of the acquisition process and by the bandwidth of the detector. There are two primary methods for acquiring FT time-resolved spectra, the continuous scan and the noncontinuous step scan.[27,28]

A special approach to the time-resolved spectra of phenomena lasting from milliseconds to microseconds is the synchronous scanning FT technique.[29] This method requires the possibility of initiating the reaction in a pulsed mode (e.g., using a laser, electric discharge, electron bombardment, or UV discharge lamp).[15] The apparatus performs a continuous scan and reads the signal from the detector during the pulse, which corresponds to the position of the moving mirror and the time from the initial pulse reaction using the HeNe laser fringe signals generated by the interferometer. This method is called stroboscopic interferometry.[27] After accumulating a sufficient amount of data and scans, the time-shifted interferograms (usually 10 ms to 1 $\mu$s) are composed.

The continuous scanning principle was the basis for data acquisition by a modified (Bruker IFS 120, Bruker, Germany) spectrometer in our laboratory at the J. Heyrovsky Institute of Physical Chemistry, Prague, Czech Republic, and a similarly modified spectrometer was used at Okayama University, Okayama, Japan. The data acquisition system can be described as follows: The position of the traversing mirror of the Michelson interferometer is detected by reading the interference maxima of the HeNe laser emission. The input signal, which has a cosine function shape, is digitally processed into rectangular pulses and becomes the internal standard of the interferometer. The frequency of these rectangular pulses depends on the mirror speed. In the classic measurement mode, the frequency is usually 10 kHz with a discharge pulse duration of 100 $\mu$s. An external processor monitors the beginning and order of the HeNe laser digital pulse and the zero position of the mirror. During a single discharge pulse, the signal from the detector is read (30−64 readings), which is called the AD trigger. These signals are shifted in time by $\Delta t$, where $\Delta t = 1, 2, 3, ... \mu$s. A matrix $I(t_k, \delta_i)$ is acquired, where $I$ is intensity, $t_k$ is the time, and the optical path difference is $\delta_i$ ($i$ is the index of the selected optical path difference ranging from zero to the maximum value). A discharge pulse of a variable duration can be arbitrarily inserted into the data acquisition process (AD trigger). This process results in 30−64 reciprocally time-shifted interferograms.

**B. Experimental Setup.** The emission spectra of plasma from a positive column discharge in He/CH$_4$ mixtures were observed with the time-resolved Fourier transform high-resolution Bruker IFS 120 HR interferometer. The schematic of the apparatus is shown in Figure 1. High-purity CH$_4$ and He (99.999%) were used. The positive column discharge tube (25 cm long with an inner diameter of 12 mm) was covered with a glass outer jacket and had CaF$_2$ windows. The pulsed discharge was maintained by a high-voltage transistor switch (HTS 81, Behlke electronic GmbH, Frankfurt, Germany) applied between the stainless steel anode and the grounded cathode. The He/CH$_4$ plasma was cooled by water in the outer jacket of the cell. The voltage drop across the discharge was 1200 V, and the current was 100 mA. The time durations of the discharge were 10 and 40 $\mu$s. The scanner velocity of FTS was set to produce a 10 kHz HeNe laser fringe frequency, which was used to trigger the discharge pulse. The recorded spectral range was 1800−4000 cm$^{-1}$ using an optical filter and InSb detector with an unapodized resolution of 0.035 cm$^{-1}$. A reasonable signal-to-noise ratio was obtained by averaging 64 scans. The initial pressure of CH$_4$ was 0.05 Torr, and the optimal pressure of the He carrier gas was determined to be 3 Torr. The pressure was measured with a Baratron gauge placed near the cathode of the cell. The combustion products of the
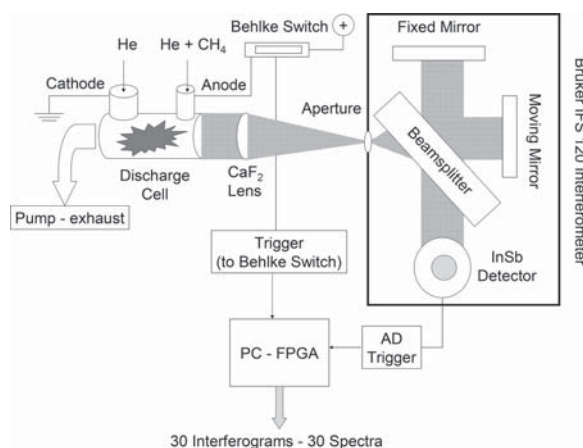


**Figure 1.** Schematic diagram of the measurement apparatus. The carrier gas (He) with the precursor (CH$_4$) enters the discharge cell. The emission from the glow discharge in the cell with out-of-axis electrodes is focused by a lens into an interferometer and onto a detector. The time-shifted signals are interpreted by a computer, which simultaneously switches the discharge pulse via a Behlke switch. The system is driven by a Field-programmable gate array (FPGA) processor, which allowed 30 time-shifted signals to be obtained.

discharge were continuously removed using an Edwards rotary oil pump.

## 3. RESULTS AND DISCUSSION

During two different discharge experiments (a short pulse of 10 $\mu$s and a long pulse of 40 $\mu$s), 30 spectra were acquired in 1 $\mu$s intervals, which were used to observe the time-resolved sequence of the decay processes in the plasma and as the source of the emission data for the chemical model. The general emission spectrum of the ac discharge in the mixture of methane, helium, and hydrogen is shown in Figure 2.
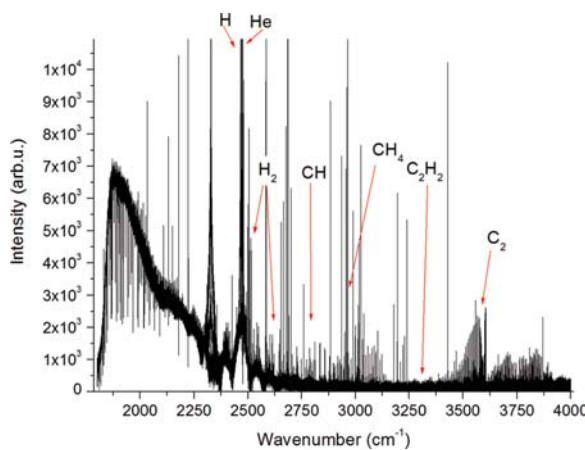


**Figure 2.** Emission spectrum of the He/CH$_4$ discharge (10 $\mu$s after the termination of the 40 $\mu$s discharge pulse). The pressures for He and CH$_4$ were 10 and 0.05 Torr, respectively.

The following emission bands were identified: acetylene ($\nu_3$ 3289 cm$^{-1}$ ($\sigma_u^+$) CH stretch); methane ($\nu_3$ stretch (f$_2$), 3019 cm$^{-1}$ and $\nu_1$ symmetric stretch (a$_1$) 2917 cm$^{-1}$); CH radical (ground state X$^2\Pi_r$ rotation−vibration transition[30−32]

from 2309 to 2953 cm$^{-1}$) (for details of the spectrum, see Figure 3); $C_2$ (electronic Bernath transition[33] $B^1\Delta_g$–$A^1\Pi_u$ from
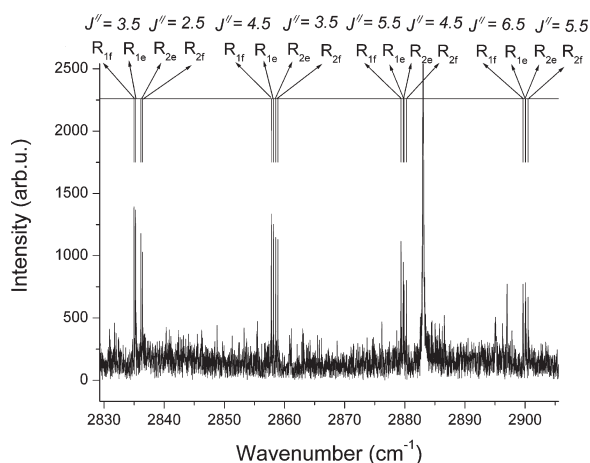


**Figure 3.** $X^2\Pi_r$ lines of CH radicals in the spectral range of 2830–2900 cm$^{-1}$ (10 $\mu$s after the termination of the 40 $\mu$s discharge pulse).

3337 to 3606 cm$^{-1}$); and emission transitions[34–36] (5g–4f and[37] 2p–2s) of molecular hydrogen, atomic hydrogen (H I), and helium[38] (He I). There is no feature in the spectra that could belong to any charged molecular species (C II, He II).

**A. Estimation of the Plasma Temperature.** Temperature is one of the important characteristics of plasma. Generally, temperature describes the energetic distribution of particles in the system. For the determination of the temperature, the system is assumed to be at thermodynamic equilibrium (Boltzmann distribution). Plasma is characterized by a set of various temperatures, the electron excitation temperature ($T_{el}$), vibrational temperature ($T_v$), rotational temperature ($T_r$), and kinetic temperature ($T_\sigma$). When the system reaches the thermodynamic equilibrium, all temperatures are equal. In the case of a nonisothermal plasma, the following relation controls the system

$$T_{el} > T_v > T_r \equiv T_\sigma \qquad (8)$$

The rotation temperature is usually taken as being the closest to the kinetic temperature, which is a key parameter for the determination of reaction rate constants. The possibility of obtaining information regarding the temperature experimentally is a major advantage of the applied experimental method.

The vibrational temperature is obtained from a simple rotation–vibration spectrum by plotting the relation

$$\ln[I/\nu^3(V+1)] = KE_v + Q \qquad (9)$$

where $K$ is the slope of the straight line, $Q$ is a constant, $\nu$ is the wavenumber, and $V$ is the vibrational number of the upper state. The temperature is obtained from the relation

$$-K = 1/kT_v \qquad (10)$$

where $k$ is the Boltzmann constant and $T_v$ is the vibrational temperature. The mean value of the vibrational temperature was 5300 K. The temperature, estimated using lines of CH radicals (experimental conditions: pressure of 3 Torr of He and a pulse length of 40 $\mu$s), is depicted in Figure 4. In the case of electronic transitions, the vibrational number $V$ was replaced by the Franck–Condon factor. Several transitions (1–0, 2–1,
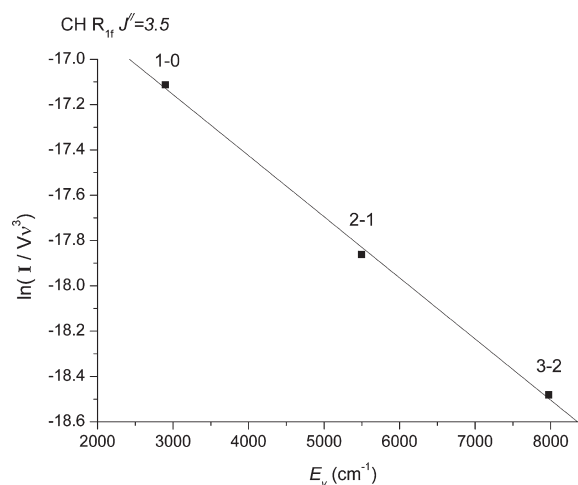


**Figure 4.** Boltzmann plot for the CH radical. The estimated vibrational temperature was 5334 K.

and 3–2) were identified. Figure 5a shows the time profile of the vibrational temperature determined from the CH $R_{1f}$ lines (2576.07, 2704.8, and 2834.97 cm$^{-1}$; $J'' = 3.5$) for the 40 $\mu$s pulse. The lines were selected because the emission intensities were suitable. The energy terms published by Ghosh et al.[32] were used. The most accurate determination of the vibrational temperature occurred at the maximum of the CH radical emission during the 40 $\mu$s discharge pulse.

In the case of pure rotational–vibrational transitions, the $T_r$ can be determined by the relation

$$\ln(I/S) = -E_r/kT_r + Q \qquad (11)$$

where $E_r$ is the energy of the upper level. The factor $S$ (Hönl–London factor) must be calculated on the basis of the parameters of the molecule and the transition under investigation. The estimation of the temperature (pressure of 3 Torr of He and a pulse length of 40 $\mu$s) is depicted in Figure 6.

According to the intensity factor, the following set of lines of the $R_{1e}$ branch were chosen for determining the rotational temperatures: vibrational transition 1–0 (2811.0, 2835.29, 2858.19, 2879.756, and 2900.03 cm$^{-1}$ with the $J''$ ranging from 2.5 to 6.5) and transition 2–1 (2681.83, 2705.051, 2726.93, 2747.54, and 2766.83 cm$^{-1}$ with the $J''$ ranging from 2.5 to 6.5). The average rotational temperature was determined to be 523 K for all vibration bands. Figure 5 shows the time profiles of temperatures (a) with the CH emission for the 40 $\mu$s discharge pulse (b).

**B. Model of the Carbon Radicals' Molecular Dynamics.** In the case of the 10 $\mu$s discharge pulse, Figure 7 depicts the time sequence (formation and decay process) of the individual transient species that were detected in the He/CH$_4$ plasma. He emission in the short discharge pulse experiment was observed 4 $\mu$s after the initiation of the discharge pulse. This delay is caused by the gradual growth of electron density after the discharge is initiated. Corbell et al.[39] reported the delays in electron concentration growth to be similar (several microseconds). The maximum He emission intensity occurred after 13 $\mu$s, which was 3 $\mu$s after the termination of the discharge. In the case of the 40 $\mu$s discharge pulse, a steady state was nearly achieved, and the helium spectrum behaved almost as a constant progression of the emissions, and 5–10 $\mu$s after the discharge ended, the species became extinct due to reactions and collisions.
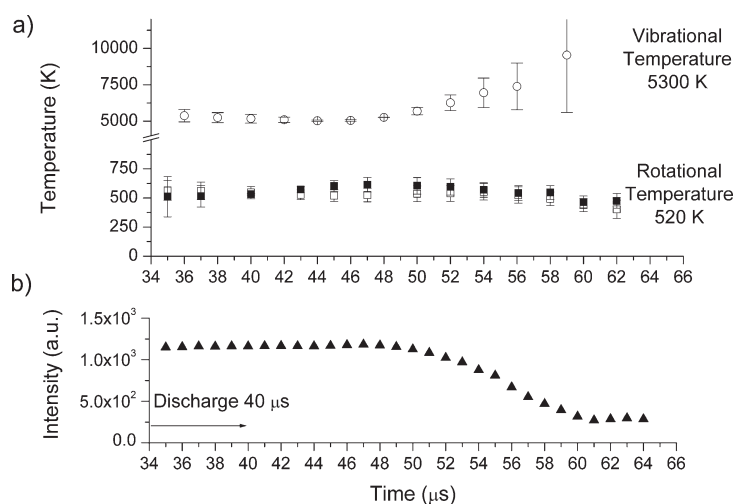
**Figure 5.** (a) Time profiles of the CH vibrational temperature ($\bigcirc$ $R_{1f}$ branch) after the 40 $\mu$s discharge pulse together with the rotational temperature time profile for the CH radical ($\blacksquare$ $R_{1e}$, $\nu = 1-0$ and $\square$ $R_{1e}$, $\nu = 2-1$). (b) The intensity profile of the CH radical (2645.48 cm$^{-1}$, $P_{1f}(3.5)$, $\nu = 1-0$, $X^2\Pi_r$).
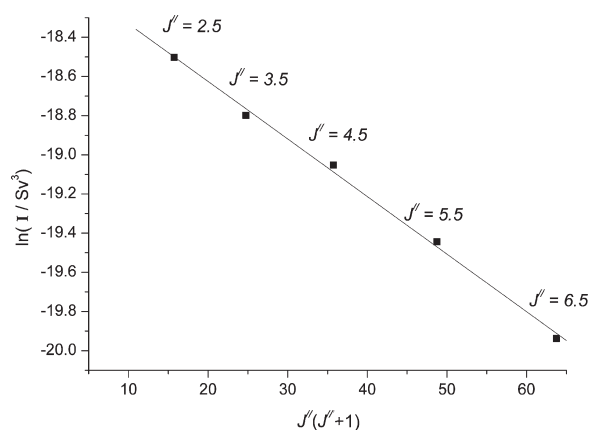


**Figure 6.** The Boltzmann plot for the CH radical. The estimated rotational temperature was 520 K.

The intensity and profile of the emission spectrum were influenced by the chemical reactions in the discharge or collision-radiation processes and by the experimental setup. In our previous study dealing with the formation of HNC/HCN in a glow discharge,[40] we showed that during the time-resolved spectra measurement process, the products from the reaction collected in the cell. Therefore, the interpretation of the time-resolved spectra requires the design of a kinetic model that accounts for these processes. The reaction model was designed for a discharge pulse with a length of 40 $\mu$s because the quantitative ratios between individual species can be determined sufficiently. The quantitative ratio determination is due to the chemical equilibrium and related stable emission profile of individual particles during the discharge.

*Kinetic Model Design.* A simplified description of the design process for the kinetic model is the following: The kinetic model of the methane discharge and afterglow was designed on the basis of the reactions listed in Table 1, while none of the rate constants were fitted. The model describes the chemistry of the discharge on the basis of published data. Kinetic

equations have been adopted from several published works dealing with selected kinetic models of methane plasma,[7,26,47] the NIST database,[41] and other works cited in Table 1. The accuracy of the calculation with the experimental data was subsequently verified on the basis of the concentration ratios of individual identified species because an absolute quantification of concentrations based on the emission spectra is extremely difficult. The Einstein emission coefficients[32,51,54,57,58] and partition functions[55,56,59] were determined for each species with an available reference, and the integral intensities of the bands during the 40 $\mu$s discharge period were determined from the experimental data. A stationary state between excitation and de-excitation during the period was assumed. Hardwick and Whipple[42] reported that the emission intensity is proportional to the concentration of the emitting species according to the equation

$$c_A = \frac{I_A Q_A}{A_A \nu_A \exp(E_A/kT)} \tag{12}$$

The ratio between the concentrations and intensities of emission bands of two species, A and B, can be expressed as

$$\frac{c_A}{c_B} = \frac{I_A}{I_B} \cdot \frac{Q_A A_B \nu_B \exp(E_B/kT)}{Q_B A_A \nu_A \exp(E_A/kT)} \tag{13}$$

where $c_A$ and $c_B$ are the concentrations of species A and B, $Q_A$ and $Q_B$ are the total partition functions of species A and B, $A_A$ and $A_B$ are the Einstein emission coefficients of species A and B, $\nu_A$ and $\nu_B$ are the vibrational frequencies of the transitions of species A and B, $E_A$ and $E_B$ are the energy levels of the emission transitions of species A and B, $k$ is the Boltzmann constant, and $T$ is the thermodynamic temperature. The partition functions were obtained from references when available,[55,56,59] and the population distribution of the levels investigated was estimated using the experimentally obtained rotation (520 K) and vibration (5300 K) temperatures. The electron excitation temperature was estimated on the basis of the results of the model at 1.5 eV (17400 K).

We suppose that vibration and rotation temperatures of different species are close to each other. This assumption can

P14
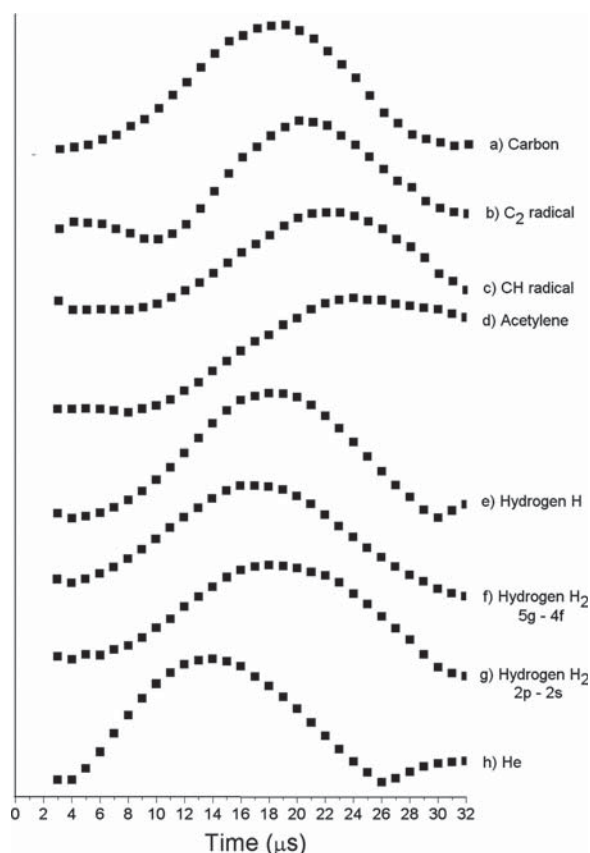
**Figure 7.** Emission time profiles of all species identified in the He/CH₄ discharge spectrum after a 10 μs long discharge pulse: (a) carbon atomic line 2222.57 cm$^{-1}$ ($^1$P°−$^1$P), (b) C$_2$ radical line 3605.42 cm$^{-1}$ R(7), $\nu$ = 0−0, B$^1\Delta_g$−A$^1\Pi_u$, (c) CH radical line 2645.48 cm$^{-1}$ P$_{1f}$(3.5), $\nu$ = 0−1, X$^2\Pi_r$ ground state, (d) acetylene line 3318.35 cm$^{-1}$, $\nu_3$ band, R$_e$(15), (e) atomic hydrogen line 2467.75 cm$^{-1}$ (alpha Brackett system), (f) H$_2$ line 2489.38 cm$^{-1}$ R$_1$(4), 5g−4f, (g) H$_2$ line 2830.92 cm$^{-1}$ Q(1) 4−3 band, 2p−2s, and (h) He atomic line 2469.74 cm$^{-1}$.

be demonstrated for example if we consider our measurement of the CN radical in the (CN)$_2$ discharge. We have estimated the rotation temperature to be $T_{rot}$ = 480 K and $T_{vib}$ = 6680 ± 835 K for the A$^2\Pi$ and 6757 ± 534 K for the X$^2\Sigma^+$ transitions. It means that temperatures $T_{vib}$ are close together for different transitions.[86] In the case of CH$_3$CN, BrCN, or HCONH$_2$

discharges,[40] we estimated the temperature for HCN to be $T_{rot}$ = 550 K. We can state that the temperatures $T_{rot}$ and $T_{vib}$ of CN or HCN are close to the values estimated in this work for CH, and we suppose that in the case of most species under similar discharge conditions, the temperatures are close to the values $T_{rot} \approx$ 500 K and $T_{rot} \approx$ 6000 K.

The other key features of the model have been summarized in previous papers,[40,79] and brief details are provided below:

- The numerical model was implemented in the Python 2.6.4 programming language using modules Numpy[43] and Scipy.[44]
- The model was constructed as a zero-dimensional model, which described only the time evolution of the concentrations in the homogeneous region of the positive column of a glow discharge.
- A set of ordinary differential equations constructed according to the postulated reaction scheme (Table 1) was numerically solved by the Scipy module using the ODEPACK library.[45] We would like to note that ion reactions were not included in the model. The total concentration of all ions in the discharge is equal to the concentration of electrons (i.e., 6 × 10$^{11}$ cm$^{-3}$). This concentration is lower than the estimated concentration of active radicals (e.g., the estimated concentration of the CH radical is about 3 × 10$^{12}$ cm$^{-3}$), and therefore, the chemistry of the discharge is simulated by a radical−radical reaction approach as well as in our previous works.[40,79,82] The model has involved the chemistry of simple carbon chains C$_1$ and C$_2$. The spectrum of the C$_3$ radical has not been observed under used conditions.
- The activity of the discharge was simulated by a rectangular pulse of an electron number density of a 40 μs duration, in accordance with the experiment. The typical values of electron densities in a glow discharge are[35,46] between 10$^9$ and 10$^{11}$ particles per cm$^3$. A value of 6 × 10$^{11}$ cm$^{-3}$ was used, which was obtained by a Langmuir probe measurement of the actual experimental discharge. The theoretical electron temperature was estimated to be 1.5 eV.
- The number densities of the precursor molecules (CH$_4$) were fixed at 8.74 × 10$^{14}$ cm$^{-3}$, which were calculated from the partial pressures (6.67 Pa) and the temperature ($T$ = 520 K). It is supposed that in the glow discharge, the kinetic temperature is close to the rotation temperature (see, e.g., ref 85). Therefore, the value $T = T_{rot}$ = 520 K has been adopted. The flow rate of the precursor into the cell and the flow rate of the products out of the cell were assumed to be

**Table 1. Results of the Chemical Model Compared with the Concentration Ratio among Selected Species Estimated Using the Appropriate Partition Function and the Einstein Emission Coefficients (references or calculations are given for the values)$^a$**

| molecule | band assig. | band position (cm$^{-1}$) | Einstein emission coefficient (s$^{-1}$) | integrated band intensity (arb. u.) | partition function $T_v$ = 5300 K, $T_r$ = 520 K | experimentally estimated ratio (%) | model ratio $T_e$ = 17000 K, $T_v$ = 5300 K, $T_r$ = 520 K | ref |
|---|---|---|---|---|---|---|---|---|
| CH$_3$ | $\nu_3$ | 3160 | 8.3 | 28.4$^{est.}$ | 1.55 × 10$^4$ | n.d. | 11.67% | 51,52 |
| CH$_2$ | X$^3$B$^1$ $\nu_3$ | 3190 | 1.0 | 1.1$^{est.}$ | 1.88 × 10$^4$ | n.d. | 4.57% | |
| | a$^1$A$^1$ $\nu_1$ | 2806 | 66.5 | 82.6$^{est.}$ | | | | 53,54 |
| | a$^1$A$^1$ $\nu_3$ | 2864 | 36.1 | 44.1$^{est.}$ | | | | |
| CH | X$^2\Pi$ $\nu_1$ | 2732 | 145.9 | 3047.0 | 2.87 × 10$^2$ | 1.16% | 1.40% | 55 |
| C$_2$ | B$^1\Delta_g$−A$^1\Pi_u$ | 3609 | 6430.0 | 4245.7 | 2.57 × 10$^3$ | 0.33% | 0.37% | 55−57 |
| C$_2$H$_2$ | $\nu_3$ | 3289 | 96.7 | 255.5 | 1.35 × 10$^5$ | 82.22% | 82.22% | 58,59 |

$^a$Values marked est. are estimated using eq 12. Values marked n.d. were not estimated because the species was not detected.

**Table 2. Kinetic Equations Used in Our Chemical Model**[a]

| dissociation reaction | activation energy (eV) | ref |
|---|---|---|
| $C_2H_6 + e^- \rightarrow C_2H_4 + H_2 + e^-$ | 1.41 | all[47] |
| $C_2H_5 + e^- \rightarrow C_2H_4 + H + e^-$ | 1.59 | |
| $C_2H_3 + e^- \rightarrow C_2H_2 + H + e^-$ | 1.72 | |
| $C_2H_5 + e^- \rightarrow C_2H_3 + H_2 + e^-$ | 1.75 | |
| $C_2H_4 + e^- \rightarrow C_2H_2 + H_2 + e^-$ | 1.81 | |
| $C_2H_4 + e^- \rightarrow 2CH_2 + e^-$ | 2.66 | |
| $C_2H_3 + e^- \rightarrow C_2H + H_2 + e^-$ | 2.89 | |
| $CH + e^- \rightarrow C + H + e^-$ | 2.9 | |
| $C_2H_6 + e^- \rightarrow C_2H_2 + 2H_2 + e^-$ | 3.22 | |
| $C_2H_5 + e^- \rightarrow C_2H_2 + H + H_2 + e^-$ | 3.39 | |
| $CH_2 + e^- \rightarrow CH + H + e^-$ | 3.89 | |
| $C_2H_4 + e^- \rightarrow C_2H_3 + H + e^-$ | 4.19 | |
| $C_2H_6 + e^- \rightarrow C_2H_5 + H + e^-$ | 4.43 | |
| $H_2 + e^- \rightarrow H + H + e^-$ | 4.53 | |
| $CH_4 + e^- \rightarrow CH_3 + H + e^-$ | 4.55 | |
| $C_2H_5 + e^- \rightarrow C_2H + 2H_2 + e^-$ | 4.64 | |
| $C_2H_6 + e^- \rightarrow 2CH_3 + e^-$ | 4.65 | |
| $CH_3 + e^- \rightarrow CH_2 + H + e^-$ | 4.76 | |
| $CH_4 + e^- \rightarrow CH_2 + H_2 + e^-$ | 4.79 | |
| $C_2H_2 + e^- \rightarrow C_2H + H + e^-$ | 5.78 | |
| $C_2H_6 + e^- \rightarrow C_2H_4 + 2H + e^-$ | 5.93 | |
| $C_2H_6 + e^- \rightarrow C_2H_3 + H + H_2 + e^-$ | 6.1 | |
| $C_2 + e^- \rightarrow 2C + e^-$ | 6.17 | |
| $C_2H_2 + e^- \rightarrow 2CH + e^-$ | 6.17 | |
| $C_2H_5 + e^- \rightarrow C_2H_3 + 2H + e^-$ | 6.27 | |
| $C_2H_4 + e^- \rightarrow C_2H_2 + 2H + e^-$ | 6.32 | |
| $C_2H_2 + e^- \rightarrow C_2 + H_2 + e^-$ | 6.33 | |
| $C_2H_3 + e^- \rightarrow C_2H + 2H + e^-$ | 7.41 | |
| $C_2H_4 + e^- \rightarrow C_2H + H + H_2 + e^-$ | 7.57 | |
| $C_2H_5 + e^- \rightarrow C_2H_2 + 3H + e^-$ | 7.91 | |
| $CH_2 + e^- \rightarrow C + 2H + e^-$ | 7.95 | |
| $C_2H_4 + e^- \rightarrow C_2 + 2H_2 + e^-$ | 8.14 | |
| $CH_4 + e^- \rightarrow C + 2H_2 + e^-$ | 8.2 | |
| $C_2H_6 + e^- \rightarrow C_2 + 3H_2 + e^-$ | 8.3 | |
| $C_2H + e^- \rightarrow C_2 + H + e^-$ | 8.59 | |
| $C_2H_6 + e^- \rightarrow C_2H + H + 2H_2 + e^-$ | 8.98 | |
| $CH_4 + e^- \rightarrow CH + H_2 + H + e^-$ | 9.19 | |
| $CH_4 + e^- \rightarrow CH_2 + 2H + e^-$ | 9.31 | |
| $C_2H_5 + e^- \rightarrow C_2 + H + 2H_2 + e^-$ | 9.72 | |
| $CH_3 + e^- \rightarrow CH + 2H + e^-$ | 9.73 | |
| $C_2H_6 + e^- \rightarrow C_2H_3 + 3H + e^-$ | 10.61 | |
| $C_2H_2 + e^- \rightarrow C_2 + 2H + e^-$ | 10.85 | |
| $C_2H_4 + e^- \rightarrow C_2H + 2H + e^-$ | 12.09 | |
| $C_2H_6 + e^- \rightarrow C_2H_2 + 4H + e^-$ | 12.26 | |
| $C_2H_3 + e^- \rightarrow C_2 + 2H + e^-$ | 12.49 | |
| $C_2H_5 + e^- \rightarrow C_2H + 3H + e^-$ | 13.7 | |
| $CH_4 + e^- \rightarrow CH + 3H + e^-$ | 13.71 | |
| $CH_3 + e^- \rightarrow C + 3H + e^-$ | 14.34 | |
| $C_2H_4 + e^- \rightarrow C_2 + 4H + e^-$ | 17.17 | |
| $CH_4 + e^- \rightarrow C + 4H + e^-$ | 17.24 | |
| $C_2H_6 + e^- \rightarrow C_2H + 5H + e^-$ | 18.02 | |

| dissociation reaction | activation energy (eV) | ref |
|---|---|---|
| $C_2H_5 + e^- \rightarrow C_2 + 5H + e^-$ | 18.77 | |
| $H_2 + e^- \rightarrow 2H + e^-$ | 4.52 | |

| recombination reaction | rate constant $T_r$ = 520 K ($cm^3$ molecule$^{-1}$ sec$^{-1}$) | ref |
|---|---|---|
| $2CH \rightarrow C_2H_2$ | $1.99 \times 10^{-10}$ | 60 |
| $CH + H \rightarrow C + H_2$ | $2.49 \times 10^{-10}$ | 61 |
| $CH + H_2 \rightarrow CH_3$ | $2.19 \times 10^{-10}$ | 62 |
| $CH + CH_3 \rightarrow C_2H_2 + H_2$ | $1.64 \times 10^{-10}$ | 18 |
| $H_2 + C \rightarrow CH + H$ | $1.50 \times 10^{-10}$ | 63 |
| $CH_2 + H_2 \rightarrow CH_3 + H$ | $1.20 \times 10^{-10}$ | 47,64 |
| $CH + H \rightarrow C + H_2$ | $1.15 \times 10^{-10}$ | 61 |
| $C + CH_3 \rightarrow C_2H_2 + H$ | $8.30 \times 10^{-11}$ | 47,64 |
| $CH_3 + CH_2 \rightarrow C_2H_4 + H$ | $8.30 \times 10^{-11}$ | 65 |
| $CH_2 + H \rightarrow CH + H_2$ | $6.64 \times 10^{-11}$ | 66 |
| $C_2H_5 + H \rightarrow 2CH_3$ | $6.18 \times 10^{-11}$ | 67 |
| $2CH_2 \rightarrow C_2H_2 + H_2$ | $5.25 \times 10^{-11}$ | 26 |
| $C_2H_3 + H \rightarrow C_2H_2 + H_2$ | $4.98 \times 10^{-11}$ | 47,60 |
| $C_2H_5 + H \rightarrow C_2H_4 + H_2$ | $4.98 \times 10^{-11}$ | 47,60 |
| $CH_2 + CH \rightarrow H_2 + C_2H$ | $4.98 \times 10^{-11}$ | 47,60 |
| $CH_2 + CH_3 \rightarrow C_2H_4 + H$ | $2.99 \times 10^{-11}$ | 47,60 |
| $2CH_3 \rightarrow C_2H_6$ | $2.97 \times 10^{-11}$ | 71 |
| $CH_4 + CH_2 \rightarrow C_2H_6$ | $1.66 \times 10^{-11}$ | 29 |
| $H_2 + C \rightarrow CH_2$ | $1.47 \times 10^{-11}$ | 67 |
| $CH + H_2 \rightarrow CH_2 + H$ | $9.68 \times 10^{-12}$ | 68 |
| $C_2H_5 + H \rightarrow C_2H_4 + H_2$ | $2.82 \times 10^{-12}$ | 69 |
| $CH_4 + CH \rightarrow C_2H_4 + H$ | $2.49 \times 10^{-12}$ | 70 |
| $C_2H + H_2 \rightarrow C_2H_2 + H$ | $1.20 \times 10^{-12}$ | 65,70 |
| $C_2H_2 + H \rightarrow C_2H_3$ | $3.42 \times 10^{-13}$ | 65,70 |
| $C_2H_4 + H \rightarrow C_2H_3 + H_2$ | $2.86 \times 10^{-14}$ | 60,65 |
| $C_2H_6 + H \rightarrow C_2H_5 + H_2$ | $2.61 \times 10^{-14}$ | 60,65 |
| $CH_4 + H \rightarrow CH_3 + H_2$ | $5.25 \times 10^{-15}$ | 71 |
| $CH_3 + CH_3 \rightarrow C_2H_5 + H$ | $8.48 \times 10^{-16}$ | 60,65 |
| $CH_3 + H \rightarrow CH_2 + H_2$ | $1.69 \times 10^{-16}$ | 72 |
| $CH_3 + H_2 \rightarrow CH_4 + H$ | $8.82 \times 10^{-17}$ | 60,65 |
| $C_2H_6 + CH_3 \rightarrow C_2H_5 + CH_4$ | $5.70 \times 10^{-17}$ | 60,65 |
| $C_2H_4 + CH_3 \rightarrow C_2H_3 + CH_4$ | $2.67 \times 10^{-17}$ | 60,65 |
| $CH_3 + CH_3 \rightarrow C_2H_4 + H_2$ | $1.60 \times 10^{-20}$ | 72 |
| $CH_2 + C \rightarrow CH + CH$ | $2.23 \times 10^{-29}$ | 73 |
| $C_2 + H_2 \rightarrow C_2H + H$ | $1.39 \times 10^{-13}$ | 74 |
| $CH_4 + C_2H \rightarrow C_2H_2 + CH_3$ | $1.98 \times 10^{-12}$ | 65 |
| $CH_4 + CH_2 \rightarrow CH_3 + CH_3$ | $7.34 \times 10^{-16}$ | 75 |
| $CH_4 + C_2H_3 \rightarrow CH_3 + C_2H_4$ | $3.60 \times 10^{-15}$ | 65 |
| $CH_2 + C_2H \rightarrow CH + C_2H_2$ | $3.01 \times 10^{-11}$ | 65 |
| $CH_3 + H \rightarrow CH_4$ | $1.56 \times 10^{-10}$ | 65 |
| $CH_2 + H \rightarrow CH_3$ | $2.61 \times 10^{-10}$ | 65 |
| $CH + H \rightarrow CH_2$ | $2.51 \times 10^{-10}$ | 65 |
| $C_2 + H \rightarrow C_2H$ | $2.76 \times 10^{-10}$ | 65 |
| $C_2H + H \rightarrow C_2H_2$ | $2.89 \times 10^{-10}$ | 76 |
| $C_2H + H \rightarrow C_2 + H_2$ | $3.16 \times 10^{-21}$ | 77 |
| $C_2H_3 + H \rightarrow C_2H_4$ | $2.32 \times 10^{-10}$ | 76 |
| $C_2H_5 + H \rightarrow C_2H_6$ | $2.24 \times 10^{-10}$ | 76 |
| $C_2H_6 + CH \rightarrow C_2H_4 + CH_3$ | $1.30 \times 10^{-10}$ | 78 |

[a]The values of the rate constants are calculated for a temperature of 520 K. The values given by Morrison, William, and Milne[47] were used for the activation energies.

constant (4.78 s$^{-1}$). This constant was estimated using the pumping speed of the pump (5 m$^3$h$^{-1}$) and inner volume of the cell (290 cm$^3$).
- The accumulation of reaction products from the previous discharge pulses was accounted for by modeling a sequence of 3000 pulses.

- The rate constant of electron dissociation was calculated according to a formula used by Morrison et al.,[47,48] which is described in our previous work.[40]

The ratios between the concentrations of the individual species obtained from the emission spectra and from the

P16

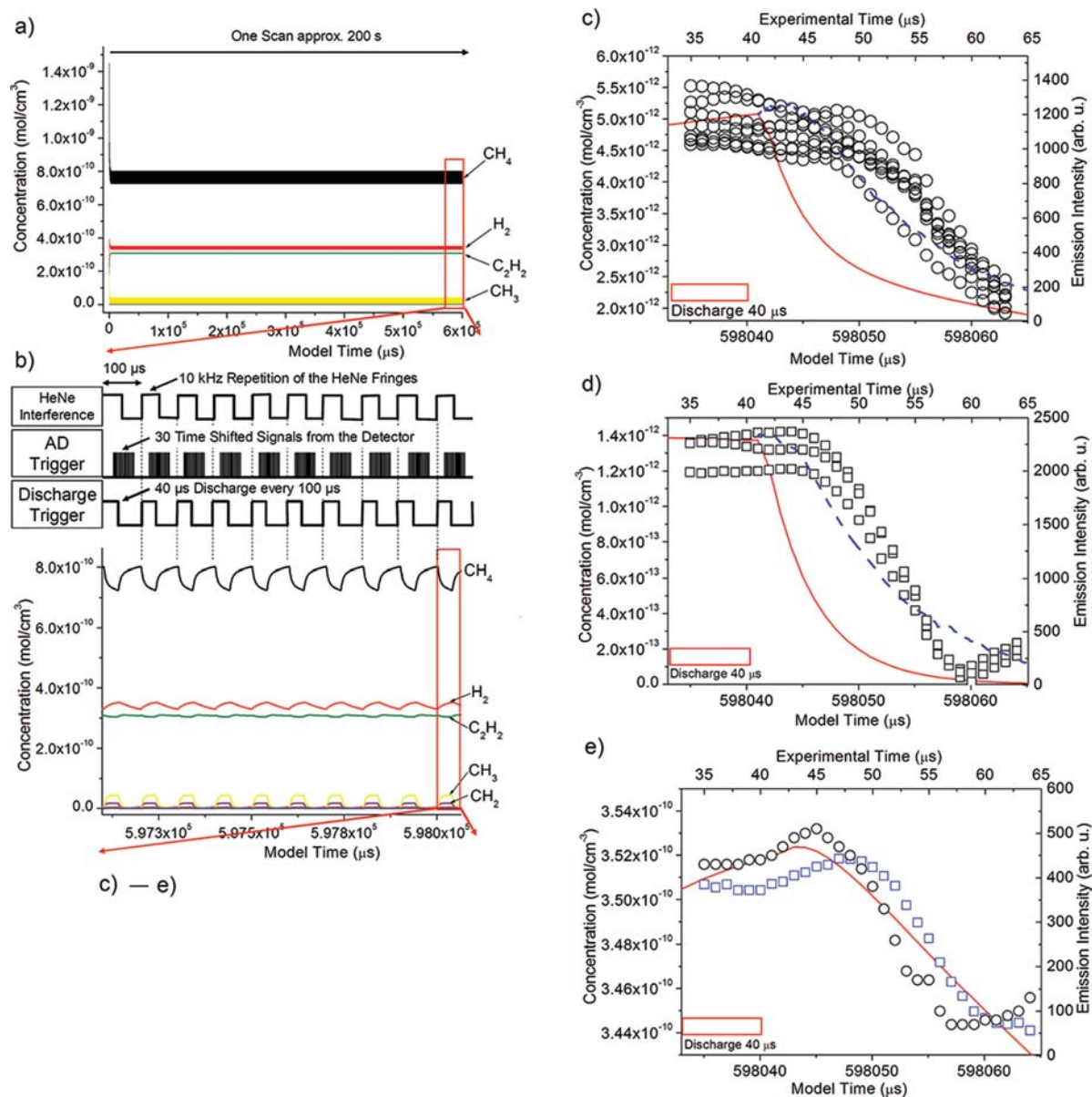**Figure 8.** The results of the chemical model compared with the experimental emission time profiles of selected species in the He/CH$_4$ discharge spectrum after a 40 $\mu$s long discharge pulse. (a) Development of the concentrations of the most abundant species in the discharge over time according to the model. The maximized areas depicted in (b–f) are marked in red. (b) Digitalized signal of the HeNe interference, AD trigger for the data acquisition, and discharge trigger together with the concentration profiles of the most abundant species. (c) ($\square$) The emission profile of the CH X$^2\Pi_r$ ground-state transition ($\nu$ = 1−0, J'' = 3.5) compared with the concentration profile predicted by the chemical model (red line) and the emission profile obtained if collision processes are considered (blue line). (d) ($\square$) The emission profile of the selected C$_2$ Q branch lines of the B$^1\Delta_g$−A$^1\Pi_u$ transition compared with the concentration profile that was predicted from the chemical model (red line) and the emission profile if the collision processes are considered (blue line). (e) The emission profile of the H$_2$ line ($\square$) at 2489.38 cm$^{-1}$, R1(4), 5 g−4f transition, and the line ($\bigcirc$) at 2830.92 cm$^{-1}$ Q(1), 4−3 band, 2p−2s transition, compared with the concentration profile predicted by the chemical model (red line).

discharge model are given in Table 2. The calculated ratios between the individual identified species are in good accord with the experimental values. Figure 8 shows the results of the chemical model. Figure 8a indicates that although the system is designed to allow the discharge products to be continuously removed using a mechanical pump, the products collect in the discharge cell throughout hundreds to thousands of discharge pulses, and a steady

state between the rate of product formation from chemical reactions and the rate of product removal from the cell is established. Figure 8b shows a comparison between the concentration profiles of the species with the highest abundance and the profile of discharge pulses (discharge trigger). The discharge pulses are synchronized with the acquisition of the time-shifted signals from the detector (AD trigger) using the digitalized signal of the HeNe laser.

*Chemistry of the Discharge.* The dehydrogenation of the methane molecule is the main dissociation mechanism in the discharge process. The first step of methane dissociation requires a minimum energy[47] of 4.55 eV (eq 1). This energy is far less than that required for methane ionization, that is, 13 eV. The increase in emission signals from hydrogen can be attributed to the cleavage of hydrogen atoms from the methane molecule because hydrogen gas was not added into the discharge mixture. Emission lines from atomic hydrogen and molecular hydrogen in highly excited states were observed in the infrared spectral range that was measured (2500–3000 cm$^{-1}$). Emission signals attributed to H, H$_2$, and He were observed 4 $\mu$s after the discharge pulse was triggered. The sequential observation of C, H, and H$_2$ and unidentified emissions immediately after atomic He indicate that these species are the primary dissociation products of methane fragmentation.

The first reaction step during the discharge was the excitation of helium, which was followed by Penning ionization and dissociation (eqs 3–7). High-energy Penning electrons are produced via eq 3, which originated 4 $\mu$s after the discharge was initiated, according to the following equation

$$CH_n + e^- \rightarrow CH_{n-1} + H + e^- \tag{14}$$
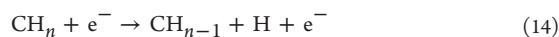
where n = 1–4.

The dissociation of methane due to collisions with electrons requires[47] 4.55 and 9.31 eV according to reactions 1 and 2, respectively. The direct dehydrogenation of methane, which leads to the production of CH, requires 13.71 eV. The ionization potential of helium is 24.59 eV; therefore, the energy required for the fragmentation of methane is available from the discharge. The dissociation is followed by the formation of molecular hydrogen, which results from the collision of the H atom with a hydrocarbon species:
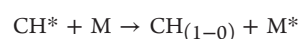
$$CH_n + H \rightarrow CH_{n-1} + H_2 \tag{15}$$
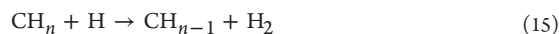
The dehydrogenation of methane leads to the formation of CH$_3$, CH$_2$, and CH fragments. However, only a strong signal was observed for the CH fragment in the emission spectrum. Kado et al.[49] used deuterium isotopes in various abundances found in the products to show that the reaction pathways of methane dissociation by electrons effectively lead to the production of atomic carbon and subsequently to the formation of CH, C$_2$ radicals, and acetylene. The dehydrogenation of CH$_2$ and CH$_3$ is a very fast process. The results of our model show (see Table 2) that the concentrations of the CH$_3$ and CH$_2$ radicals were approximately 8 and 3 times higher, respectively, than the concentration of the CH radical. The reason that the CH$_3$ and CH$_2$ fragments were difficult to detect compared to CH was determined by calculating the integral intensities in the emission spectrum and using relevant values of the Einstein emission coefficient and estimated partition function. The integral intensities of the CH$_3$ and CH$_2$ bands were predicted to be 2 orders lower than the intensity of the CH bands, that is, under the detection threshold of the technique.
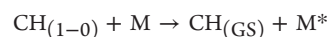
Although the ratios of estimated emission intensities of individual species were consistent with the results of the chemical model (Table 2), the time developments of the emission lines of the observed species (Figure 8c and d) do not agree with the time development of concentrations predicted by the model. In addition to the chemistry of the discharge, the emission lines were assumed to be strongly influenced by collision–radiation processes. The radical and atomic fragments

in the discharge are formed in excited states and subsequently relax into the ground states via radiation and collision processes.

For example, this process can be observed in the emission spectrum of the CH radical (Figure 8c). After the termination of the 40 $\mu$s discharge, the intensity of the emission line of the ground state did not decay until as late as 50 $\mu$s (i.e., 10 $\mu$s after the termination of the discharge). However, the model predicted the decrease in concentration to occur immediately following termination of the discharge. This discrepancy indicates that the observed ground state is complemented by the de-excitation of higher states, which is schematically shown as follows
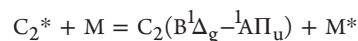
$$CH_4 \rightarrow CH^* + \text{other fragments} \tag{16}$$

$$CH^* + M \rightarrow CH_{(1-0)} + M^*$$
$$k_{(17)} = 7.0 \times 10^{-13} \text{ cm}^3 \text{ s}^{-1} \tag{17}$$

$$CH_{(1-0)} + M \rightarrow CH_{(GS)} + M^*$$
$$k_{(18)} = 5 \times 10^{-13} \text{ cm}^3 \text{ s}^{-1} \tag{18}$$

GS signifies the ground state of the CH radical. In our previous study[40] of the HNC/HCN isomers, the implementation of collision–radiation processes into the model allowed emission line profiles to be simulated more precisely. The system for methane is very complicated, and the chemical model was supplemented by the processes described by eqs 17 and 18. For simplification, we assumed that all states of the CH radical react with the same rate constant to form other products. The concentration of species M, which causes the de-excitation upon collision, was assumed to be the concentration of He ($5.26 \times 10^{16}$ cm$^{-3}$) and the number of molecules in the ground state and excited states that relaxed to the ground state, which were determined using the Boltzmann distribution at the temperature of the discharge ($T_v$ = 5300 K, $T_e$ = 17 000 K). The root-mean-square values of the rate constants ($k_{(13)}$ = $7.0 \times 10^{-13}$ cm$^3$ s$^{-1}$ and $k_{(14)}$ = $5 \times 10^{-13}$ cm$^3$ s$^{-1}$) were obtained by fitting the data to the following equations, which was the same method used to determine the relaxation constants of the C$_2$ radical

$$C_2^* + M = C_2(B^1\Delta_g - ^1A\Pi_u) + M^*$$
$$k_{(13)} = 4.5 \times 10^{-13} \text{ cm}^3 \text{ s}^{-1} \tag{19}$$
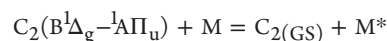
$$C_2(B^1\Delta_g - ^1A\Pi_u) + M = C_{2(GS)} + M^*$$
$$k_{(14)} = 1.0 \times 10^{-13} \text{ cm}^3 \text{ s}^{-1} \tag{20}$$

Figure 8c–e shows the profiles of several emission lines of the CH radicals (c), C$_2$ radicals (d), and molecular H$_2$ (e) with the concentration profile predicted by the chemical model (red line) and the emission profile predicted by the collision–radiation model (blue line). The inclusion of the collision–radiation processes caused the model to be consistent with experimental data. In the case of H$_2$ excited to high Rydberg states, changes to the emission lines and concentration overtime were in agreement (see Figure 8e). It was assumed that the transfer of energy during a collision between the individual states was not relevant and that the emission line is influenced mainly by the concentration profile.

Article

In the previous model[40] for the relaxation of excited HNC, a relaxation constant of $k_{2-1} = 1.15 \times 10^{-11}$ cm$^3$ s$^{-1}$ was obtained for the relaxation of the 2−1 vibration state, which was analogous to eq 17. Similarly, for the reaction analogous to eq 18, a relaxation constant of $k_{1-GS} = 2.2 \times 10^{-12}$ cm$^3$ s$^{-1}$ was obtained. Smith et al.[50] determined the relaxation rates of highly excited states of NCNO, which were on the order of $10^{-14}$ cm$^3$ s$^{-1}$ for collisions with He and Ar atoms but $10^{-10}$ cm$^3$ s$^{-1}$ for the molecular gas $N_2$. The values obtained were closer to the relaxation rates that are achieved with a rare gas buffer, which corresponds to experimental conditions with an abundance of the carrier gas (3 Torr of He) and an addition of the precursor (0.05 Torr of $CH_4$).

In the future, we plan to measure absorption in the MIR, vis, and UV regions using a spectrometer, with the majority of the excited states to be observed. Additionally, we plan to examine the discharges and the consequences of chemicals in the LIDB plasma[80−82] in methane.[1] A pilot study using deuterium isotopes is now under preparation.

All of the measurements will be complemented with experiments in the absorption setup. The measurements will enable the collision−radiation processes of the series of excited states to be included in the model with precision. These measurements will also allow the preferred excited states responsible for the production of the radicals that were studied to be determined.

## 4. CONCLUSION

One of the reactions that led to the breakdown of methane was collisions with electrons. These reactions led to the formation of atomic carbon and hydrogen, which was followed by the formation of $CH_3$, $CH_2$, CH, $C_2$, and other radicals.[83,84] The emission spectra of the discharge in the short pulse mode (10 $\mu$s duration) showed that the first emission spectra of excited helium, atomic carbon, and hydrogen could be detected 4 $\mu$s after the initiation of the discharge. The emission maximum occurred at 13 $\mu$s, followed by the maxima of C and H at 18 $\mu$s. The CH and $C_2$ bands were detected at 8 and 10 $\mu$s, respectively, with the maxima at 23 and 21 $\mu$s, respectively.

A kinetic model was constructed for the emission spectra of the discharge in the long pulse mode (40 $\mu$s duration), which was expected to nearly be in a steady state. Using the kinetic model complemented by the calculation of the emission intensities of the $CH_3$, $CH_2$, CH, and $C_2$ fragments, it was determined that the $CH_3$ and $CH_2$ radicals were not observed in the glow discharge emission spectra due to the low intensity of the emission spectra, rather than low concentrations, which was initially assumed (e.g., the study of pulsed discharge at atmospheric pressure by Kado et al.[49]). The ratio of integral intensities of the CH and $C_2$ bands corresponded well with the results of the kinetic model designed on the basis of current knowledge of the values of rate constants. The decay processes were, however, apart from the chemical reactions, significantly influenced by collision−radiation processes. It should be noted that the model was valid for the experimental setup and conditions used in this study. However, if the experimental conditions (precursor concentration, pumping speed, or voltage) are changed, then the discharge chemistry will be greatly influenced.

The estimated rotation and vibration temperatures of the plasma were 520 ± 42 and 5300 ± 8 K, respectively. These values indicate that nonequilibrium plasma was present during the glow discharge.

## AUTHOR INFORMATION

**Corresponding Author**

*E-mail: martin.ferus@jh-inst.cas.cz. Tel. +420 266 05 3685.

**Notes**

The authors declare no competing financial interest.

## REFERENCES

(1) Babankova, D.; Civis, S.; Juha, L. *Prog. Quantum Electron.* **2006**, *30*, 75−88.
(2) Wiener, H; Burton, M. *J. Am. Chem. Soc.* **1953**, *75*, 5815−5823.
(3) Delacal, E.; Tafalla, D.; Tabares, F. L. *J. Appl. Phys.* **1993**, *73*, 948−954.
(4) Homann, V. H.; Lange, W.; Wagner, H. G. *Ber. Bunsen-Ges. Phys. Chem* **1971**, *2*, 121−&.
(5) Peters, K.; Wagner, O. H. *Z. Phys. Chem.* **1931**, *A153*, 161−186.
(6) Kline, L. E.; Partlow, D. W.; Bies, W. E. *J. Appl. Phys.* **1989**, *65*, 70−78.
(7) Gogolides, E.; Mary, D.; Rhallabi, A.; Turban, G. *Jpn. Appl. Phys.* **1995**, *34*, 261−270.
(8) Vandentop, G. J.; Kawasaki, M.; Nix, R. M.; Brown, I. G.; Salmeron, M.; Samorjai, G. A. *Phys. Rev. B* **1990**, *41*, 3200−3210.
(9) Rhallabi, A.; Catherine, Y. *IEEE Trans. Plasma Sci.* **1991**, *19*, 270−277.
(10) Coburn, J.; Chen, M. *J. Appl. Phys.* **1980**, *51*, 3134−3136.
(11) Keudell, A.; Jacob, W. *Prog. Surf. Sci.* **2004**, *76*, 21−54.
(12) Catherine, Y.; Pastol, A.; Athouel, L.; Fourrier, C. *IEEE Trans. Plasma Sci.* **1990**, *18*, 923−929.
(13) Kawaguchi, K.; Baskakov, O.; Hosaki, Y.; Hama, Y.; Kugimiya, Ch. *Chem. Phys. Lett.* **2003**, *369*, 293−298.
(14) Hosaki, Y.; Civiš, S.; Kawaguchi, K. *Chem. Phys. Lett.* **2004**, *383*, 256−260.
(15) Civiš, S.; Kubát, P.; Nishida, S.; Kawaguchi, K. *Chem. Phys. Lett.* **2006**, *418*, 448−453.
(16) Pastol, A.; Catherine, Y *J. Phys. D* **1990**, *23*, 799−805.
(17) Zhu, W.; Inspektor, A.; Badzian, A. R.; McKenna, T.; Messier, J. *J. Appl. Phys.* **1990**, *68*, 1489−1496.
(18) Kirikov, A. V.; Ryzhov, V. V.; Suslov, A. I. *Tech. Phys. Lett.* **1999**, *10*, 794−795.
(19) Kozlov, K. V. *Czech. J. Phys.* **1998**, *10*, 1199−1207.
(20) Yencha, A. J. *Electron Spectrosc.: Theory, Tech., Appl.* **1984**, *5*, 197.
(21) Tokue, I.; Sakai, Y.; Yamasaki, K. *J. Chem. Phys.* **1997**, *106*, 4491−4498.
(22) Moore, C. E. *Atomic Energy Levels I-III*; U.S. Government Printing Office: Washington, DC, 1949.
(23) Cermák, V. *J. Chem. Phys.* **1966**, *44*, 3781.
(24) Serdioutchenko, A.; Möller, I.; Soltwisch, H. *Spectrochim. Acta, Part A* **2004**, *60*, 3311−3318.
(25) Fischer, F.; Peters, K. *Z. Phys. Chem.* **1929**, *A141*, 180−194.
(26) Tachibana, K.; Nishida, M.; Harima, H.; Urano, Y. *J. Phys. D* **1984**, *17*, 1727−1742.
(27) Smith, G. D.; Palmer, R. A. In *Handbook of Vibrational Spectroscopy*; Chalmers, J.M.; Griffiths, P.R., Eds.; Wiley: Chichester, U.K., 2002; Vol. *1*, pp 625−640.

P19

(28) Rödig, C.; Siebert, F. In *Handbook of Vibrational Spectroscopy*; Chalmers, J.M.; Griffiths, P.R., Eds.;Wiley: Chichester, U.K., 2002; Vol. *1*, pp 641−654.

(29) Kawaguchi, K.; Hama, Y.; Nishida, S. *J. Mol. Spectrosc.* **2005**, *232*, 1−13.

(30) Lubic, K. G.; Amano, T. *J. Chem. Phys.* **1984**, *81*, 1655−1660.

(31) Bernath, P. F. *J. Chem. Phys.* **1987**, *86*, 4838−4842.

(32) Ghosh, P. N.; Deo, M. N.; Kawaguchi, K. *Astrophys. J.* **1999**, *525*, 539−542.

(33) Douay, M.; Nietmann, R.; Bernath, P. F. *J. Mol. Spectrosc.* **1988**, *131*, 261−271.

(34) Davies, P. B.; Guest, M. A.; Stickland, R. J. *J. Chem. Phys.* **1990**, *93*, 5408−5416.

(35) Davies, P. B.; Guest, M. A.; Stickland, R. J. *J. Chem. Phys.* **1990**, *93*, 5417−5423.

(36) Chang, E. S.; Pulchtopek, S.; Eyler, E. E. *J. Chem. Phys.* **1984**, *80*, 601−605.

(37) Dabrowski, I.; Herzberg, G. *Acta Phys. Hung.* **1984**, *55*, 219−228.

(38) *NIST database*. http://physics.nist.gov/PhysRefData/ASD/lines_form.html (downloaded March 20, 2008).

(39) Corbella, C.; Polo, M. C.; Oncins, G.; Pascual, E.; Andújar, J. L.; Bertran, E. *Thin Solid Films* **2005**, *482*, 172−176.

(40) Ferus, M.; Kubelík, P.; Kawaguchi, K.; Dryahina, K.; Španěl, P.; Civiš, S. *J. Phys. Chem. A* **2011**, *115*, 1885−1899.

(41) *NIST Chemical Kinetics Database: Standard Reference Database 17*, version 7.0, Web version release 1.4.3, Data Version 2009.01. http://kinetics.nist.gov/kinetics/index.jsp (dowloaded Oct. 25, 2010).

(42) Hadrwick, J. L.; Whipple, G. C. *J. Mol. Spectrosc.* **1991**, *147*, 267−273.

(43) *NumPy*. http://numpy.org/ (downloaded Oct. 25, 2010).

(44) URL <http://scipy.org/>, downloaded Oct. 25, 2010.

(45) *ODEPACK, Ordinary Differential Equation Solvers*. http://people.sc.fsu.edu/~jburkardt/f77_src/odepack/odepack.html (downloaded Oct. 25, 2010).

(46) Winchester, M.; Payling, R. *Spectrochim. Acta, Part B* **2004**, *59*, 607−666.

(47) Morrison, N. A.; William, C.; Milne, W. I. *J. Appl. Phys.* **2003**, *94*, 7031−7043.

(48) Lieberman, M. A.; Lichtenberg, A. J. *Principles of Plasma Discharges and Materials Processing*, 1st ed.; Wiley: New York, 1994; p 79.

(49) Kado, S.; Urasaki, K.; Sekine, Y.; Fujimoto, K.; Nozaki, T.; Okazaki, K. *Fuel* **2003**, *82*, 2291−2297.

(50) Wright, S. M. A.; Sims, I. R.; Smith, I. W. M. *Phys. Chem. Chem. Phys.* **2001**, *3*, 2203−2208.

(51) Tanarro, I.; Sanz, M. M.; Domingo, C.; Bermejo, D.; Santos, J.; Domenech, J. L. *J. Phys. Chem.* **1994**, *98*, 5862−5866.

(52) Goldmann, A.; Gamache, R. R.; Perrin, A.; Flaud, J. M.; Rinsland, C. P.; Rothmann, L. S. *J. Quant. Spectrosc. Radiat. Transfer* **2000**, *66*, 455−486.

(53) Hollis, J. M.; Jewell, P. R.; Lovas, F. *Astrophys. J.* **1995**, *438*, 259−264.

(54) Bunker, P. R.; Langhoff, S. R. *J. Mol. Spectrosc.* **1983**, *102*, 204−211.

(55) Sauval, A. J.; Tatum, J. B. *Astrophys. J. Suppl. Ser.* **1984**, *56*, 193−209.

(56) Tatum, J. B. *Publ. Dom. Astrophys. Obs.* **1963**, *1*, 12.

(57) Bruna, P. J.; Wright, J. S. *Chem. Phys.* **1991**, *157*, 111−121.

(58) Varanasi, P.; Bangaru, R. P. *J. Quant. Radiat. Transfer* **1974**, *14*, 839−844.

(59) Gamache, R. R.; Kennedy, S.; Hawkins, R.; Rothman, L. S. *J. Mol. Struct.* **2000**, *517*, 407−425.

(60) Braun, W.; McNesby, J. R.; Bass, A. N. *J. Chem. Phys.* **1967**, *46*, 2071.

(61) Harding, L. B.; Guadagnini, R.; Schatz, G. C. *J. Phys. Chem.* **1993**, *97*, 5472−5481.

(62) Fulle, D.; Hippler, H. *J. Chem. Phys.* **1997**, *106*, 8691−8698.

(63) Lin, S. Y.; Guo, H. *J. Phys. Chem. A* **2004**, *108*, 10066−10071.

(64) Frenklach, M.; Wang, H. *Phys. Rev. B* **1991**, *43*, 1520−1545.

(65) Tsang, W.; Hampson, R. F. *J. Phys. Chem. Ref. Data* **1986**, *15*, 1087−1279.

(66) Baulch, D. L.; Cobos, C. J.; Cox, R. A.; Esser, C.; Frank, P.; Just, Th.; Kerr, J. A.; Pilling, M. J.; Troe, J.; Walker, R. W.; Warnatz, J. *J. Phys. Chem. Ref. Data* **1992**, *21*, 411−734.

(67) Pratt, G. L.; Wood, S. W. *J. Chem. Soc., Faraday Trans. 1* **1984**, *80*, 3419−3427.

(68) Zabarnick, S.; Fleming, J. W.; Lin, M. C. *J. Chem. Phys.* **1986**, *85*, 4373−4376.

(69) Camilleri, P.; Marshall, R. M.; Purnell, J. H. *J. Chem. Soc., Faraday Trans. 1* **1974**, *70*, 1434−1444.

(70) Braun, W.; McNesby, J. R.; Bass, A. N. *J. Chem. Phys.* **1967**, *66*, 2071.

(71) Sepehrad, A.; Marshall, R. M.; Purnell, H. *J. Chem. Soc., Faraday Trans. 1* **1979**, *75*, 835−843.

(72) Warnatz, J. *Combustion Chemistry*; Springer-Verlag: New York, 1984.

(73) Mayer, S. W.; Schieler, L.; Johnston, H. S. *Symp. Int. Combust. Proc.* **1967**, *11*, 837−844.

(74) Kruse, T.; Roth, P. *J. Phys. Chem. A* **1997**, *101*, 2138−2146.

(75) Bohland, T.; Dobe, S.; Temps, F.; Wagner, H.Gg. *Ber. Bunsen-Ges. Phys. Chem.* **1985**, *89*, 1110−1116.

(76) Harding, L. B.; Georgievskii, Y.; Klippenstein, S. J. *J. Phys. Chem. A* **2005**, *109*, 4646−4556.

(77) Beck, W. H.; Mackie, J. C. *J. Chem. Soc., Faraday Trans. 1* **1975**, *71*, 1363−1371.

(78) Galland, N.; Caralp, F.; Hannachi, Y.; Bergeat, A.; Loison, J.-C. *J. Phys. Chem. A* **2003**, *107*, 5419−5426.

(79) Ferus, M.; Civiš, S.; Kubelík, P.; Nevrlý, V.; Bitala, P.; Grygorova, E.; Střižík, M.; Kubát, P.; Zelinger, Z. *Plasma Chem. Plasma Proc.* **2011**, *31*, 417−426.

(80) Babankova, D.; Civis, S.; Juha, L.; Bittner, M.; Cihelka, J.; Pfeifer, M.; Skala, J.; Bartnik, A.; Fiedorowicz, H.; Mikolajczyk, J.; et al. *Phys. Chem.* **2006**, *110*, 12113−12120.

(81) Civis, S.; Juha, L.; Babankova, D.; Cvacka, J.; Frank, O.; Jehlicka, J.; Kralikova, B.; Krasa, J.; Kubat, P.; Muck, A.; et al. *Chem. Phys. Lett.* **2004**, *386*, 169−173.

(82) Ferus, M.; Kubelík, P.; Civiš, S. *J. Phys. Chem. A* **2011**, *115*, 12132−12141.

(83) Tokaryk, D. W.; Civiš, S. *J. Chem. Phys.* **1995**, *103*, 3928−3941.

(84) Civiš, S.; Tokaryk, D. W. *J. Mol. Spectrosc.* **1995**, *172*, 543−551.

(85) Touzeau, M.; Vialle, M.; Zellagui, A.; Gousset, G.; Lefebvre, M.; Pealat, M. *J. Phys. D* **1991**, *24*, 41−47.

(86) (a) Civis.; et al. *J. Mol. Spectrosc.* **2008**, *250*, 20−26. (b) Civiš, S.; Šedivcová-Uhlíková, T.; Kubelík, P.; Kawaguchi, K. *J. Mol. Spectrosc.* **2008**, *250*, 20−26.

P20

# HNC/HCN Ratio in Acetonitrile, Formamide, and BrCN Discharge

Martin Ferus,[†,‡] Petr Kubelík,[†,‡] Kentarou Kawaguchi,[§] Kseniya Dryahina,[†] Patrik Španěl,[†] and Svatopluk Civiš*,[†]

[†]J. Heyrovský Institute of Physical Chemistry, Academy of Sciences of the Czech Republic, Dolejškova 3, 18223 Prague 8, Czech Republic

[‡]Institute of Physics, Czech Academy of Sciences, Na Slovance 2, 182 21 Prague 8, Czech Republic

[§]Faculty of Science, Okayama University, Tsushima-naka, Okayama 700-8530, Japan

**ABSTRACT:** Time-resolved Fourier transform (FT) spectrometry was used to study the dynamics of radical reactions forming the HCN and HNC isomers in pulsed glow discharges through vapors of BrCN, acetonitrile ($CH_3CN$), and formamide ($HCONH_2$). Stable gaseous products of discharge chemistry were analyzed by selected ion flow tube mass spectrometry (SIFT-MS). Ratios of concentrations of the HNC/HCN isomers obtained using known transition dipole moments of rovibrational cold bands $\nu_1$ were found to be in the range 2.2−3%. A kinetic model was used to assess the roles the radical chemistry and ion chemistry play in the formation of these two isomers. Exclusion of the radical reactions from the model resulted in a value of the HNC/HCN ratio 2 orders of magnitude lower than the experimental results, thus confirming their dominant role. The major process responsible for the formation of the HNC isomer is the reaction of the HCN isomer with the H atoms. The rate constant determined using the kinetic model from the present data for this reaction is 1.13 ($\pm$0.2) $\times 10^{-13}$ $cm^3$ $s^{-1}$.
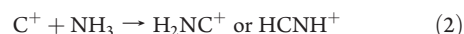
## I. INTRODUCTION

**A. HNC/HCN Ratio in Astronomically Observed Environments.** HNC is a metastable isomer of hydrogen cyanide. Its origin and the mechanisms of its formation in interstellar space are still not entirely understood. The HNC isomer was first detected by radio-astronomical observations of the center of the Milky Way in the constellation of Sagittarius (dense molecular cloud Sgr B2) by Snyder and Buhl[1] in 1971. Its existence has since been proven in other environments, including cold, dense molecular clouds,[2] diffuse clouds,[3] cool carbon stars,[4] comets, and planetary atmospheres.[5]

The abundance of HNC in these various environments varies significantly. In cold molecular clouds (e.g., TMC-1, which has a temperature around 10 K), the HNC/HCN ratio[6] is around 1.55. In warmer or hot regions (e.g., OMC-1, a region of high mass star formation,[7] and hot core regions with temperatures around 200 K; a circumstellar envelope of red giant stars[8] with temperatures of 2800 K), the values range from $10^{-3}$ to 0.2. All of these observations reveal that temperature plays a key role in high HNC/HCN ratios.

The HCNH$^+$ ion, which has been observed by millimeter wave spectroscopy,[9] has been implicated in the formation of HNC and HCN in interstellar clouds. HCNH$^+$ ions are formed in a sequence of reactions initiated by proton donors ionized by cosmic rays, with a general formula XH$^+$ (e.g., H$_3^+$, CH$^+$, NH$^+$, H$_3$O$^+$, HCO$^+$) and with HCN according to the equation:[10]

$$XH^+ + HCN \rightarrow HCNH^+ + X \qquad (1)$$

or in reactions of ions with certain molecules and radicals, e.g.,

$$C^+ + NH_3 \rightarrow H_2NC^+ \text{ or } HCNH^+ \qquad (2)$$

$$N^+ + CH_3 \rightarrow HCNH^+ + H \qquad (3)$$

The H$_2$NC$^+$ isomer also can be transformed to HCNH$^+$ by the absorption of radiation:

$$H_2NC^+ + h\nu \rightarrow HCNH^+ \qquad (4)$$

Finally, the dissociative recombination of the molecular ion[11−13] HCNH$^+$

$$HCNH^+ + e^- \rightarrow HNC/HCN + H \qquad (5)$$

is considered to be the main process for the production of both HNC and HCN, with a branching ratio[14] close to 1:1, thus forming both HNC and HCN in approximately equal amounts, which explains the observational data in cold clouds.

Another possible source of HNC/HCN in interstellar clouds apart from reactions 1−5 is the neutral−neutral radical reactions.[15] According to Talbi et al.,[16] one example of such reactions is

$$C + NH_2 \rightarrow HNC + H \qquad k_{300} = 6.8 \times 10^{-11} \text{ cm}^3 \text{ s}^{-1} \qquad (6)$$

The authors, however, state that any considerable contribution from these reactions is disputable because of what is known of rate constants at low temperatures and the possible isomerization of HNC to HCN due to excitation by the energy released in exothermic reaction.

HNC can also be produced by photochemical processes, for example, in cometary comae, as illustrated by observations of comet Hale-Bopp.[17,18] During Hale-Bopp's approach toward the Sun, the observed HNC/HCN ratio grew from 0.02 to 0.2.

It is supposed that the exchange reaction of suprathermal hydrogen atoms between HCN and HNC plays an important role in the cometary comae. The suprathermal hydrogen atoms originate from the photoinduced decay of H-containing species[19] and both isomers are formed:

$$HCN + H \rightarrow HNC + H \qquad (7)$$

$$HNC + H \rightarrow HCN + H \qquad (8)$$

Sumathi and Nguyen et al.[20] and Talbi et al.[21] have given the following values for the rate constants: $k_7 = 5.6 \times 10^{-15}$ cm$^3$ s$^{-1}$ for the forward reaction 7 and $k_8 = 5 \times 10^{-12}$ cm$^3$ s$^{-1}$ for the reverse reaction 8. The activation barrier of reaction 7 was determined to be 17.8 kcal/mol (0.77 eV) for the forward reaction and 4.2 kcal/mol (0.18 eV) for the reverse reaction.[22] It was found that the HNC/HCN equilibrium obtained via reaction 7 is an important factor affecting the chemistry of cometary comae;[23] however, it is not the only mechanism of HNC production, and it does not always fully explain the observed HNC/HCN ratios. For this reason, it is assumed that HNC could also be directly the decay product of an unknown parent compound.

**B. Laboratory Detection of HNC.** In the laboratory, HNC was first observed in an argon matrix in the mid-infrared spectral range (600−4000 cm$^{-1}$) by Milligan and Jacox,[24] and more comprehensive measurements were obtained by Burkholder[25] or Mellau.[26] As HNC cannot be distinguished by mass from its isomer, HCN, spectroscopy is the only applicable method for the detection of this molecule, apart from collision-induced dissociative ionization measurements.[27] Deuterated isotopologues DNC and DCN have also been detected in space[28] and studied in the laboratory.[27]

In addition to the above-mentioned low-temperature mechanisms, which are typical for interstellar clouds, the simple heating[29] of HCN can be used to measure the highly resolved spectra of gaseous HNC while the spontaneous isomerization of HCN into HNC occurs. The potential energy barrier separating the two species is 50.5 kcal/mol (2.19 eV), while the energy of HNC is higher than the energy of HCN[30] by 11 kcal/mol (0.47 eV). According to the theoretical calculation of the partition function, as presented by Tennyson,[31] extremely high temperatures are necessary to reach a higher HNC/HCN ratio. The equilibrium constant of plain isomerization

$$HC\equiv N \rightleftharpoons {}^-C\equiv \overset{+}{H}N \qquad (9)$$

under 1400 K is less than 1%. It is assumed that it is actually this thermal isomerization of HCN into HNC in reaction 9 that plays the main role in cool carbon stars, which have inner atmosphere temperatures of several thousand K.[32]

HNC/HCN can also be observed in discharges,[33,34] e.g., in the mixture of CH$_4$/N$_2$ or acetonitrile/Ar or by the reaction of translationally excited H atoms with CN containing molecules (e.g., BrCN, ClCN, ICN). These atoms have been generated by



**Figure 1.** Schematic diagram of the experimental apparatus.



**Figure 2.** Schematic diagram of the SIFT-MS spectrometer.

the photolysis[35] of CH$_3$SH (248 nm) or directly by breaking down the parent compounds with excimer laser radiation.[36] Hydrogen reacts with the parent compound in the following way:

$$H + BrCN \rightarrow HNC + Br \quad \sigma = 1.45 \times 10^{-16} \text{ cm}^2 \qquad (10)$$

$$H + BrCN \rightarrow HCN + Br \quad \sigma = 2.21 \times 10^{-17} \text{ cm}^2 \qquad (11)$$

$$H + BrCN \rightarrow HBr + CN \quad \sigma = 2.89 \times 10^{-18} \text{ cm}^2 \qquad (12)$$

where $\sigma$ is the total reaction cross section. These reaction profiles were studied in a photolytic experiment by Macdonald,[37,38] who estimated the ratio of the total reaction cross section (0.85/0.13/0.017) and the total cross section ($1.7 \times 10^{-16}$ cm$^2$). Brupbacher et al.[88] estimated the branching ratio between (11) and (12) to be 1:1. The ratios of the reaction cross sections preferring the formation of HNC were also found. However, these ratios contradicted the thermodynamics data because, according to the theoretical prediction made by Song et al.,[39] the activation barriers of reactions 10 and 11 are 24.4 kcal/mol (1.05 eV) and 4.6 kcal/mol (0.19 eV), respectively. Therefore, the formation of HCN is favorable from an energetic point of view. Other studies have indicated that the reaction channel 10 leading to the formation of HNC is less important. For example, Arunan et al.,[40] using a flowing afterglow technique, found that the branching ratio between reactions 10 and 11 is 1:3 in favor of HCN. Arunan, however, in opposition to the theoretical assumptions,[39] determined the activation barrier of reaction 9

1886

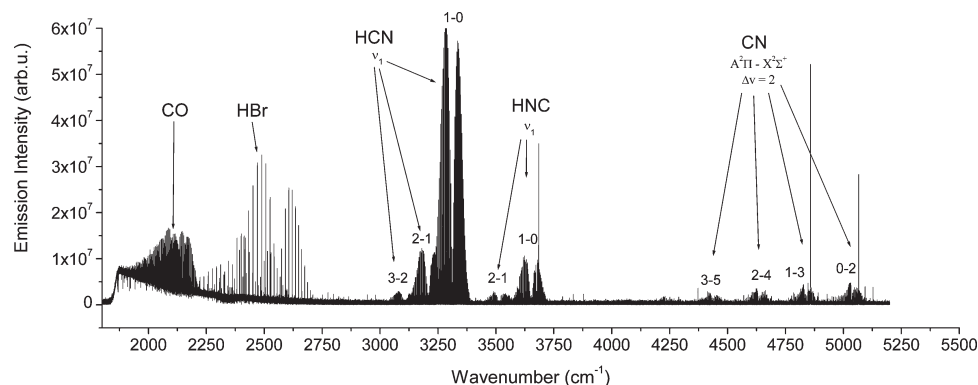dx.doi.org/10.1021/jp1107872 |*J. Phys. Chem. A* 2011, 115, 1885–1899

P22

**Figure 3.** Emission spectrum of the BrCN + H₂ discharge (10 $\mu$s after the discharge pulse).
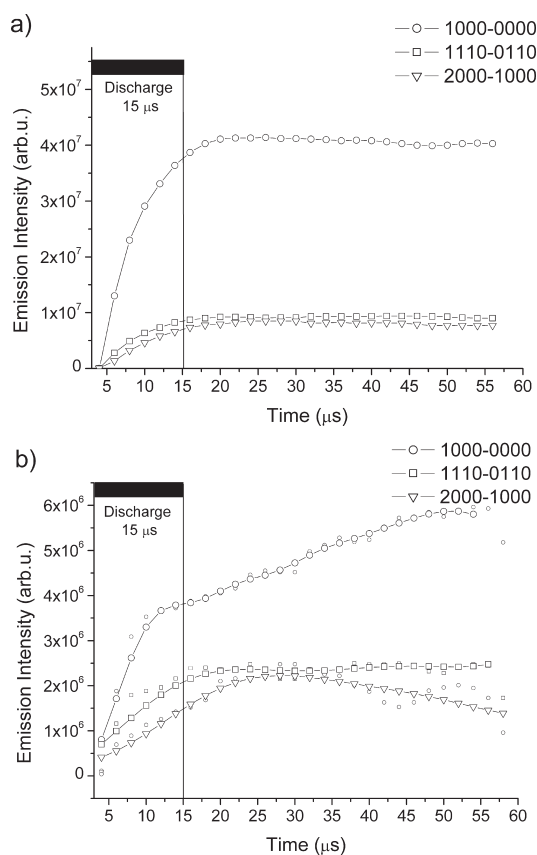


**Figure 4.** Time dependence of intensity profiles of HCN (a) and HNC (b) bands in the BrCN + H₂ discharge.

to be 7.8 kcal/mol (0.34 eV). The activation barrier of reaction 12 was determined[42] to be 14.1 kcal/mol (0.61 eV).

HNC has been identified as a minor product in reactions of the CN radical with hydrocarbons. Copeland et al.[41] found that the rate constants of HCN formation from hydrocarbons have values of approximately $10^{-11}$ cm³ s⁻¹, but the overall emission intensity of HNC in the observed region $(3425-3825$ cm⁻¹) reaches only 1% of the emission intensity of HCN.

HNC has also been observed in an Ar matrix during the breakdown of formamide,[42] diazomethane,[43] and a mixture of hydrogen azide HN₃ with CO.

Precursors related to stellar and interstellar chemistry were chosen in our work. Acetonitrile was first found in space[44] in 1971 in a molecular cloud near Sgr A and Sgr B, and in 1974, it was identified in the comet Kohoutek.[45] As in the case of BrCN, acetonitrile is a simple compound, and its decay produces the CN radical. Formamide, which does not contain the CN group, was also detected[46] in Sgr A and Sgr B in 1971. In 2000, formamide was identified in comet Hale-Bopp.[47] The problematic origin of biomolecules from simple compounds is widespread,[48] and formamide is regarded as one of the possible precursors of nucleic bases.[49] The chemistry of formamide's decay is, therefore, important for understanding the mechanism of the origin of nucleic bases.

## II. EXPERIMENTAL SECTION

**A. Experimental Setup.** The experimental setup is shown in Figure 1. A 25-cm-long positive column discharge tube with an inner diameter of 12 mm was placed in front of the interferometer window in emission configuration. The radiation was focused using a CaF₂ lens. The ac glow discharge was maintained by an HTS 81 high voltage transistor switch (Behlke electronic GmbH, Frankfurt, Germany), which was applied between the stainless steel anode and the grounded cathode. The voltage drop across the discharge was 1200 V, with a pulse width of 15 $\mu$s (BrCN) or 22 $\mu$s (CH₃CN, HCONH₂) and a peak-to-peak current of 0.5 A. The pressure was measured using a Baratron gauge.

An InSb detector was used at a spectral range of 1800−4000 cm⁻¹ or 2000−6000 cm⁻¹ with Ge interference optical filters at an unapodized resolution of 0.05 cm⁻¹. Fifty scans were averaged to obtain a reasonable signal-to-noise ratio. Synchronization of the data acquisition (AD trigger) and the discharge (discharge trigger) was provided by a FPGA processor. The system was driven by a HeNe laser interference signal (Bruker 120 IFS spectrometer) with frequencies of 5 or 10 kHz.

The stable gas phase products were analyzed using a SIFT-MS technique.

**B. Continuous Scanning Time-Resolved FT Spectroscopy.** Time-resolved FT spectroscopy is a wide-spectrum technique used for studying the dynamics of chemical reactions or the

**Table 1. List of All Compounds Detected in the Emission Spectra (Upper Part of the Table) Using FTIR and in the Mass Spectra Using SIFT-MS (Bottom Part of the Table)**[a]

| compound | system | | | note |
|---|---|---|---|---|
| | acetonitrile | formamide | BrCN | |
| Spectral Data, 0.6 A Peak-to-Peak Current Discharges (1.2 kV) | | | | |
| HCN | $2.5 \times 10^7$ | $1.1 \times 10^8$ | $1.4 \times 10^8$ | max band intensity (arb units) $- \nu_1$ |
| HNC | $3.0 \times 10^6$ | $1.7 \times 10^7$ | $2.0 \times 10^7$ | max band intensity (arb units) $- \nu_1$ |
| HNC/HCN | 2.80% | 2.20% | 3.00% | |
| CO | | s | | $\nu_1$ band |
| CO$_2$ | | s | | $\nu_3$ band |
| N$_2$ | not observed | s | not observed | electronic transition, see ref 86 |
| CH | | w | | $^2\Pi^-$ ground state |
| NH | | w | | $X^3\Sigma^-$ ground state |
| CN | s | s | s | $X^2\Sigma$ band $\Delta \nu = 1$ |
| CN | s | s | s | $A^2\Pi - X^2\Sigma$ band $\Delta \nu = 2$ |
| CN | s | s | s | $A^2\Pi - X^2\Sigma$ band $\Delta \nu = 3$ |
| C | s | s | s | atomic lines |
| H | s | s | s | atomic lines |
| N | s | s | s | atomic lines |
| H | s | s | s | atomic lines |
| SIFT Data, 0.6 A Peak-to-Peak Current Discharges (1.2 kV) | | | | |
| HNC/HCN | 671 | 3562 | | |
| C$_2$H$_2$ | | 147 | | |
| CH$_4$ | 56 | 897 | | |
| HCHO | | 21 | not measured | signal in arb units |
| NO | | 21 | | |
| CH$_3$OH | | 9 | | |
| (CH$_3$)$_2$CO | | 7 | | |

[a] The emission intensity of HNC/HCN is expressed in arbitrary units; in the case of other species, w means weak intensity and s means strong intensity.
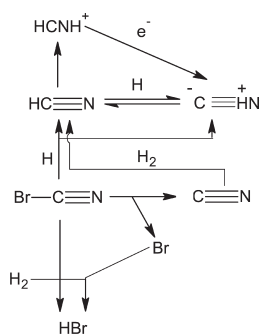


**Figure 5.** Scheme of the BrCN decomposition.

dynamic properties of molecules, radicals, and ions in liquid, gas, and solid states.[50] The time-resolved continuous scanning principle was the basis for the data acquisition, which was conducted using a modified Bruker IFS 120 spectrometer in our laboratory at the J. Heyrovsky Institute of Physical Chemistry, and a similarly modified spectrometer was used in Okayama, Japan. The principle of the used method has been described in detail in previous papers.[51,52]

The data acquisition system can be described as follows: The position of the traversing mirror of the Michelson interferometer was detected by reading the interference maxima of the HeNe

laser emission. The input signal in a cosine function shape was digitally processed into rectangular pulses, and it became the internal standard of the interferometer. The frequency of these rectangular pulses depends on the mirror speed. In the classic measurement mode, the frequency is usually 10 kHz with a pulse duration of 100 $\mu$s. An external processor monitors the beginning of the HeNe laser digital pulse, its order, and the zero position of the mirror. During one pulse, the signal from the detector is read (30 or up to 64 readings), which is the so-called AD trigger. A discharge pulse of variable length can be arbitrarily inserted into the data acquisition process (AD trigger). This process results in 30−64 reciprocally time-shifted spectra.

**C. Selected Ion Flow Tube Mass Spectrometry.** Selected ion flow tube mass spectrometry (SIFT-MS; see Figure 2) is a technique that allows the quantification of trace amounts of gases and vapors present in air. SIFT-MS is based on chemical ionization using reagent ions $H_3O^+$, $O_2^+$, and $NO^+$. These ions do not react with the major components of air, but they selectively ionize trace amounts of other gases and vapors. Absolute quantification is achieved on the basis of a well-defined reaction time, during which chemical ionization takes place in the helium carrier gas flowing through a flow tube into which the reagent ions are injected and the sample is introduced at a known flow rate. In this study, we used SIFT-MS to analyze stable compounds produced during the decomposition of formamide and acetonitrile in a discharge pulse. Only qualitative analysis is possible under glow discharge conditions due to the highly complicated composition and possible ion
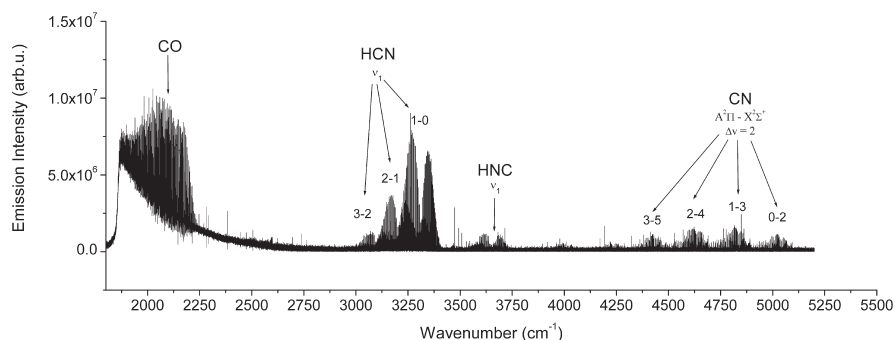
P24

**Figure 6.** Emission spectrum of the acetonitrile discharge (10 $\mu$s after the discharge pulse).

chemical reactions of the products in the flow tube. SIFT-MS has been used to study trace gases in various biological systems[53] and gases produced in controlled combustion.[54]

## III. RESULTS AND DISCUSSION

**A. The BrCN/H$_2$ Discharge.** The emission spectrum of the mixture of 0.5 mbar BrCN, 0.5 mbar H$_2$, and 2 mbar He discharge is shown in Figure 3. The HCN and HNC emission profiles (integrated intensity of the band) detected in the discharge are shown in Figure 4. The following species were detected: HBr, HCN, HNC, and CN, atomic lines of Br, C, and N, and the emission spectrum of CO (presented as an impurity). A summary of the emission bands of the identified species is given in Table 1. A summary of the other identified species, which were characteristic for the individual types of discharge, including the detection results from the SIFT-MS method for the individual systems, is also given in Table 1.

The reaction pathways of BrCN decomposition proposed on the basis of a search of the literature are shown in Figure 5. During the 15 $\mu$s discharge and 15 $\mu$s into the afterglow in the BrCN/He + H$_2$ mixture, collisions with electrons cause the excitation and dissociation of the hydrogen molecules into H atoms:

$$H_2 + e^- \rightarrow 2H + e^- \tag{13}$$
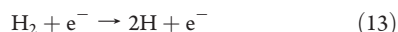
as well as the direct dissociation of the BrCN precursor following the equation

$$BrCN + e^- \rightarrow CN + Br + e^- \tag{14}$$

The process of Penning ionization[55,56] occurring in discharges in carrier gases with high ionization energies also produces energetic electrons in reactions involving metastable atoms with molecules M. The energy of such Penning electron is between the ionization energy of the collision partner and the energy of the excited rare gas atom (e.g., He $\approx$ 20 eV):

$$He^* + M \rightarrow He + M^+ + e^- \tag{15}$$

The energetic electrons contribute to the dissociation of the precursor molecules. The dissociation energy of the Br−CN bond is 3.69 eV. In the case of the collision with atomic hydrogen, and analogous to the photolytic experiment, some contributions from reactions 10−12 can be taken into account in addition to the mechanism of direct dissociation via (13) and (14).

The emissions of the atomic species of H, Br, and He reach their maxima at the time of the termination of the discharge (15
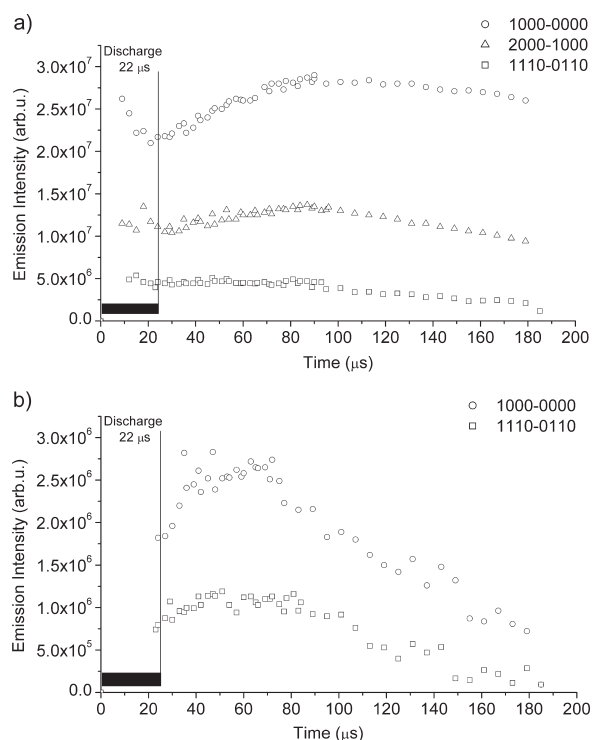


**Figure 7.** Time dependence of intensity profiles of HCN (a) and HNC (b) bands in the CH$_3$CN discharge.

$\mu$s), and they are followed by the emission maximum of the A$^2\Pi$−X$^2\Sigma$ CN band.

The maximum emission of HNC $\nu_1$ − GS (GS = ground state) is reached within 40−50 $\mu$s, but the excited $2\nu_1$ − $\nu_1$ band reaches its maximum immediately after the discharge pulse. The HCN maximum occurs around 25 $\mu$s.

The reverse decay of hydrogen cyanide into the CN radical[57] and molecular hydrogen is a reaction with a low rate constant:

$$H + HCN \rightarrow H_2 + CN \quad k_{500} = 1.07 \times 10^{-20} \text{ cm}^3 \text{ s}^{-1} \tag{16}$$
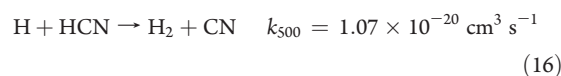
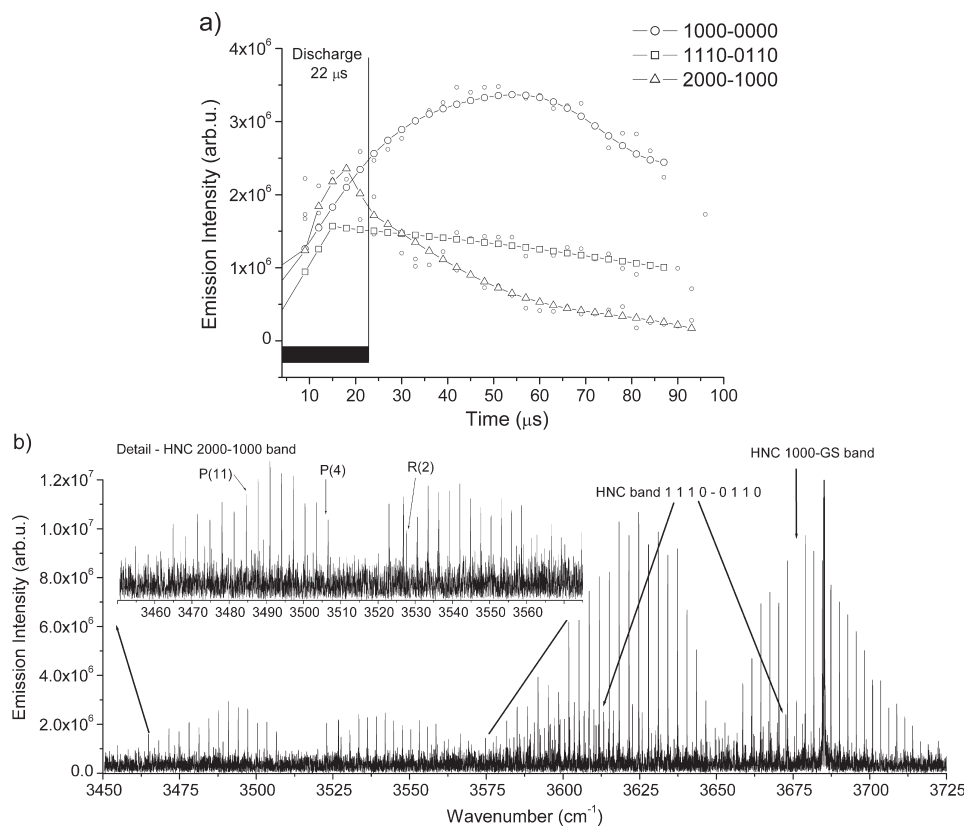The produced CN radical can react with the precursor molecule according to the equation[58]

**Figure 8.** Time dependence of intensity profiles of HNC (a) bands in the $CH_3CN + H_2$ together with details of the $2\nu_1 - \nu_1$ band 10 $\mu$s after the discharge pulse (b).



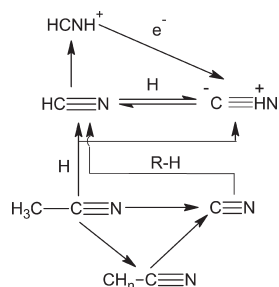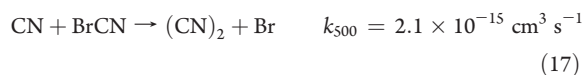**Figure 9.** Scheme of the $CH_3CN$ decomposition.

$$CN + BrCN \longrightarrow (CN)_2 + Br \qquad k_{500} = 2.1 \times 10^{-15} \text{ cm}^3 \text{ s}^{-1}$$

$$(17)$$

However, $(CN)_2$ was detected neither in the discharge nor in its products. Due also to the low rate constant when compared to the H + CN reaction and the fast dissociation of BrCN, this reaction can be neglected. We assume that the equilibrium is also affected by reactions of HCN and HNC with the hydrogen radical according to eqs 7 and 8.

**B. The $CH_3CN$ Discharge.** HCN and HNC as well as CN, H, N, and C radicals were identified in the emission spectra of a discharge in 0.5 mbar acetonitrile and 2.5 mbar He/Ar. In some

cases $0.5-1.5$ mbar of $H_2$ have been used. Using the SIFT-MS method, HCN and methane were found to be the most abundant in the discharge products. The emission spectrum is shown in Figure 6. The time progression of the HNC and HCN formation is shown in Figure 7. The addition of 0.5 mbar hydrogen led to an increase in the emission intensity of both HNC and HCN, while a clearly visible HNC $2\nu_1 - \nu_1$ band was also found. The time progression in comparison to the other HNC and HCN transitions is shown in Figure 8. A summary of the identified species and their emission bands is given in Table 1.

The reaction diagram of acetonitrile decomposition, drawn on the basis of a search of the literature, is shown in Figure 9. During 22 $\mu$s of the discharge and 15 $\mu$s into its afterglow, acetonitrile is dissociated by a collision with a fast electron, and species H and C as well as the CN radical are produced. The CN emission spectrum was observed at 25 $\mu$s, i.e., 3 $\mu$s after the discharge termination, as it was the case in the BrCN/He + $H_2$ discharge. The acetonitrile dissociation process is described by the following equation:

$$CH_3CN + e^- \longrightarrow CN + \text{other products} + e^-$$

$$\sigma_{(8\,eV)} = 1 \times 10^{-20} \text{ cm}^2 \qquad (18)$$
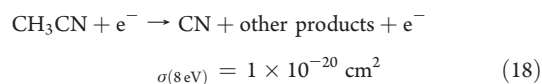
The reaction cross section given with eq 18 is valid for acetonitrile dissociation in an electron beam resulting in $CN^-$ and $CH_3$, as stated by Märk et al.[59] The dissociation of only a single hydrogen from the molecule producing $CH_2CN$ has a reaction cross section of $\sigma_{(3.5\,eV)} = 4 \times 10^{-19}$ cm$^2$. Märk et al. found that the ratios of
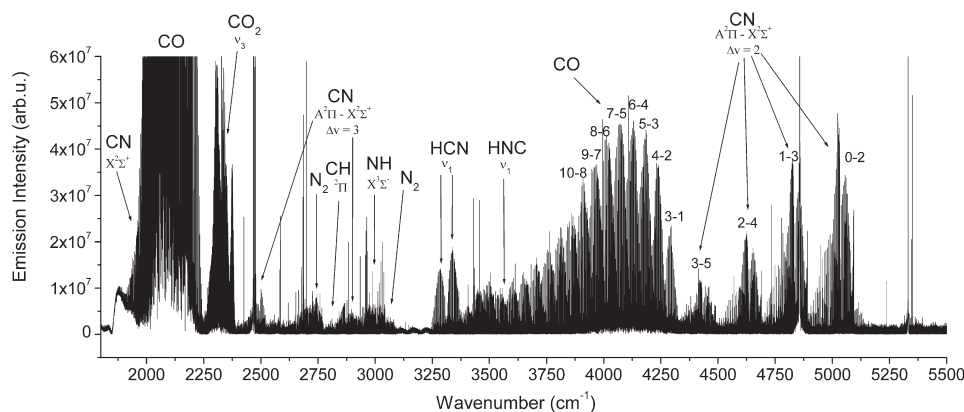
**Figure 10.** Emission spectrum of the formamide discharge (10 $\mu$s after the discharge pulse).
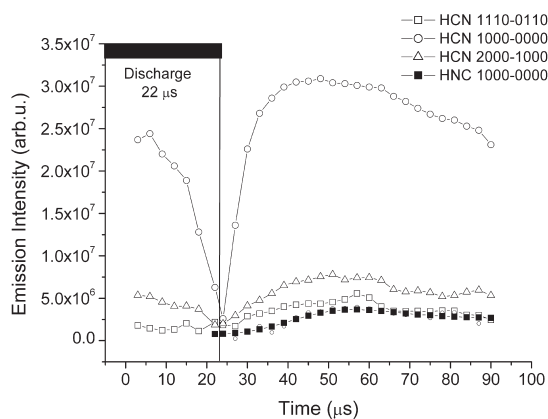


**Figure 11.** Time dependence of intensity profiles of HCN and HNC bands in the formamide discharge.

reaction cross sections for the products are 2000:35:7:50 for $CH_2CN^-$, $CHCN^-$, $CCN^-$, and $CN^-$, respectively. With regard to these conclusions, it can be assumed that reaction 18 is composed of the following partial dissociation reactions:

$$CH_nCN \rightarrow CH_{n-1}CN + H \qquad (19)$$

while the last step is the split into atomic carbon and the CN radical

$$CCN \rightarrow C + CN \qquad (20)$$

The $CH_3$, $CH_2$, and CH radicals are, therefore, produced in smaller concentrations than CN. Neither the $CH_3$, $CH_2$, and CH nor the C—CN species were detected in the emission spectra. This fact, explained in the conclusion of our paper, deals with the decomposition of methane in a glow discharge.

The emission lines of CH, $C_2$, and molecular hydrogen were detected in the observed spectra. It was found that the CH radical is produced by the dehydrogenation of the parent compound, that is, in the same way as we expected in the case of the elimination of CN from $CH_3CN$. This process is generally described by the equation

$$CH_n \rightarrow CH_{n-1} + H \qquad (21)$$

We found that only the CH radical was present in a detectable concentration. We therefore assume that the mechanism is the same as in the case of $CH_3CN$ and the CN radical. The results of the SIFT-MS method of measuring the product composition also
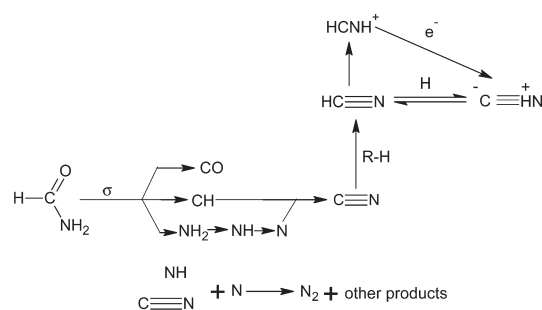


**Figure 12.** Scheme of the formamide decomposition.

showed that the main reaction product is HCN (about 80 %) and not hydrocarbons.

Analogous to the case of BrCN and reaction 12, we could assume that CN is also produced in the reaction of hydrogen radicals with the parent compound according to the equation[60]

$$CH_3CN + H \rightarrow CH_4 + CN \qquad k_{550} = 1.09 \times 10^{-14} \text{ cm}^3 \text{ s}^{-1} \qquad (22)$$
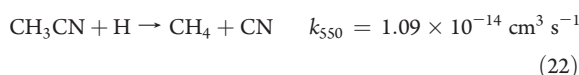
Note that reactions similar to 10 and 11 leading to the formation of HNC/HCN + $CH_3$ are possible, but no accurate information regarding their rates is available.

**C. The HCONH$_2$ Discharge.** The discharge in formamide is chemically different from the discharges in compounds like BrCN and $CH_3CN$, which contain the CN group. In the case of formamide dissociation, the CN radical is a product of subsequent reactions. The study of formamide decomposition is, therefore, important as a reference experiment. For this reason, the formamide dissociation is mentioned in the presented article, although its exact mechanism, and a comparison with the dissociation by UV ArF laser, will be described in detail in a separate work.[61]

The following species were identified in the emission spectra of the discharge in formamide (Figure 10): molecular nitrogen, CO, $CO_2$; CN, CH, and NH radicals, HNC, HCN, and the atomic lines of C, N, O, and H. The HNC and HCN emission progression is shown in Figure 11. Among the species identified in the discharge products by the SIFT-MS method were HCN, acetylene, methane, formaldehyde, nitrous oxide, and methanol. Some species, such as carbon monoxide or dinitrogen oxide,

could not be detected due to their low reactivity with the ions used in the SIFT-MS method. Spectral analysis is an important counterpart of this type of mass detection.

The reaction mechanism of the formamide decomposition composed on the basis of a search of the available literature is summarized in Figure 12. The major primary dissociation channel is known to be[62]

$$HCONH_2 + e^- \rightarrow HCO + NH_2 + e^- \tag{23}$$

This reaction was studied at 193 nm in an Ar matrix by Fourier transform IR spectroscopy,[44] and HCO was identified as the main product. In the discharge, the mentioned dissociation by the collision with a fast electron takes place again during the 22 $\mu$s discharge period and in the afterglow. The HCO radical is dissociated (the dissociation energy is 0.68 eV), producing CO, which is a stable product (dissociation energy 11.14 eV).

The species with general formula $NH_n$ ($n$ = 1, 2, 3) are dehydrogenated in the glow discharge

$$NH_n + e^- \rightarrow NH_{n-1} + H + e^- \tag{24}$$

and subsequently, CN is formed in the reaction of CH with atomic nitrogen:[63]

$$HC + N \rightarrow CN + H \qquad k_{500} = 1.58 \times 10^{-10} \text{ cm}^3 \text{ s}^{-1} \tag{25}$$

The reaction of the reverse formation of NH has a significantly lower rate constant than in the CN formation:[64]

$$CH + N \rightarrow NH + C \qquad k_{500} = 1.58 \times 10^{-12} \text{ cm}^3 \text{ s}^{-1} \tag{26}$$
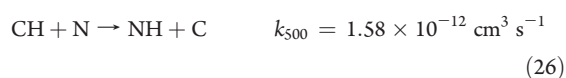
Molecular nitrogen $N_2$ was detected exclusively in the spectra of formamide; it was not detected in the experiments with acetonitrile or BrCN. We assume that, in this system, $N_2$ is produced in the reaction of atomic nitrogen with NH and CN according to the following equations:[65,66]

$$NH + N \rightarrow N_2 + H \qquad k_{500} = 2.49 \times 10^{-11} \text{ cm}^3 \text{ s}^{-1} \tag{27}$$

$$CN + N \rightarrow N_2 + C \qquad k_{500} = 1.12 \times 10^{-11} \text{ cm}^3 \text{ s}^{-1} \tag{28}$$
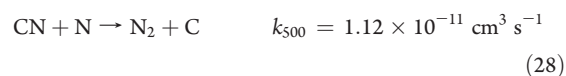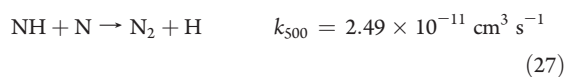
The absence of molecular nitrogen in the acetonitrile and BrCN spectra can be explained by the large dissociation energy of the CN radical (6.11 eV), so that CN, instead of dissociation, more probably enters a reaction, producing stable HNC/HCN. In contrast, the formamide molecule is dissociated into $NH_2$ and NH, i.e., species with lower dissociation energies (3.29 and 3.27 eV, respectively). $NH_2$ and NH subsequently break down and produce reactive atomic nitrogen. This atomic nitrogen reacts with these radicals in reverse according to eqs 25, 27, and 28, producing molecular nitrogen or CN.

The CN radical in the formamide/Ar discharge subsequently reacts with molecules containing hydrogen (HCO, $NH_n$), e.g.,

$$HCO + CN \rightarrow HCN + CO \tag{29}$$

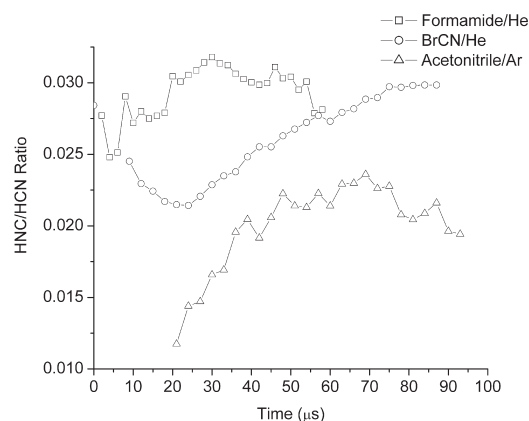producing hydrogen cyanide as the product of this discharge.



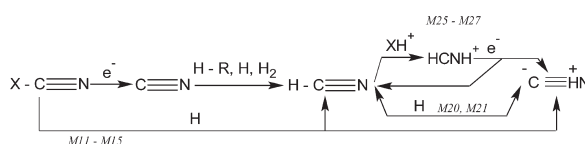**Figure 13.** Time dependence of HNC/HCN ratios in formamide, BrCN, and acetonitrile.



**Figure 14.** Proposed scheme of the HNC formation in the glow discharge. M is related to the chemical equation in the model. The precursor (general formula X—CN) is dissociated to the CN radical. The second possibility is a reaction with the atomic hydrogen. The CN radical reacts with hydrogen containing species (R—H) or hydrogen, and HNC/HCN is formed. HCN reacts with H to HNC or it is protonated to $HCNH^+$, which forms HNC by the dissociation recombination with the electron.

**D. Determining the Ratios of HNC/HCN and the Mechanism of HNC Formation.** Knowledge of the transition moment or the band strength of a particular molecule provides information on its quantitative abundance. The transition dipole moment of the HCN band $\nu_1$ is 0.083 D, and the transition dipole moment of the HNC band[67] $\nu_1$ is 0.156 D. According to Tennyson et al.,[68] the equation for the intensity of the band using common SI units can be written as

$$S_{ji} = \frac{2\pi^2 N_A \nu_{ji}}{3hc\varepsilon_0}\left[1 - \exp\left(\frac{-hc\nu_{ji}}{kT}\right)\right] \cdot |\langle j|\mu|i\rangle|^2 \tag{30}$$

where $N_A$ is Avogadro's number, $\nu_{ji}$ is the frequency of the transition, $h$ is the Planck constant, $c$ is the speed of light, $\varepsilon_0$ is the permittivity of the vacuum, $|\langle j|\mu|i\rangle|$ is the transition dipole moment, and $T$ is the thermodynamic temperature. The factor in square brackets in eq 30 is the population difference between the two vibrational states $i$ and $j$. This factor gives rise to induced emission and is very close to unity for the temperature typical for the glow discharge (approximately 500−600 K). After substitution and conversion of the dipole moment to the Debye units (1 D = 3.336 × 10^{-30} Cm) and the wavenumber to cm$^{-1}$, this equation can be enumerated as follows:

$$S_{ji} = 2.5066379 \cdot 10^5 \cdot \nu_{ji} \cdot |\langle j|\mu|i\rangle|^2 \tag{31}$$

The intensity of the HCN band $\nu_1$ calculated from eq 31 is $S_{HCN}$ = 5.78 × 10^6 cm/mol, which conforms to the data from the literature. The intensity of $S_{HNC}$ = 2.27 × 10^7 cm/mol was

**Table 2. Reactions Used in the Model of HNC/HCN Chemistry**

| reaction type | no. | reaction | threshold energy (eV) | remark |
|---|---|---|---|---|
| electron impact dissociation | M0 | $BrCN + e^- \rightarrow Br + CN + e^-$ | 3.30 | predicted using eq 37 |
| | M1 | $CH_3CN + e^- \rightarrow CH_3 + CN + e^-$ | 5.30 | |
| | M2 | $CH_3CN + e^- \rightarrow H + CH_2CN + e^-$ | 3.12 | |
| | M3 | $CH_2CN + e^- \rightarrow CHCN + H + e^-$ | 3.12 | |
| | M4 | $CHCN + e^- \rightarrow CCN + H + e^-$ | 3.12 | |
| | M5 | $CCN + e^- \rightarrow C + CN + e^-$ | 6.29 | |
| | M6 | $HCN + e^- \rightarrow H + CN + e^-$ | 5.41 | |
| | M7 | $HNC + e^- \rightarrow H + CN + e^-$ | 4.92 | |
| | M8 | $H_2 + e^- \rightarrow H + H + e^-$ | 4.17 | |
| | M9 | $D_2 + e^- \rightarrow D + D + e^-$ | 4.55 | |

| reaction type | no. | reaction | rate constant ($cm^3 \cdot s^{-1}$) | remark |
|---|---|---|---|---|
| HCN channels | M10 | $H_2 + CN \rightarrow HCN + H$ | $5.38 \times 10^{-13}$ | ref 87 |
| | M11 | $BrCN + H \rightarrow Br + HCN$ | $1.02 \times 10^{-12}$ | estimated using ref 88 |
| | M14 | $CH_3CN + H \rightarrow HCN + CH_3$ | $1.36 \times 10^{-14}$ | ref 62 |
| | M16 | $CN + CH_3CN \rightarrow HCN + CH_2CN$ | $3.01 \times 10^{-12}$ | estimated using ref 89 |
| | M17 | $CN + CH_2CN \rightarrow HCN + CHCN$ | $1.00 \times 10^{-13}$ | |
| | M18 | $CN + CHCN \rightarrow HCN + CCN$ | $1.00 \times 10^{-13}$ | |
| | M19 | $CN + HBr \rightarrow HCN + Br$ | $3.74 \times 10^{-12}$ | ref 78 |
| | M20 | $HNC + H \rightarrow HCN + H$ | $5.00 \times 10^{-12}$ | refs 21 and 22 |
| | M22 | $M + CN + H \rightarrow HCN + M$ | $7.19 \times 10^{-31}$ | ref 90 |
| | M48 | $CH_4 + CN \rightarrow CH_3 + HCN$ | $4.17 \times 10^{-12}$ | ref 91 |
| | M49 | $CH_3 + CN \rightarrow CH_2 + HCN$ | $4.17 \times 10^{-12}$ | estimated using ref 91 |
| | M50 | $CH_2 + CN \rightarrow CH + HCN$ | $4.17 \times 10^{-12}$ | |
| | M51 | $CH + CN \rightarrow C + HCN$ | $4.17 \times 10^{-12}$ | |
| | M56 | $CCN + H \rightarrow CH + HCN$ | $1.36 \times 10^{-14}$ | estimated using ref 87 |
| HNC channels | M12 | $BrCN + H \rightarrow Br + HNC$ | $3.33 \times 10^{-13}$ | refs 42 and 88 |
| | M21 | $HCN + H \rightarrow HNC\,(v' = 2) + H$ | $9.28 \times 10^{-14}$ | fitted using refs 20–22 |
| | D1 | $HNC\,(v' = 2) + M = HNC\,(v'' = 1) + M^*$ | $1.15 \times 10^{-11}$ | fitted |
| | D2 | $HNC\,(v' = 1) + M = HNC\,(GS) + M^*$ | $2.2 \times 10^{-12}$ | fitted |
| | M15 | $CH_3CN + H \rightarrow HNC + CH_3$ | $4.53 \times 10^{-15}$ | estimated using refs 42 and 88 |
| | M23 | $M + CN + H \rightarrow HNC + M$ | $7.19 \times 10^{-32}$ | ref 92 |
| ionic chemistry | M24 | $HCN + MH^+ \rightarrow HCNH^+ + M$ | $7.41 \times 10^{-09}$ | ref 81 |
| | M25 | $HCNH^+ + e^- \rightarrow HNC + H$ | $1.18 \times 10^{-07}$ | |
| | M26 | $HCNH^+ + e^- \rightarrow HCN + H$ | $1.18 \times 10^{-07}$ | |
| | M27 | $HCNH^+ + e^- \rightarrow CN + H + H$ | $1.13 \times 10^{-07}$ | |
| other reactions | M53 | $CH_3CN + H \rightarrow CH_4 + CN$ | $1.36 \times 10^{-14}$ | ref 62 |
| | M54 | $CH_2CN + H \rightarrow CH_3 + CN$ | $1.09 \times 10^{-14}$ | estimated using ref 62 |
| | M55 | $CHCN + H \rightarrow CH_2 + CN$ | $1.09 \times 10^{-14}$ | estimated using ref 62 |
| | M57 | $CH_2CN + H \rightarrow CH_3CN$ | $1.60 \times 10^{-10}$ | estimated using ref 62 |
| | M58 | $CHCN + H \rightarrow CH_2CN$ | $1.60 \times 10^{-10}$ | estimated using ref 62 |
| | M59 | $CCN + H \rightarrow CHCN$ | $1.60 \times 10^{-10}$ | estimated using ref 62 |
| | M61 | $Br + H_2 \rightarrow HBr + H$ | $1.20 \times 10^{-18}$ | ref 93 |
| | M52 | $M + CH_3 + H \rightarrow CH_4 + M$ | $2.13 \times 10^{-29}$ | ref 94 |
| | M13 | $BrCN + H \rightarrow HBr + CN$ | $1.02 \times 10^{-12}$ | estimated using refs 39, 40, and 87 |

found[69] for the same band of HNC. The HCN absorption band $v_1$ is, therefore, about 4 times weaker than the band of HNC. Equation 30 can be expressed using a formalism based on the Einstein coefficient $A_{ji}$ instead of the transition dipole moment

$$A_{ij} = \frac{16\pi^3 v_0^3}{3\varepsilon_0 h} \cdot |\langle j|\mu|i\rangle|^2 \qquad (32)$$

and we obtain the equation

$$S_{ji} = \frac{A_{ij} \cdot N_A}{8\pi c v_{ji}^2} \left[ 1 - \exp\left(\frac{-hcv_0}{kT}\right) \right] \qquad (33)$$

For the observed HNC band $v_1$, the Einstein coefficient of $A_{ij} = 370$ s$^{-1}$ can be calculated from the dipole moment. The obtained value of the Einstein coeffcient of HCN was[69] 77.2 s$^{-1}$. The
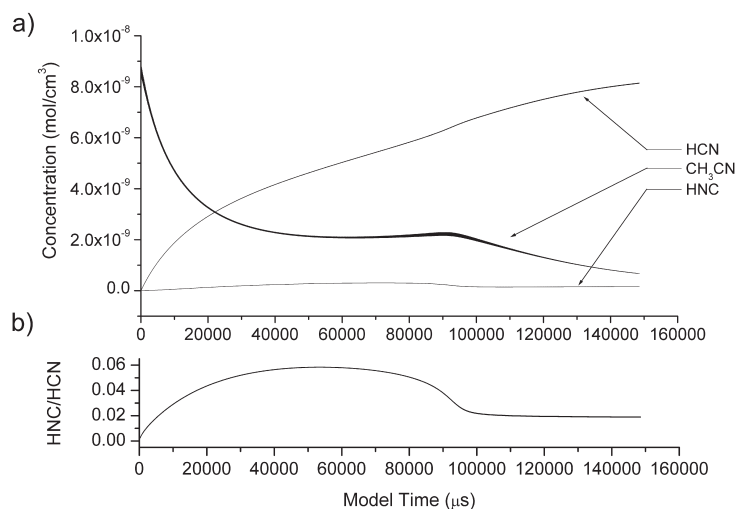
**Figure 15.** Concentration of HCN, HNC, and the precursor molecule estimated using the model (a). HNC/HCN ratio predicted by the model (b). After 1000 pulses, an equilibrium concentration of about 2% HNC/HCN is reached.

emission spectrum of HNC is stronger in comparison with the spectra of HCN; therefore, it can be easily detected despite relatively lower concentrations.

If we consider the reverse absorption of the emitted radiation to be negligible, the calculated Einstein coefficients of the spontaneous emission of the $\nu_1$ cold band transitions for HNC and HCN can be used to correct the HNC emission spectrum strength and calculate the HNC/HCN ratio in the afterglow of the studied systems. The rotational temperature of the discharge at 550 K determined by the Boltzmann plot showed that, during the afterglow, the system was in thermal equilibrium.

The intensity of spontaneous emission is directly proportional to the population of the excited state of the particular species. Therefore, with regard to the detector response to an emission quantum with the energy of $h\nu_0$, the quantitative ratio in thermal equilibrium can be written in the following way:

$$\frac{[\text{HNC}]}{[\text{HCN}]} \approx \frac{I(\text{HNC})}{I(\text{HCN})} \cdot \frac{A_{ij}(\text{HCN}) \cdot \nu_0(\text{HCN})}{A_{ij}(\text{HNC}) \cdot \nu_0(\text{HNC})} \approx \frac{I(\text{HNC})}{I(\text{HCN})} \cdot \frac{1}{5.26} \quad (34)$$

where $I$ is the emission intensity of the band, $A_{ij}$ is the Einstein coefficient of spontaneous emission, and $\nu_0$ is the band origin in wavenumber of the observed bands.

To obtain the band intensity, 56 lines in the HCN and HNC spectra were assigned and integrated in a C++ program. The intensity was subsequently corrected using the Einstein $A_{ij}$ coefficient, and the HNC/HCN ratio was determined.

The time-resolved development of the HNC/HCN ratio in the afterglow of the studied systems is shown in Figure 13. The highest ratio, HNC/HCN $\approx$ 3.0%, was found in the discharge in the mixture of formamide and He. In the discharge in BrCN/He, the ratio was found to be HNC/HCN $\approx$ 2.8%, and in the acetonitrile/Ar system, the ratio was found to be HNC/HCN $\approx$ 2.2%. Although the individual systems had different precursors, the HNC/HCN ratios were always close to 3%. We assume this result indicates that the mechanisms of HNC/HCN production are similar, regardless of the discharge type. This ratio is unlikely

to result from thermal chemical equilibrium via reaction, because the HNC abundance calculated for the temperature of 550 K, typical for a glow discharge, is only[33] $6 \times 10^{-4}$ %.

Comparing the reaction mechanisms found on the basis of a search of the literature, we found that numerous reactions take place in all systems. The simplified pathway of HNC/HCN formation is shown in Figure 14. It is a key objective of the kinetic model of the processes occurring in the experimentally studied gas discharges that will be discussed in the following section to identify the dominant reaction channels with respect to the formation of HNC.

**E. Kinetic Model of HNC/HCN Hydrogen Chemistry.** A kinetic model of the BrCN and acetonitrile HNC/HCN discharge and afterglow was designed on the basis of the reactions listed in Table 2 to provide a description of the radical and hydrogen chemistry and to explain the observed emission time profiles and HNC/HCN ratio. The model focuses on the radical chemistry because no ions were directly observed.

The key features of the model are summarized in the following points:

- The numerical model was implemented in the Python 2.6.4 programming language. The decrease of calculation speed caused by the interpreted nature of Python was partially compensated by using modules Numpy[70] and Scipy[71] for the acceleration of numerical algorithms.
- The model was constructed without spatial dimensions as a so-called zero-dimensional model describing only the time evolution of the concentrations. This type of model is appropriate for data originating from the homogeneous region of the positive column of a glow discharge.
- A set of ordinary differential equations constructed according to the postulated reaction scheme (Table 2) was numerically solved by the Scipy module using the ODE-PACK library.[72] The time dependencies of the concentrations of the individual species were obtained for the given initial conditions.
- The activity of the discharge was simulated by a rectangular pulse of electron number density of 22 and 15 $\mu$s duration in accordance with the experiment. The typical values of electron densities in a glow discharge are[73,74] between $10^9$
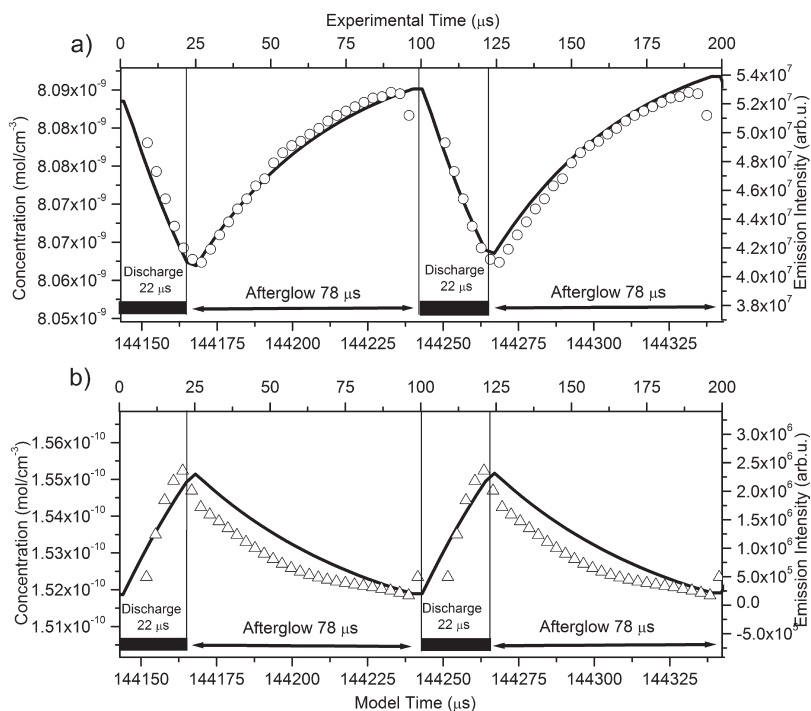
**Figure 16.** Comparison of the HCN concentration profile predicted by the acetonitrile discharge model (solid line) with the emission profile (circles) of the $\nu_1 - $ GS band (a). Comparison of the HNC concentration profile predicted by the acetonitrile discharge model (solid line) with the emission profile (triangles) of the $2\nu_1 - \nu_1$ band (b).
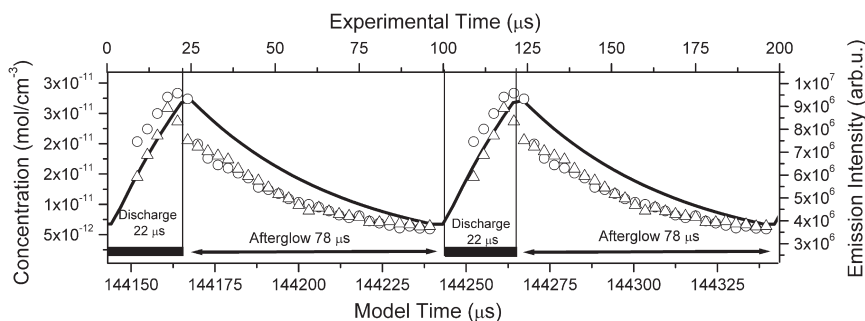


**Figure 17.** Comparison of the CN concentration profile in the acetonitrile discharge model (solid line) with the CN emission profile of the ground state $X^2\Sigma^+$ (triangles: 2 − 1, circles: 1 − GS bands).

and $10^{11}$ particles/cm$^3$. We used a value of $6 \times 10^{11}$ cm$^{-3}$ obtained by a Langmuir probe measurement in the actual experimental discharge. The electron temperature not obtained by measurement was estimated as 1 eV and was treated as a free parameter for the fitting of the experimental results by the model.

- The concentration of MH$^+$ ions in reaction M24 was forced to be proportional to the electron number density and was thus represented by a rectangular pulse.
- The number densities of the precursor molecules and the hydrogen molecules were fixed at $6.58 \times 10^{15}$ cm$^{-3}$, as calculated from their partial pressures of 50 Pa and temperature 550 K.
- The electron temperature and the rate constant M21 were treated as free parameters for fitting the model results to the

experimental values of the HNC/HCN ratios (2.2% for CH$_3$CN and 3% for BrCN + H$_2$) using the Nelder−Mead simplex algorithm.[75]
- The accumulation of reaction products from the previous discharge pulses (illustrated in Figure 7) was accounted for by modeling a sequence of 3000 pulses in each run (2−4 h of CPU time) while accounting for the loss of the products by convection in a flow of the buffer gas into the pump. The concentrations during the last pulse were used for the fitting.

*Rate Constants.* The rate constants of reactions involved in the hydrogen chemistry of HNC/HCN were adopted from the NIST[76] database and original literature (citations listed in Table 2). The temperature dependence of the rate constants

was estimated using the Arrhenius plot of the experimental data according to the equation:

$$\ln k = K(1000/T) + Q \qquad (35)$$

where the slope is $K = -E_A/R$ ($R$ is the universal gas constant, and $E_A$ is the activation energy), and the constant term $Q$ represents the temperature-independent logarithm of preexponential factor $A$. From the Boltzmann plot of the HCN lines, the rotational temperature of the discharge was estimated to be 550 K. The values of the rate constants given in Table 2 for reactions M10−M61 were calculated using eq 35 where possible.

The main mechanism of the dissociation of the molecules in the glow discharge is the collisions with free electrons generated by electron ionization and by Penning ionization (15). The second-order dissociation reaction can be generally written as

$$X - CN + e^- \rightarrow X + CN + e^- \qquad (36)$$

The rate constant of electron dissociation was calculated according to the formulation used by Morrison et al.[77,78] as

$$k(T_e) = \pi \left( \frac{e}{4\pi\varepsilon_0 E_A} \right)^2 \cdot \left( \frac{8eT_e}{\pi m_e} \right)^{1/2} \cdot \left( 1 + \frac{2T_e}{E_A} \right)$$
$$\exp(-E_A/T_e) \qquad (37)$$

Here, $e$ and $m_e$ are the electronic charge and mass, $\varepsilon_0$ is the permittivity of the vacuum (all in SI units), $E_A$ is the activation energy for dissociation in eV, and $T_e$ is the electron temperature expressed in eV (11600 K = 1 eV). Thus, the rate constants for reactions M0−M9 were calculated from the $E_a$ values given in Table 2 using eq 37.

As the rate constants for the formation of HNC are not accurately known, they were treated as free model parameters, and they were fitted so that the resulting HNC/HCN ratios were within a range of 2.2−3%. The following constraints were used for the rate constants:

- The ratio of the rate constants M11/M12 and M14/M15 was fixed at 3:1 on the basis of work by Arunan.[42]
- The initial value of the rate constant for reaction M21 was taken as $k_{M21} = 5.6 \times 10^{-15}$ cm$^3$ s$^{-1}$ according to theory by Sumathi et al.[21] The final value resulting from the fitting in the present model and the importance of reaction M21 will be discussed below.
- The rate constant for the formation of HCNH$^+$ by the protonation of HCN (M24) was taken as the rate constant of the reaction[79] of H$_3^+$, which has the quickest reaction among all the potential proton donors. The concentration of proton donors MH$^+$ was fixed as 1/10 of the electron number density.
- The dissociative recombination[80] reactions M25−M27 were assumed to produce HNC and HCN in equal amounts.

*Results of Modeling, Reaction Channels Important for HNC Production.* As discussed in the previous sections, collisions of HCN molecules with molecules and atoms in the ground internal energy states at the 550 K discharge temperature represent a negligible contribution to the HCN $\rightarrow$ HNC isomerization. Also, the energies of the lowest excited states of Ar ($^2P^\circ_{3/2}$ = 11.55 eV) and He ($^3S$ = 19.81 eV) do not overlap with the energy barrier for the isomerization of 2.19 eV. Thus, the collisions of excited He or Ar atoms with HCN are likely to lead to Penning ionization (the ionization energy of HCN is 13.61 eV) or to the dissociation of HCN to the H atom and the CN radical (dissociation energy $E_{dis}$ = 4.8 eV).

The numerical kinetic model confirmed that the reaction products are accumulated in the discharge cell during a sequence of pulses and that the molecules remaining from the previous pulses significantly affect the experimentally obtained emission spectra (see Figure 15). Especially important for the present study is the accumulation of HCN after several thousands of pulses (several tenths of a second after the beginning of the experimental sequence). Due to the substantial initial concentration of HCN at the onset of the pulse, the equilibrium between the HNC/HCN isomers is established by the conversions of HCN to HNC and back in reactions with hydrogen atoms H (eqs 7 and 8 in the Introduction, designated as M20 and M21 in the model) or by the protonation of HCN producing HNCH$^+$, followed by its dissociative recombination with electrons producing HNC/HCN (eq 5, designated as M25 − M27). The experimental time profiles of HNC and HCN emissions are compared with the modeled profiles in Figure 16. A similar comparison for the CN radical is shown in Figure 17. Other species mentioned in the model have significantly lower concentration than CN, HCN, and HNC except HBr and H. However, their emission profiles are in agreement with the model. The main question now is which mechanism is more important for the formation of HNC molecules in the glow discharges: is it the ion chemistry or the radical chemistry?

The simplest ions that can form in a discharge in mixtures containing hydrogen are H$_2^+$ and H$_3^+$. However, H$_2^+$ reactions with the CN radical[81] and HCN molecules

$$CN + H_2^+ \rightarrow HNC^+ + H \qquad (39)$$

$$HCN + H_2^+ \rightarrow HCN^+ + H_2 \qquad (40)$$
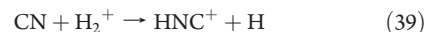
do not produce the HCNH$^+$ ion or the HNC isomer. However, the H$_3^+$ ions that are so important in interstellar chemistry do react with HCN by proton transfer to produce HCNH$^+$ according to eq 1, as mentioned in the Introduction (designated M24 in the model).

The method of continuous scanning time-resolved Fourier transform spectroscopy has been used in the 1800−4000 cm$^{-1}$ spectral region to observe the formation of the H$_3^+$ ion in a hydrogen discharge.[82] To generate high concentrations of this ion, a high pressure of molecular hydrogen is required at several tens of mbar, much greater than the pressure used in the present study. It is noteworthy that, in the present experiments, molecular hydrogen, a precursor of H$_3^+$ that is easily detected in this spectral region,[83] was not detected. There was also no evidence for the presence of the HCNH$^+$ ions.

Ion molecule reactions are generally rapid and can thus play an important role even when the ion concentrations are below the detection limit of the spectroscopy methods. Thus, it is necessary to use the results of modeling to assess their contribution to the formation of HNC. If the neutral radical reaction channels leading to HNC formation (reactions M12, M15, M21, and M23) are excluded from the model, the resulting HNC/HCN ratio is only 0.07% and, notably, it does not depend on the MH$^+$ concentration, because the reverse conversion of HNC back to HCN (reaction M20) involves the H atoms produced both by the dissociative recombination of HCNH$^+$ and the dissociation of H$_2$. Reaction M20 thus significantly controls the HNC/HCN ratio. When the neutral reactions M12, M15, M21, and M23 are enabled, the modeled ratio of HNC/HCN rises to 2.2−3%, indicating that these reactions represent the main route to the

formation of HNC in the positive column of the glow discharge. The value of the HNC/HCN ratio is in accordance with the model result of equilibrium in reactions M20 and M21.

Recently, Amano et al.[84] studied the negative column of a glow discharge in a mixture of $CH_4/N_2$ at liquid nitrogen temperature, and they observed a 33% HNC/HCN ratio. This result, which is much higher than our observations in the positive columns, was attributed to dissociative recombination (eq5, M25 and M26). Extended negative glow discharge is a good source of positive ions, including the $HCNH^+$ that was actually observed. At liquid nitrogen temperature and at low pressures of $10^{-3}$ mbar, the neutral radical processes (including reactions M20 and M21) are insignificant due to the low collisional frequencies and lower reaction rate constants, and the ion chemistry dominates. However, in the positive column at 550 K and 1 mbar in this study, the neutral radical chemistry played the major role, and this is also supported by our model.

The fitting of the chemistry models in the BrCN and $CH_3CN$ discharges to the experimental data provided rate constants for reaction M21 of $1.33 \times 10^{-13}$ and $9.3 \times 10^{-14}$ cm$^3$ s$^{-1}$, respectively. This difference demonstrates the accuracy of our results. The previous values reported in the literature ranged from $5.6 \times 10^{-15}$ cm$^3$ s$^{-1}$, obtained by theoretical calculation,[21] to $7 \times 10^{-11}$ cm$^3$ s$^{-1}$, obtained by the modeling of cometary chemistry,[20] and no direct experimental data are available in the current literature. Our results are thus closer to the lower theoretical value by Sumathi.[21] However, it must be kept in mind that the conditions of our experiments are given by the plasma environment of the glow discharge at a temperature of 550 K, an electron temperature of 1 eV, and a number density of electrons of $6 \times 10^{10}$ cm$^{-3}$.

*Emission and Concentration Profiles.* The model results for the time profiles of the species concentrations in the discharge correspond to the observed experimental data qualitatively, but not quantitatively (as shown in Figures 16 and 17). The modeled change

of concentration during one pulse was relatively small, while the change of the emission intensity recorded by the detector was comparatively large. This mismatch can be explained by the excitation of the radiating species in the active discharge and by their subsequent collisional relaxation (quenching). The details of these processes can be illustrated by the HNC and HCN emission profiles:

The ground state of HCN in collisions with excited hydrogen atoms H* produces HNC ($\nu' = 2$, observed band $2\nu_1 - \nu_1$):

$$HCN + H^* \rightarrow HNC\ (\nu' = 2) + H \quad k_{M21} = 9.28 \times 10^{-14}\ cm^3\ s^{-1} \quad (41)$$

Then, HNC ($\nu' = 2$) is quenched in collisions with a molecule M to $\nu'' = 1$ (observed band $\nu_1 - GS$) and is further quenched to the ground vibrational state (GS).
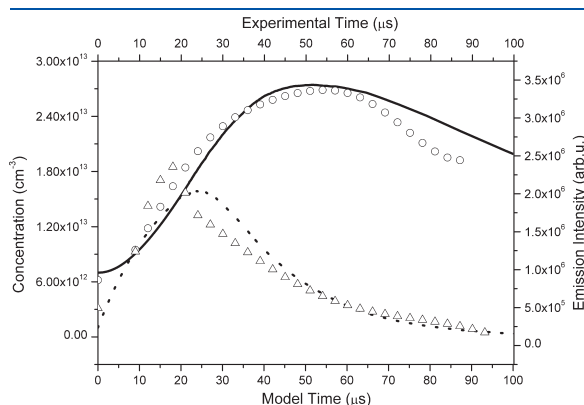


**Figure 18.** Comparison of the acetonitrile discharge model of HNC excited $\nu' = 2$ formation (dashed line) followed by the collisional deexcitation to the $\nu'' = 1$ state (solid line) and to the GS with the experimental profiles of these bands (circles, $\nu_1 - GS$ band; triangles, $2\nu_1 - \nu_1$ band).



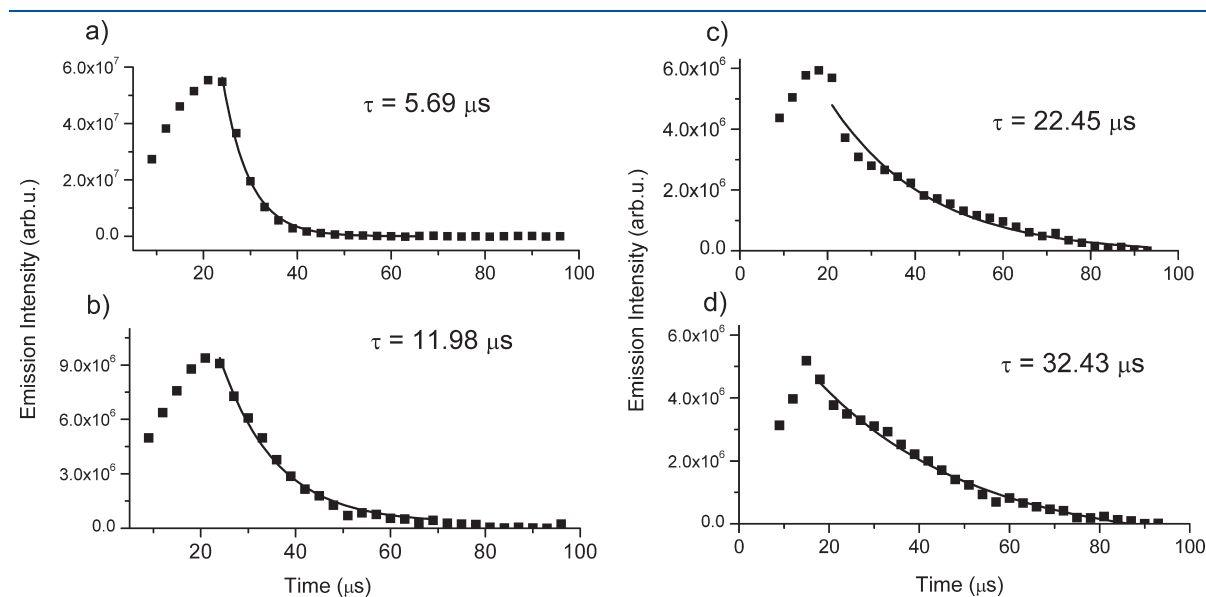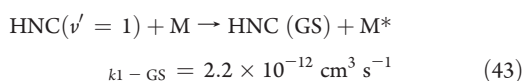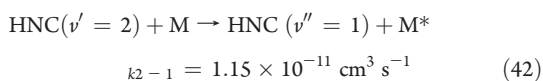**Figure 19.** Emission profiles of the CN $X^2\Sigma^+$ $2 - 1$ (a) and $1 - GS$ (b) bands in the case of $CH_3CN + H_2$ discharge compared with the profiles of the same bands in the case of $CH_3CN$ discharge without extra added molecular hydrogen (c, d).

P33

$$\text{HNC}(v' = 2) + \text{M} \rightarrow \text{HNC} \; (v'' = 1) + \text{M}^*$$

$$k_{2-1} = 1.15 \times 10^{-11} \; \text{cm}^3 \; \text{s}^{-1} \qquad (42)$$

$$\text{HNC}(v' = 1) + \text{M} \rightarrow \text{HNC} \; (\text{GS}) + \text{M}^*$$

$$k_{1-\text{GS}} = 2.2 \times 10^{-12} \; \text{cm}^3 \; \text{s}^{-1} \qquad (43)$$

The results of the kinetic model of this sequence involving the same number of collision partners and molecules HCN and HNC ($4.85 \times 10^{15} \; \text{cm}^{-3}$) are shown in Figure 18. The agreement of the presented emission profiles with the experimental results indicates that quenching significantly influences the time profiles of the emission intensities. The actual rate of quenching is strongly influenced by the nature of the colliding species and by the differences in the excitation levels of the exciting species and the energy acceptor. The rate constants for quenching by rare gas atoms are known to be slow. For example, the relaxation rates of highly excited states[85] of NCNO are in the order of $10^{-14} \; \text{cm}^3 \; \text{s}^{-1}$ for collisions with He and Ar atoms, but for collisions with molecular gas $N_2$, the quenching rate constant is $10^{-10} \; \text{cm}^3 \; \text{s}^{-1}$. This value is close to a typical collisional rate constant. Spontaneous emission lifetimes are comparatively long and do not strongly influence the observed time profiles. For HNC, the spontaneous emission lifetime is 2702.7 $\mu$s, while the observed exponential time constant of decay in the discharge is only 115.2 $\mu$s. The effect of collisions on the experimental lifetime $\tau_{\text{exp}}$ of the CN emission lines is also demonstrated experimentally with the addition of $H_2$. In the acetonitrile/Ar discharge without the added hydrogen, the lifetime of the emission line R(8) in the ground state $X^2\Sigma^+$, $2 - 1$, was $\tau_{\text{exp}} = 22.45 \; \mu$s (not truly exponential, see Figure 19); in the case of the R(8) line in the ground state $X^2\Sigma^+$, $1 - \text{GS}$, it was $\tau_{\text{exp}} = 32.43 \; \mu$s. After the addition of 0.5 mbar of hydrogen to the discharge, these lifetimes shortened to $\tau_{\text{exp}} = 5.69 \; \mu$s and $\tau_{\text{exp}} = 11.98 \; \mu$s, respectively.

## IV. CONCLUSIONS

Time-resolved Fourier transform emission spectroscopy was used to study the formation of HNC and HCN. On the basis of the strength of the HCN and HNC bands, the HNC/HCN ratios were studied in the glow discharge in three different mixtures: acetonitrile/Ar, BrCN/$H_2$/He, and formamide/He. The aim of the work was to determine whether the HNC/HCN ratio depends on the type of precursor used. In all three mixtures, HNC/HCN experimental ratios between 2 and 3% were found. The final products of the discharges in the acetonitrile/He and the formamide were detected using the SIFT-MS method. The main decay products in both acetonitrile and formamide were HCN, methane, and acetylene.

Kinetic modeling was conducted to identify the reaction channels responsible for the formation of HNC in the given concentration ratio to the HCN present in the gas mixture. A numerical kinetic model was constructed that contained 61 reactions covering both ion chemistry and neutral radical chemistry. The results of fitting the model predictions to the experimental data revealed the following:

- The products of the discharge chemistry are accumulated in the cell in a sequence of pulses.
- The ratio of HNC/HCN was 2 orders of magnitude smaller than the experimental results when the radical chemistry was excluded and only the ion chemistry was enabled. The full model, including the radical chemistry, reproduced the experimental results.
- HNC is formed primarily by the reaction of HCN with the H atoms (equations M21 and M20), and the rate constant for reaction M21 was determined to be in the range $9.3 \times 10^{-14}$ to $1.33 \times 10^{-13} \; \text{cm}^3 \; \text{s}^{-1}$.
- The time profiles of emission intensities are influenced by the collisional quenching of the vibrationally excited states in addition to the concentration profiles of the chemical compounds produced by the discharge chemistry. The value of HNC/HCN ratio can therefore be influenced by collisions, and rate constant M21 must be accepted like an effective value.

## ■ AUTHOR INFORMATION

**Corresponding Author**
*E-mail: civis@jh-inst.cas.cz. Phone: +420-286 591 766.

## ■ REFERENCES

(1) Snyder, L. E.; Buhl, D. *Bull. Am. Astron. Soc.* **1971**, *3*, 388.
(2) Goldsmith, P. F.; Langer, W. D.; Ellder, J.; Irvine, W.; Kollberg, E. *Astrophys. J.* **1981**, *249*, 524.
(3) Liszt, H.; Lucas, R. *Astron. Astrophys.* **2001**, *370*, 576.
(4) Nyman, L., A.; Olofsson, H.; Johansson, L. E. B.; Carstrom, U.; Wolstencroft, R. *Astron. Astrophys.* **1993**, *1*, 377.
(5) Lellouch, E.; Romani, P. N.; Rosenqvist, J. *Icarus* **1994**, *108*, 112.
(6) Irvine, W. M.; Schloerg, F. P. *Astrophys. J.* **1984**, *282*, 516.
(7) Schilke, P.; Walmsley, M. C.; Pineau des Forests, G.; Rouell, E.; Flower, D. R.; Guilloteau, S. *Astron. Astrophys.* **1992**, *256*, 595.
(8) Ziurys, L. M.; Tenenbaum, E. D.; Pulliam, R. L.; Woolf, N. J.; Milam, S. N. *Astrophys. J.* **2009**, *695*, 1604.
(9) Schilke, P.; Walmsley, C. M.; Millar, T. J.; Henkel, C *Astron. Astrophys.* **1991**, *247*, 487.
(10) Brown, R. D.; Burden, F. R.; Cuno, A. *Astrophys. J.* **1989**, *347*, 855.
(11) Watson, W. D. *Rev. Mod. Phys.* **1976**, *48*, 513.
(12) Turner, B. E.; Pirogov, L.; Minh, Y. C. *Astrophys. J.* **1997**, *483*, 235.
(13) Allen, T. L.; Goddard, J. D.; Shaefer, H. F. *J. Chem. Phys.* **1980**, *73* (7), 3255.
(14) Talbi, D.; Ellinger, Y. *Chem. Phys. Lett.* **1998**, *288*, 155.
(15) Graedel, T. E.; Langer, W. D.; Frerking, M. A. *Astrophys. J.* **1982**, *48*, 321.
(16) Herbst, E.; Terzieva, R.; Talbi, D. *Mon. Not. R. Astron. Soc.* **2000**, *311*, 869.
(17) Kawaguchi, K.; Hirota, T.; Yamamoto, S.; Sakamoto, A.; Ukuta, N. *Astrophys. J.* **1999**, *520*, 895.
(18) Irvine, W. M.; Dickens, J. E.; Loverll, A. J.; Schloerb, P. F.; Senay, M.; Bergin, E. A.; Jewitt, D.; Matthews, E. *Faraday Discuss.* **1998**, *109*, 475.
(19) Rodgers, S. D.; Charnley, S. B. *Astrophys. J.* **1998**, *501*, L227.
(20) Sumathi, R.; Nguyen, M. T. *J. Phys. Chem. A* **1998**, *102*, 8013.
(21) Talbi, D.; Ellinger, Y; Herbst, E *Astron. Astrophys.* **1996**, *314*, 688.
(22) Talbi, D.; Ellinger, Y. *Chem. Phys. Lett.* **1996**, *263*, 385.

P34

(23) Rodgers, S. D.; Charnley, S. B. *Mon. Not. R. Astron. Soc.* **2005**, *356*, 1542.

(24) Milligan, D. E.; Jacox, M. E. *J. Chem. Phys.* **1963**, *3* (39), 712.

(25) Burkholder, J. B.; Sinha, A.; Hamer, P. H.; Howard, C. J. *J. Mol. Spectrosc.* **1987**, *126*, 72.

(26) Maki, A. G.; Mellau, G. Ch. *J. Mol. Spectrosc.* **2001**, *206*, 47.

(27) Burgers, P. C.; Holmes, J. L.; Mommers, A. A.; Terlouw, J. K. *Chem. Phys. Lett.* **1983**, *1*, 1.

(28) Snell, R. L.; Wootten, H. A. *Astrophys. J.* **1977**, *216*, L111.

(29) Maki, A. G.; Sams, R. L. *J. Chem. Phys.* **1981**, *75*, 4178.

(30) Kumeda, Y.; Minami, Y.; Takano, K.; Taketsugu, T.; Hirano, T. *THEOCHEM* **1999**, *458*, 285.

(31) Barber, R. J.; Harris, G. J.; Tennyson, J. *J. Chem. Phys.* **2002**, *24* (117), 11239.

(32) Harris, G. J.; Pavlenko, Y. V.; Jones, H. R. A.; Tennyson, J. *Mon. Not. R. Astron. Soc.* **2003**, *344*, 1107.

(33) Nezu, M.; Amano, T.; Kawaguchi, K. *J. Mol. Spectrosc.* **1998**, *192*, 41.

(34) Kawaguchi, K.; Fujimoto, J. Time-resolved Fourier transform infrared emission spectra of HNC/HCN. 62nd OSU International Symposium on Molecular Spectroscopy, Columbus, OH, 2007.

(35) He, G.; Macdonald, R. G. *Chem. Phys. Lett.* **1999**, *301*, 175.

(36) Northrup, F. J.; Bethardy, G. A.; Macdonald, R. G. *J. Mol. Spectrosc.* **1997**, *186*, 349.

(37) Decker, B. K.; He, G.; Tokue, I.; Macdonald, R. G. *J. Phys. Chem. A* **2001**, *105*, 5759.

(38) He, G.; Tokue, I.; Macdonald, R. G. *J. Chem. Phys.* **2000**, *112*, 6689.

(39) Song, Y; Sushan, D. *J. Mol. Struct.* **1996**, *362*, 387.

(40) Arunan, E.; Manke, G.; Setser, D. W. *Chem. Phys. Lett.* **1993**, *1*, 81.

(41) Copeland, L. R.; Mohammad, F.; Zahedi, M.; Volman, D. H. *J. Chem. Phys.* **1992**, *96*, 5817.

(42) Lundell, J.; Krajewska, M.; Räsänen, M. *J. Phys. Chem. A* **1998**, *102*, 6643.

(43) Moore, M. H.; Hudson, R. L. *Icarus* **2003**, *161*, 486.

(44) Solomon, P. M.; Jefferts, K. B.; Penzias, A. A.; Wilson, R. W. *Astrophys. J.* **1971**, *168*, L107.

(45) Ulick, B. L.; Conklin, E. K. *Nature* **1974**, *248*, 121.

(46) Rubin, R. H.; Swenson, G. W., Jr.; Solomon, R. C.; Flygare, H. L. *Astrophys. J.* **1971**, *169*, L39–L44.

(47) Bockelée-Morvan, D.; Lis, D. C.; Wink, J. E.; Despois, D.; Crovisier, J.; Bachiller, R.; Benford, D. J.; Biver, N.; Colom, P.; Davies, J. K.; Gérard, E.; Germain, B.; Houde, M.; Mehringer, D.; Moreno, R.; Paubert, G.; Phillips, T. G.; Rauer, H. *Astron. Astrophys.* **2000**, *353*, 1101–1114.

(48) Civis, S.; Juha, L.; Babankova, D. *Chem. Phys. Lett.* **2004**, *386*, 169.

(49) Saladino, R.; Crestini, C.; Ciciriello, F.; Costanzo, G.; Di Mauro, E. *Chem. Biodiversity* **2007**, *4*, 694.

(50) Tokaryk, D. W.; Civis, S. *J. Chem. Phys.* **1995**, *10*, 3928.

(51) Results will be published.

(52) Kawaguchi, K.; Hama, Y.; Nishida, S. *J. Mol. Spectrosc.* **2005**, *232*, 1.

(53) Smith, D.; Spanel, P. *Mass Spectrom. Rev.* **2005**, *24*, 661–700.

(54) Sovova, K.; Ferus, M.; Matulkova, I.; Spanel, P.; Dryahina, K.; Dvorak, O.; Civis, S. *Mol. Phys.* **2008**, *106*, 1205–1214.

(55) Tokue, I.; Sakai, Y.; Yamasaki, K. *J. Chem. Phys.* **1997**, *106* (11), 4491.

(56) Yencha, A. J. *Electron spectroscopy: theory, techniques and applications*; Bundle, C. R., Baker, A. D., Eds.; Academic: London, 1984; Vol. 5.

(57) Baulch, D. L.; Duxbury, J.; Grant, S. J.; Montague, D. C. *J. Phys. Chem. Ref. Data* **1981**, *10*, 1.

(58) Haruhiko, I.; Kawamura, Y. *J. Non-Cryst. Solids* **2008**, *354*, 3267.

(59) Sailer, W.; Pelc, A.; Limao-Vieira, P.; Mason, N. J.; Limtrakul, J.; Scheier, P.; Probst, M.; Märk, T. D. *Chem. Phys. Lett.* **2003**, *381*, 216.

(60) Jamieson, J. V. S.; Brown, G. R.; Tanner, J. S. *Can. J. Chem.* **1970**, *48*, 3619.

(61) Results will be published.

(62) Liu, D.; Fang, W.; Fu, X. *Chem. Phys. Lett.* **2000**, *318*, 291.

(63) Brownsword, R.A.; Gatenby, S.D.; Herbert, L.B.; Smith, I.W. M.; Stewart, D.W.A.; Symonds, A. C. *J. Chem. Soc., Faraday Trans.* **1996**, *92*, 723.

(64) Mayer, S.W.; Schieler, L. *J. Chem. Phys.* **1966**, *45*, 385.

(65) Caridade, P. J. S. B.; Rodrigues, S. P. J.; Sousa, F.; Varandas, A. J. C. *J. Phys. Chem. A* **2009**, *109*, 2356.

(66) Atakan, B.; Kocis, D.; Wolfrum, J.; Nelson, P. *Symp. Int. Combust. Proc.* **1992**, *24*, 691.

(67) Nezu, M.; Amano, T.; Kawaguchi, K. *J. Mol. Spectrosc.* **1999**, *198*, 186.

(68) Harris, G. J.; Polynsky, O. L.; Tennyson, J. *Spectrochim. Acta, Part A* **2002**, *58*, 673.

(69) Botschwina, P. *Chem. Phys.* **1983**, *81*, 73.

(70) URL: http://numpy.org/, downloaded Oct 25, 2010.

(71) URL: http://scipy.org/, downloaded Oct 25, 2010.

(72) URL: http://people.sc.fsu.edu/~jburkardt/f77_src/odepack/odepack.html, downloaded Oct 25, 2010.

(73) Winchester, M.; Payling, R. *Spectrochim. Acta, Part B* **2004**, *59*, 607.

(74) Corbella, C.; Polo, M. C.; Oncins, G.; Pascual, E.; Andújar, J. L.; Bertran, E. *Thin Solid Films* **2005**, *482*, 172.

(75) Scientific Tools for Python, SciPy, <http://scipy.org/>.

(76) NIST Chemical Kinetics Database: Standard Reference Database 17, Version 7.0 Web Version, Release 1.4.3, Data Version 2009.01 <http://kinetics.nist.gov/kinetics/index.jsp>, dowloaded Oct 25, 2010.

(77) Morrison, N. A.; William, C.; Milne, W. I. *J. Appl. Phys.* **2003**, *11*, 7031.

(78) Lieberman, M. A.; Lichtenberg, A. J. *Principles of Plasma Discharges and Materials Processing*, 1st ed.; Wiley: New York, 1994; p 79.

(79) Mackay, G. I.; Betowski, L. D.; Payzant, J. D.; Shiff, H. I.; Bohme, D. K. *J. Phys. Chem.* **1976**, *80*, 29919.

(80) Semaniak, J.; Minaev, B. F.; Derkatch, A. M.; Hellberg, F.; Neau, A.; Rosén, S.; Thomas, R.; Larsen, M; Danaid, H.; Paál, A.; Ugglas, M. *Astrophys. J. Suppl.* **2001**, *135*, 275.

(81) The UMIST database for Astrochemistry, <http://www.udfa.net/>.

(82) Civiš, S.; Kubát, P.; Nishida, S.; Kawaguchi, K. *Chem. Phys. Lett.* **2005**, *418*, 448.

(83) Dabrowski, I.; Herzber,g, G. *Acta Phys. Hung.* **1984**, *55*, 219.

(84) Amano, T.; Zelinger, Z.; Hirao, T.; Takano, J.; Toyoda, R. *J. Mol. Spectrosc.* **2008**, *251*, 252.

(85) Wright, S. M. A.; Sims, I. R.; Smith, I. W. M. *Phys. Chem. Chem. Phys.* **2001**, *3*, 2203.

(86) Saum, K. A.; Benesch, W. M. *Appl. Opt.* **1970**, *9*, 195.

(87) Sun, Q; Yang, D. L; Wang, N. S; Bowman, J. M; Lin, M. C. *J. Chem. Phys.* **1990**, *93*, 4730.

(88) Brupbacher, J. M; Esneault, C. P; Kern, R. D. *J. Phys. Chem.* **1977**, *81*, 1128.

(89) Yang, D. L.; Yu, T.; Lin, M. C.; Melius, C. F. *Chem. Phys.* **1993**, *177*, 174.

(90) Tsang, W. *Chem. Kinet. Data* **1992**, *21*, 753.

(91) Baulch, D. L.; Cobos, C. J.; Cox, R. A.; Frank, P.; Hayman, G.; Just, Th.; Kerr, J. A.; Murrells, T.; Pilling, M. J.; Troe, J.; Walker, R. W.; Warnatz, J. *J. Phys. Chem. Ref. Data* **1994**, *23*, 847.

(92) Tsang, W *Chem. Kinet. Data* **1992**, *21*, 753.

(93) Seakins, P. W.; Pilling, M. J. *J. Phys. Chem.* **1991**, *95*, 9878.

(94) Golden, D. M. *Int. J. Chem. Kinet.* **2008**, *40*, 310.

1899

dx.doi.org/10.1021/jp1107872 |*J. Phys. Chem. A* 2011, 115, 1885–1899

P35

ORIGINAL PAPER

# Time-Resolved Fourier Transform Emission Spectroscopy of $CF_3Br$ and $CF_3CFHCF_3$ in a Pulsed Electrical Discharge

**Martin Ferus · Svatopluk Civiš · Petr Kubelík · Václav Nevrlý ·
Petr Bitala · Eva Grigorová · Michal Střižík · Pavel Kubát ·
Zdeněk Zelinger**

**Abstract** The environmentally important decomposition of halogenated species $CF_3Br$ and $CF_3CHFCF_3$ in helium discharge plasma was investigated by time-resolved high-resolution Fourier transform infrared emission spectroscopy. Contrary to classical pyrolysis, a deeper fragmentation of precursors up to atoms and lower molecular species was observed. Excited molecular products CF, $CF_2$ and $CF_4$ achieved the maximal concentration in the afterglow. The high concentration of all these species is in agreement with a kinetic model based on radical chemistry. The non-detectable concentration of $CF_3$ can be connected to its high reactivity and the formation of more stable products, $CF_4$ and $CF_2$, by addition or release of a fluorine atom, respectively. Other products included HF, HBr, CO and cyano compounds that were produced by secondary reactions with traces of water vapor, atmospheric oxygen and nitrogen present in original industrial samples as impurities.

**Keywords** Helium discharge plasma · $CF_3Br$ · $CF_3CHFCF_3$ · Fluorocarbon radicals · Time-resolved FTIR

## Introduction

Halogenated fire extinguishing agents have been traditionally utilized in many applications to protect fixed enclosures or in applications requiring rapid extinguishing. The most commonly used halogenated hydrocarbon extinguishing agents were bromine-containing

M. Ferus · S. Civiš · P. Kubelík · P. Kubát · Z. Zelinger (✉)
J. Heyrovský Institute of Physical Chemistry, v.v.i., Academy of Sciences of the Czech Republic,
Dolejškova 3, 18223 Prague 8, Czech Republic
e-mail: zelinger@jh-inst.cas.cz

M. Ferus · P. Kubelík
Institute of Physics, v.v.i., Academy of Sciences of the Czech Republic, Na Slovance 2,
18221 Prague 8, Czech Republic

V. Nevrlý · P. Bitala · E. Grigorová · M. Střižík
VŠB—Technical University of Ostrava, Faculty of Safety Engineering, Lumírova 13,
70030 Ostrava—Výškovice, Czech Republic

compounds, e.g., $CF_3Br$ (Halon[TM] 1301). The Montreal Protocol and its attendant amendments have mandated that their production be discontinued [1] because these compounds have been linked to the ozone depletion [2, 3] and to the formation of toxic products [4, 5]. Nonbrominated fluorohydrocarbons [6], e.g., $CF_3CHFCF_3$ are suitable alternatives of growing importance for both fixed and portable fire extinguishing systems. The behavior of these agents in thermal and non-thermal plasma as well as related environmental aspects and their decomposition products are still challenging tasks in the context of fire safety science.

In previous papers, high resolution spectroscopic studies of halogenated radicals were performed [7–10], and time-resolved high-resolution Fourier transform infrared (FTIR) spectroscopy was used to study plasma processes in an electrical discharge [11, 12] and/or in a plasma plume formed by laser ablation of various materials [13, 14]. Although the time-resolved spectroscopy can significantly contribute to the better understanding of the processes, so far, no study has been published on the measurement of time resolved spectra of the decomposition products of $CF_3Br$ or $CF_3CHFCF_3$. Because of the high stability of fluorohydrocarbons, pulsed helium discharge plasma was used, which allows the generation of the high concentration of unstable species that is expected to occur at moderate temperatures with low yields but at conditions far from the thermal equilibrium with excitation temperature of about 3,500 K [15]. Non-thermal fluorocarbon plasma serves as an effective source of high-energy electrons and chemically active particles with applications in material science, where it is widely used for etching semiconductors [16, 17].

The time-resolved data provide more detailed information about the kinetics of unstable species than the classical steady-state FTIR of fluorocarbons [18]. The high resolution (typically 0.05 cm$^{-1}$) can resolve lines of individual species in a wide spectral range, and the individual formation and decay processes can be studied simultaneously. The limitation of this method is the sensitivity of the FTIR emission technique (commonly at least about $10^9$–$10^{12}$ particles per cm$^3$) and the considerable time required to obtain the data because signal accumulation is necessary.

## Experimental

The emission spectra were measured using a time-resolved Fourier transform high-resolution Bruker IFS 120 HR interferometer. The basic principle of this method, described in previous papers [11, 19] is the acquisition of signals from the detector during discharge pulses for different optical path differences. These signals are shifted in time by $\Delta t$ (where $\Delta t = 1$, 2 or 3 μs). In this way, a matrix $I(t_k, \delta_i)$ of intensity $I$ at times $t_k$ is acquired for the given optical path difference $\delta i$ ($i$ is the index of the selected optical path difference, from its zero to maximum values). This process results in 30 to 64 reciprocally time-shifted interferograms computed as a spectrum using the Fourier transformation.

The scheme of experimental set-up is depicted in Fig. 1. The positive column discharge tube, covered with a glass outer jacket, was 25 cm long with an inner diameter of 12 mm. KBr windows were used. The pulsed discharge was maintained by a high voltage transistor switch HTS 81 (Behlke electronic GmbH, Frankfurt, Germany) and applied between the stainless steel anode and the grounded cathode.

The He/precursor plasma was cooled by water in the outer jacket of the cell. The voltage drop across the discharge was 1,200 V, with a pulse width of 20 μs and 0.6 A peak-to-peak current. The scanner velocity of FTS was set to produce a 5 or 10 kHz HeNe laser fringe frequency, which was used to trigger the discharge pulse. The recorded spectral
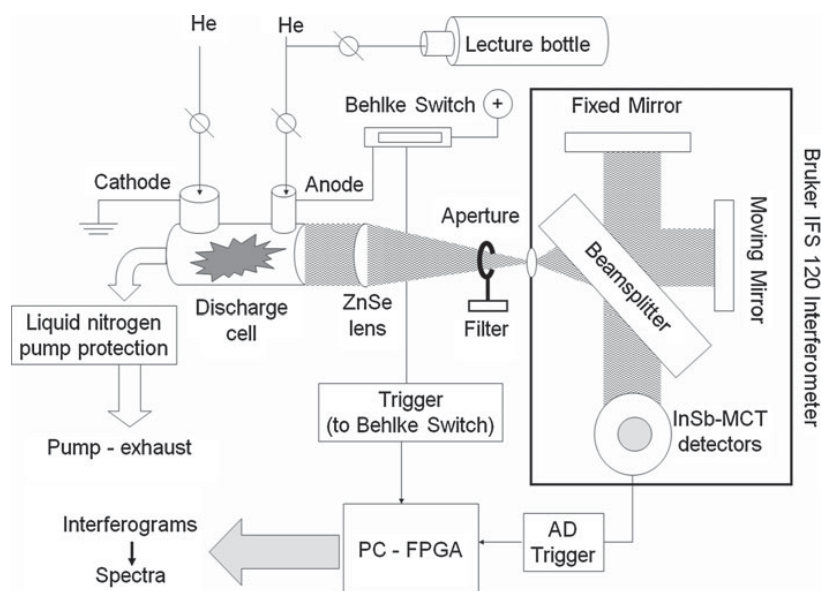
**Fig. 1** Experimental set-up

range was 600–2,000 cm$^{-1}$ and 2,000–6,000 cm$^{-1}$ using a ZnSe lens and a series of Ge optical filters at an unapodized resolution of 0.05 cm$^{-1}$. This spectral range is very wide, commonly only one of these spectral regions is measured. Fifty scans were averaged to obtain a reasonable signal-to-noise ratio. The signal was detected by MCT and InSb detectors. Samples from the industry reservoir that contain air impurities (oxygen, moisture) were taken to the small lecture bottle at a pressure of 8 atm. The initial pressure of the extinguish agent, 0.5 mbar, was sampled from the lecture bottle, and the He buffer gas (99.999% purity) at a pressure in the range 2–4 mbar was co-added to obtain a stable glow discharge. Discharge products were pumped-out from the cell by the rotational pump (Edwards) after each pulse, and the He/precursor system was continually refreshed.

## Results and Discussion

FTIR Emission Spectra

The FTIR spectra of He/$C_3F_7H$ and He/$CF_3Br$ mixtures in pulsed discharge are shown in Figs. 2 and 3, respectively.

    Among the many atomic transitions of excited He* in the IR region, the strongest lines were assigned to the He I (e.g. $^3S$-$^3P^o$ line 918.92 cm$^{-1}$ ∼ 23.7 eV), system of transitions at 2,469.75 cm$^{-1}$, He I $^3P^o$-$^3D$ (line 2,700.09 cm$^{-1}$ ∼ 24.0 eV) or very strong He I $^1S$-$^1P^o$ (line 4,857.46 cm$^{-1}$ ∼ 21.2 eV). Energies in brackets corresponding to the upper level of given transitions show that electrons with energies close to the first ionization energy of He (24.58 eV) are available due to Penning ionization. However, He II was not detected,
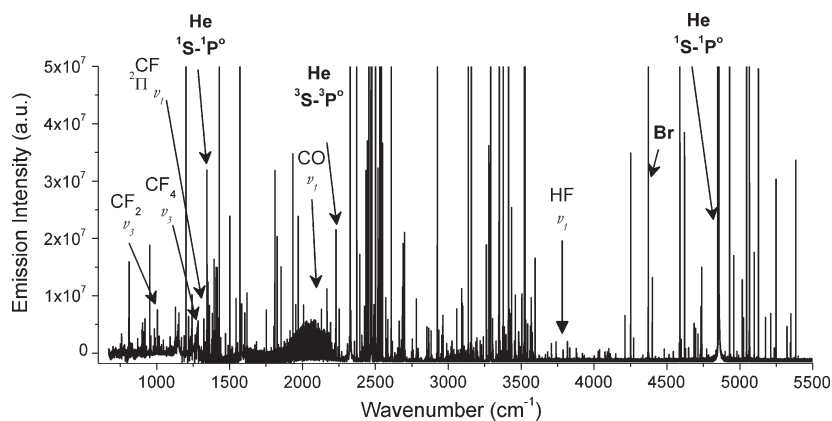
**Fig. 2** FTIR spectrum (600–5,500 cm$^{-1}$) observed for He/CF$_3$Br mixture in a pulsed discharge
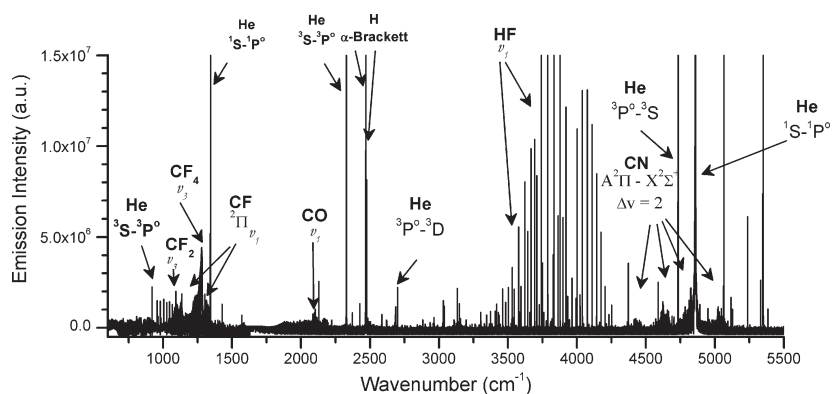


**Fig. 3** FTIR spectrum (600 –5,500 cm$^{-1}$) observed for He/CF$_3$CHFCF$_3$ mixture in a pulsed discharge

which is in agreement with the observed electron energy distribution in helium discharge [20], where the energy continuously decreases into area of the first ionization potentials with an energy maximum of several electron volts.

The lines of atomic hydrogen H I ($\alpha$-Brackett series at 2,467.73 cm$^{-1}$ $\sim$ 13.0 eV) for CF$_3$CHFCF$_3$ and atomic bromine Br I (e.g., transitions at 4,372.07 cm$^{-1}$) for CF$_3$Br were observed as well. Surprisingly, a low intensity was observed at the atomic lines of carbon, and the strongest line at 2,963.984 cm$^{-1}$ was assigned to the $^3$D-$^3$F$^\circ$ transition. The atomic spectrum of fluorine F I in the IR region has not been studied before. The data were calculated on the basis of the extrapolation of results in the visible spectral region; [21] however, the lines of F I in the FTIR spectra of both compounds cannot be assigned due to their low intensity and/or overlapping with other lines.

The molecular species formed in the helium discharge plasma include predominantly the decomposition products of CF$_3$Br and CF$_3$CHFCF$_3$, namely HBr ($v_1$ band at 2,558 cm$^{-1}$, Fig. 2), HF ($v_1$ band at 3,962 cm$^{-1}$, Figs. 2 and 3), CF (P branch of $^2\Pi_{1/2}$
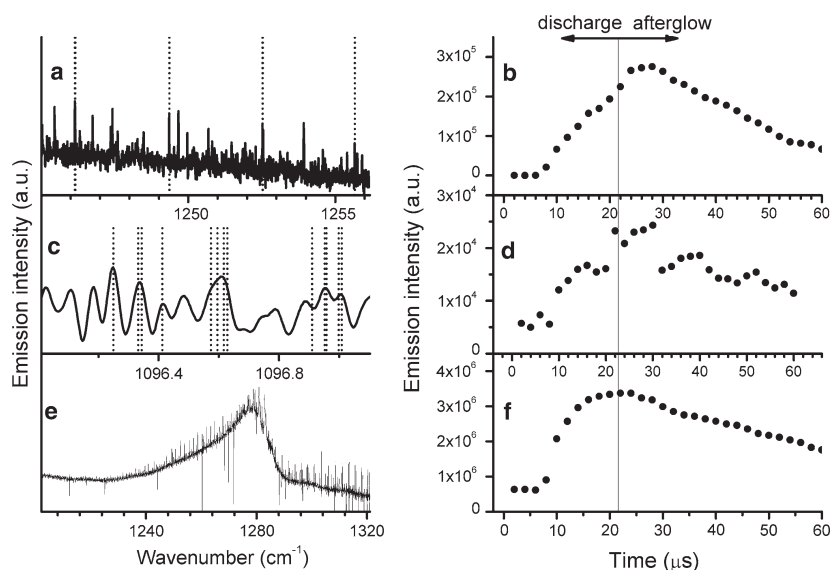
**Fig. 4** Assignments of CF (**a**), CF$_2$ (**c**) and CF$_4$ (**e**) lines in high resolution FTIR spectra in He/CF$_3$CHFCF$_3$ discharge and their comparison with literature data (*dotted lines*). Corresponding time profiles of integrated intensities of CF $^2\Pi_{1/2}$ band (**b**), CF$_2$ $v_3$ band (**d**) and CF$_4$ $v_3$ band (**f**) are shown in the right side of this figure

band at 1,286 cm$^{-1}$, Fig. 4a) [22], CF$_2$ (P branch of $v_3$ band, Fig. 4c) [23, 24], and CF$_4$ ($v_3$ band at 1,281 cm$^{-1}$, Fig. 4e). Although the CF$_3$Br molecule does not contain hydrogen, HF was identified in the spectra of both CF$_3$Br and CF$_3$CHFCF$_3$ decomposition products, probably due to presence of water traces in industrial samples.

The lines of CF$_3$ radical [25] that can be expected in plasma discharge were not explicitly assigned due to congested spectra and possible overlap with lines of similar species, e.g., C$_2$F$_6$. The non-detectable concentration of CF$_3$ can be connected to its reactivity and the formation of more stable products, CF$_4$ and CF$_2$, by the addition or release of fluorine, respectively. No direct evidence of CF$_3$ formation is in agreement with results of the pyrolysis of CF$_3$CHFCF$_3$, where the most favored reaction is the elimination of HF at lower temperatures and the formation of CF$_2$ radicals at higher temperatures [26].

Lines of carbon monoxide CO at 2,143 cm$^{-1}$ and the electronic transition A$^2\Pi$-X$^2\Sigma^+$ of the CN radical around 4,750 cm$^{-1}$ (Figs. 2 and 3) were also found. The addition of water vapor to discharge led to the formation of HCN ($v_1$ band at 3,311 cm$^{-1}$). All these species are toxic, and their origin is in secondary reactions of reactive decomposition products in the discharge with air traces and/or water vapor, which are the main contaminants of industrial samples of fire extinguishing agents CF$_3$Br and CF$_3$CHFCF$_3$.

### Kinetics and Chemical Processes in the Discharge

The use of time-resolved FTIR data (Figs. 3 and 4) permits a detailed description of the kinetics of the formation and decay of unstable species. The individual processes were studied in the wide spectral range of 600–6,000 cm$^{-1}$. These results provide information about the time profiles of the unstable species concentrations in excited states. The time

**Fig. 5** Time resolved
concentration profiles of atomic
lines of Br (**a**), He (**b**), H (**c**), and
C (**d**) observed for He/CF$_3$Br
mixture in a pulse discharge
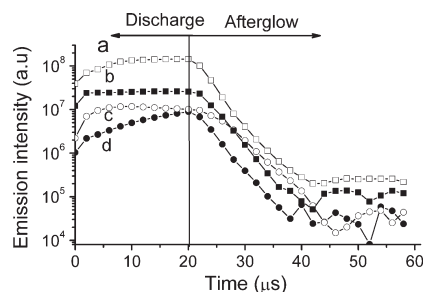


profiles show the difference between the deactivation of atoms (Fig. 5) and molecular species (Fig. 4b, d, f). Whereas atomic species deactivate spontaneously immediately after pulsed discharge with lifetime of several μs (Fig. 5), excited molecular species of CF (Fig. 4b), CF$_2$ (Fig. 4d) and CF$_4$ (Fig. 4f) achieve their maximal concentration in the afterglow. This observation could be connected to their formation from atoms and lower molecular fragments and/or deactivation from higher energy levels.

The emission profiles do not reflect the absolute total concentration of species, which are predominantly quenched to the ground state. Knowledge of the Einstein coefficients for spontaneous emission and bimolecular quenching rate constants is, therefore, essential for their quantification. The total concentrations of the species may be different from the concentration of excited species as forbidden transitions for the metastable levels, and radiation trapping for the resonant levels can change energy distribution inside individual species significantly.

Unstable species (ions, excited states) in helium discharge plasma are formed by Penning ionization (Eq. 1) and/or by molecular dissociation due to collisions with He* (Eq. 2) and electrons (Eq. 3): [27, 28]
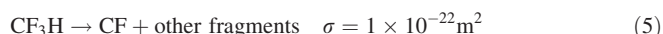
$$AB + He* \rightarrow AB^+ + He + e^- \tag{1}$$

$$AB + He* \rightarrow A + B + He \tag{2}$$

$$AB + e^- \rightarrow A + B + e^- \tag{3}$$
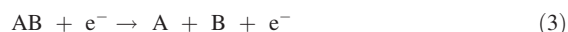
He* represents a helium atom (metastable states $2^1S$ with energy of 20.6 eV and $2^3S$ with energy of 19.8 eV), and AB denotes a molecule with fragments A and B. In comparison with the lowest lying He ($2^3S$), the energies required for the ionization of CF$_3$Br (ionization potential of 11.4 eV) and CF$_3$CHFCF$_3$ (12.4 eV) are significantly lower [24].

The dissociation energy for the C-X bond decreases in the following order: C–F > C–H > C–C > C–Br [29]. The energies of excited He* atoms are significantly higher than the literature data for C–F bonds with the highest dissociation energy ($E_{diss}$ <5.7 eV), and they allow simultaneous splitting of a few bonds during one collision with excited He* atoms and the formation of the observed CF and CF$_2$ fragments (Eq. 2). In reactions where multiple bonds are broken, the bond dissociation energy of a particular bond can be changed by the cleavage of ancillary bonds within the molecule. That is, once the first bond is broken, the remaining bond dissociation energies are often altered, e.g., the experimental values for C–F bonds are 5.31 eV (CF$_4$) [30], 4.00 eV (CF$_3$) [30], 4.59 eV (CF$_2$) [31], and 5.67 eV (CF) [32].

Electron impact data for both precursors (Eq. 3) are not available; however, similar studies with CF$_3$H and CF$_4$ were carried out. The minimal energy for hydrogen (Eq. 4) and

fluorine release (Eq. 6) was calculated to be 11 and 13 eV, respectively. The threshold energy for the direct formation of CH was found to be 19.5 eV. For comparison, the threshold energy of $CF_4$ dissociation to $CF_3$ and $CF_2$ fragments by electron impact was experimentally measured to be 12.5 eV with an optimum of 125 eV [33]. The highest effective cross-sections $\sigma$ for an energy of 20 eV were observed for reactions (Eqs. 4–6) leading to the formation of CF and $CF_3$ radicals:[34]

$$CF_3H \rightarrow CF_3 + H \quad \sigma = 2 \times 10^{-22} m^2 \tag{4}$$

$$CF_3H \rightarrow CF + \text{other fragments} \quad \sigma = 1 \times 10^{-22} m^2 \tag{5}$$

$$CF_3H \rightarrow CHF_2 + F \quad \sigma = 1 \times 10^{-23} m^2 \tag{6}$$
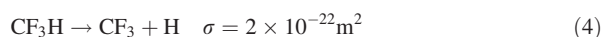
In summary, the energetics of all processes described by Eqs. 4–6 show that both collisions with excited helium atoms and/or with fast electrons can be responsible for the deep fragmentation of $CF_3Br$ and $CF_3CHFCF_3$.

Kinetic Model of $CF_3Br$ Chemistry

A kinetic model of $CF_3Br$ discharge and afterglow was designed on the basis of the reactions listed in Table 1. This model was presented in a previous paper [35] in detail, and it focuses on the radical chemistry because no ions were directly observed.

Briefly, the numerical model was implemented in the Python 2.6.4 programming language using the modules Numpy [36] and Scipy [37] as a zero-dimensional model describing only the time evolution of the concentrations. This type of model is appropriate for data originating from the homogeneous region of the positive column of a glow discharge. The activity of the discharge was simulated by a rectangular pulse with an electron number density of 22 μs in duration in accordance with the experiment. The typical values of electron densities in a glow discharge are between $10^9$ and $10^{11}$ particles per cm³ (ref [38, 39].). A value of $6 \times 10^{11}$ particles per cm³ obtained by a Langmuir probe measurement in the actual experimental discharge was used. The electron temperature not obtained by measurement was set as a free parameter in the range of 0.5–4 eV. The number densities of the precursor molecules were fixed at $6.58 \times 10^{15}$ cm⁻³, as calculated from their partial pressures of 50 Pa and the temperature of the glow discharge of 550 K. The temperature was obtained from a Boltzmann plot of the CF lines. The possible accumulation of reaction products from the previous discharge pulses was taken into account by modeling a sequence of 3,000 pulses in each run (12 h of CPU time) while accounting for the loss of the products by convection in a flow of the buffer gas into the pump. The rates of reactions were adopted from the NIST database [21] and original literature (citations listed in Table 1).

The main mechanism of the dissociation of the molecules in the glow discharge is the collisions with free electrons generated by electron ionization and by Penning ionization. The rate constant of electron dissociation was calculated according to Morrison et al.: [40]

$$k(T_e) = \pi \left( \frac{e}{4\pi\varepsilon_0 E_A} \right)^2 \cdot \left( \frac{8eT_e}{\pi m_e} \right)^{1/2} \cdot \left( 1 + \frac{2T_e}{E_A} \right) \exp(-E_A/T_e) \tag{7}$$

Here, $e$ and $m_e$ are the electronic charge and mass, $\varepsilon_0$ is the permittivity of the vacuum (all in SI units), $E_A$ is the activation energy for dissociation in eV and $T_e$ is the electron temperature expressed in eV.

**Table 1** Reactions in the CF₃Br discharge and afterglow

| No. | Dissociation reaction | Threshold energy (eV) | Ref. |
|---|---|---|---|
| D0 | $CF_3Br + e^- \rightarrow CF_3 + e^- + Br$ | 2.60 | [42, 43] |
| D1 | $CF_2Br + e^- \rightarrow CF_2 + e^- + Br$ | 2.79 | Estimated |
| D2 | $CF_4 + e^- \rightarrow CF_3 + e^- + F$ | 5.31 | [30] |
| D3 | $CF_3 + e^- \rightarrow CF_2 + e^- + F$ | 3.94 | [44] |
| D4 | $CF_2 + e^- \rightarrow CF + e^- + F$ | 4.59 | [30] |
| D5 | $CF + e^- \rightarrow C + e^- + F$ | 5.60 | Estimated |
| D6 | $C_2F + e^- \rightarrow C + e^- + CF$ | 6.16 | Estimated |
| D7 | $C_2F_2 + e^- \rightarrow CF + e^- + CF$ | 5.76 | [30] |
| D8 | $C_2F_2 + e^- \rightarrow C_2F + e^- + F$ | 5.24 | Estimated |
| D9 | $C_2F_4 + e^- \rightarrow C_2F_3 + e^- + F$ | 5.11 | Estimated |
| D10 | $C_2F_6 + e^- \rightarrow C_2F_5 + e^- + F$ | 5.04 | Estimated |
| D11 | $C_2F_5 + e^- \rightarrow C_2F_4 + e^- + F$ | 4.95 | Estimated |
| D12 | $C_2F_3 + e^- \rightarrow C_2F_2 + e^- + F$ | 4.95 | Estimated |
| D14 | $C_2F_3 + e^- \rightarrow CF_2 + e^- + CF$ | 0.44 | [45] |
| D15 | $C_2F_4 + e^- \rightarrow 2\,CF_2 + e^-$ | 3.70 | Estimated |
| D16 | $C_2F_6 + e^- \rightarrow 2\,CF_3 + e^-$ | 3.32 | Estimated |
| D17 | $C_2F_5 + e^- \rightarrow CF_3 + e^- + CF_2$ | 0.44 | [45] |

| No. | Radical–radical reaction | Rate constant (cm³s⁻¹) | Ref. |
|---|---|---|---|
| R0 | $CF_3 + CF_3 \rightarrow C_2F_6$ | $5.25 \times 10^{-12}$ | [46] |
| R1 | $CF_3 + F \rightarrow CF_4$ | $4.40 \times 10^{-11}$ | [47] |
| R2 | $CF_3 + Br \rightarrow CF_3Br$ | $4.40 \times 10^{-11}$ | Estimated using [47] |
| R3 | $CF_2 + F \rightarrow CF_3$ | $4.30 \times 10^{-14}$ | [48] |
| R4 | $CF_3 + CF_2 \rightarrow C_2F_5$ | $8.80 \times 10^{-13}$ | [48] |
| R5 | $CF_2 + CF_2 \rightarrow C_2F_4$ | $4.01 \times 10^{-14}$ | [49] |
| R6 | $CF + F \rightarrow CF_2$ | $1.00 \times 10^{-13}$ | [50] |
| R7 | $CF_4 + F \rightarrow CF_3 + F_2$ | $4.15 \times 10^{-15}$ | Estimated using [51] |
| R8 | $CF_3 + F \rightarrow CF_2 + F_2$ | $4.15 \times 10^{-15}$ | |
| R9 | $CF_2 + F \rightarrow CF + F_2$ | $4.15 \times 10^{-15}$ | |
| R10 | $CF_3 + F_2 \rightarrow CF_4 + F$ | $7.00 \times 10^{-14}$ | Estimated using [48] |
| R11 | $CF_2 + F_2 \rightarrow CF_3 + F$ | $8.32 \times 10^{-14}$ | [52] |
| R12 | $CF + F_2 \rightarrow CF_2 + F$ | $8.32 \times 10^{-14}$ | Estimated using [52] |
| R13 | $C + F_2 \rightarrow CF + F$ | $8.32 \times 10^{-14}$ | |
| R14 | $CF_3 + CF_3 \rightarrow CF_4 + CF_2$ | $1.00 \times 10^{-15}$ | |
| R15 | $CF_3 + CF_2 \rightarrow CF_4 + CF$ | $1.00 \times 10^{-15}$ | |
| R16 | $CF_2 + CF_2 \rightarrow CF_3 + CF$ | $1.00 \times 10^{-15}$ | |
| R17 | $CF + CF_3 \rightarrow 2CF_2$ | $3.90 \times 10^{-12}$ | [53] |
| R18 | $CF_2 + CF \rightarrow C_2F_3$ | $1.00 \times 10^{-12}$ | [47] |
| R19 | $C_2F_3 + F \rightarrow C_2F_4$ | $5.00 \times 10^{-14}$ | |
| R20 | $C_2F_4 + F \rightarrow CF_3 + CF_2$ | $4.00 \times 10^{-11}$ | |
| R21 | $C_2F_5 + F \rightarrow 2\,CF_3$ | $1.00 \times 10^{-11}$ | |
| R22 | $C_2F_6 + F \rightarrow CF_3 + CF_4$ | $1.00 \times 10^{-11}$ | |

**Fig. 6** Calculated time resolved concentration profiles of $CF_4$ (**a**), CF (**b**), $CF_2$ (**c**), $CF_3Br$ (**d**) and $CF_3$ (**e**) in $CF_3Br$ pulse discharge as a function of the number of discharge/afterglow periods
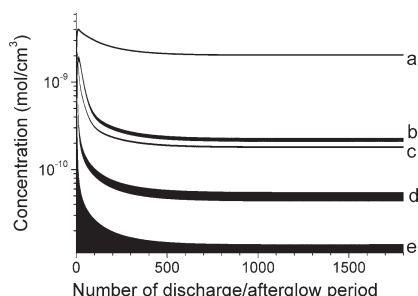


The results of this model applied to the $CF_3Br$ discharge are summarized in Fig. 6. The system achieved the equilibrium between dissociation and recombination reactions after several thousand discharge/afterglow periods. The calculated concentration of $CF_4$ was higher than that of CF and $CF_2$, which is in agreement with the experimental data (see above). The concentrations of $CF_3$ and $C_xF_yBr_z$ species not observed by FTIR measurements were about two orders of magnitude lower than those of CF and $CF_2$. Both experimental and calculated data that predict a high concentration of CF are in agreement with the literature data of Kim et al. [41] for a $CF_4$ discharge. A similar model can be applied to the $CF_3CFHCF_3$ discharge.

## Conclusion

The time-resolved emission spectra of $CF_3Br$ and $CF_3CFHCF_3$ in helium discharge plasma were measured in the $600–6,000$ $cm^{-1}$ region using a high resolution Fourier transform spectrometer. The reaction mechanism that was suggested on the basis of time resolved data starts by Penning ionization and the reaction of precursors with excited helium atoms and/or fast electrons up to atoms and low molecular fragments. The major unstable products were $CF_4$, CF and $CF_2$, which is in agreement with a kinetic model. The formation of stable molecules and vibrational cooling to the ground state were observed in the range of tens of microseconds. All measurements show the formation of toxic and/or reactive stable products, e.g., HF, HBr, CO and HCN.

## References

1. Zurer PS (1993) Chem Eng News 71:12
2. Velders G, Madronich S, Clerbaux C, Derwent R, Grutter M, Hauglustaine D, Incecik S, Ko M, Libre J-M, Neilson O, Stordal F, Zhu T, Blake D, Cunnold D, Daniel J, Forster P, Fraser P, Krummel P, Manning A, Montzka S, Myhre G, O'Doherty S, Oram D, Parther M, Prinn R, Reimann S, Simmonds P, Wallington T, Weiss R (2005) Chemical and Radiative Effects of Halocarbons and Their Replacement

Compounds. IPCC/TEAP Special Report on Safeguarding the Ozone Layer and the Global Climate System: Issues Related to Hydrofluorocarbons and Perfluorocarbons, IPCC Working Group I & III and TEAP. Cambridge University Press, Cambridge, UK

3. Murphy AB, Farmer AJD, Horrigan EC, McAllister T (2002) Plasma Chem Plasma Process 22:371
4. Takigami H, Suzuki G, Hirai Y, Sakai S-i (2009) Chemosphere 76:270
5. Windham GC, Pinney SM, Sjodin A, Lum R, Jones RS, Needham LL, Biro FM, Hiatt RA, Kushi LH (2010) Environ Res 110:251
6. Zegers EJP, Williams BA, Fisher EM, Fleming JW, Sheinson RS (2000) Combust. Flame 121:471
7. Bailleux S, Dréan P, Godon M, Zelinger Z, Duan C (2004) Phys Chem Chem Phys 6:3049
8. Bailleux S, Dréan P, Zelinger Z, Civiš S, Ozeki H, Saito S (2005) J Chem Phys 122:1
9. Bailleux S, Dréan P, Zelinger Z, Godon M (2005) J Mol Spectrosc 229:140
10. Zelinger Z, Dréan P, Walters A, Avilès JR, Bogey M, Pernice H, Von Ahsen S, Willner H, Breidung J, Thiel W, Bürger H (2003) J Chem Phys 118:1214
11. Civiš S, Kubát P, Nishida S, Kawaguchi K (2006) Chem Phys Lett 418:448
12. Civiš S, Šedivcová-Uhlíková T, Kubelík P, Kawaguchi K (2008) J Mol Spectrosc 250:20
13. Civiš S, Matulková I, Cihelka J, Kawaguchi K, Chernov VE, Buslov EY (2010) Phys Rev A. 81
14. Kawaguchi K, Sanechika N, Nishimura Y, Fujimori R, Oka TN, Hirahara Y, Jaman AI, Civiš S (2008) Chem Phys Lett 463:38
15. Jonkers J, Van Der Mullen JAM (1999) J Quant Spectrosc Rad Transfer 61:703
16. Schaepkens M, Standaert TEFM, Rueger NR, Sebel PGM, Oehrlein GS, Cook JM (1999) J Vac Sci Technol A 17:26
17. Chang MB, Chang J-S (2006) Ind Eng Chem Res 45:4101
18. Modiano SH, McNesby KL, Marsh PE, Bolt W, Herud C (1996) Appl Opt 35:4004
19. Kawaguchi K, Hama Y, Nishida S (2005) J Mol Spectrosc 232:1
20. Alexandrov VM, Flender U, Kolokolov NB, Rykova OV, Wiesemann K (1996) Plasma Sources Sci Technol 5:523
21. NIST (2010) in NIST database, URL: http://webbook.nist.gov/chemistry/ downloaded 3 Nov 2010
22. Nakanaga T, Ito F, Takeo H (1994) J Mol Spectrosc 165:88
23. Burkholder JB, Howard CJ, Hamilton PA (1988) J Mol Spectrosc 127:362
24. Gabriel O, Stepanov S, Pfafferott M, Meichsner J (2006) Plasma Sources Sci Technol 15:858
25. Yamada C, Hirota E (1983) J Chem Phys 78:1703
26. Copeland G, Lee EPF, Dyke JM, Chow WK, Mok DKW, Chau FT (2010) J Phys Chem A 114:3540
27. Bell KL, Dalgarno A, Kingston AE (1968) J Phys B 1:18
28. Tokue I, Sakai Y, Yamasaki K (1996) J Chem Phys 106:4491
29. Blanksby SJ, Ellison GB (2003) Acc Chem Res 36:255
30. Modica AP, Sillers SJ (1968) J Chem Phys 48:3290
31. Modica AP (1966) J Chem Phys 44:1585
32. Hildenbrand DL (1975) Chem Phys Lett 32:523
33. Nakano T, Sugai H (1992) Jpn J Appl Phys 31:2919
34. Goto M, Nakamura K, Toyoda H, Sugai H (1994) Jpn J Appl Phys 33:3602
35. Ferus M, Kubelík P, Kawaguchi K, Dryahina K, Španěl P, Civiš S (2011) J Phys Chem A. (in press)
36. http://numpy.org/ downloaded 25 Oct 2010
37. URL: http://scipy.org/, downloaded 25 Oct 2010
38. Corbella C, Polo MC, Oncins G, Pascual E, Andujar JL, Bertran E (2005) Thin Solid Films 482:172
39. Winchester MR, Payling R (2004) Spectrochim Acta B 59:607
40. Morrison NA, William C, Milne WI (2003) J Appl Phys 94:7031
41. Kim JH, Chung KH, Yoo YS (2005) J Korean Phys Soc 47:249
42. Hidaka Y, Nakamura T, Kawano H (1989) Chem Phys Lett 154:573
43. Hidaka Y, Nakamura T, Kawano H, Koike T (1993) Int J Chem Kinet 25:983
44. Srinivasan NK, Su MC, Michael JV, Jasper AW, Klippenstein SJ, Harding LB (2008) J Phys Chem. A 112:31
45. Li K, Kennedy EM, Dlugogorski BZ (2000) Chem Eng Sci 55:4067
46. Geigl M, Peters S, Gabriel O, Krames B, Meichsner J (2005) Contrib Plasma Phys 45:369
47. Ryan KR, Plumb IC (1986) Plasma Chem Plasma Process 6:231
48. Plumb IC, Ryan KR (1986) Plasma Chem Plasma Process 6:205
49. BattinLeclerc F, Smith AP, Hayman GD, Murrells TP (1996) J Chem Soc-Faraday Trans 92:3305
50. Vanhoeymissen J, Deboelpaep I, Uten W, Peeters J (1994) J Phys Chem 98:3725
51. Westbrook CK (1983) Combust Sci.Technol 34:201
52. Seeger C, Rotzoll G, Lubbert A, Schugerl K (1982) Int J Chem Kinet 14:457
53. Peeters J, Vanhoeymissen J, Vanhaelemeersch S, Vermeylen D (1992) J Phys Chem 96:1257

# Investigation of laser–plasma chemistry in CO–N$_2$–H$_2$O mixtures using $^{18}$O labeled water

Martin Ferus [a,b], Irena Matulková [a], Libor Juha [b], Svatopluk Civiš [a,*]

[a] J. Heyrovský Institute of Physical Chemistry, Academy of Sciences of the Czech Republic, Dolejškova 3,182 23 Prague 8, Czech Republic
[b] Institute of Physics, Academy of Sciences of the Czech Republic, Na Slovance 2, 182 21 Prague 8, Czech Republic

## ARTICLE INFO

## ABSTRACT

A large-scale plasma was created in CO–N$_2$–H$_2$O gas mixtures by high-power laser-induced dielectric breakdown. The composition of the mixtures used corresponded to a cometary and/or meteoritic impact into the Earth's early atmosphere. A multiple-centimeter-sized fireball was created by focusing near-infrared laser pulse into the centre of cell. The laser–plasma formation in the mixtures mainly leads to a production of CO$_2$. The competition of the CO + CO → CO$_2$ + C and CO + OH → CO$_2$ + H reactions in the CO$_2$ production was investigated using $^{18}$O labeled water. An analysis of the isotopomers was carried out by means of high-resolution FTIR spectroscopy.

© 2009 Elsevier B.V. All rights reserved.

## 1. Introduction

The majority of current models of the atmosphere during the period of life's origin on our planet prefer an atmosphere composed mostly of carbon dioxide, emphasizing its volcanic origin. The fundamental hypothesis is that the gases were the same as those produced in present volcanic eruptions. Most models are inclined to downplay the existence of strongly reducing atmospheres, which were previously considered to have played the main role in prebiotic syntheses [1].

In this Letter, as well as in those previously published [2,3], it has been shown that a CO–CO$_2$–N$_2$–H$_2$O mixture can be used for the creation of a series of organic molecules, as in the case of strongly reducing atmospheres. An atmosphere containing CO could therefore be an environment for prebiotic syntheses leading to the formation of biologically relevant organic compounds [4]. An atmosphere dominated by carbon monoxide could have existed only under the precondition that the production rate of CO was high. However, a CO dominated atmosphere could not have existed for a long period of time, because the CO was depleted from it. There are several ways of explaining the sink of CO in the early Earth's system.

One possibility is the chemical reaction of CO with the other molecules present, resulting in more complex organic compounds [5]. Groth [6] studied the reaction:

$$2CO + H_2O \rightarrow H_2CO + CO_2. \tag{1}$$

This leads to a shortened half-life of carbon monoxide in the atmosphere due to the formation of formaldehyde. The reaction is thermodynamically unfavorable, but occurs when an high-energy event takes place in its initiation. For example, absorption of 129.5 nm or 147 nm radiation, such as produced from Xe lines, in the gas produces H$_2$CO with quantum yields of 1.0.

Maksimov et al. [7] carried out detailed studies of reactions leading to the formation and decomposition of CO$_2$ taking place in an electric glow discharge in CO. Amongst other things, they found out that the reaction rate constant of

$$CO + O \rightarrow CO_2. \tag{2}$$

could, under certain conditions, be considerably lower than the reaction rate constant of

$$CO + CO \rightarrow CO_2 + C. \tag{3}$$

Essenhigh et al. [8] studied the CO disproportionation reaction (3) (Boudouard reaction) between two highly vibrationally excited CO molecules in the ground electronic state. The inferred reaction activation energy, 11.6 eV (close to the CO dissociation energy of 11.09 eV) was evaluated using the statistical transition state theory, by comparing the dependence of the measured CO$_2$ concentration and the calculated reaction rate constant on helium partial pressure. This suggests that the gas phase Boudouard reaction occurs in collisions of two highly vibrationally excited CO molecules by pooling their vibrational energies. The gas phase disproportionation reaction which does not involve electronically excited species may only occur if the activation barrier is overcome at the expense of translational or vibrational energy of the reactants. The former channel would require extremely high gas temperatures available in a shock tube experiment. The disproportionation reaction rate constant measured at that conditions was $k_f = 9 \times 10^{-18}$ cm$^3$ s$^{-1}$ (3).

Another CO sink in the primitive atmosphere is due to its reaction with hydroxyl radicals [9].

* Corresponding author.
E-mail address: civis@jh-inst.cas.cz (S. Civiš).

$$CO + OH \rightarrow CO_2 + H. \tag{4}$$
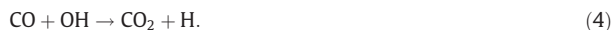
The reaction (4) has been generally accepted to be a major sink of both the OH radical and CO in the atmosphere [10]. In the primitive atmosphere, OH would come from water photolysis and from the reaction of excited oxygen atoms with water vapor [11].

The reaction of OH with CO in the presence of a large quantity of $N_2$ was studied by Biermann et al. [12] at 300 K using pulsed discharge UV photolysis of $H_2O$. The rate constant of this reaction ($1.95 \times 10^{-13}$ cm$^3$ mol$^{-1}$ s$^{-1}$ at 750 Torr $N_2$) was found to be independent of pressure. However, trace impurities may cause the rate constant to increase at high pressure.

If we use Brinkmann's estimate [13] for simultaneous production of the OH radical by the photolysis of water ($1.6 \times 10^9$ mol cm$^{-2}$ s$^{-1}$), we come to the conclusion that the CO in the atmosphere at the pressure of 1 bar would have been converted to $CO_2$ within 430 my (million years) even by this reaction alone. However, it needs to be taken into account that OH in the atmosphere can also react with $CH_4$ and numerous other species [14].

A detailed study of the mechanism of CO conversion in a mixture with nitrogen and water, representing the CO-dominant transient atmosphere model, was carried out using large laser sparks generated on the high-power laser facility PALS (Prague Asterix Laser System) [15]. The main aim of the present experiment, carried out with stable isotope labelling, is to compare the rates of the reactions (3) and (4) in a 1:1 mixture of CO and $N_2$ under the presence of water in both, the liquid and the gas phase. The concentration of water in the gas phase corresponded to a partial pressure of water in the atmosphere at 50 °C. The reactions (3) and (4) can be distinguished by using $H_2^{18}O$. $C^{16}O$ and $H_2^{18}O$ were used as the key laser–plasma chemical reactants and high-resolution Fourier transform infrared (FTIR) spectroscopy was used for the analysis of isotopomeric products of the reaction:

$$C^{16}O(g) + H_2^{18}O(g) + N_2(g) \text{ [LIDB]} \rightarrow \text{products}. \tag{5}$$

$C^{16}O$, $C^{18}O$, $C^{16}O^{18}O$, $C^{18}O_2$, and $H_2^{16}O$ represent the main products formed in this reaction system.

In this Letter, we present experimental results allowing us to evaluate the particular role of the reactions (3) and (4) in laser–plasmas produced in carbon monoxide rich systems. The production rates (i.e., yields, formation efficiencies) of the isotopomeric products from these reactions are compared as a function of the amount of the laser radiation energy deposited in the reactor, i.e., of the number of laser shots fired into the cell.

## 2. Experimental

Laser-induced dielectric breakdown was achieved in the molecular gas mixture using the high-power iodine photo-dissociation laser system PALS [15]. A single pulse of radiation at a wavelength of 1.3152 µm (pulse duration of 400 ps and energy of 100 J) was extracted behind the 4th amplifier of the laser system. The diameter of the laser beam behind the 4th amplifier was 15 cm. One pulse was delivered every 30 min.

The laser beam was focused into a gas cell using a plano-convex lens with a diameter of 15 cm and a focal length of 25 cm. The pulse energy lost at the focusing lens and the cell window did not exceed 15%.

For the static LIDB experiments, a 15 L glass cell was used. The shape of the cell body was a cross with length and width of 40 cm each, with four windows. The main laser beam entrance windows were made of 4 cm thick glass, with a diameter of 20 cm. 1.5 cm thick inspection windows with a diameter of 10 cm served for collection of the OES signals. The windows were mounted onto the glass body with stainless-steel flanges and sealed with viton rings. The cell was mounted on a 1 cm thick aluminum platform for eas-

ier manipulation and positioning. The cell body was equipped with two vacuum valves (ACE glass, USA) for gas handling.

The clean glass cell (the main body of cell was oven-annealed at 450 °C) was evacuated to a pressure of $3 \times 10^{-5}$ Torr and then filled with high-purity $N_2$ and CO gases up to atmospheric pressure (1:1, CO - Linde 99.99%, $N_2$ - Messer 99.996%). 2 mL of liquid water containing 97% of $^{18}O$ (Cambridge Isotope Laboratories, USA) was added to the gas mixture. After filling, the cell was closed and transported to the laser facility. Another cell was used as a control, filled with the same gaseous mixture and 2 mL of distilled water $H_2^{16}O$.

After each laser spark was created in the gas mixture, an approximately 5 mL sample of the gaseous mixture was taken and transferred into a previously evacuated glass IR absorption spectroscopy cell with a length of 30 cm, equipped with KBr windows. The optimal pressure for the high-resolution spectra measurement was chosen with regard to minimal spectral broadening of individual rotation–vibration lines (usually 3.25 Torr). The absorption spectra were measured in the spectral range of 1860–5500 cm$^{-1}$ with a Bruker IFS 120 Fourier transform infrared spectrometer (Bruker, Germany) using an InSb detector and 0.01 cm$^{-1}$ spectral resolution. It was usually necessary to accumulate 100 scans to obtain a sufficient signal-to-noise ratio.

All spectra were compared with a blank sample taken from the cell before the first laser spark.

## 3. Results and discussion

In each sample taken from the 1:1 mixture of CO and $N_2$ with $H_2^{18}O$ water present in the gas phase, we determined the increase of $C^{18}O$, $C^{16}O^{18}O$, and $C^{18}O_2$ concentrations in relation to the number of laser pulses (a pulse energy of 100 J is shot into the cell every 30 min). The reaction scheme proposed including reactions (3) and (4) is shown in the Fig. 1. The quantity of carbon dioxide in the original sample and in the samples after the irradiation was measured by gas chromatography (GC) with FID detection. However, this technique does not allow the determination of the isotope composition in the gas. The abundance of particular isotopomers was determined by high-resolution Fourier transform infrared absorption spectroscopy of samples of the gaseous mixture. Absolute concentrations were determined combining these results with total concentrations of the compound obtained by the gas chromatography. The isotope composition of the original mixture corresponded to the natural abundance of $^{18}O$ and, after the irradiation, the abundance rose in CO and in $CO_2$. To compare the efficiencies of reactions (3) and (4), in accordance with the database HITRAN, the rotation–vibration lines of both isotopomers were selected in such a way that their absorption coefficients were very close each other (Table 1). In the case of the isotopomer $C^{18}O_2$, the strongest spectral line was found, its absorption coefficient was extracted from the HITRAN database, and a spectral line of $C^{16}O_2$ with a similar absorption coefficient was selected. When the formation of $C^{18}O$ as a function of the number of laser shots was studied, the strongest line of this isotopomer was selected, it was quantified on the basis of data on the natural abundance of $^{18}O$ in CO, and finally the result was compared with the formation efficiency of other isotopomers. The integration of the areas of the individual rotation–vibration lines and the plotting of their dependence on supplied energy provided us with gradients of the reactions (3) and (4) leading to isotopomers $C^{16}O_2$ and $C^{16}O^{18}O$ and reactions providing the isotopomer $C^{18}O$. The dependence of integral absorbance, or rather concentration on total deposited energy (i.e., number of laser pulses) in the studied range is linear. The slopes of these lines provide information about the rates of particular reactions under the given conditions.
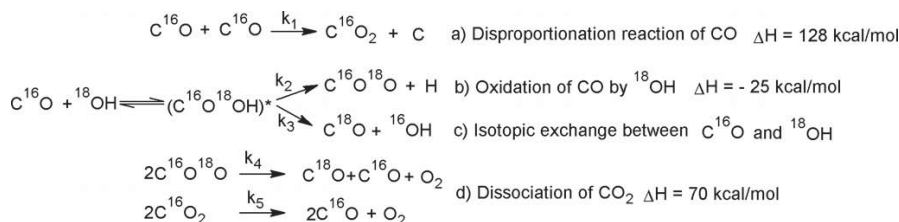
$C^{16}O + C^{16}O \xrightarrow{k_1} C^{16}O_2 + C$    a) Disproportionation reaction of CO   $\Delta H = 128$ kcal/mol

$C^{16}O + {}^{18}OH \rightleftharpoons (C^{16}O^{18}OH)^* \begin{array}{c} \xrightarrow{k_2} C^{16}O^{18}O + H \\ \xrightarrow{k_3} C^{18}O + {}^{16}OH \end{array}$    b) Oxidation of CO by ${}^{18}OH$   $\Delta H = -25$ kcal/mol

c) Isotopic exchange between $C^{16}O$ and ${}^{18}OH$

$2C^{16}O^{18}O \xrightarrow{k_4} C^{18}O + C^{16}O + O_2$

$2C^{16}O_2 \xrightarrow{k_5} 2C^{16}O + O_2$    d) Dissociation of $CO_2$   $\Delta H = 70$ kcal/mol

**Fig. 1.** The proposed isotopic reaction scheme.

Other species are formed in the CO–N$_2$–H$_2$O mixture in very low concentrations and their contribution to the chemical reactions studied in this Letter is neglected. For example N$_2$O was detected by GC method (0.81 ppm). It was necessary to use a liquid nitrogen trap to detect such a small concentration by FTIR spectroscopy [3].

### 3.1. $C^{16}O^{18}O$ formation

A comparison of the slopes of product integral absorbance dependencies on the number of laser shots shows which is the preferred reaction path. The ratio of slopes of the formation curves of carbon dioxide isotopomer $C^{16}O_2$ (a product of the disproportionation reaction (3)) and the isotopomer $C^{16}O^{18}O$ (a product of the oxidation of $C^{16}O$ by radical ${}^{18}OH$ (4)) is 1.53. Therefore, according to the scheme in Figs. 1 and 2, we can conclude $k_1/k_2 = 1.53$. Disproportionation of carbon monoxide is therefore dominating the formation of carbon dioxide in CO–N$_2$–H$_2$O gas mixtures irradiated by a large laser spark.

### 3.2. $C^{18}O_2$ formation

Isotopomer $C^{18}O_2$ is likely a product of isotope reactions where ${}^{18}O$ is transferred from other species to the $C^{16}O^{18}O$ molecule. A comparison of the slopes of linear fits to the measured curves of the isotopomer formation showed (Fig. 3) that during the irradiation, the concentration of $C^{18}O_2$ isotopomer increases 13.3 times less efficiently than $C^{16}O_2$ produced in the reaction Fig. 1a. This demonstrates, that the isotope exchange reactions forming $C^{18}O_2$ play a minor role in the reaction system. (see Fig. 3).

### 3.3. $C^{18}O$ formation

We assume that the isotopomer $C^{18}O$ is a product of isotope exchange between the ${}^{18}OH$ radical and the carbon monoxide $C^{16}O$

molecule, and at the same time a product of the reverse decay of $C^{16}O^{18}O$ to $C^{18}O$. The dissociation of $CO_2$ into CO and oxygen is a competitive reaction to the disproportionation (3) and the oxidation by OH (4). It can also be assumed that both isotopomers ($C^{16}O^{18}O$ a $C^{16}O_2$) decay in the same way. The reverse decay of $CO_2$ to CO cannot be measured by any of the methods of CO chemical analysis because of the great excess of CO in the reaction mixture. However, the described decay can be observed following the concentration of $C^{18}O$ as a function of increasing number of laser shots (see Fig. 4).

It was found that the ratio of the slopes of the $C^{16}O_2$ formation and the $C^{18}O$ formation is 0.98, which, in the context of the scheme in Fig. 1c and d, means $k_1/(k_3 + k_4) = 0.98$. Therefore, the abundance of $C^{18}O$ in the mixture increases at the same rate as the product of the disproportionation reaction of $C^{16}O_2$ is formed. According to the scheme presented in Fig. 1, we can assume that the dynamic equilibrium of the formation of $CO_2$ from CO and the reverse decay of $CO_2$ to CO takes place. If we consider the isotope exchange c) being less probable, the slope $k_4$ of the $C^{18}O$ formation line gives the rate of $C^{16}O^{18}O$ decay:

$$2C^{18}O^{16}O \rightarrow C^{18}O + C^{16}O + {}^{16}O^{18}O. \tag{6}$$
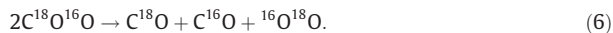
(see Fig. 1) and assuming the equal rate of $C^{16}O_2$ decay, also the half rate of the $C^{16}O_2$ isotopomer decay:

$$2C^{16}O_2 \rightarrow 2C^{16}O + {}^{16}O_2. \tag{7}$$

It can therefore be assumed that the disproportionation rate is actually almost three fold greater

$$k_{dis} = k_1 + 2k_4. \tag{8}$$

**Table 1**
Rotation–vibration lines used for the analysis of isotopomers.

| Isotopomer | Line wavenumber (cm$^{-1}$) | Line | Absorption coefficient (cm$^2$ mol$^{-1}$) |
|---|---|---|---|
| $C^{16}O^{18}O$ compared with | 2308.416 | P (29) | $\varepsilon = 1.03 \times 10^{-18}$ |
| $C^{16}O_2$ | 2317.195 | P (36) | $\varepsilon = 1.01 \times 10^{-18}$ |
| $C^{16}O^{18}O$ compared with | 2342.461 | R (14) | $\varepsilon = 1.71 \times 10^{-18}$ |
| $C^{16}O_2$ | 2352.953 | R (4) | $\varepsilon = 1.70 \times 10^{-18}$ |
| $C^{18}O_2$ compared with | 2302.298 | P (16) | $\varepsilon = 3.08 \times 10^{-18}$ |
| $C^{16}O_2$ | 2365.388 | R (22) | $\varepsilon = 3.11 \times 10^{-18}$ |
| $C^{18}O_2$ compared with | 2327.351 | R (20) | $\varepsilon = 3.19 \times 10^{-18}$ |
| $C^{16}O_2$ | 2332.369 | P (20) | $\varepsilon = 3.18 \times 10^{-18}$ |
| $C^{18}O$ | 2113.406 | R (5) | $\varepsilon = 3.96 \times 10^{-21}$ |



**Fig. 2.** Comparison of slopes of linear fits of dependences of the P(36) $C^{16}O_2$ (2317.195 cm$^{-1}$) and P(29) $C^{16}O^{18}O$ (2308.416 cm$^{-1}$) absorption lines on the increasing number of laser shots, i.e., on the growing amount of laser energy accumulated in the system.
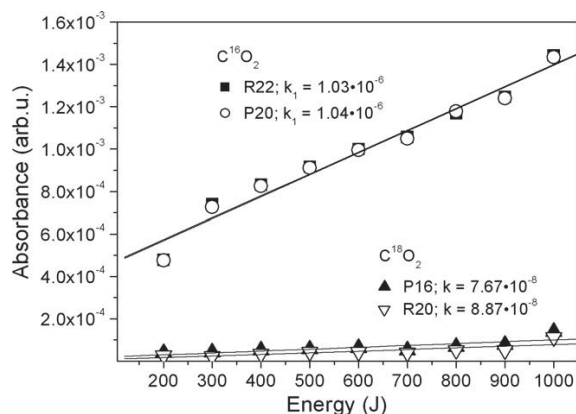
**Fig. 3.** Comparison of the slopes of dependences of $C^{16}O_2$ (2365.3878, 2332.3691 cm$^{-1}$) and $C^{18}O_2$ (2302.2975, 2327.351 cm$^{-1}$) absorbance on increasing amount of laser energy deposited in the cell.
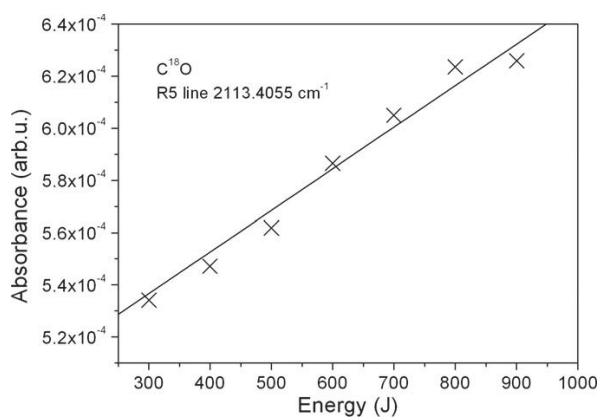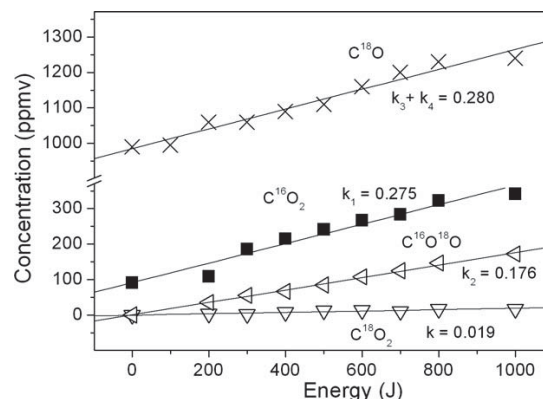


**Fig. 5.** Isotopomeric concentrations, determined by a combination of GC and FTIR analysis, as a function of increasing number of laser shots. $C^{16}O_2$–P20, $C^{16}O^{18}O$–P29, $C^{18}O_2$–R20, $C^{18}O$–R5 absorption lines were utilized in the analysis.
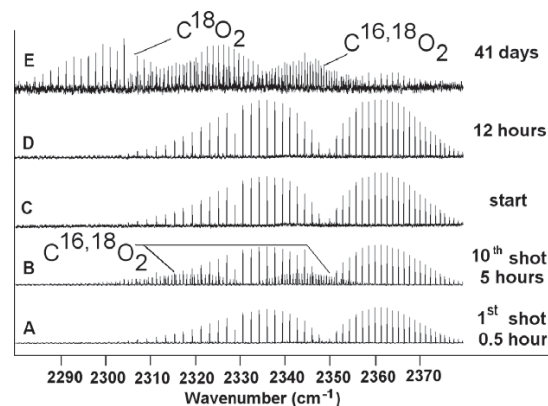


**Fig. 4.** An increase of $C^{18}O$ (2113.4055 cm$^{-1}$ line R5) concentration during the laser exposure.



**Fig. 6.** Spontaneous isotope exchange in a mixture (CO, N$_2$, H$_2^{18}$O containing 93 ppmv $C^{16}O_2$) (C–E) is compared with the LIDB experiment carried out in the same mixture (A,B). No spontaneous isotope exchange was indicated during the first 12 h (D).

### 3.4. Chemical and isotopic analysis of the gaseous mixture

As has been mentioned, the abundance of CO and $CO_2$ isotopomers in the initial, i.e., unirradiated, gas mixture is given by the ratios of the $^{16}O$ and $^{18}O$ natural abundances (quotation HITRAN). Gas chromatography revealed that the unirradiated mixture contained 93 ppmv of $CO_2$. The isotope composition of the mixture is shown in Table 2. After the irradiation, the isotopomeric composition changed and the concentration of $CO_2$ determined by GC increased. If we use rotation–vibration lines with equal absorption coefficient, the abundances of the individual isotopomers will be approximately equal to the ratio of the integral absorbances of the individual isotopomer lines. The total abundance of $CO_2$ can be divided in this ratio to obtain the quantitative data given in Fig. 5.

Finally, we are able to compare ratios of reaction constants obtained from spectral data (the constant is expressed in A J$^{-1}$, where A is the absorbance in arbitrary units) with the ratios of the same constants obtained from spectral data combined with data from gas chromatography (rate constant in ppm J$^{-1}$).

The ratios of gradients in Fig. 5 refer to data obtained exclusively on the basis of spectra and GC: the ratio between reactions (3) and (4) being $k_1/k_2$ = 1.6, and in the case of $C^{18}O_2$ formation,

Let us assume that the dissociation rate constant is $k_5 = 2k_4$ (see Eqs. (6) and (7)). Therefore the rate constant of oxidation is expressed as:

$$k_{ox} = k_2 + 2k_4. \tag{9}$$

The constant $k_5$ cannot be determined from our experiment, because of the high pressure of $C^{16}O$. Intensities of the $C^{16}O$ lines are too strong to detect their small changes by FTIR spectroscopy. The oxidation rate ($k_{ox}$) is in reality more than four times greater than predicted above (Eq. (9)).

The reaction of $CO_2$ decay into CO has been studied in detail [16]. In our laboratory, it was observed, for example, in a glow discharge where $CO_2$ is the source of CO emission bands.

**Table 2**
Concentrations of particular isotopomers in the gas mixture before and after laser exposure.

|  | Isotopomer | | | |
|---|---|---|---|---|
|  | $C^{16}O_2$ | $C^{16}O^{18}O$ | $C^{18}O_2$ | $C^{18}O$ |
| Initial concentration (ppm) | 93 | 0.4 | $3.6 \times 10^{-4}$ | 990 |
| Final concentration (ppm) | 363.9 | 175.9 | 19.2 | 1264 |

13.6. The resulting isotope composition of the mixture is seen in Table 2.

### 3.5. Control experiment without laser–plasma exposure

In this Letter, the oxygen isotope $^{16}O/^{18}O$ fractionation between $CO_2$, CO and $H_2O$ is studied in gas mixtures exposed to a large laser spark. For comparison, we carried out an experiment using the same analytical procedures to investigate evolution of an identical gas mixture which was not irradiated by laser pulses. A long-term study of the reaction mixture using the high-resolution FTIR technique indicated that a spontaneous isotope exchange (Fig. 6) occurs between $H_2^{18}O(g)$ and $C^{16}O_2(g)$. In Fig. 6D, we do not see any sign of $C^{16}O^{18}O$ and $C^{18}O_2$ formation in a period of time comparable to the duration of the whole irradiation series at the PALS facility, which provides one laser pulse per half an hour. This gives a proof that their production is caused by laser–plasma initiated processes.

### 4. Conclusion

Our experiments show that carbon monoxide can be efficiently converted into carbon dioxide by high-energy density events in a CO-rich transient atmosphere, both in the presence of water vapor and in its absence. This is given by the fact that both, CO disproportionation and CO oxidation by OH radicals significantly contribute to the conversion of CO into $CO_2$. Although these reactions take place simultaneously, the disproportionation rate seems to be slightly higher than the rate of that OH reaction under the given conditions. This was found by using the isotopically labeled water. Analysis of the isotopomeric products was carried out by a combination of gas chromatography and high-resolution Fourier transform infrared absorption spectroscopy.

The ratio of slopes of linear fits of the particular isotopomeric product formation curves depicts the ratio of the rates of corresponding reactions occurring in the gas mixture exposed to LIDB plasmas. The calculation of the ratio was carried out for two independent sets of absorption lines of isotopomeric products. It gives a value of 1.5 for the disproportionation and oxidation reactions.

Thus, the disproportionation should be 1.5 times more efficient in $CO_2$ production than oxidation of CO by OH radicals. However, a part of the $CO_2$ formed by the laser spark is decomposed back to CO. Taking this into account, while assuming the low probability of the isotope exchange between the $C^{16}O$ and the $^{18}OH$ radical, the increase of $C^{16}O_2$ (the disproportionation product) concentration with increasing number of laser shots can actually be considered to be three times higher and the $C^{16}O^{18}O$ (the OH oxidation product) formation rate 4.2 times higher than values calculated from a reaction scheme not considering the $CO_2$ decomposition by the laser-produced plasma.

### References

[1] S.L. Miller, Science 117 (1953) 147.
[2] D. Babánková et al., J. Phys. Chem. A110 (2006) 12113.
[3] S. Civiš, D. Babánková, J. Cihelka, P. Sazama, L. Juha, J. Phys. Chem. A112 (2008) 7162.
[4] S. Miyakawa, H. Yamanashi, K. Kobayashi, H.J. Cleaves, S.L. Miller, Proc. Nat. Acad. Sci. USA 99 (2002) 14628.
[5] S. Miyakawa, K. Murasawa, K. Kobayahi, A.B. Sawaoka, J. Amer. Chem. Soc. 121 (1999) 8144.
[6] W. Groth, Z. Phys. Chem. B16 (1932) 77.
[7] A.I. Maksimov, L.S. Polak, A.F. Sergienko, D.I. Slovetskii, Khim. Vys. Energy 13 (1979) 358.
[8] K.A. Essenhigh, Y.G. Utkin, Ch. Bernard, I.V. Adamovich, J.W. Rich, Chem. Phys. 330 (2006) 506.
[9] J.E. Van Trump, S.L. Miller, Earth Planet. Sci. Lett. 20 (1973) 145.
[10] J. Pressman, P. Warneck, J. Atm. Sci. 27 (1970) 155.
[11] H. Levy II, Science 173 (1971) 141.
[12] H.W. Biermann, C. Zetzsch, F. Stuhl, Ber. Bunsenges. Phys. Chem. 82 (1978) 639.
[13] R.T. Brinkmann, J. Geophys. Res. 74 (1969) 5355.
[14] J.L. Franklin, Annu. Rev. Phys. Chem. 18 (1967) 261.
[15] K. Jungwirth et al., Phys. Plasmas 8 (2001) 2495.
[16] I.I. Galakitionov, T.D. Korovkina, High Temp. 7 (1969) 1128.

# Laser Spark Formamide Decomposition Studied by FT-IR Spectroscopy

M. Ferus,[†,‡] P. Kubelík,[†,‡] and S. Civiš*,[†]

[†]J. Heyrovský Institute of Physical Chemistry, Academy of Sciences of the Czech Republic, Dolejškova 3, 18223 Prague 8, Czech Republic

[‡]Institute of Physics, Academy of Sciences of the Czech Republic, Na Slovance 2, 182 21 Prague 8, Czech Republic

**ABSTRACT:** High-resolution FT-IR spectroscopy was used for the analysis of the products of formamide dissociation using a high-energy Asterix laser. In the experiment, the detected products of the formamide LIDB dissociation were hydrogen cyanide, ammonia, carbon monoxide, carbon dioxide, nitrous oxide, hydroxylamine, and methanol. The molecular dynamics of the process was simulated with the use of a chemical model. The chemistry shared by formamide and the products of its dissociation is discussed with the respect to the formation of biomolecules.
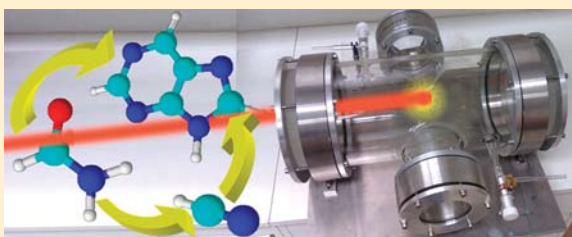
## I. INTRODUCTION

Since the hypothesis of a "primitive soup", suggested by Oparin, one-carbon fragments have been proposed as the starting material for the synthesis of nucleic acid components, amino acids, and sugars. Simple molecules, such as methane, carbon oxides, nitrogen, water, and hydrogen cyanide, are transformed to fragments with a potential significance for the formation of prebiotic molecules:[1] cyanogen, $(CN)_2$; acetonitrile, $CH_3CN$; formaldehyde, $HCHO$; glycolaldehyde, $HOCH_2CHO$; formic acid, $HCOOH$; ammonium cyanide, $NH_4CN$; urea, $NH_2CO-NH_2$; and formamide, $NH_2CHO$ in, for example, an electric discharge,[2] shock wave,[3] or laser spark.[4,5]

Formamide is, from this point of view, an interesting molecule, because it contains all the main constituents of biomolecules: carbon, nitrogen, oxygen, and hydrogen. The formamide molecule is also the simplest model of a peptide or nucleic base linkage. According to Yamada et al.[6] purine has been produced from pure liquid formamide with a yield of up to 55% when it is heated to 170−200 °C. Yamada et al.[7] have found that, with the use of carbon ^{13}C, adenine (a nucleic base derived from purine) is formed in the reaction mixture of HCN and formamide from two molecules of formamide and three molecules of HCN. Saladino et al.[8−10] and Constanzo et al.[11] have studied the formation of nucleic acid bases from formamide diluted in pure water under a reducing atmosphere and subjected to UV radiation or heated at 110−160 °C in the presence of metal oxides and minerals. It should be noted that Saladino et al.[8] have stated that the yield of the purine synthesis without a catalyst is only 1.7%. The formation of amino acids from formamide is the subject of a study published by Sedaghat et al.[12] Experimental works focused on the irradiation of formamide with UV light show that the molecule is photoactive.[13,35]

According to the theory published by Saladino et al., formamide chemistry was one of the paths leading to the formation of nucleic bases for the following reasons[14] (the described processes are shown schematically in Figure 1):

- It is supposed that seawater was abundant with HCN, salts, and other chemical compounds.[15] Formamide is formed by the hydrolysis of HCN (a) in such an environment.[14] We would like to note that formamide has been found in interstellar space,[16] young stellar objects,[17] and comets.[18] When a comet entered the Earth's atmosphere, formamide could therefore have been directly released from the melting cometary ice (b).

- It is a stable liquid over a wide range of temperatures (2.5−210 °C). In periodically drying lagoons, it could have been concentrated (c) from the theoretical values of $10^{-6}$ M predicted by Miller et al.[19] and then entered the subsequent reactions (d). It should be noted that Miller et al.[19] express a negative opinion in their work, as concerns a formamide contribution to the formation of nucleic bases, and they suggest that the bases were formed directly by the increase in the concentration of the HCN solution, for example, via eutectic freezing (e).

However, to deepen the understanding of the formation of these biomolecules, formamide dissociation chemistry must be studied thoroughly because it lies at the beginning of these reaction channels. The study of this dissociation using a high-energy laser Asterix[20−22] is important because processes with a high energy density played a significant role during the period of late heavy bombardment,[23,24] during lightning discharges (f), and also when comets entered the Earth's atmosphere at the time of the formation of our solar system.
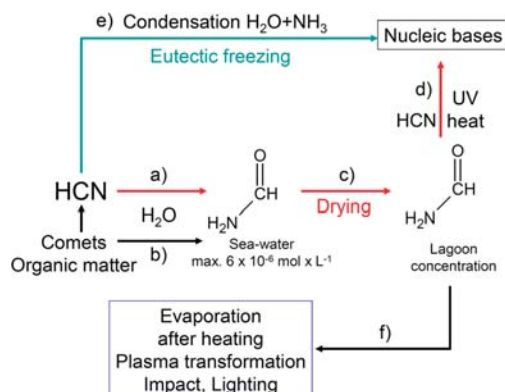
**Figure 1.** Scheme of the formamide transformation under early Earth conditions.

The aim of our experiment was to study the plasma chemistry of pure formamide in the gas phase without other added substances.

## II. EXPERIMENTAL SECTION

**A. Bruker IFS 125 HR Spectrometer.** FT-IR spectroscopy is a suitable absolute method for enabling the direct and sensitive detection of the absorption bands of small molecules in a gaseous mixture of unknown composition. The spectrum allows the identification and direct quantification of the detected molecules. The measurement of the absorption spectra was performed using a Bruker IFS 125 HR apparatus with MCT (HgCdTe) and InSb nitrogen-cooled semiconductor detectors in the $680-3500$ and $1800-5500$ cm$^{-1}$ ranges, with a resolution of 0.02 cm$^{-1}$. To obtain an optimal signal-to-noise ratio, $100-300$ scans were accumulated. A multipass cell of our own design, with an optical path of 30 m, was used for the measurements.

To obtain the product concentrations, calibration measurements were performed at different pressures with various standards of pure gases: HCN (Messer Technogas, 186 ppm/He), CO (Linde Gas, 5.3), N$_2$O (Linde Gas, 2.7), CO$_2$ (Linde Gas, 5.3), NH$_3$ (Linde Gas, 3.8), and CH$_3$OH (Lach-Ner, UV-spectroscopy grade).

**B. Laser-Induced Dielectric Breakdown (LIDB) Plasma and the Asterix Laser System.** The high-energy laser PALS[25] is an iodine chemical laser with a wavelength of 1315 nm. Amplifiers that generate laser radiation by flash photolysis of isopropyliodide (C$_3$F$_7$I) are located along its 160 m optical path. The peak energy of the laser reaches 1 kJ and, because of the pulse width of $\approx$350 ps, power up to 3 TW is obtained. For the purpose of formamide decomposition, the experiment used a cell filled with 10 mL of pure formamide and 760 Torr of inert buffer gas (Ar). A scheme of the cell is shown in Figure 2. A lens was used to focus a 29 cm wide laser beam with an energy of 150 J into the cell to create LIDB plasma. The irradiation was repeated 10 times at 25 min intervals. These intervals are necessary for the charging of the laser.

The contents of the cell were subsequently frozen in a glass vessel that was cooled with liquid nitrogen. The contents were then heated to laboratory temperature and evaporated into a multipass cell. The pressure of the products prepared for measurement inside the cell was 0.056 Torr.
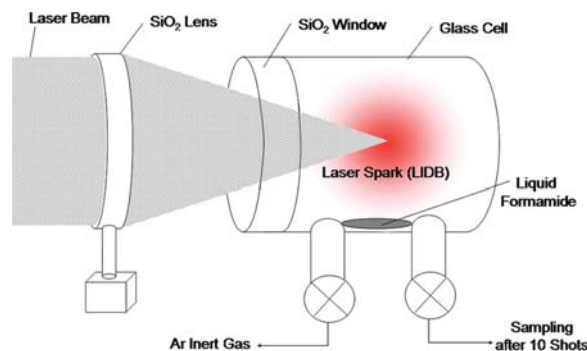


**Figure 2.** LIDB experiment setup.

## III. RESULTS AND DISCUSSION

Hydrogen cyanide, ammonia, carbon dioxide, carbon monoxide, nitrous oxide, hydroxylamine, and methanol were detected as the products of formamide decomposition. Figure 3 shows the spectrum of the blank (a) together with the sample of products of formamide dissociation (b). A summary of all the detected compounds and their percentage ratios estimated using calibration and their infrared intensities is given in Table 1.

To concentrate the volatile organic compounds, a $-196$ °C nitrogen bath was used. It should be noted that with regard to carbon monoxide, which exhibits a melting temperature of $-205$ °C, the freezing method does not trap this gas effectively and, therefore, the CO was not quantified. Methanol was present as the impurity in the gas phase sample of the formamide itself. However, its concentration increased 20× after the formamide irradiation, and it was, therefore, considered to be a reaction product. Although hydroxylamine is also found among the products, it is not quantified in the gas phase because at laboratory temperature it is a volatile solid substance (vapor pressure[26] $0.27-5.3$ Torr at $0-33$ °C).

**A. Model of Formamide Decomposition.** The model of formamide decomposition was designed in the Chemical Kinetics Simulator program.[27] From a general point of view, the processes in the LIDB plasma are very complex. The LIDB laser spark is generated by photon ionization of the molecules, followed by a chain ionization of the gas. Around the expanding plasma, processes of mixing with the surrounding gas, thermal dissociation, dissociation by radiation generated by excited molecules, and shock-wave dissociation take place.

The laser spark is generated on the first harmonic frequency of the Asterix system ($\lambda_1 = 1315$ nm), and a direct photolysis of formamide by laser radiation can therefore be neglected. Because of this fact, a simplification of the formamide vapor decomposition to the process of shock-wave thermolysis at the experimentally found plasma temperature[28] of 4500 K was used in the model. This thermolysis was followed by the subsequent formation of stable molecules after the mixture was cooled to laboratory temperature (293 K). The temperature dependence of the rate constant $k$ was found using the Arrhenius plot:

$$k = 10^{A + 1000B/T} \tag{1}$$

where $k$ is the reaction rate constant in units of cm, mol, and s, $A$ and $B$ are parameters obtained from the fit of the Arrhenius plot, and $T$ is temperature in K. A summary of the reactions used and their parameters is given in Table 2. The activation energy
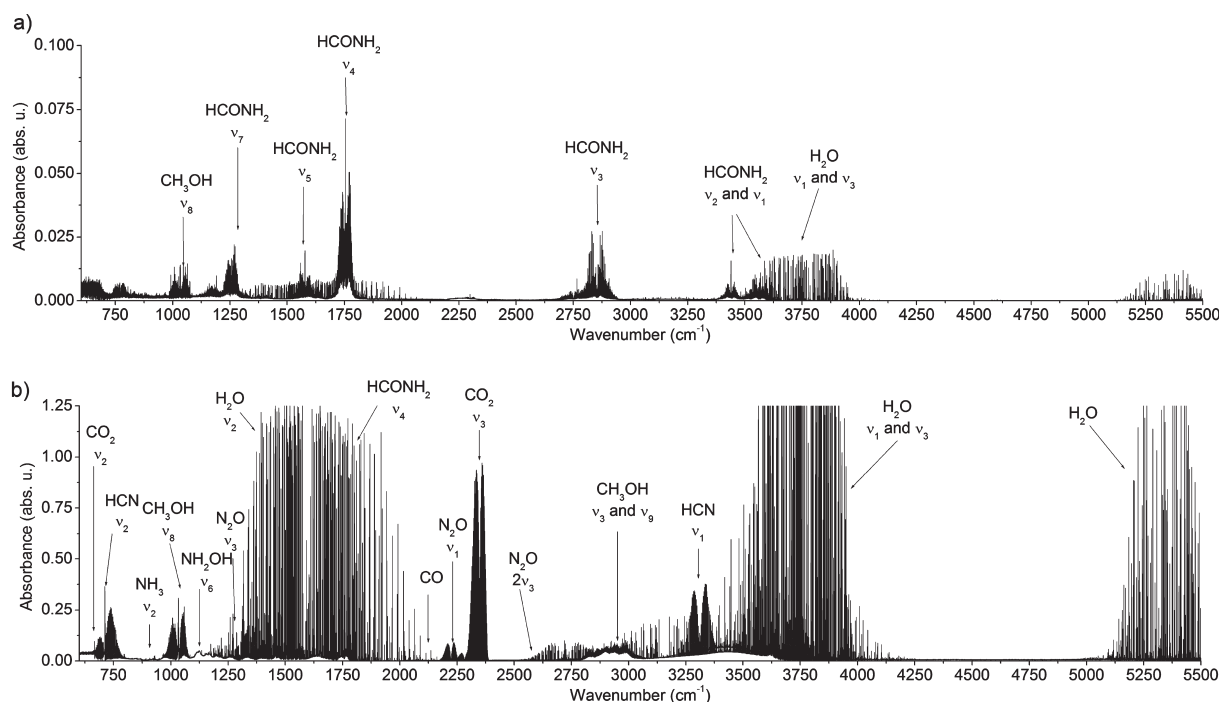
**Figure 3.** Absorption spectrum of formamide blank (a) together with the spectrum of the LIDB dissociation products after evaporation from the liquid-nitrogen trap (b).

**Table 1. Concentrations and Percentages of Abundance of Gaseous Products Identified Using FTIR Spectrometry and Compared with the Results of Chemical Models**

| molecule | band center (cm$^{-1}$) | assig. | band intensity (km/mol) | LIDB plasma | | |
| --- | --- | --- | --- | --- | --- | --- |
| | | | | pressure (mTorr) | ratio (%) | model ratio (%) |
| HCN | 712 | $\nu_2$ | 62.8[62] | 43.3 | 77.3 | 73.4 |
| CH$_3$OH | 1033 | $\nu_8$ | | 7 | 12.4 | 14.5 |
| NH$_3$ | 950 | $\nu_2$ | 51.1[63] | 1.4 | 2.6 | 3 |
| CO$_2$ | 2349 | $\nu_3$ | 538.9[64] | 3.9 | 6.9 | 8.4 |
| CO | 2143 | $\nu_1$ | 64.6[65] | not quantified | | |
| N$_2$O | 2224 | $\nu_3$ | 312.0[66] | 0.4 | 0.8 | 1 |
| total pressure: | | | | 56 mTorr | | |

in kJ·mol$^{-1}$ can be calculated from this dependence from the equation:

$$E_A = 2.303 B R_T \qquad (2)$$

where 2.303 is the conversion factor between the natural and decadic logarithms, $B$ is the slope of the Arrhenius plot and $R_T$ is the universal gas constant ($R_T = 8.3145$ J·mol$^{-1}$·K$^{-1}$).

No rate constant was fitted and the results of the model are based on the current knowledge of rate constants, the values are discussed further in the text. The rate constants were taken from the references and from the NIST database. The concentration of formamide for the purpose of the model was set for the gas phase on the basis that the formamide vapor pressure at laboratory temperature (295 K) is 0.08 Torr. Because of the excess liquid phase in the cell, the formamide pressure remains constant during the irradiation period.

**B. Reaction Channels of the Formamide Decomposition.** *Formation of HCN.* The most abundant product of the LIDB formamide dissociation (77.3%) is, according to our measurement, HCN. The formation of this molecule from formamide was studied in an electric discharge for the first time by Jamiesson[29] and during photolysis by Boden and Back,[30] who have mainly described reactions that form other species: NH$_3$ and CO. Boden and Back have mentioned that when an unfiltered mercury arc is used as a light source, a trace amount of hydrogen cyanide is a further product of the photochemical decomposition of heated formamide. The pure thermal decomposition of formamide has been studied by Cataldo et al.[31] This author has detected HCN as a product at temperatures above 220 °C. According to his results, HCN polymerizes after the formamide decomposition.

The most recent study has been carried out by Nguyen et al.,[32] who have, among other things, theoretically studied formamide thermal decomposition via an intramolecular dehydration process

12134

dx.doi.org/10.1021/jp205413d |*J. Phys. Chem. A* 2011, 115, 12132–12141

P53

**Table 2. Reactions Used in the LIDB Model**[a]

| No. | dissociation reaction | $E_a$ (eV) | Arrhenius parameters | | rate constant s$^{-1}$, cm$^3$ mol$^{-1}$ s$^{-1}$ (4500 K) | note and ref. |
|---|---|---|---|---|---|---|
| | | | B | A | | |
| D0 | HCONH$_2$ → H$_2$O + HCN | 3.18 (HCN)† 3.59 (HNC)† | −16.5677 | 16.2033 | $3.32 \times 10^{12}$ | 32 |
| D1 | HCONH$_2$ → HCO + NH$_2$ | 3.16 | −15.9338 | −7.6520 | $6.41 \times 10^{-12}$ | 37 |
| D2 | HCONH$_2$ → NH$_3$ + CO | 3.25*, 3.12‡ 3.39† | −11.2006 | −5.7340 | $5.98 \times 10^{-9}$ | 37 |
| | | | −17.6577 | 16.4002 | $2.99 \times 10^{12}$ | 32 |
| D3 | HCONH$_2$ → HCON•(H) + H | 5.95*, 3.9‡ | −14.0330 | −8.1170 | $1.94 \times 10^{-12}$ | 37 |
| D4 | HCONH$_2$ → •CONH$_2$ + H | 5.03,* 3.86‡ | −14.0330 | −8.1170 | $5.82 \times 10^{-12}$ | 37 |
| D5 | HCONH$_2$ → H$_2$ + +HNCO | 3.42 | −17.2553 | 14.6212 | $6.12 \times 10^{10}$ | 32 |
| D6 | HCONH → HCO• + :NH | 3.16 | | | $5.90 \times 10^{12}$ | 67 |
| D7 | HCONH·(H) → HCN → •OH | 3.16 | | | $5.90 \times 10^{12}$ | 67 |
| D8 | •CONH$_2$ → •NH$_2$ + CO | 3.16 | | | $5.90 \times 10^{12}$ | 67 |
| D9 | HCO• → H + CO | 0.67 | −3.3536 | −10.2215 | $1.08 \times 10^{-11}$ | 68 |
| D10 | NH$_3$ → •NH$_2$ + H | 4.07 | −20.4986 | −7.3798 | $1.16 \times 10^{-12}$ | 69 |
| D11 | NH$_2$ → :NH + H | 3.29 | −16.5892 | −8.7010 | $4.10 \times 10^{-13}$ | 70 |
| D12 | :NH$_2$ → :NH + H | 3.24 | −16.3284 | −9.5247 | $7.03 \times 10^{-14}$ | 70 |
| D13 | H$_2$O → •OH + H | 4.63 | −23.3176 | −9.1830 | $4.32 \times 10^{-15}$ | 71 |
| D14 | CO → C + O | 9.24 | −46.5840 | −9.4296 | $1.65 \times 10^{-20}$ | 72 |
| D15 | •OH → H + O | 4.31 | −21.7146 | −8.3976 | $5.98 \times 10^{-14}$ | 73 |
| D16 | NO → N + O | 6.43 | −32.4005 | −8.6178 | $1.52 \times 10^{-16}$ | 74 |
| D17 | N$_2$O → N$_2$ + O | 2.5 | −12.5944 | −9.0217 | $1.51 \times 10^{-12}$ | 75 |
| D18 | HCN → H + •CN | 4.79 | −24.1502 | −7.2533 | $2.40 \times 10^{-13}$ | 73 |
| D19 | N$_2$ → 2N | 8.415 | −42.4063 | −9.4425 | $1.36 \times 10^{-19}$ | 76 |
| D20 | CH$_3$OH → •CH$_2$OH + H | 2.35 | −11.8270 | −8.7430 | $4.25 \times 10^{-12}$ | 77 |
| D21 | CH$_3$OH → CH$_3$O• + H | 4.48 | −22.5700 | 9.3350 | $2.09 \times 10^{4}$ | 78 |
| D22 | CH$_2$O• → CH$_2$O | 0.59 | −2.9490 | −10.043 | $2.00 \times 10^{-11}$ | 79 |
| D23 | CH$_2$O → •CHO + •H | 3.18 | −16.0280 | −8.388 | $1.12 \times 10^{-12}$ | 80 |
| D24 | CH$_3$OH → •CH$_3$ + •OH | 2.66 | −13.4040 | −8.028 | $9.85 \times 10^{-12}$ | 81 |
| D25 | H$_2$ → 2H | 4.17 | −21.0176 | −8.8242 | $3.20 \times 10^{-14}$ | 82 |
| D26 | CO$_2$ → CO + O | 4.21 | −21.2363 | −9.7424 | $3.46 \times 10^{-15}$ | 83 |
| D27 | NH$_2$OH → NH$_2$ + •OH | 3.00 | | | $1.00 \times 10^{-12}$ | estim. |
| D28 | •CN → C + N | 6.12 | −30.83495 | −9.37631 | $5.90 \times 10^{-17}$ | 84 |
| D29 | NHCO → CO + :NH | 4.43 | −20.866 | −6.325 | $1.09 \times 10^{-11}$ | 83 |

| no. | recombination reaction | Arrhenius parameters | | rate constant s$^{-1}$, cm$^3$ mol$^{-1}$ s$^{-1}$ | | note and ref. |
|---|---|---|---|---|---|---|
| | | B | A | 293 K | 4500 K | |
| R0 | •CH$_3$ + •OH + M → CH$_3$OH + M | 4.9550 | −32.7830 | $1.03 \times 10^{-16}$ | $2.08 \times 10^{-32}$ | 85 |
| R1 | HCO• + H$_2$O → CH$_2$O + •OH | −6.1418 | −10.7922 | $2.44 \times 10^{-32}$ | $6.97 \times 10^{-13}$ | 73 |
| R2 | HCO• + NH$_2$ → CO + NH$_3$ | | | $1.00 \times 10^{-10}$ | $1.00 \times 10^{-10}$ | estim. |
| R3 | HCO• + H → CO + H$_2$ | | | $1.83 \times 10^{-10}$ | $1.83 \times 10^{-10}$ | 86 |
| R4 | HCO• + •OH → H$_2$O + CO | | | $1.83 \times 10^{-10}$ | $1.83 \times 10^{-10}$ | 87 |
| R5 | CO + H + M → HCO• + M | −0.1608 | −33.2761 | $1.51 \times 10^{-34}$ | $4.88 \times 10^{-34}$ | 73 |
| R6 | CO + •OH → CO$_2$ + H | −0.4811 | −12.0315 | $1.45 \times 10^{-13}$ | $7.27 \times 10^{-13}$ | 88 |
| R7 | HCO• + H + M → CH$_2$O + M | 2.0040 | −32.6726 | $1.32 \times 10^{-26}$ | $5.93 \times 10^{-33}$ | 89 |
| R8 | CH$_2$O + H + M → •CH$_2$OH | −0.2593 | −13.6804 | $2.76 \times 10^{-15}$ | $1.83 \times 10^{-14}$ | 90 |
| R9 | CH$_2$O + H → CH$_3$O• | −0.8904 | −10.3999 | $3.82 \times 10^{-14}$ | $2.52 \times 10^{-11}$ | 91 |
| R10 | CH$_2$O + H → H$_2$ + HCO• | −0.7571 | −10.8409 | $3.91 \times 10^{-14}$ | $9.79 \times 10^{-12}$ | 92 |
| R11 | CH$_3$O• + H → CH$_3$OH• | −0.2120 | −9.4880 | $1.74 \times 10^{-10}$ | $2.92 \times 10^{-10}$ | 93 |
| R12 | CH$_3$O• + H → CH$_2$O + H$_2$ | −0.2613 | −8.4283 | $4.85 \times 10^{-10}$ | $3.26 \times 10^{-9}$ | 94 |
| R13 | •CH$_2$OH + H → CH$_3$OH | −0.0070 | −9.5160 | $2.89 \times 10^{-10}$ | $3.04 \times 10^{-10}$ | 92 |
| R14 | •CH$_2$OH + H → CH$_2$ + H$_2$ | | | $1.66 \times 10^{-11}$ | $1.66 \times 10^{-11}$ | 95 |
| R15 | H + •NH$_2$ + M → NH$_3$ + M | | | $6.07 \times 10^{-30}$ | $6.07 \times 10^{-30}$ | 96 |
| R16 | H + •OH$_2$ + M → H$_2$O + M | 0.3290 | −30.4550 | $1.78 \times 10^{-31}$ | $4.15 \times 10^{-31}$ | 97 |
| R17 | N$_2$ + O + M → N$_2$O + M | | | $5.00 \times 10^{-38}$ | $5.00 \times 10^{-38}$ | 98 |
| R18 | N + :NH → N$_2$ + H | −0.3126 | −10.0400 | $7.95 \times 10^{-12}$ | $7.75 \times 10^{-11}$ | 99 |

**Table 2. Continued**

| no. | recombination reaction | Arrhenius parameters | | rate constant $s^{-1}$, $cm^3$ $mol^{-1}$ $s^{-1}$ | | note and ref. |
|---|---|---|---|---|---|---|
| | | $B$ | $A$ | 293 K | 4500 K | |
| R19 | $CO + N \rightarrow {}^{\bullet}CN + O$ | −15.6370 | −8.4160 | $3.78 \times 10^{-62}$ | $1.29 \times 10^{-12}$ | 100 |
| R20 | ${}^{\bullet}CN + NH_3 \rightarrow HCN + NH_2$ | 0.0780 | −10.8180 | $2.80 \times 10^{-11}$ | $1.58 \times 10^{-11}$ | 101 |
| R21 | ${}^{\bullet}CN + NH_3 \rightarrow HCN + {}^{\bullet}NH_2$ | 0.0780 | −10.8180 | $2.80 \times 10^{-11}$ | $1.58 \times 10^{-11}$ | estim. |
| R22 | $CH + N \rightarrow {}^{\bullet}CN + H$ | 0.0130 | −9.8260 | $1.65 \times 10^{-10}$ | $1.50 \times 10^{-10}$ | 102 |
| R23 | $CH + N \rightarrow :NH + C$ | −0.8800 | −9.8230 | $1.56 \times 10^{-13}$ | $9.58 \times 10^{-11}$ | 103 |
| R24 | $:NH + NCO \rightarrow HNCO + N$ | −1.6649 | −16.9414 | $2.60 \times 10^{-23}$ | $4.88 \times 10^{-18}$ | 104 |
| R25 | $:NH + O \rightarrow NO + H$ | | | $1.16 \times 10^{-10}$ | $1.16 \times 10^{-10}$ | 105 |
| R26 | $NO + NH \rightarrow {}^{\bullet}OH + N2$ | 0.2640 | −11.8670 | $1.07 \times 10^{-11}$ | $1.55 \times 10^{-12}$ | 106 |
| R27 | $:NH + O \rightarrow {}^{\bullet}OH + N$ | | | $1.16 \times 10^{-11}$ | $1.16 \times 10^{-11}$ | 105 |
| R28 | $:NH + :NH \rightarrow {}^{\bullet}NH_2 + N$ | −2.8290 | −9.8020 | $4.06 \times 10^{-20}$ | $3.71 \times 10^{-11}$ | 107 |
| R29 | ${}^{\bullet}NH_2 + {}^{\bullet}OH \rightarrow NH_2OH$ | −0.0240 | −9.9490 | $9.32 \times 10^{-11}$ | $1.11 \times 10^{-10}$ | 108 |
| R30 | ${}^{\bullet}NH_2 + {}^{\bullet}OH \rightarrow H_2O + :NH$ | −1.5980 | −10.0770 | $3.21 \times 10^{-16}$ | $3.70 \times 10^{-11}$ | 109 |
| R31 | ${}^{\bullet}NH_2 + {}^{\bullet}OH \rightarrow NH_3 + O$ | −0.2930 | −12.0590 | $8.87 \times 10^{-14}$ | $7.51 \times 10^{-13}$ | 105 |
| R32 | $NH_3 + NH \rightarrow 2{}^{\bullet}NH_2$ | −5.8680 | −9.2770 | $6.78 \times 10^{-30}$ | $2.62 \times 10^{-11}$ | 110 |
| R33 | ${}^{\bullet}CN + N \rightarrow N_2 + C$ | 0.7690 | −12.4900 | $1.31 \times 10^{-10}$ | $4.80 \times 10^{-13}$ | 111 |
| R34 | ${}^{\bullet}CN + O \rightarrow C + NO$ | −3.2340 | −11.2770 | $5.76 \times 10^{-23}$ | $1.01 \times 10^{-12}$ | 112 |
| R35 | ${}^{\bullet}CN + O \rightarrow CO + N$ | 0.0003 | −9.9490 | $1.13 \times 10^{-10}$ | $1.12 \times 10^{-10}$ | 113 |
| R36 | ${}^{\bullet}CN + H + M \rightarrow HCN + M$ | 0.7560 | −31.3400 | $1.67 \times 10^{-29}$ | $6.73 \times 10^{-32}$ | 113 |
| R37 | ${}^{\bullet}CN + HCO \rightarrow HCN + CO$ | | | $1.00 \times 10^{-10}$ | $1.00 \times 10^{-10}$ | 113 |
| R38 | $CO + O + M \rightarrow CO_2 + M$ | −0.6558 | −32.7692 | $1.02 \times 10^{-35}$ | $1.22 \times 10^{-33}$ | 114 |
| R39 | $:NH + H + M \rightarrow {}^{\bullet}NH_2 + M$ | | | $6.07 \times 10^{-30}$ | $6.07 \times 10^{-30}$ | estim. |
| R40 | $NO + N \rightarrow N_2 + O$ | | | $1.00 \times 10^{-31}$ | $1.00 \times 10^{-31}$ | estim. |
| R41 | $N_2 + {}^{\bullet}OH \rightarrow N_2O + H$ | −17.5882 | −11.2754 | $1.27 \times 10^{-71}$ | $6.55 \times 10^{-16}$ | 115 |
| R42 | $NO + NO \rightarrow N_2O + O$ | −14.2879 | −11.2224 | $2.21 \times 10^{-60}$ | $4.00 \times 10^{-15}$ | 116 |
| R43 | $NO + :NH \rightarrow N_2O + H$ | 0.0657 | −11.0270 | $1.54 \times 10^{-11}$ | $9.71 \times 10^{-12}$ | 115 |
| R44 | $NO + :NH \rightarrow N_2O + H$ | 0.1833 | −11.0683 | $2.78 \times 10^{-11}$ | $7.27 \times 10^{-12}$ | 117 |
| R45 | $N_2 + O \rightarrow NO + N$ | −16.5025 | −9.7800 | $1.90 \times 10^{-66}$ | $3.57 \times 10^{-14}$ | 118 |

[a] Dissociation reaction channels are marked D0−D27, radical−radical recombination channels are marked R0−R45. Activation energies are taken from the literature: [†]indicates the value estimated for the first-order constant by Nguyen et al.[32]; [*]indicates the value estimated by Kang et al.[46]; [‡]indicates the value estimated for the second-order constant by Kakumoto et al.[37]

that produces HCN and HNC and they have found that the process has several transition states, schematically described by eq 3:

$$HCONH_2 \rightarrow [several\ transition\ states] \rightarrow HCN + H_2O \quad (3)$$

has an activation barrier of 306.7 and 346.0 kJ/mol (when the products are HCN and HNC, respectively). This activation energy is comparable to the activation barrier of the formation of $NH_3$ and CO that, according to Nguyen et al.,[32] is 322.2 kJ/mol.

The key to understanding HCN formation via this intramolecular rearrangement is the structure of the planar[33] formamide molecule itself, because the bond between nitrogen and oxygen has a partially double character;[34] therefore, the molecule can be described by a resonance structure:



(4)
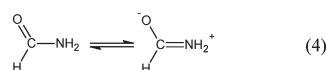
According to the study by Barks et al.,[35] who have dealt with the photochemically induced formation of nucleic bases in a formamide solution, hydrogen cyanide is produced by the rearrangement of the hydrogen atom in its enol form (formidic acid) according to the following equation:



(5)
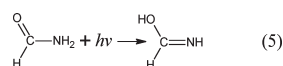
The enol form subsequently decomposes, producing HCN and water.



(6)
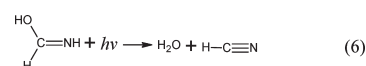
These chemical reactions have been observed by Duvernay[36] in various matrices under UV light irradiation with $\lambda = 240$ nm. According to this author, the enol form decomposes in the matrix, producing HCN and HNC under VUV light irradiation at $\lambda = 160$ nm. This wavelength corresponds to the dissociation energy of the C−H and O−H bonds in HCN and water, respectively.

A second mechanism has been suggested in an experimental paper by Jamiesson et al.,[29] who studied the reaction of formamide vapors with H radicals generated in a hydrogen discharge. Jamiesson has presumed a direct fast reaction of hydrogen atoms with the parent formamide molecule:

$$HCONH_2 + H \rightarrow HCON(H) + H_2 \quad (7)$$

$$HCON^{\bullet}(H) \rightarrow HCN + {}^{\bullet}OH \quad (8)$$
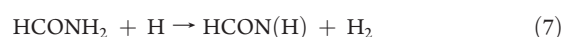
To summarize the possible HCN formation pathways, we can state that HCN is directly formed from the formamide molecule via two known channels: (a) dehydrogenation rearrangement
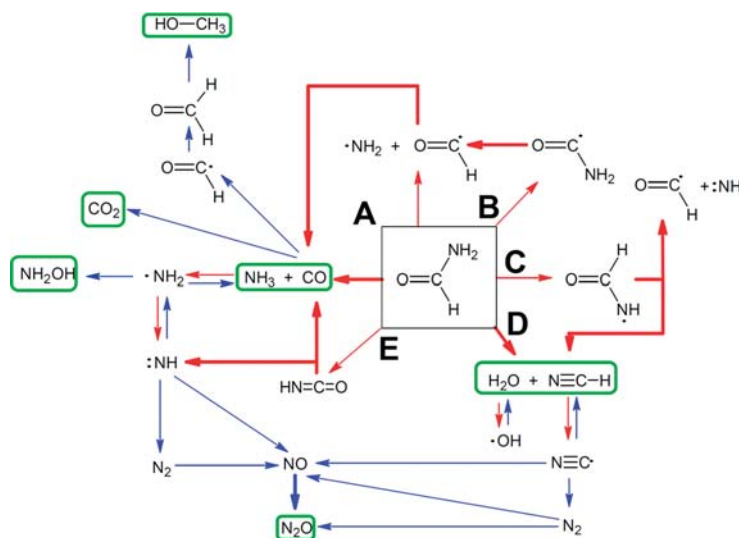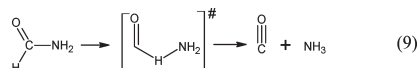
**Figure 4.** Diagram showing formamide dissociation in a laser spark. The dissociation channels are marked with a red arrow, and the recombination channels are marked with a blue arrow. The compounds detected by the FTIR spectrometer are in the green frame.

according to reactions 3, or (b) the reactions of H radicals described by eqs 7 and 8.

The rate coefficient for reaction 7 is not known, and this mechanism is, therefore, not included in our kinetic model.

*Formation of CO and NH₃.* According to the studies of Kakumoto et al.,[37] Liu et al.,[38] and, more recently, Nguyen et al.,[32] the formamide molecule is also dissociated, forming $NH_3$ and CO. Liu et al.[38] and Nguyen et al.[32] have proposed the mechanism of the direct decarbonylation of the formamide molecule in the ground state, which produces $NH_3$ and CO:

$$\underset{H}{\overset{O}{\parallel}}C-NH_2 \longrightarrow \left[ \underset{H}{\overset{O}{\cdots}}\underset{}{\cdots}NH_2 \right]^{\#} \longrightarrow \overset{O}{\underset{}{\parallel}}C \ + \ NH_3 \qquad (9)$$

As detected in the experiment, apart from CO and significant concentrations of $CO_2$ among the products, it can be assumed that the CO produced via reaction 9 is oxidized by an ${}^\bullet OH$ radical[88] or atomic oxygen[114]

$$CO + {}^\bullet OH \rightarrow CO_2 + H \qquad (10)$$

$$CO + O \rightarrow CO_2 \qquad (11)$$

OH radical originates from the thermolysis of water.[71]

$$H_2O \rightarrow {}^\bullet OH + H \qquad (12)$$

Kakumoto et al.[37] have experimentally and theoretically studied, in addition to channel (9), the direct dissociation of formamide into $HCO^\bullet$ and ${}^\bullet NH_2$ radicals:

$$HCONH_2 \rightarrow HCO + {}^\bullet NH_2 \qquad (13)$$
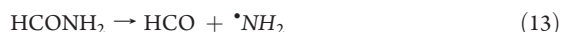
Formamide is a photoactive molecule and decomposition according (13) is considered the most effective photodissociation channel. The characteristic of the formamide excitation in the VUV region of its absorption bands[39] is of the $n-\pi^*$ type,[40] where the excitation of an electron from a bonding orbital of oxygen to an antibonding $\pi^*$ orbital of carbon takes place. The excited formamide subsequently decomposes according to eq 13.

The products $NH_3$ and CO are formed by the following reaction:

$$HCO^\bullet + {}^\bullet NH_2 \rightarrow NH_3 + CO \qquad (14)$$

Reactions 9, 13, and 14 have been studied by Lundell et al.[41] in an Ar matrix (UV laser, 193 nm) by Petersen et al.[42] in the liquid phase, where a ${}^\bullet NH_2$ radical was detected (UV femtosecond laser, 200 nm), and by Boden and Back[43] in the gas phase at high temperatures (UV iodine resonance lamp, 206.2 nm, 115−400 °C). Boden and Back have also designed a reaction model that predicts that the formation of ${}^\bullet NH_2$, $NH_3$, and CO constitues 80% of the photochemical reaction channels.

*Direct Splitting of the CH and NH Bond.* The dissociation channels leading to a direct splitting of hydrogen from the carbon and nitrogen atoms of the formamide molecule have also been referenced.[44,45,37] The splitting forms the respective radicals according to the following equations:

$$HCONH_2 \rightarrow HCON^\bullet(H) + H \qquad (15)$$

$$HCONH_2 \rightarrow {}^\bullet CONH_2 + H \qquad (16)$$
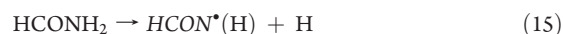
Although the strengths of the C−H and N−H bonds should theoretically be the same, the photochemical decomposition of the isotopically labeled formamide, $DCONH_2$, suggests that the ratio[46] of the rate constants of the reactions is $k_{(15)}/k_{(16)} \approx 1/3$ and activation energies are 5.95 and 5.03 eV, respectively. This conclusion also corresponds with the results of Boden and Back[43] and shows that the CH bond is weaker than the NH bond.

Boden and Back,[30,43] in their photochemical studies, have suggested that the ${}^\bullet CONH_2$ radical decomposes into $:NH_2$ and CO:

$$NH_2CO \rightarrow {}^\bullet NH_2 + CO \qquad (17)$$

The final products of such a pathway are $NH_3$ and CO. For the decomposition of the radical $HCON^\bullet(H)$, Jamiesson et al.[29] have suggested reaction 8, and therefore this reaction channel can be associated with the formation of HCN. For the simplification of our model, the values of the rate constants of the radicals $HCON^\bullet(H)$ and ${}^\bullet CONH_2$ decomposition have been estimated
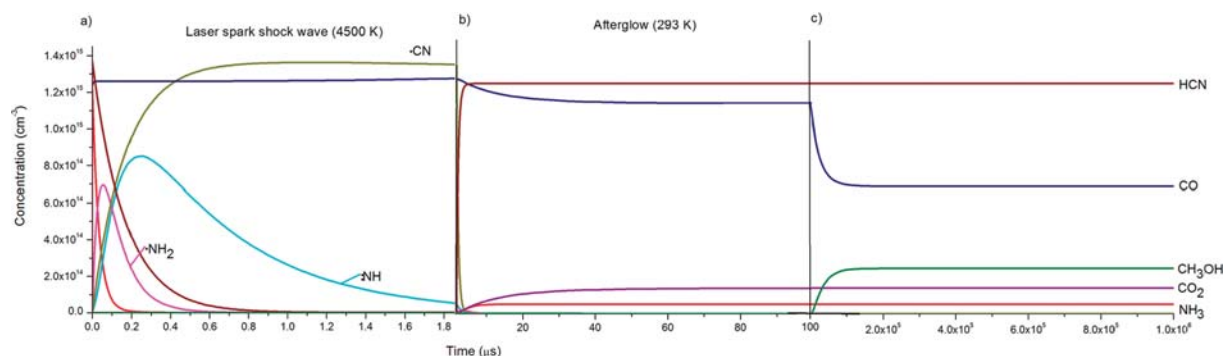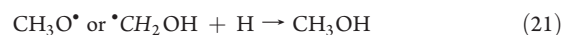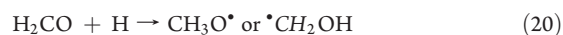
**Figure 5.** Time development of the $NH_3$, HCN, and relevant radical concentrations together with CO, $CO_2$, and $CH_3OH$, according to the model of the LIDB plasma.

to be the same according to the results of Yokota and Back[67] for reaction 17.

*Formation of $CH_3OH$, $NH_2OH$, and $N_2O$.* Methanol ($CH_3OH$) is formed in further reactions of the $HCO^{\bullet}$ radical from reaction 13, in which formaldehyde is an intermediary and methanol is the final product. However, the formamide molecule in the plasma is primarily dissociated into CO, HCN, and $NH_3$. The formed $HCO^{\bullet}$ radical is broken down to CO as a product immediately after the laser pulse. The $HCO^{\bullet}$ radical is, therefore, being produced by the following sequence of reactions:[73,89−93]

$$H + CO \rightarrow HCO^{\bullet} \tag{18}$$

$$HCO^{\bullet} + H \rightarrow H_2CO \tag{19}$$

$$H_2CO + H \rightarrow CH_3O^{\bullet} \text{ or } {}^{\bullet}CH_2OH \tag{20}$$

$$CH_3O^{\bullet} \text{ or } {}^{\bullet}CH_2OH + H \rightarrow CH_3OH \tag{21}$$

In contrast to this complicated reaction chain, we suppose that hydroxylamine ($NH_2OH$) is formed by the direct reaction of the[108] ${}^{\bullet}OH$ radical with ${}^{\bullet}NH_2$

$$ {}^{\bullet}NH_2 + {}^{\bullet}OH \rightarrow NH_2OH \tag{22}$$

Nitrous oxide ($N_2O$) is a typical product of plasma chemistry; it was detected for example in the electric discharge plasma (results to be published). We assume that this molecule is formed by sequence of reactions involving atomic oxygen, NO, or :NH radical:[105,115,118]

$$:NH + O \rightarrow NO + H \tag{23}$$

$$:NH + NO \rightarrow N_2O + H \tag{24}$$

$$N_2 + O \rightarrow NO + N \tag{25}$$

*Formation of HNCO.* According to the studies by Liu et al.[38] and Nguyen et al.,[32] another reaction channel of the dissociation of the formamide molecule is the formation of isocyanic acid, HNCO, by the dehydrogenation of formamide:

$$HCONH_2 \rightarrow HNCO + H_2 \tag{26}$$
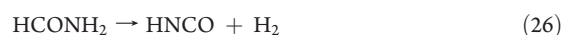
HNCO has a strong $\nu_2$ band[47] at approximately 2269 cm$^{-1}$, which was not identified in our spectrum of the gaseous LIDB

products. This observation could indicate that isocyanic acid is further dissociated into the :NH radical and carbon monoxide:[83]

$$HNCO \rightarrow :NH + CO \tag{27}$$

Although the rate constant of the reverse reaction was not obtained experimentally, it can be assumed that, because of the low reactivity and high stability of CO, its value is very low ($\approx$10$^{-15}$ cm$^3$ mol$^{-1}$ s$^{-1}$ at 295 K).

In summary, the formamide molecule is fully broken down into radicals and atomic fragments by the laser spark, and the fragments are subsequently combined into stable molecules. Therefore, under such drastic conditions in the laser spark, it is not important which molecule containing the basic elements H, C, N, and O is decomposed, but it is the nature and ratio of the fragments which are significant.

**C. Reaction Dynamics.** On the basis of the rate constants calculated according to the study by Kakumoto et al.[37] and Nguyen et al.,[32] the half-life of formamide decomposition at a temperature of 4500 K could be determined in the order of $10^{-12}$ s (in our experiment, the concentration of formamide, $2.83 \times 10^{15}$ cm$^{-3}$, is set by vapor pressure at laboratory temperature, and the concentration of inert gas Ar at atmospheric pressure $2.5 \times 10^{19}$ cm$^{-3}$). This means that, during a laser pulse with a duration of $350 \times 10^{-12}$ s, the precursor vapors are fully decomposed.

A simplified reaction scheme of formamide dissociation in a laser spark was proposed on the basis of the results of the kinetic LIDB model (see Figure 4). For details, see the list of reactions summarized in Table 2. The concentrations of the products that resulted from our model are compared with the spectra of liquid-nitrogen-trapped molecules from the irradiated mixture (see Table 1). The best agreement of our model with experimental results was achieved in the case of the shock-wave temperature of 4500 K for a time interval of $1.86 \times 10^{-6}$ s. These results correspond with previous time-resolved OES measurements of the LIDB plasma[20] during the afterglow laser spark period.

The main products of formamide decomposition immediately after the laser pulse are $H_2O$, HCN, CO, HNCO, $NH_3$ and radicals $HCO^{\bullet}$, $HCON^{\bullet}(H)$, ${}^{\bullet}NH_2$, and ${}^{\bullet}CONH_2$. These molecules subsequently break down, producing significant concentrations of reactive radicals ${}^{\bullet}CN$, :NH, and ${}^{\bullet}OH$ and atoms H, C, O, and N. Other species like NO, $NH_2OH$, $N_2$, and $H_2$ are formed by subsequent reactions during laser spark and plasma cooling. During this period at laboratory temperature, reactive
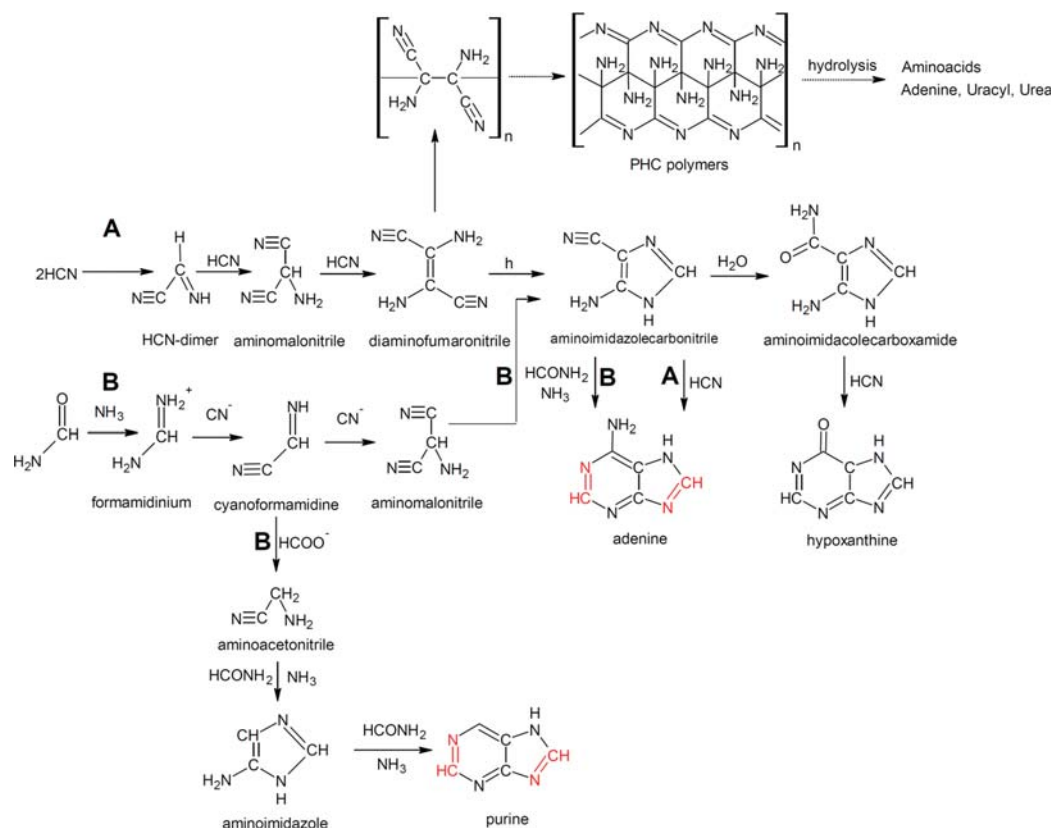
**Figure 6.** Schematic diagram of the formation of adenine, purine, and hypoxanthine by a common chemistry of HCN, $NH_3$, and formamide. Atoms originating from this molecule are marked in red.

species recombine and subsequent products are formed ($N_2O$, $CO_2$, $NH_2OH$, and $CH_3OH$), whereas the radicals $^{\bullet}OH$, $^{\bullet}NH_2$, $:NH$, H, and $^{\bullet}CN$ recombine back into $NH_3$, $H_2O$, and HCN. NO and CO are converted via reactions 23—25, 18—21, 10, and 11 to $N_2O$, $CH_3OH$, and $CO_2$. The model demonstrates that the longer the chosen time interval of thermal dissociation, the higher the HCN concentration and the lower the $NH_3$ concentration after the recombination. This result was obtained because ammonia is thermally less stable. Figure 5 shows the concentration profiles of the selected most abundant radical species together with the stable products detected using FT-IR during the period of the laser spark (a), immediately after the laser spark (b), and during the 1 s after the laser spark (c). The concentrations are predicted by the model.

**D. Formamide Dissociation Products and the Origin of Biomolecules.** HCN is the main product of formamide decomposition by high-energy laser radiation. Saladino et al.[48] suggest that HCN is formed from the formamide molecule due to the presence of catalysts. However, according to our results, HCN together with $NH_3$ are formed without any need of a catalyst, directly in the gas phase during the shock wave thermal decomposition of the parent molecule.

The HCN molecule in the presence of $NH_3$ is able to condense gradually and to produce a series of organic compounds that react to form nucleic bases[49—51] (see Figure 6). The reaction chain is terminated by the formation of polymers,[52—54] so-called cyanopolyynes (sometimes also called *alzulmins*[55,44]). Cyanopolyynes are not formed only in solutions, but also in ice[56] or in

discharges.[57] Nucleic acids and amino acids can be produced from these polymers by repeated hydrolysis.[58,59] The reaction leading to the formation of nucleic bases and polymers from the HCN molecule arranged according to refs 10, 35, 51, 54 and 31, is shown in Figure 6: reaction channels marked **A**.

However, in the systems containing formamide, HCN reacts with its parent molecule. Saladino et al.[11] have stated that, from the point of view of the conversion between formamide and HCN, the chemistry of these molecules cannot be strictly divided. The important fact is that the reverse reactions producing formamide from HCN are also possible, for example, formamide is a product of the hydrolysis or radiolysis[60] of HCN solutions. The formation of nucleic bases within the common chemistry of formamide, HCN, and $NH_3$, according to the results published by Springsteen et al.,[61] is shown in Figure 6: reaction channels marked **B**.

It has been found that the formation of nucleic bases from HCN is a strongly exothermic process, which cannot take place in an isolated state (gas phase), but rather it takes place in a solution.[51] Formamide therefore cannot be dissociated within the studied event of high energy density into HCN and $NH_3$, but to form the nucleic bases, it is necessary for the products to react retroactively with formamide in the liquid phase.

From the point of view of the abundance of individual products after the laser spark, low concentrations of $NH_3$ have to be apparent. As we have mentioned earlier, ammonia is thermally less stable than HCN and it decomposes further. The longer the

12139    dx.doi.org/10.1021/jp205413d |*J. Phys. Chem. A* 2011, 115, 12132–12141

P58

shock wave (thermolysis) lasts, the lower the representation of NH₃ found among the resulting products. It is, however, presumed that $NH_3$, together with HCN, is an important reactant contributing to the formation of nucleic bases (see Figure 6). From this point of view, it therefore cannot be said that the environment in which formamide was dissociated due to an event with high energy density is plausible for the formation of nucleic bases via reactions of formamide with its decomposition products. On the other hand, it can be presumed that suitable conditions are established either where formamide is dissociated into both $NH_3$ and HCN or where $NH_3$ and HCN are generated by other sources in the presence of formamide. For this reason, our next study will be focused on the detection of nucleic bases formed (or not formed) by formamide dissociation in a laser spark (in a solution or ice).

## IV. CONCLUSION

The analysis of the gaseous products of formamide dissociation by the laser LIDB plasma showed that the products of the decomposition are HCN, $NH_3$, CO, $CO_2$, $CH_3OH$, and $NH_2OH$. With the help of the chemical model, it was demonstrated that dissociation, atomization, and subsequent reactions take place in the LIDB plasma, which change the ratio of the final products; $NH_3$ and HNCO are dissociated and their ratio among the products is therefore diminished: CO is converted to $CH_3OH$ and $CO_2$, and NO is converted to $N_2O$ and $N_2$. Additionally, no catalyst for the HCN formation is needed and HCN is the main product of the plasmochemistry. With the formamide dissociation, the whole path leading to the formation of nucleic bases returns to its origin, to the HCN or HNC molecule.[119]

The chemical model was based on the rate constants of formamide dissociation, which have been determined theoretically by Nguyen et al.[32] and Liu et al.[38] and experimentally by Kakumoto et al.[37] With regard to the agreement between the model and experimental results, their theoretical calculations are confirmed. Further study of formamide chemistry is planned with the use of isotopically labeled compounds.

## ■ AUTHOR INFORMATION

**Corresponding Author**
*Tel.: +42 (0) 266 05 3275. E-mail: svatopluk.civis@jh-inst. cas.cz.

## ■ ACKNOWLEDGMENT

## ■ REFERENCES

(1) Balucani, N. *Int. J. Mol. Sci.* **2009**, *10*, 2304–2335.
(2) Miller, S. L.; Urey, H. C. *Science* **1959**, *3370*, 245.
(3) Bar-Nun, A. *Origins Life Evol. Biospheres* **1975**, *1–2*, 109.
(4) Civis, S; Juha, L.; Babankova, D; Cvacka, J.; Frank, O.; Jehlicka, J.; Kralikova, B.; Krasa, J.; Kubat, P.; Muck, A.; Pfeifer, M.; Skala, J.; Ullschmied, J. *Chem. Phys. Lett.* **2004**, *386*, 169.
(5) Ferus, M.; Matulková, I.; Juha, L.; Civiš, S. *Chem. Phys. Lett.* **2009**, *472*, 14.
(6) Yamada, H.; Okamoto, T. *Chem. Pharm. Bull.* **1972**, *20*, 623.

(7) Yamada, H.; Hirobe, M.; Higashiyama, K.l; Takahashi, H.; Suzuki, K. T. *J. Am. Chem. Soc.* **1978**, *14* (100), 4617.
(8) Saladino, R.; Crestini, C.; Costanzo, G.; DiMauro, E. *Top. Curr. Chem.* **2005**, *259*, 29.
(9) Saladino, R.; Ciambecchini, U.; Crestini, C.; Costanzo, G.; Negri, R.; Di Mauro, E. *ChemBioChem* **2003**, *4*, 514.
(10) Saladino, R.; Crestini, C.; Costanzo, G.; DiMauro, E. *Curr. Org. Chem.* **2004**, *8*, 1425.
(11) Costanzo, G.; Saladino, R.; Crestini, C.; Ciciriello, F.; Di Mauro, E. *BMC Evol. Biol.* **2007**, *7* (Suppl 2), S1.
(12) Sedaghat, S.; Leveque, J.-M.; Draye, M. *Chem. Nat. Compd.* **2010**, *1*, 75.
(13) Senanayake, S. D.; Idriss, H. *Proc. Natl. Acad. Sci. U.S.A.* **2006**, *5*, 1194.
(14) Saladino, R.; Crestini, C.; Ciciriello, F.; Di Mauro, E.; Costanzo, G. *J. Biol. Chem.* **2006**, *281*, 5790.
(15) Bada, J. L. *Earth Planet. Sci. Lett.* **2004**, *226*, 1.
(16) Rubin, R.; Swenson, G.; Benson, R.; Tigelaar, H.; Flygare, W. *Astrophys. J.* **1971**, *169*, L39.
(17) Schutte, W. A.; Boogert, A. C. A.; Tielens, A. G. G. M.; Whittet, D. C. B.; Gerakines, P. A.; Chiar, J. E.; Ehrenfreund, P.; Greenberg, J. M.; van Dishoeck, E. F.; de Graauw, T. *Astron. Astrophys.* **1999**, *343*, 966.
(18) Lis, D.; Mehringer, D.; Benford, D.; Gardner, M.; Phillips, T.; Bockelée-Morvan, D.; Biver, N.; Colom, P.; Crovisier, J.; Despois, D.; Rauer, H. *Earth, Moon, Planets* **1997**, *78*, 13.
(19) Miyakawa, S.; Cleaves, H. J.; Miller, S. L. *Origin Life Evol. Biospheres* **2002**, *32*, 195.
(20) Babánková, D.; Civiš, S.; Juha, L. *Prog. Quantum Electron.* **2006**, *30*, 75.
(21) Civiš, S.; Babánková, D.; Cihelka, J.; Sazama, P.; Juha, L. *J. Phys. Chem. A* **2008**, *112*, 7162.
(22) Babánková, D.; Civiš, S.; Juha, L.; Bittner, M.; Cihelka, J.; Pfeifer, M.; Skála, J.; Bartnik, A.; Fiedorowicz, H.; Mikolajczik, J.; Rýć, L.; Šedivcová, T. *J. Phys. Chem. A* **2006**, *110*, 12113.
(23) Wetherill, G. W. Lunar and Planetary Science Conference Proceedings, 1975, p 1539.
(24) Gomes, R.; Levison, H.; Tsiganis, K.; Morbidelli, A. *Nature* **2005**, *435*, 466.
(25) Rus, B.; Rohlena, K.; Skala, J.; Králíkova, B.; Jungwirth, K.; Ullschmied, J.; Watte, K. J.; Baumhacker, H. *Laser Part. Beams* **1999**, *17*, 179.
(26) Krishna, K.; Wang, Y.; Saraf, S. R.; Rodgers, W. J.; Baldwin, J. T.; Gupta, J. P.; Mannan, M. S. *Rel. Eng. Syst. Safety* **2003**, *2*, 215.
(27) URL: http://www.almaden.ibm.com/st/computational_science/ck/?cks, downloaded May 17, 2010.
(28) Babánková, D.; Civiš, S.; Juha, L.; Bittner, M.; Cihelka, J.; Pfeifer, M.; Skála, J.; Bartnik, A.; Fiedorowicz, H.; Mikolajczik, J.; Rýć, L.; Šedivcová, T. *J. Phys. Chem. A* **2006**, *110*, 12113.
(29) Jamieson, J. W. S. *Can. J. Chem.* **1963**, *41*, 1568.
(30) Boden, J. C.; Back, R. A. *Trans. Faraday Soc.* **1970**, *66*, 175.
(31) Cataldo, F.; Patane, G.; Compagnini, G. *J. Macromol. Sci., Part A: Pure Appl. Chem.* **2009**, *46*, 1039.
(32) Nguyen, V. S.; Abbott, H. L.; Dawley, M. M.; Orlando, T. M.; Leszczynski, J.; Nguyen, M. T. *J. Phys. Chem. A* **2011**, *115*, 841.
(33) Fogarasi, G.; Szalay, P. G. *J. Phys. Chem. A* **1997**, *101*, 1400.
(34) Basch, H.; Hoz, S. *Chem. Phys. Lett.* **1998**, *294*, 117.
(35) Barks, H. L.; Buckley, R.; Grieves, G. A.; Di Mauro, E.; Hud, N.; Orlando, T. M. *ChemBioChem* **2010**, *11*, 1240.
(36) Duvernay, F.; Trivella, A.; Borget, F.; Coussan, S.; Aycard, J. P.; Chiavassa, T. *J. Phys. Chem. A* **2005**, *109*, 11155.
(37) Kakumoto, T.; Saito, K.; Imamura, A. *J. Phys. Chem.* **1985**, *89*, 2286.
(38) Liu, D.; Fang, W. H.; Fu, X. Y. *Chem. Phys. Lett.* **2000**, *318*, 291.
(39) Gingell, J. M.; Mason, N. J.; Zhao, H.; Walker, I. C.; Siřel, M. R. F. *Chem. Phys.* **1997**, *220*, 191.
(40) Besley, N. A.; Oakley, M. T.; Cowan, A. J.; Hirst, J. D. *J. Am. Chem. Soc.* **2004**, *126*, 13502.
(41) Lundell, J.; Kraječka, M.; Rsnen, M. *J. Phys. Chem. A* **1998**, *102*, 6643.

12140 dx.doi.org/10.1021/jp205413d |*J. Phys. Chem. A* 2011, 115, 12132–12141

P59

(42) Petersen, Ch.; Dahl, N. H.; Jensen, S. K.; Poulsen, J. A.; Thøgersen, J.; Keiding, S. R. *J. Phys. Chem. A* **2008**, *112*, 3339.

(43) Boden, J. C.; Back, R. A. *Can. J. Chem.* **1970**, *48*, 88.

(44) Robinson, P. J.; Holbrook, K. A. *Unimolecular Reactions*; Wiley: New York, 1972.

(45) Baer, T.; Hase, W. L. *Unimolecular Reaction Dynamics*; Oxford University Press: New York, 1996.

(46) Kang, T. Y.; Kim, H. L. *Chem. Phys. Lett.* **2006**, *431*, 24.

(47) Teles, J. H.; Maier, G.; Hess, B. A., Jr.; Schaad, L. J.; Winnewisser, M.; Winnewisser, B. P. *Chem. Ber.* **1989**, *122*, 753.

(48) Saladino, R.; Crestini, C.; Ciciriello, F.; Constanzo, G.; Di Mauro, E. *Chem. Biodiversity* **2007**, *4*, 694.

(49) Oró, J. *Biochim. Biophys. Res. Commun.* **1962**, *2*, 407.

(50) Oró, J. *Nature* **1961**, *191*, 1193.

(51) Roy, D.; Najafian, K.; Schleyer, P. R. *Proc. Natl. Acad. Sci. U.S.A.* **2007**, *44*, 17272.

(52) Liebman, S. A.; Pesce-Rodriguez, R.; Matthews, C. N. *Adv. Space Res.* **1995**, *15*, 71.

(53) Borquez, E.; Cleaves, H. J.; Lazcano, A.; Miller, S. L. *Origins Life Evol. Biosphere* **2005**, *35*, 79.

(54) Matthews, C. N.; Minard, R. D. *Faraday Discuss.* **2006**, *133*, 393.

(55) Ferris, J. P.; Wos, J. D.; Ryan, T. J.; Lobo, A. P.; Donner, D. B. *Origins Life Evol. Biospheres* **1974**, *1−2*, 153.

(56) Miyakawa, S.; Cleaves, H. J.; Miller, S. L. *Origins Life Evol. Biospheres* **2002**, *32*, 209.

(57) Umemoto, K.; Takahashrand, M.; Yokota, K. *Origins Life Evol. Biospheres* **1987**, *3−4*, 283.

(58) Ferris, J. P.; Wos, J. D.; Nooner, D. W.; Oró, J. *J. Mol. Evol.* **1974**, *3*, 225.

(59) Liebman, S. A.; Pesce-Rodriguez, R. A.; Matthews, C. N. *Adv. Space Res.* **1995**, *3*, 71.

(60) Moore, M. H.; Hudson, R. L. *Proc. IAU Colloq.* **2005**, *231*, 119.

(61) Hudson, J.; Eberle, J.; Vachhani, R.; Rodgers, L.; Springsteen, G. ISSOL and Bioastronomy Joint Internation Conference, 2011.

(62) Devi, V. M.; Benner D., Ch.; Smith, M. A. H.; Rinsland, C. P.; Predoi-Cross, A.; Sharpe, S .W.; Sams, R. L.; Boulet, C.; Bouanich, J. P. *J. Mol. Spectrosc.* **2005**, *231*, 66.

(63) Kim, K. *J. Quant. Spectrosc. Radiat. Transfer* **1985**, *33*, 611.

(64) Rothman, L. S.; Hawkins, R. L.; Wattson, R. B.; Gamache, R. R. *J. Quant. Spectrosc. Radiat. Transfer* **1992**, *48*, 537.

(65) Kim, K. *J. Quant. Spectrosc. Radiat. Transfer* **1983**, *30*, 413.

(66) Varanasi, P.; Ko, F. K. *J. Quant. Spectrosc. Radiat. Transfer* **1977**, *18*, 465.

(67) Yokota, T.; Back, R. A. *Int. J. Chem. Kinet.* **1973**, *5*, 37.

(68) Krasnopetrov, L. N.; Chesnokov, E. N.; Stark, H.; Ravishankara., A. R. *J. Phys. Chem. A* **2004**, *108*, 11526.

(69) Hanson, R. K.; Salimian, S. *Comb. Chem.*, Survey of rate constants in the N/H/O system; Springer-Verlag: New York, 1984.

(70) Deppe, J.; Friedrichs, G.; Ibrahim, A.; Romming, H. J.; Wager., H. G. *Ber. Bunsenges. Phys. Chem.* **1998**, *102*, 1474.

(71) Javoy, S.; Naudet, V.; Abid, S.; Paillard, C. E. *Exp. Therm. Fluid Sci.* **2003**, *27*, 371.

(72) Mick, H. J.; Burmeister, M.; Roth., P. *AIAA J.* **1993**, *31*, 671.

(73) Tsang, W.; Hampson, R. F. *J. Phys. Chem. Ref. Data* **1986**, *15*, 1087.

(74) Tsang, W.; Herron, J. T. *J. Phys. Chem. Ref. Data* **1991**, *20*, 609.

(75) Ross, S. K.; Sutherland, J. W.; Kuo, S. C.; Klemm, R. B. *J. Phys. Chem. A* **1997**, *101*, 1104.

(76) Thielen, K.; Roth, P. *AIAA J.* **1986**, *24*, 1102.

(77) Cribb, P. H.; Dove, J. E.; Yamazaki, S. *Combust. Flame* **1992**, *88*, 169.

(78) Ing, W. C.; Sheng., C. Y.; Bozzelli, J. W. *Fuel Process. Technol.* **2003**, *83*, 111–145.

(79) Choudhury, T. K.; He, Y.; Sanders, W. A. *J. Phys. Chem. A* **1990**, *94*, 2394.

(80) Troe, J. *J. Phys. Chem. A* **2005**, *109*, 8320.

(81) Vasudevan, V.; Cook, R. D.; Hanson, R. K.; Bowman, C. T.; Goden, D. M. *Int. J. Chem. Kinet.* **2008**, *40*, 488.

(82) Baulch, D. L.; Cobos, C. J.; Cox, R. A.; Esser, C.; Frank, P.; Just, Th.; Kerr, J. A.; Pilling, M. J.; Troe, J.; Walker, R. W.; Warnatz, J. *J. Phys. Chem. Ref. Data* **1992**, *21*, 411.

(83) Eremin, A. V.; Ziborov, V. S.; Shumova, V. V.; Voiki, D.; Roth, P. *Kinet. Catal. (Engl. Transl.)* **1997**, *38*, 1.

(84) Tsang, W. *J. Phys. Chem. Ref. Data* **1992**, *21*, 753.

(85) Baulch, D. L.; Cobos, C. J.; Cox, R. A.; Frank, P.; Hayman, G.; Just, Th.; Kerr, J. A.; Murrells, T.; Pilling, M. J.; Troe, J.; Walker, R. W.; Warnatz, J. *J. Phys. Chem. Ref. Data* **1994**, *23*, 847.

(86) Friedrichs, G.; Herbon, J. T.; Davidson, D. F.; Hanson, R. K. *Phys. Chem. Chem. Phys.* **2002**, *4*, 5778.

(87) Temps, F.; Wagner, H. G. *Ber. Bunsenges. Phys. Chem.* **1984**, *88*, 415.

(88) Lissianski, V.; Yang, H.; Qin, Z.; Mueller, M. R.; Shin, K. S.; Gardiner, W. C., Jr. *Chem. Phys. Lett.* **1995**, *240*, 57.

(89) Eiteneer, B.; Yu, C.-L.; Goldenberg, M.; Frenklach, M. *J. Phys. Chem. A* **1998**, *102*, 5196.

(90) Tsuboi, T.; Katoh, M.; Kikuchi, S.; Hashimoto, K. *Jpn. J. Appl. Phys.* **1981**, *20*, 985.

(91) Curran, H. J. *Int. J. Chem. Kinet.* **2006**, *38*, 250.

(92) Oehlers, C.; Wagner, H. Gg.; Ziemer, H.; Temps, F.; Dobe, S. *J. Phys. Chem. A* **2000**, *104*, 10500.

(93) Jasper, A. W.; Klippenstein, S. J.; Harding, L. B.; Ruscic, B. *J. Phys. Chem. A* **2007**, *111*, 3932.

(94) Li, Q. S.; Zhang, Y.; Zhang, S. W. *J. Chem. Phys.* **2004**, *121*, 9474.

(95) Cribb, P. H.; Dove, J. E.; Yamazaki, S. *Combust. Flame* **1992**, *88*, 169.

(96) Gordon, S.; Mulac, W.; Nangia, P. *J. Phys. Chem. A* **1971**, *75*, 2087.

(97) Sellevag, S. R.; Georgievskii, Y.; Miller, J. A. *J. Phys. Chem. A* **2008**, *112*, 5085.

(98) Schofield, K. *J. Phys. Chem. Ref. Data* **1973**, *2*, 25.

(99) Caridade, P.; Rodrigues, S. P. J.; Sousa, F.; Varandas, A. J. C. *J. Phys. Chem. A* **2005**, *109*, 2356.

(100) Ibragimova, L. B. *Kinet. Catal.* **1986**, *27*, 467.

(101) Sims, I. R.; Smith, I. W. M. *J. Chem. Soc., Faraday Trans.* **1988**, *84*, 527.

(102) Brownsword, R. A.; Gatenby, S. D.; Herbert, L. B.; Smith, I. W. M.; Stewart, D. W. A.; Symonds, A. C. *J. Chem. Soc., Faraday Trans.* **1996**, *92*, 723.

(103) Mayer, S. W.; Schieler, L. *J. Chem. Phys.* **1966**, *45*, 385.

(104) Xu, Z. F.; Zun, C. C. *J. Mol. Struct.* **1999**, *459*, 37.

(105) Cohen, N.; Westberg, K. R. *J. Phys. Chem. Ref. Data* **1991**, *20*, 1211.

(106) Bozzelli, J. W.; Chang, A.; Dean, A. M. *Symp. Int. Combust. Proc.* **1994**, *25*, 965.

(107) Zu, Z.-F.; Fang, D.-C.; Fu, X.-Y. *Chem. Phys. Lett.* **1997**, *275*, 386.

(108) Fagerstrom, K.; Jodkowski, J. T.; Lund, A.; Ratajczak, E. *Chem. Phys. Lett.* **1995**, *236*, 103.

(109) Mackie, J. C.; Bacskay, G. B. *J. Phys. Chem. A* **2005**, *109*, 11967.

(110) Rohrig, M.; Romming, H.-J.; Wagner, H. Gg. *Ber. Bunsenges. Phys. Chem.* **1994**, *98*, 1332.

(111) Atakan, B.; Kocis, D.; Wolfrum, J.; Nelson, P. *Symp. Int. Combust. Proc.* **1992**, *24*, 691.

(112) Andersson, S.; Markovic, N.; Nyman, G. *J. Phys. Chem. A* **2003**, *107*, 5439.

(113) Tsang, W. *J. Phys. Chem. Ref. Data* **1992**, *21*, 753.

(114) Tsang, W.; Hampson, R. F. *J. Phys. Chem. Ref. Data* **1986**, *15*, 1087.

(115) Albers, E. A.; Hoyermann, K.; Schacke, H.; Schmatjko, K. J.; Wagner, H. G.; Wolfrum, J. *Symp. Int. Combust. Proc.* **1975**, *15*, 765.

(116) Lin, M. C.; He, Y.; Melius, C. F. *J. Phys. Chem.* **1993**, *36*, 9124.

(117) Bozzelli, J. W.; Chang, A.; Dean, A. M. *Symp. Int. Combust. Proc.* **1994**, *25*, 965.

(118) Michael, J. V.; Lim, K. P. *J. Chem. Phys.* **1992**, *97*, 3228.

(119) Ferus, M.; Kubelík, P.; Kawaguchi, K.; Dryahina, K.; Španěl, P.; Civiš, S. *J. Phys. Chem. A* **2011**, *115*, 1885.

12141

dx.doi.org/10.1021/jp205413d |*J. Phys. Chem. A* 2011, 115, 12132–12141

P60

Dynamic Article Links ▶ View Online

**COMMUNICATION**

# Oxygen-isotope labeled titania: Ti$^{18}$O$_2$†

Ladislav Kavan,*[a] Marketa Zukalova,[a] Martin Ferus,[a] Jenő Kürti,[b] János Koltai[b] and Svatopluk Civiš*[a]

$^{18}$O-isotope labelled titania (anatase, rutile) was synthesized. The products were characterized by Raman spectra together with their quantum chemical modelling. The interaction with carbon dioxide was investigated using high-resolution FTIR spectroscopy, and the oxygen isotope exchange at the Ti$^{18}$O$_2$/C$^{16}$O$_2$ interface was elucidated.

Titanium dioxide is an attractive material for (photo)catalysis, solar cells, electrochromics and batteries,[1] and various fundamental studies would benefit from the availability of $^{18}$O-exchanged material, Ti$^{18}$O$_2$. For instance, O-isotope labeling of titania would allow deeper understanding of Raman spectra. Second motivation for the synthesis of Ti$^{18}$O$_2$ is the possibility to study isotope exchange reactions at the titania surface.[3]

Isotopically pure Ti$^{18}$O$_2$ can be prepared from suitable Ti-precursors *via* hydrolysis by heavy-oxygen water, H$_2$$^{18}$O. The reaction must be carried out in a hermetically closed apparatus to avoid contact with $^{16}$O-containing species, including air. Such a strategy obviously rules out the application of Ti(IV) alkoxides, which are the usual reagents for titania synthesis, and selects Ti(IV) halides as possible starting compounds. Titanium tetrafluoride, TiF$_4$, is converted hydro-thermally in HF medium into TiO$_2$ (anatase) with unusual morphology of truncated bipyramid.[12] On the other hand, hydrothermal conversion of TiCl$_4$ provides usually TiO$_2$ rutile, but other phases (anatase, brookite) can be grown from solutions containing 0.53 to 1.40 mol L$^{-1}$ titanium tetrachloride.[2] In our case (see S1, ESI†), a stoichiometric reaction mixture was used (TiCl$_4$ + H$_2$$^{18}$O; molar ratio 0.5, in vacuum) formally representing 25 mol L$^{-1}$ of TiCl$_4$ in aqueous solution. The hydrolysis proceeds according to the equation:

$$TiCl_4 + 2H_2^{18}O \rightarrow Ti^{18}O_2 + 4HCl \qquad (1)$$

The reaction mixture precipitated spontaneously towards a yellowish solid, containing, presumably, intermediates such as

Ti$^{18}$OCl$_2$. The raw product was heated to 200 °C in the still closed apparatus, while the evolved HCl was collected in a side trap cooled by liquid N$_2$. The final white powder material is further labeled as A200. It contained some adsorbed HCl (see below), which can be removed at 450 °C in vacuum. This material is further labeled as A450. Both A200 and A450 exhibited the X-ray diffraction pattern of pure anatase. The surface area, determined from nitrogen adsorption isotherms by the BET method, was 31 m$^2$ g$^{-1}$ independent of the synthetic history (A200, A450). Eventually, the A450 was calcined at 1000 °C in vacuum producing phase-pure rutile, further labeled as R1000. Its BET surface area was 5 m$^2$ g$^{-1}$. To prepare reference materials, the reaction (1) was reproduced with water of natural isotopic composition, and the obtained products passed the same heat treatment history as A200, A450 and R1000. X-Ray diffraction on powder samples indicated negligible differences caused by isotope labeling (see S1, ESI†).

Raman spectroscopy can easily distinguish crystallographic phases of titania, but detailed understanding of the spectra is still lacking, and various controversies persist in the literature, even for the most common phases, *viz.* rutile[11] and anatase.[4] Some of these problems can be addressed by isotope labeling. Fig. 1 compares the Raman spectra of our $^{18}$O-labeled titania samples (A450 and R1000) with those of unlabeled reference materials. Anatase TiO$_2$ (space group $D_{4h}^{19}$-$I4_1/amd$) has six Raman active vibrations: A$_{1g}$ + 2B$_{1g}$ + 3E$_g$. Rutile TiO$_2$ (space group $D_{4h}^{14}$-$P4_2/mnm$) has four Raman active vibrations: A$_{1g}$ + B$_{1g}$ + B$_{2g}$ + E$_g$, and there is also a combination band

[a] *J. Heyrovský Institute of Physical Chemistry, v.v.i. Academy of Sciences of the Czech Republic, Dolejskova 3, 18223 Prague 8, Czech Republic. E-mail: kavan@jh-inst.cas.cz, civis@jh-inst.cas.cz*
[b] *Institute of Physics, Loránd Eötvös University, Pázmány Péter sétány 1/A, H-1117 Budapest, Hungary*
† Electronic supplementary information (ESI) available: Experimental procedures, calculations details and additional data. See DOI: 10.1039/c1cp20775j
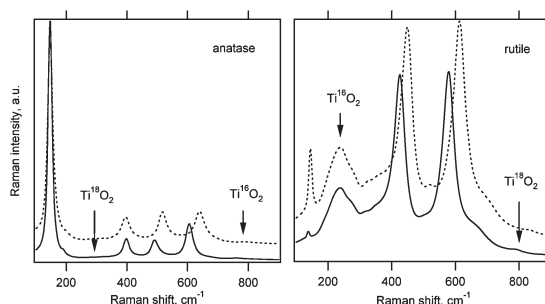
**Fig. 1** Raman spectra of the prepared materials excited by 514.5 nm laser. Full curves are for $^{18}$O labeled titania samples and dashed curves are for reference unlabeled samples. Spectra are offset for clarity, but the intensity scale is identical in each chart.

This journal is © the Owner Societies 2011

*Phys. Chem. Chem. Phys.*, 2011, **13**, 11583–11586 | 11583

P61

**Table 1** Experimental and calculated Raman frequencies of Ti$^{16}$O$_2$ ($\upsilon_{16}$) and Ti$^{18}$O$_2$ ($\upsilon_{18}$) in anatase and rutile. Experimental data were acquired using 514.5 nm excitation. Calculations were carried out by first-principles density functional theory

| Sample | $\upsilon_{16}$ (cm$^{-1}$) Ti$^{16}$O$_2$ | $\upsilon_{18}$ (cm$^{-1}$) Ti$^{18}$O$_2$ | $\upsilon_{16}$ (cm$^{-1}$) Ti$^{16}$O$_2$ | $\upsilon_{18}$ (cm$^{-1}$) Ti$^{18}$O$_2$ | Assignment | $\upsilon_{16}$–$\upsilon_{18}$ exp. | $\upsilon_{16}$–$\upsilon_{18}$ calc. |
|---|---|---|---|---|---|---|---|
| | Experimental | | Calculated | | | | |
| Anatase (A450) | 146 | 146 | 146.5 | 145.5 | E$_g$(1) | 0 | 1 |
| | 197 | 187 | 154.5 | 146.5 | E$_g$(2) | 10 | 8 |
| | 397 | 397 | 381.8 | 381.8 | B$_{1g}$(1) | 0 | 0 |
| | 516$^a$ | 492$^a$ | 503.7 | 474.9 | B$_{1g}$(2) | 24 | 28.8 |
| | 516$^a$ | 492$^a$ | 526.9 | 496.8 | A$_{1g}$ | 24 | 30.1 |
| | 640 | 604 | 653.6 | 616.6 | E$_g$(3) | 36 | 37 |
| Rutile (R1000) | 145 | 138 | 141.2 | 133.1 | B$_{1g}$ | 7 | 8.1 |
| | 238 | 238 | — | — | Comb. | 0 | — |
| | 448 | 426 | 466.3 | 439.6 | E$_g$ | 22 | 26.7 |
| | 613 | 579 | 614.5 | 579.4 | A$_{1g}$ | 34 | 35.1 |
| | 826 | 788 | 819.1 | 772.3 | B$_{2g}$ | 38 | 46.8 |

$^a$ Overlapping bands in the experimental spectrum.

around 240 cm$^{-1}$. Table 1 summarizes the observed Raman frequencies and their assignment. The frequencies of $^{18}$O-labeled isotopologues are intact or red-shifted. The largest shifts (36 and 38 cm$^{-1}$) are detected for the anatase E$_g$(3) mode and the rutile B$_{2g}$ modes (Table 1). They are sufficient to prove the isotope purity of our Ti$^{18}$O$_2$ (anatase, rutile).

Table 1 further summarizes the theoretically calculated Raman frequencies (see S2, ESI†). For all four peaks of rutile, the relative isotope shifts, ($\upsilon_{16}$–$\upsilon_{18}$)/$\upsilon_{16}$, are 5.7% and the experimental values are between 5 to 6%. As the Ti atoms in rutile are located in inversion centers, they cannot take part in vibrations with *gerade* symmetry, and for all the Raman active modes only the oxygen atoms are moving (see Table 1-S2 in ESI†). Hence, the Raman frequencies should scale exactly with the mass of oxygen isotope. The downshift for $^{16}$O $\rightarrow$ $^{18}$O substitution is:

$$1 - (16/18)^{1/2} \qquad (2)$$

Remarkable agreement of this value with both experiment and theory (Table 1) further confirms the isotope purity of our R1000.

In contrast to rutile, the Ti atoms in anatase do not occupy inversion centers. Hence, most of the modes involve both Ti and O atoms movement. There is only one Raman active mode, the A$_{1g}$, where the symmetry does not allow the movement of Ti atoms. This mode exhibits the expected shift of 5.7% (eqn (2) and Table 1), although in this case, the experimental analysis is complicated by the overlap of the A$_{1g}$ and B$_{1g}$(2) bands (see Fig. 1 and Table 1). On the other hand, both experiment and theory show in unison that there are two modes with no oxygen isotope shift: E$_g$(1) and B$_{1g}$(1). Symmetry analysis shows that it is possible to construct a displacement pattern with E$_g$(1) and B$_{1g}$(1) symmetry, so that the oxygen atoms do not vibrate at all.

The Raman spectra of our Ti$^{18}$O$_2$ materials (A450, R1000) did not change markedly even after months of storage of the samples in air at room temperature. Both samples still showed the Raman spectra like pure $^{18}$O-isotopologues (Fig. 1) in spite of their long-time contact with air oxygen and humidity (with dominating $^{16}$O-content; 99.8% natural abundance). However, Raman scattering mostly comes from the bulk sample and surface reactions may thus be unnoticed.

To settle this question, the isotope exchange on the $^{18}$O labeled titania was studied. In general, the $^{18}$O/$^{16}$O-exchange between gaseous molecules and oxidic surfaces was studied carefully since the middle of the last century, due to its impact on catalysis and photocatalysis.[8,9] The classical studies employed common (unlabeled) solid oxides exposed to $^{18}$O-labeled molecules and mass spectroscopy was the usual analytical technique.

We upgraded this traditional approach by two inputs. First, we explored the behavior of a 'reverse system', *i.e.* $^{18}$O-labeled titania plus unlabeled model gaseous molecules. Secondly, we developed a new analytical technique based on a high-resolution Fourier transform infrared spectroscopy (HR-FTIR) of the gas phase contacting the titania surface. This technique is ideal for characterization of molecules having many IR-active rotation–vibration transitions. A generic case is carbon dioxide, CO$_2$, exhibiting rich and well-known IR spectrum. Secondly, CO$_2$ is attractive as the final product of photocatalytic mineralization of organic molecules on titania,[1] and CO$_2$ can be also photoreduced on titania to fuels.[5] The application of Ti$^{18}$O$_2$ as a photocatalyst and analysis of products by HR-FTIR would be a powerful strategy for mechanistic studies of photocatalytic reactions. However, understanding of the CO$_2$/Ti$^{18}$O$_2$ interaction in dark is a logical prerequisite for correct interpretation of photocatalytic processes based on isotope tracing.

To address this problem, we contacted gaseous CO$_2$ (with natural isotope composition) with solid Ti$^{18}$O$_2$ and measured the HR-FTIR spectra of the gas phase (see S1, ESI†). Fig. 2 (top curve) shows the reference spectrum of CO$_2$ in the absence of titania. Our starting carbon dioxide was mostly C$^{16}$O$_2$ (partial pressure 2.06 Torr; abbreviated 16–16). It contained some natural C$^{16}$O$^{18}$O (0.008 Torr; abbreviated 16–18) but negligible amount of C$^{18}$O$_2$ (8.25.10$^{-6}$ Torr, abbreviated 18–18). When CO$_2$ was exposed to our sample A200, no marked oxygen isotope exchange took place, but we detected the diagnostic rotation–vibration band of HCl in the region of 2600–3100 cm$^{-1}$ and also small amount of water in the 3600–3800 cm$^{-1}$ region. Hydrogen chloride is the obvious impurity in the A200 sample (*cf.* reaction (1)) and it is not completely removed by heat treatment at 200 °C during the synthesis in a closed apparatus (see S1, ESI†). Hence HCl is desorbed from A200 into the studied gas phase.
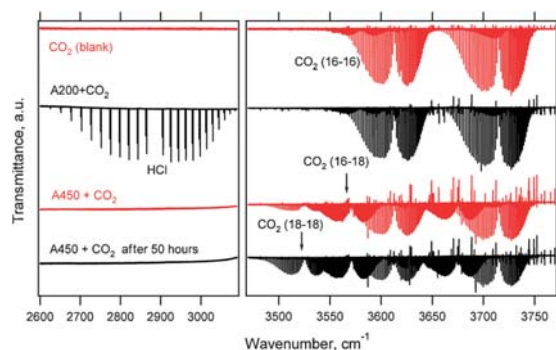
This journal is © the Owner Societies 2011

**Fig. 2** FTIR spectra of the gas-phase. [CO$_2$ (blank)]: reference spectrum of the starting C$^{16}$O$_2$; [A200 + CO$_2$]: spectrum of this gas phase after *ca.* 30 min contact with Ti$^{18}$O$_2$, sample A200; [A450 + CO$_2$]: spectrum of this gas phase immediately after contact with Ti$^{18}$O$_2$, sample A450; [A450 + CO$_2$ after 50 hours]: spectrum of this gas phase after 50 hours of contact with Ti$^{18}$O$_2$ at 30 °C, sample A450. Spectra are offset for clarity, but the transmittance scale is identical. The assignment of characteristic bands is marked by arrows.

The sample A450 exhibited strikingly different behavior from that of A200. If a freshly vacuum-calcined sample, A450, contacted CO$_2$, the isotope exchange started immediately (Fig. 2, third curve from top) producing mostly C$^{16}$O$^{18}$O. No HCl was found in the gas phase even after 50 hours of contact (Fig 2), indicating its complete removal from the titania surface by calcination at 450 °C in vacuum (see S1, ESI†). The isotope exchange progressed in this time scale as shown in Fig. 2 (bottom curve). To highlight the isotope-specific effects for the A450 + CO$_2$ interaction, only small part of the spectrum was zoomed in Fig. 3.
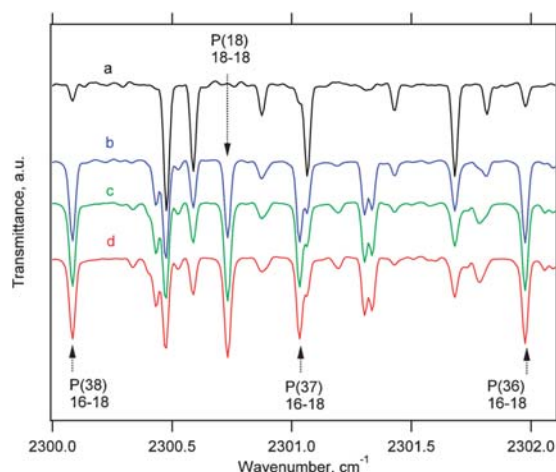


**Fig. 3** Details of FTIR spectra of the gas-phase showing several rotation–vibration lines of the $\nu_3$ band of carbon dioxide. (a) Reference spectrum of the starting C$^{16}$O$_2$; (b) spectrum of this gas phase immediately after contact with Ti$^{18}$O$_2$ powder (A450); (c) spectrum of this gas phase after 15 hours of contact with Ti$^{18}$O$_2$ powder at 30 °C; (d) spectrum of this gas phase after 50 hours of contact with Ti$^{18}$O$_2$ powder at 30 °C. Spectra are offset for clarity, but the transmittance scale is identical. The assignment of characteristic spectral lines is marked by arrows.

The concentrations of isotopologues were determined from the intensities of these diagnostic rotation–vibration lines. During the initial *ca.* 20 min of interaction, there was a marked decrease of the 16–16 isotopologue, with the corresponding increase of the 18–18 isotopologue. The 16–18 isotopologue acted as an intermediate: its concentration increased abruptly when the reaction started, but then remained almost constant (see Fig. 1-S3, ESI†).

The oxygen-exchange activity of vacuum-annealed Ti$^{18}$O$_2$ (sample A450) towards C$^{16}$O$_2$ stems obviously from lattice-oxygen vacancy and the corresponding Ti$^{4+}$/Ti$^{3+}$ exchange.[6] The surface vacancies in titania lattice act as traps for C$^{16}$O$_2$ molecules, and are thus filled by $^{16}$O. The anchored carbon dioxide molecules may behave like 'truly' adsorbed CO$_2$, that is the Ti–O–C–O structure, but the majority of surface complexes mimic a carbonate anion, (Ti–O–CO–O–), in four different configurations: bridging, bidentate, monodentate or free.[6] This can be schematically depicted as follows:

$$C^{16}O_2 + -\square-Ti-^{18}O- \rightarrow Ti\cdots CO_3, \square \text{ is vacancy} \quad (3)$$

Apart from its complicated structure, the surface complex may decompose towards C$^{16}$O$^{18}$O which is evolved into the gas phase. This molecule can further react on the Ti$^{18}$O$_2$ surface to give C$^{18}$O$_2$ in the next step. No CO was detected in the products of reaction (3) in dark. (Carbon monoxide, solely the C$^{16}$O isotopologue, was, however, generated upon UV-excitation of the A200 sample.)[7] The crucial role of surface activation (*cf.* eqn (3)) is confirmed if we compare the behavior of A450 and A200. The latter sample shows no oxygen isotope scrambling because the surface of A200 is blocked by the adsorbed HCl and water molecules. Surface hydroxyls, –$^{18}$OH (which obviously occur on A200 but not on *in-situ* calcined A450; see S1, ESI†), have negligible effect for the C$^{16}$O$_2$/ Ti$^{18}$O$_2$ isotope exchange, compared to the effect of heat-treatment activation (*cf.* eqn (3)). This conclusion is reminiscent of the report by Sato *et al.*[10] who found highly enhanced activity of calcined Ti$^{16}$O$_2$ for the photocatalytic exchange with $^{18}$O$_2$.

In summary, we synthesized pure Ti$^{18}$O$_2$ both in anatase and rutile forms. Raman spectra together with quantum chemical modeling indicated different isotope shifts ($^{18}$O/$^{16}$O) for the known vibration modes of anatase and rutile. The interaction with carbon dioxide was investigated with the aim to explore oxygen isotope exchange at the Ti$^{18}$O$_2$/C$^{16}$O$_2$ interface. To this purpose, high-resolution Fourier transform infrared spectroscopy of the gas phase turned to be a powerful analytical technique.

## Acknowledgements

P63

## Notes and references

1 X. Chen and S. S. Mao, *Chem. Rev.*, 2007, **107**, 2891.
2 H. Cheng, J. Ma, Z. Zhao and L. Qi, *Chem. Mater.*, 1995, **7**, 663.
3 U. Diebold, *Surf. Sci. Rep.*, 2003, **48**, 5.
4 M. Giarola, A. Samson, F. Monti and G. Mariotto, *Phys. Rev. B: Condens. Matter*, 2010, **81**, 174305.
5 V. P. Indrakanti, J. D. Kubicki and H. H. Schobert, *Energy Environ. Sci.*, 2009, **2**, 745.
6 L. F. Liao, C. F. Lien, D. L. Shieh, M. T. Chen and J. L. Lin, *J. Phys. Chem. B*, 2002, **106**, 11240.
7 S. Civis, M. Ferus, P. Kubat, M. Zukalova and L. Kavan, *J. Phys. Chem. C*, 2011, DOI: 10.1021/jp201935e.
8 J. Novakova, *Catal. Rev.*, 1970, **4**, 77.
9 P. Pichat, H. Courbon, R. Enriquez, T. T. Y. Tan and R. Amal, *Res. Chem. Intermed.*, 2007, **33**, 239.
10 S. Sato, T. Kadowaki and K. Yamaguti, *J. Phys. Chem.*, 1984, **88**, 2930.
11 V. Swamy, *Phys. Rev. B: Condens. Matter*, 2008, **77**, 195414.
12 H. G. Yang, C. H. Sun, S. Z. Qiao, J. Zou, G. Liu, S. C. Smith, H. M. Cheng and G. Q. Lu, *Nature*, 2008, **453**, 638.

11586 | *Phys. Chem. Chem. Phys.*, 2011, **13**, 11583–11586

This journal is © the Owner Societies 2011

P64

# Oxygen-Isotope Exchange between $CO_2$ and Solid $Ti^{18}O_2$

Svatopluk Civiš,*,[†] Martin Ferus,[†,‡] Pavel Kubát,[†] Markéta Zukalová,[†] and Ladislav Kavan[†]

[†]J. Heyrovský Institute of Physical Chemistry, v.v.i, Academy of Sciences of the Czech Republic, Dolejškova 3, 182 23 Prague 8, Czech Republic

[‡]Institute of Physics, v.v.i., Academy of Sciences of the Czech Republic, Na Slovance 2, 182 21 Prague 8, Czech Republic

Ⓢ *Supporting Information*

**ABSTRACT:** The light—induced oxygen-isotope exchange between gaseous $CO_2$ and solid $Ti^{18}O_2$ (anatase) and the spontaneous thermal isotope exchange that takes place between the vacuum-calcined solid $Ti^{18}O_2$ and $CO_2$ were studied by gas-phase high-resolution Fourier transform infrared absorption spectroscopy over a period of several days. The absorption ro-vibrational spectra of all the measured carbon dioxide isotopologues were assigned and served as the quantification of the time-dependent isotope exchange between the oxygen atoms from the $Ti^{18}O_2$ solid and the oxygen related to the gaseous $CO_2$. The $C^{18}O_2$ was formed as the dominating final product with a minor content of $C^{16}O^{18}O$. The rate of oxygen-isotope exchange is highly sensitive to the conditions of the titania pretreatment; vacuum-annealed $Ti^{18}O_2$ at 450 °C exhibited a very high spontaneous oxygen exchange activity with gaseous $C^{16}O_2$. A mechanism for the $^{18}O/^{16}O$ exchange process is discussed at the molecular level. The photocatalytic formation of methane, acetylene, and $C^{16}O$ released from the $Ti^{18}O_2$ surface was observed after irradiation by an excimer laser.
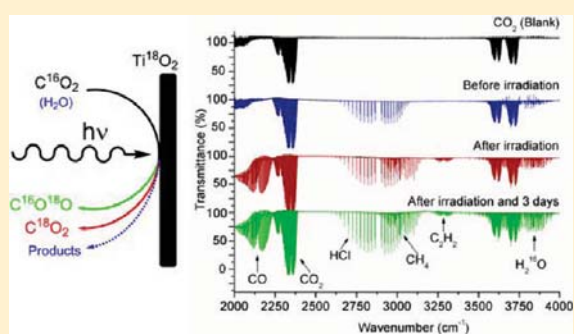
## 1. INTRODUCTION

Titanium dioxide has attracted considerable interest due to its numerous applications in photocatalysis, solar cells, gas sensors, Li-ion batteries, electrochromics, and catalysis.[1,2] These applications require a detailed understanding of the surface science of solid titania (for a review, see ref 3). Chemical processes on the titania surface, both thermally and photochemically activated, can be conveniently followed by oxygen isotope labeling. These reactions have been carefully studied since the middle of the last century.[4−6] The traditional approach is based on the use of "ordinary" $Ti^{16}O_2$ exposed to gaseous reactants, which comprise various $^{18}O$-isotope-labeled molecules, such as $H_2^{18}O$ or $^{18}O_2$, and their corresponding $^{16}O$-isotope counterparts. The isotope exchange (e.g., between $^{18}O_2(g)$ and $^{16}O_2(g)$) may or may not involve the replacement of the lattice oxygen ($^{16}O$) in titania by $^{18}O$. In particular, the reactions of $H_2^{18}O$ on photoexcited titania led to the fundamental questions that are relevant to photocatalysis.[7] This approach is smoothly extendable to photoassisted isotopic exchange reactions involving other molecules, such as gaseous oxygen,[6] formic acid,[8,9] alcohols,[10] carbon monoxide, carbon dioxide,[9,11−13] and carbonates.[9]

A variant of the strategy of employing "ordinary" $Ti^{16}O_2$ for the isotope exchange is the use of titania with a deliberately $^{18}O$-enriched surface. This material can be prepared by simply exposing $Ti^{16}O_2$ to $^{18}O_2$ at 750 K[14] or to $H_2^{18}O$ with simultaneous UV irradiation[10] or by electrochemical oxidation in an $^{18}O$-containing electrolyte solution.[8] In all these cases, the isotope exchange $Ti^{16}O_2/Ti^{18}O_2$ is restricted to the surface layers only and is hardly perfect in these products. For instance, the thermal reaction with oxygen gas provides an $^{18}O$-enriched surface of titania with an $^{18}O/^{16}O$ ratio of 2.5 (ref 14). Reports on the isotopically pure solid $Ti^{18}O_2$ are surprisingly scarce in the literature. To the best of our knowledge, there is only one paper that discusses the transformation of titanium nitride TiN to $TiO_2$ in oxygen ($^{18}O_2$) plasma.[15] Although this reaction, in principle, could lead to a pure solid $Ti^{18}O_2$, the product was not characterized in the report.[15] It is obvious that this material would lead to the reconsideration of classical studies on the isotopic exchange of $^{18}O$ on the gas/solid oxide interface.[5] In particular, the release of lattice oxygen and its transfer to the surrounding molecules can be studied on a clean system, in which solely the solid oxide is isotopically labeled. The investigation of adsorption, catalytic, and photocatalytic processes in the "reverse direction", that is, from the $^{18}O$-labeled oxide toward the gaseous molecules at the interface, could lead to novel input in this old,[4,5] yet enduring,[6,7,10] story.

In this study, the oxygen isotope $^{16}O/^{18}O$ exchange between gaseous $C^{16}O_2$ and solid $Ti^{18}O_2$ was explored. Although there have been several earlier studies focused on isotope exchange reactions involving carbon dioxide, the reactions have been

studied either on the $C^{18}O_2/Ti^{16}O_2$ system[13] or on a complicated gaseous mixture containing $C^{16}O_2$, $^{18}O_2$ or $H_2^{18}O$, and ordinary $Ti^{16}O_2$.[9,11] Recently, stoichiometrically pure $Ti^{18}O_2$ was synthesized. The samples showed Raman spectra of the pure $Ti^{18}O_2$ isotopologue,[16] and its interaction with $CO_2$ in the dark was explored. However, to the best of our knowledge, the reaction of $CO_2$ with photoexcited $Ti^{18}O_2$ is presented here for the first time. Carbon dioxide offers several advantages as the target molecule for these studies: (i) the isotope exchange can be readily followed by high-resolution FTIR; (ii) it is the final product of the photocatalytic oxidation of organic molecules; (iii) the adsorption mechanism and surface chemistry of $CO_2$ are known in detail;[17] and (iv) photoinduced reactions on the $TiO_2$ surface are of prospective environmental impact for $CO_2$ removal from the atmosphere and its conversion to fuels.[18]

This study has as its primary goal the determination of the time scale of the spontaneous and light-induced isotope exchange between carbon dioxide and solid $TiO_2$. In addition to affirming that the spontaneous reaction cannot compete with the UV laser-induced rapid processes, the spontaneous process is quantified by evaluating its absorption ro-vibrational spectra, and the corresponding reaction mechanism is described.

## 2. EXPERIMENTAL SECTION

**2.1. Materials.** Methane, acetylene, and $CO_2$ (all Linde Technogas, Czech Republic) were used as received. The synthesis of $Ti^{18}O_2$ was described in a previous paper.[16] Briefly, $Ti^{18}O_2$ was prepared in a closed all-glass vacuum apparatus from titanium tetrachloride (99.98%, Aldrich) and $H_2^{18}O$ (Cambridge Isotope Laboratories, 97% of $^{18}O$). The HCl produced was collected in a side ampule cooled by liquid nitrogen. Subsequently, the solid product was heated at 200 °C overnight in the still-closed vacuum apparatus, while the HCl trap remained in the liquid nitrogen cooling bath. Finally, the apparatus was opened in a glovebox under Ar, and the solid white powder was collected. This product is subsequently abbreviated as A200. The material was stored under Ar at room temperature. In the next synthetic step, part of the A200 powder was heated at 450 °C in a vacuum ($10^{-5}$ Pa) for 30 h. This material is subsequently abbreviated as A450.

Both samples were characterized by Raman spectroscopy on a LabRam HR spectrometer (Horiba Jobin Yvon) interfaced to an Olympus BX41 microscope and by X-ray diffraction (Bruker D8 Advance diffractometer, Cu Kα radiation). It exhibited the pattern of pure anatase (data not shown).[16] BET (Brunauer–Emmett–Teller measurement of the specific surface area of a material) surface areas were calculated from the $N_2$ adsorption isotherms (Micromeritics ASAP 2020 instrument). The samples were degassed at 400 °C in the vacuum prior to measurement. The BET surface area was found to be 31 $m^2$/g, independent of the synthetic history (A200/A450).

**2.2. Methods.** FTIR spectra were measured in a 20 cm long (2.5 cm diameter) glass optical cell equipped with $CaF_2$ windows. The cell was interfaced to a sealable glass-tube joint for the transference of the powder material under vacuum from a side ampule, in which the calcination of $TiO_2$ also took place.[19] The optical cell was further equipped with a second vacuum valve (ACE glass, USA) for the gas handling and connection to the vacuum line. The optical cell containing 0.8 g of $Ti^{18}O_2$ in the powder form spread over the walls was filled with $CO_2$. The pressure in the measuring cell was approximately 2 Torr, but it was precisely measured with a MKS Baratron pressure gauge (0–10 Torr).
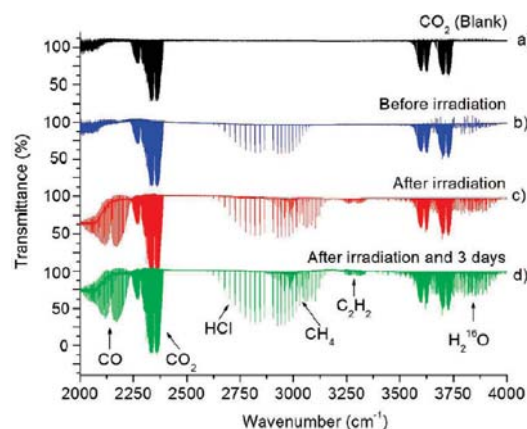


**Figure 1.** Comparison of the $CO_2$ FTIR spectrum (a) with the spectrum of the gas phase in the mixture of $Ti^{18}O_2$ (sample A200) and $CO_2$ before irradiation (b), after the irradiation with 4500 pulses of the XeCl laser (308 nm; pulse width, 28 ns; energy, 180 mJ) (c), and after irradiation and 75 h in the dark at 30 °C (d). Spectra are offset.

The spectral measurement was performed using the Bruker IFS 120 HR spectrometer ($CaF_2$ beam splitter, InSb detector) in a spectral range of 1800–6000 $cm^{-1}$. The spectra were measured in the gas phase with a resolution of 0.01 $cm^{-1}$ with 30 scans using the Blackmann–Harris apodization function. The optical cell was left in the dark inside a thermostat at a temperature of 30 ± 0.1 °C for several days, after which the high-resolution infrared spectra were acquired.

For photochemical experiments, a XeCl excimer laser (308 nm, COMPEX 200, Lambda Physik, Germany) and UV light source lamp (340 nm, Omnilux) were used for the irradiation of the powdered $TiO_2$ material. In the case of the pulse XeCl laser, the nonfocused beam (180 mJ/pulse, 28 ns pulse length) was collimated through the $CaF_2$ inlet window directly onto the $TiO_2$ surface. The 160 W UV lamp source was set vertically (20 cm) to the sample cell, and the $TiO_2$ surface was irradiated through the glass body of the cell (transparency of approximately 70%).

## 3. RESULTS AND DISCUSSION

**3.1. Chemistry of $CO_2$ at the $Ti^{18}O_2$ Surface (Sample A200).** The dark and photoinduced oxygen isotope exchange between $Ti^{18}O_2$ calcined in a vacuum at 200 °C (sample A200) and $CO_2$ was complicated by other processes.

The obtained spectrum of the gas phase over A200 containing 2 Torr of $CO_2$ is shown in Figure 1, curve b, in addition to the reference spectrum of carbon dioxide in a $TiO_2$-free optical cell (Figure 1, curve a). A ro-vibrational band of HCl was detected in the 2800–3000 $cm^{-1}$ spectral region, and a small quantity of water (mostly $H_2^{16}O$) is apparent by the band at 3600–3800 $cm^{-1}$ (Figure 1, curve b).[16]

Hydrogen chloride is an obvious impurity in the A200 sample resulting from its synthesis by the reaction of $TiCl_4$ with $H_2^{18}O$ (see the Experimental Section). The calcination at 200 °C in a closed apparatus does not quantitatively remove it from the final product. The adsorbed HCl is released from A200 into the gas phase in the optical cell (Figure 1, curve b).

For stimulation of physical/chemical processes on the $TiO_2$ surface (e.g., isotope exchange), high-energy UV irradiation for
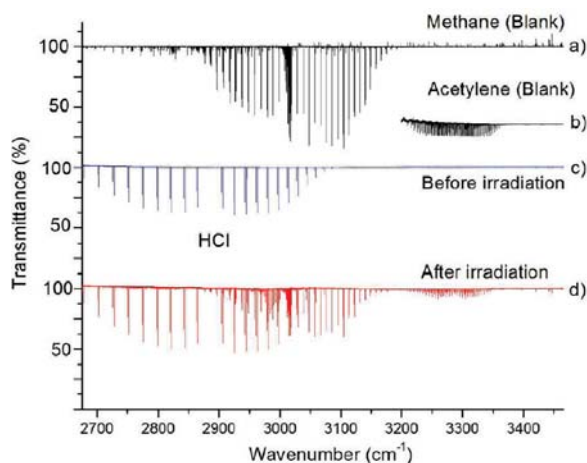
**Figure 2.** Reference FTIR spectra of methane (a) and acetylene (b) compared with the spectra of the gas phase in the mixture of $Ti^{18}O_2$ (sample A200) and $CO_2$ before irradiation (c) and the sample after irradiation with 4500 pulses from the XeCl laser (308 nm; pulse width, 28 ns; energy, 180 mJ) (d).
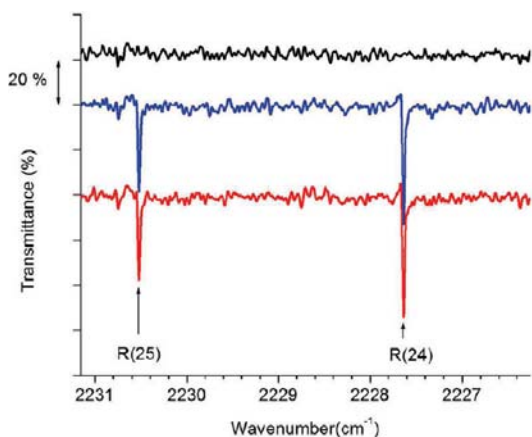


**Figure 3.** Two selected ro-vibrational lines of $C^{16}O$ in the spectrum before the $Ti^{18}O_2$ (A200) irradiation (black line), after the irradiation with 4500 pulses from the XeCl laser, and after irradiation and 75 h in the dark (red line). Spectra are offset.

$TiO_2$ band-gap excitation was used. Upon UV photoexcitation, the desorption of HCl progressed (Figure 1, curve c), and the formation of additional products was observed. In the actual experiment, the surface of A200 was irradiated with 4500 pulses of the XeCl laser (308 nm, energy of 180 mJ), which were focused by a quartz lens directly onto the A200 surface through the calcium fluoride window of the optical cell. After the irradiation of the A200 surface, ro-vibrational bands of methane and acetylene were found (Figures 1 and 2, curve d), together with bands of CO in the region of 2050—2200 $cm^{-1}$ (Figure 1, curves c and d). The assignment of ro-vibrational lines of methane and acetylene was supported by the measurement of the reference pure molecules (Figure 2, spectra a and b). The concentration of $H_2O$ increased during the UV-laser treatment (Figure 1, curve c). All the main ro-vibrational lines belong to the $H_2^{16}O$ isotopologue.
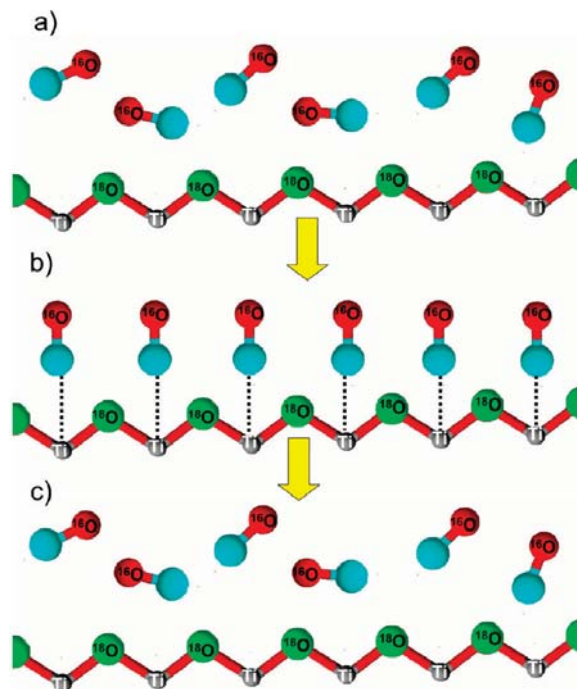


**Figure 4.** Diagram of the oxygen isotope exchange between the surface of crystalline $Ti^{18}O_2$ and carbon monoxide. CO binds directly with the titanium atom. After laser irradiation or thermal exposure at low pressure, this complex breaks down into $C^{16}O$.

The lines of $H_2^{18}O$ appeared only in their natural isotopic abundance; that is, no exchange of oxygen atoms $^{18}O$ from the solid phase $Ti^{18}O_2$ took place.

Both hydrocarbons $CH_4$ and $C_2H_2$ were formed by photocatalytic conversion of $CO_2$ and water or HCl on the surface of $Ti^{18}O_2$ irradiated by the XeCl excimer laser. After UV irradiation, the still closed optical cell was stored at a temperature of 30 °C in the dark, and the spectra were measured after 50 and 75 h of storage. The concentration of CO (Figure 1, curve d and Figure 3) and hydrocarbons remained constant after 75 h in the dark; that is, the formation of these products did not proceed.

Similar to $H_2O$, absorption lines of the $C^{16}O$ isotopologue only were found; that is, the labeled carbon monoxide, $C^{18}O$, was not generated. Obviously, $^{16}O$ can originate only from $CO_2$ because there was no other source of this isotope in this closed system.

Because $CO_2$ does not absorb UV radiation of wavelengths larger than 200 nm, another mechanism of $C^{16}O$ formation includes two-photon photolysis of $C^{16}O_2$ by the XeCl excimer laser. This mechanism is supported by experiments where the irradiation by a low-intensity UV lamp (340 nm, 160 W) did not lead to the formation of CO (Figure S1 in the Supporting Information).

CO adsorption on anatase and rutile $TiO_2$ has been studied previously.[20] The observed infrared bands (2192 and 2209 $cm^{-1}$) were assigned to the adsorbed CO bound to the $Ti^{4+}$ ions with a binding energy of 17 kcal/mol.[21] The direct binding of CO to the metal atom explains that the isotope exchange does not take
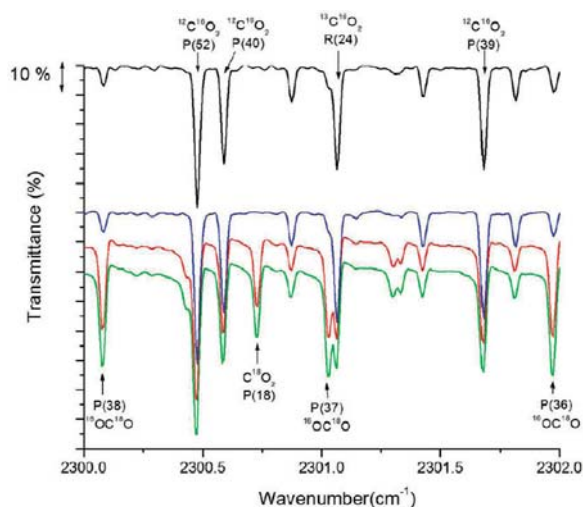
**Figure 5.** Several ro-vibrational lines of the $\nu_3$ band of $CO_2$ (2 Torr) over the $Ti^{18}O_2$ surface in the spectral range of $2300-2302$ cm$^{-1}$ measured immediately after filling the cell (blue line), after irradiation by the XeCl laser (red line), and after irradiation and 75 h in the dark (green line) together with the reference spectrum of $C^{16}O_2$ (black line). Spectra are offset.

**Table 1. Oxygen-Isotope Exchange in $CO_2$ on $Ti^{18}O_2$ Induced by the XeCl Laser and Followed by the Spontaneous Process[b]**

| sample | time (h) | partial pressures (Torr) | | | note |
|---|---|---|---|---|---|
| | | $CO_2$ (16-16) | $CO_2$ (16-18) | $CO_2$ (18-18) | |
| A200 | 0 | $2.26^a$ | $0.009^a$ | $8.25 \times 10^{-6a}$ | before irradiation |
| | 1 | 3.07 | 0.027 | 0.148 | 4500 pulses |
| | 50 | 3.80 | 0.031 | 0.168 | spontaneous |
| | 75 | 3.90 | 0.032 | 0.169 | spontaneous |
| A450 | 0 | 2.250 | 0.031 | 0.097 | before irradiation |
| | 1 | 2.100 | 0.044 | 0.240 | 4500 pulses |
| | 15 | 1.990 | 0.052 | 0.330 | spontaneous |
| | 72 | 1.980 | 0.053 | 0.340 | spontaneous |

$^a$ Natural abundance. $^b$ Concentrations of $^{16}O-C-^{16}O$, $^{18}O-C-^{16}O$, and $^{18}O-C-^{18}O$ isotopologues determined from the calibration curves for selected ro-vibrational lines (Table 2).

place between the oxygen in the carbon monoxide molecule and the oxygen in the structure of $Ti^{18}O_2$ (Figure 4).

**3.2. Oxygen-Isotope Exchange between $CO_2$ and $Ti^{18}O_2$ (Sample A200).** Oxygen-isotope exchange was observed in the $\nu_3$ region of the spectral band, where the absorption lines of all three isotopologues ($^{16}O-C-^{16}O$, $^{18}O-C-^{16}O$, $^{18}O-C-^{18}O$) can be found.[22] Figure 5 shows a selected part of the relevant spectra. The reference spectrum of $^{16}O-C-^{16}O$ (black) confirms the presence of the ro-vibrational transitions of individual isotopologues of $CO_2$ in natural abundance. In the $CO_2$-containing gas phase over the nonirradiated titania sample A200, no additional lines corresponding to the individual transitions of the $^{18}O-C-^{16}O$ and $^{18}O-C-^{18}O$ molecules were found (Figure 5, blue curve), and the resulting spectrum fully corresponds to the spectrum of the pure $C^{16}O_2$ with a natural abundance of $C^{18}O_2$.

**Table 2. Wavenumbers of the Ro-Vibrational Transitions of $\nu_3$ Bands of $^{16}O-C-^{16}O$, $^{18}O-C-^{16}O$, and $^{18}O-C-^{18}O$ Isotopologues Used for Spectroscopic Quantification**

| wavenumber (cm$^{-1}$) | isotopologue $CO_2$ | assignment |
|---|---|---|
| 2321.134 | 16-16 | P(32) |
| 2337.658 | 16-16 | P(14) |
| 2332.369 | 16-16 | P(20) |
| 2315.436 | 16-18 | P(21) |
| 2311.972 | 16-18 | P(25) |
| 2327.351 | 18-18 | R(20) |
| 2326.188 | 18-18 | R(18) |

After irradiation with 4500 pulses of the excimer laser (Figure 5, red curve), the $^{18}O-C-^{16}O$ line grew in intensity, and a new line assigned to the $^{18}O-C-^{18}O$ isotopologue appeared in the spectrum of the gaseous phase over the A200 sample. The concentration of both isotopologues increased with time when the sample was stored in the dark (Figure 5, green curve; Table 1). The individual lines in the spectra were fitted and quantified. The quantification of the spectra was based on the calibration measurements of the absorption spectra of individual isotopologues (reference gases) of $CO_2$ at different pressures. Thus, the calculated concentrations of individual isotopologues (Table 1) determined from the intensity profiles of the individual ro-vibrational lines (Table 2) showed an incremental jump of the $^{16}O-C-^{18}O$ and $^{18}O-C-^8O$ concentrations after the laser irradiation. An increase of the $^{16}O-C-^{16}O$ isotopologue can correspond to its adsorption on the $Ti^{18}O_2$ surface before irradiation. Irradiation of the A200 induced release of the adsorbed $^{16}O-C-^{16}O$ that led to an increase of its concentration in the gas phase.

The oxygen atoms of $CO_2$ each have a lone pair of electrons and can donate these electrons to Lewis acid centers in the surface. The carbon atom could also gain electrons from Lewis base centers, such as oxide ions, forming stable carbonate-like species that could prevent desorption of $CO_2$ from the titania surface. Formation of this complex can be the reason that the slow desorption process progressing several hours after irradiation in the dark (Table 1). Additionally, the $\pi$ electrons of $C-O$ bonds can also participate in reactions with Lewis base centers. To a large extent, the processes of isotope exchange and the adsorption of $CO_2$ are influenced by the presence of water and OH groups on the surface of $TiO_2$.[23] The release of water can be explained either by simple desorption or by the breakdown of the carbonic acid bonded to the surface of $TiO_2$ (eq 1):

$$H_2CO_3 \rightarrow CO_2 + H_2O \quad (1)$$
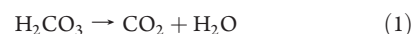
Similar to the beginning of the experiment, $H_2{}^{18}O$ is adsorbed on the surface of $Ti^{18}O_2$, and the carbonic acid is composed of a mixture of $^{16}O$ and $^{18}O$. The increased concentration of $H_2{}^{16}O$ in the gas phase above the $TiO_2$ surface after 75 h is traceable by comparing curves c and d in Figure 1. It can be explained by the breakdown of the carbonate complex and the spontaneous isotope exchange reaction taking place in the dark (eq 2):[23,24]

$$H_2{}^{18}O + {}^{16}O-C-{}^{16}O \rightarrow {}^{16}O-C-{}^{18}O + H_2{}^{16}O \quad (2)$$
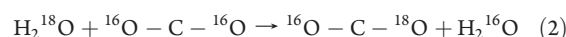
This isotope exchange reaction can influence the enrichment of $CO_2$ with the oxygen isotope $^{18}O$.
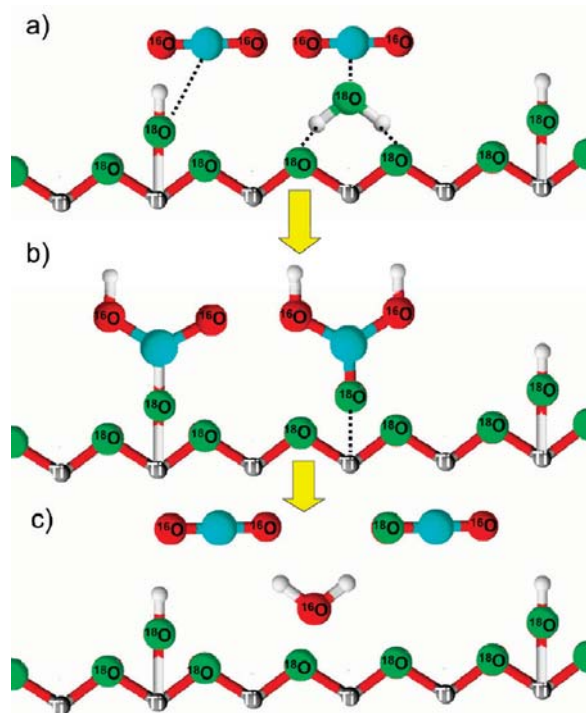
**Figure 6.** Diagram of the isotope exchange on the surface of crystalline Ti$^{18}$O$_2$. The surface layer is composed of Ti$^{4+}$ onto which the $^{18}$OH groups and H$_2$$^{18}$O are bonded. The gaseous CO$_2$ reacts with the water and OH groups, creating a hydrogen and dihydrogen complex bonded onto the Ti atoms. This complex breaks down after the laser irradiation, or thermally at low pressure, into molecules of H$_2$$^{16}$O, $^{16}$O$-$C$-$$^{16}$O, and partially into $^{16}$O$-$C$-$$^{18}$O.



**Figure 7.** Several ro-vibrational lines of the $\nu_3$ band of CO$_2$ (2 Torr) over the Ti$^{18}$O$_2$ surface (A450) in the spectral range of 2300$-$2302 cm$^{-1}$ measured immediately after filling the cell (blue line), after 15 h (red line), and after 50 h (green line) together with the reference spectrum of C$^{16}$O$_2$ (black line). Spectra are offset.



**Figure 8.** Conversion curves: oxygen isotope exchange between CO$_2$ and vacuum-annealed Ti$^{18}$O$_2$ (A450). Concentrations of $^{16}$O$-$C$-$$^{16}$O (black line), $^{18}$O$-$C$-$$^{16}$O (green line), and $^{18}$O$-$C$-$$^{18}$O (red line) isotopologues were estimated from the calibration curves for selected ro-vibrational lines (Table 2).

The spontaneous exchange of the oxygen isotopes in the CO$_2$ and H$_2$O mixtures has been studied in aqueous solutions in a series of earlier publications. In 1940, Mills and Urey[21] performed measurements for several pH values from acidic through mildly alkaline media (leading to the prevalence of bicarbonate ions), up to very alkaline environments. They proved that the oxygen exchange in acidic and mildly alkaline solutions occurs through the formation of carbonic acid by the simple hydration of CO$_2$. The mechanism of the oxygen exchange between carbon dioxide and water following atmospheric sampling using glass flasks was explained in refs 25 and 26. The oxygen-isotope exchange between CO$_2$ and water adsorbed on Al$_2$O$_3$ or Fe$_2$O$_3$ was studied by Baltrusaitis et al.[23] The rate constants of the spontaneous exchange in the solution were strongly temperature-dependent.

In summary, the sample A200 showed low oxygen exchange activity between CO$_2$ and Ti$^{18}$O$_2$. The mechanism of possible processes taking place on the surface of TiO$_2$ is shown in Figure 6.

### 3.3. Oxygen-Isotope Exchange between CO$_2$ with Ti$^{18}$O$_2$ (Sample A450).
The sample A200 was heated to 450 °C in vacuum (sample A450) to remove HCl and water from Ti$^{18}$O$_2$. The isotopic exchange between CO$_2$ and Ti$^{18}$O$_2$ was monitored by observation of the fundamental $\nu_3$ band of CO$_2$ at approximately 2300 cm$^{-1}$. For the sake of easy comparison, Figure 7 (black curve) depicts a part of the reference spectrum of CO$_2$ (as

in Figure 5). The FTIR spectrum measured immediately after mixing both components (Figure 7, blue line) shows that the oxygen exchange between the surface of Ti$^{18}$O$_2$ (sample A450) and CO$_2$ molecules is a very fast process. The obtained spectrum presents the ro-vibrational lines of $^{16}$O$-$C$-$$^{18}$O with the lines of $^{18}$O$-$C$-$$^{18}$O. The profiles of the individual lines of selected isotopologues (isolated lines in the spectrum) were fitted and quantified similarly to the A200 sample. The concentrations of individual isotopologues are characterized by the decrease in the $^{16}$O$-$C$-$$^{16}$O isotopologue and the increase in the $^{18}$O$-$C$-$$^{18}$O isotopologue (Figure 8). The $^{18}$O$-$C$-$$^{16}$O acts as an intermediate in the mixture, and its concentration remains quite low and almost constant.

Liao et al.[9] studied the infrared spectra of TiO$_2$ after the interaction of the TiO$_2$ surface with 0.1 Torr of CO$_2$. Several absorption bands appeared in the spectrum at 1319 and 1579 cm$^{-1}$,

**Figure 9.** Schematic diagram of the spontaneous isotope exchange on the surface of crystalline $Ti^{18}O_2$. The white square means a vacancy in the solid A450 $Ti^{18}O_2$.



**Figure 10.** Conversion curves: isotopic exchange on the surface of A450 $Ti^{18}O_2$ (passivated 15 min with 11 Torr of $H_2^{16}O$ water vapor). Panel A: fresh sample. Panel B: sample refilled with fresh $CO_2$ after 80 h. Panel C: sample refilled with fresh $CO_2$ after 160 h. The black, green, and red lines and symbols correspond to $^{16}O-C-^{16}O$, $^{18}O-C-^{16}O$, and $^{18}O-C-^{18}O$ isotopologues, respectively.

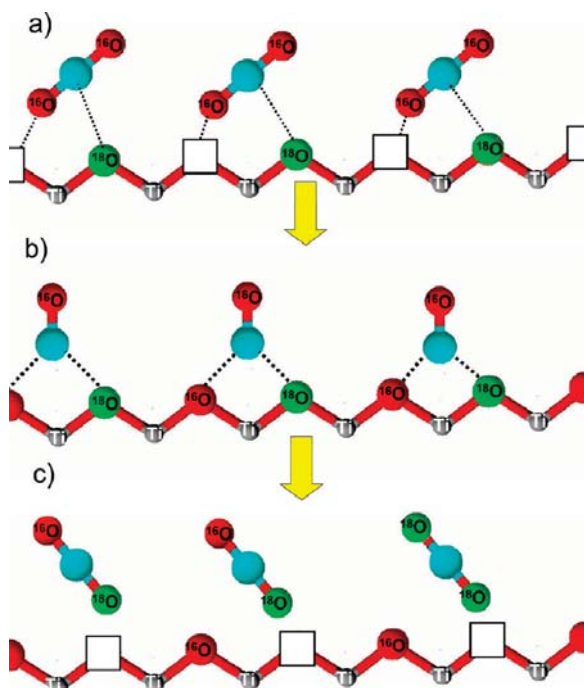which were attributed to bidentate-bonded carbonate. On the basis of the spectral intensity and the isotopic exchange measurements, the data were in good agreement with the proposal of the formation of the bidentate-bonded carbonate as the major species for $CO_3$ on $TiO_2$. Figure 9 schematically shows the formation of bidentate $CO_3$ from $CO_2$ adsorption on the $Ti^{18}O_2$ surface sites involved and the consecutive thermal isotopic exchange of the surface-oxygen atoms $^{18}O$ of $Ti^{18}O_2$ and molecules of $C^{16}O_2$.

The surface layer of our vacuum outgased sample (A450) is composed of a nonstoichiometric mixture of $Ti^{4+}$ and $Ti^{3+}$, on which the $^{18}O$ oxygen atoms are bound. The calcination under vacuum creates vacancies (white squares). During the isotope exchange, (a) the $^{16}O$ oxygen from the gaseous $^{16}O-C-^{16}O$ bonds to the vacancy on the surface of the $TiO_2$ crystal, (b) bidentate $CO_3$ from the $CO_2$ adsorption is formed, and (c) the $^{18}O$ oxygen from the surface layer bonds to the carbon dioxide molecule, subsequently releasing gaseous $^{16}O-C-^{18}O$.

**3.4. Oxygen-Isotope Exchange between $CO_2$ with $Ti^{18}O_2$ Treated with $H_2^{16}O$ (Sample A450/$H_2^{16}O$).** Because $CO_2$ molecules could compete for adsorption sites with water,[27] the A450 material was treated with $H_2^{16}O$ (11 Torr) for approximately 15 min at laboratory temperature to suppress fast spontaneous isotope exchange between $CO_2$ and $Ti^{18}O_2$. The cell was evacuated and then filled with 2 Torr of $CO_2$. However, the rate of oxygen isotope exchange in this material and the major production of $C^{18}O_2$ (Figure 10A) was similar in comparison with the behavior of material that was not treated with water (Figure 8). These results show that adsorbed water does not block $CO_2$ adsorption sites. The A450 material retained the oxygen isotope exchange activity even after 80 h (Figure 10B) and 160 h (Figure 10C) of passivation by 2 Torr of $CO_2$. The rate



**Figure 11.** Spectra of the A450/$H_2^{16}O$ sample before (blue line) and after (red line) excimer laser irradiation together with CO and $CH_4$ reference spectra (black lines).

of oxygen isotope exchange was decreased by the time of passivation (Figure 10, compare panels B and C).

Irradiation of A450/$H_2^{16}O$ by the XeCl laser enhanced the oxygen isotope exchange between $Ti^{18}O_2$ and $CO_2$ similar to A200. Similar to sample A200, methane and $C^{16}O$ were observed as products of the photocatalytic reaction (Figure 11). It is interesting to note that no acetylene is formed on HCl-free titania. The usual product of photocatalytic reduction of $CO_2$ is methane, which is also reproduced here; the formation of acetylene is favored only on specific photocatalysts, such as Cu, Fe-doped $TiO_2$ (see ref 18).

## 4. CONCLUSION

The completely $^{18}$O-isotope-exchanged titanium dioxide, Ti$^{18}$O$_2$ (anatase), was prepared from TiCl$_4$ and H$_2^{18}$O. The as-received material (A200), heat-treated at 200 °C, still contained a considerable amount of adsorbed water and HCl from the synthesis. This HCl was released into an environment composed of 2 Torr of CO$_2$. When the same material was calcined at 450 °C in a high vacuum, pure, HCl-free Ti$^{18}$O$_2$ (A450) was obtained.

Both the Ti$^{18}$O$_2$ materials exhibited spontaneous $^{18}$O-isotope exchange with the surrounding C$^{16}$O$_2$, which was monitored by high-resolution FTIR spectroscopy of the gas phase over the Ti$^{18}$O$_2$ surface. The formation of C$^{18}$O$_2$ with both exchanged oxygen atoms was dominant with a minor content of C$^{16}$O$^{18}$O. The oxygen-isotope exchange activity of A450 was not suppressed by the addition of H$_2^{16}$O. After the irradiation of the Ti$^{18}$O$_2$ surface with the excimer laser, ro-vibrational bands of methane, acetylene, and water were identified in the gaseous phase. The isotope exchange does not take place between the oxygen in the carbon monoxide and water molecules and the oxygen atom from the Ti$^{18}$O$_2$ structure.

The possible processes taking place on the surface of Ti$^{18}$O$_2$ can be summarized as follows: $^{18}$OH groups and H$_2^{18}$O are bound to the surface layer of Ti$^{4+}$. The gaseous carbon dioxide reacts with the water and OH groups, creating a carbonate complex bound to the Ti atoms. This complex breaks down after laser irradiation or following thermal exposure at low pressures, both completely into molecules of H$_2^{16}$O, $^{16}$O−C−$^{16}$O, and partially into $^{16}$O−C−$^{18}$O. On the basis of the spectral intensity and the isotopic exchange measurements, the data are in good agreement with the proposal of the formation of bidentate-bonded carbonate as the major species for CO$_3$ on TiO$_2$. The surface layer of vacuum-annealed Ti$^{18}$O$_2$ is composed of a nonstoichiometric mixture of Ti$^{4+}$ and Ti$^{3+}$, on which the $^{18}$O oxygen atoms are bound. The calcination under vacuum creates vacancies. During the isotope exchange, the $^{16}$O oxygen from the gaseous $^{16}$O−C−$^{16}$O bonds to the vacancy on the surface of the TiO$_2$ crystal, and bidentate CO$_3$ from the CO$_2$ adsorption is formed. The $^{18}$O oxygen from the surface layer is bound to the carbon dioxide molecule, and, subsequently, gaseous $^{16}$O−C−$^{18}$O and $^{18}$O−C−$^{18}$O are released.

## ■ ASSOCIATED CONTENT

**Ⓢ Supporting Information.** FTIR spectra of the gas phase over the irradiated Ti$^{18}$O$_2$. This material is available free of charge via the Internet at http://pubs.acs.org.

## ■ AUTHOR INFORMATION

**Corresponding Author**
*E-mail: civis@jh-inst.cas.cz.

## ■ ACKNOWLEDGMENT

## ■ REFERENCES

(1) Chen, X.; Mao, S. S. *Chem. Rev.* **2007**, *107*, 2891.

(2) Kavan, L. *Adv. Sci. Technol.* **2006**, *51*, 20.

(3) Diebold, U. *Surf. Sci. Rep.* **2003**, *48*, 53.

(4) Winter, E. R. S. *J. Chem. Soc. A* **1968**, 2889.

(5) Novakova, J. *Catal. Rev.* **1970**, *4*, 77.

(6) Pichat, P.; Courbon, H.; Enriquez, R.; Tan, T. T. Y.; Amal, R. *Res. Chem. Intermed.* **2007**, *33*, 239.

(7) Nakamura, R.; Nakato, Y. *J. Am. Chem. Soc.* **2004**, *126*, 1290.

(8) Bogdanoff, P.; Alonsovante, N. *J. Electroanal. Chem.* **1994**, *379*, 415.

(9) Liao, L. F.; Lien, C. F.; Shieh, D. L.; Chen, M. T.; Lin, J. L. *J. Phys. Chem. B* **2002**, *106*, 11240.

(10) Zhang, M.; Wang, Q.; Chen, C. C.; Zang, L.; Ma, W. H.; Zhao, J. C. *Angew. Chem., Int. Ed.* **2009**, *48*, 6081.

(11) Sato, S. *J. Phys. Chem.* **1987**, *91*, 2895.

(12) Kalamaras, C. M.; Panagiotopoulou, P.; Kondarides, D. I.; Efstathiou, A. M. *J. Catal.* **2009**, *264*, 117.

(13) Yanagisawa, Y. *Energy Convers. Manage.* **1995**, *36*, 443.

(14) Henderson, M. A. *J. Phys. Chem.* **1995**, *99*, 15253.

(15) Jimenez, C.; Perriere, J.; Palacio, C.; Enard, J. P.; Albella, J. M. *Thin Solid Films* **1993**, *228*, 247.

(16) Kavan, L.; Civiš, S.; Ferus, M.; Zukalová, M. *Phys. Chem. Chem. Phys.* **2011**; doi: 10.1039/c1cp20775j.

(17) Freund, H. J.; Roberts, M. W. *Surf. Sci. Rep.* **1996**, *25*, 225.

(18) Indrakanti, V. P.; Kubicki, J. D.; Schobert, H. H. *Energy Environ. Sci.* **2009**, *2*, 745.

(19) In certain experiments, the in situ calcination and vacuum transfer of TiO$_2$ were avoided; in this case, the optical cell was loaded with TiO$_2$ in a glovebox under Ar and then evacuated.

(20) Hadjiivanov, K.; Lamotte, J.; Lavalley, J. C. *Langmuir* **1997**, *13*, 3374.

(21) Mills, G. A. *J. Am. Chem. Soc.* **1940**, *62*, 1019.

(22) Rothman, L. S.; Gordon, I. E.; Barbe, A.; Benner, D. C.; Bernath, P. E.; Birk, M.; Boudon, V.; Brown, L. R.; Campargue, A.; Champion, J. P.; Chance, K.; Coudert, L. H.; Dana, V.; Devi, V. M.; Fally, S.; Flaud, J. M.; Gamache, R. R.; Goldman, A.; Jacquemart, D.; Kleiner, I.; Lacome, N.; Lafferty, W. J.; Mandin, J. Y.; Massie, S. T.; Mikhailenko, S. N.; Miller, C. E.; Moazzen-Ahmadi, N.; Naumenko, O. V.; Nikitin, A. V.; Orphal, J.; Perevalov, V. I.; Perrin, A.; Predoi-Cross, A.; Rinsland, C. P.; Rotger, M.; Simeckova, M.; Smith, M. A. H.; Sung, K.; Tashkun, S. A.; Tennyson, J.; Toth, R. A.; Vandaele, A. C.; Vander Auwera, J. *J. Quant. Spectrosc.Radiat. Transfer* **2009**, *110*, 533.

(23) Baltrusaitis, J.; Schuttlefield, J. D.; Zeitler, E.; Jensen, J. H.; Grassian, V. H. *J. Phys. Chem. C* **2007**, *111*, 14870.

(24) Ferus, M.; Matulková, I.; Juha, L.; Civiš, S. *Chem. Phys. Lett.* **2009**, *472*, 14.

(25) Brenninkmeijer, C. A. M.; Janssen, C.; Kaiser, J.; Rockmann, T.; Rhee, T. S.; Assonov, S. S. *Chem. Rev.* **2003**, *103*, 5125.

(26) Gemery, P. A.; Trolier, M.; White, J. W. C. *J. Geophys. Res.* **1996**, *101*, 14415.

(27) Baltrusaitis, J.; Schuttlefield, J.; Zeitler, E.; Grassian, V. H. *Chem. Eng. J.* **2011** in press.

11162

dx.doi.org/10.1021/jp201935e |*J. Phys. Chem. C* 2011, 115, 11156–11162

P71

# Photochemistry and Gas-Phase FTIR Spectroscopy of Formic Acid Interaction with Anatase Ti$^{18}$O$_2$ Nanoparticles

Svatopluk Civiš,* Martin Ferus, Markéta Zukalová, Pavel Kubát, and Ladislav Kavan

J. Heyrovský Institute of Physical Chemistry, v.v.i., Academy of Sciences of the Czech Republic, Dolejškova 3, 18223 Prague 8, Czech Republic

**ABSTRACT:** The photoinduced isotope exchange between $^{18}$O atoms in the lattice of vacuum-calcinated solid Ti$^{18}$O$_2$ and $^{16}$O atoms of formic acid and its photoproducts was studied with gas-phase high-resolution Fourier transform infrared absorption spectroscopy. The rotation–vibration absorption spectra of all products from the photochemical reactions of formic acid were measured over a broad infrared spectral range and used to quantify the time-dependent isotope exchange between the oxygen atoms on solid Ti$^{18}$O$_2$ and the oxygen atoms in gaseous HC$^{16}$O$^{16}$OH and the isotopologues of CO$_2$, CO, and H$_2$O. It was found that formic acid did not exchange oxygen with titania during adsorption and decomposition processes; strongly bonded formate species blocked active sites and thereby inhibited the exchange between CO$_2$ and Ti$^{18}$O$_2$. Similar blocking was observed by adsorbed water. The isotopologues C$^{16}$O$^{18}$O and C$^{18}$O$_2$ are the products of the spontaneous exchange of oxygen atoms in C$^{16}$O$_2$ and the active sites on Ti$^{18}$O$_2$ that are unblocked during the irradiation of the surface by UV photons. The C$^{18}$O molecules are a product of the UV decomposition of C$^{16}$O$^{18}$O or C$^{18}$O$_2$ that is formed during the spontaneous exchange process.
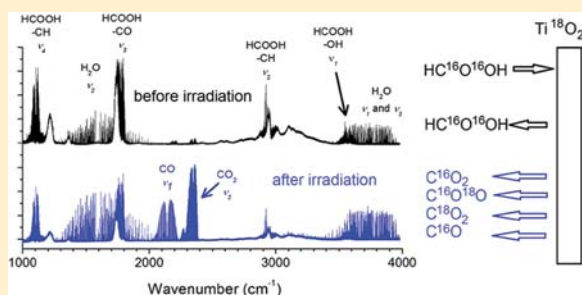
## 1. INTRODUCTION

Formic acid is a model molecule for the investigation of photocatalytic reactions on illuminated titania.[1−3] Furthermore, HCOOH is formed as an intermediate in the photocatalytic oxidation of other molecules such as ethanol, acetic acid, acetaldehyde, and formaldehyde,[4,5] the last of which is one of the most widespread indoor pollutants. Formic acid spontaneously dissociates on TiO$_2$ (rutile) to form a surface proton and adsorbed formate, HCOO$_{(ads)}$, which can further decompose thermally to CO and H$_2$O. This reaction occurs at 450 K even without photoexcitation, but these dark thermal reactions produce little or no CO$_2$.[6] However, the photocatalytic oxidation of formic acid easily leads to CO$_2$ because the redox potential for the reaction

$$HCOOH \rightarrow CO_2 + 2H^+ + 2e^- \qquad (1)$$
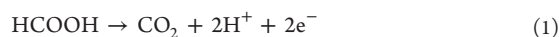
is only 0.19 V vs the standard hydrogen electrode (at pH 0.3), which is near the flat-band potential of TiO$_2$.[2] Hence, the driving force for reaction 1 is large because the valence-band holes are approximately 3 V more positive on the electrochemical scale.

Isotope labeling ($^{18/16}$O, H/D) is a useful strategy in mechanistic studies of TiO$_2$ surfaces under both dark and photoexcited conditions.[7,8] Mass spectroscopy[2,6] or vibration spectroscopy of the titania surface[1,7] can be used to observe the labeled species in the reactions under study. In this work, one of the fundamental questions concerns the participation of lattice oxygen atoms from dark-excited or photoexcited TiO$_2$

surfaces in the catalytic reactions of model molecules. The O isotope transfer between titania and the model molecule(s) can be studied in two ways: (i) using "ordinary" Ti$^{16}$O$_2$ and labeled reactant(s) such as H$_2$$^{18}$O (refs 8 and 9) and $^{18}$O$_2$ (ref 1) or (ii) using a labeled catalyst, Ti$^{18}$O$_2$, and unlabeled molecules.[1,6] The first approach was used by Liao et al.[1] to follow the photocatalytic conversion of HC$^{16}$O$^{16}$O$_{(ads)}$ + $^{18}$O$_2$ to HC$^{16}$O$^{18}$O$_{(ads)}$ or HC$^{18}$O$^{18}$O$_{(ads)}$.

The second approach was demonstrated by Henderson,[6] who investigated the reactions of formic acid on TiO$_2$ (rutile) with $^{18}$O-enriched surfaces ($^{18}$O/$^{16}$O ratio of 2.5) under dark conditions. This work demonstrated that lattice $^{18}$O takes part in the evolution of gaseous products (H$_2$$^{18}$O, H$_2$C$^{18}$O, and HC$^{18}$O$^+$), including the formation of HC$^{16}$O$^{18}$OH. Bogdanoff and Alonso-Vante[2] pioneered the application of isotope tracing to the photoelectrochemical oxidation of formic acid in the presence of $^{18}$O-enriched TiO$_2$ (with an unknown $^{18}$O/$^{16}$O ratio), but no transfer of $^{18}$O from the photocatalyst to CO$_2$ (cf. reaction 1) was detected.

It is obvious that convincing data about the reactions of the second type can only be obtained with an isotopically pure photocatalyst such as Ti$^{18}$O$_2$. We recently prepared this material in both anatase and rutile forms via hydrolysis of TiCl$_4$ by H$_2$$^{18}$O (97% purity).[10,11] High-quality titania was

obtained in an evacuated system, and Raman spectroscopy detected no measurable contamination from $^{16}O$.[10] Livraghi et al.[12] subsequently used a similar reaction to grow $Ti^{17}O_2$ from $TiCl_4$ and $H_2^{17}O$ (40% $^{17}O$ enrichment). Our pure $Ti^{18}O_2$ is a benchmark system for isotope tracing at solid/gas interfaces. High-resolution Fourier transfer infrared spectroscopy (HR-FTIR) can be used to analyze the gas phase over dark or illuminated titania. Our initial study focused on the $Ti^{18}O_2/C^{16}O_2$ interface, where we detected the products $C^{16}O^{18}O$, $C^{18}O^{18}O$, $C^{16}O$, methane, and acetylene through their rich rotational−vibrational spectra.[10,11] In this work, we extended that study to analyze formic acid.

## 2. EXPERIMENTAL SECTION

**2.1. Materials.** The chemicals used in this work included formic acid (HCOOH; Sigma-Aldrich, ACS reagent grade, ≤98% purity), carbon dioxide ($CO_2$; Linde Gas, 99.9993% purity), water ($H_2^{18}O$; Cambridge Isotope Laboratories, 97% purity).

The measurements were based on the calibration of the absorption intensities of isotopologues of $CO_2$, $H_2O$, and $CO$ at different pressures. The partial pressures of the individual isotopologues were calculated using the natural abundances of 0.003947 ($C^{16}O^{18}O$), 0.984204 ($C^{16}O_2$), 0.001978 ($C^{18}O$), 0.986544 ($C^{16}O$), 0.997317 ($H_2^{16}O$) and 0.00199983 ($H_2^{18}O$). The isotopologue $C^{18}O_2$ was produced by isotopic exchange between $H_2^{18}O$ and $C^{16}O_2$ and measured separately. In addition, all of the data were confirmed using wavenumbers and intensities of individual lines from the HITRAN database.[13] The list of lines selected for the calibration is shown in Table 1.

**Table 1. List of Individual Isotopologue Lines Selected for the Calibration**

| isotopologue | wavenumber ($cm^{-1}$) | assignment ($\nu$, $J$, $K_A$, $K_C$) |
| --- | --- | --- |
| $C^{16}O_2$ | 2367.8776 | $\nu_3$, $R(26)_e$ |
| $C^{16}O^{18}O$ | 2343.1041 | $\nu_3$, $R(15)_e$ |
| $C^{18}O_2$ | 2300.71252 | $\nu_3$, $P(18)_e$ |
| $C^{16}O$ | 2172.7588 | $\nu_1$, $R(7)$ |
| $C^{18}O$ | 2113.4055 | $\nu_1$, $R(5)$ |
| $H_2^{16}O$ | 3606.9935 | $\nu_3$, $5_{14}-6_{15}$ |
| $H_2^{18}O$ | 3738.0241 | $\nu_3$, $2_{20}-2_{21}$ |

The completely $^{18}O$ isotope exchanged titanium dioxide ($Ti^{18}O_2$) was prepared from $TiCl_4$ and $H_2^{18}O$.[10] The preparation of $Ti^{18}O_2$ was carried out in a closed all-glass vacuum apparatus. $TiCl_4$ (Sigma-Aldrich, 99.98%) was distilled twice under vacuum before use. Then 1 g of $H_2^{18}O$ (Cambridge Isotope Laboratories, 97%) was frozen under high vacuum with liquid nitrogen, and ice was brought into contact with 2.8 mL of $TiCl_4$ through a breakable glass valve. After the reactants were mixed, the cooling bath was removed, and the reaction mixture was stored at room temperature overnight. The reaction byproduct HCl was collected in a side ampule that was cooled by liquid nitrogen. Then the solid product was heated at 450 °C under vacuum ($10^{-5}$ Torr) for 30 h in the closed vacuum apparatus to remove traces of HCl.[10] Afterward, the apparatus was opened in a glovebox under an Ar atmosphere, and the solid white powder was collected. This powder form of $Ti^{18}O_2$ was placed in a 20 cm long absorption cell and stored under an argon atmosphere at room temperature. The $Ti^{18}O_2$ was characterized by Raman spectroscopy and X-ray diffraction,[10] and it exhibited the pattern of pure anatase. The BET

(Brunnauer−Emmett−Teller) surface area calculated from the $N_2$ adsorption isotherms was 31 $m^2/g$. The samples were degassed at 450 °C under vacuum prior to these measurements.

**2.2. Methods.** FTIR spectra were measured in a 20 cm long (2.5 cm diameter) glass optical cell with $CaF_2$ windows and a 25 cm long glass tube finger in which additional calcination of $TiO_2$ took place. (In certain experiments, in situ calcination was performed and the vacuum transfer of $TiO_2$ was avoided.) The optical cell containing 0.8 g of $TiO_2$ was further equipped with two vacuum valves (ACE Glass, Vineland, NJ) for gas handling and connection to the vacuum line that was used to fill the cell with gases while it was inside the evacuated sample compartment of the spectrometer. The pressure of $CO_2$ and formic acid in the cell was approximately 2 Torr, and it was measured precisely during the acquisition process with an MKS Baratron pressure gauge (0−10 Torr). The spectral measurements were performed using a Bruker IFS 125 HR spectrometer (KBr beam splitter, Mercury Cadmium Telluride (MCT) detector) in a spectral range from 1000 to 4000 $cm^{-1}$. The spectra were measured with a resolution of 0.01−0.02 $cm^{-1}$ with 30−50 scans using the Blackmann−Harris apodization function.

In the photochemical studies, a XeCl excimer laser (308 nm) and a UV light source (340 nm, 160 W, E27 Omnilux Lamp) were used to irradiate the powder $TiO_2$ sample. In the case of the XeCl pulse laser, the nonfocused beam (energy of 150 mJ/pulse, 28 ns pulse length) was collimated through the $SiO_2$ window directly onto the $TiO_2$ surface. The 160 W UV lamp source was positioned vertically through a quartz window (3 cm diameter) to the sample cell, and the $TiO_2$ surface was irradiated through this window.

## 3. RESULTS AND DISCUSSION

**3.1. Photocatalytic Decomposition of Formic Acid on $Ti^{18}O_2$ Using a XeCl Laser.** Previous studies reported that formic acid decomposes photocatalytically by first forming the formate anion (eq 2)[4,14] and then $CO_2$ and $H_2O$.[15] The

$$h^+ + HCOOH_{(ads)} \rightarrow HCOO^-_{(ads)} + H^+ \qquad (2)$$

majority of the mechanism for the decomposition of formate is still not well understood. The decomposition is assumed to proceed by means of electron transfer to photogenerated valence-band holes ($h^+$, eq 3) and/or reaction with $OH^\bullet$ radicals (eq 4) produced from water and the formation of $CO_2$ (eq 5).[16]

$$HCOO^-_{(ads)} + h^+ \rightarrow COO^{\bullet-} + H^+ \qquad (3)$$

$$HCOO^-_{(ads)} + OH^\bullet \rightarrow COO^{\bullet-} + H_2O \qquad (4)$$

$$COO^{\bullet-} \rightarrow CO_2 + e^- \qquad (5)$$

The reaction mechanisms become more complicated when the side reactions of different species and their adsorption on the $TiO_2$ surface obscure the basic processes. The following FTIR experiments with $^{18}O$-labeled $TiO_2$ are intended to clarify the involvement of the lattice oxygen atoms and defects in the overall mechanism of the photocatalytic process.

The clean surface of $Ti^{18}O_2$ was placed in an evacuated cell and then exposed to gaseous formic acid (10 Torr) for 24 h. After this treatment, the partial pressure of formic acid was reduced to 2 Torr. Figure 1 shows the FTIR absorption spectrum of the gas phase over the $Ti^{18}O_2$ sample in the range

**Figure 1.** High-resolution FTIR absorption spectra of formic acid in the gas phase over the $Ti^{18}O_2$ surface in the range of 1000–4000 cm$^{-1}$ (A) and details of the $\nu_3$ band of formic acid (B, C): nonirradiated sample of formic acid (a) and sample with $Ti^{18}O_2$ irradiated by the XeCl laser (308 nm, 8500 pulses, energy of 150 mJ/pulse) (b).



**Figure 2.** Formate adsorption on $TiO_2$: monodentate species (a), bidentate bridging species (b), and bidentate chelating species (c).

from 1000 to 4000 cm$^{-1}$ before (a) and after irradiation (b) of the $Ti^{18}O_2$ surface with the XeCl laser (8500 pulses). The characteristic features of the rotational−vibrational bands for the simple gaseous species were used to assign the IR transitions according to the HITRAN database,[13] where the Lambert−Beer law was used to calculate partial pressures of the individual components. The concentration of formic acid was evaluated using the $\nu_3$ rotational−vibrational band of carbonyl at approximately 1750 cm$^{-1}$. High-resolution spectra between 1760.00 and 1762.25 cm$^{-1}$ for nonirradiated (Figure 1C, spectrum a) and irradiated (Figure 1C, spectrum b) samples were nearly identical; only their intensities di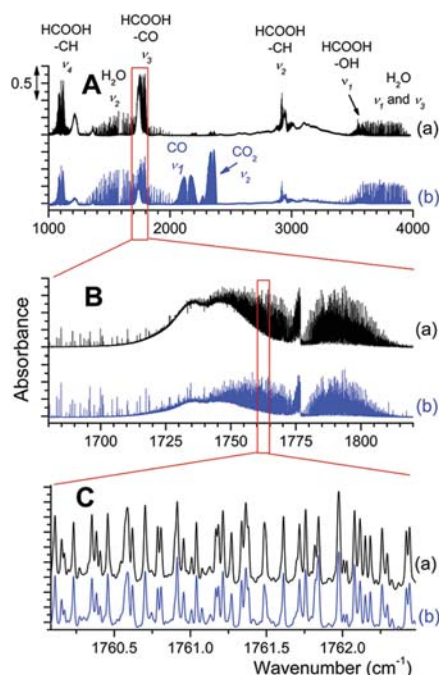ffered. There was no evidence of the formation of formic acid isotopologues with one or two $^{18}O$ atoms in the gas phase, which shift the $\nu_3$ band. These results mean that there was no desorption of any $^{18}O$-labeled isotopologues of formic acid/formate from the $Ti^{18}O_2$ surface. Note that formic acid can migrate between different surface-active sites of titania,[17] and its desorption was observed elsewhere at relatively low temperatures (below 250 K).[14]

Our gas-phase measurements are in good agreement with in situ FTIR spectra of adsorbed formic acid/formate on different $TiO_2$ surfaces. According to literature data,[4,18−21] formic acid/formate molecules can adsorb in different ways. All three proposed geometries (Figure 2) are based on interactions of titanium atoms with formate oxygen atoms and no direct interactions of lattice $^{18}O$ with carbon atoms (and isotope exchange).

Isotope exchange between oxygen atoms of formic acid adsorbed on $TiO_2$ surfaces and gaseous molecular oxygen $^{18}O_2$ was observed by Liao et al.[1] They recorded a shift of the spectral band of adsorbed formic acid/formate from 1555 to

1548 cm$^{-1}$ after the $TiO_2$ surface was exposed to UV radiation for 180 min in 10 Torr of $^{18}O_2$; they interpreted this shift to indicate the formation of formic acid/formate isotopologue(s) with $^{18}O$ atoms. Thermal desorption data from the decomposition of $HC^{16}O^{16}OH$ on the $^{18}O$-enriched $TiO_2(110)$ surface also indicated that oxygen exchange between the surface and the formic acid adlayer resulted in significant amounts of $^{18}O$-containing products (carbon monoxide, water, and formaldehyde).[14]

In this work, the $TiO_2$ photocatalyst was surrounded by gas-phase formic acid molecules and irradiated with the XeCl laser (8500 pulses, 308 nm, fluence approximately 160 J cm$^{-2}$). Note that formic acid has no absorption band above 250 nm, and only weak absorption of formate is expected.[13] The decomposition of formic acid occurred preferentially via photoactivation of the $TiO_2$. A detailed analysis of the observed vibrational−rotational bands in the FTIR spectrum after irradiation (Figure 1, spectra b) revealed the presence of $C^{16}O_2$, $C^{16}O^{18}O$, $C^{18}O_2$ ($\nu_2$ band at 2350 cm$^{-1}$, Figure 3), $H_2^{16}O$, $H_2^{18}O$ ($\nu_3$ band at 3600 cm$^{-1}$, Figure 4), and $C^{16}O$, $C^{18}O$ ($\nu_1$ band at 2150 cm$^{-1}$, Figure 5) that were formed as products of photocatalytic decomposition.

**3.2. Photocatalytic Decomposition of Formic Acid on $Ti^{18}O_2$ Using a 160 W UV Lamp.** A continuous UV lamp was used to irradiate $TiO_2$ to measure the kinetics of the formation of the individual isotopologues and eliminate the effects of the high energy of the pulsed XeCl laser. Figure 6 shows the decrease of the concentration of formic acid in the gas phase during 70 min after irradiation (panel A) and the kinetics of the decomposition products (panels B−D) that were monitored on the basis of their absorption bands (Figures 1 and 3−5). The kinetics of all reactions were measured in the gas phase. The reaction rate was strongly influenced by the adsorption/desorption processes and diffusion behavior because these measurements were carried out in an unstirred cell.

Carbon dioxide $C^{16}O_2$ was the main impurity in the FTIR spectrum of formic acid (Figure 2a). We did not find any absorption lines from the $C^{16}O^{18}O$ and $C^{18}O_2$ isotopologues even when the $TiO_2$ surface was exposed to a gaseous sample for 140 h prior to irradiation. We assume that formic acid and/or formate adsorbed on the surface of $Ti^{18}O_2$ partially blocked the active sites and prevented spontaneous isotope exchange between $CO_2$ and lattice oxygens. During the irradiation of the $Ti^{18}O_2$ surface with a UV lamp, all isotopologues of $C^{16}O^{18}O$ and $C^{18}O_2$ were formed (Figure 6). The formic acid/formate decomposed and allowed the active sites to become available for the adsorption of decomposition products such as $CO_2$. It is well-known that adsorbed $CO_2$ readily exchanges oxygen atoms with $Ti^{18}O_2$.[11] The isotope exchange and reactivity of adsorbed $CO_2$ during irradiation of $Ti^{18}O_2$ may be facilitated also by

**Figure 4.** Rotation−vibration lines of $H_2O$ isotopologues in the spectral range 3380−3381 cm$^{-1}$: $H_2O$ formed from formic acid over the irradiated $Ti^{18}O_2$ surface (XeCl laser, 8500 pulses) (a), $H_2^{16}O$ (b) and $H_2^{18}O$ (c) from the HITRAN database[13] and simulated with the Winproof program, and the pure water standard with natural abundances of oxygen atoms (d). Transitions were assigned to the fundamental $\nu_3$ band with rotational assignments in the $J$, $K_A$, and $K_C$ quantum numbers according to convention.



**Figure 3.** (A) Rotation−vibration lines of the $\nu_3$ band of $CO_2$ in the spectral range 2270−2380 cm$^{-1}$: $CO_2$ standard with natural abundances of oxygen isotopes (a), $CO_2$ formed from formic acid over the irradiated $Ti^{18}O_2$ surface (XeCl laser, 8500 pulses) (b), and individual isotopologues from the HITRAN database[13] simulated with the Winproof program (c−e). (B) High-resolution FTIR spectrum (2298−2302 cm$^{-1}$) of the $CO_2$ standard (a) and the $CO_2$ formed from formic acid over the irradiated $Ti^{18}O_2$ surface (XeCl laser, 8500 pulses) (b). Lines were assigned for all isotopologues.



**Figure 5.** Rotation−vibration lines of the $\nu_1$ band of CO in the spectral range 2000−2250 cm$^{-1}$: CO standard with natural abundances of oxygen isotopes (a), CO formed by irradiation of HCOOH over the irradiated $Ti^{18}O_2$ surface (XeCl laser, 8500 pulses) (b), and $C^{18}O$ isotopologue from the HITRAN database[13] simulated with the Winproof program (c).

formation of $CO_2^-$ with lower reduction potential in the adsorbed state.[22]

Water is another product of the photocatalytic decomposition of formic acid; its concentration increased slightly during irradiation (Figure 6D). The abundances of the individual isotopologues (96% for $H_2^{16}O$ and 4% for $H_2^{18}O$) were nearly constant (Figure 7), which suggests that the oxygen atoms in the lattice were not involved in the formation of water.

Carbon monoxide $C^{16}O$ was a minor product formed during the irradiation of $TiO_2$ with a UV lamp (Figure 6C), but no $C^{18}O$ was detected. In our previous study,[11] we discovered that CO does not react with oxygen in the lattice; instead, it bonds directly with Ti atoms. In other words, there is no oxygen exchange between CO and $Ti^{18}O_2$.

However, the $C^{18}O$ isotopologue was observed in experiments with the XeCl laser (Figure 5b). The abundance of $C^{18}O$ in the reaction mixture after the irradiation of $TiO_2$ with 4500

laser pulses was 0.6%, which is significantly higher than the usual abundance (0.2%) according to the HITRAN database.[13] Trace concentrations of $C^{18}O$ can be formed by the two-photon photolysis of $C^{18}O_2$ or $C^{16}O^{18}O$ (eq 6).[23] In this case, the oxygen atoms of the titania are not involved in the process, and there is no interfacial isotope exchange.

$$2C^{16}O^{18}O \rightarrow C^{18}O + C^{16}O + {}^{16}O^{18}O \qquad (6)$$

**3.3. Passivation with Water and Isotopic Exchange between $C^{16}O_2$ and $Ti^{18}O_2$.** Because most applications of $TiO_2$ involve a water-containing environment, there is considerable interest in the effects of water on the chemistry of simple organic molecules such as formic acid at $TiO_2$ surfaces. Water has been observed to significantly affect the photocatalytic decomposition of several compounds on $TiO_2$. In some cases, water can reduce catalytic activity through

D

dx.doi.org/10.1021/jp303011a | J. Phys. Chem. C XXXX, XXX, XXX−XXX

P75

**Figure 6.** Photocatalytic decomposition of formic acid on a Ti$^{18}$O$_2$ surface that was irradiated with a UV lamp (A) and the formation of CO$_2$ (B), CO (C), and H$_2$O (D) isotopologues: partial pressures of individual species in the gas phase.



**Figure 7.** Photocatalytic decomposition of formic acid on a Ti$^{18}$O$_2$ surface that was irradiated with a UV lamp: abundances of individual isotopologues during irradiation.

competitive adsorption with the reactant; in other cases, water can accelerate a reaction through mechanisms that are not fully understood yet.[24,25]

Our previous study[11] showed that Ti$^{18}$O$_2$ can spontaneously exchange oxygen atoms with the CO$_2$, which is the major product of the photocatalytic decomposition of formic acid. Therefore, we studied the influence of water on isotope exchange of CO$_2$ in this work. The Ti$^{18}$O$_2$ powder was placed in a cell and exposed to water (15.2 Torr) for 24 h. Then the pressure was reduced to 0.1 Torr, and the cell was filled with CO$_2$ (1.8 Torr). Figure 8 shows the abundances of the individual isotopologues of CO$_2$ and H$_2$O in the gas over the nonirradiated Ti$^{18}$O$_2$. The spontaneous isotope exchange



**Figure 8.** Influence of water passivation (24 h by 15.2 Torr of water) on the relative abundances of individual H$_2$O and CO$_2$ isotopologues observed during spontaneous isotopic exchange of oxygen atoms between the surface of Ti$^{18}$O$_2$ and H$_2$O and CO$_2$ followed by laser irradiation of the titania surface (2000 pulses) (a) and during laser-induced isotope exchange (b): sample 0, before irradiation; sample 1, after irradiation with the XeCl laser (5000 pulses); sample 2, after irradiation and spontaneous isotope exchange (2 h).

between CO$_2$ and the titania surface was limited; the relative abundance of the C$^{16}$O$^{18}$O isotopologue (1−2%) was similar to the natural values published in the HITRAN database.[13] These results demonstrate that water blocks the active sites on Ti$^{18}$O$_2$. That is, water prevents CO$_2$ adsorption and spontaneous isotope exchange between CO$_2$ and the titania surface. Finally, the Ti$^{18}$O$_2$ surface was kept in the dark for 23.5 h, and then it was irradiated with the XeCl laser. The laser irradiation (2000 pulses, energy of 150 mJ/pulse) accelerated the desorption of water from TiO$_2$, and the H$_2$$^{18}$O/H$_2$$^{16}$O isotopologue ratio remained constant. This experiment was repeated with a higher number of laser pulses (Figure 8b). The data show that the CO$_2$ in the gas phase was enriched with the C$^{18}$O$_2$ isotopologue. The laser radia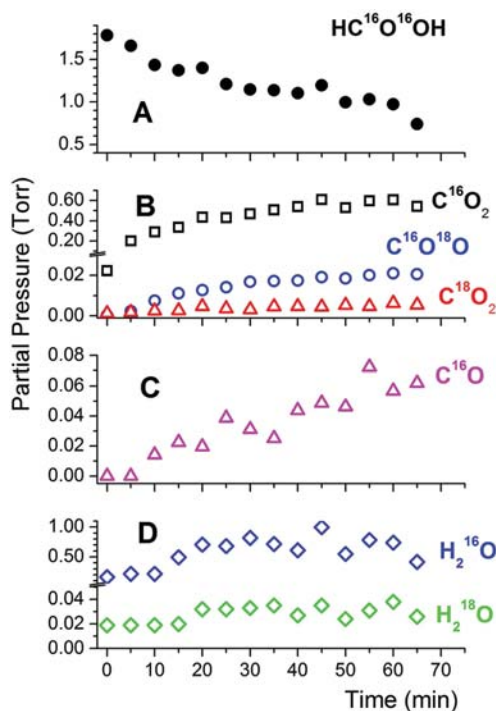tion likely induced photo-desorption or thermal desorption of water into the gas phase. As a result, the binding sites on the TiO$_2$ surface were available. Then CO$_2$ molecules adsorbed onto the titania, and light-driven isotope exchange took place followed by spontaneous exchange.

After Ti$^{18}$O$_2$ passivation by water in the previous experiment, the cell was evacuated to $2 \times 10^{-3}$ Torr for 120 min. Then the cell was filled with CO$_2$ (1.7 Torr), and the gas phase was monitored using FTIR spectroscopy. Each FTIR spectrum was accumulated from an average of five scans with a resolution of 0.02 cm$^{-1}$. The intervals between the collection of consecutive individual spectra were between 20 s and 1 h. The abundances of the CO$_2$ isotopologues in the first spectrum (immediately after the addition of gaseous CO$_2$) were consistent with the natural abundances listed in the HITRAN database.[13] The fast spontaneous exchange of $^{18}$O atoms with the Ti$^{18}$O$_2$ surface was observed subsequently (Figure 9). The abundance of the C$^{18}$O$_2$ isotopologue with both exchanged oxygen atoms significantly increased to ~15% in the first 10 min and remained nearly constant for 24 h (Figure 9 b). Similar behavior was observed when freshly prepared TiO$_2$, which was heated at 450 °C in a vacuum (10$^{-5}$ Torr) for 30 h in the absence of water.

## 4. CONCLUSION

High-resolution FTIR spectroscopic measurements showed that formic acid underwent photocatalytic decomposition over Ti$^{18}$O$_2$, and CO$_2$, CO, and H$_2$O isotopologues containing $^{18}$O

**Figure 9.** Isotopic exchange after water removal by evacuating the cell at $2 \times 10^{-3}$ Torr for 120 min: relative abundances of the individual $CO_2$ isotopologues after several minutes (a) and several hours (b) of spontaneous isotope exchange between the $CO_2$ molecules (1.8 Torr) and the $Ti^{18}O_2$ surface.

atoms were formed. Formic acid does not exchange oxygen atoms with the lattice oxygen atoms of $Ti^{18}O_2$ spontaneously and/or during photocatalytic decomposition; moreover, it blocks the active sites on the lattice. This blocking behavior was demonstrated in an experiment where HCOOH was adsorbed on a titania surface and no spontaneous exchange occurred between $C^{16}O_2$ and $Ti^{18}O_2$. Adsorbed water also inhibits the activity of the calcinated $Ti^{18}O_2$. When the surface of the $Ti^{18}O_2$ with adsorbed HCOOH was irradiated with the XeCl laser and the UV lamp, the main decomposition products were $C^{16}O_2$, $H_2^{16}O$, and $C^{16}O$. The isotopologues $C^{16}O^{18}O$ and $C^{18}O_2$ are the products of the spontaneous exchange of oxygen atoms between the $C^{16}O_2$ and the active sites on the $Ti^{18}O_2$ that became available during the irradiation of the surface by UV photons. The $C^{18}O$ is a product of the UV decomposition of the $C^{16}O^{18}O$ or $C^{18}O_2$ that formed during the spontaneous exchange process.

## ■ AUTHOR INFORMATION

**Corresponding Author**
*E-mail: civis@jh-inst.cas.cz.
**Notes**
The authors declare no competing financial interest.

## ■ ACKNOWLEDGMENTS

## ■ REFERENCES

(1) Liao, L. F.; Lien, C. F.; Shieh, D. L.; Chen, M. T.; Lin, J. L. *J. Phys. Chem. B* **2002**, *106*, 11240−11245.
(2) Bogdanoff, P.; Alonso-Vante, N. *J. Electroanal. Chem.* **1994**, *379*, 415−421.
(3) Liao, L. F.; Wu, W. C.; Chen, C. Y.; Lin, J. L. *J. Phys. Chem. B* **2001**, *105*, 7678−7685.
(4) Hauchecorne, B.; Terrens, D.; Verbruggen, S.; Martens, J. A.; Van Langenhove, H.; Demeestere, K.; Lenaerts, S. *Appl. Catal., B* **2011**, *106*, 630−638.
(5) Wen, B.; Li, Y.; Chen, C.; Ma, W.; Zhao, J. *Chem.—Eur. J.* **2010**, *16*, 11859−11866.
(6) Henderson, M. A. *J. Phys. Chem.* **1995**, *99*, 15253−15261.
(7) Sato, S. *J. Phys. Chem.* **1987**, *91*, 2895−2897.
(8) Nakamura, R.; Nakato, Y. *J. Am. Chem. Soc.* **2004**, *126*, 1290−1298.
(9) Wu, T.; Kaden, W. E.; Anderson, S. L. *J. Phys. Chem. C* **2008**, *112*, 9006−9015.
(10) Kavan, L.; Zukalová, M.; Ferus, M.; Kurti, J.; Koltai, J.; Civiš, S. *Phys. Chem. Chem. Phys.* **2011**, *13*, 11583−11586.
(11) Civiš, S.; Ferus, M.; Kubát, P.; Zukalová, M.; Kavan, L. *J. Phys. Chem. C* **2011**, *115*, 11156−11162.
(12) Livraghi, S.; Maurelli, S.; Paganini, M. C.; Chiesa, M.; Giamello, E. *Angew. Chem., Int. Ed.* **2011**, *50*, 8038−8040.
(13) Rothman, L. S.; Gordon, I. E.; Barbe, A.; Benner, D. C.; Bernath, P. E.; Birk, M.; Boudon, V.; Brown, L. R.; Campargue, A.; Champion, J. P.; et al. *J. Quant. Spectrosc. Radiat. Transfer* **2009**, *110*, 533−572.
(14) Henderson, M. A. *J. Phys. Chem. B* **1997**, *101*, 221−229.
(15) McMurray, T. A.; Byrne, J. A.; Dunlop, P. S. M.; McAdams, E. T. *J. Appl. Electrochem.* **2005**, *35*, 723−731.
(16) Mitoraj, D.; Beránek, R.; Kisch, H. *Photochem. Photobiol. Sci.* **2010**, *9*, 31−38.
(17) Chen, J.; Kubota, J.; Wada, A.; Kondo, J. N.; Domen, K. *J. Am. Chem. Soc.* **2009**, *131*, 4580−4581.
(18) Miller, K. L.; Falconer, J. L.; Medlin, J. W. *J. Catal.* **2011**, *278*, 321−328.
(19) Tanner, R. E.; Sasahara, A.; Liang, Y.; Altman, E. I.; Onishi, H. *J. Phys. Chem. B* **2002**, *106*, 8211−8222.
(20) Brownson, J. R. S.; Tejedor-Tejedor, M. I.; Anderson, M. A. *J. Phys. Chem. B* **2006**, *110*, 12494−12499.
(21) Halasi, G.; Schubert, G.; Solymosi, F. *Catal. Lett.* **2012**, *142*, 218−223.
(22) He, H.; Zapol, P.; Curtiss, L. A. *J. Phys. Chem. C* **2010**, *114*, 21474−21481.
(23) Ferus, M.; Matulková, I.; Juha, L.; Civiš, S. *Chem. Phys. Lett.* **2009**, *472*, 14−18.
(24) Miller, K. L.; Musgrave, C. B.; Falconer, J. L.; Medlin, J. W. *J. Phys. Chem. C* **2011**, *115*, 2738−2749.
(25) Peral, J.; Domènech, X.; Ollis, D. F. *J. Chem. Technol. Biotechnol.* **1997**, *70*, 117−140.

**Přílohy**

# Laser ablation of CsI: time-resolved Fourier-transform infrared spectra of atomic cesium in the 800–8000 cm$^{-1}$ range

**S. Civiš,[1,*] M. Ferus,[1] P. Kubelík,[1] P. Jelínek,[1] V. E. Chernov,[1,2] and M.Yu. Knyazev[2]**

[1]*J. Heyrovský Institute of Physical Chemistry, Academy of Sciences of the Czech Republic,*
*Dolejškova 3, 18223 Prague 8, Czech Republic*
[2]*Voronezh State University, 394693 Voronezh, Russia*
*\*Corresponding author: civis@jh-inst.cas.cz*

Fourier-transform time-resolved spectroscopy of laser-induced breakdown of Cs vapor in a vacuum has been used for the measurement of atomic Cs emission spectra in the 800–8000 cm$^{-1}$ range with a resolution of 0.02 cm$^{-1}$. The $6h$ and $7h$ levels of Cs are observed. The dipole transition matrix elements (transition probabilities, oscillator, and line strengths) between the observed levels are calculated using quantum defect theory.   © 2012 Optical Society of America

*OCIS codes:*   300.6210, 300.6300, 300.6340, 020.4900.

## 1. INTRODUCTION

The spectrum of neutral Cs atom has become one of the most important and well studied [1] due to a number of modern atomic physics experiments involving atomic cesium, such as the cooling and trapping of atoms, ultracold atom collisions and the formation of cold molecules, and evidence for effects of quantum electrodynamics and parity nonconservation, not to mention the atomic Cs frequency standard.

The most complete compilation of Cs levels available in the literature [1] includes the states with orbital angular momentum $l \leq 4$, but it lacks the levels with higher angular momenta. Such high-$l$ states are of interest for various problems of atomic and molecular physics [2], such as the excitation and decay of autoionizing states [3,4] or the extraction of multipole moments and/or polarizabilities of ions from the high-$l$ Rydberg electron spectra of corresponding neutral atoms [5] obtained using precise microwave [6] or optical [7] measurements of high-$l$ states.

Unlike the high-excited Rydberg levels, the low-excited high-$l$ states (for example, the $nh$ series begins with the principal quantum number $n = 6$) can be observed only in the infrared (IR) spectral range. Indeed, $nh$ states are linked by dipole transitions to $n'g$ states, and the transition energy for the minimal $n' = 5$ is about 1330 cm$^{-1}$ ($n = 6$) and 810 cm$^{-1}$ ($n = 7$). This estimate is given according to the Rydberg formula with zero quantum defects (the outer electron's interaction with the atomic core is weak in high-$l$ states, so these states have small quantum defects decreasing with $l$ [5]). The transitions between higher $n, n'$ lie below 600 cm$^{-1}$.

The transitions in the spectral ranges mentioned above can be observed by analyzing the light spectrum emitted from a plasma created on the sample surface by laser radiation. The corresponding technique, laser-induced breakdown spectroscopy (LIBS), is a versatile and sensitive probe for the detection and identification of trace substances. LIBS has many practical advantages over the conventional methods of chemical analysis of elements and is consequently being considered for a growing number of applications [8–12].

In this work LIBS is used together with time-resolved Fourier-transform infrared (FTIR) spectroscopy for recording Cs emission spectra in the 800–8000 cm$^{-1}$ range. From these spectra one can extract the energies of some Cs levels involved in the observed transitions. Although most of these energies are available in literature with very good accuracy, our energy values for $7p_{\frac{3}{2}}$ and $8p_{\frac{3}{2}}$ levels have smaller uncertainties.

A part of the above mentioned spectral region (the 1200–1600 cm$^{-1}$ range) has been measured for Cs in our recent work [13] reporting the $6h$ Cs level energy that was previously unknown. In this paper we have extended the measured range to cover the 800–1200 cm$^{-1}$ spectral region and determine the $7h$ Cs level energy. No experimental measurement of Cs IR lines the 800–2500 cm$^{-1}$ range is reported in literature or NIST database [14]. To our knowledge, no alkali atom lines have been experimentally measured in the 800–1600 cm$^{-1}$ range previously due to several problems. First, the HgCdTe (MCT) detectors used in this range are not always characterized by sensitivity and/or sufficient signal-to-noise ratio (SNR). Second, the background blackbody radiation inside the spectrometer chamber (at laboratory temperature) decreases readability of the spectra recorded in this domain. Third, as mentioned above, the spectral lines in this spectral region are due to transition from high-excited states and their complex population dynamics requires using the time-resolution technique for reliable recording of the emission spectra (see our earlier works [15–17]). This work attempts to fill this gap. In addition to our recent work [13] (where we have observed seven Cs lines not reported previously), we report here 15 new Cs lines in the 800–1200 and 1600–2500 cm$^{-1}$ ranges. We also present the dipole transition matrix elements (transition probabilities, oscillator and line strengths) between the observed levels calculated using quantum defect theory (QDT).

## 2. METHODS

### A. Experimental

The sketch of the experimental setup is presented in Fig. 1. Time-resolved FTIR spectroscopy was applied for observation of the emission arising after the irradiation of a CsI target with a pulsed nanosecond ArF ($\lambda = 193$ nm) laser. A high repetition rate ArF laser ExciStar *S*-Industrial V2.0 1000 (193 nm, laser pulse width 12 ns, frequency 1 kHz) with 15 mJ pulse energy was focused on a rotating and linearly traversing target (CsI tablet) inside a vacuum chamber (average pressure $10^{-1}$ Torr). The IR emission of the laser plume was measured in the probed area at axial distance $L$ ranging from 1 to 9 mm from the target. The emission from this area was focused into the spectrometer by $CaF_2$ (100 mm) or ZnSe (127 mm) lenses (for 1600–7700 $cm^{-1}$ or 800–1600 $cm^{-1}$ spectral range, respectively). Two different detectors (MCT and InSb) and two beamsplitters (KBr and $CaF_2$) were used to cover the whole measured spectral range. The measurements were carried out with a resolution of 0.02 $cm^{-1}$ for five values of the distance $L$: 1, 3, 5, 7, and 9 mm. The emission was observed in seven spectral ranges: 800–1000, 1000–1300, 1200–1600, 1600–2000, 2000–3500, 4100–5000, and 5000–7700 $cm^{-1}$.

The continuous scanning method was used for the measurement of the time-resolved FTIR spectra. After each ArF laser trigger point, several data points were sampled during the continual movement of the interferometer mirror. The synchronization of the laser ablation, which is the source of the emission, with the signal acquisition requires a special technique. In the case of the common time-resolved FT measurement, the time shifted signals from a detector are sampled at each zero-crossing point of HeNe laser fringes. A complication comes from the fact that the repetition rate of the lasers suitable for ablation experiments is lower then the frequency of the HeNe laser fringes produced by the interferometer. Therefore the laser pulse is triggered only in the chosen (every second, third, or fourth, etc.) zero-cross point of the HeNe laser fringes. As a result $1/n$ of each time-resolved interferogram is obtained after each scan [18]. The timing diagram is shown in Fig. 2, where the time sequence corresponds to the case of $n = 3$; several measurements were carried out with the divider $n = 4$. An assembly of the $n$ parts of the interferogram sampled at the same time after the laser pulse provides the complete interferogram. The output of this process is a set of time-resolved interferograms (30–64).

Our system was designed using a field programmable gate array (FPGA) processor. The main role of the FPGA processor in our experiment was to initiate a laser pulse and AD trigger signals (the signal for data collection from the detector) synchronously with the HeNe laser fringe signals from the spectrometer. The FPGA processor also controls the data transmission from the digital input board to the PC. The width of the ablation laser pulse can be preset, as well as the offset value between the beginning of the laser pulse and the data acquisition.

In the present experiments we used a 60 $\mu$s offset followed by the 30 AD trigger acquisition signals covering a 30 $\mu$s interval. The matrix of data signals corresponding to the AD triggers is stored and Fourier-transformed. The acquired interferograms were postzero filled using the OPUS Bruker program [19] and subsequently corrected by subtracting the blackbody background spectrum. The wavenumbers, line widths, and their intensities were then obtained using the OPUS peak picking procedure.

### B. Line Identification and Dipole Transition Matrix Elements

To record Cs spectra we studied the plasma formed by a laser ablation of the cesium iodide CsI. To ensure that our plasma spectra contained only Cs lines, we made a control measurement with a cesium bromide (CsBr) target, which did not result in appearing or disappearing of the spectral lines as compared to the case of CsI. However, the SNR achieved for the CsI target was better, so we report only the results of CsI ablation. We do not expect any emissions from the halogen atoms for the following reason. The Cs levels from which the emission was registered have excitation energies not higher than ~30000 $cm^{-1}$, while the lowest excited levels (those from which dipole radiative transitions are possible) of the halogen atoms have much higher energies [14]: ~64000 $cm^{-1}$ ($4s^2 4p^4(^3P_2)5s$ ($^2P$) levels of Br) and ~56000 $cm^{-1}$ ($5s^2 5p^4(^3P_2)6s$ ($^2[2]$) levels of I). So these halogen atoms' levels should be much less populated as compared to the Cs levels so that no emission lines of I or Br are expected in our ablation plasma spectra.

All the lines observed are classified as belonging to transitions between the neutral Cs $(5p^6)nl_j$ atom states. The transition between the states with the orbital angular momentum $l < 5$ is easily identified using the available Cs level list [1,14]. However, since the $(5p^6)6h$ ($l = 5$) level has not been observed previously, at first approximation we assumed it to have very small quantum defect $\mu \simeq 0.01$ and used the Rydberg formula:

$$E(nl_j) = V_{\text{ion}} - \frac{Z^2 \mathcal{R}_{\text{Cs}}}{n^{*2}} = V_{\text{ion}} - \frac{Z^2 \mathcal{R}_{\text{Cs}}}{(n - \mu_{lj})^2}, \quad (1)$$

where $V_{\text{ion}} = 31406.46766$ $cm^{-1}$ [1] stands for the ionization potential of the Cs atom whose $(5p^6)$ core's charge is $Z = 1$; $\mathcal{R}_{\text{Cs}} = 109736.86254$ $cm^{-1}$ [1] is the mass-corrected Rydberg constant for Cs.

However, this first approximation can have an error of order of tens of $cm^{-1}$. The only transition possible from the $6h$ level can be to the $5g$ level, and the only line appearing in the corresponding spectral region is the 1348.359 $cm^{-1}$ line. To ensure this line is indeed due to the $5g$–$6h$ transition, we



Fig. 1.    (Color online) Experimental setup for LIBS.

Fig. 2.   (Color online) Timing diagram for the interleaved sampling. During the scan, the laser pulse and the AD trigger sampling are induced with a rate of $1/n$ times of the HeNe laser fringe frequency. The complete interferograms are obtained after $n$ scans ($n = 3$ here).

estimate its relative intensity. The same considerations apply to the 6$g$–7$h$ transition.

For an optically thin plasma at local thermal equilibrium (LTE), the emission transition from an upper state $k$ to a lower state $i$ has the intensity $I_{ki}$ proportional to the transition probability $A_{ki}$ and to the transition wavenumber $\nu_{ki}$:

$$I_{ki} \sim g_k A_{ki} \nu_{ki} \, \exp\left(-\frac{E_k}{k_{\mathrm{B}} T}\right), \qquad (2)$$

where $k_{\mathrm{B}}$ is the Boltzmann constant, $T$ is the excitation temperature, and $E_k$ and $g_k$ are the energy and the degeneracy factor of the upper state, respectively.

Since at the low pressures used in our experiment, the atom concentration is low, we can consider our plasma to be optically thin. However, in the same conditions, some deviations from LTE conditions can occur [20], but the Boltzmann distribution of the atomic populations remains valid [21], although with different temperatures of electrons and atoms [20]. This means that even if the observed line intensities display some deviations from the proportionality to the $A$-values, they should describe the qualitative picture of the relative line intensities well enough to assign the lines.

The Boltzmann plot made according to Eq. (2) is presented in Fig. 3, displaying a typical example of calculating the excitation temperature from tour data (e.g., for the 2000–3500 cm$^{-1}$ range). The linear fitting gives the plasma

temperature $T = 2250 \pm 560$ K. The uncertainty of $T$ is small enough to consider the Boltzmann population distribution [Eq. (2)] to be valid for our experiment. The moderate distortion of the Boltzmann plot from the straight line can be considered as an evidence that $A_{ik}$ values are be calculated with enough accuracy (at least to confirm our line identifications).

The investigation of atomic emission in our LIBS experiment is complicated by nonequilibrium and nonstationary conditions of the plasma for the excited states [12]. In particular, the emission intensities of the spectral lines show a complex dependence on the time delay $\tau$ after the ArF laser



Fig. 3.   Boltzmann plot of the ablation plasma.

pulse shot (see Fig. 5 below). So the use of the time-resolved scheme is essential in our experiment. For analyzing the excitation temperature, there is no good substitute for calculating $T$ separately for each distance $L$ between the probed area and the target surface and delay time $\tau$ after the laser shot. We cannot identify any dependence that could simplify such an analysis. There are hints in the data at some rich dynamics in the plasma that cause $T$ to evolve in some complex way as a function of time and location, but the uncertainties in $T$ as measured (300…600 K) are too great to explore those dynamics in detail.

The dipole matrix elements required for knowledge of $A_{ki}$ were calculated using single-channel QDT [22–24]. This technique is quite similar to the FMP method used in our previous papers (see, e.g., [16]) with the radial wavefunction of $nl_j$ state given in terms of Whittaker functions by

$$
R_{nlj}(r) = \frac{Z^{1/2}}{r\,n^*}\left[\frac{\Xi_l(E(nl_j))}{\Pi_l(n^*)}\right]^{1/2} W_{n^*,l+1/2}\left(\frac{2Zr}{n^*}\right)
$$
$$
\times \left[\Gamma(l+1+n^*)\Gamma(n^*-l)\left(1+\frac{\partial\mu_{lj}(n^*)}{\partial n^*}\right)\right]^{-1/2}, \quad (3)
$$

where the effective principal quantum number $n^*$ is connected to the energy level $E(nl_j)$ and quantum defect $\mu_{lj}$ via the Rydberg formula [Eq. (1)]. The functions $\Xi_l(E(nl_j))$ and $\Pi_l(n^*)$ in Eq. (3) are connected with an interpolation of the quantum defect function $\mu_{lj}(n^*)$ [24]. The core polarization effects were taken into account according to [25].

The adequacy of the QDT approximation was tested by comparison the dipole matrix elements for $6s–np$ transitions with the values from the NIST database [14] and with *ab initio*

Dirac–Hartree–Fock calculations [26]. The results are presented in Table 1, where the line strengths ($S$-values) are listed; these $S$-values are the squared reduced dipole matrix elements given in [26]. The maximal discrepancy between our and NIST values was about 25% for $6s–6p$ transitions; for transitions involving higher principal quantum numbers, the discrepancy is considerably lower. This comparison shows the QDT technique to be adequate for the calculation of matrix elements of the transition between the levels observed in the present experiment

## 3. RESULTS AND DISCUSSION

A part of the recorded Cs emission spectrum is shown in Fig. 4 without subtraction of the background blackbody radiation signal component. The list of the observed lines with their parameters and identification is presented in Table 2. Since the measurements were done in seven spectral ranges, 800–1000, 1000–1300, 1200–1600, 1600–2000, 2000–3500, 4100–5000, and 5000–7700 cm$^{-1}$, intensity values have the same scale only for lines within the same range of wavenumbers. A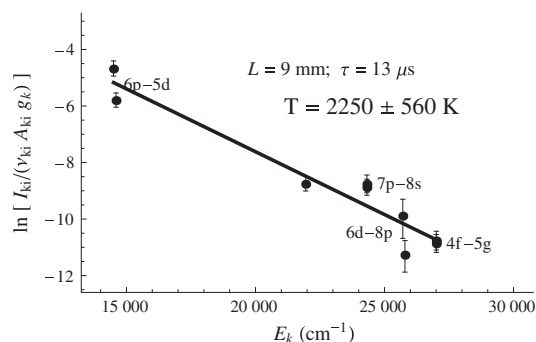ll the uncertainties in the tables below are given in round brackets after the corresponding values and should be treated as their rightmost significant digits; e.g., 123.4(56) means $123.4 \pm 5.6$.

As mentioned above, the intensities of the emission lines display a complex nonmonotonic behavior as functions of the time delay $\tau$ after the ArF laser pulse shot. These dependencies, or the time profiles of the emission lines, have maxima at different delay times $\tau$ ranging from about 10 to 20 $\mu$s. Some examples of time profiles of the observed lines are presented in Fig. 5. The dependence of the time profiles on the

**Table 1.   Comparison Of QDT-Calculated $S$-Values of Cs (this work) With The Experimental And *ab initio* Dirac–Hartree–Fock (DHF) Calculation Results Listed In [26] And The NIST Database [14] (for the $6s – np$ and $6p – 5d$ transitions)**

| $np_j$ level | $6s_{\frac{1}{2}} – np_j$ | | | $8s_{\frac{1}{2}} – np_j$ | |
|---|---|---|---|---|---|
| | This work | DHF [26] | NIST [14] | This work | DHF [26] |
| $6p_{\frac{1}{2}}$ | $1.655 \times 10^1$ | $2.015 \times 10^1$ | $2.023 \times 10^1$ | $9.711 \times 10^{-1}$ | $1.055 \times 10^0$ |
| $6p_{\frac{3}{2}}$ | $3.301 \times 10^1$ | $3.999 \times 10^1$ | $4.009 \times 10^1$ | $1.963 \times 10^0$ | $2.137 \times 10^0$ |
| $7p_{\frac{1}{2}}$ | $6.829 \times 10^{-2}$ | $7.618 \times 10^{-2}$ | $7.59 \times 10^{-2}$ | $8.375 \times 10^1$ | $8.558 \times 10^1$ |
| $7p_{\frac{3}{2}}$ | $2.981 \times 10^{-1}$ | $3.434 \times 10^{-1}$ | $3.44 \times 10^{-1}$ | $1.911 \times 10^2$ | $1.96 \times 10^2$ |
| $8p_{\frac{1}{2}}$ | $5.467 \times 10^{-3}$ | $6.561 \times 10^{-3}$ | $5.22 \times 10^{-3}$ | $3.098 \times 10^2$ | $3.136 \times 10^2$ |
| $8p_{\frac{3}{2}}$ | $4.271 \times 10^{-2}$ | $4.752 \times 10^{-2}$ | $4.44 \times 10^{-2}$ | $5.915 \times 10^2$ | $5.983 \times 10^2$ |
| $9p_{\frac{1}{2}}$ | $9.662 \times 10^{-4}$ | $1.849 \times 10^{-3}$ | $1.04 \times 10^{-3}$ | $3.002 \times 10^0$ | $3.038 \times 10^0$ |
| $9p_{\frac{3}{2}}$ | $1.284 \times 10^{-2}$ | $1.613 \times 10^{-2}$ | $1.33 \times 10^{-2}$ | $8.693 \times 10^0$ | $8.815 \times 10^0$ |
| $10p_{\frac{1}{2}}$ | $2.522 \times 10^{-4}$ | $2.209 \times 10^{-3}$ | $2.64 \times 10^{-4}$ | $4.465 \times 10^{-1}$ | $4.02 \times 10^{-1}$ |
| $10p_{\frac{3}{2}}$ | $5.455 \times 10^{-3}$ | $1.3 \times 10^{-2}$ | $5.21 \times 10^{-3}$ | $1.513 \times 10^0$ | $1.341 \times 10^0$ |
| $11p_{\frac{1}{2}}$ | $8.352 \times 10^{-5}$ | $1.156 \times 10^{-3}$ | $9.16 \times 10^{-5}$ | $1.388 \times 10^0$ | $1.211 \times 10^{-1}$ |
| $11p_{\frac{3}{2}}$ | $2.825 \times 10^{-3}$ | $7.225 \times 10^{-3}$ | $2.8 \times 10^{-3}$ | $5.166 \times 10^{-1}$ | $4.449 \times 10^{-1}$ |
| $12p_{\frac{1}{2}}$ | $3.254 \times 10^{-5}$ | $6.76 \times 10^{-4}$ | $3.93 \times 10^{-5}$ | $6.065 \times 10^{-2}$ | $5.198 \times 10^{-2}$ |
| $12p_{\frac{3}{2}}$ | $1.66 \times 10^{-3}$ | $4.489 \times 10^{-3}$ | $1.59 \times 10^{-3}$ | $2.404 \times 10^{-1}$ | $2.034 \times 10^{-1}$ |
| $13p_{\frac{1}{2}}$ | $1.429 \times 10^{-5}$ | $4.41 \times 10^{-4}$ | $1.79 \times 10^{-5}$ | $3.212 \times 10^{-2}$ | $2.723 \times 10^{-2}$ |
| $13p_{\frac{3}{2}}$ | $1.063 \times 10^{-3}$ | $3.025 \times 10^{-3}$ | $1.04 \times 10^{-3}$ | $1.331 \times 10^{-1}$ | $1.116 \times 10^{-1}$ |
| $14p_{\frac{1}{2}}$ | $6.881 \times 10^{-6}$ | $2.89 \times 10^{-4}$ | $8.86 \times 10^{-6}$ | $1.923 \times 10^{-2}$ | $1.613 \times 10^{-2}$ |
| $14p_{\frac{3}{2}}$ | $7.256 \times 10^{-4}$ | $2.116 \times 10^{-3}$ | $6.28 \times 10^{-4}$ | $8.239 \times 10^{-2}$ | $6.864 \times 10^{-2}$ |
| $15p_{\frac{1}{2}}$ | $3.564 \times 10^{-6}$ | $2.25 \times 10^{-4}$ | $3.4 \times 10^{-6}$ | $1.252 \times 10^{-2}$ | $1.04 \times 10^{-2}$ |
| $15p_{\frac{3}{2}}$ | $5.185 \times 10^{-4}$ | $1.521 \times 10^{-3}$ | $3.9 \times 10^{-4}$ | $5.498 \times 10^{-2}$ | $4.537 \times 10^{-2}$ |
| $6p_j$ level | $6p_j – 5d_{\frac{3}{2}}$ | | $6p_j – 5d_{\frac{5}{2}}$ | |
| | This work | NIST [14] | This work | NIST [14] |
| $6p_{\frac{1}{2}}$ | $4.88 \times 10^1$ | $4.92 \times 10^1$ | | |
| $6p_{\frac{3}{2}}$ | $1.00 \times 10^1$ | $9.97$ | $9.21 \times 10^1$ | $9.84 \times 10^1$ |
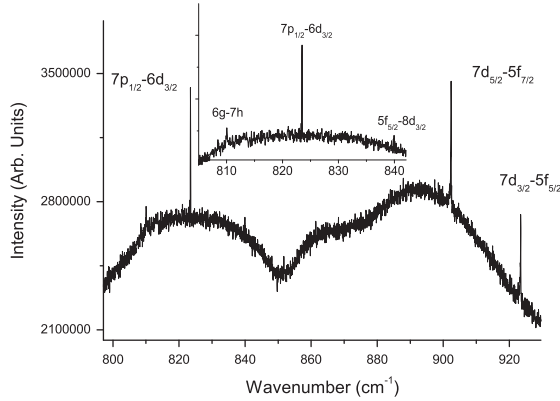
Fig. 4. A part of the recorded Cs emission spectrum (without subtraction of the background blackbody radiation signal component).

distance $L$ between the probed area at the target surface is shown in Fig. 6. Note that for the closest distance $L = 1$ mm, we observed quite high noise in the measured spectra. This is probably due to thermal radiation from the target heated by the laser pulses.

A nonmonotonic decay of the emission intensity shown in Figs. 5 and 6 could be due to the complex population kinetics of the atomic Cs states in the ablation plasma and the transfer processes in ablation products [27,28]. While complete understanding of the time profiles is not necessary for the main results of this work, it seems possible that the profiles may vary with $\tau$ and $L$ in a way that might be useful if one wished to investigate in detail the dynamics of the plasma [29].

The energies $E_k$ of the levels involved in the corresponding transitions can be extracted from the measured $\nu_{ki}$ values. The procedure for extracting the energy values for the levels involved in the observed transitions is briefly described in

**Table 2.** **Cs IR Line Wavenumbers $\nu_{ki}$, Intensities $I_{ki}$, SNRs, FWHMs, And Oscillator Strengths $f_{ik}$ For The Observed Lines. Each of the seven spectral ranges, 800–1000, 1000–1300, 1200–1600, 1600–2000, 2000–3500, 4100–5000, and 5000–7700 cm$^{-1}$, has its own scale of arbitrary units for the emission intensity $I_{ki}$. Only the fractional parts are given for the NIST wavenumber values. The oscillator strengths $f_{ki}$ are calculated using the QDT technique [Eq. (3)]**

| $\nu_{ki}$(cm$^{-1}$), this work | $\nu_{ki}$(cm$^{-1}$), NIST [1] | $I_{ki}$ (arb. u.) | SNR | FWHM (cm$^{-1}$) | Identification | $f_{ki}$ |
|---|---|---|---|---|---|---|
| 642.439(10) | | $2.29 \times 10^4$ | 2.88 | 0.099(37) | $7p_{\frac{3}{2}} - 6d_{\frac{3}{2}}$ | $3.13 \times 10^{-2}$ |
| 685.289(8) | | $2.31 \times 10^4$ | 5.26 | 0.056(21) | $7p_{\frac{3}{2}} - 6d_{\frac{5}{2}}$ | $3.03 \times 10^{-1}$ |
| 810.050(16) | | $2.99 \times 10^4$ | 4.24 | 0.105(43) | $6g - 7h$ | 2.91 |
| 823.478(5) | | $9.23 \times 10^4$ | 6.95 | 0.072(16) | $7p_{\frac{1}{2}} - 6d_{\frac{3}{2}}$ | $3.98 \times 10^{-1}$ |
| 839.938(10) | | $2.14 \times 10^4$ | 6.47 | 0.066(25) | $5f_{\frac{5}{2}} - 8d_{\frac{3}{2}}$ | $2.87 \times 10^{-1}$ |
| 851.739(10) | | $8.82 \times 10^3$ | 3.81 | 0.051(17) | $5f_{\frac{7}{2}} - 8d_{\frac{5}{2}}$ | $3.02 \times 10^{-1}$ |
| 902.367(16) | | $1.41 \times 10^5$ | 1.42 | 0.014(7) | $7d_{\frac{5}{2}} - 5f_{\frac{7}{2}}$ | 1.25 |
| 923.437(11) | | $9.51 \times 10^4$ | 1.55 | 0.030(16) | $7d_{\frac{3}{2}} - 5f_{\frac{5}{2}}$ | 1.33 |
| 1119.152(2) | | $1.12 \times 10^4$ | 3.52 | 0.081(18) | $8p_{\frac{3}{2}} - 9s_{\frac{1}{2}}$ | $4.87 \times 10^{-1}$ |
| 1201.816(8) | | $6.84 \times 10^3$ | 5.35 | 0.083(20) | $8p_{\frac{1}{2}} - 9s_{\frac{1}{2}}$ | $4.63 \times 10^{-1}$ |
| 1348.359(2) | | $6.21 \times 10^3$ | 8.85 | 0.043(7) | $5g - 6h$ | 3.04 |
| 1381.126(3) | | $5.12 \times 10^2$ | 3.35 | 0.041(12) | $5f_{\frac{5}{2}} - 6g_{\frac{7}{2}}$ | 1.13 |
| 1381.277(8) | | $1.52 \times 10^3$ | 2.38 | 0.038(32) | $5f_{\frac{7}{2}} - 6g_{\frac{9}{2}}$ | 1.30 |
| 1391.662(8) | | $4.80 \times 10^3$ | 4.29 | 0.089(26) | $8s_{\frac{1}{2}} - 8p_{\frac{1}{2}}$ | $6.55 \times 10^{-1}$ |
| 1474.332(6) | | $9.68 \times 10^3$ | 6.91 | 0.105(19) | $8s_{\frac{1}{2}} - 8p_{\frac{3}{2}}$ | 1.32 |
| 1575.605(8) | | $3.28 \times 10^3$ | 5.58 | 0.067(25) | $4f_{\frac{5}{2}} - 7d_{\frac{3}{2}}$ | $1.34 \times 10^{-1}$ |
| 1596.726(7) | | $4.29 \times 10^3$ | 5.90 | 0.062(15) | $4f_{\frac{7}{2}} - 7d_{\frac{5}{2}}$ | $1.40 \times 10^{-1}$ |
| 1840.348(5) | | $1.26 \times 10^6$ | 4.60 | 0.110(18) | $6d_{\frac{5}{2}} - 4f_{\frac{7}{2}}$ | $8.23 \times 10^{-1}$ |
| 1883.397(3) | | $6.63 \times 10^6$ | 24.6 | 0.114(8) | $6d_{\frac{3}{2}} - 4f_{\frac{5}{2}}$ | $8.79 \times 10^{-1}$ |
| 2031.380(14) | | $7.08 \times 10^4$ | 3.71 | 0.105(47) | $8p_{\frac{3}{2}} - 8d_{\frac{5}{2}}$ | $2.82 \times 10^{-1}$ |
| 2102.423(12) | | $6.15 \times 10^4$ | 6.12 | 0.099(37) | $8p_{\frac{1}{2}} - 8d_{\frac{3}{2}}$ | $2.63 \times 10^{-1}$ |
| 2370.750(5) | | $6.58 \times 10^3$ | 10.5 | 0.037(19) | $7p_{\frac{3}{2}} - 8s_{\frac{1}{2}}$ | $3.44 \times 10^{-1}$ |
| 2535.825(5) | .8272(160) | $5.99 \times 10^3$ | 3.71 | 0.046(8) | $4f_{\frac{5}{2}} - 5g_{\frac{7}{2}}$ | 1.32 |
| 2536.011(2) | .0113(160) | $8.05 \times 10^3$ | 5.06 | 0.051(5) | $4f_{\frac{7}{2}} - 5g_{\frac{9}{2}}$ | 1.29 |
| 2551.800(6) | .8036(30) | $3.35 \times 10^3$ | 8.75 | 0.066(33) | $7p_{\frac{1}{2}} - 8s_{\frac{1}{2}}$ | $3.25 \times 10^{-1}$ |
| 2766.948(4) | .9518(240) | $1.00 \times 10^5$ | 12.9 | 0.063(2) | $6p_{\frac{3}{2}} - 5d_{\frac{5}{2}}$ | $2.11 \times 10^{-2}$ |
| 2864.529(1) | .5377(300) | $3.52 \times 10^5$ | 4.29 | 0.092(3) | $6p_{\frac{3}{2}} - 5d_{\frac{5}{2}}$ | $2.00 \times 10^{-1}$ |
| 3229.818(7) | .818(30) | $2.77 \times 10^4$ | 5.12 | 0.064(10) | $7s_{\frac{1}{2}} - 7p_{\frac{1}{2}}$ | $4.97 \times 10^{-1}$ |
| 3320.984(1) | .992(30) | $2.96 \times 10^5$ | 9.71 | 0.107(4) | $6p_{\frac{1}{2}} - 5d_{\frac{3}{2}}$ | $2.46 \times 10^{-1}$ |
| 3410.862(4) | .868(30) | $5.27 \times 10^4$ | 5.62 | 0.059(5) | $7s_{\frac{1}{2}} - 7p_{\frac{3}{2}}$ | 1.01 |
| 4122.382(5) | .3801(60) | $7.56 \times 10^4$ | 9.68 | 0.055(28) | $7p_{\frac{3}{2}} - 7d_{\frac{5}{2}}$ | $2.80 \times 10^{-1}$ |
| 4282.499(4) | .5017(90) | $3.02 \times 10^5$ | 4.29 | 0.084(8) | $7p_{\frac{1}{2}} - 7d_{\frac{3}{2}}$ | $2.68 \times 10^{-1}$ |
| 4339.464(10) | .4733(50) | $5.07 \times 10^4$ | 3.93 | 0.038(23) | $6d_{\frac{5}{2}} - 5f_{\frac{7}{2}}$ | $5.12 \times 10^{-2}$ |
| 4382.478(12) | .4894(50) | $1.71 \times 10^4$ | 3.70 | 0.097(40) | $6d_{\frac{3}{2}} - 5f_{\frac{5}{2}}$ | $4.73 \times 10^{-1}$ |
| 4964.280(12) | .2659(50) | $1.48 \times 10^4$ | 5.26 | 0.082(36) | $7p_{\frac{3}{2}} - 9s_{\frac{1}{2}}$ | $2.76 \times 10^{-2}$ |
| 6803.221(5) | .2186(21) | $1.52 \times 10^6$ | 5.37 | 0.081(4) | $6p_{\frac{3}{2}} - 7s_{\frac{1}{2}}$ | $1.93 \times 10^{-1}$ |
| 7173.343(14) | .3044(22) | $2.93 \times 10^4$ | 4.01 | 0.068(42) | $7s_{\frac{1}{2}} - 8p_{\frac{1}{2}}$ | $9.11 \times 10^{-3}$ |
| 7266.091(14) | .0848(30) | $4.58 \times 10^4$ | 3.65 | 0.123(54) | $5d_{\frac{3}{2}} - 7p_{\frac{1}{2}}$ | $2.15 \times 10^{-2}$ |
| 7349.552(6) | .5497(30) | $4.56 \times 10^4$ | 2.80 | 0.056(25) | $5d_{\frac{5}{2}} - 7p_{\frac{3}{2}}$ | $2.12 \times 10^{-2}$ |
| 7357.260(6) | .2644(30) | $6.77 \times 10^5$ | 3.15 | 0.085(12) | $6p_{\frac{1}{2}} - 7s_{\frac{1}{2}}$ | $1.79 \times 10^{-1}$ |
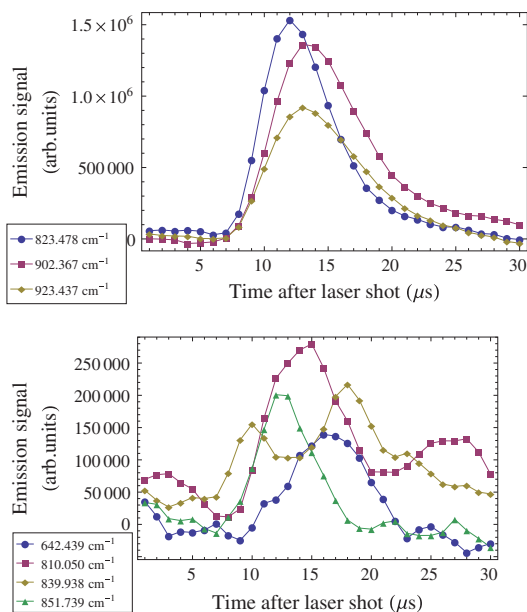
Fig. 5. (Color online) Time profiles of several Cs emission lines for $L = 9$ mm.

**Table 3. Energy Values $E_k$ Of The Cs I Levels Involved In The Observed Transitions**

| Term | $E_k(\mathrm{cm}^{-1})$ | NIST values |
|------|------------------------|-------------|
| 7h | 29162.472(43) | |
| 6h | 28356.426(45) | |
| $8p_{\frac{3}{2}}$ | 25791.480(12) | .508(30) |
| $7p_{\frac{3}{2}}$ | 21946.395(14) | .397(26) |
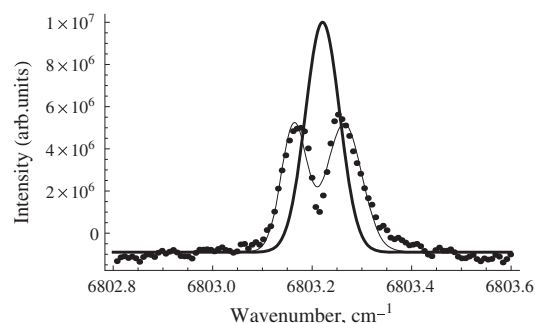


Fig. 7. The $6p_{\frac{3}{2}}$–$7s_{\frac{1}{2}}$ doublet lines of Cs. The hyperfine components are fitted to Gaussian shape (normal curve), and the parameters of the averaged line (bold curves) are calculated according to the authors' previous work [30].

our previous paper [16]. The extracted $E_k$ values coincide within the calculated uncertainties with the level values taken from NIST [1,14]. The latter have far higher precision apart from the $7p_{\frac{3}{2}}$ and $8p_{\frac{3}{2}}$ levels, for which we report values with a slightly lower uncertainty. These values, together with the newly reported $h$-level energies, are presented in Table 3. Our spectral resolution does not allow us to resolve the fine structure of the 6h level. Indeed, the fine-structure separation of $h$ levels should be less than that of $g$ levels. The latter is quite low, while the $5f$ level has fine separation of about $0.15$ cm$^{-1}$ [1], and it is clearly seen from the our measured wavenumbers (see Table 2).

Some of the measured lines (for instance, 6803.221 and 7357.26 cm$^{-1}$) display a hyperfine structure like that shown in the Fig. 7. Note that no hyperfine structure has been mentioned previously in the Cs IR line list [1] where these lines' wavenumbers are reported with a comparatively high precision (of about 0.002–0.01 cm$^{-1}$).

Since, to the authors' knowledge, the dipole transition matrix elements are available only for the transitions listed in Table 1, in this work we make QDT-calculations of these matrix elements (oscillator strengths $f_{ik}$) for the observed transitions in Table 2.

## 4. CONCLUSION

Using FTIR spectroscopy of a plasma formed by ablation of a CsI target by a pulsed nanosecond ArF laser in a vacuum, we report the IR spectrum of atomic cesium in the 800–8000 cm$^{-1}$ region. We have substantially extended the spectral range (as compared to the 1200–1600 cm range measured in our recent work [13]). No spectra of alkali metals were measured previously in the 800–1200 cm$^{-1}$ domain. The recorded spectra allowed us to extract the excitation energy of $5p^6\,7h$ state of Cs (in addition to the $5p^6\,6h$ level reported in our recent paper [13]), which has not been measured before. The other Cs levels extracted from the observed lines are in good agreement with NIST Atomic Spectra Database. We also calculate the probabilities of transitions for the observed lines. We show an asymmetric and multiple-peak behavior of the emission intensity as a function of the time delay after the ablating laser shot and of the distance between the probed area and the target surface. While complete understanding of the time profiles is not necessary for the main results of this work, it seems possible that the profiles may vary with time and location in a way that might be useful if one wished to investigate in detail the dynamics of the plasma.
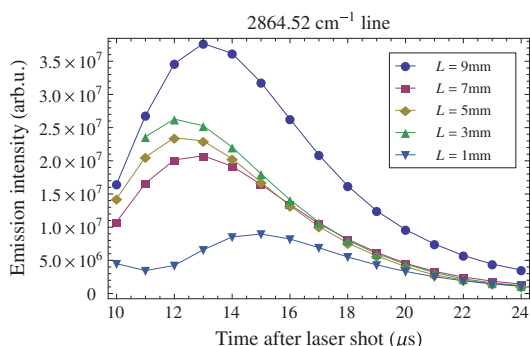


Fig. 6. (Color online) The dependence of the time profile of the 2864.52 cm$^{-1}$ on the distance $L$ between the probed area at the target surface.

## REFERENCES

1. J. E. Sansonetti, "Wavelengths, transition probabilities, and energy levels for the spectra of cesium (Cs I–Cs LV)," J. Phys. Chem. Ref. Data **38**, 761–923 (2009).
2. W. Clark and C. H. Greene, "Adventures of a Rydberg electron in an anisotropic world," Rev. Mod. Phys. **71**, 821–833 (1999).
3. S. A. Napier, D. Cvejanović, J. F. Williams, and L. Pravica, "Effect of electron correlations on the excitation of neutral states of zinc in the autoionizing region: a photon emission study," Phys. Rev. A **78**, 032706 (2008).
4. S. I. Themelis, "Partial widths with interchannel coupling for the P-3(0) Wannier-ridge states of $H^-$," Phys. Rev. A **81**, 064504 (2010).
5. S. R. Lundeen, "Fine structure in high-$L$ Rydberg states: a path to properties of positive ions," in *Advances In Atomic, Molecular, and Optical Physics*, Vol. **52**, P. R. Berman and C. C. Lin, eds. (Academic Press, 2005), pp. 161–208.
6. M. E. Hanni, J. A. Keele, S. R. Lundeen, and W. G. Sturrus, "Microwave spectroscopy of high-$L$ $n = 10$ Rydberg states of argon," Phys. Rev. A **78**, 062510 (2008).
7. J. A. Keele, S. L. Woods, M. E. Hanni, S. R. Lundeen, and W. G. Sturrus, "Optical spectroscopy of high-$l$ Rydberg states of nickel," Phys. Rev. A **81**, 022506 (2010).
8. W.-B. Lee, J.-Y. Wu, Y.-I. Lee, and J. Sneddon, "Recent applications of laser-induced breakdown spectrometry: a review of material approaches," Appl. Spectrosc. Rev. **39**, 27–97 (2004).
9. D. Babánková, S. Civiš, and L. Juha, "Chemical consequences of laser-induced breakdown in molecular gases," Prog. Quantum Electron. **30**, 75–88 (2006).
10. A. Gomes, A. Aubreton, J. J. Gonzalez, and S. Vacquie, "Experimental and theoretical study of the expansion of a metallic vapour plasma produced by laser," J. Phys. D **37**, 689 (2004).
11. O. Barthelemy, J. Margot, M. Chaker, M. Sabsabi, F. Vidal, T. W. Johnston, S. Laville, and B. L. Drogoff, "Influence of the laser parameters on the space and time characteristics of an aluminum laser-induced plasma," Spectrochim. Acta, Part B **60**, 905–914 (2005).
12. C. Aragon and J. A. Aguilera, "Characterization of laser induced plasmas by optical emission spectroscopy: a review of experiments and methods," Spectrochim. Acta, Part B **63**, 893–916 (2008).
13. S. Civiš, P. Kubelík, P. Jelínek, V. E. Chernov, and M. Y. Knyazev, "Atomic cesium 6h states observed by time-resolved FTIR spectroscopy," J. Phys. B **44**, 225006 (2011).
14. Y. Ralchenko, A. Kramida, and J. Reader, and NIST ASD Team, "NIST Atomic Spectra Database (version 4.1.0)" (2011).
15. S. Civiš, I. Matulková, J. Cihelka, K. Kawaguchi, V. E. Chernov, and E. Y. Buslov, "Time-resolved Fourier-transform infrared emission spectroscopy of Au in the 1800–4000−$cm^{-1}$ region: Rydberg transitions," Phys. Rev. A **81**, 012510 (2010).
16. S. Civiš, I. Matulková, J. Cihelka, P. Kubelík, K. Kawaguchi,, and V. E. Chernov, "Time-resolved Fourier-transform infrared emission spectroscopy of Ag in the $(1300−3600)−cm^{-1}$ region: transitions involving $f$ and $g$ states and oscillator strengths," Phys. Rev. A **82**, 022502 (2010).
17. S. Civiš, I. Matulková, J. Cihelka, P. Kubelík, K. Kawaguchi, and V. E. Chernov, "Time-resolved FTIR emission spectroscopy of Cu in the 1800–3800 $cm^{-1}$ region: transitions involving $f$ and $g$ states and oscillator strengths," J. Phys. B **44**, 025002 (2011).
18. K. Kawaguchi, Y. Hama, and S. Nishida, "Time-resolved Fourier transform infrared spectroscopy: application to pulsed discharges," J. Mol. Spectrosc. **232**, 1–13 (2005).
19. "Opus spectroscopy software," http://www.brukeroptics.com/opus.html (2010).
20. A. D. Giacomo, V. Shakhatov, and O. D. Pascale, "Optical emission spectroscopy and modeling of plasma produced by laser ablation of titanium oxides," Spectrochim. Acta, Part B **56**, 753–776 (2001).
21. H. Qi, Y. Sun, X. Liu, X. Hou, and Y. Li, "Spatial spectroscopic diagnose of the plasma produced from laser ablation of a KTA crystal," Laser Phys. Lett. **4**, 212–217 (2007).
22. C. H. Greene, A. R. P. Rau, and U. Fano, "General form of the quantum-defect theory. II," Phys. Rev. A **26**, 2441–2459 (1982).
23. V. Chernov, N. Manakov, and A. Starace, "Exact analytic relation between quantum defects and scattering phases with applications to Green's functions in quantum defect theory," Eur. Phys. J. D **8**, 347–359 (2000).
24. V. E. Chernov, D. L. Dorofeev, I. Y. Kretinin, and B. A. Zon, "Method of the reduced-added Green function in the calculation of atomic polarizabilities," Phys. Rev. A **71**, 022505 (2005).
25. B. N. Chichkov and V. P. Shevelko, "Dipole transitions in atoms and ions with one valence electron," Phys. Scr. **23**, 1055–1065 (1981).
26. A. Sieradzan, M. D. Havey, and M. S. Safronova, "Combined experimental and theoretical study of the $6p^2P_j \rightarrow 8s^2S_{1/2}$ relative transition matrix elements in atomic Cs," Phys. Rev. A **69**, 022502 (2004).
27. A. Khalil and N. Sreenivasan, "Study of experimental and numerical simulation of laser ablation in stainless steel," Laser Phys. Lett. **2**, 445–451 (2005).
28. K. Kawaguchi, N. Sanechika, Y. Nishimura, R. Fujimori, T. N. Oka, Y. Hirahara, A. Jaman, and S. Civiš, "Time-resolved Fourier transform infrared emission spectroscopy of laser ablation products," Chem. Phys. Lett. **463**, 38–41 (2008).
29. M. Rossa, C. A. Rinaldi, and J. C. Ferrero, "Internal state populations and velocity distributions of monatomic species ejected after the 1064 nm laser irradiation of barium," J. Appl. Phys. **105**, 063306 (2009).
30. S. Civiš, I. Matulková, J. Cihelka, P. Kubelík, K. Kawaguchi, and V. E. Chernov, "Low-excited $f$-, $g$- and $h$-states in Au, Ag and Cu observed by Fourier-transform infrared spectroscopy in the 1000–7500 $cm^{-1}$ region," J. Phys. B **44**, 105002 (2011).

**Astronomy & Astrophysics**

# Potassium spectra in the 700–7000 cm⁻¹ domain: Transitions involving f-, g-, and h-states

S. Civiš[1], M. Ferus[1], P. Kubelík[1], P. Jelinek[1], and V. E. Chernov[1,2]

[1] J. Heyrovský Institute of Physical Chemistry, Academy of Sciences of the Czech Republic, Dolejškova 3, 18223 Prague 8, Czech Republic
e-mail: civis@jh-inst.cas.cz

[2] Voronezh State University, 394693 Voronezh, Russia

## ABSTRACT

*Context.* The infrared (IR) range is becoming increasingly important to astronomical studies of cool or dust-obscured objects, such as dwarfs, disks, or planets, and in the extended atmospheres of evolved stars. A general drawback of the IR spectral region is the much lower number of atomic lines available (relative to the visible and ultraviolet ranges).

*Aims.* We attempt to obtain new laboratory spectra to help us identify spectral lines in the IR. This may result in the discovery of new excited atomic levels that are difficult to compute theoretically with high accuracy, hence can be determined solely from IR lines.

*Methods.* The K vapor was formed through the ablation of the KI (potassium iodide) target by a high-repetition-rate (1.0 kHz) pulsed nanosecond ArF laser ($\lambda$ = 193 nm, output energy of 15 mJ) in a vacuum ($10^{-2}$ Torr). The time-resolved emission spectrum of the neutral atomic potassium (K I) was recorded in the 700–7000 cm⁻¹ region using the Fourier transform infrared spectroscopy technique with a resolution of 0.02 cm⁻¹. The $f$-values calculated in the quantum-defect theory approximation are presented for the transitions involving the reported K I levels.

*Results.* Precision laboratory measurements are presented for 38 K I lines in the infrared (including 25 lines not measured previously in the laboratory) range using time-resolved Fourier transform infrared spectroscopy. The 6g, 6h, and 7h levels of K I are observed for the first time, in addition to updated energy values of the other 23 K I levels and the $f$-values for the transitions involving these levels.

*Conclusions.* The recorded wave numbers are in good agreement with the data from the available solar spectrum atlases. Nevertheless, we correct their identification for three lines (1343.699, 1548.559, and 1556.986 cm⁻¹).

**Key words.** atomic data – line: identification – methods: laboratory – infrared: general – techniques: spectroscopic

## 1. Introduction

Understanding the chemical evolution of our Galaxy requires the determination of the element abundances in stars of different metallicities. Potassium is an odd-$Z$ element that is mainly produced in massive stars by explosive oxygen burning (see Zhang et al. 2006b, and references therein).

An analysis of K abundances of 58 metal-poor stars (Zhang et al. 2006b) found that the dependence of [K/Fe] versus [Fe/H] agrees with the theoretical predictions of the chemical evolution models of the Galaxy. The spectroscopic determination of potassium abundances in metal-poor stars is difficult to obtain only because the resonance doublet (K I at 7665 Å and 7699 Å) lines are available in this analysis; moreover, these K I lines are often blended with very strong telluric $O_2$ lines.

Since it is one of the most important references in astronomy, the solar spectrum forms the basis of the description of the chemical evolution of our Galaxy. An analysis of the absorption lines found in the solar spectrum provides detailed information about the isotopic and elemental abundance distribution of a very large number of elements found in the solar system (Lodders 2003).

One of the most important problems of atmospheric line formation, is the assumption of local thermodynamic equilibrium (LTE), which is usually applied to the computation of atomic populations and radiative transfer (Gehren et al. 2001). Non-local thermal equilibrium (NLTE) occurs under high temperatures and low pressures, when the photon absorption rate exceeds the atom-electron collision rate. These conditions occur, for example, in metal-poor stars where electron collisions have lower rates because the free electron density is correlated with metal abundance (Gehren et al. 2001).

The level populations of the atoms with low ionization potentials are particularly sensitive to deviations from LTE. As for other atoms with one electron in the outermost shell, K I has one of the lowest ionization energies (4.34 eV) in the periodic system. Neutral sodium constitutes approximately 0.7% of the sodium atoms under the conditions of the solar photosphere, whereas neutral potassium represents only 0.1%. The photospheric solar potassium abundance based on the theoretical NLTE model atmospheres is $\log \varepsilon_\odot(K) = 5.12 \pm 0.03$ (Zhang et al. 2006a); the Fe abundance is also calculated by accounting for NLTE (Gehren et al. 2001). There are several stellar atmosphere models that predict different photospheric/coronal abundance ratios as a function of ionization potential. Hence, K I abundance can be used to test these models for different stars. For instance, CORONAS-F solar spacecraft measurements (Sylwester et al. 2010) yielded possible values of the coronal abundance of K with a peak at $\log \varepsilon_\odot(K) = 5.86$ and a half-peak range of 5.63–6.09. The latter measurements were based on the resonant line of the He-like K (K XVIII) ion in the X-ray range.

P86

In addition to the optical, UV, and X-ray ranges, the infrared (IR) range is becoming increasingly important to astronomical research, for instance in studies of dust-obscured objects and interstellar clouds, cool objects such as dwarfs, disks, or planets and the extended atmospheres of evolved stars, including objects at cosmological distances from the Earth (Kerber et al. 2009).

The IR spectrum of the most studied object, the Sun, has been recorded from the ground (Wallace et al. 1996) and the stratosphere (Goldman et al. 1996), but, even in the atmospheric window regions, the recorded spectra contain many telluric atmosphere absorption lines. Pure solar IR spectra were recorded by the ATMOS (Atmospheric Trace Molecule Spectroscopy) Fourier transform spectrometer (FTS) during four Space Shuttle missions (Farmer et al. 1989) in the 600–4800 cm$^{-1}$ range at a resolution of 0.01 cm$^{-1}$ ($R = \lambda/\Delta\lambda \sim 6 \times 10^4$–$5 \times 10^5$). A more recent program, the Atmospheric Chemistry Experiment with a space-borne FTS (ACE-FTS), has been performed on board a SCISAT-1 satellite (Hase et al. 2010). The ACE solar atlas covers the 700–4430 cm$^{-1}$ frequency range at a resolution of 0.02 cm$^{-1}$ ($R \sim 2 \times 10^4$–$2 \times 10^5$).

The current space-born spectrographs performing IR studies of objects other than the Sun, have lower spectral resolutions. The *Spitzer* Space Telescope has a resolution of $R \sim 600$ in the $\lambda = 10$–37 micron range (Houck et al. 2004); the AKARI satellite (Murakami et al. 2007) is equipped with a Far-Infrared Surveyor (FTS with resolution $\Delta\nu = 0.19$ cm$^{-1}$) and a near- and mid-IR camera with a resolution of up to $\Delta\lambda = 0.0097$ microns ($R \sim 100$–1000). Nevertheless, the forthcoming spatial and airborne telescopes are expected to have a much higher resolution. For instance, the airborne Stratospheric Observatory For Infrared Astronomy (SOFIA) (Gehrz et al. 2009) is planned to be complemented with the Echelon-cross-Echelle Spectrograph (EXES) with a resolution of $R \sim 10^5$ in the wavelength region of 4.5 to 28.3 microns (Richter et al. 2010). The future SPace Infrared telescope for Cosmology and Astrophysics (SPICA) (Goicoechea et al. 2011) will carry a mid-IR, high resolution spectrometer (MIRHES) operating in the 4–18 micron range with a spectral resolution of $R \sim 3 \times 10^4$.

The great advantages of Fourier transform infrared spectroscopy (FTIR), such as its constant high resolution and energy throughput, have made the IR spectral region more accessible for laboratory spectral measurements (Nilsson 2009). Nevertheless, the powerful capacities of IR astronomy, including the existing VLT with CRyogenic Infra-Red Echelle Spectrograph, (CRIRES) and the future ground-based (e.g., E-ELT) or satellite-borne (e.g., Gaia, 0.33–1.05 micron range) IR telescopes, cannot be fully utilized without detailed spectroscopic information on atomic line features (in particular, wavelengths and oscillator strengths) in the IR region (Biémont 1994; Grevesse & Noels 1994; Pickering 1999; Jorissen 2004; Johansson 2005; Pickering et al. 2011).

A general drawback of the IR spectral region is the much lower number of atomic and ionic lines available (relative to the visible and ultraviolet ranges) (Ryde 2010). Modern laboratory spectral features are lacking for most elements with wavelengths longer than 1 micron (Wahlgren 2011). On the other hand, atlases of stellar spectra often provide only a short list of identified lines (Lobel 2011). Even in the solar IR atlas (Hase et al. 2010), there are a number of lines with doubtful or missing identifications.

New laboratory spectra may help us to identify spectral lines in IR and potentially discover new excited atomic levels. These levels are difficult to compute with high accuracy theoretically, hence they can be determined solely from IR lines

(Wahlgren 2011). The inclusion of additional atomic lines and higher energy levels will increase the reliability of astrophysical calculations such as stellar atmosphere models. For instance, modern analyses of solar chemical compositions (Asplund et al. 2009) measure substantially lower metallicities than determined two decades ago. The use of high-resolution solar spectra (Hase et al. 2010) for the computation of the Sun's irradiance spectrum is still in its initial stage of development (Kurucz 2011).

The above-mentioned development of IR astronomy, together with the lack of high-resolution laboratory data for atomic spectral features, illustrates the importance of reporting new IR atomic lines, highly-excited levels, and oscillator strengths. For instance, the identification of IR atomic lines may be used for reliable temperature, gravity, and abundance analyses for a wide range of ultra-cool dwarfs, from M dwarf stars to brown dwarfs as well as extra-solar giant planets (Lyubchik et al. 2004). A comparison of these atomic lines with computed profiles can be used as key diagnostics of ultra-cool dwarf atmospheres (Lyubchik et al. 2007). Laboratory-measured manganese IR line features were used to determine the Mn abundance in the atmospheres of the Sun, Arcturus, and a dwarf (Blackwell-Whitehead et al. 2011). Together with the molecular IR bands, atomic (including K I) IR lines provide good diagnostics for a self-consistent pure-infrared spectral classification scheme in most cases for both L and T dwarfs (McLean et al. 2003). The investigation of the gravity-sensitive features of atomic (including K I) IR line features was used as a way to distinguish between young and old brown dwarfs (McGovern et al. 2004). Even without a direct application to the stellar atmosphere and abundance models, information on atomic spectral features is in constant demand from the astrophysical community (Raassen et al. 1998; Blackwell-Whitehead et al. 2005; Wallace & Hinkle 2007; Brown et al. 2009; Wallace & Hinkle 2009; Deb & Hibbert 2010; Thorne et al. 2011).

Parts of the spectra in the 800–1800 cm$^{-1}$ (12.5–5.6 microns) range are difficult to observe from the ground owing to the heavy contamination of the spectrum by telluric absorption lines. This infrared spectrum represents a great challenge for laboratory observations of new, unknown infrared atomic transitions involving atomic levels with a high orbital momentum (Civiš et al. 2011b) and their comparison with the available stellar (e.g., solar) spectra. An attempt to fill this gap for K I is made in the present paper.

After K I spectrum measurements were made by Risberg (1956) in the 0.3101–1.1772 $\mu$m range a half of century ago, potassium IR lines were reported by Johansson & Svendenius (1972) who extended the measurements up to 3.735 $\mu$m and by Litzen (1970) who reported the 5g-levels of K I from his measurement of 4.0169 $\mu$m line. In these hollow-cathode measurements, no lines with longer wavelengths were recorded, nor was emission from ng (with $n > 5$) or nh-levels observed. Here, we report the results of a FTIR spectroscopy study of K I transitions in the following IR ranges: 1.4–2.5, 2.7–5.0, 5.9–9.1 and 11.1–14.3 microns.

## 2. Method

Time-resolved FTIR spectroscopy was applied to observing the emission arising after the irradiation of a potassium iodine (KI) target with a pulsed nanosecond ArF ($\lambda = 193$ nm) laser. A high-repetition-rate ArF laser ExciStar S-Industrial V2.0 1000 (193 nm, laser pulse width 12 ns, frequency 1 kHz) with 15 mJ pulse energy was focused on a rotating and linearly traversing target (CsI tablet) with a vacuum chamber (average pressure $10^{-1}$ Torr). The IR emission of the laser plume was measured
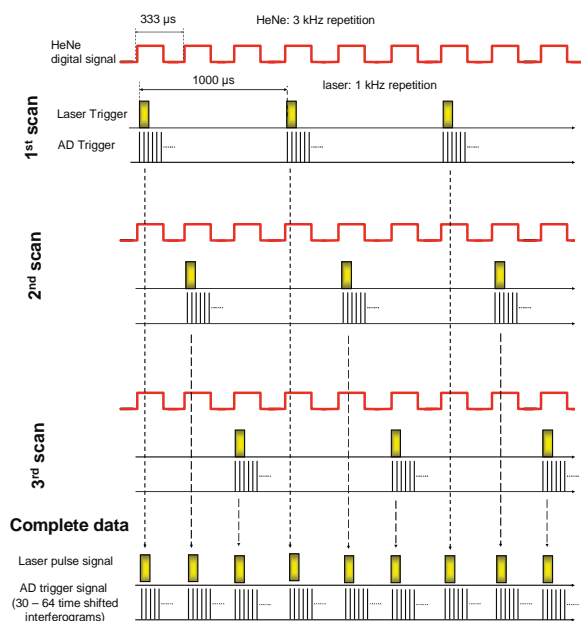
**Fig. 1.** Timing diagram for the interleaved sampling. During the scan, the laser pulse and the AD trigger sampling are induced with a rate of $1/n$ times of the He–Ne laser fringe frequency. The complete interferograms are obtained after $n$ scans ($n = 3$ here).

in the probed area at an axial distance of $L = 9$ mm from the target. The emission from this area was focused into the spectrometer by CaF$_2$ (100 mm) or ZnSe (127 mm) lenses (for the 1600–7700 cm$^{-1}$ or 800–1600 cm$^{-1}$ spectral ranges, respectively). Two different detectors (MCT and InSb) and two beamsplitters (KBr and CaF$_2$) were used to cover the measured spectral range. The measurements were performed with a resolution of 0.017 cm$^{-1}$.

The continuous scanning method was used to measure the time-resolved FTIR spectra. After each ArF laser trigger point, several data points were sampled during the continual movement of the interferometer mirror. The synchronization of the laser ablation, which is the source of the emission, with the signal acquisition requires a special technique. In the case of the common time-resolved FT measurement, the time-shifted signals from a detector are sampled at each zero-crossing point of the HeNe laser fringes. A complication is that the repetition rate lasers suitable for ablation experiments is lower then the frequency of the HeNe laser fringes produced by the interferometer. Therefore, the laser pulse is triggered only in the chosen (every second, third, or fourth etc.) zero-cross point of the HeNe laser fringes. As a result, $1/n$ of each time-resolved interferogram is obtained after each scan Kawaguchi et al. (2005). The timing diagram is shown in Fig. 1, where the time sequence corresponds to the case of $n = 3$; several measurements were performed with the divider $n = 4$. An assembly of the $n$ parts of the interferogram sampled at the same time after the laser pulse provides the complete interferogram. The output of this process is a set of time-resolved interferograms (30–64).

Our system was designed using a field programable gate array (FPGA) processor. The main role of the FPGA processor in our experiment was to initiate a laser pulse and AD trigger signals (the signal for data collection from the detector) synchronously with the He–Ne laser fringe signals from the spectrometer. The FPGA processor also controls the data

transmission from the digital input board to the PC. The width of the ablation laser pulse, as well as the offset value between the beginning of the laser pulse and the data acquisition, can be preset.

In the present experiments, we used a 60 $\mu$s offset followed by the 30 AD trigger acquisition signals covering a 30 $\mu$s interval. The matrix of data signals corresponding to the AD triggers was stored and Fourier-transformed. The acquired interferograms were post-zerofilled using the OPUS Bruker program OPUS (2010) and subsequently corrected by subtracting the blackbody background spectrum. The wavenumbers, line widths, and their intensities were then obtained using the OPUS peak picking procedure. For more details of the experimental setup, we refer to our previous papers (Civiš et al. 2010a; Kawaguchi et al. 2008).

The use of the time-resolved scheme is essential because the emission intensities of the spectral lines depend on the time delay after the ArF laser pulse shot. The maxima of time profiles of the emission lines arise at different delay times $\tau \simeq 3$–10 $\mu$s, hence one should examine a wide time-domain range (0–30 $\mu$s) to avoid missing a line in the resulting spectra. The intensities reported in Table 1 below were obtained as the emission values at the time profile maxima. This non-monotonic decay of the emission intensity could be due to the complex population kinetics of the atomic K I states in the ablation plasma.

Such a complex system was not solely used to excite the spectrum of a neutral atom. Although inexpensive potassium hollow cathode lamps are commercially available, they are apparatuses of quite moderate power used mostly with visible range optics. Their usage in the IR requires substantial modifications (e.g., IR optics and windows). We note that previous hollow-cathode studies of the K I spectrum did not report many of the IR lines that are listed in this work. In addition, our scheme was designed to perform measurements of the IR spectra of several targets, not solely potassium (see our previous results, Civiš et al. 2010a; Civiš et al. 2010b, 2011b).

In this paper we record FTIR spectra in the five spectral ranges of 700–900, 1100–1700, 2000–3700, 4100–5000 and 5000–7000 cm$^{-1}$ (11–14, 5.9–9.1, 2.7–5.0, 2.0–2.4 and 1.4–2.0 $\mu$m, respectively). An InSb detector was used for all spectral domains except the 700–900 and 1100–1700 cm$^{-1}$ domain, where an MCT detector was used. All of the observed emission lines were classified as to transitions between 3p$^6$ $nl_j$ K I levels with $n = 3...7$ and $l = 0...4$. No halogen (Cl, Br, F or I) lines were observed in the recorded emission spectra. The spectral resolution was either 0.1 cm$^{-1}$ (four scans, higher signal-to-noise ratio (S/N)) or 0.017 cm$^{-1}$ (one scan, lower S/N). The acquired interferograms were post-zerofilled (zero filling 2, trapezoid apodization function, for details see, e.g., the book by Stuart 2004) using Bruker OPUS software and subsequently corrected by subtracting the blackbody background spectrum.

The results of the line measurement and assignment are presented in Table 1. The wavenumbers, line widths, and their intensities (as well as the uncertainties in these quantities) were obtained by fitting a Lorentzian line shape.

To identify the observed lines, we assumed that, under LTE conditions and negligible self-absorption (optically thin plasma), the intensity of a spectral line due to radiative transition from the upper state $|k\rangle$ to the lower state $|i\rangle$ is proportional to the line strength $S_{ik}$, which is related to the oscillator strength $f_{ik}$ according to $S_{ik} = \dfrac{3\hbar e^2 g_i}{2m_e \omega_{ik}} f_{ik}$ (Larsson 1983), where $\omega_{ik}$ is $2\pi$ multiplied by the transition frequency, $g_i$ is the degeneracy factor of the lower level, and $m_e$ and $e$ are the electron mass and

**Table 1.** K I lines and their identification.

| Wavenumber (cm$^{-1}$) | Wavelength ($\mu$m) | Intensity (arb. units) | $S/N$ | HWHM (cm$^{-1}$) | Identification | Laborat. | ACE [3][b] |
|---|---|---|---|---|---|---|---|
| 729.694(8) | 13.7006 | $1.41 \times 10^4$ | 5.32 | 0.057(26) | $4d_{\frac{3}{2}}$–$4f_{\frac{5}{2}}$ | | |
| 730.755(6) | 13.6807 | $1.10 \times 10^4$ | 5.04 | 0.048(37) | $4d_{\frac{5}{2}}$–$4f_{\frac{7}{2}}$ | | |
| 795.575(16) | 12.5661 | $5.98 \times 10^3$ | 3.34 | 0.049(60) | $7s_{\frac{1}{2}}$–$7p_{\frac{1}{2}}$ | | |
| 800.081(12) | 12.4953 | $1.15 \times 10^4$ | 5.38 | 0.047(32) | $7s_{\frac{1}{2}}$–$7p_{\frac{3}{2}}$ | | |
| 809.189(12) | 12.3547 | $2.15 \times 10^4$ | 4.33 | 0.107(39) | $6g$ –$7h$ | | |
| 884.125(11) | 11.3075 | $1.63 \times 10^4$ | 4.62 | 0.073(38) | $5d_{\frac{3}{2}}$–$7p_{\frac{1}{2}}$ | | |
| 889.117(8) | 11.2441 | $2.55 \times 10^4$ | 7.70 | 0.075(22) | $5d_{\frac{5}{2}}$–$7p_{\frac{3}{2}}$ | | |
| 1177.545(3) | 8.489930 | $1.86 \times 10^5$ | 35.5 | 0.083(9) | $6p_{\frac{3}{2}}$–$5d_{\frac{5}{2}}$ | | NA / NA /.55 |
| 1178.041(13) | 8.486355 | $1.66 \times 10^4$ | 2.97 | 0.066(57) | $6p_{\frac{3}{2}}$–$5d_{\frac{3}{2}}$ | | |
| 1186.478(2) | 8.426009 | $1.00 \times 10^5$ | 34.9 | 0.071(9) | $6p_{\frac{1}{2}}$–$5d_{\frac{3}{2}}$ | | |
| 1266.577(4) | 7.893144 | $6.16 \times 10^4$ | 17.6 | 0.073(11) | $6p_{\frac{3}{2}}$–$7s_{\frac{1}{2}}$ | | |
| 1275.007(3) | 7.840956 | $3.30 \times 10^4$ | 14.2 | 0.061(15) | $6p_{\frac{1}{2}}$–$7s_{\frac{1}{2}}$ | | |
| 1343.699(4) | 7.440114 | $1.61 \times 10^5$ | 16.1 | 0.136(13) | $5g$ –$6h$ | | .702/.698/.703 (Mg I 6g $^3$G–8h $^3$H) |
| 1352.873(5) | 7.389662 | $5.34 \times 10^4$ | 8.72 | 0.106(17) | $5f$ –$6g$ | | |
| 1548.559(5) | 6.455856 | $1.17 \times 10^5$ | 5.10 | 0.097(17) | $6s_{\frac{1}{2}}$–$6p_{\frac{1}{2}}$ | | .566/.561/.564 (CO 12–11) |
| 1556.986(4) | 6.420915 | $2.10 \times 10^5$ | 15.0 | 0.096(11) | $6s_{\frac{1}{2}}$–$6p_{\frac{3}{2}}$ | | .99/.986/ NA (unassigned) |
| 1601.103(3) | 6.243992 | $9.40 \times 10^4$ | 16.6 | 0.091(11) | $4d_{\frac{3}{2}}$–$6p_{\frac{1}{2}}$ | | |
| 1609.533(12) | 6.211289 | $1.60 \times 10^4$ | 2.60 | 0.083(54) | $4d_{\frac{3}{2}}$–$6p_{\frac{3}{2}}$ | | |
| 1610.601(3) | 6.207170 | $1.72 \times 10^5$ | 30.5 | 0.093(10) | $4d_{\frac{5}{2}}$–$6p_{\frac{3}{2}}$ | | |
| 2057.382(8) | 4.859221 | $8.97 \times 10^2$ | 3.79 | 0.078(24) | $4f_{\frac{7}{2}}$–$5d_{\frac{5}{2}}$ | | |
| 2057.898(15) | 4.858003 | $7.69 \times 10^2$ | 2.68 | 0.086(54) | $4f_{\frac{5}{2}}$–$5d_{\frac{3}{2}}$ | | |
| 2489.439(3) | 4.015874 | $5.40 \times 10^4$ | 7.92 | 0.111(8) | $4f$ –$5g$ | .462 [1] | .446/.438/.46 |
| 2676.927(4) | 3.734608 | $1.11 \times 10^5$ | 4.16 | 0.126(12) | $5p_{\frac{3}{2}}$–$4d_{\frac{5}{2}}$ | .938 [2] | .936/.928/.938 |
| 2678.012(10) | 3.733095 | $8.23 \times 10^3$ | 2.88 | 0.105(34) | $5p_{\frac{3}{2}}$–$4d_{\frac{3}{2}}$ | .008 [2] | .011/.003/.008 |
| 2696.757(3) | 3.707147 | $6.08 \times 10^4$ | 4.23 | 0.123(11) | $5p_{\frac{1}{2}}$–$4d_{\frac{3}{2}}$ | .765 [2] | .767/.759/.765 |
| 2730.542(3) | 3.661278 | $2.87 \times 10^4$ | 5.09 | 0.118(10) | $5p_{\frac{3}{2}}$–$6s_{\frac{1}{2}}$ | .554 [2] | .556/.548/.571 |
| 2749.299(3) | 3.636299 | $1.43 \times 10^4$ | 6.01 | 0.115(11) | $5p_{\frac{1}{2}}$–$6s_{\frac{1}{2}}$ | .309 [2] | .283/.274/.328 |
| 3164.389(4) | 3.159306 | $3.38 \times 10^4$ | 5.07 | 0.118(11) | $3d_{\frac{3}{2}}$–$5p_{\frac{1}{2}}$ | .396 [2] | .401/.392/.394 |
| 3183.135(4) | 3.140700 | $6.32 \times 10^3$ | 4.11 | 0.112(14) | $3d_{\frac{3}{2}}$–$5p_{\frac{3}{2}}$ | .153 [2] | .154/.144/.151 |
| 3185.455(3) | 3.138413 | $6.34 \times 10^4$ | 5.00 | 0.118(10) | $3d_{\frac{5}{2}}$–$5p_{\frac{3}{2}}$ | .461 [2] | .467/.458/.459 |
| 3208.542(7) | 3.115831 | $5.11 \times 10^3$ | 3.36 | 0.104(21) | $4d_{\frac{3}{2}}$–$5f_{\frac{5}{2}}$ | | NA / NA /.583 |
| 3209.628(4) | 3.114776 | $9.90 \times 10^3$ | 5.68 | 0.120(14) | $4d_{\frac{5}{2}}$–$5f_{\frac{7}{2}}$ | | NA / NA /.653 |
| 3674.823(7) | 2.720477 | $1.03 \times 10^3$ | 6.10 | 0.088(20) | $5s_{\frac{1}{2}}$–$5p_{\frac{1}{2}}$ | .827 [2] | .825/.814/.831 |
| 3693.570(4) | 2.706669 | $5.37 \times 10^3$ | 5.20 | 0.107(12) | $5s_{\frac{1}{2}}$–$5p_{\frac{3}{2}}$ | .585 [2] | .58 /.569/.586 |
| 4555.000(8) | 2.194791 | $2.94 \times 10^4$ | 2.99 | 0.058(36) | $4d_{\frac{3}{2}}$–$6f_{\frac{5}{2}}$ | | |
| 4556.057(11) | 2.194281 | $5.55 \times 10^4$ | 3.83 | 0.095(38) | $4d_{\frac{5}{2}}$–$6f_{\frac{7}{2}}$ | | |
| 6590.857(10) | 1.516839 | $1.87 \times 10^5$ | 6.51 | 0.069(16) | $3d_{\frac{3}{2}}$–$4f_{\frac{5}{2}}$ | | |
| 6593.169(3) | 1.516307 | $2.39 \times 10^5$ | 8.89 | 0.069(9) | $3d_{\frac{5}{2}}$–$4f_{\frac{7}{2}}$ | | |

**Notes.** Each of the five spectral ranges (700–900, 1100–1700, 2000–3700, 4100–5000, and 5000–7000 cm$^{-1}$) has its own scale of arbitrary units for the emission intensity. [a] Only the fractional part of the wavenumbers in cm$^{-1}$. [b] Data format: line list 1 (corrected)/line list 1 (observed)/line list 2 (see Hase et al. 2010, Sect. 4). NA means that the line is not listed in the corresponding line list.

**References.** [1] Johansson & Svendenius (1972); [2] Litzen (1970); [3] Hase et al. (2010).

charge, respectively. When LTE is fulfilled and self-absorption is negligible (or properly taken into account), the $f$-values can be determined from the laser-ablation plasma spectra if the temperature of the atom energy distribution is known (Manrique et al. 2011).

Since the atom concentration is low at the low pressures used in our experiment, we can consider our plasma to be optically thin. However, under the same conditions, some deviations from LTE conditions can occur, but the Boltzmann distribution of the atomic populations remains valid (Giacomo et al. 2001), though

with different temperatures for electrons and atoms. This means that even if the observed line intensities display some deviations from the proportionality to the $S$-values, they should describe the qualitative picture of the relative line intensities adequately enough to assign the lines. A typical example of a Boltzmann plot for the ablation plasma can be found in Civiš et al. (2011a). The uncertainty in the excitation temperature is small enough to consider the Boltzmann population distribution to be a satisfactory approximation for our experiment. The moderate deviation of the Boltzmann plot's points away from the straight line

**Table 2.** Comparison of the QDT-calculated (this work) K I oscillator strengths with other works.

| Transition | $\nu$ (cm$^{-1}$) | $\lambda$ ($\mu$)m | $\log(g_i f_{ik})$ | | $f_{ik}$ |
|---|---|---|---|---|---|
| $4s_{\frac{1}{2}}$–$10p_{\frac{3}{2}}$ | 33 411.3986 | 0.299211788 | $-10.8$ | $1.00 \times 10^{-5}$ | $8.46 \times 10^{-6}$ [1] |
| $4s_{\frac{1}{2}}$–$10p_{\frac{1}{2}}$ | 33 410.2306 | 0.299222249 | $-12.$ | $3.22 \times 10^{-6}$ | $2.91 \times 10^{-6}$ [1] |
| $4s_{\frac{1}{2}}$–$9p_{\frac{3}{2}}$ | 32 941.9262 | 0.303476190 | $-10.1$ | $1.99 \times 10^{-5}$ | $1.86 \times 10^{-5}$ [1] |
| $4s_{\frac{1}{2}}$–$9p_{\frac{1}{2}}$ | 32 940.203 | 0.30349207 | $-11.2$ | $6.78 \times 10^{-6}$ | $6.6 \times 10^{-6}$ [1] |
| $4s_{\frac{1}{2}}$–$8p_{\frac{3}{2}}$ | 32 230.11 | 0.3101789 | $-9.29$ | $4.62 \times 10^{-5}$ | $4.68 \times 10^{-5}$ [1] |
| $4s_{\frac{1}{2}}$–$8p_{\frac{1}{2}}$ | 32 227.44 | 0.3102046 | $-10.3$ | $1.69 \times 10^{-5}$ | $1.76 \times 10^{-5}$ [1] |
| $4s_{\frac{1}{2}}$–$7p_{\frac{3}{2}}$ | 31 074.4 | 0.321715 | $-8.21$ | $1.36 \times 10^{-4}$ | $1.54 \times 10^{-4}$ [1] |
| $4s_{\frac{1}{2}}$–$7p_{\frac{1}{2}}$ | 31 069.9 | 0.321762 | $-9.14$ | $5.37 \times 10^{-5}$ | $6.18 \times 10^{-5}$ [1] |
| $4s_{\frac{1}{2}}$–$6p_{\frac{3}{2}}$ | 29 007.71 | 0.3446372 | $-6.74$ | $5.91 \times 10^{-4}$ | $5.92 \times 10^{-4}$ [1] |
| $4s_{\frac{1}{2}}$–$6p_{\frac{1}{2}}$ | 28 999.27 | 0.3447375 | $-7.6$ | $2.51 \times 10^{-4}$ | $2.58 \times 10^{-4}$ [1] |
| $4s_{\frac{1}{2}}$–$5p_{\frac{3}{2}}$ | 24 720.139 | 0.40441422 | $-4.53$ | $5.40 \times 10^{-3}$ | $5.69 \times 10^{-3}$ [1] |
| $4s_{\frac{1}{2}}$–$5p_{\frac{1}{2}}$ | 24 701.382 | 0.40472132 | $-5.31$ | $2.48 \times 10^{-3}$ | $2.63 \times 10^{-3}$ [1] |
| $4p_{\frac{1}{2}}$–$9d_{\frac{3}{2}}$ | 20 586.9392 | 0.485609209 | $-5.92$ | $1.34 \times 10^{-3}$ | $1.3 \times 10^{-3}$ [2] |
| $4p_{\frac{1}{2}}$–$9d_{\frac{3}{2}}$ | 20 529.2289 | 0.486974338 | $-7.49$ | $1.39 \times 10^{-4}$ | $1.2 \times 10^{-4}$ [2] |
| $4p_{\frac{3}{2}}$–$9d_{\frac{5}{2}}$ | 20 529.1632 | 0.486975896 | $-5.29$ | $1.26 \times 10^{-3}$ | $1.1 \times 10^{-3}$ [2] |
| $4p_{\frac{1}{2}}$–$10s_{\frac{1}{2}}$ | 20 229.041 | 0.49420087 | $-6.26$ | $9.52 \times 10^{-4}$ | $7.8 \times 10^{-4}$ [2] |
| $4p_{\frac{1}{2}}$–$8d_{\frac{3}{2}}$ | 20 193.0467 | 0.495081800 | $-5.63$ | $1.79 \times 10^{-3}$ | $1.6 \times 10^{-3}$ [2] |
| $4p_{\frac{3}{2}}$–$10s_{\frac{1}{2}}$ | 20 171.3307 | 0.495614801 | $-5.58$ | $9.47 \times 10^{-4}$ | $7.83 \times 10^{-4}$ [2] |
| $4p_{\frac{3}{2}}$–$8d_{\frac{3}{2}}$ | 20 135.3364 | 0.496500783 | $-7.2$ | $1.86 \times 10^{-4}$ | $1.7 \times 10^{-4}$ [2] |
| $4p_{\frac{3}{2}}$–$8d_{\frac{5}{2}}$ | 20 135.2379 | 0.496503212 | $-5.$ | $1.68 \times 10^{-3}$ | $1.4 \times 10^{-3}$ [2] |
| $4p_{\frac{1}{2}}$–$9s_{\frac{1}{2}}$ | 19 663.1654 | 0.508423398 | $-5.79$ | $1.53 \times 10^{-3}$ | $1.36 \times 10^{-3}$ [2] |
| $4p_{\frac{1}{2}}$–$7d_{\frac{3}{2}}$ | 19 613.258 | 0.50971714 | $-5.35$ | $2.38 \times 10^{-3}$ | $2.3 \times 10^{-3}$ [2] |
| $4p_{\frac{3}{2}}$–$9s_{\frac{1}{2}}$ | 19 605.4551 | 0.509920004 | $-5.1$ | $1.52 \times 10^{-3}$ | $1.4 \times 10^{-3}$ [2] |
| $4p_{\frac{3}{2}}$–$7d_{\frac{3}{2}}$ | 19 555.5477 | 0.511221379 | $-6.92$ | $2.48 \times 10^{-4}$ | $2.2 \times 10^{-4}$ [2] |
| $4p_{\frac{3}{2}}$–$7d_{\frac{5}{2}}$ | 19 555.3921 | 0.511225447 | $-4.71$ | $2.24 \times 10^{-3}$ | $2.1 \times 10^{-3}$ [2] |
| $4p_{\frac{1}{2}}$–$8s_{\frac{1}{2}}$ | 18 780.191 | 0.53232786 | $-5.22$ | $2.71 \times 10^{-3}$ | $2.7 \times 10^{-3}$ [2] |
| $4p_{\frac{3}{2}}$–$8s_{\frac{1}{2}}$ | 18 722.4807 | 0.533968732 | $-4.53$ | $2.70 \times 10^{-3}$ | $2.69 \times 10^{-3}$ [2] |
| $4p_{\frac{1}{2}}$–$6d_{\frac{3}{2}}$ | 18 710.9804 | 0.534296928 | $-5.13$ | $2.96 \times 10^{-3}$ | $3.4 \times 10^{-3}$ [2] |
| $4p_{\frac{3}{2}}$–$6d_{\frac{3}{2}}$ | 18 653.2701 | 0.535949978 | $-6.69$ | $3.10 \times 10^{-4}$ | $3.3 \times 10^{-4}$ [2] |
| $4p_{\frac{3}{2}}$–$6d_{\frac{5}{2}}$ | 18 653.0045 | 0.535957610 | $-4.49$ | $2.81 \times 10^{-3}$ | $3.0 \times 10^{-3}$ [2] |
| $4p_{\frac{1}{2}}$–$7s_{\frac{1}{2}}$ | 17 289.063 | 0.57823999 | $-4.47$ | $5.71 \times 10^{-3}$ | $6.17 \times 10^{-3}$ [2] |
| $4p_{\frac{3}{2}}$–$7s_{\frac{1}{2}}$ | 17 231.3527 | 0.580176621 | $-3.78$ | $5.68 \times 10^{-3}$ | $6.21 \times 10^{-3}$ [2] |
| $4p_{\frac{1}{2}}$–$5d_{\frac{3}{2}}$ | 17 200.5619 | 0.581215207 | $-5.29$ | $2.52 \times 10^{-3}$ | $2.8 \times 10^{-3}$ [2] |
| $4p_{\frac{3}{2}}$–$5d_{\frac{3}{2}}$ | 17 142.8516 | 0.583171849 | $-6.82$ | $2.72 \times 10^{-4}$ | $2.8 \times 10^{-4}$ [2] |
| $4p_{\frac{3}{2}}$–$5d_{\frac{5}{2}}$ | 17 142.3479 | 0.583188985 | $-4.62$ | $2.47 \times 10^{-3}$ | $2.4 \times 10^{-3}$ [2] |
| $4p_{\frac{1}{2}}$–$6s_{\frac{1}{2}}$ | 14 465.5247 | 0.691108150 | $-3.38$ | $1.71 \times 10^{-2}$ | $1.95 \times 10^{-2}$ [2] |
| $4p_{\frac{1}{2}}$–$4d_{\frac{3}{2}}$ | 14 412.961 | 0.69362862 | $-7.08$ | $4.19 \times 10^{-4}$ | $3.8 \times 10^{-4}$ [2] |
| $4p_{\frac{3}{2}}$–$4d_{\frac{3}{2}}$ | 14 355.251 | 0.69641712 | $-9.04$ | $2.96 \times 10^{-5}$ | $3.7 \times 10^{-5}$ [2] |
| $4p_{\frac{3}{2}}$–$4d_{\frac{5}{2}}$ | 14 354.181 | 0.69646903 | $-6.88$ | $2.56 \times 10^{-4}$ | $3.4 \times 10^{-4}$ [2] |
| $4s_{\frac{1}{2}}$–$4p_{\frac{3}{2}}$ | 13 042.896027 | 0.76648991044 | $+0.162$ | $5.88 \times 10^{-1}$ | $6.7 \times 10^{-1}$ [3] |
| $4s_{\frac{1}{2}}$–$4p_{\frac{1}{2}}$ | 12 985.185724 | 0.76989645407 | $-0.534$ | $2.93 \times 10^{-1}$ | $3.33 \times 10^{-1}$ [3] |
| $4p_{\frac{1}{2}}$–$3d_{\frac{3}{2}}$ | 8551.802 | 1.169024 | $+0.536$ | $8.55 \times 10^{-1}$ | $9.02 \times 10^{-1}$ [2] |
| $4p_{\frac{3}{2}}$–$3d_{\frac{3}{2}}$ | 8494.092 | 1.176967 | $-1.07$ | $8.54 \times 10^{-2}$ | $9.02 \times 10^{-2}$ [2] |
| $4p_{\frac{3}{2}}$–$3d_{\frac{5}{2}}$ | 8491.784 | 1.177287 | $+1.12$ | $7.69 \times 10^{-1}$ | $8.08 \times 10^{-1}$ [2] |
| $4p_{\frac{1}{2}}$–$5s_{\frac{1}{2}}$ | 8041.365 | 1.243230 | $-1.07$ | $1.71 \times 10^{-1}$ | $1.8 \times 10^{-1}$ [2] |
| $4p_{\frac{3}{2}}$–$5s_{\frac{1}{2}}$ | 7983.655 | 1.252217 | $-0.374$ | $1.72 \times 10^{-1}$ | $1.83 \times 10^{-1}$ [2] |

**References.** [1]: Shabanova & Khlyustalov (1985a,b); [2]: Villars (1952); [3]: Wang et al. (1997).

can be considered as evidence that $S_{ik}$ values are calculated with enough accuracy (at least to confirm our line identifications).

Using K I atomic-level energy data (Ralchenko et al. 2011, and references therein), we checked all of the transitions in the 700–7000 cm$^{-1}$ range allowed by the electric dipole rules. In the cases of transitions with close wavenumbers, we chose those with greater line strength. For the calculation of the oscillator strengths, we used single-channel quantum defect theory (QDT), which has proved its efficiency for the calculation of first- (Alcheev et al. 2002) and second- (Chernov et al. 2005; Akindinova et al. 2009) order matrix elements in atoms and molecules. We tested our QDT technique by comparing the QDT calculations with the experimental oscillator strengths available at NIST (Ralchenko et al. 2011). The results of this comparison
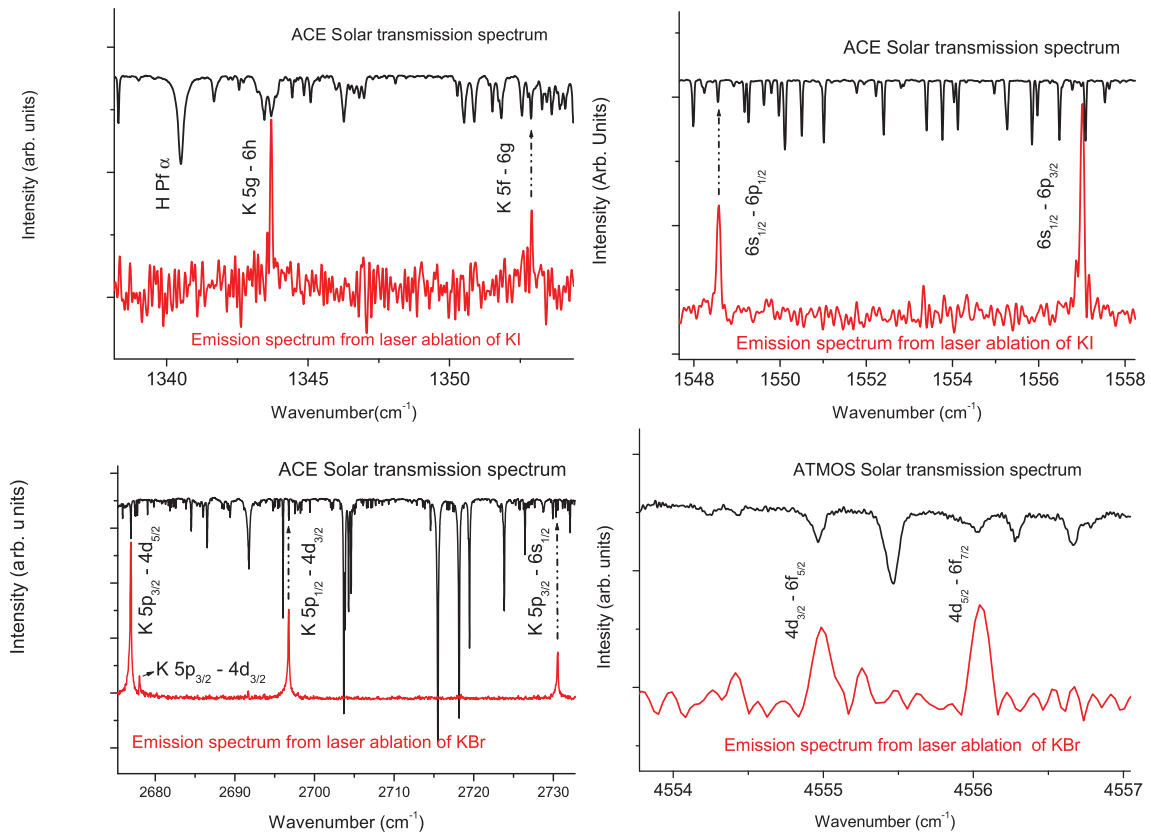
**Fig. 2.** K I emission spectra from the ablation plasma and the Solar spectra recorded from space-born spectrometers.

are presented in Table 2 with references to the original papers. For the majority of K I transitions, the QDT calculations indicate that there is closer agreement with the experimental data of Ralchenko et al. (2011) than the Fues model potential used in our previous works (Civiš et al. 2010a; Civiš et al. 2010b, 2011c). There are a number of other (not listed in Table 2) transitions for which only theoretical $f$-values are available at NIST. These values were calculated (Anderson & Zilitis 1964) using the Coulomb approximation (CA), which is somewhat similar to the QDT and FMP techniques. Some of these CA $f$-values are closer to our FMP values than QDT calculations. We do not present these large data lists here, and give these CA values only for the transitions between the K I levels observed in the present work, which are listed in Table 3. This table was used to classify the observed lines.

After classification, we refined the energy values for some levels involved in the assigned transitions. To this end, we applied a procedure similar to that used in our previous studies (Civiš et al. 2010b, 2011c,b). Table 4 presents some K I revised energy values, $E_i$, and their uncertainties.

## 3. Results

The FTIR spectra of K I were recorded in five spectral regions (700–900, 1100–1700, 2000–3700, 4100–5000, and 5000–7000 cm$^{-1}$). The measured emission lines are presented in Table 1 (with different intensity unit scales for different spectral regions). This table also contains the wavenumbers of some K I lines in the above spectral regions measured both in the laboratories (Litzen 1970; Johansson & Svendenius 1972) and space (the ACE-FTS solar atlas described by Hase et al. 2010). The

ACE-FTS spectral data actually represented as three data lists. The second data list (according to Hase et al. 2010) contains the set of wavenumbers and transitions specified in the graphic ACE atlas pages. A simple analysis shows that the K I line wavenumbers encountered in the data list 2 are simply the Ritz wavenumbers obtained from the K I level energies stored in the NIST database (Ralchenko et al. 2011). The first data list is presented in two variants: (a) the list of observed lines and (b) the corrected (by an empirical calibration factor of 1.00000294) version of the observed data; the correction was made to achieve closer agreement with the line positions specified in the second data list. All three variants (list 1 corrected, list 1 observed and list 2) are compared in Table 1 with the K I lines observed in the present work.

We consider the ACE data list 1 (uncorrected) to be the most relevant to compare with our results since the above correction (by a calibration factor of 1.00000294) was performed in the ACE atlas (Hase et al. 2010) to aid the assignment of the spectral signatures in the ACE solar spectrum with the line positions given in current spectroscopic line-lists. The uncertainty in ACE peak picking is 0.001 cm$^{-1}$, which is better than those of our lines. At the same time, for a number of lines our uncertainties are better than those of the previous laboratory measurements, including the values of 0.005 cm$^{-1}$ in Johansson & Svendenius (1972) and 0.01 cm$^{-1}$ in Litzen (1970). Both of these previous laboratory measurements and our results coincide with ACE data within the corresponding uncertainties. However, our wavenumbers are generally closer to those of ACE compared to the wavenumbers from the previous measurements (Johansson & Svendenius 1972; Litzen 1970).

Some parts of the measured emission spectra in the vicinity of the most prominent lines are shown in Fig. 2 (upper red curve), together with the ACE-FTS or ATMOS solar transmission spectra (upper black curve) in the corresponding ranges. The majority of our emission peaks are lined up with the closest ACE features. As shown in Table 1, the majority of the line wavenumbers measured in the present work in the 2000–3700 cm$^{-1}$ range are in good agreement (within 0.01 cm$^{-1}$) with the values from the non-corrected list 1 of ACE. The spectral regions (4100–5000 and 5000–7000 cm$^{-1}$) are not covered by the ACE atlas. In the 1100–1700 cm$^{-1}$ range, the most prominent line observed in the present work is the 1343.699 cm$^{-1}$ line. According to Table 3, this line should be the most prominent for all of the spectral ranges considered. The ACE data list 2 attributes its identification to the Mg I 6g$^3$G–8h$^3$H transition. This is probably incorrect since the ACE data list 2 identification is based only on a Ritz wavenumber obtained from the NIST database (Hase et al. 2010, Table 3). However, to our knowledge, there has been no report of a measured Mg I line near 1343.7 cm$^{-1}$. Moreover, our preliminary FTIR measurements in the laser ablation of magnesium salts do not show an Mg line at this position. Thus, we consider that the solar 1343.699 cm$^{-1}$ line belongs to K I according to Table 1.

The revised energy values of the K I levels obtained from the present measurement are presented in Table 4. The majority of the energies coincide with the previously reported values within the uncertainty limits. Given the smaller (as compared to the previous measurements) uncertainty in our values for f-, g-, and 7p-level energies, the revised energy values can be considered as the recommended ones.

Table 3 presents the oscillator strengths for the transitions between the 3p$^6$ states of K I observed in the present work. When possible, we also included in Table 3 the $f$-values from the NIST database (Ralchenko et al. 2011). All of these NIST $f$-values were calculated using a Coulomb approximation (Anderson & Zilitis 1964); thus, as one would expect, the majority of these $f$-values are in good (within 10% accuracy) agreement with our QDT calculations, which also use the wave functions with Coulomb asymptotics.

Some transitions listed in this table were not observed in our experiment, and we present them for completeness only. We note that the intensities that are measured are not strictly proportional to the line strengths because the coefficient of this proportionality depends on the upper state population, even for the equilibrium population distribution. For example, in the 1100–1700 cm$^{-1}$ range, the largest line strength corresponds to the 1343.699 cm$^{-1}$ line, while, in our laser-ablated plasma, the 1548.559, 1556.986, and 1610.601 cm$^{-1}$ lines appear to be much more prominent. However, in the solar ACE spectra (Hase et al. 2010), the 1548.559 and 1556.986 cm$^{-1}$ lines are very weak compared to the 1343.699 cm$^{-1}$ line (and the 1610.601 cm$^{-1}$ line does not appear at all in the ACE spectra). Obviously the $f$-values are insufficient for an accurate determination of the intensities of solar lines, which are also determined by the populations of the atomic and ionic states in the line-forming regions of the solar photosphere.

## 4. Conclusion

While current and future satellite-based spectrometers are and will be capable of recording the IR spectra of various objects in almost the full IR range, there are great difficulties in analyzing laboratory IR spectroscopy for wavelengths longer than 5 microns. To our knowledge, there are no laboratory measured

**Table 4.** Revised energy values (cm$^{-1}$) of some levels of K I.

| Level | Present work | Other sources |
|---|---|---|
| 7h | 32768.775(27) | |
| 6h | 31961.001(10) | |
| 6g | 31959.583(20) | |
| 6f$_{\frac{7}{2}}$ | 31953.141(11) | 31953.17(6) (Risberg 1956) |
| 6f$_{\frac{5}{2}}$ | 31953.154(9) | 31953.17(6) (Risberg 1956) |
| 8s$_{\frac{1}{2}}$ | 31765.377(3) | 31765.3767(30) (Thompson et al. 1983) |
| 7p$_{\frac{3}{2}}$ | 31074.378(14) | 31074.40(6) (Risberg 1956) |
| 7p$_{\frac{1}{2}}$ | 31069.865(19) | 31069.90(6) (Risberg 1956) |
| 5g | 30617.306(8) | 30617.31(1) (Litzen 1970) |
| 5f$_{\frac{7}{2}}$ | 30606.710(8) | 30606.73(6) (Risberg 1956) |
| 5f$_{\frac{5}{2}}$ | 30606.700(9) | 30606.73(6) (Risberg 1956) |
| 7s$_{\frac{1}{2}}$ | 30274.252(3) | 30274.2487(30) (Thompson et al. 1983) |
| 5d$_{\frac{3}{2}}$ | 30185.748(3) | 30185.7476(30) (Thompson et al. 1983) |
| 5d$_{\frac{5}{2}}$ | 30185.244(3) | 30185.244(3) (Thompson et al. 1983) |
| 6p$_{\frac{3}{2}}$ | 29007.685(3) | 29007.71(5) (Risberg 1956) |
| 6p$_{\frac{1}{2}}$ | 28999.262(4) | 28999.27(5) (Risberg 1956) |
| 4f$_{\frac{7}{2}}$ | 28127.855(4) | 28127.85(5) (Risberg 1956) |
| 4f$_{\frac{5}{2}}$ | 28127.865(4) | 28127.85(5) (Risberg 1956) |
| 6s$_{\frac{1}{2}}$ | 27450.701(2) | 27450.7104(30) (Thompson et al. 1983) |
| 4d$_{\frac{3}{2}}$ | 27398.152(4) | 27398.147(5) (Johansson & Svendenius 1972) |
| 4d$_{\frac{5}{2}}$ | 27397.079(3) | 27397.077(5) (Johansson & Svendenius 1972) |
| 5p$_{\frac{3}{2}}$ | 24720.142(3) | 24720.139(5) (Johansson & Svendenius 1972) |
| 5p$_{\frac{1}{2}}$ | 24701.390(3) | 24701.382(5) (Johansson & Svendenius 1972) |
| 3d$_{\frac{3}{2}}$ | 21536.997(4) | 21536.988(5) (Johansson & Svendenius 1972) |
| 3d$_{\frac{5}{2}}$ | 21534.683(4) | 21534.680(5) (Johansson & Svendenius 1972) |
| 5s$_{\frac{1}{2}}$ | 21026.560(4) | 21026.551(5) (Johansson & Svendenius 1972) |

spectra of metals above 5.5 microns. In the present work, we have reported the results of an FTIR spectroscopy study of K I transitions in the IR wavelength ranges, 1.4–2.5, 2.7–5.0, 5.9–9.1, and 11.1–14.3 microns. We list 38 IR lines of K I (at a resolution of 0.017 cm$^{-1}$), 25 of which had not been previously experimentally observed in a laboratory. The recorded wave numbers are in good agreement with the data from the ACE solar spectrum. We corrected the ACE identification of three lines (1343.699, 1548.559, and 1556.986 cm$^{-1}$). From the 809.189, 1352.873, and 1343.698 cm$^{-1}$ lines, we report the energy values of the 7h, 6g, and 6h levels, which had not been observed for K I. We also update the energies of another 23 K I levels, most of which had been reported some decades ago. The $f$-values calculated assuming the quantum-defect theory approximation are presented for the transitions involving the reported K I levels. Some of these $f$-values have not been previously calculated, while the others are in good agreement with the $f$-values available from the NIST database.

## References

Akindinova, E. V., Chernov, V. E., Kretinin, I. Y., & Zon, B. A. 2009, Phys. Rev. A, 79, 032506
Alcheev, P. G., Chernov, V. E., & Zon, B. A. 2002, J. Mol. Spectrosc., 211, 71
Anderson, E. M., & Zilitis, V. A. 1964, Opt. Spectrosk., 16, 177
Asplund, M., Grevesse, N., Sauval, A. J., & Scott, P. 2009, ARA&A, 47, 481

Biémont, E. 1994, in Infrared Solar Physics, ed. D. M. Rabin, J. T. Jefferies, & C. Lindsey, Int. Astron. Union (Dordrecht, The Netherlands: Kluwer Academic Publ.), 501, 154th Symposium of the International-Astronomical-Union, 1st International Meeting devoted to Infrared Physics, Tucson, AZ, Mar. 02–06, 1992, IAU Symp., 154,

Blackwell-Whitehead, R. J., Pickering, J. C., Pearse, O., & Nave, G. 2005, ApJS, 157, 402

Blackwell-Whitehead, R., Pavlenko, Y. V., Nave, G., et al. 2011, A&A, 525, A44

Brown, M. S., Federman, S. R., Irving, R. E., Cheng, S., & Curtis, L. J. 2009, ApJ, 702, 880

Chernov, V. E., Dorofeev, D. L., Kretinin, I. Y., & Zon, B. A. 2005, Phys. Rev. A, 71, 022505

Civiš, S., Matulková, I., Cihelka, J., et al. 2010a, Phys. Rev. A, 81, 012510

Civiš, S., Matulková, I., Cihelka, J., et al. 2010b, Phys. Rev. A, 82, 022502

Civiš, S., Kubelík, P., Jelínek, P., Chernov, V. E., & Knyazev, M. Y. 2011a, J. Phys. B, 44, 225006

Civiš, S., Matulková, I., Cihelka, J., et al. 2011b, J. Phys. B, 44, 105002

Civiš, S., Matulková, I., Cihelka, J., et al. 2011c, J. Phys. B, 44, 025002

Deb, N. C., & Hibbert, A. 2010, ApJ, 711, L104

Farmer, C. B., Norton, R. H., & Geller, M. 1989, NASA Reference Publication, 1224

Gehren, T., Butler, K., Mashonkina, L., Reetz, J., & Shi, J. 2001, A&A, 366, 981

Gehrz, R., Becklin, E., de Pater, I., et al. 2009, Adv. Space Res., 44, 413

Giacomo, A. D., Shakhatov, V., & Pascale, O. D. 2001, Spectrochimica Acta Part B: Atomic Spectroscopy, 56, 753, 1st International Conference on Laser-Induced Plasma Spectroscopy and Applications (LIBS 2000), Tirrenia, Italy, Oct. 08–12, 2000

Goicoechea, J. R., Nakagawa, T., & on behalf of the SAFARI/SPICA teams 2011, in Conditions and impact of star formation: New results with Herschel and beyond, The 5th Zermatt ISM Symposium (EDP Sciences)

Goldman, A., Blatherwick, R. D., Murcray, F. J., & Murcray, D. G. 1996, Appl. Opt., 35, 2821

Grevesse, N., & Noels, A. 1994, Phys. Scr., T51, 47

Hase, F., Wallace, L., McLeod, S. D., Harrison, J. J., & Bernath, P. F. 2010, J. Quant. Radiat. Transf., 111, 521

Houck, J. R., Roellig, T. L., van Cleve, J., et al. 2004, ApJS, 154, 18

Johansson, S. 2005, in High Resolution Infrared Spectroscopy In Astronomy, Proceedings, ed. H. U. Kaufl, R. Siebenmorgen, & A. Moorwood, ESO Astrophysics Symposia, ESO (Heidelberger Berlin, Germany: Springer–Verlag Berlin), 62, ESO Workshop on High Resolution Infrared Spectroscopy in Astronomy, Garching, Germany, Nov. 18–21, 2003

Johansson, I., & Svendenius, N. 1972, Phys. Scr., 5, 129

Jorissen, A. 2004, Phys. Scr., T112, 73

Kawaguchi, K., Hama, Y., & Nishida, S. 2005, J. Mol. Spectrosc., 232, 1

Kawaguchi, K., Sanechika, N., Nishimura, Y., et al. 2008, Chem. Phys. Lett., 463, 38

Kerber, F., Nave, G., Sansonetti, C. J., & Bristow, P. 2009, Phys. Scr., T134, 014007

Kurucz, R. L. 2011, Can. J. Phys., 89, 417

Larsson, M. 1983, A&A, 128, 291

Litzen, U. 1970, Phys. Scr., 1, 253

Lobel, A. 2011, Can. J. Phys., 89, 395

Lodders, K. 2003, ApJ, 591, 1220

Lyubchik, Y., Jones, H., Pavlenko, Y., et al. 2004, A&A, 416, 655

Lyubchik, Y., Jones, H. R. A., Pavlenko, Y. V., et al. 2007, A&A, 473, 257

Manrique, J., Aguilera, J., & Aragón, C. 2011, J. Quant. Spec. Radiat. Transf., 112, 85

McGovern, M. R., Kirkpatrick, J. D., McLean, I. S., et al. 2004, ApJ, 600, 1020

McLean, I., McGovern, M., Burgasser, A., et al. 2003, ApJ, 596, 561

Murakami, H., Baba, H., Barthel, P., et al. 2007, PASJ, 59, S369

Nilsson, H. 2009, Phys. Scr., T134, 014009

OPUS 2010, Opus Spectroscopy Software, http://www.brukeroptics.com/opus.html

Pickering, J. C. 1999, Phys. Scr., T83, 27

Pickering, J., Blackwell-Whitehead, R., Thorne, A., Ruffoni, M., & Holmes, C. 2011, Can. J. Phys., 89, 387

Raassen, A. J. J., Pickering, J. C., & Uylings, P. H. M. 1998, A&AS, 130, 541

Ralchenko, Y., Kramida, A., Reader, J., & NIST ASD Team 2011, NIST Atomic Spectra Database (version 4.1.0)

Richter, M. J., Ennico, K. A., McKelvey, M. E., & Seifahrt, A. 2010, Proc. SPIE, 7735, 77356Q

Risberg, P. 1956, Ark. Fys. (Stockholm), 10, 583

Ryde, N. 2010, Astron. Nachr., 331, 433

Shabanova, L. N., & Khlyustalov, A. N. 1985a, Opt. Spectrosk., 59, 207,

Shabanova, L. N., & Khlyustalov, A. N. 1985b, Opt. Spectrosc., 59, 123

Stuart, B. H. 2004, Infrared Spectroscopy: Fundamentals and Applications (Analytical Techniques in the Sciences (AnTs), 1st edn. (Wiley)

Sylwester, J., Sylwester, B., Phillips, K. J. H., & Kuznetsov, V. D. 2010, ApJ, 710, 804

Thompson, D. C., O'Sullivan, M. S., Stoicheff, B. P., & Xu, G. X. 1983, Can. J. Phys., 61, 949

Thorne, A. P., Pickering, J. C., & Semeniuk, J. 2011, ApJS, 192, 11

Villars, D. S. 1952, J. Opt. Soc. Am., 42, 552

Wahlgren, G. M. 2011, Can. J. Phys., 89, 345

Wallace, L., & Hinkle, K. 2007, ApJS, 169, 159

Wallace, L., & Hinkle, K. 2009, ApJ, 700, 720

Wallace, L., Livingston, W., Hinkle, K., & Bernath, P. 1996, ApJS, 106, 165

Wang, H., Li, J., Wang, X. T., et al. 1997, Phys. Rev. A, 55, R1569

Zhang, H. W., Butler, K., Gehren, T., Shi, J. R., & Zhao, G. 2006a, A&A, 453, 723

Zhang, H. W., Gehren, T., Butler, K., Shi, J. R., & Zhao, G. 2006b, A&A, 457, 645

**Table 3.** Calculated oscillator strengths, $f_{ik}$, for the transitions between the 3p$^6$ states of K I observed in the present work.

| Transition | $\nu$ (cm$^{-1}$) | $\lambda$ ($\mu$)m | $\log(g_i f_{ik})$ (QDT) | $f_{ik}$ QDT | $f_{ik}$ NIST |
|---|---|---|---|---|---|
| 3d$_{\frac{5}{2}}$–6f$_{\frac{5}{2}}$ | 10 418.47 | 959.571 | $-3.86$ | $3.52 \times 10^{-3}$ | $3.3 \times 10^{-3}$ |
| 3d$_{\frac{5}{2}}$–6f$_{\frac{7}{2}}$ | 10 418.456 | 959.572 | $-0.863$ | $7.03 \times 10^{-2}$ | $6.4 \times 10^{-2}$ |
| 3d$_{\frac{3}{2}}$–6f$_{\frac{5}{2}}$ | 10 416.157 | 959.784 | $-1.22$ | $7.38 \times 10^{-2}$ | $6.8 \times 10^{-2}$ |
| 5s$_{\frac{1}{2}}$–7p$_{\frac{3}{2}}$ | 10 047.818 | 994.968 | $-4.94$ | $3.57 \times 10^{-3}$ | $4.2 \times 10^{-3}$ |
| 5s$_{\frac{1}{2}}$–7p$_{\frac{1}{2}}$ | 10 043.305 | 995.415 | $-5.71$ | $1.66 \times 10^{-3}$ | $2.1 \times 10^{-3}$ |
| 3d$_{\frac{5}{2}}$–7p$_{\frac{3}{2}}$ | 9539.695 | 1047.96 | $-4.26$ | $2.35 \times 10^{-3}$ | $1.9 \times 10^{-3}$ |
| 3d$_{\frac{3}{2}}$–7p$_{\frac{3}{2}}$ | 9537.381 | 1048.22 | $-6.46$ | $3.92 \times 10^{-4}$ | $3.1 \times 10^{-4}$ |
| 3d$_{\frac{3}{2}}$–7p$_{\frac{1}{2}}$ | 9532.868 | 1048.71 | $-4.86$ | $1.93 \times 10^{-3}$ | $1.6 \times 10^{-3}$ |
| 3d$_{\frac{5}{2}}$–5f$_{\frac{7}{2}}$ | 9072.024 | 1101.99 | $+0.0545$ | $1.76 \times 10^{-1}$ | $1.6 \times 10^{-1}$ |
| 3d$_{\frac{5}{2}}$–5f$_{\frac{5}{2}}$ | 9072.013 | 1101.99 | $-2.94$ | $8.78 \times 10^{-3}$ | $8.0 \times 10^{-3}$ |
| 3d$_{\frac{3}{2}}$–5f$_{\frac{5}{2}}$ | 9069.7 | 1102.27 | $-0.307$ | $1.84 \times 10^{-1}$ | $1.7 \times 10^{-1}$ |
| 5s$_{\frac{1}{2}}$–6p$_{\frac{3}{2}}$ | 7981.119 | 1252.61 | $-3.23$ | $1.98 \times 10^{-2}$ | $2.1 \times 10^{-2}$ |
| 5s$_{\frac{1}{2}}$–6p$_{\frac{1}{2}}$ | 7972.695 | 1253.94 | $-3.97$ | $9.42 \times 10^{-3}$ | $1.1 \times 10^{-2}$ |
| 3d$_{\frac{5}{2}}$–6p$_{\frac{3}{2}}$ | 7473.001 | 1337.78 | $-3.05$ | $7.88 \times 10^{-3}$ | $6.6 \times 10^{-3}$ |
| 3d$_{\frac{3}{2}}$–6p$_{\frac{3}{2}}$ | 7470.688 | 1338.2 | $-5.25$ | $1.31 \times 10^{-3}$ | $1.1 \times 10^{-3}$ |
| 3d$_{\frac{3}{2}}$–6p$_{\frac{1}{2}}$ | 7462.264 | 1339.71 | $-3.65$ | $6.48 \times 10^{-3}$ | $5.5 \times 10^{-3}$ |
| 5p$_{\frac{1}{2}}$–8s$_{\frac{1}{2}}$ | 7063.987 | 1415.24 | $-4.04$ | $8.84 \times 10^{-3}$ | $8.7 \times 10^{-3}$ |
| 5p$_{\frac{3}{2}}$–8s$_{\frac{1}{2}}$ | 7045.235 | 1419.01 | $-3.35$ | $8.77 \times 10^{-3}$ | $8.8 \times 10^{-3}$ |
| 3d$_{\frac{5}{2}}$–4f$_{\frac{5}{2}}$ | 6593.18 | 1516.3 | $-1.45$ | $3.92 \times 10^{-2}$ | $3.4 \times 10^{-2}$ |
| 3d$_{\frac{5}{2}}$–4f$_{\frac{7}{2}}$ | 6593.17 | 1516.31 | $+1.55$ | $7.85 \times 10^{-1}$ | $6.9 \times 10^{-1}$ |
| 3d$_{\frac{3}{2}}$–4f$_{\frac{5}{2}}$ | 6590.867 | 1516.84 | $+1.19$ | $8.24 \times 10^{-1}$ | $7.8 \times 10^{-1}$ |
| 5p$_{\frac{1}{2}}$–7s$_{\frac{1}{2}}$ | 5572.862 | 1793.92 | $-2.92$ | $2.71 \times 10^{-2}$ | $2.7 \times 10^{-2}$ |
| 5p$_{\frac{3}{2}}$–7s$_{\frac{1}{2}}$ | 5554.11 | 1799.98 | $-2.23$ | $2.70 \times 10^{-2}$ | $2.7 \times 10^{-2}$ |
| 5p$_{\frac{1}{2}}$–5d$_{\frac{3}{2}}$ | 5484.357 | 1822.87 | $-4.2$ | $7.49 \times 10^{-3}$ | $7.8 \times 10^{-3}$ |
| 5p$_{\frac{3}{2}}$–5d$_{\frac{3}{2}}$ | 5465.605 | 1829.12 | $-5.9$ | $6.83 \times 10^{-4}$ | $8.0 \times 10^{-4}$ |
| 5p$_{\frac{3}{2}}$–5d$_{\frac{5}{2}}$ | 5465.101 | 1829.29 | $-3.71$ | $6.10 \times 10^{-3}$ | $7.1 \times 10^{-3}$ |
| 4d$_{\frac{5}{2}}$–6f$_{\frac{5}{2}}$ | 4556.075 | 2194.27 | $-3.22$ | $6.65 \times 10^{-3}$ | $6.7 \times 10^{-3}$ |
| 4d$_{\frac{5}{2}}$–6f$_{\frac{7}{2}}$ | 4556.061 | 2194.28 | $-0.226$ | $1.33 \times 10^{-1}$ | $1.3 \times 10^{-1}$ |
| 4d$_{\frac{3}{2}}$–6f$_{\frac{5}{2}}$ | 4555.001 | 2194.79 | $-0.58$ | $1.40 \times 10^{-1}$ | $1.4 \times 10^{-1}$ |
| 4f$_{\frac{7}{2}}$–6g$_{\frac{9}{2}}$ | 3831.728 | 2609.08 | $+0.365$ | $1.80 \times 10^{-1}$ | |
| 4f$_{\frac{7}{2}}$–6g$_{\frac{7}{2}}$ | 3831.728 | 2609.08 | $-3.19$ | $5.15 \times 10^{-3}$ | |
| 4f$_{\frac{5}{2}}$–6g$_{\frac{7}{2}}$ | 3831.718 | 2609.08 | $+0.104$ | $1.85 \times 10^{-1}$ | |
| 5s$_{\frac{1}{2}}$–5p$_{\frac{3}{2}}$ | 3693.577 | 2706.66 | $+0.669$ | $9.76 \times 10^{-1}$ | 1.0 |
| 4d$_{\frac{5}{2}}$–7p$_{\frac{3}{2}}$ | 3677.299 | 2718.65 | $-2.09$ | $2.06 \times 10^{-2}$ | $1.8 \times 10^{-2}$ |
| 4d$_{\frac{3}{2}}$–7p$_{\frac{3}{2}}$ | 3676.226 | 2719.44 | $-4.29$ | $3.44 \times 10^{-3}$ | $3.1 \times 10^{-3}$ |
| 5s$_{\frac{1}{2}}$–5p$_{\frac{1}{2}}$ | 3674.825 | 2720.48 | $-0.0263$ | $4.87 \times 10^{-1}$ | $5.0 \times 10^{-1}$ |
| 4d$_{\frac{3}{2}}$–7p$_{\frac{1}{2}}$ | 3671.713 | 2722.78 | $-2.69$ | $1.70 \times 10^{-2}$ | $1.6 \times 10^{-2}$ |
| 6s$_{\frac{1}{2}}$–7p$_{\frac{3}{2}}$ | 3623.677 | 2758.88 | $-2.72$ | $3.31 \times 10^{-2}$ | |
| 6s$_{\frac{1}{2}}$–7p$_{\frac{1}{2}}$ | 3619.164 | 2762.32 | $-3.45$ | $1.59 \times 10^{-2}$ | |
| 4d$_{\frac{5}{2}}$–5f$_{\frac{7}{2}}$ | 3209.629 | 3114.78 | $+0.858$ | $3.93 \times 10^{-1}$ | $3.9 \times 10^{-1}$ |
| 4d$_{\frac{5}{2}}$–5f$_{\frac{5}{2}}$ | 3209.618 | 3114.79 | $-2.14$ | $1.97 \times 10^{-2}$ | $1.9 \times 10^{-2}$ |
| 4d$_{\frac{3}{2}}$–5f$_{\frac{5}{2}}$ | 3208.544 | 3115.83 | $+0.502$ | $4.13 \times 10^{-1}$ | $4.2 \times 10^{-1}$ |
| 3d$_{\frac{5}{2}}$–5p$_{\frac{3}{2}}$ | 3185.459 | 3138.41 | $-0.0661$ | $1.56 \times 10^{-1}$ | $1.4 \times 10^{-1}$ |
| 3d$_{\frac{3}{2}}$–5p$_{\frac{3}{2}}$ | 3183.146 | 3140.69 | $-2.26$ | $2.61 \times 10^{-2}$ | $2.2 \times 10^{-2}$ |
| 3d$_{\frac{3}{2}}$–5p$_{\frac{1}{2}}$ | 3164.394 | 3159.3 | $-0.646$ | $1.31 \times 10^{-1}$ | $1.1 \times 10^{-1}$ |
| 6p$_{\frac{1}{2}}$–8s$_{\frac{1}{2}}$ | 2766.115 | 3614.19 | $-2.62$ | $3.65 \times 10^{-2}$ | |
| 6p$_{\frac{3}{2}}$–8s$_{\frac{1}{2}}$ | 2757.692 | 3625.23 | $-1.93$ | $3.62 \times 10^{-2}$ | |
| 5p$_{\frac{1}{2}}$–6s$_{\frac{1}{2}}$ | 2749.309 | 3636.29 | $-0.462$ | $3.15 \times 10^{-1}$ | $3.2 \times 10^{-1}$ |
| 5p$_{\frac{3}{2}}$–6s$_{\frac{1}{2}}$ | 2730.557 | 3661.26 | $+0.237$ | $3.17 \times 10^{-1}$ | $3.2 \times 10^{-1}$ |
| 5p$_{\frac{1}{2}}$–4d$_{\frac{3}{2}}$ | 2696.762 | 3707.14 | $+0.892$ | 1.22 | 1.2 |
| 5p$_{\frac{3}{2}}$–4d$_{\frac{3}{2}}$ | 2678.01 | 3733.1 | $-0.717$ | $1.22 \times 10^{-1}$ | $1.2 \times 10^{-1}$ |
| 5p$_{\frac{3}{2}}$–4d$_{\frac{5}{2}}$ | 2676.936 | 3734.6 | $+1.47$ | 1.09 | 1.1 |
| 4f$_{\frac{7}{2}}$–5g$_{\frac{7}{2}}$ | 2489.451 | 4015.85 | $-1.21$ | $3.73 \times 10^{-2}$ | |
| 4f$_{\frac{7}{2}}$–5g$_{\frac{9}{2}}$ | 2489.451 | 4015.85 | $+2.34$ | 1.30 | |

**Table 3.** continued.

| Transition | $\nu$ (cm$^{-1}$) | $\lambda$ ($\mu$m) | $\log(g_i f_{ik})$ (QDT) | $f_{ik}$ QDT | NIST |
|---|---|---|---|---|---|
| $4f_{\frac{5}{2}}$–$5g_{\frac{7}{2}}$ | 2489.441 | 4015.87 | +2.08 | 1.34 | |
| $5g_{\frac{9}{2}}$–$7h_{\frac{9}{2}}$ | 2151.469 | 4646.72 | −3.3 | $3.69 \times 10^{-3}$ | |
| $5g_{\frac{9}{2}}$–$7h_{\frac{11}{2}}$ | 2151.469 | 4646.72 | +0.688 | $1.99 \times 10^{-1}$ | |
| $5g_{\frac{7}{2}}$–$7h_{\frac{9}{2}}$ | 2151.469 | 4646.72 | +0.485 | $2.03 \times 10^{-1}$ | |
| $4f_{\frac{5}{2}}$–$5d_{\frac{3}{2}}$ | 2057.884 | 4858.04 | −1.07 | $5.69 \times 10^{-2}$ | |
| $4f_{\frac{7}{2}}$–$5d_{\frac{5}{2}}$ | 2057.39 | 4859.2 | −0.717 | $6.10 \times 10^{-2}$ | |
| $4f_{\frac{5}{2}}$–$5d_{\frac{5}{2}}$ | 2057.38 | 4859.23 | −3.71 | $4.07 \times 10^{-3}$ | |
| $5d_{\frac{5}{2}}$–$6f_{\frac{5}{2}}$ | 1767.91 | 5654.85 | −2.66 | $1.16 \times 10^{-2}$ | |
| $5d_{\frac{5}{2}}$–$6f_{\frac{7}{2}}$ | 1767.896 | 5654.9 | +0.331 | $2.32 \times 10^{-1}$ | |
| $5d_{\frac{3}{2}}$–$6f_{\frac{5}{2}}$ | 1767.406 | 5656.47 | −0.0243 | $2.44 \times 10^{-1}$ | |
| $4d_{\frac{5}{2}}$–$6p_{\frac{3}{2}}$ | 1610.606 | 6207.15 | +0.627 | $3.12 \times 10^{-1}$ | $3.0 \times 10^{-1}$ |
| $4d_{\frac{3}{2}}$–$6p_{\frac{3}{2}}$ | 1609.532 | 6211.29 | −1.57 | $5.21 \times 10^{-2}$ | $5.0 \times 10^{-2}$ |
| $4d_{\frac{3}{2}}$–$6p_{\frac{1}{2}}$ | 1601.108 | 6243.97 | +0.0431 | $2.61 \times 10^{-1}$ | $2.4 \times 10^{-1}$ |
| $6s_{\frac{1}{2}}$–$6p_{\frac{3}{2}}$ | 1556.985 | 6420.92 | +0.94 | 1.28 | |
| $6s_{\frac{1}{2}}$–$6p_{\frac{1}{2}}$ | 1548.561 | 6455.85 | +0.248 | $6.41 \times 10^{-1}$ | |
| $5f_{\frac{5}{2}}$–$6g_{\frac{7}{2}}$ | 1352.883 | 7389.61 | +1.95 | 1.17 | |
| $5f_{\frac{7}{2}}$–$6g_{\frac{9}{2}}$ | 1352.873 | 7389.66 | +2.21 | 1.14 | |
| $5f_{\frac{7}{2}}$–$6g_{\frac{7}{2}}$ | 1352.873 | 7389.66 | −1.35 | $3.25 \times 10^{-2}$ | |
| $5g_{\frac{7}{2}}$–$6h_{\frac{9}{2}}$ | 1343.698 | 7440.12 | +2.6 | 1.68 | |
| $5g_{\frac{9}{2}}$–$6h_{\frac{11}{2}}$ | 1343.698 | 7440.12 | +2.8 | 1.65 | |
| $5g_{\frac{9}{2}}$–$6h_{\frac{9}{2}}$ | 1343.698 | 7440.12 | −1.19 | $3.05 \times 10^{-2}$ | |
| $5g_{\frac{7}{2}}$–$6f_{\frac{5}{2}}$ | 1335.849 | 7483.84 | −2.77 | $7.85 \times 10^{-3}$ | |
| $5g_{\frac{7}{2}}$–$6f_{\frac{7}{2}}$ | 1335.835 | 7483.91 | −6.06 | $2.91 \times 10^{-4}$ | |
| $5g_{\frac{9}{2}}$–$6f_{\frac{7}{2}}$ | 1335.835 | 7483.91 | −2.51 | $8.14 \times 10^{-3}$ | |
| $6p_{\frac{1}{2}}$–$7s_{\frac{1}{2}}$ | 1274.99 | 7841.06 | −0.0965 | $4.54 \times 10^{-1}$ | |
| $6p_{\frac{3}{2}}$–$7s_{\frac{1}{2}}$ | 1266.567 | 7893.21 | +0.601 | $4.56 \times 10^{-1}$ | |
| $6p_{\frac{1}{2}}$–$5d_{\frac{3}{2}}$ | 1186.487 | 8425.95 | +1.12 | 1.53 | |
| $6p_{\frac{3}{2}}$–$5d_{\frac{3}{2}}$ | 1178.063 | 8486.2 | −0.491 | $1.53 \times 10^{-1}$ | |
| $6p_{\frac{3}{2}}$–$5d_{\frac{5}{2}}$ | 1177.559 | 8489.83 | +1.71 | 1.38 | |
| $5d_{\frac{5}{2}}$–$7p_{\frac{3}{2}}$ | 889.134 | 11 243.8 | +1.02 | $4.64 \times 10^{-1}$ | |
| $5d_{\frac{3}{2}}$–$7p_{\frac{3}{2}}$ | 888.63 | 11 250.2 | −1.17 | $7.74 \times 10^{-2}$ | |
| $5d_{\frac{3}{2}}$–$7p_{\frac{1}{2}}$ | 884.117 | 11 307.6 | +0.44 | $3.88 \times 10^{-1}$ | |
| $6g_{\frac{9}{2}}$–$7h_{\frac{9}{2}}$ | 809.192 | 12 354.6 | −1.3 | $2.72 \times 10^{-2}$ | |
| $6g_{\frac{9}{2}}$–$7h_{\frac{11}{2}}$ | 809.192 | 12 354.6 | +2.69 | 1.47 | |
| $6g_{\frac{7}{2}}$–$7h_{\frac{9}{2}}$ | 809.192 | 12 354.6 | +2.48 | 1.50 | |
| $7s_{\frac{1}{2}}$–$7p_{\frac{3}{2}}$ | 800.126 | 12 494.6 | +1.14 | 1.57 | |
| $7s_{\frac{1}{2}}$–$7p_{\frac{1}{2}}$ | 795.613 | 12 565.5 | +0.454 | $7.87 \times 10^{-1}$ | |
| $4d_{\frac{5}{2}}$–$4f_{\frac{5}{2}}$ | 730.785 | 13 680.2 | −2.25 | $1.76 \times 10^{-2}$ | $1.7 \times 10^{-2}$ |
| $4d_{\frac{5}{2}}$–$4f_{\frac{7}{2}}$ | 730.775 | 13 680.4 | +0.75 | $3.53 \times 10^{-1}$ | $3.3 \times 10^{-1}$ |
| $4d_{\frac{3}{2}}$–$4f_{\frac{5}{2}}$ | 729.711 | 13 700.3 | +0.392 | $3.70 \times 10^{-1}$ | $3.5 \times 10^{-1}$ |
| $7p_{\frac{1}{2}}$–$8s_{\frac{1}{2}}$ | 695.512 | 14 374.0 | +0.167 | $5.91 \times 10^{-1}$ | |
| $7p_{\frac{3}{2}}$–$8s_{\frac{1}{2}}$ | 690.999 | 14 467.9 | +0.864 | $5.93 \times 10^{-1}$ | |
| $5d_{\frac{5}{2}}$–$5f_{\frac{7}{2}}$ | 421.464 | 23 720.4 | +1.42 | $6.87 \times 10^{-1}$ | |
| $5d_{\frac{5}{2}}$–$5f_{\frac{5}{2}}$ | 421.453 | 23 721. | −1.58 | $3.43 \times 10^{-2}$ | |
| $5d_{\frac{3}{2}}$–$5f_{\frac{5}{2}}$ | 420.949 | 23 749.4 | +1.06 | $7.20 \times 10^{-1}$ | |

**Notes.** The Ritz wavenumbers, $\nu$, and air wavelengths, $\lambda$, are calculated using the energy values taken from the present measurement (see Table 4). The NIST $f$-values (last column) were calculated using a Coulomb approximation (Anderson & Zilitis 1964).

Taylor & Francis
Taylor & Francis Group

## RESEARCH ARTICLE

## A study of thermal decomposition and combustion products of disposable polyethylene terephthalate (PET) plastic using high resolution fourier transform infrared spectroscopy, selected ion flow tube mass spectrometry and gas chromatography mass spectrometry

Kristýna Sovová[a], Martin Ferus[ab], Irena Matulková[a], Patrik Španěl[a], Kseniya Dryahina[a], Otto Dvořák[c] and Svatopluk Civiš[a]*

[a]*J. Heyrovský Institute of Physical Chemistry, Academy of Sciences of the Czech Republic, Dolejškova 3, 182 23 Prague 8, Czech Republic Na Slovance;* [b]*Institute of Physics of the Academy of Sciences of the Czech Republic Na Slovance 2, 182 21 Prague 8, Czech Republic;* [c]*Fire Technical Institute, Písková 42, 143 00 Prague, Czech Republic*

The industrial production of poly (ethylene terephthalate), PET, continues to increase and thus it is important to understand the composition of fumes resulting from its disposal as a part of incinerated waste. In this study samples of PET material were combusted in a furnace corresponding to the German standard DIN 53 436 at temperatures of 500°C, 800°C (in an air flow) and also uncontrolled combustion in air. The gaseous products were then analysed using three different analytical methods: high resolution Fourier transform infrared spectroscopy (FTIR), selected ion flow tube mass spectrometry (SIFT-MS) and gas chromatography mass spectrometry (GC-MS). Carbon dioxide, methane, ethylene, acetylene, formaldehyde (methanal) and acetaldehyde (ethanal) were detected by FTIR. Water, methane, acetaldehyde, ethylene, formaldehyde, methanol, acetone, benzene, terephthalic acid, styrene (ethenylbenzene), ethanol, toluene (methylbenzene), xylene (dimethylbenzene), ethylbenzene, naphthalene, biphenyl and phenol concentrations were all quantified by both SIFT-MS and GC-MS. Additionally, the fumes resulting from uncontrolled combustion in air were analysed by FTIR which resolves the rotation–vibration structure of the absorption bands of formaldehyde (2779.90 and 2778.48 $cm^{-1}$) and propane, which was identified from characteristic vibrations of $CH_3$ groups at 2977.00 and 2962.00 $cm^{-1}$. The spectra were compared with reference standards.

**Keywords:** polyethylene terephthalate (PET); combustion; high resolution FTIR spectroscopy; GC-MS, SIFT MS

### 1. Introduction

The production of waste is a fundamental problem from environmental and economic points of view. Approximately 15 million tonnes of used plastic waste are generated every year across Europe. Of this volume, a mere 7% [1–3] is recycled and the remainder is deposited or incinerated [4]. Polyethylene terephthalate (PET, systematic name poly(oxy-1,2-ethanediyl-oxycarbonyl-1,4-phenylenecarbonyl)) is a highly thermally stable polymer with many uses, most frequently as packaging material for beverages [5] in the form of the well known PET bottles. The ideal way of dealing with PET waste is recycling. One of the possible recycling methods for PET is a controlled thermal degradation of PET into oligomers with olefin and carboxylic end-groups [6] including terephthalic acid whilst yielding minimal amounts of carbonaceous residue [3,7]. The terephthalic acid thus obtained

together with other oligomers can subsequently be used in polymerization for the production of recycled materials. Alternatively, there are two commercially available depolymerization methods (methanolysis and glycolysis) available for PET recycling. Both of these methods reduce PET to either a monomer or the original raw materials which can be purified and subsequently re-reacted into 'new' PET for use in a food-contact application, packing for detergents, cosmetics, high-quality carpets, foils, car spare parts or pillow filling for allergic persons [8].

It is worth noting that some polymers are not suitable for recycling, one example being polyethylene, PE, and sometimes for logistic and other reasons PET is not separated from the mixed communal waste. Thus the incineration of carbon-rich wastes is becoming an increasingly attractive alternative to the deposition in landfills, because as much as 90% reduction in volume

[3,9] is achieved. There is a German standard DIN 53,436 [10] in place concerning the combustion of PET and any other plastic materials, which sets the maximum permitted amounts of waste products in the fumes and also gives methods for the testing of their toxicity.

Thermal stability and possible further applications of the degradation products of PET material have been widely studied. Kinetic studies of PET combustion in the presence of various amounts of oxygen and with the temperatures ranging between 25 and 800°C using thermogravimetric analysis (TGA) have recently been conducted [4,11,12]. Other studies have been carried out to identify the products of the thermal decomposition in the temperature range 270–370°C in a $N_2$ inert atmosphere using the MALDI, ^{1}H and ^{13}C NMR methods [13]. Infrared spectroscopy has previously been used to study the products of PET thermal degradation [14] and also to study hydro-thermal degradation under higher pressure [7,15]. Recently, PET degradation by laser ablation was studied using AAS spectrometry, infrared spectroscopy, gel permeation chromatography (GPC) and electron microscopy methods [16]. In one interesting experiment, PET material was also irradiated with $Ar^+$ ions and studied using the Rutherford backscattering (RBS) and elastic recoil detection (ERD) techniques [17].

High resolution Fourier transform infrared (FTIR) spectroscopy has not so far been exploited to study the products of PET thermal decomposition and combustion. Therefore, this paper presents the results of high resolution FTIR characterization of these products, paving the way for wider research into the degradation of other polymers. The same samples were also studied using selected ion flow tube mass spectrometry, SIFT-MS. This mass spectrometry method is based on chemical ionization in a flow tube and is chiefly suitable for absolute quantifications of trace amounts of volatile organic compounds in air in the presence of water vapour. SIFT-MS has been used in various fields of research [18] but this is the first time it has been utilized to study products of polymer combustion. The main objective of this study was to compare the products of thermal decomposition of PET at 500°C, controlled combustion at 800°C and fumes from uncontrolled flame in air as a simulation of imperfect PET incineration.

## 2. Experimental

### 2.1. Thermally uncontrolled combustion of PET

The material from a transparent PET bottle with a volume of 1.5 L was used for a combustion experiment mimicking burning of PET in stoves or home central heating boilers. The exact temperature of the combustion cannot be defined in this situation but it is worth noting that the self-ignition of PET is 600°C. A PET bottle was cut into strips $1 \times 2$ cm in size and weight about 2 g. The gaseous products generated were pumped directly into a vacuum line and trapped in a liquid nitrogen trap and later released into the FTIR absorption cell.

### 2.2. Thermally controlled thermal decomposition and combustion

For the controlled thermal decomposition and combustion experiments a sample of polyethylene terephthalate film ('TENOLAN'), from which PET bottles are made, was used. This time, the material was thermally decomposed and combusted at two temperatures (500°C and 800°C) in the presence of air in an apparatus corresponding to the German standard DIN 53 436. The testing apparatus was set up according to DIN 53 436 (see diagram shown in Figure 1) and consisted of a quartz-glass combustion tube 1 m length and 40 mm diameter, terminated with ball-and-socket ground joints, a quartz-glass boat of 400 mm length $(15 + 1)$ mm diameter wall thickness 1.7 mm holding the sample and a circular furnace of 100 mm width encircling the tube. A motor with a helix gear moved the furnace along the tube at the speed 1 cm/min. The temperature of the furnace was maintained by a regulation module which also controls the furnace motor. The glazed front wall enabled direct observation of the flow of fumes during the process. The compressed air from the laboratory mains passed through a pre-drying cartridge with crystalline $CaCl_2$ and a general-purpose flow meter, calibrated over the desired range of flows. The air flow was regulated using a needle valve to a flow of 150 L/h. Note that this flow entered the tube in the opposite direction to the furnace movement and thus the sample was always exposed to a supply of clean air. The PET samples were supported inside the quartz glass combustion tube by a quartz glass boat, and heated to the preset temperatures 500°C and 800°C. Resulting fumes containing the thermal decomposition and combustion products were introduced via a connecting adapter into a 5 L mixing vessel (placed inside a box thermostat with forced circulation) in which they were kept at 130°C.

Two samples of PET foil of 0.15 mm thickness were cut into $400 \times 20$ mm strips and placed inside the combustion furnace boat always in five layers. The first sample of mass 6.41 g was subjected to flameless
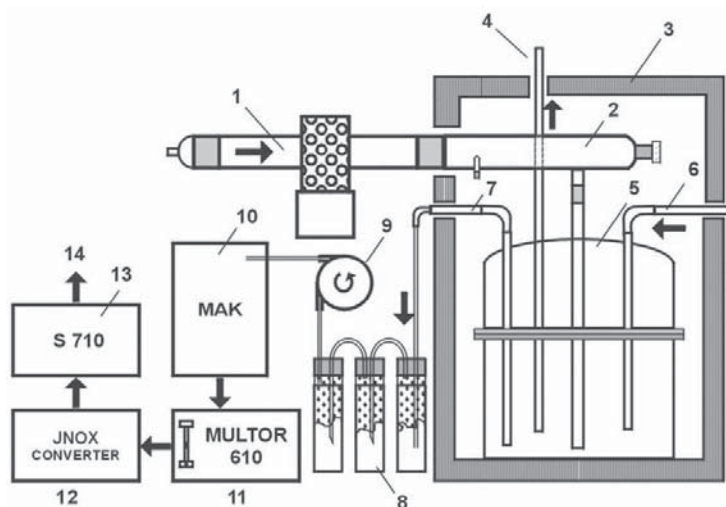
Figure 1. Tube furnace decomposition and sampling apparatus in accordance with DIN 53 436 [10,25]: 1-furnace tube; 2-connecting adapter; 3-heating thermostat; 4-fume outlet; 5-mixing and measurement vessel; 6-dilutent secondary air inlet (not used in the present study); 7-sampling line; 8-particle filters; 9-metering gas pump; 10-refrigerator; 11-CO, $CO_2$ and $O_2$ analyzers; 12-$NO_2$/NO converter; 13-$SO_2$, $NO_X$ and moisture analyzer; 14-exhaust outlet.

thermal decomposition at 500°C and the second sample of mass 6.28 g was combusted in flame at 800°C. As part of the routine protocol elementary composition of the samples was determined as: C 62.86% w/w; H 4.36% w/w; N 0.12% w/w and the stoichiometric ratio of weight of spent oxygen to the weight of fuel calculated according to ISO TR 9122 was $\Psi = 2.0928$. Samples of fumes containing combustion products were taken directly from the mixing vessel into glass volumes with PTF stoppers. The contents of the glass volumes were analysed using FTIR, GC-MS and SIFT-MS.

### 2.3. *FTIR spectroscopy*

The gaseous products of the uncontrolled and controlled combustion of PET samples (at 500°C and 800°C) were released into a vacuum line and trapped in a liquid nitrogen trap. An absorption cell was filled to a pressure of 5.5 Torr by slow re-heating of this trap. The length of the absorption cell was 36.5 cm and the diameter was 5 cm. The spectra were obtained at ambient temperature using the Bruker IFS 120 HR spectrometer in the spectral range 500–7000 cm$^{-1}$. In order to cover the near-infrared (NIR) range a halogen lamp, a CaF$_2$ beam splitter and InSb detector were used, and to cover the middle-IR (MIR) spectral region a glow bar source, KBr beam splitter and

HgCdTe detector were applied. Fifty scans of the spectra were acquired at the resolution of 0.02 cm$^{-1}$ and 0.014 cm$^{-1}$ using the Blackmann–Harris apodization function.

### 2.4. *GC-MS*

The gas chromatograph with mass spectrometer detector (GC-MS) used for this study was a 'Trace GC Ultra-DSQ II' (Thermo Electron Corporation). The parameters of the Rxi$^{TM}$ 5 ms (manufactured by Restek) chromatographic column were: 30 m × 0.25 mm × 0.25 μm. The temperature of the SL/S injector was 235°C, the liner diameter was 5 mm and the temperature range achieved was 37–300°C.

Samples of gases originating from the controlled thermal decomposition and combustion in the quartz combustion furnace were taken directly from its exhaust at the end of the combustion tube. The sampling method used a 500 μL gas-tight syringe preheated to 60°C. The standard method of the direct Head Space analysis was applied. The samples were dosed at 60°C. The volume of the sample dose was always 500 μL for both temperatures (500°C and 800°C). The individual peak assignments seen in the chromatographs were based on the measurements of standards and their comparison with NIST 05 Mass Spectral Libraries for Xcalibur [18].
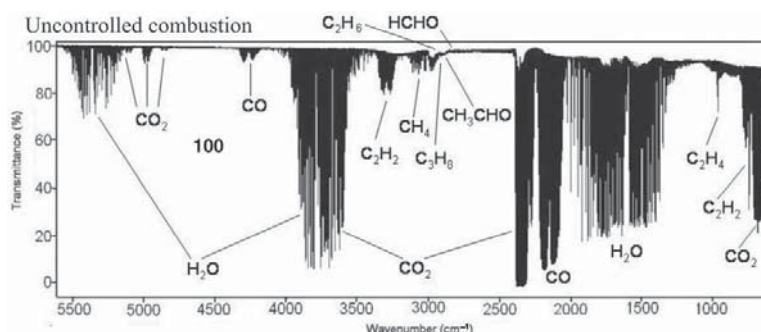
Figure 2. MIR and NIR spectra of the fumes from uncontrolled combustion of PET.

### 2.5. *SIFT-MS*

Selected ion flow tube mass spectrometry (SIFT-MS) is a technique used for simultaneous real-time quantification of several trace gases in air and exhaled breath. It relies on the chemical ionisation of the trace gas molecules in air/breath samples introduced into helium carrier gas, using $H_3O^+$, $NO^+$ and $O_2^+$ reagent (precursor). Reactions between the precursor ions and the trace gas molecules proceed for an accurately defined time, the precursor and product ions being detected and counted by a downstream mass spectrometer. The absolute concentrations of trace gases in single breath exhalation can be determined by SIFT-MS down to parts-per-billion (ppb) levels, obviating sample collection into bags or onto traps [19]. The calibration using chemical standards is not routinely required, as the concentrations are calculated using the known reaction rate constants and the measured flow rates and pressures [20]. For this study samples of the gaseous products of controlled decomposition and combustion were collected in 6 L glass vessels at atmospheric pressure, kept at an ambient temperature of 20°C and introduced into the Profile 3 SIFT-MS instrument (manufactured by Instrument Science Limited, Crewe, UK) via a heated calibrated capillary and full scan mass spectra were obtained by repeated full scans for all three precursor ions. The concentrations of main compounds identified on the mass spectra were calculated from the precursor and product ion count rates, the known carrier gas and sample flow rates and flow tube pressure, according to the general method for the calculation of absolute trace gas concentrations in air from selected ion flow tube mass spectrometry data [20]. The rate coefficients were taken from the kinetic library supplied with the SIFT-MS instrument where available or estimated theoretically [19]. The accuracy of quantification in this complex mixture is estimated to be a factor of about two, +100% −50% of estimated absolute error. The relative precision of the measurement, however, is better estimated at about ±30%. Thus the results provide an order of magnitude of information about the concentrations of the main components of the thermal decomposition and combustion products in the sampled fumes.

## 3. Results and discussion

### 3.1. *FTIR spectroscopy*

In the NIR and MIR spectra of fumes from the uncontrolled combustion (Figure 2), we successfully identified a homologous series of saturated hydrocarbons, which were assigned on the basis of stretching vibrational and rotational modes of C–H groups of methane ($3019 \, cm^{-1}$), ethane (2985, 2969 and $2954 \, cm^{-1}$) and propane (2977 and $2962 \, cm^{-1}$); the unsaturated hydrocarbon ethene, which was verified by the existence of vibrational and rotational bands of the rocking modes of the C–H group at $949 \, cm^{-1}$, and acetylene, whose stretching vibrational and rotational modes of the C–H group were observed at 3374 and $3289 \, cm^{-1}$ and deformation vibrational and rotational bands of the same group at $730 \, cm^{-1}$. The group of aldehydes was represented by acetaldehyde and formaldehyde, whose stretching vibrational and rotational modes of C–H groups lay in the FTIR spectrum at $2715 \, cm^{-1}$ (acetaldehyde) and 2780 and $2778 \, cm^{-1}$ (formaldehyde). The above-listed analysis of the IR spectra was performed using the individual vibrational and rotational lines listed in the HITRAN database [21] and using our database in a Bruker OPUS computer program.

Spectra and the analyses of the products of thermal decomposition of PET in a quartz furnace corresponding to the DIN standard, at the temperature of 500°C (Figure 3(a)) accuracy of were
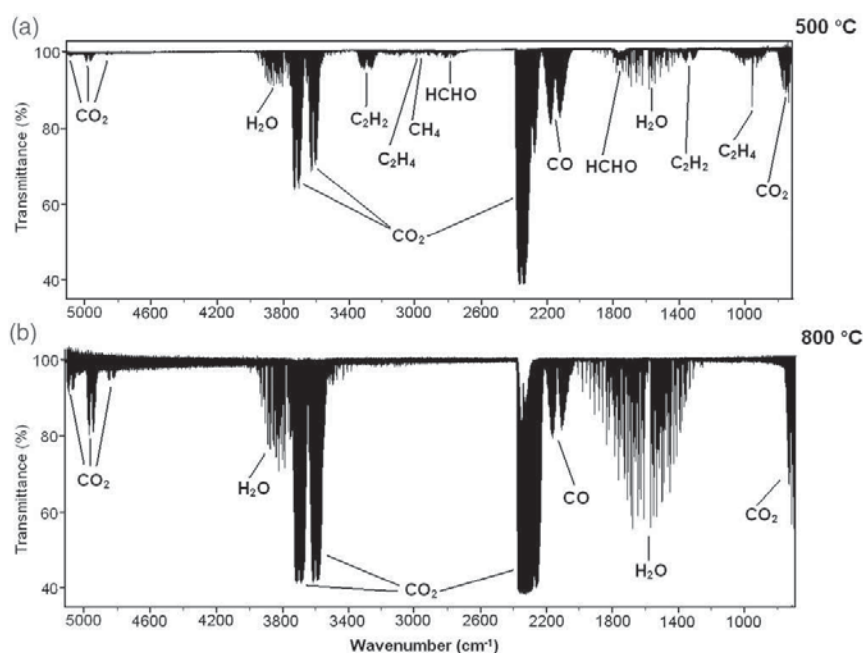
Figure 3. Comparison of the MIR and NIR spectra of fumes from controlled decomposition and combustion of PET at 500°C and 800°C.

similar to uncontrolled combustion. Thus in the FTIR spectra of products of PET decomposed at 500°C, we have identified methane, ethane, ethyne, formaldehyde, carbon dioxide, carbon monoxide and water. Figure 3(b) shows that the PET combustion at 800°C (i.e. above the inflammation point) is a process of more efficient burning and the main combustion products are carbon oxides and water. Carbohydrates and aldehydes appear only in concentrations that are lower than the detection limit of our FTIR method. The main advantage of using the high-resolution FTIR method in comparison with the more commonly used low resolution FTIR spectroscopy (resolution $1–5\,cm^{-1}$) is that it allows one to resolve the detailed structure of the vibrational bands, which often overlap in the spectra of complicated gaseous mixtures. With our high resolution method, we can, for example, differentiate the stretching rotation–vibration lines of C–H bonds in propane from the stretching rotation–vibration lines of C–H in methane (Figure 4).

### 3.2. GC-MS

Table 1 contains the analytical comparison of gaseous components obtained from thermal decomposition at a temperature of 500°C with the combustion products
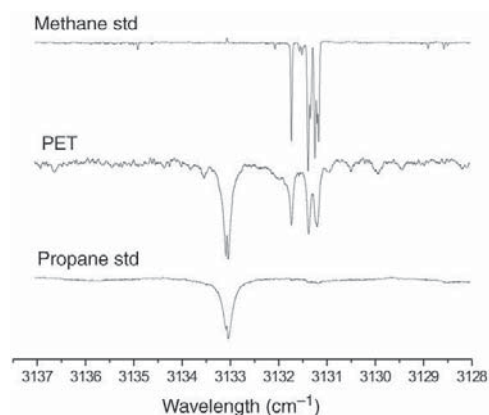


Figure 4. Rotational–vibrational structure in methane and propane (stretching bands of C–H bonds).

obtained at 800°C. Twenty-three organic molecules were identified at 500°C, and at 800°C, there were 21 different compounds. The characteristic groups of GC-MS analysis were aromatic compounds, derivates of benzoic acid, group of phthalates, biphenyles and others. Common products such as styrene, toluene and naphthalene were found in both samples. From the relative abundance of each identified compound in the

Table 1. The assignment of peaks from the gas chromatography.

| | PET film – composition of fumes | 500°C | | 800°C | |
|---|---|---|---|---|---|
| Assign | Name | Area | Ratio | Area | Ratio |
| 1 | Phenyl ethyne | | | 32.9 | 2.59 |
| 2 | Xylene | 76.5 | 0.50 | | |
| 3 | Styrene | 157 | 1.03 | 21.6 | 1.70 |
| 4 | Benzaldehyde | 103 | 0.67 | 18.2 | 1.43 |
| 5 | Phenol | 44 | 0.29 | 19 | 1.50 |
| 6 | Indene | | | 22 | 1.73 |
| 7 | Indane | 16 | 0.10 | | |
| 8 | Phenylacetaldehyde | 20.3 | 0.13 | | |
| 9 | Acetophenone | 44 | 0.29 | 29.8 | 2.35 |
| 10 | Methylbenzoate | 24 | 0.16 | 6.5 | 0.51 |
| 11 | Vinylbenzoate | 962 | 6.29 | 169 | 13.32 |
| 12 | Benzoic acid | 4789 | 31.30 | 192 | 15.14 |
| 13 | Naphthalene | 12,4 | 0.08 | 63.8 | 5.03 |
| 14 | 4-methyl-benzoic acid | 343 | 2.24 | | |
| 15 | 4-ethyl-benzoic acid, phenyl ester | 53.2 | 0.35 | | |
| 16 | 4-ethyl-benzoic acid | 323 | 2.11 | | |
| 17 | Biphenyl | 334 | 2.18 | 268 | 21.13 |
| 18 | 3,4-dimethyl acetophenone | 350 | 2.29 | | |
| 19 | Diphenylmethane | | | 14.9 | 1.17 |
| 20 | Biphenylene | | | 23 | 1.81 |
| 21 | Dibenzofurane | | | 7.1 | 0.56 |
| 22 | 6-methoxyquinoline-*N*-oxide | 553 | 3.61 | 18.4 | 1.45 |
| 23 | Phthalates (group of esters of phthalic and terephthalic acids) | 5864 | 38.33 | 259 | 20.42 |
| 24 | Terephthalic acids | 353 | 2.31 | | |
| 25 | 9-fluorenone | 83 | 0.54 | | |
| 26 | Anthracene | | | 40.2 | 3.17 |
| 27 | 4-bifenyl carboxylic acid | 540 | 3.53 | 42.1 | 3.32 |
| 28 | Pyrene | | | 3.8 | 0.30 |
| 29 | Ethylene dibenzoate | 199 | 1.30 | 13.2 | 1.04 |
| 30 | 1,4-triphenyl | 55 | 0.36 | 4 | 0.32 |
| | Footing: | 15298.4 | 100.00 | 1268.5 | 100.00 |

chromatograms (Figures 5 and 6) it is evident that their abundance at 800°C is lower than that at 500°C. This trend was confirmed also by SIFT-MS analysis (see the next section and Table 2). Exceptions were biphenyle (peak number 17) and naphthalene (peak number 13); their relative abundance was higher in the 800°C sample.

### 3.3. *SIFT-MS*

An analysis of the gaseous products originating from the controlled decomposition and combustion at 500°C and 800°C was carried out using three precursor reagent ions $H_3O^+$, $NO^+$ and $O_2^+$. Several compounds were identified from the characteristic ions present in the $H_3O^+$ spectra (Figure 7). Additionally, the spectra obtained with $NO^+$ and $O_2^+$ precursors were used to quantify those compounds which do not react with the

$H_3O^+$ precursors. The $O_2^+$ spectra were only of a limited value because of the complexity of the mixture and overlap of multiple fragmentation patterns. This has prevented unambiguous identification of more complex organic compounds, however quantification of several hydrocarbons was possible. The compounds identified on the SIFT-MS spectra are listed in Table 2 together with the characteristic product ions and their concentrations calculated for the two temperatures. SIFT-MS can be also used to quantify the concentration of water vapour in the fumes [22] and the results are given in Table 2.

To illustrate how the ions observed on the spectra are related to the compounds present in the analysed gaseous mixture, we will outline the main features of ion chemistry which are involved. The $H_3O^+$ precursor ions are known to react with unsaturated hydrocarbon alkenes ($C_nH_{2n}$) and alkynes ($C_nH_{2n-2}$) [22] and with
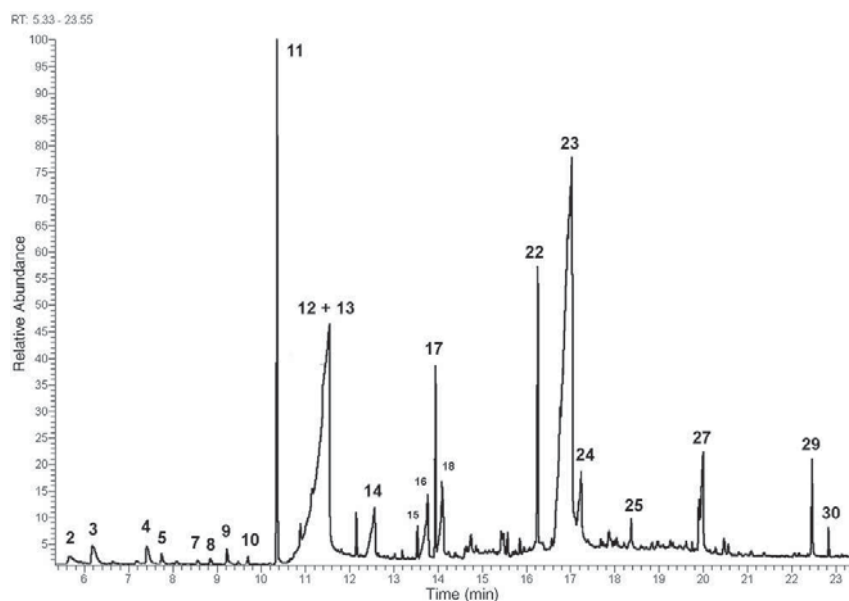
Figure 5. Chromatogram of fumes from controlled decomposition of PET at 500°C.
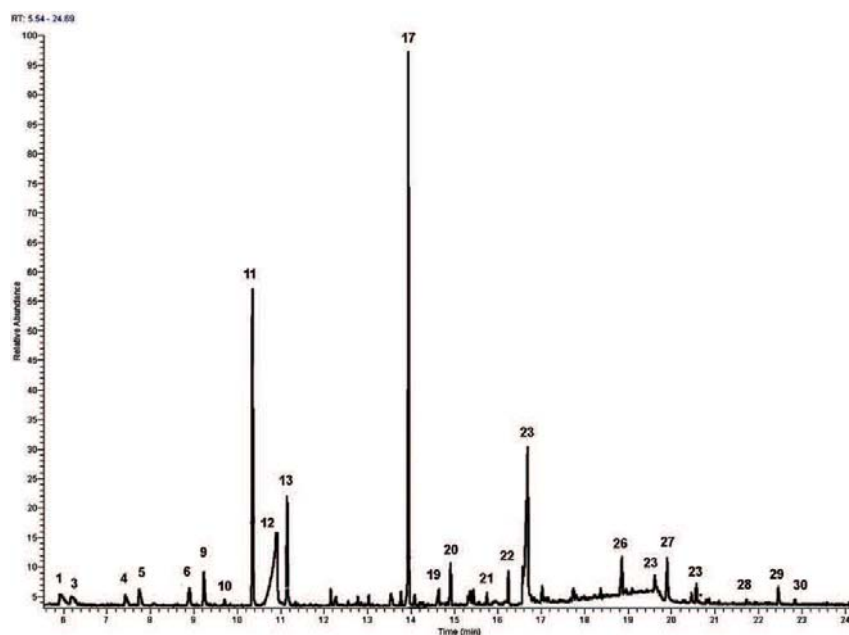


Figure 6. Chromatogram of fumes from controlled combustion of PET at 800°C.

aromatic hydrocarbons by proton transfer leading to the formation of the MH$^+$ product ions.

$$H_3O^+ + M \rightarrow MH^+ + H_2O. \qquad (1)$$
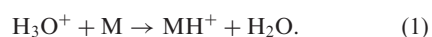
Such proton transfer also occurs with aldehydes, ketones, small alcohols and many other compounds, as is known from many previous studies [22]. However, for styrene and biphenyl (identified by

Table 2. Main compounds identified in the SIFT-MS spectra of fumes of PET thermal decomposition and combustion at 500°C and 800°C. For each compound, the stoichiometric formula is given together with its approximate molecular weight in g/mol, the precursor ions used for chemical ionization, the corresponding mass to charge ratio of the characteristic product ions and their concentrations in fumes analysed at atmospheric pressure in units of parts per million (ppm).

| Name | Formula | Molecular weight g/mol | Precursor Ions | $m/z$ of productions | Ppm 500°C | Ppm 800°C |
|---|---|---|---|---|---|---|
| Water | $H_2O$ | 18 | $H_3O^+$ | 19–37–55 | 700 | 9000 |
| Methane | $CH_4$ | 16 | $O_2^+$ | 47 | 600 | 15 |
| Acetaldehyde | $C_2H_4O$ | 44 | $H_3O^+$ | 45 | 90 | 8 |
| Ethylene | $C_2H_4$ | 28 | $O_2^+$ | 28 | 11 | 3 |
| Formaldehyde | $CH_2O$ | 30 | $H_3O^+$ | 31 | 7 | 4 |
| Methanol | $CH_4O$ | 32 | $H_3O^+$ | 33–51 | 4 | 0.3 |
| Acetone | $C_3H_6O$ | 58 | $H_3O^+$ | 59–77 | 5 | 0.03 |
| | | | $NO^+$ | 88 | | |
| | | | $O_2^+$ | 43–58 | | |
| Benzene | $C_6H_6$ | 78 | $H_3O^+$ | 79 | 4 | 2 |
| | | | $NO^+$ | 78 | | |
| | | | $O_2^+$ | 78 | | |
| Phthalates and terephthalic acid | $C_8H_6O_4$ | 166 | $H_3O^+$ | 149 | 1.4 | 0.7 |
| | | | $NO^+$ | 149 | | |
| | | | $O_2^+$ | 149 | | |
| Styrene | $C_8H_8$ | 104 | $H_3O^+$ | 105 | 0.8 | 0.5 |
| | | | $NO^+$ | 104 | | |
| | | | $O_2^+$ | 104 | | |
| Ethanol | $C_2H_6O$ | 46 | $H_3O^+$ | 47 | 0.6 | 0.3 |
| Toluene | $C_7H_8$ | 92 | $H_3O^+$ | 93 | 0.5 | 0.1 |
| | | | $NO^+$ | 92 | | |
| | | | $O_2^+$ | 92 | | |
| Xylene, ethylbenzene | $C_8H_{10}$ | 106 | $H_3O^+$ | 107 | 0.5 | 0.2 |
| | | | $NO^+$ | 106 | | |
| | | | $O_2^+$ | 106 | | |
| Naphthalene | $C_{10}H_8$ | 128 | $H_3O^+$ | 129 | 0.2 | 0.4 |
| | | | $NO^+$ | 128 | | |
| | | | $O_2^+$ | 128 | | |
| Biphenyl | $C_{12}H_{10}$ | 154 | $H_3O^+$ | 155 | 0.05 | 0.08 |
| | | | $NO^+$ | 154 | | |
| | | | $O_2^+$ | 154 | | |
| Phenol | $C_6H_6O$ | 94 | $H_3O^+$ | 95 | 0 | 0.7 |
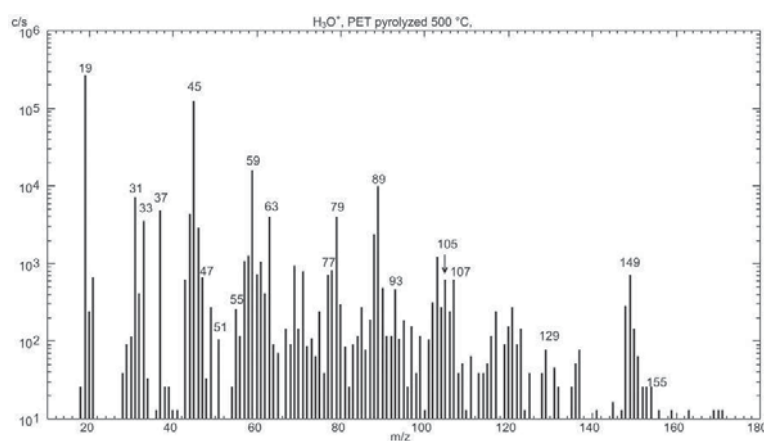


Figure 7. SIFT-MS spectrum obtained for fumes from controlled decomposition of PET at 500°C using the $H_3O^+$ reagent ion. The ion signal intensities are shown on a logarithmic scale in counts per second (c/s) as a function of the mass-to-charge ratios ($m/z$) of the ions.

GC-MS, see Section 3.2) there was so far no knowledge of the SIFT-MS product ions. Thus, we have carried out a quick study of the ion chemistry of these two compounds and found that proton transfer is indeed the only process occurring for both styrene and biphenyl and no fragmentation occurs. In fact all products of $H_3O^+$ reactions identified in Table 2 are protonated molecules $MH^+$. The aromatic hydrocarbons were responsible for the following ions in the $H_3O^+$ mass spectra: $m/z$ 79 (benzene), 93 (toluene) and 107 (xylene, ethylbenzene) and for the ions at $m/z$ 78, 92 and 106 in the $NO^+$ spectra. The ions in the $H_3O^+$ mass spectra at $m/z$ 31 and 49 ($MH^+ \cdot H_2O$) are due to the presence of formaldehyde and the ions at $m/z$ 45 a 89 are characteristic of acetaldehyde. The ions at $m/z$ 89 are proton bound acetaldehyde dimers ($MH^+ \cdot M$). The ions at $m/z$ 33 and 47 are protonated methanol and ethanol, the ions at $m/z$ 59 and 77 correspond to acetone as is confirmed by the presence of ions at $m/z$ 88 ($NO^+ \cdot M$) in the $NO^+$ spectrum.

However, it must be noted that $H_3O^+$ ions do not transfer protons to saturated alkanes and $O_2^+$ precursors may be used for their identification. This is exemplified in the case of methane:

$$O_2^+ + CH_4 \rightarrow CH_3O_2^+ + H. \qquad (2)$$
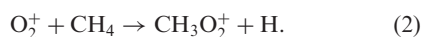
This reaction is unusually slow, the rate coefficient being only $5.2 \times 10^{-12}\,cm^3\,s^{-1}$ [23]. Thus the product ions of the reaction (2) are seen in $O_2^+$ spectra at $m/z$ 47 as characteristic product ions of methane. Ethylene reacts with $O_2^+$ by the charge transfer, thus forming product ion at $m/z$ 28.

Aromatic hydrocarbons undergo charge transfer with both $NO^+$ and $O_2^+$ precursors, thus forming molecular ions $M^+$. Using a combination of $H_3O^+$ and $NO^+$ ions was thus appropriate for the reliable quantification of aromatic hydrocarbons in the fume gas samples.

Inspection of Table 2 reveals that in general concentrations of organic products are lower at the higher combustion temperature 800°C than at a decomposition temperature of 500°C. This conforms to the results of previous studies [4,9]. The exception to this trend is the behaviour of naphthalene and biphenyl, which are seen to be more concentrated in the products of higher temperature combustion. Also there is significantly more water vapour present in the mixture obtained at 800°C. In the present study it was not possible to quantify $CO_2$ using SIFT-MS because the characteristic ion $CO_2.H_3O^+$ overlaps hydrated protonated acetaldehyde at m/z 63, thus exclusion of $CO_2$ from Table 2 does not imply its absence.

## 4. Conclusions

In this study, high resolution FTIR spectroscopy was used for the first time to analyse products of PET thermal decomposition and combustion. The spectra of a series of the products obtained were measured, even under conditions in which their spectral rotation–vibration bands overlap. The results show that high resolution FTIR spectroscopy cannot compete with methods based on mass detection in cases where trace amounts of heavier organic molecules are to be identified. This is because the rotation–vibration spectra of heavy molecules in their gas phase at room temperature are unresolved and their measurement requires the use of sub-Doppler techniques. On the other hand, the advantage of FTIR spectroscopy is that it allows observation of a very broad spectral range and that the intensities of the vibrational bands, mainly the light molecules (water, carbon monoxide, carbon dioxide, methane, formaldehyde etc.), provide a broad view of the thermal decomposition and combustion of PET and its degree of conversion into the final combustion products ($CO_2$ and $H_2O$). Although only a single-pass absorption arrangement (36.5 cm) was used, we were able to detect small concentrations of some organic substances, such as formaldehyde and propane, in the fumes.

The main aim of this work was to compare the products resulting from uncontrolled combustion of PET (burning in stoves and home boilers) with processes in which the physical conditions of the thermal decomposition (500°C) or combustion (800°C) are exactly defined and controlled. The results of this study show that uncontrolled burning in air leads to products that are similar to those from thermal decomposition in a quartz furnace at the temperature of 500°C, i.e. below the PET inflammation point of 600°C. In comparison, the products of PET combustion at 800°C contain mainly carbon oxides, water and the heavier hydrocarbons in significantly lower concentrations. The only two cases where concentration increased at the higher temperature were biphenyle and naphthalene. This was independently indicated by both GC-MS and SIFT-MS results.

From the point of view of the analysis of volatile substances, the gas chromatography method remains the best. The combination of gas chromatography with the mass detection represents a very effective combination of separation and a highly sensitive detection technique. A wide range of aromatic and polyaromatic substances such as the group of phthalates [23] was identified using gas chromatography. Concentrations of these compounds were quantified also using

SIFT-MS and the precision of this technique was sufficiently high to observe significant differences in the composition of the fumes originating from different temperatures of decomposition and combustion.

Finally, it is worth mentioning that FTIR was found to complement mass spectrometry based techniques in identification of methane and $C_2$ hydrocarbons that were not accessible to the GC-MS and SIFT-MS methods used in this study.

This study confirms the utility of the above mentioned combined analysis in providing important information both for incineration purposes and for assessment of fire effluent dangers to persons and the environment.

## Acknowledgements

## References

[1] B.G. Girija, R.R.N. Sailaja, and G. Madras, Polym. Deg. Stab. **90**, 147 (2005).

[2] F. Fraisse, V. Verney, S. Commereuc, *et al.*, Polym. Deg. Stab. **90**, 250 (2005).

[3] T. Masuda, Y. Miwa, A. Tamagawa, *et al.*, Polym. Deg. Stab. **58**, 315 (1997).

[4] I. Martin-Gullón, M. Esperanza, and R. Font, J. Anal. Appl. Pyrolysis **635**, 58 (2001).

[5] F. Villain, J. Coudane, and M. Vert, Polym. Deg. Stab. **43**, 431 (1994).

[6] G. Montaudo, C. Puglisi, and F. Semperi, Polym. Deg. Stab. **42**, 13 (1993).

[7] S.G. Kazarian and G.G. Martirosyan, Phys. Chem. Chem. Phys. **4**, 3759 (2002).

[8] http://www.petpower.nl/plastic-PET-bottles-and-jars/recycling/petpower.aspx#

[9] N.A. García, M.M. Esperanza, and Rafael Font, J. Anal. Appl. Pyrolysis **577**, 68 (2003).

[10] DIN 53 436: Erzeugung thermischer Zersetzungs product e von Werkstoffen unter Luftzufuhr und ihre toxikologische Prüfung. Teil 1. Zersetzungsgerät und Bestimmung der Versuchstemperatur (1981).

[11] J. Yang, R. Miranda, and C. Roy, Polym. Deg. Stab. **73**, 455 (2001).

[12] B. Saha and A.K. Ghoshal, Chem. Eng. J. **111**, 39 (2005).

[13] F. Samperia, C. Puglisia, R. Alicatab, *et al.*, Polym. Deg. Stab. **83**, 3 (2004).

[14] B.J. Holland and J.N. Hay, Polymer **43**, 1835 (2002).

[15] C. Sammon, J. Yarwood, and N. Everall, Polym. Deg. Stab. **67**, 149 (2000).

[16] M. Urbanová, J. Šubrt, A. Galíková, *et al.*, Polym. Deg. Stab. **91**, 2318 (2006).

[17] V. Hnatowicz, V. Peřina, V. Havránek, *et al.*, Nucl. Instr. Meth. Phys. Res. B **161**, 1099 (2000).

[18] NIST/EPA/NIH *Mass Spectral Library with Search Program* (National Institute of Standards and Technology).

[19] P. Spanel and D. Smith, Eur. J. Mass Spectrom. **13**, 77 (2007).

[20] P. Spanel, K. Dryahina, and D. Smith, Int. J. Mass Spectrom. **249**, 230 (2006).

[21] The HITRAN Database, http://cfa-www.harvard.edu/HITRAN/

[22] D. Smith and P. Spanel, Mass Spectrom. Rev. **24**, 661 (2005).

[23] V.G. Anicich, *An Index of the Literature for Bimolecular Gas Phase Cation–Molecule Reaction Kinetics* (JPL-Publication, Pasadena, 2003).

[24] S.V. Leivadara, A.D. Nikolaou, and T.D. Lekkas, Food Chem. **108**, 277 (2008).

[25] O. Dvořák and V. Charvátová, Research on dangerous effects of fire effluents from materials. Final research report, Fire Technical Institute, Prague (1999).

Referát

# FORMALDEHYD V ŽIVOTNÍM PROSTŘEDÍ – STANOVENÍ FORMALDEHYDU METODOU LASEROVÉ A FOTOAKUSTICKÉ DETEKCE

**MARTIN FERUS**[a,b]**, JAROSLAV CIHELKA**[a,b] **a SVATOPLUK CIVIŠ**[a]

*[a] Ústav fyzikální chemie Jaroslava Heyrovského v.v.i., Akademie věd České republiky, Dolejškova 3, 128 23 Praha 8, [b] Fyzikální ústav v .v. i., Akademie věd České republiky, Na Slovance 2, 182 21 Praha 8*
civis@jh-inst.cas.cz

Došlo 19.7.07, přijato 7.11.07.

---

## Obsah

## 1. Formaldehyd v životním prostředí

Formaldehyd je nejvíce zastoupenou karbonylovou sloučeninou v zemské atmosféře a byl detegován i v mezihvězdném prostoru[1]. Je zařazen do skupiny těkavých organických látek (tzv. VOC), které jsou v přírodě běžně emitovány do atmosféry. Jejich významným zdrojem je rovněž činnost člověka. Přirozená koncentrace formaldehydu ve vzduchu[2] činí průměrně 0,5 µg m^{−3}, ve městech se pohybuje v hodnotách desítek µg m^{−3}.

Zdrojem formaldehydu ve vnějším prostředí jsou zejména spalovací procesy, ve kterých je formaldehyd produkován radikálovými reakcemi, např.:

$$CH_4 = H\cdot + \cdot CH_3$$
$$\cdot CH_3 + \cdot O = CH_2O + H\cdot$$
$$\cdot CH_3 + O_2 = CH_2O + \cdot OH \text{ atd. (cit.}^{3,4})$$
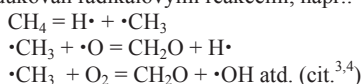
Průmyslové kotle na LPG produkují průměrně 11,2 mg formaldehydu na 1 kg paliva, kotle na zemní plyn 8,8 mg kg^{−1} a naftové 4,12 mg kg^{−1} (cit.[5]). Významným zdrojem formaldehydu je rovněž cigaretový kouř[6]. Jeho prekurzory jsou při teplotách pod 500 °C sacharidy a polysacharidy. Při vyšších teplotách se koncentrace formaldehydu v kouři snižuje[7]. Kouř z cigaret obsahuje až 130 µg m^{−3} formaldehydu a silní kuřáci (20 cigaret denně) jsou exponováni 1 mg formaldehydu denně[8]. Formaldehyd byl detegován také v kouři ze spalování dřeva[9,10]. Nezanedbatelným zdrojem je i automobilová doprava. Automobily emitují mezi 16,5–115,2 mg formaldehydu na km jízdy[11], přičemž významnějším producentem jsou vznětové motory (až 1000 mg formaldehydu na 1 kg paliva[12]).

Formaldehyd je meziproduktem fotochemických reakcí v atmosféře. Sám je fotolyzován zejména při 320 nm za vzniku oxidu uhelnatého[13]. Formaldehyd byl v městských oblastech prokázán i ve sněhu[14].

Dnešní člověk uvnitř budov tráví až tři čtvrtiny svého života, u nemocných a starších lidí pak toto číslo dosahuje téměř 100 %. Koncentrace některých látek (výjimku tvoří např. $SO_2$ nebo $O_3$) mohou dosahovat ve vnitřních prostorách vyšších hodnot než venku[15,16]. To platí zejména pro řadu těkavých organických látek (VOC) včetně formaldehydu. Jeho koncentrace zde mohou dosahovat až desetinásobku hodnot obvyklých pro venkovní prostředí[17,18] (tab. I).

Majoritním zdrojem formaldehydu ve vnitřních prostorách jsou zejména dřevěné materiály – dřevotřísky a překližky[19]. Při jejich výrobě se používá pojidel na bázi formaldehydu[20] (obr. 1). 100 g takového materiálu uvolňuje několik miligramů formaldehydu[21]. Povrchovou úpravou se emise sníží až desetkrát. Formaldehyd je uvolňován i z materiálů na bázi vinylu – PVC a gumy. Nebyl však prokázán v emisích z linolea, které je ovšem charakteris-

Tabulka I
Porovnání koncentrací formaldehydu z různých míst

| Koncentrace [µg m^{−3}] | Lokalizace | Lit. |
|---|---|---|
| 58,25 | město São Paulo | 35 |
| 8 až 23,5 | město Ljubljana | 99 |
| 6 | město Hongkong | 100 |
| max 100 | město – silný provoz, inverze | 9 |
| 25 | byty | 101 |
| 9 až 70 | byty | 102 |
| 60 až 622 | byty | 50 |
| 8 až 33 | knihovny | 114 |
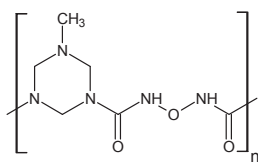
Obr. 1. **Struktura močovino-formaldehydového polymeru**

tické jinými aldehydy. Dalším zdrojem formaldehydu jsou barvy[22] a fermeže[23,24]. Emise formaldehydu ze všech materiálů časem exponenciálně klesají. Např. u nového koberce dochází ke snížení emisí VOC na polovinu cca po 3 měsících[108]. Teplota a vlhkost vzduchu[27] navyšuje emise formaldehydu na každých 10 °C asi 2−3krát[25,26]. Obměna vzduchu v místnostech snižuje koncentrace formaldehydu, zdvojnásobená cirkulace redukuje koncentrace této škodliviny o polovinu. Jestliže však vnitřní zdroje formaldehydu dominují nad cirkulací, větrání úroveň formaldehydu významně nesnižuje[27].

Formaldehyd není problémem jen ve vnitřních prostorách, ale i na pracovištích, např. v papírnách[28], provozech zpracovávajících dřevotřísku, či v nemocničním prostředí, kde i na řádně odvětrávaných patologických pracovištích se skladovanými vzorky může dosahovat koncentrace formaldehydu[29] od 375 μg m$^{-3}$ až k 2875 μg m$^{-3}$, krátkodobě i 10 750 μg m$^{-3}$.

Formaldehyd vzniká v těle jako sekundární produkt oxidace lipidů. Byl dokázán ve vzduchu vydechovaném lidmi s rakovinou plic, což je zřejmě způsobeno produkcí nekrotických proteinů indukujících právě zvýšenou oxidaci lipidů. Také u pacientek s rakovinou prsu bylo ve vydechovaném vzduchu změřeno mezi 562,5−1500 μg m$^{-3}$ formaldehydu. Zdravá žena vydechovala oproti tomu 375 až 750 μg m$^{-3}$ (cit.[30]).

Dále bylo zjištěno, že formaldehyd vzniká po smrti enzymatickou redukcí trimethylamin-*N*-oxidu v tkáních mořských ryb a korýšů určených ke konzumaci[31]. Akceptovatelný denní příjem formaldehydu je podle americké Agentury pro ochranu prostředí (EPA) 0,2 mg kg$^{-1}$. Přitom hluboce zmražená treska obsahuje kolem 4−10 mg kg$^{-1}$ formaldehydu, makrela zmražená doma a uchovávaná po dobu 2 měsíců obsahuje 10,1 mg kg$^{-1}$, sardinka kolem 6 mg kg$^{-1}$, pstruh kolem 3,5 mg kg$^{-1}$ (cit.[32]). Formaldehyd je rovněž obsažen v alkoholických nápojích, kde byl stanoven v množstvích od 0,27 mg l$^{-1}$ (značka Mistá z Itálie) až po 3,01 mg l$^{-1}$ (španělská brandy)[33]. Formaldehyd byl nalezen ve vysokých koncentracích až 494 mg kg$^{-1}$ v houbách shiitake (*Lentinula edodes*)[34].

### 1.1. Stanovené limity

Limitní koncentrace formaldehydu považované za bezpečné jsou stanoveny pro dlouhodobý pobyt řádově v desítkách μg m$^{-3}$, v případě kratších expozic ve stovkách μg m$^{-3}$.

Světová zdravotnická organizace (WHO) připouští třicetiminutový limit koncentrace formaldehydu[35] 108 μg m$^{-3}$.

Americká rada vládních hygieniků pro průmysl (ACGIH) doporučuje jako krátkodobý limit 375 μg m$^{-3}$, Americký Národní institut pro pracovní bezpečnost a zdraví (U.S.NIOSH) patnáctiminutový limit 125 μg m$^{-3}$ a dlouhodobě 20 μg m$^{-3}$.

Vyhláška Ministerstva zdravotnictví 6/2003 Sb. (cit.[36]) stanovuje limitní hodinovou koncentraci formaldehydu v místnostech na 60 μg m$^{-3}$. Pro pracoviště je stanoven podle nařízení vlády 178/2001 Sb. (cit.[37]) přípustný expoziční limit (PEL) na 0,5 mg m$^{-3}$ a nejvyšší mezní přípustná koncentrace (NPK-P) na 1 mg m$^{-3}$. Vyhláška Ministerstva zdravotnictví ČR 26/2001 Sb. zakazuje používání formaldehydu jako potravinářského aditiva (např. bakteriostatické činidlo v sýrech) E240, povoleno je množství do 5 % v kosmetických přípravcích na tvrzení nehtů. Jednotkové riziko pro formaldehyd je podle EPA 1,3·10$^{-5}$ μg m$^{-3}$. Kerns a spol.[38] zjistili, že při příjmu 14,3 mg kg$^{-1}$ den$^{-1}$ onemocní 94 ze 140 sledovaných krys rakovinou. Til a spol.[39] stanovili referenční dávku (RfD) na 0,2 mg kg$^{-1}$ den$^{-1}$, nejnižší limit, kdy ještě není pozorován škodlivý účinek (NOAEL) 15 mg kg$^{-1}$ den$^{-1}$ a nejnižší limit, kdy došlo k pozorování škodlivého účinku (LOAEL) 82 mg kg$^{-1}$ den$^{-1}$. Limit NOAEL pro poškození nosní sliznice[40,41] byl stanoven na 1,25 mg m$^{-3}$.

### 1.2. Vliv formaldehydu na zdraví

Formaldehyd je elektrofilní sloučenina, která může reagovat s makromolekulami v organismu (DNA, RNA, proteiny) za tvorby reverzibilních i ireverzibilních aduktů. Formaldehyd je produkován v organismu mj. i oxidační demethylací xenobiotik. Po vstupu do organismu se
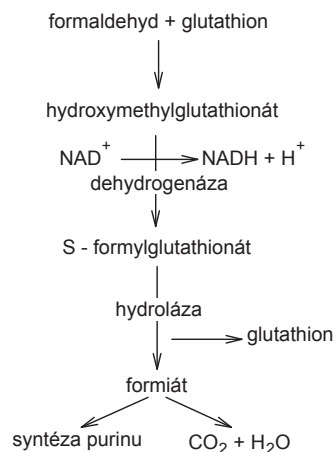


Obr. 2. **Schematické znázornění odbourávání formaldehydu v organismu**

formaldehyd váže na glutathion a enzymatickými reakcemi vzniká kyselina mravenčí, která je přeměněna na $CO_2$ a vodu, nebo se zapojuje do syntetických procesů[42,43] (obr. 2).

Expozici formaldehydu, resp. VOC ve vnitřních prostorách, je přikládána řada obtíží zahrnujících astma, astmatické symptomy jako noční dušnost, onemocnění průdušek a plicní nedostatečnost[44,45].

Formaldehyd lze vnímat čichem při koncentracích 0,0875–1,5 mg m$^{-3}$. Někteří citliví jedinci pociťují horkost v obličeji již při koncentracích 0,01 mg m$^{-3}$. Astmatici[46] pociťují symptomy při 2,5 mg m$^{-3}$. Při akutní expozici nastává podráždění hrdla (0,1 mg m$^{-3}$), podráždění očí (1 mg m$^{-3}$), únava, bolesti hlavy, nevolnost a po čase zánět spojivek. Při dlouhodobé expozici se dostavuje bronchitida, laryngitida, faryngitida[47]. Dále při větších akutních expozicích lze pozorovat ztížené dýchání (10 mg m$^{-3}$), poškození dýchacích cest (40 mg m$^{-3}$), dušení (80 mg m$^{-3}$) a smrt ($\approx$125 mg m$^{-3}$)[48]. Bylo prokázáno, že expozice formaldehydu vyšší než 60 µg m$^{-3}$ vede u dětí k prokazatelnému riziku vzniku astmatu[49]. Podráždění kůže způsobuje roztok s koncentrací vyšší než 2 %, avšak citlivé osoby nesnesou již 0,05% roztok.

Předpokládá se, že VOC včetně formaldehydu přispívají ke vzniku tzv. SBS, syndromu nemoci v budovách (Sick Building Syndrome).

Imunotoxické působení formaldehydu je stále předmětem sporů. Podle některých studií je právě toto působení příčinou pozdějšího podráždění kůže a snížené rezistence k infekcím (rhinitis, pneumonie)[50,51]. Neutrofily jsou buňky schopné migrovat tkáněmi do postižených míst a pohltit (fagocytovat) bakterie. Hrají důležitou roli v rezistenci proti infekcím[52]. Při expozici formaldehydu je znatelně snížena schopnost těchto buněk produkovat peroxid vodíku[53], kterým zabíjejí mikroby. Působení formaldehydu může vést až k dermatitidě a alergii[54,55]. Prevalence citlivosti na formaldehyd v řádech ppm se však zdá být malá[56]. Wilhelmsson a Holmström[57] zjistili, že dlouhotrvající expozice formaldehydu spouští alergickou reakci zprostředkovanou imunoglobulinem E, která je běžná při atopii (velká přecitlivělost organismu projevující se alergickou reakcí). Práce publikovaná Lindenem však tento fakt vyvrací[58]. Studie, zabývající se reakcí na krátkodobou expozici 412,5–1662,5 µg m$^{-3}$ formaldehydu během pobytu v laboratoři, nic podobného nezjistila[59]. V lidských průdušnicových buňkách vystavených formaldehydu je ve větší míře přítomen protein Hs 680. Pokusy na krysách poukazují na snížení exprese ribosomálního fosfoproteinu P2 a kalmodulinu[60]. Formaldehyd se také váže kovalentně na lidský sérový albumin (tzn. je haptenem HSA) za vzniku aduktu F-HSA, proti němuž Thrasher a spol.[61] našli v organismu protilátky. Také Carraro a spol.[62] označuje F-HSA jako biomarker expozice formaldehydu.

Mezinárodní agentura pro výzkum rakoviny (IARC) dnes formaldehyd řadí do skupiny 1 „jako karcinogenní pro člověka"[63], ačkoliv dříve byl zařazen do skupiny 2A mezi látky, které jsou z karcinogenních účinků pouze po-

dezřelé[64]. Po inhalaci formaldehydu byly pozorovány adukty DNA v nosní sliznici[65]. Chronická expozice je spojována s rakovinou nosu a nosohltanu[66], avšak karcinogenita formaldehydu byla v řadě studií prokázána typicky při vyšších koncentracích. Úmrtnost na myeloidní leukémii u dělníků, vystavených působení formaldehydu, podle studie provedené Pinkertonem[67] vzrůstá hlavně při dlouhodobé expozici (zde 20 let). Výměna sesterských chromatid (test mutagenity) byla indukována při překročení koncentrace 5 µg ml$^{-1}$ (cit.[68]). Křivka dávka-účinek přitom zaznamenává patrný nárůst při dávce 10 µg ml$^{-1}$, resp. mezi koncentracemi 2500 µg m$^{-3}$ a 7500 µg m$^{-3}$. Na buňkách savců bylo pozorováno síťování DNA s proteiny a zlomy ssDNA jak *in vitro*, tak *in vivo*. Tato poškození jsou však efektivně opravována[69].

Odhaduje se, že kolem 70–75 % předpokládaného rizika rakoviny způsobeného VOC připadá na formaldehyd v kombinaci s polycyklickými aromatickými uhlovodíky, butadienem a benzenem. Nebezpečí plynoucí z přítomnosti těchto VOC v prostředí je přirovnáváno k riziku plynoucímu z expozice radonu či cigaretovému kouři[70].

### 1.3. Stanovení formaldehydu

#### 1.3.1. Spektrofotometrická stanovení

Klasickým stanovením je reakce s kyselinou chromotropovou (4,5-dihydroxynaftalen-2,7-disulfonovou), která probíhá ve vodném 1% roztoku okyseleném kyselinou sírovou. Vzniká fialový produkt, který lze stanovit spektrofotometricky při 570–580 nm (obr. 3). Mez detekce je 81 µg m$^{-3}$. Další klasická metoda je založena na reakci pararosanilinu, siřičitanu a formaldehydu. Vzniká purpurově zbarvená látka silně absorbující při 570 nm (cit.[71–74]), v tomto případě je mez detekce v řádech desítek µg m$^{-3}$.

#### 1.3.2. Chemiluminiscenční stanovení

Chemiluminiscenční stanovení je založeno na reakci formaldehydu s kyselinou gallovou (3,4,5-trihydroxybenzoová) a peroxidem vodíku v silně alkalickém prostředí. Excitované singletové atomy kyslíku vyzařují světlo s emisními pásy 463 nm, 702 nm a 762 nm a přecházejí při tom do základního stavu[75]. Limit detekce je 12,3 µg m$^{-3}$.
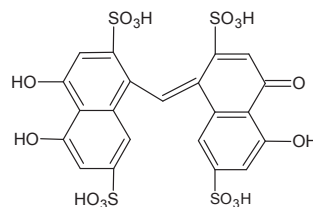


$\lambda = 570$–$580$ nm

Obr. 3. **Struktura uvažovaného produktu reakce formaldehydu s kyselinou chromotropovou**

### 1.3.3. Fluorimetrie

Fluorimetricky lze detegovat produkt Hantzschovy reakce formaldehydu s činidlem standardním fluorimetrem. Octan amonný, kyselina octová a acetylaceton (pentan-2,4-dion) reagují s formaldehydem za vzniku 3,5-diacetyl-1,4-dihydrolutidinu[76]. Stanovení lze rovněž provést v průtokovém režimu reakcí 5,5-dimethylcyklohexan-1,3-dionu (dimedonu) v prostředí octanu amonného. Excituje se zářením o vlnové délce 395 nm a emisní maximum je při 465 nm. Bylo dosaženo limitu detekce[77] 1,125 μg m$^{-3}$. Fluorimetrie byla rovněž použita při reakci HCHO s formiátdehydrogenasou (FDH). Záření o vlnové délce 350 nm excituje molekuly vzniklého NADH, které pak emitují záření s maximem o vlnové délce 450 nm (cit.[78]). Mez detekce je 0,25 μg m$^{-3}$. Jiná metoda je založena na katalytickém rozkladu formaldehydu. Produkty při přechodu do nižšího energetického stavu emitují záření. Pro rozklad formaldehydu se ukázal jako nejvhodnější katalyzátor V$_2$O$_5$-4 TiO$_2$ zahřátý na teplotu 370 °C. Je emitováno záření o vlnové délce 490 nm. Použit byl detektor s optickým filtrem a fotonásobičem. Citlivost byla v řádech[79] mg m$^{-3}$. Fluorescence indukovaná laserem[80] oproti tomu používá k excitaci molekul formaldehydu laditelný laser. Citlivost metody je 12 μg m$^{-3}$.

### 1.3.4. Chromatografické stanovení

Běžnou metodou je použití vysoce účinné kapalinové chromatografie (HPLC) v kombinaci s různými detektory, zejména typu s diodovým polem. Metoda však vyžaduje chemickou reakci formaldehydu s derivatizačním činidlem, např. směsí ethyl-3-oxobutanoátu s amoniakem v Hantzschově dihydropyridinové syntéze (reakce na obr. 4). Reakce vede ke vzniku diethyl-2,6-dimethyl-1,4-dihydropyridin-3,5-dikarboxylátu, který se stanoví HPLC s mobilní fází směsi methanolu a vody[81].

Je rovněž možné provést mikroextrakci na pevnou fázi (SPME). Sorpce VOC (vč. formaldehydu) probíhá na poly(dimethylsiloxan)divinylbenzenové vlákno (PDMS/ DVB) impregnované *O*-(2,3,4,5,6-pentafluorobenzyl) hydroxylamin-hydrochloridem (PFBHA) jakožto derivatizační látkou 2 min extrakcí vodného roztoku. Vzorkování probíhá 10 min. Následně se produkt stanoví plynovou chromatografií s plamenovým ionizačním detektorem (FID) či fotoionizačním detektorem (PID). Limit detekce[82–84] je 6,25 μg m$^{-3}$. Mikroextrakce na pevnou fázi (SPME) byla využita rovněž ve spojení s plynovou chromatografií a hmotnostní spektrometrií s isotopovým zřeďováním. Použit byl isotopově značený formaldehyd s uhlíkem $^{13}$C a formaldehyd byl derivatizován *in situ* pentafluorfenylhydrazinem[85] (reakce na obr. 5). Hmotnostní detekce SPME-GC-MS (MSD 5973 od Agilent Technologies) byla využita v práci Bianchiho a spol.[86].

### 1.3.5. Senzory

Ke stanovení formaldehydu lze použít biosenzory různých konstrukcí. Základem je reakce analytu s enzymem − např. formaldehydu a formaldehyddehydrogenasy na povrchu membrány s NAD jako kofaktorem. Tento systém byl přichycen na elektrodě pokryté platinovou černí a lipofilní látkou − solí tetrathiafulvalenu a tetrakyanchinodimethanu. Předávané elektrony jsou amperometricky detegovány[87]. Byl rovněž použit biosenzor konstruovaný ze zlatých a chromových vrstev napařených na keramickém nosiči s aktivní vrstvou alkoholoxidasy s hovězím sérovým albuminem, dextranem a laktinolem. Reakce senzoru byla měřena konduktometricky[88]. Formaldehyd lze stanovit v koncentracích desetin mmol l$^{-1}$. Problémem těchto analýz je selektivita enzymu. Jinou (starší) metodou bylo uchycení enzymatického komplexu NAD$^+$ s redukovaným glutathionem na vibrující piezoelektrický krystal. Vznikem reakčních produktů na povrchu se sníží frekvence vibrací krystalu[89]. Limit detekce je v řádu mg g$^{-1}$.

Klasickým senzorickým stanovením bez použití enzymů je např. metoda mikrosenzoru založeného na oxidaci
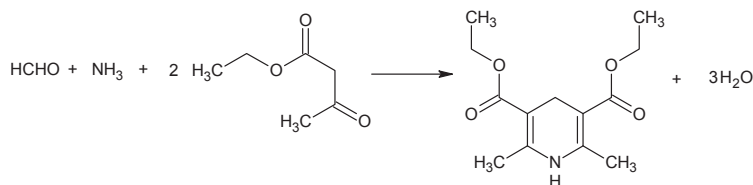


Obr. 4. **Derivatizační reakce HCHO s ethyl-3-oxobutanoátem;** produkt se stanoví metodou HPLC
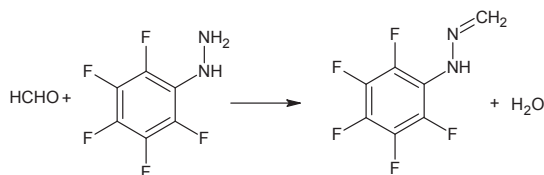


Obr. 5. **Derivatizace HCHO pentafluorfenylhydrazinem;** produkt se stanoví plynovou chromatografií

formaldehydu na žhaveném katalyzátoru NiO. Měřeny jsou elektrické vlastnosti filmu NiO s limitem detekce[90] 1500 μg m$^{-3}$.

### 1.3.6. Spektrální metody

Formaldehyd byl stanovován metodou diferenční laserové spektroskopie DOAS. Principem metody je rychlá změna absorpce látky v úzkém vlnočtovém intervalu. Výhodou stanovení je eliminace změn v prostředí (atmosféra). Diferenční laserová spektroskopie využila laserů (laser typu DFB s vlnovou délkou 1561 nm a typu DBR s vlnovou délkou 1083 nm) operujících ve spektrální oblasti 3,53 μm (2832 cm$^{-1}$) s použitím periodicky přepólovávaného krystalu LiNbO$_3$ (PPLN) a HgCdTe (MCT) detektoru. Bylo dosaženo detekčního limitu[91] 0,4 μg m$^{-3}$.

Formaldehyd byl rovněž detegován optoakustickou detekcí[92] při koncentracích v jednotkách μg m$^{-3}$ (ppb). V experimentu byl použit diodový 6 W Nd:YAG laser v kombinaci s optickým parametrickým oscilátorem a periodicky přepólovávaným krystalem LiNbO$_3$. Hrubé ladění bylo prováděno změnou teploty PPLN krystalu, jemné pak pohybem zrcadla za pomoci mikro-krokového motorku. Měřeno bylo v rozsahu 2785–2840 cm$^{-1}$ s limitem detekce 3,75 μg m$^{-3}$.

Zajímavé možnosti nabízí klasická absorpční spektroskopie za použití diodových laserů[93]. Mez detekce je obvykle 0,3 μg m$^{-3}$. Velmi nízký limit detekce byl zaznamenán Wertem[94]. Metoda založená na zmíněné laserové absorpční spektroskopii využívající diodu bázi solí olova dosáhla v multireflexní cele s optickou dráhou 100 m meze detekce 6,5·10$^{-2}$ μg m$^{-3}$ při jednominutovém integračním čase.

### 1.3.7. Standardní testy a stanovení

Standardním testem pro stanovení emise formaldehydu z materiálů je komorový test (Švédská norma SS 27 02 36, norma ENV 717-1). Provádí se uzavřením 1 m$^2$ vzorku do komory o objemu 1 m$^3$ při 23 °C, 50% vlhkosti s jednotkovou výměnou vzduchu za hodinu. Formaldehyd je stanoven fotometricky po reakci absorpčního roztoku s kyselinou chromotropovou nebo acetylacetonem. Komo-

ra s překližkou a dřevotřískou ve studii Z. Queho[95] obsahovala po 24 h 725 μg m$^{-3}$ formaldehydu. Podle NIOSH (cit.[73]) se komorový test provádí absorpcí formaldehydu do 0,1 M NaOH nebo 1% NaHSO$_3$ a následnou analýzou HPLC. Pro vzorek o objemu 60 l je limit detekce 37,5 μg m$^{-3}$. Je rovněž doporučována plynová chromatografie s FID detektorem. Metoda namáčení vzorku v 50 ml vody o teplotě 40 °C po dobu 3 h je normována podle EN 717-3/1996. Formaldehyd je stanoven fotometricky za použití acetylacetonu. Podle DIN EN 120 je materiál propírán toluenem a vodou. Formaldehyd je zachycován v destilované nebo deionizované vodě, kde následně probíhá Hantzschova reakce s amonnými ionty (octan amonný) a acetylacetonem. Reakce vede k diacetyldihydrolutidinu. Stanovení probíhá na UV spektrometru. Na základě množství formaldehydu uvolňovaného do prostředí (zde modelově do komory, resp. roztoku) jsou materiály rozděleny do tříd E1 (10 mg ze 100 g výrobku, resp. pod 1,5 mg l$^{-1}$) a E2 (do 30 mg ze 100 g výrobku, resp. 1,5 mg l$^{-1}$). Podrobné shrnutí nabízí práce Risholma[96].

Podle vyhlášky 211/2004 Sb. (cit.[97]) ve znění pozdějších předpisů se formaldehyd stanovuje Schiffovým činidlem srovnáním zabarvení roztoku se standardem a podle vyhlášky 222/1996 Sb. (cit.[98]) se formaldehyd stanovuje reakcí s kyselinou chromotropovou spektrofotometricky při 570 nm. České hygienické stanice používají ke stanovení formaldehydu pararosanilinovou metodu.

## 2. Fotoakustická a laserová detekce

### 2.1. Laserová detekce

Absorpční spektrální metody jsou založeny na měření rozdílu intenzit mezi vstupním a výstupním zářením. Při monitorování nízkých koncentrací absorbujících látek jsou rozsahy vstupních a výstupních intenzit použitého záření velmi malé.

Aplikace laserových detekčních technik má řadu výhod. Použitím laseru a technik založených na jeho aplikaci např. metodou vícenásobného odrazu (tzv. cavity ring
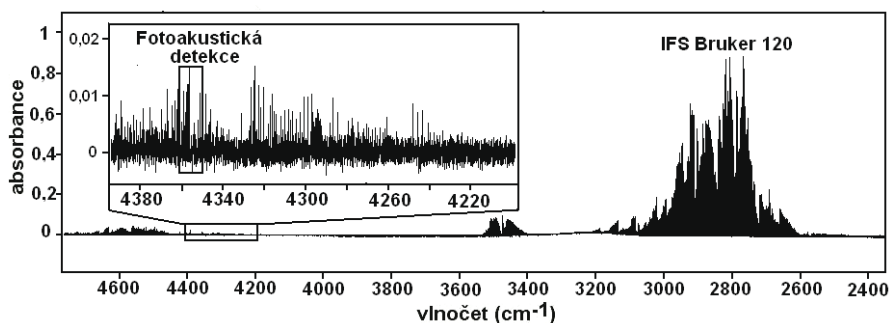


Obr. 6. **Spektrum formaldehydu v blízké infračervené oblasti při tlaku 1 Torr;** označen je spektrální rozsah MQW laseru fotoakustické detekce. Širokopásmové spektrum bylo měřeno spektrometrem IFS Bruker 120

down) nebo fotoakustické detekce lze značně zvýšit detekční citlivost i při nízkých koncentracích studovaných látek.

V této práci byl použit diodový GaInAsSb/AlGaAsSb (tzv. MQW) laser[104–106] ve spojení s fotoakustickou detekční aparaturou koncipovanou pro měření ve spektrální oblasti 2,3 μm (4356 cm$^{-1}$) (obr. 6). Diodové lasery jsou schopny pracovat za laboratorní teploty v oblasti středního infračerveného záření. V jednom módu jsou změnou proudu laditelné v rozsahu desítek reciprokých centimetrů. Dosahují dostatečného výkonu při nízkém optickém šumu. Relativně vysoký výkon dovoluje nahradit klasickou absorpční laserovou techniku rezonančním fotoakustickým uspořádáním.

## 2.2. Fotoakustická detekce

Fotoakustický systém umožňuje detegovat slabé signály za nepřítomnosti silného ofsetového signálu pozadí. Jednou z cest, jak využít této myšlenky, je opustit klasické absorpční schéma vyhodnocení na základě rozdílu vstupních a výstupních signálů a měřit absorbovanou energii jiným způsobem. Molekula, která absorbuje foton, má několik možností, jak se zbavit této energie. Za atmosférického tlaku je nejpravděpodobnější cestou kolize s jinou molekulou a konverze absorbované energie na kinetickou energii molekulárního pohybu. Jestliže se excitační záření pohybuje v infračervené spektrální oblasti, pak je absorbováno molekulami a následuje vibračně-translační relaxace. Vzrůst kinetické energie molekuly se projevuje změnou tlaku v uzavřeném objemu vzorkovací kyvety. Tato změna může být velice citlivě detegována mikrofonem. Získaný fotoakustický signál (*S*) lze jednoduše vyjádřit jako:

$$S = CN\sigma P \qquad (1)$$

kde *C* je konstanta charakterizující parametry fotoakustické cely (délka, účinný průřez a citlivost mikrofonu), *N* je počet absorbujících molekul v cm$^3$, σ je absorpční účinný průřez absorbující molekuly a *P* je výkon laseru. V porovnání s klasickou absorpční spektrometrií je fotoakustický signál měřen prakticky na nulovém pozadí. Tento fakt spolu s lineární charakteristikou mikrofonu poskytuje obrovský dynamický rozsah (až 5 řádů nebo více).

Minimální detegovatelnou fotoakustickou absorbanci $N_{min}\sigma L$ lze určit jako:

$$N_{min}\sigma L = \frac{S_{min}}{PC} = 10^{-8} \qquad (2)$$

kde $N_{min}$ je minimální detegovatelná koncentrace dané molekuly, *L* je optická dráha a $S_{min}$ je minimální šum mikrofonu ($S_{min}/P$= 30–50 nV W$^{-1}$ a $C \approx 3.5$ V cm W$^{-1}$). Z rovnice (*1*) a (*2*) lze odvodit, že malé absorbance a tudíž stopové koncentrace mohou být fotoakusticky detegovány (PA) i na malé optické dráze.

Fotoakustický jev byl poprvé popsán Grahamem Bellem v roce 1880 (cit.[107]), když přes mechanický přerušovač
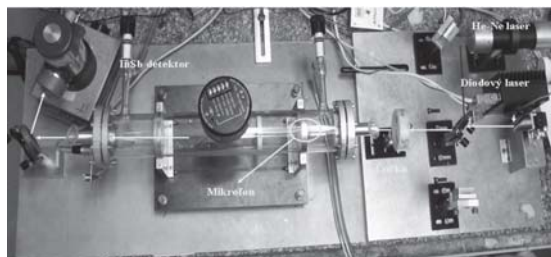


Obr. 7. **Fotoakustická aparatura;** na obrázku vpravo nahoře je He-Ne trasovací laser. Vlastní dioda je teplotně stabilizována v držáku Thorlab TCLMD M9. Paprsek je fokusován optickou soustavou do akustického rezonátoru mezi dvojici měřících mikrofonů. Svazek, který prochází kyvetou je paralelně monitorován polovodičovým InSb detektorem

zaostřil sluneční záření do kapalného vzorku a pomocí sluchátka registroval akustický signál se stejnou frekvencí, jakou měl přerušovač. Podobného jevu lze dosáhnout nejen v kapalinách, ale i ve skupenstvích plynných a pevných. Krátce po zveřejnění Bellovy práce se tímto jevem zabývali další badatelé jako Tyndall[108], Rayleigh[109] nebo Röntgen[110].

První využití tohoto jevu ke stanovení plynů, kdy již můžeme hovořit o PA detekci, lze nalézt až v práci Viengerova[111] z konce 30. let 20. století.

Velkého rozmachu dosáhla fotoakustická detekce rozvojem laserů jako zdrojů pro buzení akustického signálu. V roce 1968 byl poprvé použit $CO_2$ laser pro detekci $CO_2$ v dusíku[112]. V 80. letech vzrostla poptávka po citlivém detekčním zařízení pro studium stopových látek v atmosféře.

Při měření bylo využito rezonance signálu uvnitř akustické kyvety (vznik stojatého vlnění uvnitř rezonátoru, kdy platí vztah $k\lambda = l/2$, kde *l* je délka rezonátoru, λ vlnová délka a *k* je celé číslo). Metoda je nazývána „rezonanční fotoakustická detekce".

Fotoakustická kyveta (obr. 7) je dvouplášťová, přičemž vlastní skleněný rezonátor má průměr 5 mm a délku 200 mm. Rezonanční frekvence zařízení je cca 380 Hz. Uprostřed rezonátoru jsou proti sobě umístěny dva mikrofony Knowles EK-3024, jejichž signál je veden do fázově citlivého zesilovače (Stanford Research System-SR 530 Lock-in amplifier) a data jsou ukládána v počítači. Kyveta je v Brewsterově úhlu opatřena okénky z fluoridu vápenatého.

## 2.3. Měření spekter

Měření probíhalo za laboratorní teploty při frekvenční modulaci laseru na kmitočtu 388 Hz. Tato hodnota byla získána experimentálně kalibračním měřením pro vlnočet 4355 cm$^{-1}$. Signál byl zpracováván za použití druhé derivace (*2f*), kde *f* je fundamentální modulační frekvence. Pro kalibraci bylo použito spektrum s rozlišením 0,01 cm$^{-1}$, získané měřením spektrometrem s Fourierovou transfor-

mací Bruker IFS 120 HR.

　　Při vlastním experimentu byl plynný formaldehyd uvolňován zahříváním paraformaldehydu na 80 °C. Takto získaný vzorek byl ředěn dusíkem na výsledný tlak
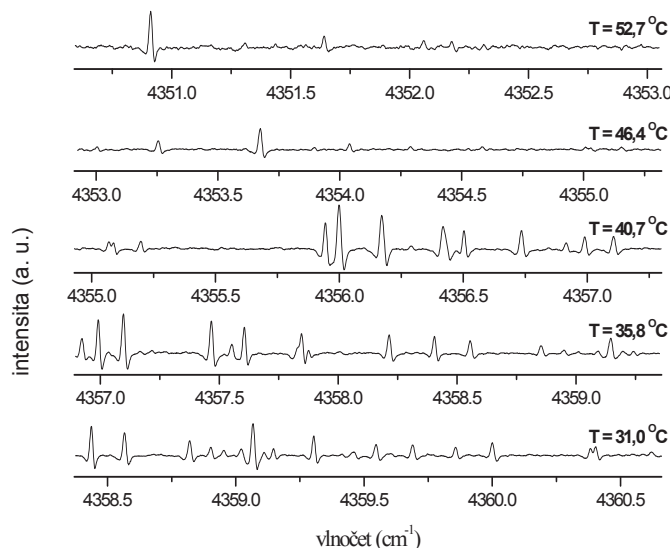


a

b

| 4350 | 4352 | 4354 | 4356 | 4358 | 4360 |

vlnočet (cm$^{-1}$)
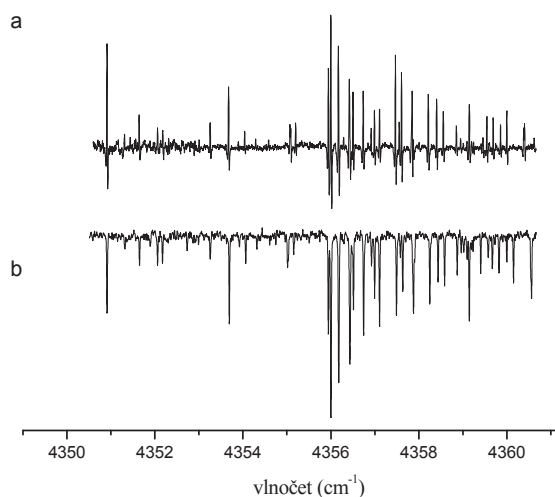
Obr. 8. **Laserdiodové fotoakustické spektrum formaldehydu** (a) **zředěného vzduchem v poměru 1:3 při tlaku 55 Torr a spektrum změřeném při tlaku 10 Torr přístrojem Bruker IFS 120** (b)

55 Torr. Měření bylo provedeno ve stacionárním stavu. Laserová dioda byla laděna v požadovaném frekvenčním rozsahu excitačním proudem od 60 do 90 mA při teplotách 31 až 52,7 °C, čímž bylo dosaženo kontinuálního proladění v rozsahu 10 cm$^{-1}$. V oblasti emise GaInAsSb/AlGaAsSb diody se nacházejí absorpční pásy formaldehydu, především $\nu_3 + \nu_5$, dále pak pásy $\nu_2 + \nu_5$, $\nu_2 + \nu_3 + \nu_6$, $\nu_2 + \nu_3 + \nu_4$ a $2\nu_3 + \nu_6$. Výsledné linie byly srovnány s velmi přesnými analýzami spekter od J. M. Flauda[113].

　　Srovnáním dat z FT spektrometru a diodového laseru byly pro fotoakustické měření vybrány tři nejintenzivnější linie v oblasti 4356 cm$^{-1}$. Na nich bylo provedeno fotoakustické měření s detekčním limitem 125 μg m$^{-3}$. Obr. 8 ukazuje diskutovanou část spektra naměřenou laserovou fotoakustickou detekcí v porovnání se spektrem měřeným spektrometrem s Fourierovou transformací. Část změřených fotoakustických a laserových spekter zachycují obr. 9 a 10, přičemž tepelné ladění laseru je ukázáno na obr. 9. Při měření nízkých koncentrací byla provedena tři měření s integračním časem 150 s. Jejich výsledky pak byly průměrovány.

## 3. Závěr

　　Formaldehyd je látkou, jež ohrožuje zdraví člověka hlavně svou prokázanou karcinogenitou. Z tohoto důvodu je třeba vyvarovat se jeho expozici zejména ve vnitřních prostorách, ale pokud možno také venku.



intensita (a. u.)

T = 52,7 °C

| 4351.0 | 4351.5 | 4352.0 | 4352.5 | 4353.0 |

T = 46,4 °C

| 4353.0 | 4353.5 | 4354.0 | 4354.5 | 4355.0 |

T = 40,7 °C

| 4355.0 | 4355.5 | 4356.0 | 4356.5 | 4357.0 |

T = 35,8 °C

| 4357.0 | 4357.5 | 4358.0 | 4358.5 | 4359.0 |

T = 31,0 °C

| 4358.5 | 4359.0 | 4359.5 | 4360.0 | 4360.5 |

vlnočet (cm$^{-1}$)

Obr. 9. **Laserem měřené spektrum formaldehydu při koncentraci 1250 μg m$^{-3}$ ve vzduchu (50 Torr);** obrázek též zachycuje stabilizační teploty laseru pro jednotlivé spektrální oblasti

423

Pro stanovení této sloučeniny byla vyvinuta řada metod a to i standardizovaných. V laboratoři FT a laserové spektrometrie byla vyzkoušena metoda rezonanční fotoakustické detekce. Fotoakustická detekce se ukázala jako velice jednoduchá, levná a prakticky použitelná metoda. Její nevýhodou však je menší citlivost ve srovnání se spektrofotometrickými technikami využívajícími absorpci či emisi záření ve viditelné oblasti světla.

Na základě studia infračervených spekter se ukázalo, že vhodným laserem konstruovaným pro oblast 3,5 μm (2800 cm$^{-1}$) by se dosáhlo o 3 řády větší citlivosti díky mnohonásobně větší absorpci základního absorpčního pásu formaldehydu oproti slabým kombinačním pásům v oblasti 4350 cm$^{-1}$. Všechny v současnosti komerčně dostupné lasery, emitující záření v oblasti 3,5 μm, pracují při teplotě kapalného dusíku či teplotách nižších. Dalšího možného zvýšení citlivosti lze docílit použitím výkonnějších laserů. Takovými lasery jsou nově konstruované kvantově kaskádové lasery, pracující v pulzním nebo kontinuálním režimu, jejichž výkon je řádově 40× větší, než u námi použitých GaInAsSb/AlGaAsSb laserů. Kombinací těchto faktorů lze tedy očekávat citlivost řádově v oblasti jednotek ppb, tedy hodnot z hlediska možných analytických aplikací již velice slibných.

Seznam zkratek

DBR　　Distributed Bragg reflector laser – typ diodového laseru
DFB　　Distributed feed-back laser – typ diodového laseru
EPA　　Environmental protection agency – Agentura ochrany prostředí (USA)
HSA　　human serum albumin – lidský sérový albumin
IARC　　International agency for research on cancer
LOAEL　lowest observable adverse effect level – nejnižší limit s pozorovaným škodlivým účinkem
MQW　　Multi-quantum well
NIOSH　National Institute for Occupational Safety and Health – Národní institut pro pracovní bezpečnost a zdraví
NOAEL　no observable adverse effect level – nejnižší limit, kdy není pozorován škodlivý účinek
NPK-P　nejvyšší přípustná koncentrace v pracovním prostředí
PA　　　fotoakustická detekce
PAH　　polycyclic aromatic hydrocarbons – PAU polycyklické aromatické uhlovodíky
PEL　　přípustný expoziční limit
PVC　　polyvinylchlorid
RfD　　referenční dávka
SBS　　sick building syndrome – syndrom onemocnění v budovách
SPME　　solid phase microextraction – mikroextrakce na pevnou fázi
VOC　　volatile organic compounds – těkavé organické sloučeniny
WHO　　World health organisation – Světová zdravotnická organizace

## LITERATURA

1. Ehrenfreund P., Charnley S. B.: Annu. Rev. Astron. Astrophys. *38*, 427 (2000).
2. *Monographs on the Evaluation of the Carcinogenic Risk of Chemicals to Humans*. Vol. 62: *Wood Dust and Formaldehyde*. IARC, Lyon 1995.
3. Turns S. R.: *An Introduction to Combustion: Concepts and Applications*. Mc Graw-Hill, New York 1996.
4. Yossefy D., Ashcroft S. J., Hacohen J.: Fuel *7*, 1061 (1995).
5. Karademir A.: Fuel *85*, 1894 (2006).
6. *Tobacco smoking*. vol. 38: *Monographs on the Evaluation of the Carcinogenic Risk of Chemicals to Humans*, IARC, Lyon 1985.
7. Baker R. R., Coburn S., Liu C.: J. Anal. Appl. Pyrol. *77*, 12 (2006).
8. *Concise International Chemical Assessment Document 40 – Formaldehyde*. WHO, Geneva 2002.
9. *Environmental Health Criteria Document 89*. WHO, Geneva 1989.
10. Lipari F., Dasch J. M., Scruggs W. F.: Sci. Technol. *18*, 326 (1984).
11. Ramdahl T., Alfheim I., Rustad S., Olsen T.: Chemosphere *11*, 601 (1982).
12. de Abrantes R., de Assuncao J. V., Hirai E. Y.: Rev. Saude Publica *39*, 479 (2005).
13. Kohoutek J., Holoubek I.: *Vývoj složení emisí z automobilové dopravy v závislosti na technickém pokroku v konstrukci vozidel*. Tocoen Report č. 116, Brno 1996.
14. Pinceloup S., Laverdet G., Magdin F.: J. Photochem. Photobiol., A *157*, 275 (2003).
15. Domine F., Shepson P. B.: Science *279*, 1506 (2002).
16. Godish T.: Atmos. Environ. *23*, 1695 (1989).
17. Hoeppe P., Martinac I.: Int. J. Biometeorol. *42*, 1695 (1998).
18. Samet J.: Am. Rev. Respir. Dis. *142*, 915 (1990).
19. Kim S., Kim J. A., Kim H. J.: Polym. Test. *25*, 605 (2006).
20. Kelly T. J., Smith D. L., Satola J.: Environ. Sci. Technol. *33*, 81 (1999).
21. Brown S. K.: Indoor Air *9*, 209 (1999).
22. Chang J. C. S., Fortmann R., Roache N., Lao H. C.: Indoor Air *9*, 253 (1999).
23. Howard E. M., McCrillis R. C., Krebs K. A., Fortman R., Lao H. C., Guo Z.: J. Air Waste Manage

*48*, 924 (1998).

24. Chang J. C. S., Guo Z., Fortmann R., Lao H. C.: Indoor Air *12*, 10 (2002).
25. Brown V., Crump D., Gavin M.: *Building Res. Establishment*. BRE report BR 299. London 1996.
26. Gilbert N. L., Gauvin D., Guay M.: Environ. Res. *102*, 1 (2006).
27. Sherman M. H., Hodgson A. T.: Indoor Air *14*, 2 (2004).
28. Kauppinen T., Teschke K., Savela A., Kogevinas M., Boffetta P.: Int. Arch. Occup. Environ. Health *70*, 119 (1997).
29. Koda S., Kumagai S., Ohara H.: Acta Med. Okayama *53*, 217 (1999).
30. Ebeler S. E.: J. Chromatogr., B *702*, 211(1997).
31. Sotelo C. G., Pineiro C., Perez-Martin R. I.: Lebensm.-Unters. Forsch. *200*, 14 (1995).
32. Bianchi F.: Food Chem. *100*, 1049 (2007).
33. Burini G., Coli R.:  Anal. Chim. Acta *511*, 15 (2004).
34. Liu J.:  Talanta *65*,  705 (2005).
35. *Update and revision of WHO air quality guidelines for Europe*. WHO, Copenhagen 1994. Dostupné z URL:   http://www.who.nl/index1.htm[2001Out17], staženo 1.8.2007.
36. Vyhláška 6/2003 Sb. *kterou se stanoví hygienické limity chemických, fyzikálních a biologických ukazatelů pro vnitřní prostředí pobytových místností některých staveb*.
37. Nařízení vlády 178/2001 Sb. *kterým se stanoví podmínky ochrany zdraví zaměstnanců při práci*.
38. Vyhláška 26/2001 Sb. *o hygienických požadavcích na kosmetické prostředky, o náležitostech žádosti neuvedení ingredience na obalu kosmetického prostředku a o požadavcích na vzdělání a praxi fyzické osoby zodpovědné za výrobu kosmetického prostředku*.
39. Kerns W. D.: Cancer Res. *43*, 4382 (1983).
40. Til H. P.: Food  Chem. Toxicol. *27*, 78 (1989).
41. Josje H. E.: Int. Arch. Occup. Environ. Health *79*, 283 (2006).
42. Bos P. M. J.: Crit. Rev. Toxicol. *21*, 423 (1992).
43. *Formaldehyde*. Chapter 5.8., WHO Regional Office for Europe, Copenhagen 2001.
44. Norback D.: Occup. Environ. Med. *52*, 388 (1995).
45. Weislander G.: Int. Arch. Occup. Environ. Health *69*, 115 (1997).
46. Witek T. J., Schachter E. N., Brody D. J.: Arch. Environ. Health *42*, 230 (1987).
47. Carrer P., Maroni M., Alcini D.: Sci. Total Environ. *270*, 33 (2001).
48. Shi Q. W., Jia D. Y., Geng S. B.: Chin. J. Contam. Contr. Air Condit. Technol. *2*, 38 (2005).
49. Rumchev K., Spickett J., Bulsara M.: Eur. Respir. J. *20*, 403 (2002).
50. Agovska A., Nosko M.: Probl. Hyg. *1*, 3 (2000).
51. Nosko M., Petrova E., Lyapina M.: Hyg. Public Health *2*, 16 (1999).

52. Sawyer D. W., Donovitz G. R., Mandell G. L.: Rev. Infect. Dis. *11*, S1532  (1989).
53. Lyapina M., Zhelezova G., Petrova E., Boev M.: Int. Arch. Occup. Environ. Health *77*, 335 (2004).
54. Garrett M. H., Rayment P. R., Hooper M. A., Abramson M. J., Hooper B. M.: Clin. Exp. Allergy *28*, 459 (1998).
55. Nordman H., Keskinen H., Tuppurainen M.: J. Allergy Clin. Immunol. *75*, 91 (1985).
56. Becher R.: Toxicol. Lett. *86*, 155 (1996).
57. Wilhelmsson B., Holmstrom M.: Scand. J. Work Environ. Health *18*, 403 (1992).
58. Linden S.: Allergy *48*, 525 (1983).
59. Ohmichi K., Komiyama M., Matsuno Y.: J. Health Sci. *52*, 642 (2006).
60. Jung Y. M., Chung H., Han B. D.: Toxicol. Lett. *164*, S299 (2006).
61. Thrasher J. D., Broughton A., Madison R.: Arch. Environ Occup. H. *45*, 271 (1990).
62. Carraro E., Gasparini S., Gilli G.: Environ. Res. *80*, 132 (1999).
63. *Monographs on the evaluation of carcinogenic risks to humans*. vol. 88: *Formaldehyde, 2-Butoxyethanol and 1-tert-Butoxy-2-propanol*. IARC, Lyon 2004.
64. *Monographs on the evaluation of carcinogenic risk of chemicals to humans*. vol 62. *Wood dust and formaldehyde*. IARC, Lyon 1995.
65. Zhong W. G., Hee S. S. Q.: Mutat. Res. – Rev. Mutat. *563*, 13 (2004).
66. *Proposed Residential Indoor Air Quality Guidelines for Formaldehyde*. Health Canada, Ottawa 2005.
67. Pinkerton L. E., Hein M. J., Stayner L. T.: J. Occup. Environ. Med. *61*, 193 (2004).
68. Kreiger R. A., Garry V. F.: Mutat. Res. *120*, 51 (1983).
69. Grafstrom R. C., Fornace A., Harris C. C.: Cancer Res. *44*, 4323 (1984).
70. Wallace L. A.: Environ. Health Perspect. *95*, 7 (1991).
71. Georghiou P. E., Ho C. K.: Can. J. Chem. *67*, 871 (1989).
72. Feigl F.: *Spot Tests in Organic Analysis*. 7. vyd. Elsevier, Amsterdam 1966.
73. *Manual of Analytical Methods (NMAM) 4th ed.* NIOSH 8/15/94. Dostupné z URL: http://www.cdc.gov/niosh/nmam/default.html, staženo 1.8.2007.
74. MacFadyen D. A.: J. Biol. Chem. *158*, 107 (1945).
75. Maeda Y., Hu X., Itou S., Kitano M., Bandow H., Munemori M.: Analyst *119*, 2237 (1994).
76. Kelly T. J., Fortune C. R.: Int. J. Environ. Annal. Chem. *54*, 249 (1994).
77. Sakai T.: Talanta *58*, 1271 (2002).
78. Lazrus A. L., Fong K. L., Lind A. J.: Anal. Chem. *60*, 1074 (1988).
79. K. Zhou.: Sens. Actuators, B *119*, 392 (2006).
80. Möhlmann G. R.: Appl. Spectrosc. *39*, 98 (1985).
81. Burini G., Coli R.:  Anal. Chim. Acta *511*, 155

(2004).

82. Liu J.: Talanta *65*, 705 (2005).
83. Koziel J. A., Noah J., Pawliszyn J.: Environ. Sci. Technol. *35*, 1481 (2001).
84. Martos P. A., Pawliszyn J.: Anal. Chem. *70*, 2311 (1998).
85. Rivero R. T., Topiwala V.: J. Chromatogr., A *1029*, 217 (2004).
86. Bianchi F. Careri M., Musci M.: Food Chem. *100*, 1049 (2007).
87. Dzyadevych S. V.: Anal. Chim. Acta *445*, 47 (2001).
88. Guilbault G. G.: Anal. Chem. *55*, 1682 (1983).
89. Rehle D., Leleux D., Erdelyi M.: Appl. Phys. B: Lasers Opt. *72*, 947 (2001).
90. Kataky R.: Talanta *56*, 451 (2002).
91. Lee C., Hsieh P., Chou C. L. P., Fu L., Chiang C.: Microsyst. Technik. *12*, 893 (2006).
92. Angelmahr M., Miklos A., Hess P.: Appl. Phys. B: Lasers Opt. *85*, 285 (2006).
93. Mackay G. I., Mayne L. K., Schiff H. I.: Aerosol. Sci. Technol. *12*, 56 (1990).
94. Wert P., Fried A, Rauenbuehler S., Walega J., Henry B.: J. Geophys. Res. *108*, ACH1/1 (2003).
95. Que Z., Furuno T.: Wood Sci. Technol. *41*, 267 (2006).
96. Risholm-Sundman M., Wallin N.: Holz Roh Werkstoff *57*, 319 (1999).
97. Vyhláška 211/2004 *o metodách zkoušení a způsobu odběru a přípravy kontrolních zorků.*
98. Vyhláška 222/1996 Sb. *kterou se stanoví metody odběru vzorků, metody laboratorního zkoušení krmiv, doplňkových látek a premixů a způsob uchovávání vzorků podléhajících zkáze.*
99. Levart A, Veber M.: Chemosphere *44*, 7014 (2001).
100. Guo H., Lee S. C., Louie P. K. K., Ho K. F.: Chemosphere *57*, 1363 (2004).
101. Clarisse B., Laurent, A. M., Seta N., Le Moullec Y., El Hasnaoui A., Momas I.: Environ. Res. *92*, 245 (2003).

102. *Guidelines for Air Quality*. WHO, Geneva (2000).
103. Yu Ch., Crump. D: Build. Environ. *33*, 357 (1998).
104. Civis S., Horka V., Simecek T.: Spectrochim. Acta, A *13*, 3066 (2005).
105. Salhi Y., Rouillard A.: Semicond. Sci. Technol. *19*, 260 (2004).
106. Tipton T., Choe J. I., Kukolich S. G., Hubbard R.: J. Mol. Spectrosc. *114*, 239 (1985).
107. Bell A. G.: Am. J. Sci. *20*, 305 (1880).
108. Tyndall J.: Proc. R. Soc. London *31*, 307 (1881).
109. Rayleigh J. W.: Nature *23*, 274 (1881).
110. Röntgen W. C.: Ann. Phys. *12*, 155 (1881).
111. Viengerov M. L.: Dokl. Akad. Nauk. SSSR *19*, 687 (1938).
112. Kerr E. L., Atwood J. G.: Appl. Opt. *7*, 915 (1968).
113. Flaud J. M., Lafferty W. J., Sams R. L, Sharpe S. W.: Mol. Phys. *104*, 1891 (2006).
114. Hanoune B., LeBris T., Allou L.: Atmos. Environ. *40*, 5768 (2006).

**M. Ferus[a,b], J. Cihelka[a,b], and S. Civiš[a]** *([a] J. Heyrovský Institute of Physical Chemistry, Academy of Sciences of the Czech Republic, Prague, [b] Institute of Physics, Academy of Sciences of the Czech Republic, Prague):* **Formaldehyde in the Environment – Determination of Formaldehyde by Laser and Photoacoustic Detection**

This work concerns the role of formaldehyde in the environment and describes the basic indoor and outdoor detection techniques. One of the laboratory techniques, laser photoacoustic spectroscopy, was used for detection of formaldehyde based on its absorption spectrum in a region around $4350 \text{ cm}^{-1}$. A new type of diode laser (GaInAsSb/AlGaAsSb – MQW (Multi-quantum well)) operating at room temperature in combination with a simple resonance photoacoustic cell provides the minimum detectable signal of formaldehyde, ca. $1250 \text{ } \mu\text{g m}^{-3}$, at $4356 \text{ cm}^{-1}$.

P115

# Dispersion of Light and Heavy Pollutants in Urban Scale Models: CO₂ Laser Photoacoustic Studies

**Z. ZELINGER,\* M. STŘIŽÍK, P. KUBÁT, S. CIVIŠ, E. GRIGOROVÁ, R. JANEČKOVÁ, O. ZAVILA, V. NEVRLÝ, L. HERECOVÁ, S. BAILLEUX, V. HORKÁ, M. FERUS, J. SKŘÍNSKÝ, M. KOZUBKOVÁ, S. DRÁBKOVÁ, and Z. JAŇOUR**

*J. Heyrovský Institute of Physical Chemistry, v.v.i., Academy of Sciences of the Czech Republic, Dolejškova 3, CZ-182 23 Prague 8, Czech Republic (Z.Z., P.K., S.C., E.G., R.J., V.H., M.F., J.S.); VŠB–Technical University of Ostrava, Faculty of Safety Engineering, Lumírova 13, CZ-700 30 Ostrava 3–Výškovice, Czech Republic (M.S., E.G., R.J., O.Z., V.N., L.H., J.S.); Laboratoire de Physique des Lasers, Atomes et Molécules, CERLA, UMR CNRS 8523, Université de Lille 1, F-59655 Villeneuve d'Ascq Cedex, France (S.B.); ETH Zurich, Laboratorium für Physikalische Chemie, Wolfgang-Pauli-Str. 10, CH-8093 Zürich, Switzerland (V.H.); VŠB – Technical University of Ostrava, Faculty of Mechanical Engineering, 17.listopadu 15, CZ-708 33 Ostrava – Poruba, Czech Republic (M.K., S.D.); and Institute of Thermomechanics, v.v.i., Academy of Sciences of the Czech Republic, Dolejškova 5, CZ-182 23 Prague 8, Czech Republic (M.S., V.N., Z.J.)*

The distribution of pollutants in two urban scale models (point emission source and street canyon with extensive transport) was investigated by means of CO₂ laser photoacoustic spectroscopy in the region of the atmospheric window (9–10 μm). The experimental results of physical modeling are in a good agreement with the numerical calculations performed in the frame of computational fluid dynamic (CFD) modeling. Methanol, ethanol, and ozone (examples of light pollutants), as well as sulfur hexafluoride and 1,2 dichlorethane (examples of heavy pollutants), were selected on the basis of their high resolution spectra acquired by Fourier transform and laser diode spectroscopy.

Index Headings: Air pollution; CO₂ laser photoacoustic spectroscopy; PAS; Laser diode spectroscopy; Fourier transform spectroscopy; Wind tunnel; Physical modeling; Computational fluid dynamics; CFD modeling.

## INTRODUCTION

Laser spectroscopic techniques are powerful tools for the investigation of air pollution.[1] Selective, sensitive, and nondestructive laser-based analytical methods have been steadily more employed to monitor trace amounts of gases present in the atmosphere.[2–5] Elevated concentration levels of both primary and secondary atmospheric pollutants mainly occur in the lower parts of the troposphere, the region where relevant physical-chemical processes are also directly influenced by the presence of earth's surface. This part of the troposphere is known as the atmospheric boundary layer.[6] Currently, information on phenomena related to the dispersion of air pollution[7,8] within the atmospheric boundary layer can be assessed only by two basic approaches.

Monitoring the motion of pollutants in a realistic atmosphere is mostly complicated and expensive, often providing incomplete results limited only to particular places. Mathematical models employing numerical calculations or methods based on physical modeling[9–11] are usually applied to overcome such lack of measurements in the realistic atmosphere. To validate the numerical models,[12–15] wind tunnel experiments are also strongly recommended. Due to their selectivity, sensitivity, and ability for on-line detection, infrared laser spectroscopic techniques are good candidates for analytical tools for physical modeling of processes taking place in the atmospheric boundary layer. One of the useful tasks supporting physical modeling is to investigate the dispersion of inert atmospheric tracers. Such tracers can be used to establish flow fields in the simulated boundary layer. The tracers to select must follow physical properties appropriate for the measurements in the wind tunnel (e.g., density of pollutants), and they should be detected by a suitable fast detection technique.[16] Simulating pollutant behavior differing by masses[17] and the chemical behavior of these pollutants[18–21] represent crucial tasks in the field of the physical modeling of air pollution dispersion.[22] In this paper, we focus mainly on studying the behavior of pollutants of different masses. In addition, we also marginally deal with the chemical behavior of the model atmospheric pollutants, with ozone serving as a model of a reactive pollutant. In view of the current approaches applied in the field of physical simulations of the atmospheric boundary layer processes, our contribution represents the first modeling study of simultaneous dispersion of light and heavy pollutants.

Monitoring trace concentration levels of atmospheric pollutants is readily carried out by absorption spectroscopy within the atmospheric window where the absorption of both H₂O and CO₂ molecules is negligible.[23] Pollutants such as ethanol, methanol, sulfur hexafluoride, 1,2-dichloroethane, and ozone that have their absorption bands within the atmospheric window (round 9–10 μm) can be monitored at their rotation-vibration bands. The molecular masses of these model pollutants span the range of two and a half orders of magnitude. To determine the reactivity of the selected model pollutants is not easy; however, ozone is a well known oxidant the reactivity of which is at least one order of magnitude higher compared to that of other model pollutants. Their absorption lines overlap fairly well with the emission spectrum of the CO₂ laser. Employing the Fourier transform infrared (FT-IR) spectrometer and a laser diode system, we have recorded the infrared absorption spectra of the above-mentioned model pollutants to find the most convenient absorption lines (analytically) before applying them to physical modeling using the CO₂ laser photoacoustic spectrometry (PAS) method. The concept of PAS detection was demonstrated to be a sensitive and suitable method for measurement of concentration profiles of pollutants in wind tunnels[4,24] (CO₂ laser as a single radiation source, time resolution 1 s). When combined with the CO₂ laser it allows measurements to be performed within a linear dynamic range up to six orders of magnitude wide.[25]

In this paper we present results of spectroscopic measurements of light (ethanol, methanol, and ozone) and heavy (sulfur hexafluoride and 1,2-dichlorethane) pollutants. This study was

aimed at the development of a step-by-step methodology employing spectroscopic techniques in physical modeling. The methodology is well-demonstrated on the two urban scale systems—a point emission source and a street canyon. Furthermore, the comprehensive study is extended by comparing the data with the results of computational fluid dynamics (CFD) modeling in the case of the point emission source.

## EXPERIMENTAL

The following model pollutants were used: methanol (company: Lach-Ner s.r.o, Czech Republic; purity: p.a. 99.5%), ethanol (company: Lach-Ner, s.r.o.; purity: 99.8%), $SF_6$ (company: Messer; purity: 99.9%), 1,2-dichlorethane (company: LACHEMA Czech Republic; purity: p.a.), and ozone (home-made production based on the use of Hg lamp ozonolyzer; concentration of ozone was calculated from absorption coefficient[26]).

The high-resolution Fourier transform infrared spectrometer Bruker IFS 120FT-IR makes use of a cell with a 20 cm path length and the resolution is 0.0035 cm$^{-1}$. The spectrometer is equipped with a Globar light source and a HgCdTe detector provided with the KBr beam splitter. Experimental details of the FT spectrometer used are shown in Ref. 27. An extensive description of the diode laser spectrometer employed was presented previously.[28,29] The diode laser (Laser Components GmbH) was placed in a laser head cooled by the He cryostat. The laser was temperature and current controlled using Laser Photonics units, model L5731, at a temperature of 30–70 K and a current of 30–500 mA. A lens focuses the laser beam into a (Czerny–Turner) monochromator to separate single laser modes from the spectrum. The radiation leaving the monochromator was directed either into a reference cell, a Ge etalon (0.04 cm$^{-1}$), or into an absorption cell loaded with the gas being studied. The absorption spectrum was recorded with a photoconductor HgCdTe detector operated at liquid nitrogen temperature. The signal from the detector was fed into a digital oscilloscope (Le Croy 9361). The spectra were measured using the current (saw-tooth) modulation of the laser.

Spectroscopic experiments aimed at the application of $CO_2$ laser photoacoustic spectrometry to physical modeling were performed within a low speed, straight open wind tunnel (constant 1.5 m × 1.5 m cross-section, length of 20.5 m, a working section 2 m long). The 30 kW ventilator with a thyristor speed regulator was used to simulate the atmospheric boundary layer with a reference speed ranging from 1 to 12 m·s$^{-1}$. Details of the whole experiment are described in our previous works.[24,30,31] The boundary layer quantities on the inlet of the working section corresponded to those of the neutrally stratified rural atmospheric boundary layer. Atmospheric samples contaminated with the model pollutant were continuously taken at individual, precisely defined places (either the urban scale street canyon model or the model of a point emission source). A movable teflon tube connected through the photoacoustic cell with a pump was used for continuous sampling of the atmosphere at defined places. Samples of the atmosphere were taken with the probe with a rate ranging from 3 to 4 cm$^3$ s$^{-1}$, which are negligible volumes considering the dynamics of the given wind tunnel. The photoacoustic cell was a thermally stabilized brass tube with a length of 38 cm and diameter of 8 mm. Detection was performed on longitudinal acoustical resonance (modulation

frequency 1.2 kHz, the phase is set on the maximum of the photoacoustic signal).

A set of silicone and/or polyethylene tubes sealed on both ends with steel balls and filled with the investigated model pollutant served as well-defined permeation standards to calibrate the equipment as well as for the analysis itself.[32] We also extended our dispersion studies using an auxiliary model pollutant, ethane, to allow better comparison, interpretation, and understanding of processes. In physical modeling ethane is often used as a reference gaseous pollutant due to its density (similar to that of air). Concentration levels of ethane were measured by a customary flame ionization detector (Rosemount Analytical NGA 2000-TFID). The emission of the model pollutants was assured by the permeation method[33,34] or by the method of gas mixing and gas flow controlling with a mass flow controller and/or by the combination of both these methods.

## NUMERICAL METHODS

Numerical models have begun to play an important and often dominant role in environmental assessment. When studying the dispersion of atmospheric pollutants emitted into the atmospheric boundary layer by the ground emission sources (located especially in urban, rural, or industrial areas), a turbulent model,[6,35,36] based on the solution of three-dimensional, time-dependent conservation equations (ideal gas law, continuity equation, Navier–Stokes equation, convection-diffusion equation, energy equation written for static enthalpy), is usually preferred over a model representing an application of the statistical theory of turbulent diffusion (commonly used Gaussian plume model). In particular the micro- and small-scale dynamical modeling employs the so-called Reynolds Average Method (RAM models) based on time-averaged quantities of turbulent flow and on Reynolds averaging the Navier–Stokes equations.[36,37] The standard k-$\varepsilon$ (kinetic turbulent energy − dissipation) model, a member of the RAM model family, currently represents the most promising tool when investigating turbulent effects on the pollutant dispersion within the atmospheric boundary layer. Employing the k-$\varepsilon$ model,[37] besides the above-mentioned conservation equations it is necessary to introduce transport equations for the turbulent kinetic energy and the dissipation rate. The transport equation for the kinetic turbulent energy is

$$\frac{\partial}{\partial t}(\rho k) + \frac{\partial}{\partial x_j}(\rho \bar{u}_j k)$$

$$= \frac{\partial}{\partial x_j}\frac{\mu_t}{\sigma_k}\frac{\partial k}{\partial x_j} + \underbrace{\mu_t\left(\frac{\partial \bar{u}_k}{\partial x_j} + \frac{\partial \bar{u}_j}{\partial x_k}\right)\frac{\partial \bar{u}_k}{\partial x_j}}_{\text{P-shear production}} \underbrace{-g_j\frac{\mu_t}{\rho\sigma_k}\frac{\partial \rho}{\partial x_j}}_{\substack{\text{G-production due} \\ \text{to buoyancy}}} - \rho\varepsilon \quad (1)$$

and the transport equation for the dissipation rate $\varepsilon$ is

$$\frac{\partial}{\partial t}(\rho\varepsilon) + \frac{\partial}{\partial x_j}(\rho\bar{u}_j\varepsilon) = \frac{\partial}{\partial x_j}\frac{\mu_t}{\sigma_\varepsilon}\frac{\partial\varepsilon}{\partial x_j} + C_{1\varepsilon}\frac{\varepsilon}{k}[P + (1 - C_{3\varepsilon})G]$$
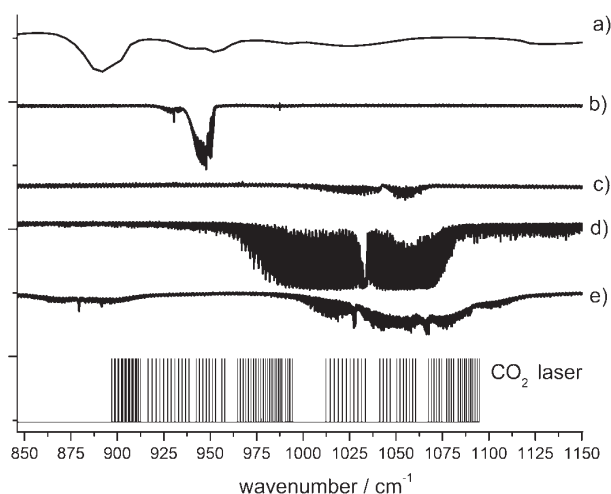$$- C_{2\varepsilon}\rho\frac{\varepsilon^2}{k}$$

$$(2)$$

FIG. 1. Absorption spectra in the 850 to 1150 $cm^{-1}$ range of (*a*) dichlorethane, 10 Torr, 0.1 $cm^{-1}$, 50 scans; (*b*) sulfur hexafluoride, 0.4 Torr, 0.01 $cm^{-1}$, 100 scans; (*c*) ozone, 20 Torr, 0.01 $cm^{-1}$, 100 scans; (*d*) methanol, 8.9 Torr, 0.01 $cm^{-1}$, 50 scans; and (*e*) ethanol 5 Torr, 0.01 $cm^{-1}$, 50 scans measured by the FT-IR spectrometer. The emission lines of the $CO_2$ laser are also shown.



FIG. 2. High resolution absorption spectra of gaseous pollutants recorded by the diode laser spectrometer at different pressures: (*a*) ethanol (231 kPa), (*b*) mixture of ethanol (231 kPa) and air (total pressure 1760 kPa), (*c*) $SF_6$ (24.9 kPa), (*d*) mixture of $SF_6$ (24.9 kPa) and air (total pressure 403.8 kPa), (*e*) ozone (5.7 kPa), and (*f*) mixture of ozone (5.7 kPa) and air (total pressure 412 kPa). The spectra are offset; the dashed line denotes the 9P(14) emission line of the $CO_2$ laser (1052.1956 $cm^{-1}$).

$P$ and $G$ occurring in Eqs. 1 and 2 written for $k$ and $\varepsilon$ denote the shear and buoyancy production of turbulent kinetic energy (TKE), and $C_{1\varepsilon}$, $C_{2\varepsilon}$, and $C_{3\varepsilon}$ are empirical constants. The ratio $G/P$ is closely related to the stability of the atmospheric boundary layer. In the convective boundary layer, the positive buoyancy contributes to the production of TKE. On the contrary, TKE is consumed under statically stable conditions. If the buoyancy term is around zero, then the boundary layer is said to be neutral. While the constants $C_{1\varepsilon}$ and $C_{2\varepsilon}$ are defined (e.g., by Launder and Spalding[38]), the value of $C_{3\varepsilon}$ depends on the buoyancy term $G$, which can be either positive or negative, and thus has to be adapted following the modeled atmospheric stratification. $\sigma_k$, and $\sigma_\varepsilon$ in the equations denote the turbulent Prandtl number [-] for $k$ and $\varepsilon$.

The standard k-ε model was developed and integrated in the customary FLUENT™ 6.2 computational fluid dynamics environment.[37] The investigated model of the point source was studied by mathematical modeling, by applying the finite-volume method. For the FLUENT™ 6.2 k-ε dynamic turbulent model used, the physical conditions (i.e., the definition of emission source and meteorological conditions) corresponded to those of the experiment performed within the simulated atmospheric boundary layer in the wind tunnel. The measuring section of the aerodynamic tunnel has a cubic shape with dimensions of 2 m (length), 1.5 m (height), and 1.5 (width). The Gambit™ 2.1.6. preprocessor was employed to prepare a three-dimensional (3D) computational grid consisting of 337 500 cells. The geometry of the aerodynamic tunnel was meshed in three basic steps. In the first step, all edges were meshed constantly. Considering the investigated problem, the mesh on edges were compressed into the middle section of the geometry moderately (with respect to the position of the pollutant source). In the second step all surfaces were meshed. Two-dimensional cells were created using the predefined scheme QUAD (elements: Quad; type: Map). Finally the volume was meshed as well. Three-dimensional cells were created using the predefined scheme HEX (elements: Hex; type:
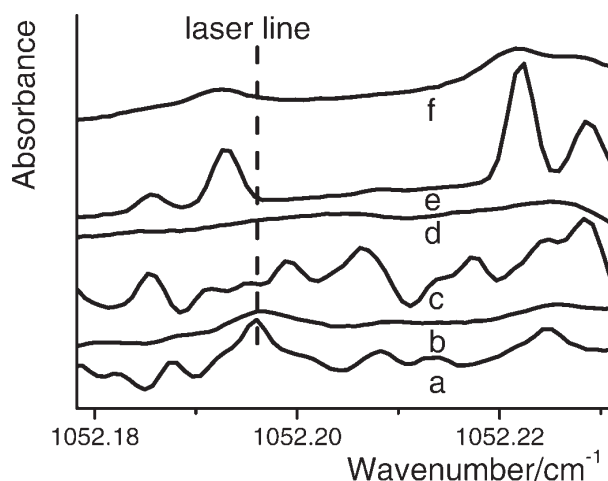
Map). The final mesh was tested using the internal Gambit™ 2.1.6. procedure and was shown to be of the best quality.

## RESULTS AND DISCUSSION

**Spectroscopic Measurements.** Absorption spectra of model pollutants were studied by FT-IR and diode laser infrared spectroscopy covering a spectral region round 10 µm that accommodates the emission bands of the $CO_2$ laser. High resolution absorption spectra of molecules measured by the Bruker IFS 120 FT-IR spectrometer (maximum resolution 0.0035 $cm^{-1}$), with emission lines of the $CO_2$ laser, are depicted in Fig. 1. From Fig. 1 it is evident that all mentioned molecules are likely candidates for monitoring in the region of the $CO_2$ laser. High resolution absorption spectra of gaseous ethanol, ozone (models of "small" pollutant), sulfur hexafluoride (example of a heavy pollutant), and their mixtures with air at different pressures are shown in Fig. 2. The widths of individual spectral lines of pure pollutants (Figs. 2a, 2c, and 2e) are influenced by pressure broadening so that the Doppler width of the lines becomes distinguishable only at pressures below 0.5 kPa. The pressure broadening caused by cumulative increments of air in the mixture leads to a large distortion of the line shapes resulting in decreased absorption coefficients (Figs. 2b, 2d, and 2f).

Several emission lines belonging to the 9P branch emission band of the $CO_2$ laser could interfere with the absorption lines of model pollutants. The information about line shapes is available from quantitative databases containing the vapor-phase infrared spectra[39] and from molecular absorption databases.[40] For instance, the 9P(14) emission $CO_2$ laser line coincides with the absorption lines of ozone (Fig. 2e) and hence seems to be an optimal candidate for ozone monitoring.[26,41,42,43] The frequency of this laser emission line, however, does not match those of absorption lines of sulfur hexafluoride[44,45] and ethanol at low pressure (Figs. 2a and 2c). Although the $CO_2$ laser line sometimes overlaps only with the wings of absorption bands broadened under higher pressure
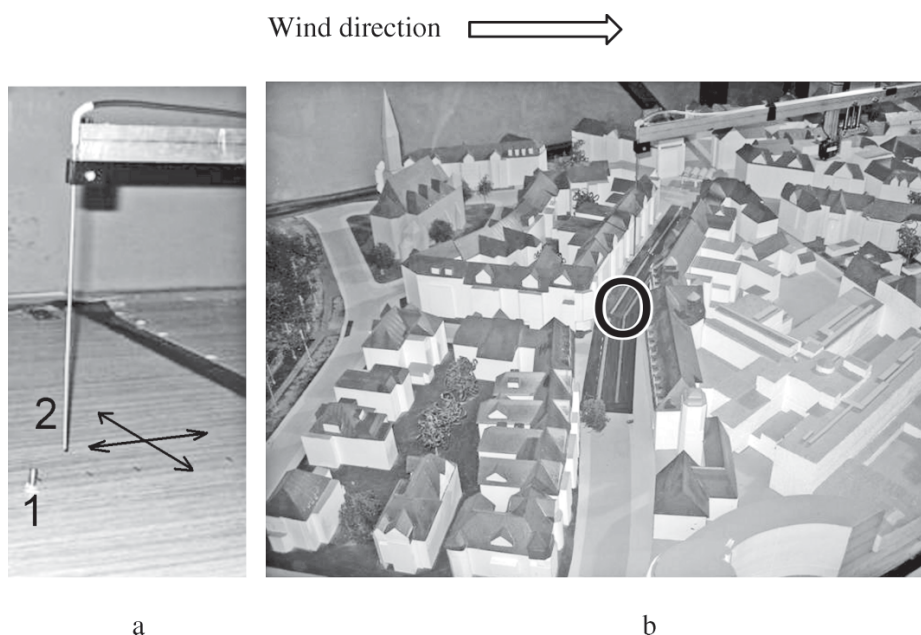
P118

Wind direction ⟹



a                    b

FIG. 3. (**a**) Model of the chimney (1) and the moveable sampling probe (2); (**b**) Urban scale model of the Podbielski street (a part of the Hannover agglomeration at a scale of 1:200), the investigated section is circled.

(Figs. 2b and 2d), the results obtained demonstrate clearly that the sensitivity and the broad linear dynamic range of the $CO_2$ laser photoacoustic technique used here is sufficient for applying this method for monitoring low concentration levels of the model gaseous pollutants in question.

Monitoring the atmosphere surrounding the models placed in the wind tunnel was ensured by using the $CO_2$ laser photoacoustic gas analyzer tuned to the $CO_2$ laser emission lines that were preselected on the basis of the Fourier transform infrared and diode laser infrared spectroscopic study described.

**Point Emission Source.** The model chimney used as a point emission source was 20 mm high and its inner diameter was 6

mm. The model was placed within the working section of the wind tunnel (Fig. 3a). A spatially adjustable sampling probe introduced into the wind tunnel was employed to continuously sample the atmosphere at precisely defined places. Each point was measured five times by 200 s scans. We estimate the level of reproducibility to be 10–15% for the whole experiment.

Figure 4a compares the experimental data of measurements carried out at individual sampling points with the numerical calculations for a light pollutant (methanol). The highest concentration was found near the point emission source; furthermore, the concentration depends strongly on the vertical position of the sampling sites. There is a balance between the
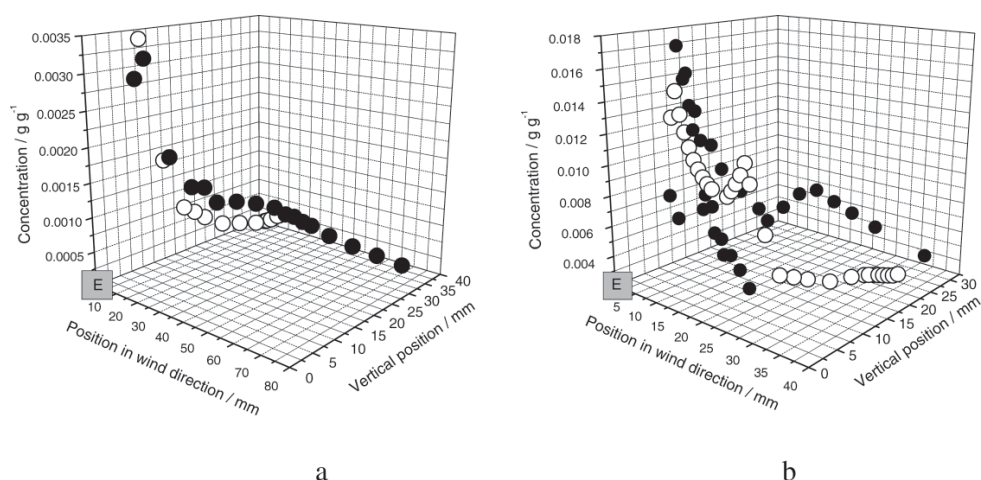


a                    b

FIG. 4. Comparison of the measured (●) and calculated (○) concentrations in a 3D view for (**a**) methanol (light pollutant) and (**b**) 1,2-dichlorethane (heavy pollutant). Sampling sites are in the direction of the wind (along the axis of the wind tunnel); the vertical position is measured relative to the bottom of the wind tunnel; the position (0, 0) denotes the location of the emission source E.
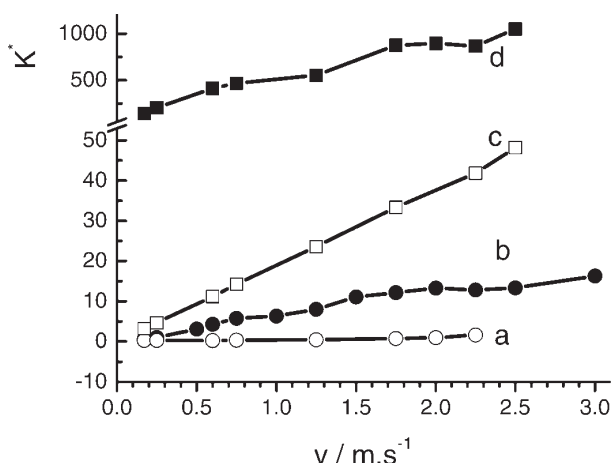
FIG. 5. Urban scale model: the dependencies of the dimensionless mean concentration $K^*$ (calculated from Eq. 3) on the reference wind speed in the wind tunnel for (*a*) ethanol, (*b*) ethane, (*c*) ozone, and (*d*) sulfur hexafluoride.

observed and the calculated concentrations: the concentration level tends to zero as the vertical position increases.

The sampling sites were chosen to follow the main stream of a plume generated by the point emission source. For the heavy pollutant (1,2-dichlorethane) the scheme of sampling points was changed due to entirely different physical behavior of the latter gas. The results of experimental measurements and numerical modeling corresponding to those sampling points are depicted in the Fig. 4b. Studies on the pollutant dispersion[46] show a similar outcome in the case of a heavy pollutant. Heavy

pollutants in particular are expected to disperse in the atmosphere similar to the larger-sized particles; however, they are greatly affected by gravity and thus have a shorter residence time in the atmosphere.[47]

In both cases the agreement between experiment and calculation is very good. Two main differences between the light and the heavy pollutant were observed: (1) for the heavy pollutant the zero concentration level was achieved at a shorter distance in the wind direction (approximately half of the magnitude) as compared to the light pollutant, and (2) the higher concentration levels were also found at sampling sites at small vertical positions up to a relatively higher position in the wind direction.

**Urban Street Canyon.** The other, much more complex, urban scale model was that of a street canyon: a model of the Podbielski street, a part of Hannover agglomeration, at a scale of 1:200 (Fig. 3b).

Vehicles slowly moving in the street in both directions were simulated by two line sources emitting continuously studied pollutant. The mentioned line source is a line consisting of 3750 parallel needle nozzles (2 cm long, inner diameter of 0.1 mm). The small diameter of the needle nozzles causes large hydrodynamic resistance.

To allow an inter-comparison of all results collected for light and heavy model pollutants, absolute concentration values (depending on emission fluxes) were converted into dimensionless ones, also reflecting the geometry of the model used. Measured concentration, $C$ [g·cm$^{-3}$] was converted into dimensionless concentration, $K$, using the height $H$ [cm] of buildings, the transverse length $L$ [cm] of the street, the reference wind speed $U$ [cm·s$^{-1}$] outside the street canyon, and the concentration flux of the pollutant line source $Q$ [g·s$^{-1}$],
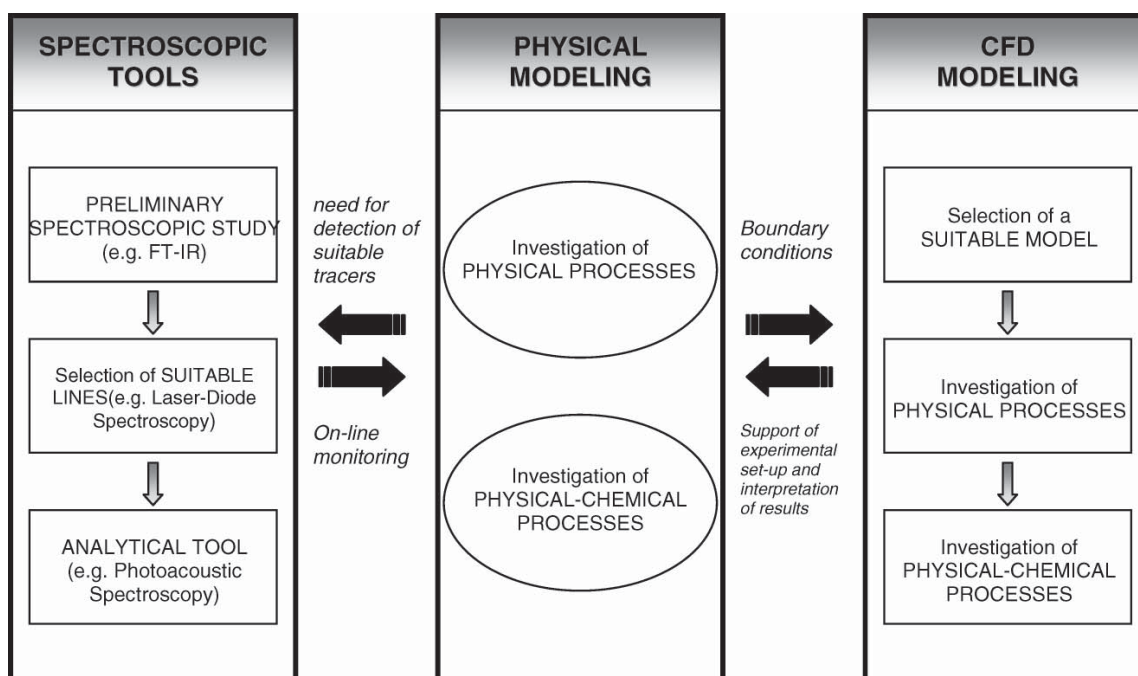


FIG. 6. Methodology combining spectroscopic methods and modeling facilities allows investigation of the dispersion of air pollutant within the atmospheric boundary layer.

P120

according to the formula

$$K = \frac{CHUL}{Q} \qquad (3)$$

The difference between the light (ethanol, ethane, and ozone) and heavy (sulfur hexafluoride) pollutants can be observed in Fig. 5. As seen in Eq. 3 the dimensionless concentration $K$ is proportional to the reference wind speed. However, the slope of this dependence is apparently larger for the heavy pollutants than it is for light and reactive pollutants. Therefore, one prefers mass dependence rather than reactivity dependence. Data of independent dispersion studies[16,17] agree with our results in the case of heavy pollutants.

The results for ozone (which are of importance for atmospheric processes) are similar to those obtained for other light pollutants (see Fig. 5). Ozone itself is not of such reactivity in the absence of reactant; it belongs to a group of moderately long living species with temporal scale ranging from a few days to one year.[48] Such similarity for all relatively stable chemical species is important for epidemiological studies, in particular when assessing exposure of population to the air pollution.[49] Differences in ozone behavior for urban air pollution within the formation of photochemical pollutants are discussed elsewhere.[18,19]

## CONCLUSION

The selected molecular models of gaseous atmospheric pollutants were studied by methods based on absorption spectroscopy. These methods were used to extend the techniques employed so far to model processes taking place in the atmospheric boundary layer. They enable the investigation of simultaneous dispersion of model atmospheric pollutants differing by their masses, as was well demonstrated in our study dealing with model light (methanol, ethanol), heavy (sulfur hexafluoride, 1,2-dichlorethane), and reactive (ozone) pollutants.

Consequently, $CO_2$ laser photoacoustic spectroscopy was applied as the main analytical tool in physical modeling the dispersion of pollutants within urban scale models. The main difference was found between the light and heavy pollutants. The drawbacks of the present system are its relatively large complexity.

Combining the spectroscopic approaches and modeling facilities (Fig. 6) for investigation of pollutant dispersion offers great possibilities for further development. On one hand it makes physical modeling easier, while being more comprehensive on the other hand (as it enables investigation of chemical reactions in a simulated atmospheric boundary layer).

1. M. W. Sigrist, "Air Monitoring, Optical Spectroscopic Methods", in *Encyclopedia of Environmental Analysis and Remediation*, R. A. Meyers, Ed. (Wiley, New York, 1998), p. 84.

2. A. Wiacek, J. R. Taylor, K. Strong, R. Saari, T. E. Kerzenmacher, N. B. Jones, and D. W. T. Griffith, J. Atmos. Ocean. Technol. **24,** 432 (2007).

3. N. Glatthor, T. von Clarmann, H. Fischer, B. Funke, S. Gil-Lopez, U. Grabowski, M. Hopfner, S. Kellmann, A. Linden, M. Lopez-Puertas, G. M. Tsidu, M. Milz, T. Steck, G. P. Stiller, and D. Y. Wang, Atmos. Chem. Phys. **6,** 2767 (2006).

4. Z. Zelinger, M. Střižík, P. Kubát, Z. Jaňour, P. Berger, A. Černý, and P. Engst, Opt. Lasers Eng. **42,** 403 (2004).

5. Z. Zelinger, B. Barret, P. Kubát, P. Ricaud, J.-L. Attie, E. LeFlochmoen, J. Urban, D. Mutargh, and M. Střižík, Mol. Phys. **104,** 2815 (2006).

6. R. B. Stull, *An Introduction to Boundary Layer Meteorology* (Kluwer Academic Publishers, Dordrecht, 1994).

7. M. Schatzmann, B. Leitl, and J. Liedtke, Environ. Monitor. Assess. **65,** 249 (2000).

8. S. Vardoulakis, B. E. A. Fischer, K. Percleous, and N. Gonzalez-Flesca, Atmos. Environ. **37,** 155 (2003).

9. A. P. G. Sagrado, J. van Beeck, P. Rambaud, and D. Olivari, J. Wind Eng. Indust. Aerodynam. **90,** 321 (2002).

10. Z. Zelinger, M. Střižík, P. Kubát, K. Lang, K. Bezpalcová, and Z. Jaňour, Intern. J. Environ. Anal. Chem. **86,** 889 (2006).

11. S. Civiš, Z. Zelinger, M. Střižík, and Z. Jaňour, "Simulation of Air Pollution in a Wind Tunnel", in *Spectroscopy from Space*, J. Demaison, Ed. (Kluwer Academic, Dordrecht, 2001), p. 275.

12. S. Di Sabatino, R. Buccolieri, B. Pulvirenti, and R. Britter, Atmos. Environ. **41,** 8316 (2007).

13. F. I. Khan and S. A. Abbasi, J. Hazardous Mater. **80,** 15 (2000).

14. M. T. Boehm and D. E. Pylor, Atmos. Environ. **39,** 4841 (2005).

15. J. Pospíšil, J. Katolicky, and M. Jicha, Sci. Total Environ. **334,** 185Sp. Iss. SI (2004).

16. J. E. Cermak, A. G. Davenport, E. J. Plate, and D. X. Virgas, Eds., *Wind Climate in Cities*, NATO ASI Series E: Applied Science (Kluwer Academic Publisher, Dordrecht, 1995), vol. 277.

17. G. Ooms and H. Tennekes, Eds., *Atmospheric Dispersion of Heavy Gates and Small Particles*, International Union of Theoretical and Applied Mechanics, Symposium, Delft, The Netherlands (Springer-Verlag, Berlin, 1984).

18. S. Sillman, Atmos. Environ. **33,** 1821 (1999).

19. M. E. Jenkin and K. C. Clemitshaw, Atmos. Environ. **34,** 2499 (2000).

20. P. Tulet, V. Crassier, and R. Rosset, Environ. Model. Software **15,** 693 (2000).

21. Z. Zelinger, P. Kubát, M. Střižík, P. Danihelka, K. Bezpalcová, Z. Jaňour, S. Drábková, M. Kozubková, P. Berger, A. Černý, and P. Engst, "Urban air pollution and its photochemistry studied by laser spectroscopic methods", in *Remote Sensing of the Atmosphere for Environmental Security*, A. Perrin, N. Ben Sari-Zizi, and J. Demaison, Eds., NATO Security Through Science Series – C: Environmental Security (Springer, Dordrecht, 2006), p. 301.

22. S. Civiš, M. Střižík, Z. Jaňour, J. Holpuch, and Z. Zelinger, J. AOAC Int. **85,** 243 (2002).

23. M. W. Sigrist, "Air Monitoring by Laser Photoacoustic Spectroscopy", in *Air Monitoring by Spectroscopic Techniques*, M. W. Sigrist, Ed., Chemical Analysis Series (Wiley, New York, 1994), vol. 127, p. 163.

24. Z. Zelinger, S. Civiš, and Z. Jaňour, Analyst (Cambridge, U.K.) **124,** 1205 (1999).

25. M. W. Sigrist, "Air Monitoring by Laser Photoacoustic Spectroscopy", in *Air Monitoring by Spectroscopic Techniques*, M. W. Sigrist, Ed., Chemical Analysis Series (Wiley, New York, 1994), vol. 127, p. 163.

26. J. Codnia and M. L. Azcarate, Opt. Lasers Eng. **39,** 619 (2003).

27. S. Civiš, T. Šedivcová-Uhlíková, P. Kubelík, and K. Kawaguchi, J. Mol. Spectrosc. **250,** 20 (2008).

28. Z. Zelinger, S. Civiš, P. Kubát, and P. Engst, Infrared Phys. Technol. **36,** 537 (1995).

29. Z. Zelinger, P. Kubát, and J. Wild, Chem. Phys. Lett. **368,** 532 (2003).

30. Z. Zelinger, I. Jančík, and P. Engst, Appl. Opt. **31,** 6974 (1992).

31. Z. Zelinger, M. Střižík, P. Kubát, and S. Civiš, Anal. Chim. Acta **422,** 179 (2000).

32. Z. Zelinger, P. Engst, Z. Papoušková, and M. Jakoubková, "Trace Analysis of Freons by Optoacoustic $CO_2$ Laser Detection", in *Photoacoustic and Photothermal Phenomena*, P. Hess and J. Pelzl, Eds., Springer Ser. Opt. Sci. (Springer-Verlag, Berlin, Heidelberg, 1988), vol. 58, p. 131.

33. Z. Zelinger, Z. Papoušková, M. Jakoubková, and P. Engst, Coll. Czech. Chem. Commun. **53,** 749 (1988).

34. V. Steiner, P. Engst, Z. Zelinger, and M. Horák, Coll. Czech. Chem. Commun. **54,** 2667 (1989).

35. F. T. M. Nieuwstadt, J. G. M. Eggels, R. J. A. Janssen, and M. B. J. M. Pourquié, "Direct and Large-Eddy Simulations of Turbulence in Fluids",

in *Future Generation Computer System* (Elsevier Science Publishers B. V., New York, 1994), vol. 10, Issues 2–3, pp. 189–205.

36. S. Drábková and P. Platoš, "Numerical Simulation as a Tool for the Solution and Understanding of Practical Air Pollution Probléme", in Proc. of the Conference on Modelling Fluid Flow (CMFF'03) (Budapest, Budapest University of Technology and Economics, 2003), pp. 501–506.

37. Fluent Inc., Fluent 6.2, available from http://sp1.vsb.cz/DOC/Fluent_6.1/html/ug/main_pre.htm.

38. B. E. Launder and D. B. Spalding, *Mathematical Models of Turbulence* (Academic Press, London, 1979).

39. S. W. Sharpe, T. J. Johnson, R. L. Sams, P. M. Chu, G. C. Rhoderick, and P. A. Johnson, Appl. Spectrosc. **58,** 1452 (2004).

40. L. S. Rothman, R. R. Gamache, R. H. Tipping, C. P. Rinsland, M. A. H. Smith, D. C. Benner, V. M. Devi, J. M. Flaud, C. Camypeyret, A. Perrin, A. Goldman, S. T. Massie, L. R. Brown, and R. A. Toth, J. Quant. Spectrosc. Radiat. Trans. **48,** 469 (1992).

41. S. Lundqvist, J. Margolis, and J. Reid, Appl. Opt. **21,** 3109 (1982).

42. J. M. Hoell, C. N. Harward, C. H. Bair, and B. S. Williams, Opt. Eng. **21,** 548 (1982).

43. J.-M. Flaud, C. Camy-Peyret, C. P. Rinsland, M. A. H. Smith, and V. M. Devi, *Atlas of Ozone Spectral Parameters from Microwave to Medium Infrared* (Academic Press, Inc., Boston, 1990).

44. H. Stafast, W. E. Schmid, and K. L. Kompa, Opt. Commun. **21,** 121 (1977).

45. R. R. Gamache, N. Lacome, G. Pierre, and T. Gabard, J. Mol. Struct. **599,** 279 (2001).

46. J. A. Havens and T. O. Spicer, "Gravity Spreading and Air Entrainment by Heavy Gas Instantaneously Released in a Calm Atmosphere", in *Atmospheric Dispersion of Heavy Gases and Small Particles*, G. Ooms and H. Tennekes, Eds. (Springer-Verlag, Berlin, 1984).

47. L. Y. Chan and W. S. Kwok, Atmos. Environ. **34,** 4403 (2000).

48. J. H. Seinfeld and S. N. Pandis, *Atmospheric Chemistry and Physics, From Air Pollution to Climate Change* (John Wiley and Sons, New York, 1998).

49. S. Kingham, D. Briggs, P. Elliott, P. Fischer, and E. Lebret, Atmos. Environ. **34,** 905 (2000).

# Spektroskopie tabákového kouře

**Vojtěch Pazdera[1], Michal Fousek[1], Martin Ferus[2,3], Kseniya Dryahina[2], Patrik Španěl[2], Violetta Shestivska[3] a Svatopluk Civiš[2]**

[1] Střední průmyslová škola sdělovací techniky, Panská 3, Praha 1
[2] Ústav fyzikální chemie J. Heyrovského, v. v. i., AV ČR, Dolejškova 3, 182 23 Praha 8 (e-mail: svatopluk.civis@jh-inst.cas.cz)
[3] Fyzikální ústav, v. v. i., AV ČR, Na Slovance 2, 182 21 Praha 8

Pomocí infračervené spektrometrie s Fourierovou transformací (FTIR), hmotnostní detekce v proudové trubici s vybranými ionty (SIFT-MS) a plynové chromatografie ve spojení s hmotnostní spektrometrií (GC-MS) bylo analyzováno složení cigaretového kouře, kouře z vodní dýmky a doutníku. Bylo kvalitativně porovnáno zastoupení jednotlivých komponent v závislosti na typu vzorku. Jsou diskutovány možnosti použitých analytických metod. Přehled konkrétních látek je doplněn fakty o jejich původu a škodlivém účinku.

Kouřením je podle medicínské definice nazývána inhalace [1] kouře zapáleného tabáku např. z dýmky, cigarety nebo doutníku. Někdy se tento pojem vztahuje i na inhalaci drog, jako je marihuana a její koncentrovaná forma hašiš nebo tzv. crack (kokain). Kuřákovu rostoucí chuť na tabákovou cigaretu způsobuje převážně vysoce návykový psychoaktivní alkaloid nikotin. Dochází ke vzniku závislosti, stavu, při němž je člověk nucen kouřit i přes znalost zdravotních následků. Ve své podstatě je závislost chronické onemocnění způsobené nejen zmíněným nikotinem, ale také chutí kouře a v některých případech se jedná pouze o společenský návyk [2].

Již v 17. stol. bylo kouření označováno za zdraví škodlivé. Rakovinotvorné účinky cigaretového kouře jsou poprvé zmíněny v publikaci Benjamina Rushe z roku 1798. Autor spojuje cigaretový kouř s rakovinou rtů. Zejména v devatenáctém století a na počátku století dvacátého bylo kouření považováno za symbol určité společenské úrovně, ačkoliv bylo ve stejné době publikováno mnoho prací, které jej jednoznačně spojovaly s řadou nemocí. Např. Joel Shew jich ve své publikaci „Tobacco: Its History, Nature, and Effects on the Body and Mind" vyjmenoval 87. Celou řadu historických faktů lze najít v přehledné publikaci Tobacco Risk Awareness Timeline [3]. Podle zprávy [4] Státního zdravotního ústavu v ČR kouří 29,2 % populace (z toho jen 2,9 % jsou nepravidelní kuřáci) a tento podíl se za posledních deset let téměř nezměnil. Podíl kuřáků mezi patnáctiletými však stoupl z 12,5 % v roce 1997 na 19,6 % v roce 2008.

Podle Mezinárodní agentury pro výzkum rakoviny [5] (IARC) jsou cigaretový kouř i tabák považovány za prokázané karcinogeny (sk. 1 A – karcinogenní pro člověka [6]). Cigaretový kouř je považován za tzv. komplexní karcinogen, tedy směs více karcinogenních látek, jejichž účinek je různým způsobem vzájemně pro-

vázán. V cigaretovém kouři bylo zjištěno kolem čtyř tisíc chemikálií ve fázi plynné, kapalné i pevné:

*Kapalná fáze* tvoří zhruba 1 % objemu vdechnutého kouře. Nejdůležitější směsí v kapalné fázi je dehet, viskózní černohnědá kapalina, jež obsahuje kolem 600 převážně karcinogenních sloučenin. Jsou to např. polycyklické aromatické uhlovodíky (např. benzo[a]pyren) způsobující rakovinu jícnu, plic, slinivky, ledvin a močového měchýře, aromatické aminy vyvolávající rakovinu močového měchýře a anorganické sloučeniny (těžké kovy – např. kadmium, železo) způsobující rakovinu plic a kůže. Nejdůležitější dehtovou látkou je psychoaktivní nikotin.

*Plynná fáze* tvoří asi 91 % a stejně jako kapalná složka kouře obsahuje promotory nádorů a látky toxické pro řasinky respiračního epitelu. Se vznikem rakoviny jsou nejčastěji spojovány nitrosaminy a formaldehyd. Mezi další toxické látky patří kyanovodík, acetaldehyd, oxid uhelnatý atd.

*Pevná fáze* tvoří 8 % a je složena převážně ze sazí, na které jsou opět navázány pro dehet typické polycyklické aromatické uhlovodíky (benzo[a]pyren, 5-methylchrysen, naftalen atd.).

## Historie kouření

Kouření tabáku se rozšířilo nejprve mezi americkými indiány, u nichž nebylo běžnou součástí každodenního života, ale bylo praktikováno během obřadů. Na rozdíl od dnešní praxe indiáni kouř nešlukovali. Evropa tabák poznala díky Kryštofu Kolumbovi a hlavně jeho námořníkům. Po jejich návratu z objevené Ameriky (duben roku 1493) představila Kolumbova posádka pěstování a používání tabáku ve Španělsku. Návyková látka v tabáku, nikotin, nese své jméno po Jeanu Nicotovi (1530–1600), francouzském vyslanci v Portugalsku. Ten tabák propagoval a přisuzoval mu zázračné léčivé schopnosti. Obklady z tabákových listů vyléčil vleklou migrénu sobě i francouzské královně.

P123
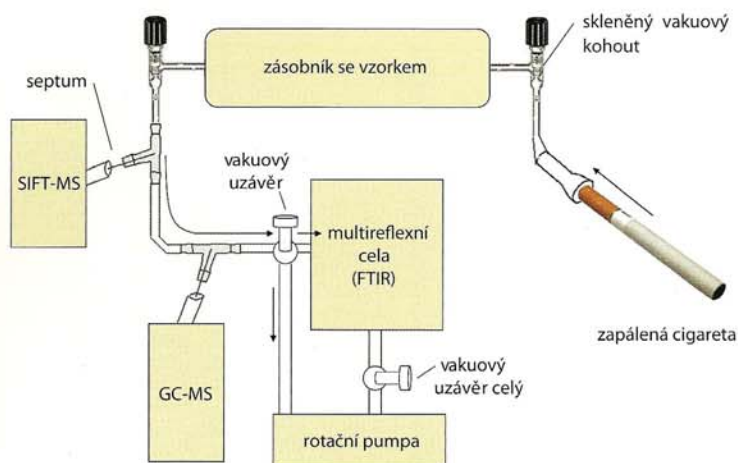
**Obr. 1** Aparatura pro odběr vzorku cigaretového kouře. Spektrometr SIFT-MS byl napojen přes septum na vakuovou linku čerpanou pomocí rotační pumpy. Do linky byl nasáván kouř, jehož vzorek byl odebírán přes septum do spektrometru SIFT-MS. Stejným způsobem byl pro analýzu GC-MS získán vzorek stříkačkou pro SPME. Pomocí zásobníku se vzorkem o objemu 5 l byla následně naplněna multireflexní cela spektrometru Bruker IFS 125.

Po několik století se kouření tabáku šířilo pomalu a zejména církev tento zlozvyk nesla nelibě. Roku 1624 vydal papež Urban VIII. bulu zakazující kouření v kostele. V Rusku bylo kouření dokonce trestáno např. useknutím nosu nebo rozseknutím horního rtu tak, aby už nesrostl a jeho majitel už nikdy nemohl pohodlně kouřit. Tyto tresty zrušil až car Petr Veliký, který byl sám náruživým kuřákem.

Vznik cigaret bývá spojován s turecko-egyptskou válkou. Egyptští dělostřelci dostali za odměnu po vítězné bitvě tabák, ale neměli jedinou dýmku. Jelikož běžnou praxí bylo balení střelného prachu do ruliček papíru, uplatnili své znalosti z bitvy a začali stejným způsobem balit tabák. Od egyptských vojáků se postup naučili vojáci turečtí a tento způsob kouření se začal rozšiřovat do celého světa [7]. Jako první začal ručně balené cigarety prodávat londýnský prodejce tabáku Philip Morris v roce 1847. V roce 1880 vynalezl James A. Bonsack stroj na výrobu cigaret, který dokázal vyrobit 200 cigaret za minutu. Kouření se stalo zcela běžnou věcí. Dnes mají stroje výkon přibližně 9 000 cigaret za minutu. Významný podíl na rozšíření cigaret měla i první světová válka, v níž dostávali vojáci všech armád příděl na povzbuzení morálky.

Během 19. století se začaly objevovat vědecké práce prokazující škodlivost kouření – např. v roce 1859 francouzský lékař M. Buisson zjistil, že rakovinou dutiny ústní jsou prokazatelně postihováni zejména kuřáci dýmek. A. Ochsner a M. E. DeBakey [8] přišli v roce 1936 na to, že většinu jejich pacientů s bronchogenním karcinomem tvořili kuřáci. Výzkumy R. Pearla [9] publikované v roce 1938 ukázaly, že nekuřáci žijí v průměru déle než kuřáci. Ve stejné době se podařilo argentinskému vědci A. H. Roffoovi prokázat karcinogenní efekt zplodin kouření tím, že vyvolal rakovinu kůže u králíků, které potíral tabákovým dehtem [10]. Ve 30. letech dvacátého století bojoval proti kouření dokonce i Adolf Hitler. Zakázal reklamu na tabákové výrobky, kouření ve veřejných budovách, veřejné dopravě a osobám mladším osmnácti let kouření na veřejnosti. V nacistickém Německu bylo vypracováno množství prací, které dokazovaly škodlivost kouření. Odborná

veřejnost v ostatních zemích nicméně soudila, že věrohodnost těchto prací je nulová. Všeobecně uznávanými se staly až práce britských vědců z počátku 50. let [5].

## EXPERIMENTY S TABÁKOVÝM KOUŘEM

Pro analýzu cigaretového kouře, kouře doutníku a vodní dýmky byly v této práci použity tři typy přístrojů – infračervený spektrometr Bruker IFS 125 HR, hmotnostní spektrometr SIFT-MS a plynový chromatograf s hmotnostní detekcí GC-MS. Cílem práce bylo porovnat možnosti uvedených metod při kvalitativní analýze složení komplexní směsi, jakou je cigaretový kouř. Analytické postupy pro cigaretový kouř jsou standardizovány např. v normách ISO 10315, ISO 4387:2000 a ISO 8454 zavedených v ČSN ISO 10315 (56 9507) Cigarety – Stanovení obsahu nikotinu v kouřových kondenzátech, kde je použita metoda plynové chromatografie a ČSN ISO 4387:2003 (56 9512) Cigarety – Stanovení dehtu za použití rutinního analytického nakuřovacího přístroje. K analýze doporučuje tato norma použití techniky nedisperzní infračervené spektrometrie.

### Plynová chromatografie s hmotnostní detekcí (GC-MS)

Plynový chromatograf (Finnigan Focus GC, ITQ 700, Thermo Electron Corp.) s hmotnostní detekcí (Xcalibur ion trap, Thermo Scientific) je komerčně dodávaným přístrojem. Odběr cigaretového kouře byl proveden plynovou stříkačkou a následně v objemu 0,2 ml vstříknut do prostoru injektoru vyhřívaného na 220 °C. Látky obsažené v analyzovaném kouři dále procházejí spolu s nosným plynem He chromatografickou kolonou, kde probíhá jejich rozdělení v čase (separace). Pro účely experimentu byla použita kapilární kolona (TR-1) o délce 30 m a průměru 0,25 mm. Kolona je naplněna vrstvou 100% dimethylpolysiloxanu (nepolární stacionární fáze) o tloušťce 1 μm. Pro nejúčinnější separaci byl použit teplotní režim postupného zahřátí kolony: iniciační teplota 38 °C byla udržována 1 minutu, následně byla teplota zvýšena rychlostí 20 °C/min na 210 °C a udržována na této hodnotě po dobu 3 min. Plynová separace jednoho vzorku tak trvala 12,60 min. Po výstupu z kolony je analyt ionizován proudem elektronů o energii 70 eV a vstupuje do iontové pasti. Jednotlivé ionty pak podle poměru hmotnosti (15–400 m/z) a náboje iontovou past opouštějí a jsou analyzovány detektorem. Přístroj je používán na citlivou kvalitativní analýzu, pro identifikaci látek byla použita databáze hmotnostních spekter NIST 2,0. Shoda hmotnostních spekter s databází byla minimálně 75 %.

### Hmotnostní spektrometrie v proudové trubici (SIFT-MS)

Princip metody SIFT-MS je shrnut v publikaci [11]. Jedná se o metodu hmotnostní spektrometrie v proudové trubici s vybranými ionty, která je založena na chemické ionizaci během přesně definovaného reakčního času a umožňuje tak přesné a citlivé stanovení stopových koncentrací látek přítomných ve vzduchu (v koncentracích $10^{-9}$ a větších). Hlavními částmi spektrometru je iontový zdroj, separátor a analyzátor. K analýze jsou použity prekurzorové ionty $H_3O^+$, $NO^+$ a $O_2^+$, které jsou generovány v mikrovlnném výboji a požadovaný ion je vybrán pomocí kvadrupólového separátoru. V proudové trubici pak ion reaguje s analytem, který vstupuje spolu s nosným plynem do spektrometru vy-
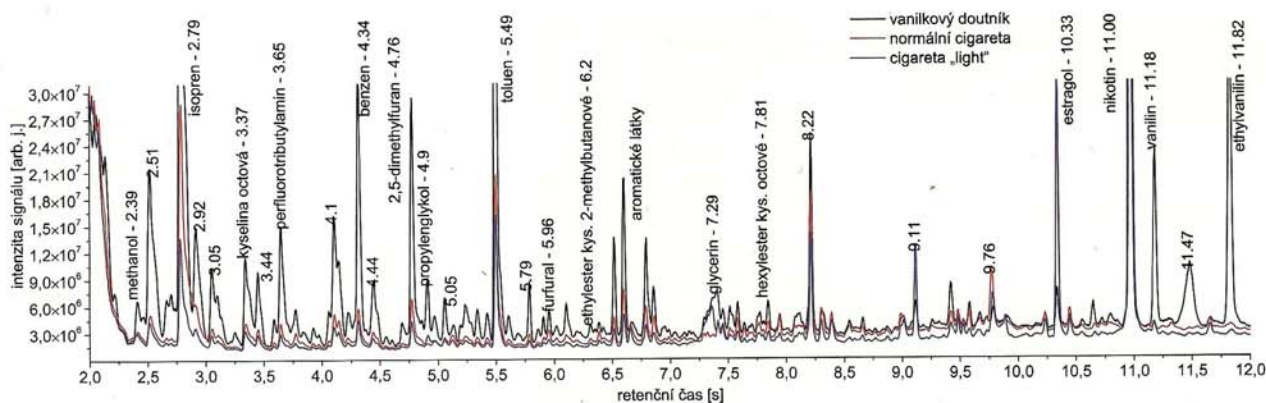
**Obr. 2** Chromatogramy jednotlivých typů kouře měřené pomocí chromatografie GC-MS.
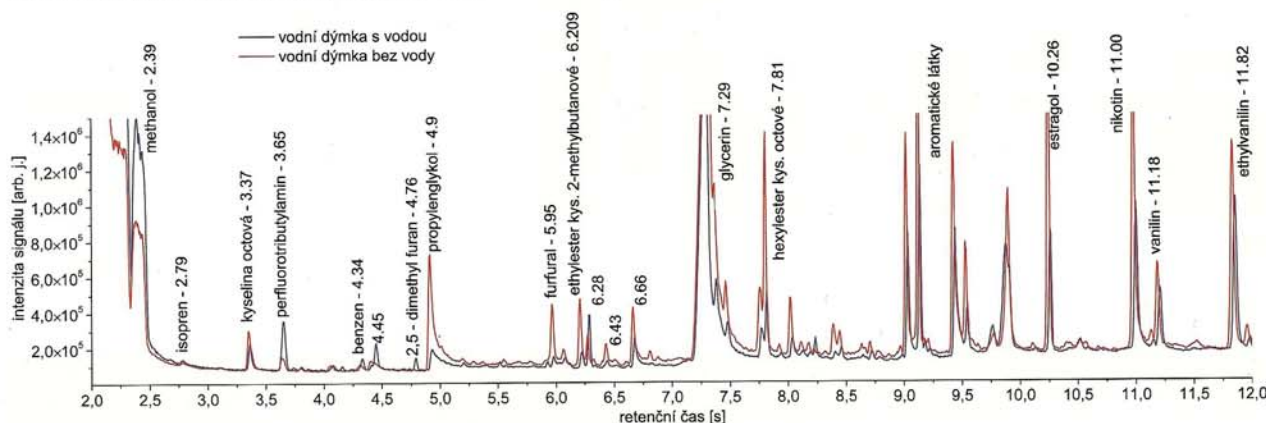


**Obr. 3** Chromatogramy jednotlivých typů kouře měřené pomocí chromatografie GC-MS.

hřívanou kapilárou. Reakční produkty jsou separovány podle poměru m/z a zachyceny detektorem. Informace o kvantitě vzorku je získána na základě znalosti reakční rychlosti vybraného iontu s molekulami analytu.

### Infračervená spektrometrie s Fourierovou transformací (FTIR)

Spektrometrem s Fourierovou transformací Bruker IFS 125 HR lze měřit jak absorpční, tak emisní spektra s rozlišením až 0,002 cm⁻¹, které odpovídá přirozené šířce spektrálních čar dané Dopplerovým jevem. Princip spektrometrie s Fourierovou transformací je shrnut v publikaci [12]. Základní součástí přístroje je Michelsonův interferometr s 2,5 m dlouhým tunelem pohyblivého zrcadla. V interferometru dochází k interferenci polychromatického záření vycházejícího ze zvoleného zdroje. Záření prochází multireflexní kyvetou s optickou dráhou 30 m a dopadá na detektor. Přístroj je schopen pokrýt rozsah od vzdáleného infračerveného záření až po UV oblast v závislosti na použitém děliči svazku, zdroji a detektoru. Pro měření v této práci byla jako zdroj použita žárovka s wolframovým vláknem nebo žhavená tyčinka z karbidu křemíku (tzv. globar), HgCdTe (MCT) a InSb dusíkem chlazené polovodičové detektory a dělič svazku z pokoveného bromidu draselného. Měření bylo provedeno v oblasti mezi 600 cm⁻¹ a 5 500 cm⁻¹ s rozlišením 0,02 cm⁻¹. K dosažení optimálního poměru signálu k šumu bylo třeba provést 100 akumulací signálu (tzv. skenů). Doba měření jednoho vzorku byla 53 minut. Komerčně dodávaný software OPUS 5.0 byl použit k vyhodnocování absorpčních intenzit a ke srovnávání rotačně vibračních pásů jednotlivých komponent s vlastní databází spekter.

### Odběr vzorku a vlastní spektrometrická měření

Vzorek kouře byl odebírán pomocí vakuové linky zobrazené na obr. 1. Cigareta, vodní dýmka a následně doutník byly zasunuty do skleněné trubičky připojené k aparatuře vakuovou hadicí Tygon. Linka byla sčerpána rotační olejovou pumpou na 10⁻² torr. Po otevření vakuového kohoutu byl kouř nasáván do linky, proud byl regulován pomocí ventilu pumpy. Přes septum byl kapilárou v průtoku odebírán vzorek pro analýzu SIFT-MS a pro GC-MS byl vzorek odebrán plynovou stříkačkou (0,2 ml). Po analýze byl prostor skleněného zásobníku o objemu 5 l naplněn kouřem a vzorek byl expandován do multireflexní cely připojené ke spektrometru FTIR. Cela byla vyčerpána na tlak 6·10⁻³ torr. Tlak vzorku v cele po expanzi kouře ze zásobníku byl u normální cigarety 25 torr, cigarety „light" 55 torr, doutníku 60 torr, vodní dýmky naplněné vodou 53 torr a kouře tabáku vodní dýmky bez vody 69 torr. Následně bylo zahájeno měření pomocí FTIR spektrometru.

### VÝSLEDKY A DISKUSE

Jako první analytická metoda byla zvolena plynová chromatografie s hmotnostní detekcí, neboť komerčně dodávané přístroje GC-MS disponují vysokou citlivostí a databází hmotnostních spekter jednotlivých látek (NIST 2.0 library), která umožňuje kvantitativní identifikaci neznámých látek přítomných ve vzorku (screening). Chromatogramy cigaretového kouře spolu s kouřem z doutníku a dýmu z vodní dýmky s a bez vody ukazují obr. 2 a obr. 3. Souhrn látek identifikovaných pomocí hmot-

P125

**Tab. 1**

| látka | vzorec | retenční čas | cigaretový kouř — klasická cigareta | cigaretový kouř — lehká cigareta | doutník | dýmka s vodou | dýmka bez vody |
|---|---|---|---|---|---|---|---|
| methanol | $CH_3OH$ | 2,43 | | | 100 % | 27 % | 16 % |
| izopren | $C_5H_8$ | 2,79 | 45 % | 20 % | 100 % | | |
| kyselina octová | $CH_3COOH$ | 3,37 | 30 % | 18 % | 100 % | 2 % | 3 % |
| perfluorotributylamin | $N(C_4F_9)_3$ | 3,65 | 22 % | 13 % | 100 % | 3 % | 1 % |
| benzen | $C_6H_6$ | 4,34 | 15 % | 11 % | 100 % | | |
| 2,5-dimethylfuran | $C_6H_8O_1$ | 4,76 | 20 % | 11 % | 100 % | | |
| propylenglykol | $C_3H_8O_2$ | 4,9 | | | 100 % | 2 % | 9 % |
| toluen | $C_6H_5CH_3$ | 5,49 | 21 % | 17 % | 100 % | | |
| furfural | $C_5H_4O_2$ | 5,96 | 50 % | 28 % | 100 % | 3 % | 9 % |
| kys. 2-methylbutanová | $C_5H_{10}O_2$ | 6,29 | | | 100 % | 8 % | 22 % |
| glycerin | $C_3H_8O_3$ | 7,29 | | | 100 % | 35 % | 49 % |
| hexylester k. octové | $C_8H_{16}O_3$ | 7,81 | 6 % | | 100 % | 9 % | 27 % |
| estragol | $C_{10}H_{12}O$ | 10,26 | 82 % | 99 % | 100 % | 3 % | 7 % |
| nikotin | $C_{10}H_{14}N_2$ | 11 | 98 % | 100 % | 50 % | 1 % | 1 % |
| vanilin | $C_8H_8O_3$ | 11,21 | | | 100 % | 2 % | 3 % |
| ethylvanilin | $C_9H_{10}O_3$ | 11,81 | | | 100 % | 3 % | 4 % |

**Tab. 1** Přehled látek detekovaných pomocí spektrometru GC-MS. Výška chromatografického píku v daném vzorku je pro každou molekulu vyjádřena procentuálně vzhledem ke své maximální hodnotě, které bylo s výjimkou nikotinu dosaženo vždy ve vzorku kouře z doutníku.

nostní databáze ukazuje tab. 1. Ačkoliv cílem práce nebyla kvantitativní analýza, intenzita signálu chromatografického píku dovoluje srovnání zastoupení jednotlivých komponent ve vzorcích. Chromatogram vanilkového doutníku ukazuje, že všechny identifikované látky kromě estragolu a také nikotinu jsou v jeho kouři přítomny ve vyšších koncentracích než v kouři obou typů cigaret. Obsah nikotinu v normální cigaretě a cigaretě „light" je oproti očekávání na základě stejné intenzity jeho chromatografického píku srovnatelný. Obsah ostatních komponent je maximálně o třetinu nižší u cigarety „light", pouze v případě izoprenu dosahuje 2× menší hodnoty.

Kouř byl metodou SIFT-MS analyzován za použití všech tří typů iontů a na základě shody mezi jednotlivými reakčními produkty byly identifikovány látky shrnuté v tabulce 2. Obr. 4 ukazuje hmotnostní spektrum reakčních produktů iontu $H_3O^+$. SIFT-MS je používána pro měření stopových koncentrací těkavých látek. Z přehledu sloučenin vidíme, že díky vysoké citlivosti metody SIFT-MS (ppb) byl zaznamenán pozitivní výsledek v případě celé řady látek, které pomocí GC-MS detekovány nebyly. Jak je vidět z obr. 4, řada látek je pomocí této metody detekovatelná již v nezapáleném vzorku tabáku. Jedná se o látky jako např. methanol, ethanol, kyselinu octovou, vanilin či estragol. Po zapálení byly identifikovány typické produkty spalovacích procesů jako kyanovodík, acetaldehyd, acetonitril, izopren, organické kyanidy, formaldehyd nebo fenol.

**Tab. 2**

| látka | vzorec | M | $H_3O^+$ detekce na pozici m/z | | | $NO^+$ detekce na pozici m/z | | $O_2^+$ detekce na pozici m/z | | klasická cigareta | doutník | dýmka s vodou | dýmka bez vody |
|---|---|---|---|---|---|---|---|---|---|---|---|---|---|
| methanol | $CH_3OH$ | 32 | 33 | 51 | 69 | 31 | 15 | 32 | | X | X | X | X |
| isopren | $C_5H_8$ | 68 | 69 | | | 68 | | 68 | 67 | X | X | X | X |
| kys. octová | $CH_3COOH$ | 60 | 61 | 43 | | 90 | | 60 | | X | X | X | X |
| benzen | $C_6H_6$ | 78 | 79 | | | 78 | | 78 | | X | X | X | X |
| toluen | $C_6H_5CH_3$ | 93 | 94 | | | 93 | | 93 | | X | X | | |
| furfural | $C_5H_4O_2$ | 96 | 97 | | | | | 96 | | X | X | X | X |
| kys. 2-methylbutanová | $C_5H_{10}O_2$ | 102 | 103 | | | 132 | | 102 | | X | X | X | X |
| glycerin | $C_3H_8O_3$ | 92 | 95 | 41 | | | | 92 | | X | X | X | X |
| hexylester kys. octové | $C_8H_{16}O_3$ | 144 | 145 | 163 | 181 | | | 144 | | X | X | X | X |
| estragol | $C_{10}H_{12}O$ | 148 | 149 | | | 148 | | 148 | | X | X | X | X |
| nikotin | $C_{10}H_{14}N_2$ | 162 | 163 | | | 162 | | 162 | | X | X | X | X |
| vanilin | $C_8H_8O_3$ | 152 | 153 | | | 152 | | 152 | | X | X | X | X |
| ethyl vanilin | $C_9H_{10}O_3$ | 166 | 167 | | | | | 166 | | X | X | X | X |
| kyanovodík | HCN | 27 | 28 | | | | | 27 | | X | X | X | X |
| amoniak | $NH_3$ | 17 | 18 | 36 | 54 | | | 17 | | X | X | X | X |
| fenol | $C_6H_5OH$ | 94 | 95 | 113 | 131 | 93 | | 94 | | X | X | X | X |
| formaldehyd | HCHO | 30 | 31 | 49 | 67 | 29 | | 30 | | | X | | X |
| aceton | $(CH_3)_2CO$ | 58 | 59 | 77 | | 41 | 88 | 58 | 43 | X | X | X | X |
| acetaldehyd | $C_2H_4O$ | 44 | 45 | 63 | 81 | 43 | | 44 | | X | X | X | X |
| acetonitril | $CH_3CN$ | 41 | 42 | | | 41 | | 41 | | X | X | X | X |
| ethanol | $CH_3CH_2OH$ | 46 | 47 | 65 | 83 | 45 | 29 | 46 | | X | X | X | X |
| propanol | $C_3H_8O$ | 60 | 61 | 43 | | | | 60 | | X | X | X | X |
| oxid dusičitý | $NO_2$ | 46 | 47 | | | | | | | X | X | X | X |
| oxid uhličitý | $CO_2$ | 44 | 63 | | | | | | | X | X | X | X |
| propylenglykol | $C_3H_8O_2$ | 76 | 77 | | | | | | | X | X | X | X |
| ethylester kys. butanové | $C_6H_{12}O2$ | 116 | 131 | | | | | | | | X | X | X |

**Tab. 2** Přehled sloučenin detekovaných pomocí metody SIFT-MS (označeno křížkem).

Souhrn látek detekovaných pomocí FTIR spektrometrie podává tab. 3 a spektra jednotlivých vzorků jsou zobrazena na obr. 5 až 9. V tab. 3 je podíl absorpční intenzity téhož pásu jednotlivých detekovaných specií vyjádřen v procentech. Vzorek kouře z doutníku obsahoval až na aceton a kyanovodík největší koncentrace látek, oproti tomu spektra normální cigarety a cigarety „light" byla odlišná jen málo. Z jedné cigarety „light" bylo získáno asi dvojnásobné množství spalin než z normální cigarety (25, resp. 55 torr). Ve shodě s GC-MS a SIFT-MS byly pomocí FTIR spektrometrie v kouři z vodní dýmky nalezeny nižší koncentrace všech látek a z tab. 3 je patrné, že i použití vody ve vodní dýmce vede k redukci jejich zastoupení. Největší pokles lze zaznamenat u methanolu, kyanovodíku a oxidu dusnatého. Sníženo je také zastoupení nepolárních látek jako methan, ethan a ethylen.

## Charakteristika látek nalezených v tabákovém kouři

V následujícím výčtu jsou shrnuty charakteristiky látek nalezených v cigaretovém kouři, jejich vznik a význam pro jeho toxicitu.

**Methanol** je běžně přítomen v listech, odpařuje se z nich a je jednou z nejběžnějších těkavých organických látek emitovaných rostlinami [13]. Vzniká demethylací pektinu v rostlinných buňkách. Další alkoholy jako **propanol** a **ethanol** vznikají při fermentaci tabáku [14]. Zdrojem methanolu v kouři je rovněž spalovací proces sám [15], stejně jako v případě **izoprenu** běžně emitovaného rostlinami. Izopren patří mezi typické karcinogeny v tabákovém kouři [16].

**Toluen** je látka obsažená v cigaretovém dehtu. Má dráždivé účinky na oči a dýchací cesty. Akutní toxicita je však relativně nízká (LC$_{50}$ 8800 ppm) [17] a z tohoto hlediska jej nelze řadit mezi látky výrazně zodpovědné za toxicitu cigaretového kouře.

**Vanilin** a **ethylvanilin** jsou aromatické chuťové látky běžně používané v potravinářství. Jejich přítomnost souvisí s aromatizací tabáku v doutníku, neboť byl použit aromatizovaný „vanilkový" doutník. Stejným způsobem byl aromatizován také tabák do vodní dýmky. V cigaretovém kouři se vzhledem k absenci aroma vanilin nevyskytuje. Aromatickou látkou přidávanou do tabáku při jeho výrobě je také **hexylester kyseliny octové** [18]. **Estragol** je běžně přítomen v tabáku, stejně jako v jiných rostlinách, jako jsou borovice, pelyněk, fenykl, bazalka a anýz. Používá se také jako potravinové aditivum k dochucování. Podle zprávy Evropské komise pro léčivé bylinné produkty [19] (HPMC) při Evropské lékařské agentuře (EMA) je podezřelým karcinogenem, a proto se doporučuje omezit jeho konzumaci. Z tohoto hlediska jej lze řadit mezi karcinogenní složky cigaretového kouře, ačkoliv jde o molekulu běžně přítomnou v rostlinách.

**2,5-dimethylfuran** je považován za látku, která je charakteristická pro tabákový kouř a může sloužit jako ukazatel přítomnosti tabákového kouře ve vzduchu [20].

Přítomnost 2,5-dimethylfuranu v krvi je považována za biomarker expozice cigaretovému kouři. Vzniká oxidací sacharidů. Cukry jsou přidávány do tabáku jako zdroj karamelové vůně, která může lákat ke kouření zejména mladé potenciální kuřáky. Přídavek cukru také zlepšuje chuť tabáku, dodává mu správnou vlhkost a organické kyseliny produkované spalováním
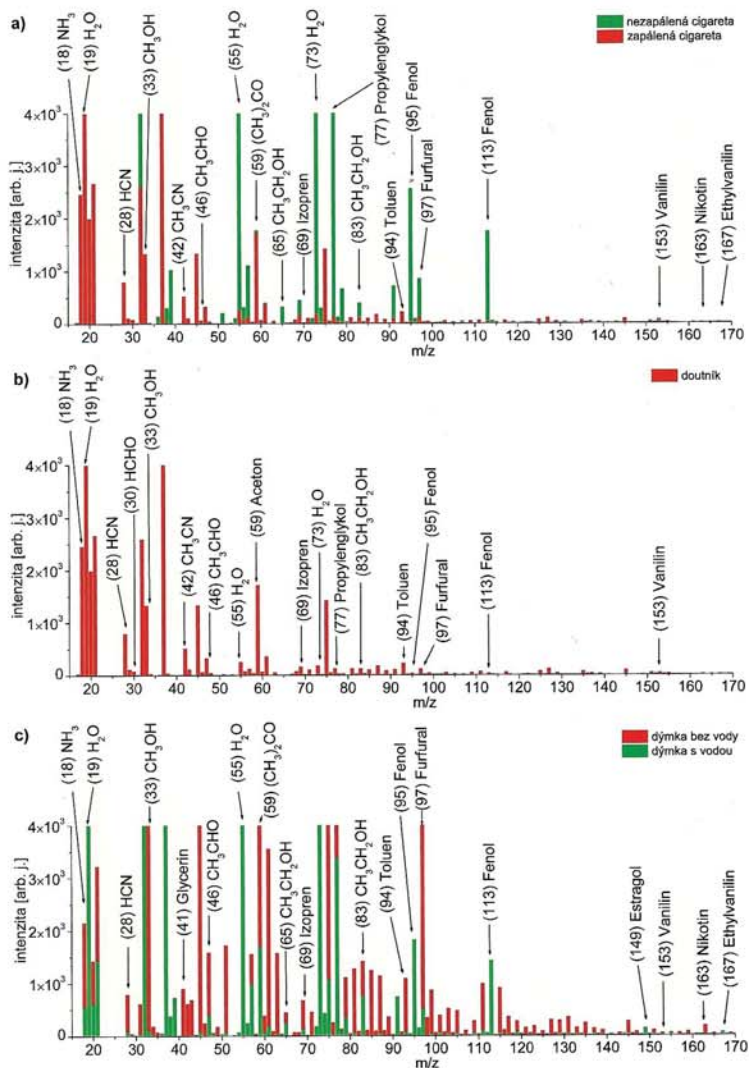


**Obr. 4** Hmotnostní spektrum SIFT reakčních produktů s iontem H$_3$O$^+$ v případě (**a**) kouře cigarety, (**b**) kouře doutníku a (**c**) vodní dýmky bez vody a s vodou.

| látka | vzorec | vlnočet pásu (cm$^{-1}$) | přiřa- zení | cigaretový kouř | | doutník | dýmka s vodou | dýmka bez vody |
|---|---|---|---|---|---|---|---|---|
| | | | | klasická cigareta | lehká cigareta | | | |
| oxid uhličitý | CO$_2$ | 668 | $\nu_2$ | 80 % | 88 % | 100 % | 81 % | 50 % |
| kyanovodík | HCN | 712 | $\nu_2$ | 95 % | 100 % | 48 % | 9 % | 6 % |
| acetylen | C$_2$H$_2$ | 729 | $\nu_5$ | 62 % | 66 % | 100 % | | |
| methanol | CH$_3$OH | 1 033 | $\nu_8$ | 83 % | 68 % | 100 % | 2 % | 2 % |
| amoniak | NH$_3$ | 967 | $\nu_2$ | | | 100 % | | 1 % |
| oxid dusný | NO | 1 875 | $\nu_1$ | 58 % | 53 % | 100 % | 5 % | 1 % |
| sulfid karbonylu | OCS | 2 062 | $\nu_1$ | 78 % | 71 % | 100 % | 9 % | |
| oxid uhelnatý | CO | 2 143 | $\nu_1$ | 47 % | 53 % | 100 % | 46 % | 68 % |
| oxid dusný | N$_2$O | 2 223 | $\nu_1$ | 27 % | 20 % | 100 % | 3 % | 2 % |
| methan | CH$_4$ | 3 019 | $\nu_3$ | 59 % | 65 % | 100 % | 39 % | 59 % |
| ethan | C$_2$H$_6$ | 2 985 | $\nu_{10}$ | 69 % | 74 % | 100 % | 34 % | 56 % |
| ethylen | C$_2$H$_4$ | 3 105 | $\nu_9$ | 68 % | 47 % | 100 % | 6 % | 11 % |
| aceton | CH$_3$COCH$_3$ | 1 731 | $\nu_3$ | 100 % | 81 % | 77 % | | |
| acetaldehyd | CH$_3$CHO | 919 | $\nu_9$ | 100 % | 85 % | 100 % | | 23 % |

**Tab. 3** Přehled látek detekovaných pomocí FTIR spektrometrie. Integrální absorbance jednotlivých molekul je vyjádřena procentuálně vzhledem ke své maximální hodnotě. Té bylo dosaženo s výjimkou kyanovodíku a acetonu ve vzorku kouře doutníku.
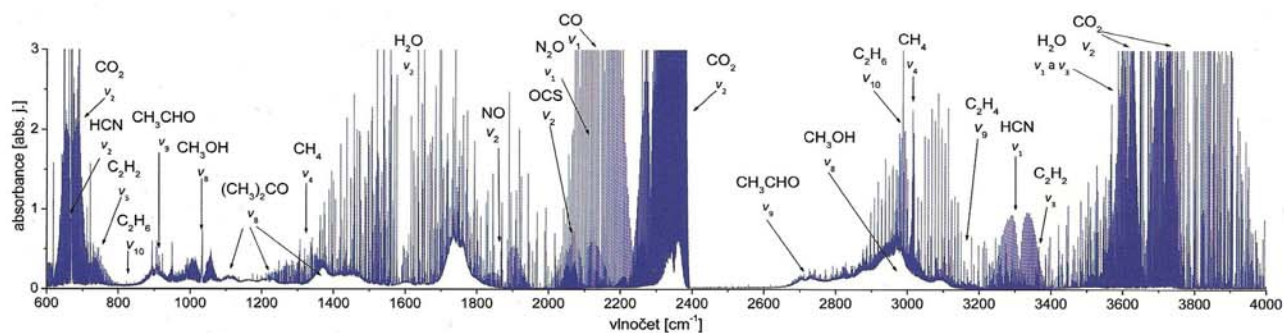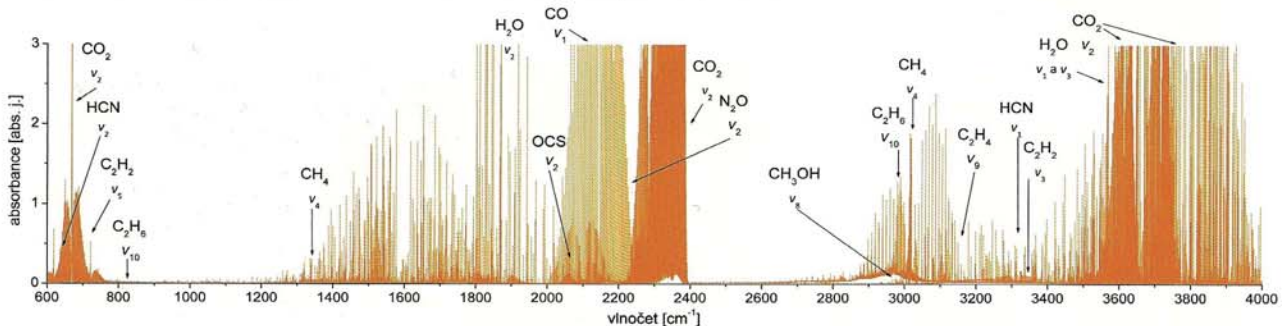
**Obr. 5** Infračervené absorpční spektrum kouře normální cigarety. Tlak vzorku v absorpční cele byl 25 Torrů.
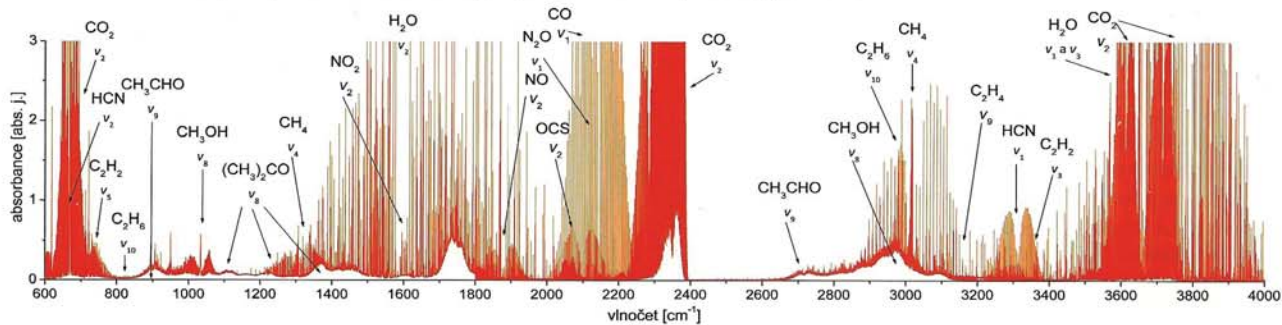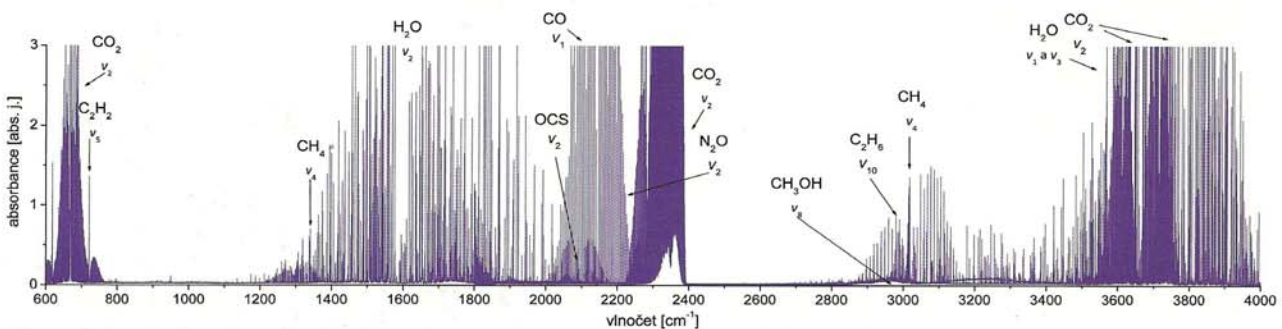


**Obr. 6** Infračervené absorpční spektrum kouře lehké cigarety. Tlak vzorku v absorpční cele byl 55 Torrů.
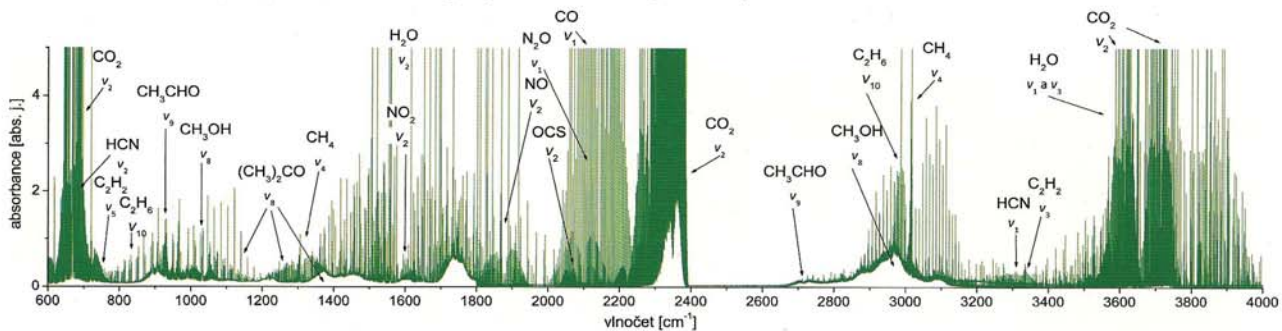


**Obr. 7** Infračervené absorpční spektrum kouře doutníku. Tlak vzorku v absorpční cele byl 60 Torrů.



**Obr. 8** Infračervené absorpční spektrum kouře vodní dýmky bez vody. Tlak vzorku v absorpční cele byl 69 Torrů.



**Obr. 9** Infračervené absorpční spektrum kouře vodní dýmky s vodou. Tlak vzorku v absorpční cele byl 53 Torrů.

cukrů neutralizují hořký zápach. 2,5-dimethylfuran je látka toxická pro vlasové buňky dýchacího epitelu.

**Glycerin** se přidává do tabáku pro vodní dýmku, aby bylo zamezeno jeho vysychání, udržena správná vlhkost [21] a aby tabák ihned neshořel při kontaktu se zapáleným uhlím. Také **propylenglykol** se přidává do tabáku jako zvlhčující látka. Americký úřad FDA (Ústav pro kontrolu potravin a léčiv) označuje propylenglykol jako nebezpečné potravinové aditivum [22] vzhledem k podezření na možný negativní vliv na játra, centrální nervovou soustavu a srdce.

**Furfural** je obsažen v dřevinách, dále také v ovoci, zelenině nebo ve víně, kam se dostává z dřevěných sudů, ve kterých se víno skladuje. Vzniká také spalováním cukrů přítomných v listech tabáku [23], stejně jako další oxo-sloučeniny, např. karcinogenní **formaldehyd** [24], relativně neškodný **aceton** nebo **acetaldehyd** [25] vyskytující se také v ovoci a kávě. Předpokládá se, že acetaldehyd, který tvoří významnou složku tabákového kouře, má synergický efekt k účinkům nikotinu [26].

Panuje obecný předpoklad, že sloučeniny **amoniaku** jsou záměrně přidávány do tabáku, aby alkalizovaly cigaretový kouř, čímž dochází k snadnějšímu vstřebávání nikotinu plicní tkání [27]. Navzdory této skutečnosti byl amoniak detekován pouze v kouři z doutníku. Nasycený roztok amoniaku se přidává také jako aromatická látka, jeho přítomnost [21] v doutníku patrně souvisí s jeho aromatizací.

Vysoce toxický **kyanovodík** je typickou složkou cigaretového kouře a spolu s **acetonitrilem** vzniká termolýzou aminokyselin [28]. Další dusíkatou látkou je biogenní **dimethylamin**, který však není sám o sobě toxický, předpokládá se však, že reakcí s oxidy dusíku mohou vznikat z aminů příslušné nitrosaminy, které jsou karcinogenní.

**Oxid uhelnatý** vzniká nedokonalým spalováním uhlíkatých látek obsažených v tabáku a cigaretovém papírku. Jedná se o jedovatou sloučeninu silně se vázající na hemoglobin. Kromě těchto akutních účinků je

znám jeho negativní vliv na kardiovaskulární systém, ke kterému dochází při dlouhodobé expozici vlivem pasivního i aktivního kouření [29, 30]. Dalšími látkami vznikajícími typicky během spalování jsou methan, acetylen, ethylen, ethan a lze je detekovat běžně ve spalinách řady materiálů [12].

**Benzen** je IARC klasifikován jako karcinogen skupiny 1, způsobuje leukémii, rakovinu plic, poškozuje imunitní systém a centrální nervovou soustavu [31]. Vzniká spalováním uhlíkatých látek nebo také trimerizací acetylenu za zvýšené teploty a tlaku [32].

**Kyselina methylbutanová** se přirozeně vyskytuje v rostlinách, a proto je obsažena v tabáku [33] stejně jako kyselina octová, která může rovněž vznikat rozpadem jejího hexylesteru, který je tabákovým aditivem [18].

Za návykovost cigaret je zodpovědný toxický tekutý alkaloid **nikotin**. Jak již bylo uvedeno výše, účinky nikotinu v tabákovém kouři zvyšuje výrazně zastoupený acetaldehyd [23]. Nikotin zlepšuje koordinaci, pracovní paměť, pozornost a dlouhodobé vizuální vnímání. Příjemné pocity, které se při kouření dostavují, jsou způsobeny především zvýšením krevního tlaku, zrychlením srdečního tepu a sekrecí hormonů jako endorfin a MSH (melanocyt-stimulating hormone). Působení nikotinu vyplývá z podobnosti s nervovým přenašečem acetylcholinem. Nikotin také uvolňuje glykogen, čímž zvyšuje hladinu cukru v krvi.

## Specifika použitých analytických metod

Použití zmíněných analytických metod na stejný typ vzorku, který je složitou směsí chemických látek různých vlastností, ukazuje, že žádná ze tří analytických metod není vhodná pro naprosto univerzální citlivou detekci všech komponent kouře zkoumaných tabákových výrobků.

Jako naprosto univerzální metoda pro detekci hlavních složek plynné fáze je vhodná infračervená spektrometrie s vysokým rozlišením, které je výhodné zejména v případě překrytí dvou pásů různých látek, jako

> » Za návykovost cigaret je zodpovědný toxický tekutý alkaloid nikotin. «
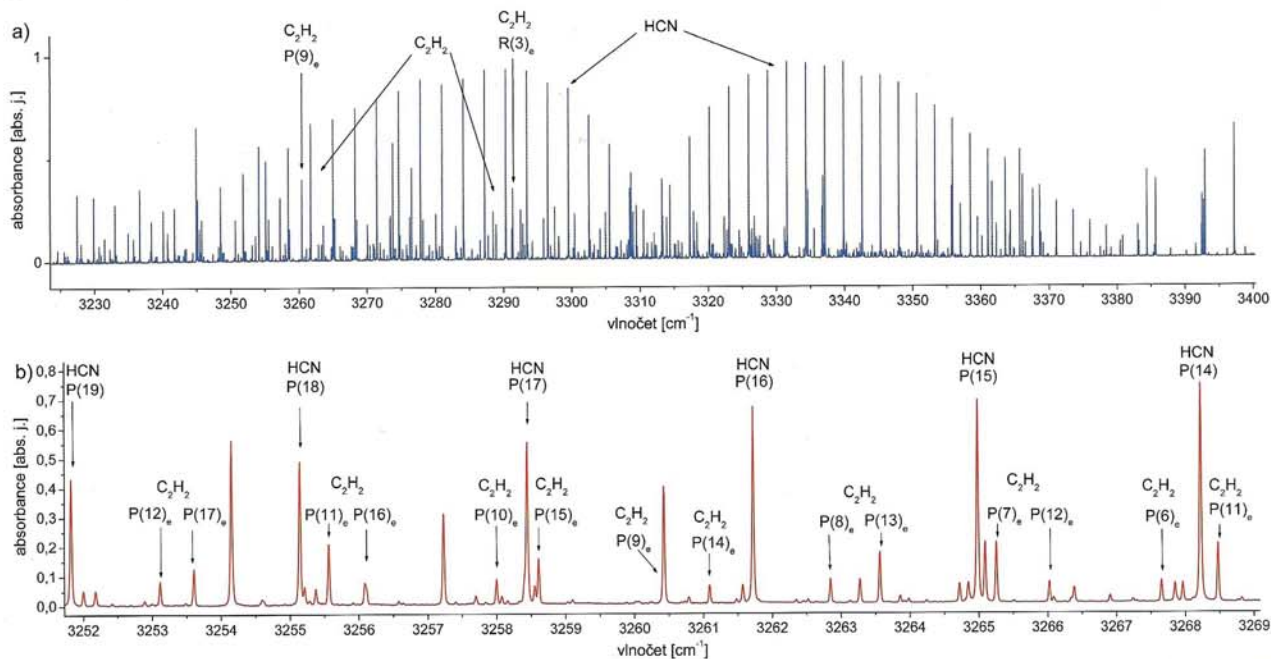


**Obr. 10 a)** Výřez spektra normální cigarety s překrývajícími se pásy HCN a $C_2H_2$. **b)** Díky vysokému rozlišení (0,02 cm$^{-1}$) lze linie obou látek vzájemně separovat.

je tomu např. v případě acetylenu a kyanovodíku v oblasti kolem 3 300 cm⁻¹. Jednotlivé linie lze pak vzájemně separovat, jak je patrné z obr. 10. Díky spojení spektrometru s multireflexní celou o optické dráze 30 m bylo dosaženo vyšší citlivosti. V základním uspořádání jsou spektrometry Bruker vybaveny pouze evakuovaným prostorem pro kyvetu s optickou dráhou do 30 cm. Kvantitativní stanovení nicméně vyžaduje kalibrovat přístroj v širokém koncentračním rozsahu pro každou

| látka | GC-MS | SIFT-MS | FTIR |
|---|---|---|---|
| methanol | X | X | X |
| isopren | X | X | |
| kys. octová | X | X | |
| benzen | X | X | |
| toluen | X | X | |
| furfural | X | X | |
| k. 2-methylbutanová | X | X | |
| glycerin | X | X | |
| hexylester kys. octové | X | X | |
| estragol | X | X | |
| nikotin | X | X | |
| vanilin | X | X | |
| ethylvanilin | X | X | |
| kyanovodík | | X | X |
| amoniak | | X | X |
| fenol | | X | |
| formaldehyd | | X | X |
| aceton | | X | X |
| acetaldehyd | | X | X |
| acetonitril | | X | |
| ethanol | | X | |
| pyridin | | X | |
| propanol | | X | |
| dimethylamin | | X | |
| oxid dusnatý | | X | X |
| oxid dusičitý | | X | X |
| oxid uhličitý | | X | X |
| propylenglykol | | X | |
| ethylester k. butanové | | X | |
| 2,5-dimethylfuran | X | | |
| perfluorotributylamin | X | | |
| propylenglykol | X | X | |
| methan | | | X |
| oxid uhelnatý | | | X |
| acetylen | | | X |
| ethan | | | X |
| ethylen | | | X |
| sulfid karbonylu | | | X |
| oxid dusný | | | X |

**Tab. 4** Přehled látek detekovaných pomocí tří použitých technik – plynové chromatografie s hmotnostní detekcí (GC-MS), hmotnostní spektroskopie v proudové trubici s vybranými ionty (SIFT-MS) a infračervené spektrometrie s Fourierovou transformací (FTIR).

látku zvlášť. Infračervená spektrometrie s Fourierovou transformací (FTIR) byla použita v řadě prací zabývajících se složením cigaretového kouře (nejnověji např. [34,35,36]). Detekovány byly stejné látky, jaké byly nalezeny při tomto měření.

Další univerzální a citlivou metodou je plynová chromatografie s hmotnostní spektrometrií (GC-MS), která je nejběžněji používána pro zkoumání složení cigaretového kouře (např. [37]), obzvláště ve spojení s mikroextrakcí na pevnou fázi k detekci těkavých látek (VOC) [38]. Tato metoda dovoluje zjištění řady molekul, které jsou pomocí infračervené spektrometrie obtížně měřitelné vzhledem k nízké koncentraci, ale také nerozlišitelnosti pásů vlivem hmotnosti molekuly. Detekovatelnost jednotlivých komponent je dána také vazbou na mikroextrakční karbonové vlákno. Na rozdíl od FTIR spektrometrie byly detekovány těžší těkavé organické molekuly. Hmotnostní spektrometrie v proudové trubici s vybranými ionty (SIFT-MS) má řadu aplikací v oblasti citlivé detekce velkého množství látek. V poslední době nalézá uplatnění při detekci stopových koncentrací biomarkerů některých nemocí přítomných v dechu. V dechu kuřáků byly rovněž metodou SIFT-MS analyzovány některé těkavé látky [39]. Pomocí této metody byla zjištěna široká paleta různých specií od lehkých molekul až po těkavé látky vyšší molekulové hmotnosti. Nevýhodou metody je nedetekovatelnost takových látek, které nereagují s vybranými ionty. Seznam těchto molekul se nicméně omezuje pouze na N₂, O₂, CO₂, CO, H₂ a alifatické uhlovodíky do C₄.

Shrnutí všech látek nalezených pomocí použitých metod poskytuje tab. 4.

### Celkové srovnání složení jednotlivých typů kouře

Porovnáním intenzity signálu jednotlivých komponent cigaretového kouře v přístroji GC-MS a FTIR bylo zjištěno, že největší koncentrace látek se nalézají v doutníku. Výjimku tvoří pouze nikotin.

Koncentrační zastoupení jednotlivých komponent kouře z normální cigarety a cigarety „light" bylo odlišné v obsahu některých těkavých látek. Největší redukce bylo dosaženo v případě izoprenu, 2,5-dimethylfuranu a furfuralu. Zastoupení nikotinu je navzdory tvrzení výrobce srovnatelné. Metodou FTIR však bylo zjištěno, že obsah některých látek v obou typech kouře je zhruba stejný, jedná se zejména o škodliviny jako oxid uhelnatý nebo kyanovodík. To je ve shodě např. s výsledky Bacsika a kol [35]. Kouř vodní dýmky s vodou a bez vody má lehce odlišné složení. Použití vody redukuje koncentraci řady látek, nicméně dým vodní dýmky ve srovnání s cigaretami a doutníkem obsahuje celkově menší koncentrace většiny složek s výjimkou ethanu, methanu, oxidu uhelnatého a uhličitého.

### ZÁVĚR

Vzhledem k zastoupení jednotlivých složek kouře doutníku, cigaret a vodní dýmky lze konstatovat, že doutník až na poloviční obsah nikotinu ve srovnání s cigaretami obsahuje největší koncentrace všech detekovaných molekul. Přitom zastoupení škodlivin, jako jsou izopren, benzen, oxid uhelnatý nebo oxidy dusíku, je zhruba dvojnásobné. Kouř vodní dýmky obsahuje ve srovnání s cigaretami menší koncentrace většiny

komponent, přičemž použití vody koncentrace většiny látek redukuje.

Jednotlivé analytické metody jsou citlivé na odlišné skupiny látek. Lehké těkavé molekuly jsou dobře detekovatelné infračervenou spektrometrií, přičemž použití multireflexní cely zvyšuje citlivost. Těžší těkavé látky (100–150 m/z) jsou dobře viditelné, detekované pomocí GC-MS. Metoda SIFT vyniká vysokou citlivostí, je používána pro měření stopových koncentrací těkavých látek a umožňuje kvantitativně detekovat řadu těkavých organických látek bez nutnosti průběžné kalibrace. SIFT-MS detekce je ovšem omezena těkavostí látek a jejich schopností reagovat s prekurzorovými ionty – například $H_2$, CO, $CO_2$, $O_2$, alifatické uhlovodíky do $C_4$. Detekční limit pro NO je snížen na 100 ppb v důsledku reakcí probíhajících v proudové trubici.

## LITERATURA

[1] *Smoking definition.* Dostupné z WWW: http://medical--dictionary.thefreedictionary.com/smoking, staženo 21. 11. 2010.

[2] *Klady kuřáctví, pozitivita kouření.* Dostupné z WWW: http://www.kurakovaplice.cz/koureni_cigaret/kurak-a--koureni/klady-koureni.html, staženo 19. 11. 2010.

[3] *Brown Williamson Tobacco.* Dostupné z WWW: http://www.cigarette.com/images/timeline.pdf, staženo 9. 2. 2011.

[4 *Zprávy SZÚ.* Dostupné z WWW: http://www.szu.cz/uploads/documents/czzp/zavislosti/koureni/Zprava2009DEF.pdf, staženo 2. 2. 2011.

[5] *Standard IARC classification.* Dostupné z WWW: http://www.greenfacts.org/glossary/ghi/iarc-classification.htm, staženo 17. 11. 2010.

[6] *Carcinogenic to humans.* Dostupné z WWW: http://monographs.iarc.fr/ENG/Classification/crthgr01.php, staženo 19. 11. 2010.

[7] *Kouření a zdraví.* Dostupné z WWW: http://www.zdn.cz/clanek/postgradualni-medicina-priloha/koureni-a-zdravi-172604, staženo 21. 11. 2010.

[8] A. Ochsner, M.E. DeBakey: Arch Surg **42**, 209 (1941).

[9] R. Pearl: Science **4**, 77 (1938).

[10] A. H. Roffo: Z. Krebsforsch. **49**, 588 (1939).

[11] D. Smith, P. Španěl: Mass Spectrom. Rev. **24**, 661 (2005).

[12] M. Ferus, S. Civiš: Čs. čas. fyz. 58, 157 (2008).

[13] R. Fall, A. A. Benson: Trends Plant Sci. **9**, 296 (1996).

[14] *Propanol.* Dostupné z WWW: http://cs.wikipedia.org/wiki/1-propanol, staženo 2. 2. 2011.

[15] R. Holzinger, C. Warneke, A. Hansel, A. Jordan, W. Lindinger, D. H. Sharffe, G. Schade, P. J. Crutzen: Geophys. Res. Lett. **8**, 1161 (1999).

[16] S. S. Hecht: J. Nat. Canc. Inst. **41**, 1194 (1999).

[17] *Toluen.* Dostupné z WWW: http://cs.wikipedia.org/wiki/Toluen, staženo 21. 11. 2010.

[18] *The Chemical Components of Tobacco and Tobacco Smoke by Alan Rodgman, Thomas A. Perfetti:* Dostupné z WWW: http://books.google.com/books?id=RiwSY-FgZ2fEC&pg=PA1166&lpg=PA1166&dq=hexyl+ester+acetic+acid+tobacco+smoke&source=bl&ots=Ka--tUNLOFV&sig=VVdDsJEnk3Bw8JRhrWqPtOXG-KQE&hl=en&ei=07EWTLCGII-YOJ3h0PoK&sa=X&oi=-book_result&ct=result&resnum=1&ved=0CBIQ6AEwA-A#v=onepage&q=hexyl%20ester%20acetic%20acid%20tobacco%20smoke&f=false, staženo 18. 11. 2010.

[19] *Committee on herbal medical product.* Dostupné z WWW: http://www.ema.europa.eu/pdfs/human/hmpc/13721205en.pdf, staženo 26. 11. 2010.

[20] *VOC and Particulate Emissions from Commercial Cigarettes: Anylysis of 2,5-DMF as an ETS Tracer.* Dostupné z WWW: http://pubs.acs.org/doi/pdf/10.1021/es072062w?cookieSet=1, staženo 21. 11. 2010.

[21] C. Merckel, F. Pragst: J. Verbr. Lebensm. **2**, 287 (2007).

[22] *Co je propylenglykol?* Dostupné z WWW: http://www.gamuccishop.cz/dotazy19-co-je-propylenglykol.html, staženo 22. 11. 2010.

[23] R. Talhout, A. Opperhuizen, J. G. C. van Amsterdam: Food Chem. Tox. **44**, 1789 (2006).

[24] *Formaldehyd.* Dostupné z WWW: http://formaldehyd.navajo.cz/, staženo 24. 11. 2010.

[25] *Acetaldehyde.* Dostupné z WWW: http://en.wikipedia.org/wiki/Acetaldehyde, staženo 27. 11. 2010.

[26] R. Talhout R., Opperhuizen A., J. G. C van Amsterdam: Eur. Neuropsychopharm. **17**, 627 (2007).

[27] *Z čeho se cigareta skládá.* Dostupné z WWW: http://www.ulekare.cz/clanek/kuraci-v-zajeti-specialnich-tabakovych-smesi-13537, staženo 27. 11. 2010.

[28] I. Schmeltz, D. Hoffmann: Chem. Rev. **3**, 295 (1977).

[29] A. P. Jones: Atm. Env. **33**, 4535 (1999).

[30] K. Steenland: J. Am. Med. Assoc. **267**, 94 (1992).

[31] *Tobacco Smoke and Involuntary Smoking.* Dostupné z WWW: http://monographs.iarc.fr/ENG/Monographs/vol83/volume83.pdf, staženo 2. 2. 2011.

[32] *Benzen.* Dostupné z URL: http://www.irz.cz/repository/latky/benzen.pdf, staženo 2. 2. 2011.

[33] *Kyselina 3-methylbutanová.* Dostupné z URL: http://cs.wikipedia.org/wiki/Kyselina_3-methylbutanov%C3%A1, staženo 2. 2. 2011.

[34] J. Zhang, L. Z. Wang, Y. H. Zhang: Spect. Spectral Anal. **4**, 821 (2008).

[35] Z. Bacsik, J. McGregor, J. Mink: Food Chem. Tox. **45**, 266 (2007).

[36] M. E. Parrish, J. L. Lyons-Hart, K. H. Shafer: Vibr. Spectr. **27**, 29 (2001).

[37] J. Z. Dong, J. N. Glass, S. C. Moldoveanu: J. Microcolumn Sep. **12**, 142 (2000).

[38] Y. Qing: J. Chromat. A **1213**, 239 (2008).

[39] S. T. Senthilmohan, M. J. McEwan, P. F. Wilson, D. B. Milligan, C. G. Freeman: Redox Rep. **6**, 185 (2001).